Eulerian modeling and numerical methods for the description of turbulent polydisperse sprays

Macole Sabat

Macole Sabat. Eulerian modeling and numerical methods for the description of turbulent polydisperse sprays. Fluids mechanics [physics.class-ph]. Université Paris-Saclay, 2016. English. NNT : . tel-02876013

HAL Id: tel-02876013
https://theses.hal.science/tel-02876013
Submitted on 20 Jun 2020

NNT : 2016SACLC086

THÈSE DE DOCTORAT DE L'UNIVERSITÉ PARIS-SACLAY,

préparé à CentraleSupélec.

ÉCOLE DOCTORALE N°579

Sciences Mécaniques et Énergétiques, MAtériaux et Géosciences.

Spécialité Mécanique des Fluides, Mathématiques Appliquées.

Présentée par

Macole SABAT

Eulerian modeling and numerical methods for the description of turbulent polydisperse sprays

Thèse soutenue à Châtenay-Malabry, le 3 novembre 2016.

Composition du jury:

M. BERTHON, Christophe	Professeur, Université de Nantes	Rapporteur
M. SIMONIN, Olivier	Professeur, Université de Toulouse, INPT	Rapporteur
M. BOURGOIN, Mickael	Directeur de recherche, CNRS	Examinateur
M. DEMOULIN, François-Xavier	Professeur, Université de Rouen	Examinateur
Mme. RIBER, Eleonore	Chercheuse Sénior, CERFACS	Examinatrice
M. JADAYEL, Oussama	Professeur, University of Balamand	Invité
Mme MASI, Enrica	Maître de Conférences, Université de Toulouse	Invitée
M. MERY, Yoann	Ingénieur expert, Safran Aircraft Engines	Invité
M. MASSOT, Marc	Professeur, CentraleSupélec	Directeur de Thèse
M. LARAT, Adam	Chargé de Recherche, CNRS	Encadrant
M. VIÉ, Aymeric	Maître de Conférences, CentraleSupélec	Encadrant

Laboratoire d'Énergétique Moléculaire et Macroscopique, Combustion
CNRS, CentraleSupélec.

Acknowledgment

I would like to express appreciation to a number of persons who have contributed, directly or indirectly, in this thesis.
First and foremost, I would like to express my deepest gratitude to Professor Marc Massot for his invaluable guidance and advice. His constant enthusiasm and support helped me brave the rough times when things did not seem to go in the right direction. I will always remember when you once told me that working in the interface of engineering and mathematics is not at all easy or straightforward but one should know how to use his strongpoints and where to exactly position himself.
I gratefully acknowledge Dr. Aymeric Vié for accompanying me during this thesis and helping me to understand and solve many problems of different scales. His support and motivation were key points toward the successful completion of this work. Aymeric, your office was one of my favorite places in the lab, the place where a barrier seemed smaller and a difficulty seemed easier. I certainly owe you a lot whether during the project, training or thesis. Marc and Aymeric, thank you both for introducing me to my new favorite chocolat and for your tremendous patience. You are both an idol, each in his own way.
I also thank Dr. Adam Larat for his help and for pushing me to become a better person. I believe that if my students value me especially as a project advisor, it is in many ways because of the advising team of my PhD.
I am grateful to Professor Olivier Simonin for accepting to review my manuscript and for his valuable comments. I am thankful to Professor Christophe Berthon for reviewing the thesis and participating in my viva. I would like to thank Professor Mickael Bourgoin for chairing my thesis defense, Professor François-Xavier Demoulin and Dr Eleonore Riber for being an important part of the jury.
Professor Oussama Jadayel, I think it is the right time to express my gratutide, if it was not for you I would have been today in a totally different place, probably designing ads and modeling visual communication systems. Thank you for being a great Professor and a wonderful leader and boss. Of course thank you also for your valuable comments on the manuscript.
I would like to thank Dr Enrica Masi for her interest in this work and for her comments on the thesis. I am indeed greatful for the discussions that we had and for the time Dr Masi invested in reading the manuscript.

Dr. Yoann Mery, I thank you for being a very helpful link with SAFRAN Propulsion and for your presence on my viva.
I would like to thank the financial support of SAFRAN-SNECMA.
This work was granted access to the HPC resources of CINES under the allocation x2015026172 made by GENCI (Grand Equipement National de Calcul Intensif). IDRIS is also acknowledged for the computation resources on Ada and Occigen.
The help of Dr Matthieu Boileau, Dr Jorge Cesar Brändle de Motta, Dr Olivier Thomine and Dr Lucie Freret on ASPHODELE/MUSES3D codes is gratefully recognized.
This PhD is done in the EM2C laboratories, thus I greatfully thank Professor Sebastion Ducruix and all the Professors, Researchers in the lab. Many thanks to Professor Frederique Laurent Nègre for the discussions we had during the thesis. Dr Matthieu Boileau, Jean-Michel Dupays and Sebastien Turgis thank you for your help. For the teaching experience, I would like to acknowledge Pr. Sebastien Candel, Pr. Frank Richecoeur, Pr. Thierry Schuller and Dr Laurent Zimmer and Dr Ronan Vicquelin.
I am thankfull to Mrs. Nathalie Rodrogez, Mrs Brigitte Llobel, Mrs. Noi Laveaud and Mrs Catherine Lhopital for their assistance, you were friendly all the time even when you had all the admnisitrative problems to solve. Brigitte there were time when you made me feel that home is not only a place, that it can be someone willing to do anything to solve your paper problem with the prefecture and who will have tears in his eyes if did not succeed to find a way out.
I also acknowledge François, Layal, Daniel, Nasser, Christophe, Valentin, David M., Florence, Davy, Pedro R., Sergei, Mohamed, Abigail, David Ch., Philippe S., Erika and Alain.
Thank you for my office mates: Marie, Maxim, Manuel, Thomas, Marc-Arthur, Jan, Philippe, Mabelle, Vincent and Claire.
I would like to thank my friends who made France a better place, just by being their: Gizem, Pedro (Bidro), Adrien (A....u), Mélodie, Mihaela, Jorge (JCBdM), P. Elie, Elie F., Doumet, Eddy, Paula, Wassim, Léo, Aurelien (Aulerien) and Livia. Your friendship, warmth and cheerfulness mean so much to me.
To my sister sent from above, Dona, your prayers in the moments of diffuclties, and there were many, helped me to move on forward. Ghada, my second chosen sister and sent from heaven, you've been the best shoulder to weep on and best neighbor to laugh with. Luckily we don't have to agree that Matlab is one of the best software to be best friends. Thank you dear Ghada for the hommous and meghle, though I know that a great deal of this thanks goes to your mom. Ghada of course thank you for the fork meals, my level of creatinine is finally normal.
Charbel, thank you for being present during my viva and for the tasty "pot de these". Dad, thank you for the tons of chocolat and baklavas. Kiko, I am

thankful for all your advices and more for the za3tar. The homemade man2ouch with your zaatar, was my ticket to Lebanon.
Mira and Simona, I am blessed to have you in my life. Side by side or miles apart, being your sisters means that I will always have a reason to smile.
Finally I would like to dedicate this work to my family and beloved ones especially my mother Georgette, my angels Micho, Clara, Tony, Maria and Angelina and to the dearest Charbel Makhlouf.

Abstract

In aeronautical combustion chambers, the ability to simulate two-phase flows gains increasing importance nowadays since it is one of the elements needed for the full understanding and prediction of the combustion process. This matter is motivated by the objective of improving the engine performance and better predicting the pollutant emissions. On the industrial scale, the description of the fuel spray found downstream of the injector is preferably done through Eulerian methods. This is due to the intrinsic statistical convergence of these methods, their natural coupling to the gas phase and their efficiency in terms of High Performance Computing compared to Lagrangian methods. In this thesis, the use of Kinetic-Based Moment Method with an Anisotropic Gaussian (AG) closure is investigated. By solving all velocity moments up to second order, this model reproduces statistically the main features of small scale Particles Trajectories Crossing (PTC). The resulting hyperbolic system of equations is mathematically well-posed and satisfies the realizability properties. This model is compared to the first order model in the KBMM hierarchy, the monokinetic model MK which is suitable for low inertia particles. The latter leads to a weakly hyperbolic system that can generate δ-shocks. Several schemes are compared for the resolution of the hyperbolic and weakly hyperbolic system of equations. These methods are assessed based on their ability to handle the naturally encountered singularities due to the moment closures, especially without globally degenerating to lower order or violating the realizability constraints. The AG is evaluated for the Direct Numerical Simulation of 3D turbulent particle-laden flows by using ASPHODELE solver for the gas phase, and MUSES3D solver for the Eulerian spray in which the new model is implemented. The results are compared to the reference Lagrangian simulation as well as the MK results. Through the qualitative and quantitative results, the AG is found to be a predictive method for the description of moderately inertial particles and is a good candidate for complex simulations in realistic configurations where small scale PTC occurs. Finally, within the framework of industrial turbulence simulations a fully kinetic Large Eddy Simulation formalism is derived based on the AG model. This strategy of directly applying the filter on the kinetic level is helpful to devise realizability conditions. Preliminary results for the AG-LES model are evaluated in 2D, in order to investigate the sensitivity of the LES result on the subgrid closures.

Keywords Spray, turbulence, moment method, kinetic based closures, realizability, particle trajectory crossing, Large Eddy Simulation, realizability-preserving high order numerical schemes

Résumé

De nos jours, la simulation des écoulements diphasiques a de plus en plus d'importance dans les chambres de combustion aéronautiques en tant qu'un des éléments requis pour analyser et maîtriser le processus complet de combustion, afin d'améliorer la performance du moteur et de mieux prédire les émissions polluantes. Dans les applications industrielles, la modélisation du combustible liquide trouvé en aval de l'injecteur sous forme de brouillard de gouttes polydisperse, appelé spray, est de préférence faite à l'aide de méthodes Eulériennes. Ce choix s'explique par les avantages qu'offrent ces méthodes par rapport aux méthodes Lagrangiennes, notamment la convergence statistique intrinsèque, le couplage aisé avec la phase gazeuse ainsi que l'efficacité pour le calcul haute performance. Dans la présente thèse, on utilise une approche Eulérienne basée sur une fermeture au niveau cinétique de type distribution Gaussienne Anisotrope (AG). L'AG résout des moments de vitesse jusqu'au deuxième ordre et permet de capter les croisements des trajectoires (PTC) à petite échelle de manière statistique. Le système d'équations obtenu est hyperbolique, le problème est bien-posé et satisfait les conditions de réalisabilité. L'AG est comparé au modèle monocinétique (MK) d'ordre 1 en vitesse. Il est approprié pour la description des particules faiblement inertielles. Il mène à un système faiblement hyperbolique qui peut générer des singularités. Plusieurs schémas numériques, utilisés pour résoudre les systèmes hyperboliques et faiblement hyperboliques, sont évalués. Ces schémas sont classifiés selon leur capacité à traiter les singularités naturellement présentes dans les modèles Eulériens, sans perdre l'ordre global de la méthode ni rompre les conditions de réalisabilité. L'AG est testé sur un champ turbulent 3D chargé de particules dans des simulations numériques directes. Le code ASPHODELE est utilisé pour la phase gazeuse et l'AG est implémenté dans le code MUSES3D pour le spray. Les résultats sont comparés aux de simulations Lagrangiennes de référence et aux résultats du modèle MK. L'AG est validé pour des gouttes modérément inertielles à travers des résultats qualitatifs et quantitatifs. Il s'avère prometteur pour les applications complexes comprenant des PTC à petite échelle. Finalement, l'AG est étendu à la simulation aux grandes échelles nécessaire dans les cas réels turbulents dans le domaine industriel en se basant sur un filtrage au niveau cinétique. Cette stratégie aide à garantir les conditions de réalisabilités. Des résultats préliminaires sont évalués en 2D pour tester la sensibilité des résultats LES sur les paramètres des modèles de fermetures de sous mailles.

Mots clés Spray, turbulence, méthodes des moments, fermetures cinétique, réalizabilité, croisement des trajectoires, simulation aux grandes échelles, schémas numérique d'ordre élevé préservant la réalizabilité

أعطنا ربِّ قبل كل عطاء أن نحطَّ التفاتة في سناك
كل ما دون وجهك الجمِّ وهمٌ
اعطنا ربِّ أن نراك

Even the smallest stone makes ripples in the water...

To Georgette Jabbour and Charbel Makhlouf

Contents

List of Tables

List of Figures

Nomenclature

The notations used in this thesis are given here in the following order: Roman characters, Greek Characters, non-dimensional numbers, operarors and abbreviations.

Latin Characters:

$\vec{\boldsymbol{c}}$	Disperse phase velocity in the phase space
c_1	x-component of $\vec{\boldsymbol{c}}$
c_2	y-component of $\vec{\boldsymbol{c}}$
c_3	z-component of $\vec{\boldsymbol{c}}$
$\vec{\boldsymbol{c}}_k$	k^{th} droplet velocity
$C_{i,j,k}$	Central $(i+j+k)^{th}$ order velocity moment
$\mathbb{D}$	Dissipation matrix
D_Y	Slope for the linear reconstruction of Y
$\vec{\boldsymbol{e}}$	A given unit vector
$\mathcal{E}$	Scalar total kinetic energy
$\mathbf{E}$	Total kinetic energy tensor
E_1	Exchange term between sections
E_2	Exchange term with the gas
E_m	Energy spectrum model
f	Number density function
f_L	Non-dimensional function governing the shape of the energy containing range
f_{long}	Longitudinal velocity autocorrelation function
f_η	Non-dimensional function governing the shape of the dissipation range
f_Σ	Autocorrelation function of the trace of the internal energy tensor
$f(u)$	Flux function
$\boldsymbol{\mathcal{F}}^*$	Numerical flux
$\boldsymbol{\mathcal{F}}(\mathbf{W})$	Conservative flux
$\boldsymbol{F}_{i+1/2}$	Flux at the interface $x_{i+1/2}$
$\overrightarrow{\mathbf{F}}$	Acceleration of the droplets due to external force
g_{pp}	Number density autocorrelation
G_Δ	LES filter
$\widehat{G}_\Delta$	Transfer function of the LES filter
G_{pp}^Δ	Segregation
h_l	Spray enthalpy
$\mathscr{H}_{f,p}$	Two-phase flow realizations
I_i	i^{th} control volume or element
H_T	Rate of change of the droplet temperature
$-_L$	At the left side of the interface
L_0	Representative length scale of the flow
L_{11}	Longitudinal integral length scale of the gas motion
L_{Long}	Longitudinal integral length scale of the spray motion
L_p	Integral length scale of the number density autocorrelation function

L_Σ	Integral length scale autocorrelation of the trace of the internal energy tensor
$m^{(p)}$	Mass concentration in section p
$\mathcal{M}$	Mass matrix
${}^{l}M^{m}_{i,j,k}$	Moment of order l in size, m in temperature and $i+j+k$ in velocity
$M_{i,j,k}$	General $(i+j+k)^{th}$ order moment in velocity
n	Number density of the disperse phase
$-^{n}$	At time t_n
$\mathcal{N}$	Joint Gaussian distribution
N_d	Number of dimensions
N_{eul}	Number of Eulerian grid elements in a given direction
N_s	Number of particles
N_s	Number of samples for DSMC
$\mathbf{P}$	Scalar pressure
$\mathbf{P}$	Pressure tensor
P_1	Pressure at the compressor intake
P_2	Pressure at the compressor exit
P_m	Fine grained PDF
$-^{r}$	Residual terms
r	Separation distance
Q	Secondary break-up operator
$-_R$	At the right side of the interface
R_{ij}	Two-point velocity correlation
R_S	Evaporation rate
R_Σ	Autocorrelation of the trace of the internal energy tensor

S	Size of droplets
$\mathbf{S}_F$	Drag source terms in moment equation
s	Entropy
s_{ij}	ij^{th} element of the strain rate tensor
$\mathcal{S}$	Space of realizable moments of boundary $\partial\mathcal{S}$
S_k	k^{th} droplet size
S_S	Evaporation rate source terms in moment equation
S_T	Heat exchange rate source terms in moment equation
t	Time
T	Temperature
T_i	i^{th} triangle of the 2D mesh
T_k	k^{th} temperature
T_L^r	Lagrangian integral timescale of the residual gas field velocity
$\mathbb{T}$	Stiffness matrix
TKE^r	Subgrid total kinetic energy
$\vec{\mathbf{u}}$	Mean velocity of the disperse phase
$\boldsymbol{\mathcal{U}}$	Set of primitive variables
$\tilde{\boldsymbol{\mathcal{U}}}$	Set of cell reconstructed primitive variables
$\overline{\boldsymbol{\mathcal{U}}}$	Set of corrected cell value of reconstructed primitive variables
u_h	Discrete approximate solution of u
$\vec{\boldsymbol{u}}_{\mathrm{g}}$	Gas phase velocity
$\overrightarrow{\mathbf{U_g}}$	Gas velocity
$\overrightarrow{\mathbf{U_l}}$	Liquid fuel velocity
$\mathbf{W}$	Unknown set of moments
$\mathbf{W}_h$	Piecewise polynomial solution
w_{pk}	Weight for sample k in DSMC

x_k	k^{th} droplet position
x_q	q^{th} Gauss-Lobatto quadrature points
$\vec{\boldsymbol{x}}$	Position
X	characteristic length of the interface

Greek Characters:

γ	Gas heat capacity ratio
$\vec{\gamma}$	Subgrid term accounting for the inhomogeneity of the flow into the drag force.
Γ	Collision/coalescence operator
$\delta\Theta_p$	Kinetic energy of the random uncorrelated motion
Δ	Filter width
Δt	Time step
Δx	Grid size
ε	Turbulence dissipation rate
ε^r	Dissipation rate of the residual gas velocity field
η	Kolmogorov lengthscale
η_{Br}	Thermodynamic efficiency of the Brayton cycle
κ	Wavenumber
κ_{DI}	Wavenumber separating the dissipation range and the inertial subrange
κ_{EI}	Wavenumber separating the inertial subrange and the energy-containing range
κ_p	Affine by part reconstruction
$\boldsymbol{\lambda}$	Subgrid term modeling the correlations of the turbulence
λ_0	Mean free path of the droplets
λ_f	Longitudinal Taylor microscale
λ_g	Transverse Taylor microscale
λ_{min}	Slowest characteristic wave of the states on the left and right side of the interface
λ_{max}	Fastest characteristic wave of the states on the left and right side of the interface
$\boldsymbol{\mu}$	Subgrid term modeling the fact that the particle agitation energy tends towards the one of the gas subgrid scales because of the drag force, and acts as a white-noise
μ_l	Liquid fuel dynamic viscosity
ν	Gas kinematic viscosity
ν_l	Liquid fuel kinematic viscosity
$\boldsymbol{\xi}$	Internal phase space
$\boldsymbol{\xi}_{pk}$	Coordinate of each sample k for DSMC in the phase space
${}^{l}\boldsymbol{\xi}^{m}_{i,j,k}$	Powers of the internal phase space variables: i, j, k for respectively the x, y and z components of the velocity, l for the size and m for the temperature
$\boldsymbol{\Omega}$	Vorticity tensor of spray
ρ_g	Gas density
ρ_l	Liquid fuel density
σ	Isotropic velocity dispersion
$\boldsymbol{\Sigma}$	Covariance matrix of spray

σ_{ij}	Element ij of the covariance matrix
$\sigma_{l,g}$	Liquid surface tension
$\widetilde{\boldsymbol{\Sigma}}$	Favre-filtered internal energy tensor
$\boldsymbol{\Sigma}^{\overline{f}}$	Internal energy tensor obtained from the filtered NDF
$\boldsymbol{\Sigma}_r$	Subgrid energy contribution
τ_p	Droplets relaxation time
$\boldsymbol{\tau}_g^r$	Subgrid stress tensor
τ_G	Characteristic time scale of the gas
τ_K	Kolmogorov time scale of the gas
φ	Basis functions
$\varphi_S^{(p)}$	Constant repartition of sizes in section p
φ_v	Spray volume fraction
χ_{I_i}	Characteristic function of I_i
ψ	Weighting or test function
ω_q	Weight of the q^{th} Gauss-Lobatto quadrature points

Non-dimensional numbers:

Kn	Knudsen number
$\mathrm{Ma_e}$	energy based disperse phase Mach number
$\mathrm{Ma_p}$	disperse phase Mach number
Oh	Ohnesorge number
Re	Reynolds number
Re_L	Reynolds number based on the integral length scale
Re_λ	Reynolds number based on the transverse Taylor microscale
St	Stokes number
St_E	Stokes number relative to Eulerian integral time scale of the gas
St_K	Stokes number relative to Kolmogorov time scale of the gas
St_L	Stokes number relative to Lagrangian integral time scale of the gas
St_L^r	Stokes number relative to the Lagrangian integral timescale of the residual gas field velocity
We	Weber number

Operators:

$\partial_{\vec{\boldsymbol{x}}}\cdot$	Divergence with respect to $\vec{\boldsymbol{x}}$
$\widetilde{\ }$	Favre-averaging
$\overline{\ }$	Filtered quantity
D_t	Material derivative
$(y)_+$	$\max\{0, y\}$
$(y)_-$	$\min\{0, y\}$
$-_t$	Partial derivative with respect to time

$-_x$	Partial derivative with respect to space
$(\ )^r$	Residual correlation between two variables a and b where $(ab)^r = \overline{ab} - \overline{a}\,\overline{b}$
$\vee$	$Symmetrictensorouterproduct$
$\mathrm{Tr}(\boldsymbol{Y})$	Trace of a matrix $\boldsymbol{Y}$
$-^T$	Transpose
$\langle .,. \rangle$	Standard scalar product
$\Delta^+ Y$	$Y_{i+1} - Y_i$
$\Delta^- Y$	$Y_i - Y_{i-1}$
$\langle . \rangle$	Averaging operator over the whole domain

Abbreviations:

ACARE	Advisory Council for Aviation Research and innovation in Europe
ACBMM	Algebraic Closure Based Moment Methods
AG	Anisotropic Gaussian closure based model
AMR	Adaptive mesh refinement
ATAG	Air Transport Action Group
CDF	Cumulative Distribution Function
CFL	Courant-Friedrichs-Lewy condition
CPR	Correction Procedure using Reconstruction
CQMOM	Conditional Quadrature Method Of Moment
CSVM	Coupled Size Velocity Moments method
CV	Control Volume
DG	Discontinuous Galerkin scheme
DiTurBC	Downstream Inflow Turbulent Boundary Condition
DNS	Direct Numerical Simulation
DoF	Degrees of Freedom
DPS	Discrete Particle Simulation
DQMOM	Direct Quadrature Method Of Moment
DSMC	Direct Simulation Monte-Carlo method
ENO	Essentially non-oscillatory schemes
EQMOM	Extended Quadrature Method Of Moment
EMSM	Eulerian Multi-Size Moment model
FC-DFS	Fully controlled deterministic forcing scheme
FD	Finite difference
FE	Finite element
FIM-UR	Fuel Injection Method by Upstream Reconstruction
FR	Flux reconstruction
FV	Finite volume
FVKS	Finite Volume Kinetic Scheme

GPBE	Generalized Population Balance Equation
GRP	Generalized Riemann problem
HIT	Homogeneous Isotropic Turbulence
HLL	Harten-Lax-van Leer Riemann solver
HPC	High Performance Computing
Iso	Isotropic Gaussian closure based model
KBMM	Kinetic Based Moment Methods
Lag	Lagrangian
LES	Large Eddy Simulation
LHDI	Lagrangian History Direct Interaction
LHS	Left Hand Side
LPP	Lean Premixed Prevaporized
LS	Level Set
MAC	Marker-And-Cell
MCE	Mean Central (or internal) energy
MC	Monotonized central-difference limiter, also called double minmod
MF	Multi-Fluid method
MG	Multi-Gaussian closure based model
Minmod	Minimum-modulus limiter
MK	MonoKinetic closure based model
MOMIC	Method Of Moment with Interpolative Closure
MTE	Mean Total energy
MUSES3D	the three dimensional MUlti-fluid Solver for Eulerian Spray
MUSCL	Monotone Upstream Scheme for Conservation Laws
NDF	Number Density Function
ODE	Ordinary Differential Equations
OSM	One Size Moment multi-fluid method
PBE	Population Balance Equation
PDE	Partial Differential Equations
PDF	Probability Density Function
PGD	Pressureless Gas Dynamics system
PIC	Particle-in-cell
PR-DNS	Particle Resolved Direct Numerical Simulation
PTC	Particle Trajectory Crossing
PVC	Precessing Vortex Core
QMOM	Quadrature Method Of Moment
RANS	Reynolds Averaged Navier Stokes method
RHS	Right Hand Side
RKDG	Runge-Kutta discontinous Galerkin method
RMS	Root Mean Square
RP	Riemann problem
RUE	Random Uncorrelated Energy

RUM	Random Uncorrelated Motion
SCE	Subgrid correlated energy
SP	Stochastic Parcel method
SSP	Strong Stability Preserving
SUPG	Streamline-Upwind Petrov-Galerkin
TKE	Turbulent kinetic energy
TSM	Two Size Moments multi-fluid method
TTGC	Two-Steps Taylor-Galerkin scheme
TVD	Total Variation Diminishing
TVB	Total Variation Bounded
UCE	Uncorrelated central energy of the unfiltered motion
VOF	Volume-Of-Fluid
WBE	Williams-Boltzmann equation
WENO	Weighted essentially non-oscillatory schemes

Introduction

Environmental context and regulations

In the actual global context, air transportation traffic is constantly increasing, and its impact on global climate change and pollutant emissions is a major concern for regulation entities. Even with the emergence of alternatives to fossil fuel that are still ongoing research topics (bio-fuels, synthetic kerosene, hydrogen), the liquid fuel combustion is currently the only viable solution for aircraft engines and their efficiency as well as their emissions have to be better controlled. In fact, the Advisory Council for Aviation Research and innovation in Europe (ACARE) (*Darecki et al. 2011*) have envisaged the goals of reducing by respectively 75% and 90% the CO_2 and NO_x emissions per passenger kilometer based on the ATAG target. These values are being calculated relative to the emission level of aircraft in year 2000. One of the main milestones towards this direction as stated by ACARE is the full understanding of the combustion process and the prediction of emitted species and their concentrations for all aeronautical engine types, fuel types and engine operating points.

Aeronautical combustion chambers

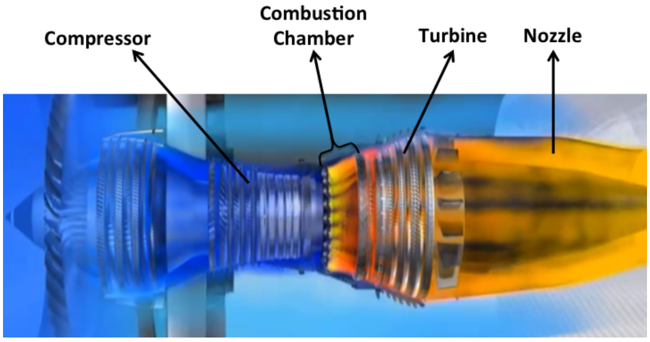

Figure 1: *An example of a gas turbine: the CFM56-7b turbofan single-aisle commercial jet engine. (Adapted from the website of SAFRAN)*

In order to understand the parameters influencing the general performance of aeronautical engines, a brief summary of the thermodynamics of this problem is presented. The typical configuration of an aircraft engine is made of three essential elements, as illustrated in Figure 1:

- a compressor used to increase the pressure of the intake air,

- a combustor used to burn the mixture of air and fuel and exhaust energetic burnt gases,
- a turbine used to expand the burnt gases and transform their energy into mechanical power.

In the ideal case, the compression and expansion are isentropic and the combustion is isobaric: this is called the Brayton cycle that is shown in Figure 2. The efficiency of this cycle is $\eta_{Br} = 1 - (P_1/P_2)^{(\frac{\gamma-1}{\gamma})}$. This means that for a given mass flow rate entering the engine, the output power can be increased by increasing the compression ratio P_2/P_1 and thus the inlet temperature of the turbine.

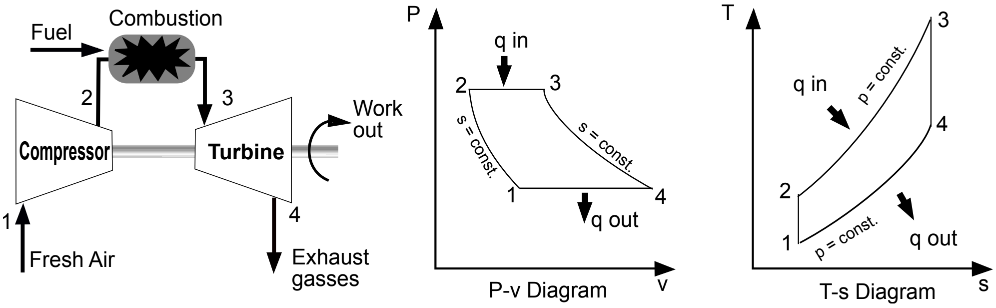

Figure 2: *Simplified sketch of the thermodynamic cycle of a gas turbine in the case of the idealized Brayton cycle (Source wikipedia)*

Practically, this ideal aerodynamic efficiency is never attained due to the different kind of losses in the system. The increase of the compression ratio is limited by the technological constraints such as the thermo-mechanic resistance of the turbine that limits inlet temperature of the turbine. Moreover, increasing the temperature may lead to increased pollutant emission such as NOx emissions. In order to limit the temperature increase while increasing the compression ratio, engine manufacturers are interested in very lean combustors for which the burnt gases temperature may be decreased. New burners are designed for this purpose, such as LPP burners (Lean Premixed Prevaporized) which target to provide a lean and homogeneous mixture before reaching the flame zone in order to limit the generation of NOx by thermal pathway. As a consequence, extensive studies are required to understand the behavior of these new systems.

Experiments and Simulations

In combustion chambers, complex and intricate physics takes place as illustrated in Figure 3. To generate compact flames, the flow is generally swirled (*Syred 2006*), leading to recirculation zones and hydrodynamics instabilities such as the Precessing Vortex Core (PVC) that play an important role in the flame ignition and stabilization. Moreover, fuel is generally stored in liquid phase, and injected directly in the combustion chamber to generate a spray composed of droplets that will eventually burn. Finally, thermo-acoustics instabilities may also take place and be promoted because of the interaction of the flame with the chamber acoustics modes. As a consequence, the flow covers a wide range of scales, from the system size of about 10cm to the smallest droplets below 1μm, and the resulting physics to be investigated involve many research field in a coupled context: aerodynamics, turbulence, two phase flow, atomization, combustion...

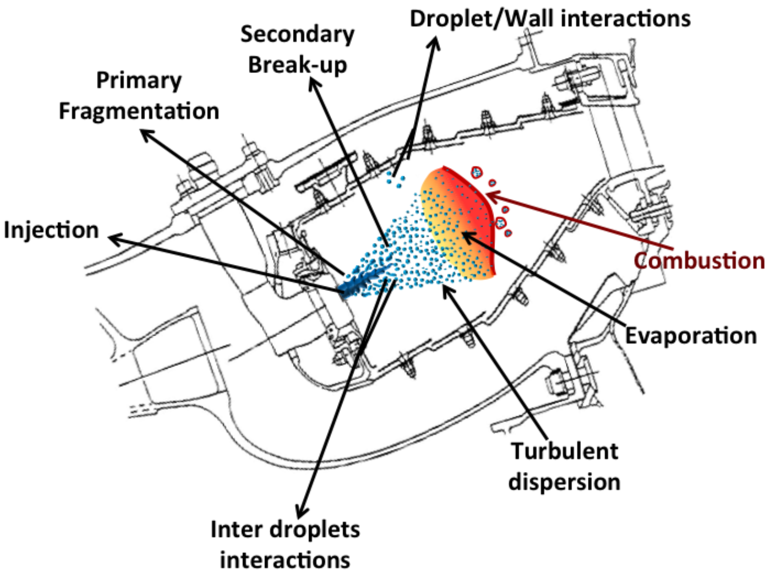

Figure 3: *Complex physics and interactions in the combustion chamber*

To understand the physics within the combustion chamber, one can conduct either experiments or simulations, complemented by theoretical investigations. In experiments, one might face technical difficulties and challenging experimental environment and conditions such as high temperature and pressure and complex interactions between the different physical phenomena. In addition, the similarity between the full realistic scale and the experimental subscale is not flawless. Due to these possible discrepancies, some physical phenomena may not occur in the same regime at the experimental scale as it is in the reality. However, due to the advancements in the experimental diagnostics and the post processing techniques, many achievements in this field can be found in the literature (*Presser et al. 1993*; *Sommerfeld and Qiu 1998*; *Sornek and Hirano 2000*; *Renaud 2015*; *Itani et al. 2015*; *Tachibana et al. 2015*; *O'Connor et al. 2016*).

On the other hand, simulations present some advantages compared to experiments. First, simulations are rich in information, which is directly accessible, whereas experimental data can be limited by the post processing techniques. Second, it could be simpler to carry parametric geometrical studies and optimizations in the combustion domain through simulations. This is an important matter in the industrial field for the design of new components. As a consequence the numerical simulations are considered to be of paramount importance for the research and development of two phase combustion. However, numerical simulations might be misleading since the results are governed by the models and the numerical methods used. For this reason, great attention must be given to the choice of the modeling approach and the underlying numerical methods in order to guarantee reliable and predictive physical results.

In summary, experiments and numerical simulations both have their advantages and limitations. These two approaches are complementary. Any improvement of either approach will lead to a better comparison between the two and a better understanding of the combustion chamber behavior. In this work, we are focusing our attention on the development of simulation techniques.

Modeling frameworks

Because of the multi-scale character of the combustion chamber, solving for all the scales of the flow through Direct Numerical Simulation (DNS) is unreachable. To circumvent this issue, modeling approaches have been proposed:

- the Reynolds Averaged Navier Stokes (RANS) methods were designed, see *Pope (2000)*, in which only an ensemble-averaged mean flow is solved. This method is still widely used in industry because of its low cost, but cannot predict unsteady phenomena such as instabilities.
- the Large Eddy Simulation (LES, *Smagorinsky (1963); Sagaut (1998)*): this strategy consists in filtering the equations to be solved in order to limit the level of details that have to be reproduced. This leads to the resolution of the large energetics structure while the small dissipative ones are modeled. This method has gained a lot of interest for academic and industrial studies because of the rise of the computational resources, as it requires to solve more information than for RANS simulations.

Nowadays, considering the new regulations and the new design problems, which require the understanding of highly unsteady behaviors, LES seems to be the best choice. However, in the context of the combustion process in turbulent regimes, modeling challenges are faced in LES.

Liquid fuel injection and atomization

Despite the fact that a lot of studies have been performed in purely gaseous systems, in reality, liquid fuel is injected directly in the combustion chamber. As a consequence the physics of injection is an important issue. Once injected in the combustion chamber, the liquid faces primary atomization and is broken into clusters, ligaments and droplets of large sizes. This atomization takes place since the external stresses on the liquid sheet predominate the surface tension that provides stability. The two phases at this stage are known as separated phase. The two phases interact with each other causing the division of the ligaments into smaller droplets that form the disperse phase. The separated phase as well as the disperse phase are illustrated in Figure 4.

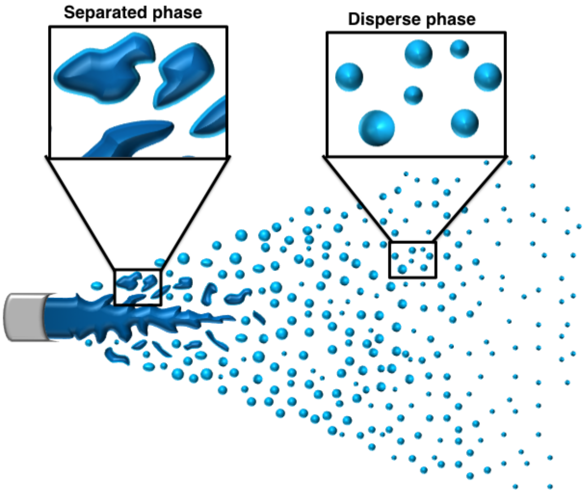

Figure 4: *Injected fuel topology: separated phase and disperse phase*

The resolution of the separated and disperse phase though sharp interface capturing methods lead to accurate description and it is used in various academic configurations (*Hirt et al. 1974; Popinet and Zaleski 1994; Aulisa et al. 2003; Tanguy and Berlemont 2005; Menard et al. 2007; Fuster et al. 2009; Herrmann 2008; Desjardins et al. 2013; le Chenadec and Pitsch 2013; Arienti and Sussman 2014*) especially for the description of the separated phase. However, this approach does not describe efficiently the disperse phase. In addition, it is very expensive and cannot be used for aircraft engines applications.
Another choice is to use reduced order models for the separated phase based on diffuse interface capturing approaches (*Baer and Nunziato 1986; Drew and Passman 1999; Le Martelot et al. 2014; Saeedipour and Priker 2016; Vu et al. 2016; Drui et al. 2016*). This approach is efficient for the separated phase but it cannot describe the disperse phase. As a consequence, the disperse phase is treated with another approach. In this case, the simulation of the full liquid jet faces the challenge of the accurate description of the transition between the separated phase regime to the spray regime. This on-going research can be found in the work of *Reveillon et al. (2013); Le Touze (2015); Zuzio et al. (2016); Drui et al. (2016); Essadki et al. (2016)*.

However, up to now, there is no available approach able to simulate the two phase flow with the high Reynolds and Weber numbers faced in real applications with an accurate transition between the separated regime and the spray regime. A practical solution used to simulate realistic burners with liquid fuel injection consists in using reduced models for the injection boundary conditions (*Martinez et al. 2010; Sanjosé et al. 2011*) in order to start the simulation directly with the spray without having to simulate the separated phases and the atomization. For this reason, the focus of this thesis is on the disperse phase regime.

Turbulent spray combustion

Once the liquid fuel is atomized into droplets, the resulting spray will feed the combustion process through its evaporation into gaseous fuel. In the case of the aeronautical combustors, the combustion takes place mainly in the diluted regime far from the atomization region, where the liquid volume fraction is below 1%. Thus, studying the combustion of a spray of droplets is justified.
In the literature, single-phase turbulent combustion has been widely studied using simulation and experiments (*Borghi 1988; Vervisch et al. 2004; Boudier et al. 2007; Cant 2011; Vervisch and Poinsot 1998; Veynante and Vervisch 2002; Vervisch et al. 2004; Poinsot et al. 1993; Poinsot and Veynante 2005*) and has led to the development of many LES strategies, handling the chemistry as well as its interaction with turbulence, see *Fiorina et al. (2015)* and references therein. At the end, turbulent gaseous combustion has reached a level of maturity that makes possible the simulations of complex configurations. LES was used for example for spark ignition engines (*Richard 2005*), combustion instabilities (*Selle et al. 2006; Martin et al. 2006; Franzelli et al. 2012*) and ignition of annular multiple-injector combustor (*Philip et al. 2015*). Many other references can be found in this field (*Pitsch and Duchamp de Lageneste 2003; Pierce and Moin 2004; Pitsch 2006*). For more information one can refer to the review of *Gicquel et al. (2012)*.
Compared to gaseous combustion, two-phase turbulent combustion is a recent topic, which has received more interest in the last decade because of the use of direct fuel injection in combustion chambers. Because of the presence of spray, the overall physics may be modified and a fundamental understanding of the underlying phenomena is still required (*Sirignano 2010; Jenny et al. 2012*). Even in laminar conditions, additional physics has to be taken into account in order to reflect the impact of the spray (*Fujita et al. 2013; Watanabe et al. 2007; Martinez-Ruiz et al. 2013; Sanchez et al. 2014; Massot et al. 1998; Laurent and Massot 2001*). When it comes to interaction with vortices, *Franzelli et al. (2016)* demonstrated that the presence of the spray may modify the interaction regimes, leading to additional phenomena to be taken into account in LES models. It also clearly appears that the spray-turbulence interaction plays an important role in two-phase combustion, as it generates spatial inhomogeneities that are not present in gaseous combustion, and shall strongly

affect the combustion process, see *Vié et al. (2014)*. Moreover, in spray combustion, isolated combustion may occur depending on the droplet interspace, and additional modeling is required to capture such regimes (*Paulhiac 2015*).
Despite the lack of complete modeling framework, reactive spray simulations of complex configurations are performed, see *Hannebique et al. (2013); Franzelli et al. (2013); Cheneau et al. (2015); Jones et al. (2014); Guedot (2015)* for example, but generally lacks models for the interactions of the spray in the turbulent combustion process.
At this point, it is clear that it is mandatory to have an accurate description of the spray phase before going to spray combustion. Actually, one of the main issue is about the spray-turbulence interaction, which is the objective of this work. Because of the strong scale separation between the droplet size (up to 100 μm) and the flame thickness (about 1 mm), the spray description may not change in reactive conditions, thus justifying a separate study on the spray itself.

Modelling Challenges

From the above discussion, five main challenging topics should be treated in a sequential manner, in order to reach an accurate and robust simulation of the spray in the combustion chamber:

(C1) The level of description: many approaches exist in the literature and one should be careful while choosing one of these descriptions to be able to reproduce the right physics at a minimal cost for the industrial application.

(C2) The modeling assumptions: if closures are needed in this model, then the suitable closure must be chosen in an attempt to recover the information lost in the reduced modeling process.

(C3) The coupling with the gas phase: the selected model should be easily coupled to the gas. In order to simulate the interaction between the two phases, and thus the turbulence/droplets interactions, the coupling terms should be properly closed.

(C4) The description of the unresolved scales: depending on how the turbulent gas phase is simulated, particular attention need to be paid to have the same level of model reduction for the disperse phase and to be precise on the coupling of the two phases in this case. For RANS, the turbulent velocity correlations between the two phases should be correctly modeled and for LES the appropriate subgrid term must be applied. Since the LES is chosen here, the second challenge is faced.

(C5) The numerical resolution: once the modeling process is finalized, the resulting systems of equations should be solved, in both DNS and LES, to obtain accurate and robust results.

In the following, we navigate through theses challenges, identifying the choices made in this work in order to delineate the objectives and contributions of this thesis.

Level of description (C1)

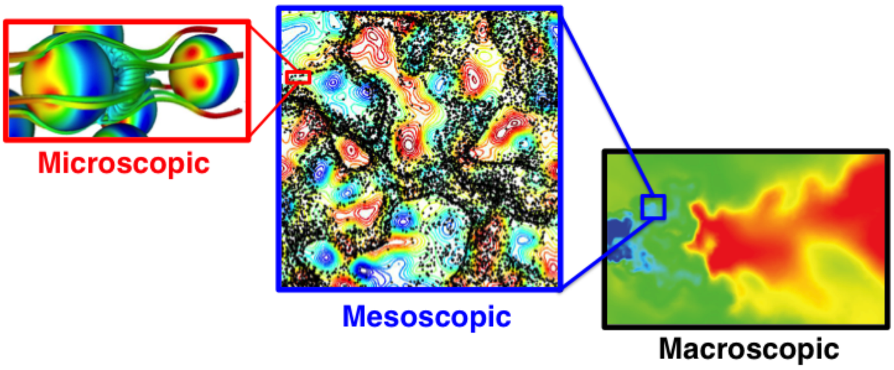

Figure 5: *Hierarchy of scales from microscopic (left), mesoscopic (center) to macroscopic (right)*

The level of description defines the details of the flow field that will be solved in both phases, see Figure 5. In fact, solving all the physics would require the solution of the flow inside the droplet, outside the droplet and at the interface level. Such a simulation corresponds to the microscopic level and is called droplet-resolved direct numerical simulation. In the context of solid particles, the problem is simplified by imposing boundary conditions at the presumed solid surface of each particles (*Xu and Subramaniam 2010; Tryggvason et al. 2010; Subramaniam 2013*). Such level of description is very rich in information for each particle but is therefore computationally very expensive and its usage is limited to the academic field (*Tenneti and Subramaniam 2014; Brändle De Motta et al. 2016; Rosso et al. 2016; Richter et al. 2016*), for instance to extract closure laws for the velocity fluctuations, drag and heat transfer (*Tenneti et al. 2011; Tenneti and Subramaniam 2014*).

In aeronautical burners, the microscopic level of description is indeed unreachable because of the number of droplets involved. However, a point-particle assumption is generally made, for which the details of the flow at the droplet scale are embedded into mesoscopic closures such as Stokes drag law[1]. Such a resolution relies on a scale separation and ends up to be a mesoscopic description of the disperse phase. The first method in this level is the Discrete Particle Simulation (DPS), where the droplets are tracked (*Riley and Paterson 1974*). The accuracy of this method is directly dependant on the accuracy of the mesoscopic closures, but ends up being highly intuitive and easy to im-

---

[1] The point-particle assumption is justified since the microscopic interactions are dissipated by the viscous effects and do not affect the mesoscopic behavior.

plement, at least in sequential codes. For this reason, this method is highly used in the literature whether for example for solid particle dispersion (*Squires and Eaton 1991b; Squires and Eaton 1991a; Elghobashi and Truesdell 1992*) or for droplet in the combustion applications (*Mashayek et al. 1997; Miller and Bellan 2000; Reveillon and Vervish 2005; Fréret et al. 2012*). The challenges of this method are its coupling with the Eulerian description of the gas and its parallel implementation. In addition, it gives only one realization of the flow and is therefore not practical when one is interested in the knowledge of global statistical variables, except in some academic configurations where ensemble averaging can be replaced by another averaging, such as time averaging thanks to ergodicity.

Still at the mesoscopic level, another approach consists in using a statistical averaging method. This is the most suitable approach to describe the disperse phase when a very high number of droplets constitutes the spray in the combustion chamber. This statistical method uses the Williams-Boltzmann equation (WBE) on the Number Density Function (NDF) of the disperse phase in order to statistically describe the dynamics of the disperse phase. Solving this WBE should be performed using Lagrangian methods such as the direct simulation Monte-Carlo method (DSMC) (*Bird 1994*) that approximates the NDF by a sample of discrete statistical particles representing a droplet, or the Stochastic Parcel method (*Crowe and Willoughby 1977; O'Rourke 1981*) in which a group of several droplets assumed to have identical properties are represented by a numerical particle. However these methods face the same issue as the DPS concerning the coupling with the gas phase, and may also be highly expensive to reach statistical convergence.
The final level of description is the macroscopic level: instead of solving individual particles (physical or statistical), one can look at integrated quantities, called moments, such as the concentration of droplets or their overall momentum. Such quantities can be obtained through the integration of the WBE in the phase space, and lead to conservation equations on the moments. This method called Eulerian Method of Moments presents a suitable choice and can be easily coupled with the gas phase since they are both continuous descriptions. It can be also efficiently parallelized and it is naturally statistical converged. For this reason, the present work focuses on the development of this method.

Modeling assumptions (C2)

Even if the moment methods present advantages over the Lagrangian methods, they demand additional modeling effort because of the integration in the phase space of the WBE, which implies a loss of information. To recover part of this information, one has to use closure assumptions that will drive the accuracy of the method. Two of the main issues concern the description of size dispersion (polydispersity) and velocity dispersion (polykineticity):

- Polydispersity: because the injection systems generate droplets of various sizes called polydisperse, this issue is of paramount importance in aeronautical engines. Various solutions were developed in the literature, which can be based on the discretization of the phase space into sections (*Laurent and Massot 2001; de Chaisemartin 2009*), on quadrature approximations (QMOM, DQMOM, *McGraw (1997); Fox et al. (2008)*), or on continuous approximation of the NDF through the use of high order moments and entropy maximization (*Massot et al. 2010; Kah 2010; Emre 2014; Vié et al. 2013; Essadki et al. 2016; Essadki et al. 2016*). Despite the great efficiency of the latter type, in the present work, we focus on multi-fluid methods (MF) which have a great flexibility when it comes to coupling with polykinetic methods, such as in *Vié et al. (2013)* and can even be extended to high order moments in the sections.
- Polykineticity: this issue is related to the inertia of the droplets. Droplets with low inertia will have a velocity close to the one of the carrier phase, and droplets in the same vicinity will have the same velocity. On the other hand, droplet with moderate to high inertia will not follow the gas phase and will generate a complex weak correlation with the carrier velocity. The dynamics of the moderately inertial to inertial particles is governed by the velocity dispersion (*Vié et al. 2015*) also called random uncorrelated motion (RUM) (*Février et al. 2005*) or granular temperature (*Fox 2014*). In the literature, Eulerian polykinetic models are divided into two main categories according to the closure methodology: algebraic closure based moment methods (ACBMM) for which the moment equations are closed based on assumptions on the moments (*Février et al. 2005; Masi 2010*), and kinetic based moment methods (KBMM) for which the moment equations are closed by using assumptions on the underlying NDF itself (*Laurent et al. 2012*). The former strategy has already been used to performed simulations in complex aeronautical configurations (*Jaegle 2009; Sanjosé et al. 2011; Vié et al. 2013*), but suffers from realizability[2] issues (*Sierra 2012*) that prevents from the design of stable and accurate schemes. On the other hand, KBMM can lead to hyperbolic systems of equations that are a preferable basis for the design of numerical scheme, which leads this work to be dedicated to this family of methods.

At the end, in the present work, we will investigate a modeling strategy that is based on KBMM closures for the polykinetic character of the spray and multi-fluid methods in order to capture polydispersity.

Coupling with the gas phase (C3)

The influence of the spray on the gas phase may be of great importance in several applications, especially when the spray is dense and with high mass

---

[2] The realizability is the ability of associating a positive NDF with every set of moments.

loading (*Elghobashi 1991*). It can modify the mass and momentum of the gas. In the combustion chamber, the two-way coupling is necessary in order to take into account the evaporation of the fuel droplets into fuel vapor before mixing with the oxidizer, igniting and burning.

For the Eulerian spray descriptions, this two-way coupling (*Doisneau et al. 2014; Emre 2014*) can be taken into account more easily than for the Lagrangian description because spray and carrier phase description share the same Eulerian framework (*Boivin et al. 1998; Capecelatro and Desjardins 2013a; Zamansky et al. 2014*).

In fact, for DNS simulation, the gas influence on the spray is taken into account through the terms of acceleration, rate of change of the droplets size and rate of change of droplet temperature in the kinetic equation. These terms depend on both gas and liquid local properties. According to the degree of complexity of the modeling of these terms, their evaluation might add a degree of complexity to the method.

The influence of the spray on the gas is taken into account by source terms in the gas phase equations modeling the exchange of mass, momentum and energy.

In the combustion chamber, the mass, momentum and energy exchanges between the two phases are characterized by very rapid variations. This means that numerical efforts are needed in order to not be limited by these small characteristic times. This can be done by using a special splitting technique that can be found in *Descombes et al. (2016); Duarte et al. (2013); Doisneau et al. (2014)* and the references therein.

Description of the unresolved scales (C4)

Since the spray is turbulent and contains a wide range of length scales, we are interested in the LES for the Eulerian description of this spray. In the literature, two classes of LES strategies have been proposed depending on the filtering strategy:

- the classical approach where the LES filter is applied at the macroscopic level by filtering directly the moment equations (*Shotorban and Balachandar 2007; Moreau et al. 2010*)
- the kinetic approach where the filter is applied at the mesoscopic kinetic level (*Zaichik et al. 2009; Pandya and Mashayek 2002*).

In this thesis, the kinetic approach is preferred since a direct link is kept between the filtered kinetic equation and the final moment system. This is helpful to guarantee the realizability conditions on the moments, which is of primary importance for developing accurate, robust and parameter-free numerical schemes. Following this strategy, the resulting moment equations have to be closed, as the highest order fluxes are unknown. To do so, we use a KBMM on the filtered WBE.

Numerical resolution (C5)

The realizability of the moment set used to describe the disperse phase in not enough to guarantee accurate results. Actually, the numerical scheme used to solve the resulting equations should be realizability-preserving in the sense that it should respect the constraints coming from the underlying kinetic representation in the sense that the updated moment set should always be associated to a non-negative NDF.

In addition, a high order robust numerical method is needed in order to minimize the numerical diffusion, which may be of the same order of magnitude of some underlying physics. In this way the numerical scheme will be able to capture the fine structures appearing in the solution and to reproduce the large variations that might be encountered in the density field (going from vacuum zones to high concentration regions) without inducing spurious oscillations.

To sum up, the numerical scheme should be:

- accurate to be able to reproduce the large variations of the density,
- preserve the realizability in order to maintain a physical sense to the solution. For example, the solution should not include any negative density, or negative pressure,
- applicable to unstructured mesh computations needed to simulate disperse phase flows in real configurations including complex geometries,
- as cost effective as possible, otherwise it would not be suitable for industrial use,
- parameter free: no need for example for artificial viscosities to stabilize the scheme and suppress spurious oscillations that can be generated near high gradients.

Contributions

In this work, the contributions are of two types. The first one concerns the development of a complete modeling approach.

- Modeling of turbulent sprays: in this work, the Anisotropic Gaussian (AG) closure suggested in *Vié et al. (2015)* is investigated. Up to now, the AG closure had been properly derived and validated in 1D and 2D cases. In this work, this model is now extended to 3D turbulent cases and validated using:
    - the qualitative results of the number density, velocity and covariance elements fields;
    - the statistical results evaluated after averaging over the whole physical domain;
    - the results of the PDF of the different quantities studied such as the number density and the disperse phase Mach number
    - the autocorrelation function for the velocity and the number density.

  The conducted test case is 3D a forced homogeneous isotropic turbulence

(HIT) which is a canonical academic case. When it comes to the Stokes numbers studied, different simulations can be found in the litterature for these levels of particles inertia whether based on the point-particles assumption used in this work or based on the fully resolved method by taking into account the effect of the finite size of the particles. Also various experimental results were carried out in the litterature for these levels of particles inertia. A non-exhaustive list of examples of the simulations and experiments of different particle-laden turbulent is illustrated in Figure 6 and the details of this list can be found in the work of *Brändle De Motta et al. (2016)*. The simulations conducted in this thesis are added and depicted by the black squares.

This evaluation on the HIT is considered to be nearly extensive in comparison with the literature.

- Extension to polydisperse sprays: the AG model is extended to polydisperse sprays based on the Multi-Fluid method. By using a high order MF, the obtained polydisperse-polykinetic model is of high order in size and velocity, while keeping the cost affordable in comparison with other quadrature based methods capable of treating the polykineticity more accurately.
- Large Eddy Simulation formalism: The extension of the AG model to the LES context is carried out leading to a new fully kinetic based closure formalism for the LES of spray. By doing so, the link between the filtered kinetic equation and the filtered moment equation is kept leading to a realizable model, unlike most of the two phase LES present in the litterature.

When it comes to the second axis of this thesis, the numerical methods, two main achievements are fulfilled.

- Development of a new scheme for unstructured grids: of the latest developments in the field of numerical methods, a realizability preserving Discontinuous Galerkin scheme is used for the resolution of two models of the KBMM namely the MK and the isotropic Gaussian one. The DG results are eventually compared in 1D configurations to a third order finite element scheme (TTGC) and two second order finite volumes schemes, namely the realizable MUSCL/HLL and the finite volume kinetic scheme. It is also evaluated and compared on a 2D test case qualitatively and quantitatively to the Lagrangian results and to the reference simulations provided by a second order structured MUSCL/HLL. Through these comparisons, the DG method is shown to be competitive for the description of the disperse phase flow. This scheme stays robust even when facing the severe singularities created by the models, especially the MK model that generate dirac δ-shocks at each crossing event. It can accurately reproduce the high preferential concentration that characterizes the dynamics of low inertia particles.

It is accurate, robust and preserves the realizability and no additional efforts are needed for its application on unstructured grid.

- Second order scheme for 3D structured grids computations: the extension of the MUSCL/HLL scheme for the resolution of the AG system to 3D is done. It is accurate and realizable and easily parallelized especially on structured grids. This scheme is implemented in the parallel academic code MUSES3D.

These contributions were published in three papers and conferences proceedings along with two articles in preparation:

- Comparison of realizable schemes for the Eulerian simulation of disperse phase flows (*Sabat et al. 2014*) (proceedings of the 7th International Symposium of Finite Volumes for Complex Applications).
- On the development of high order realizable schemes for the Eulerian simulation of disperse phase flows: a convex-state preserving Discontinuous Galerkin method (*Sabat et al. 2014*) (selected for a special edition from the 8th International Conference on Multiphase Flow).
- Fully Eulerian simulation of 3D turbulent particle laden flow based on the Anisotropic Gaussian Closure (*Sabat et al. 2016*) (proceedings of the 9th International Conference on Multiphase Flow).
- Statistical description of turbulent particle-laden flows in the very dilute regime using the Anisotropic Gaussian Moment Method (in preparation) (*Sabat et al. 2018*).

In addition, the results of this work were presented in several international conferences and seminars, where the presenter is underlined in the following:

- Sabat, M., Larat, A., Vié, A.,Massot, M.. Toward modeling and LES of droplet-gas flows with a Kinetic-Based Moment Method (KBMM) approach. Annual Meeting of the Centre de Recherche sur la Combustion Turbulente, Chatenay-Malabry, France, Mars 2014.
- Sabat, M., Vié, A., Larat, A., Doisneau, F., Chalons, C., Massot, M.. On DNS and LES of turbulent particle-laden flows: Kinetic-Based Moment Methods based on the Anisotropic Gaussian Closure. 2nd International Conference on Numerical Methods in Multiphase Flows, Darmstadt, Germany, July 2014.
- Sabat, M., Vié, A., Larat, A., Doisneau, F., Chalons, C., Massot, M.. Kinetic-Based Moment Methods for DNS and LES of particle-laden flows: Anisotropic Gaussian Closure. American Physical Society, 67th Annual Meeting of the Division of Fluid Dynamics, San Francisco, USA, November 2014.
- Larat, A., Sabat, M., Vié, A., Chalons, C., Massot, M.. Development of high order numerical methods for particle-laden flows on unstructured grids: A realizability-preserving Discontinuous Galerkin method for moderate Stokes number flows. American Physical Society, 67th Annual Meeting of the Division of Fluid Dynamics, San Francisco, USA, November

2014.

- Sabat, M., Vié, A., Larat, A., Massot, M.. Toward the realizable Large Eddy Simulation of spray: the Anisotropic Gaussian Eulerian model. 15th International Conference on Numerical Combustion, Avignon, France, April 2015.
- Sabat, M., Vié, A., Larat, A., Massot, M.. Eulerian simulation of droplet-laden flows. Poster session at: Séminaire de mécanique des fluides numérique, Institut Henri Poincaré, Paris, France, February 2015.
- Sabat, M., Vié, A., Larat, A., Massot, M.. Kinetic-Based Moment Methods for the Eulerian Large Eddy Simulation of fuel sprays: the Anisotropic Gaussian model. 2nd Frontiers in Computational Physics Conference: Energy Sciences, Zurikh, Switzerland, June 2015.
- Sabat, M., Vié, A., Larat, A., Massot, M.. A Kinetic-Based Moment Method for DNS and LES of turbulent particle-laden flows. Turbulence and Interactions, Cargèse, France, November 2015.

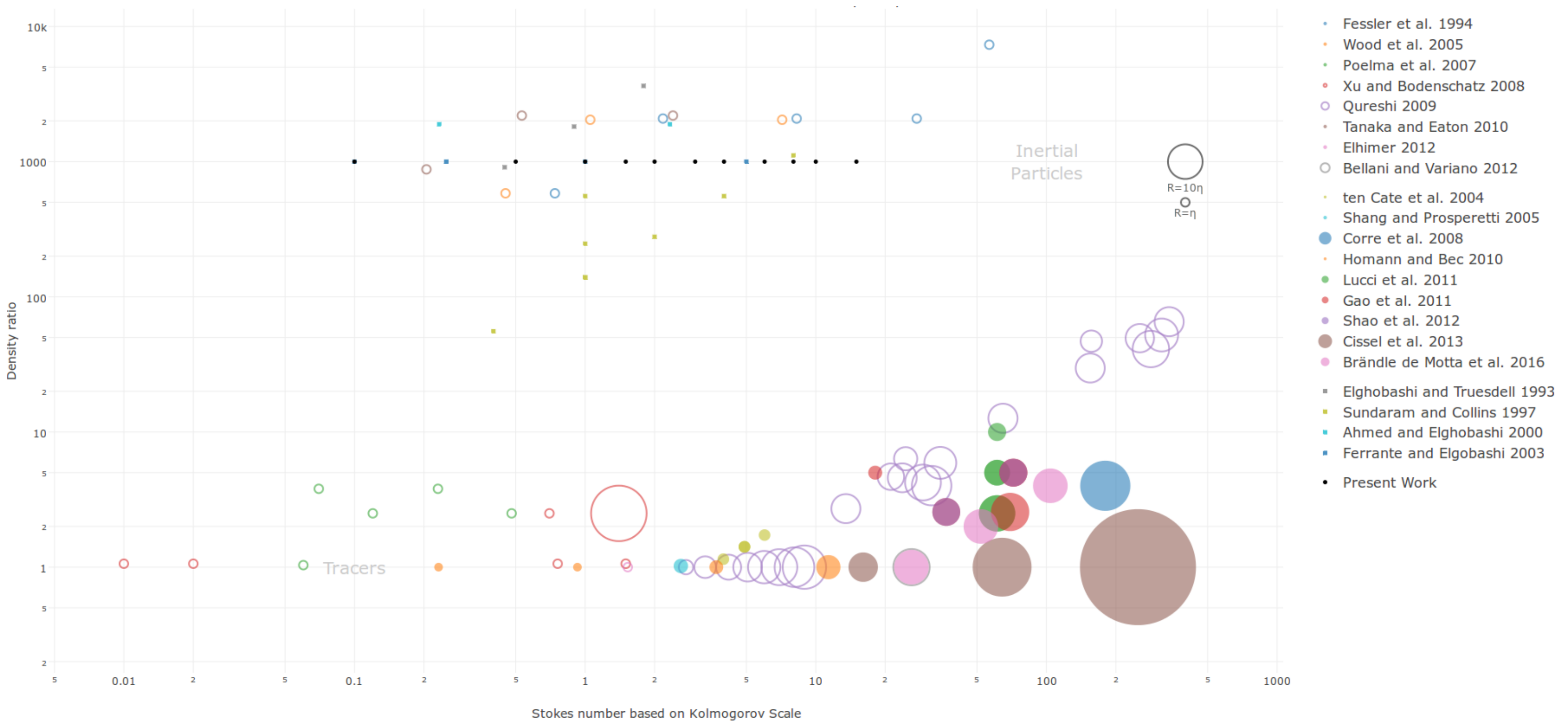

Figure 6: *Non-exhaustive list of examples of experiments (in open circles) and simulations based on point-particle assumption (in squares) and finite-size particles assumption (in filled circles) of turbulent particle-laden flows. The 3D simulations conducted in this thesis depicted by the black squares (adapted from Brändle De Motta et al. (2016))*

Organization of the manuscript

The manuscript is organized in four parts that are the DNS modeling of the disperse phase, the numerical methods, the computational dynamics of the particle laden flows and the first step toward LES modeling of the disperse phase.

In **Part I**, the DNS modeling of the disperse phase is presented and the part is divided into three chapters.

- The general context of the study is first defined in Chapter 1 along with the physics and specificities of the disperse phase needed to be modeled and the underlying assumptions. Then, the various models for the spray are presented with their advantages and disadvantages. The challenges, in the selected Eulerian moment method, are afterwards nominated. Finally, the classification of the presented modeling approaches is added.
- The polykinetic moment methods are the subject of Chapter 2 where the method of moment is presented in an attempt to describe velocity dispersion with two families of closure the ACBMM and the KBMM. The second is detailed with different closures in the hierarchy and a comparison of these closures on a theoretical two crossing jet configuration is depicted.
- Chapter 3 discusses the existing methods that handles polydispersion in size namely the size sampling method, the pivot method, the method of moments with interpolative closure, the multi-fluid method, the quadrature-based moment method and the Eulerian multi-size moment model. The focus is brought one the multi-fluid method since it describes accurately the evaporating sprays. The extension of this method to treat polykineticity based on the Anisotropic Gaussian closure for the velocity distribution is introduced for one size moment and two size moments.

Part II discusses the numerical schemes used for the resolution of the resulting hyperbolic (or weakly hyperbolic) system of equation.

- In chapter 4, an overview of numerical methods is presented including Finite Difference, Finite Volumes, continuous and Discontinuous Finite Elements. A brief non-exhaustive summary of the existing academic, semi-industrial and industrial codes is exhibited. The meshing types and classification is briefly recalled for the academic and industrial configurations. Finally, in this chapter the systems of conservation laws to solve is presented and characterized along with the objectives that govern the selection of a given numerical scheme.
- The numerical schemes are presented in Chapter 5. These schemes are the Two-step Taylor Galerkin scheme (TTGC) which is the most used scheme in AVBP code, along with the three realizability-preserving numerical schemes namely: finite volume kinetic scheme, finite volume MUSCL/HLL scheme and a convex state preserving Runge-Kutta discontinuous Galerkin method (RKDG).

- The evaluation of these numerical schemes is carried out in Chapter 6 on 1D and 2D test cases.

In **Part III**, the AG model is evaluated on 3D a turbulent test case.

- The test case is depicted in Chapter 7: a 3D Forced Homogeneous Isotropic Turbulence, and initial investigations using the Lagrangian reference method are presented.
- In Chapter 8, comparison with the monokinetic model and the Lagrangian results are performed. This comparison is carried out for a range of Stokes numbers going from particles of very small inertia to high inertia. The qualitative results such as the number density field, the velocity magnitude and the elements of the covariant matrix are put forward. Then, quantitative mean statistical results are assessed, namely the segregation, the mean total energy and the mean internal energy.
- The distribution of the number density, the velocity, the pressure and the disperse phase Mach number are presented in Chapter 9 along with the number density autocorrelation and the longitudinal velocity autocorrelation. Based on the autocorrelations, a characteristic length of the clusters and a longitudinal inertial length scale are calculated and assessed for the different Stokes numbers.

Part IV is dedicated to LES.

- The different LES modeling strategies for the disperse phase are reviewed in Chapter 10. These models are then classified and presented along with the proposed fully kinetic LES formalism (AG LES).
- The sensitivity of the AG LES model to subgrid closures parameters is presented through preliminary results in Chapter 11.

Finally, the general conclusions and prospects of the overall work are announced.

Part I

DNS modeling of the disperse phase

This part deals with the modeling of the disperse phase in the context of DNS. The term DNS in this case does not refer to the level of details that one can reach with the disperse phase modeling but to the level of description of the carrier phase coupled to this disperse phase. The physics of the injected liquid fuel and more specifically of the disperse phase is introduced in Chapter 1. In addition, the modeling strategies are presented for the different levels of description of the disperse phase from the microscopic to the macroscopic ones. The focus is put on the Eulerian method of moments along with the detailed treatement of two challenges, namely modeling polykineticity and polydispersity. The different Eulerian strategies for the treatement of the dispersion in velocity and size are then presented in chapters 2 and 3 respectively. First, in a monodisperse context, the available polykinetic approaches found in the litterature are briefly introduced. These models belong to two families: Algebraic Closure Based Moment Methods (ACBMM) and Kinetic Based Moment Methods (KBMM). The focus in Chapter 2 is on the Kinetic Based Moment Methods for being realizable and leading to well posed systems of equations. From this family, the Anisotropic Gaussian model is chosen as a compromise between its ability to statistically capture the velocity dispersion and the cost of the method compared to the higher order polykinetic methods. Second, the different strategies to account for polydispersion in a monokinetic context are presented in Chapter 3, namely the sampling method, the pivot method, the method of moments with interpolative closure, the multi-fluid (MF) method, the quadrature-based moment method and the eulerian multi-size moment model. Finally, the extension of the classical MF method and the high order MF method to statistically treat the velocity dispersion is introduced based on the AG model.

Chapter 1

Two-phase flow modeling

In this chapter the physics of the injected liquid fuel is presented along with the various existing models for the disperse phase dynamics. These strategies range from the microscopic to the macroscopic level of description. Since the microscopic resolution is very expensive and is not suitable for realistic configurations, a mesoscopic point of view is rather considered. This mesoscopic level is obtained through the Williams-Boltzmann equation (WBE) that gives the evolution of the statistical description of the spray number density function. This description is based on a point-particle assumption. To solve the resulting WBE, two families of approaches can be used the Lagrangian and the Eulerian description. These two descriptions are presented with a focus on the Eulerian method since it is chosen in this work for its ease of coupling with the carrier phase, its efficiency in parallel computing and its intrinsic statistical convergence. The main two difficulties for this Eulerian method are also depicted, namely to account for polykineticity and polydispersity.

1.1 Physics and scales of the injected liquid fuel

The two phase combustion depends on the distribution of the fuel vapor resulting from the liquid phase evaporation and therefore depends on the dynamics of the liquid phase, see Figure 1.1. In fact, due to its interaction with the gas phase present in the combustion chamber, the liquid core injected is then broken up into clusters, ligaments and droplets of large size. This is called the primary atomization. The two phases at this stage are known as separated phases. The resulting discontinuous liquid phase interacts with the gas phase, causing the division of the ligaments into smaller droplets that form the disperse phase or spray. This is the secondary atomization.

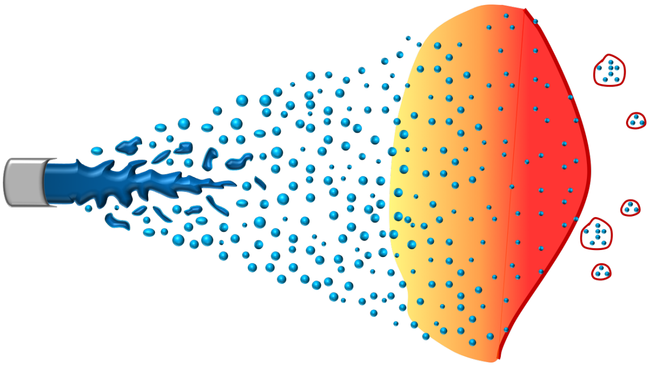

Figure 1.1: *Primary atomization of the fuel injected in the combustion chamber (navy blue), the secondary atomization (light blue), the fuel vapor (orange) and flame front (velvet red)*

The atomization is essential since the flammable fuel in its liquid state will not burn, and ignition can only happen once the liquid core has been atomized into droplets and evaporated. The topology and characteristic of the spray depends on many parameters such as the type of the injector and its geometry, the bulk liquid velocity, the turbulence level, the injection pressure and the properties of the carrier phase.

There exists many types of injectors such as the rotary atomizers, the pressure atomizers and the airblast atomizers (*Lefebvre 1989*).

- In the rotary atomizers the liquid jet is forced into a rotating device that governs the size of the droplets. They can generate very fine sprays and they are relatively cheap. However, they lead to poor high-altitude relighting conditions.
- The pressure swirl atomizers convert the pressure into kinetic energy and thus lead to a conical spray with high relative velocity between the fuel and the carrier phase.
- The airblast atomizers generate an accelerated air flow parallel to the fuel injection. This creates a shear that helps atomizing the liquid jet. It is best suited when having a high-speed airflow to generate a spray of low relative speed.

In the aeronautical combustors, both airblast and pressure swirl atomizers can be found but the mostly used is the pressure swirl atomizer.

As an example, for air assisted atomization, the influence of the dynamic forces is depicted through the increase of the aerodynamic Weber number and decrease of Ohnesorge number in Figure 1.2. The Weber number (*Weber 1931*) is the ratio of the dynamic forces over the surface ones, defined as:

$$\mathrm{We} = \frac{\rho_g X (|\overrightarrow{\mathbf{U_l}} - \overrightarrow{\mathbf{U_g}})|^2}{\sigma_{l,g}}, \tag{1.1}$$

where X is a characteristic length of the interface, ρ_g is the gas density, $(\overrightarrow{\mathbf{U_l}} -$

$\overrightarrow{\mathbf{U_g}}$) is the drift velocity between the two phases and $\sigma_{l,g}$ is the liquid surface tension. Its gives a degree of the external stresses acting on the droplet or the liquid column to the stability of the droplet ensured by the surface tension.
The Ohnesorge number (*Ohnesorge 1936*) is the ratio of the viscous forces to surface tension and inertial forces:

$$\mathrm{Oh} = \frac{\mu_l}{\sqrt{\rho_l \sigma_{l,g} X}}, \tag{1.2}$$

where ρ_l is the liquid fuel density and μ_l is the liquid fuel dynamic viscosity. High Oh indicates that liquid is too viscous to atomize properly. And low Oh means that multiple atomization can occur (*McKinley and Renardy 2011*).

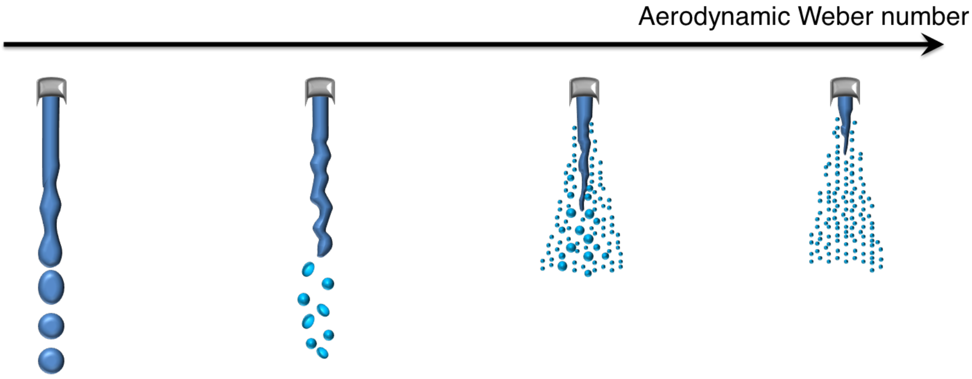

Figure 1.2: *Influence of the drift velocity on the atomization*

For the liquid fuel used in aeronautical burners, the Ohnesorge number is small: $\mathrm{Oh} < 0.1$ (*Renaud 2015*). The choice of such a liquid is very important in order to have a compact atomization process, reduce the region of separated phases and therefore to be able to ignite the spray at a relatively short distance from the injector.
With the pressure swirl and airblast injectors, near the injector, We is high leading to primary atomization. The resulting spray far from the injector is characterized by a moderate We.
Based on these dimensionless numbers, we can assume that in the aeronautical combustion chamber the disperse phase is predominant, it contains droplets of various sizes that are quasi spherical. This assumption was validated through experiments on several test rig of aeronautical-type spray burners. For example, the experimental results on MERCATO showed that the separated phase is confined to the immediate vicinity of the injector, namely at 6 mm from the atomizer. After this distance, only spherical dispersed droplets of fuel of different sizes were observed (*Garcia-Rosa 2008*).

1.1.1 Modeling levels and related numerical strategies

The injection and primary atomization can be either solved through the simulation of the separated phases or modeled through physics-based and/or geometrical based assumptions.

The modeling and simulation of the separated phases that is shown in navy blue in Figure 1.1 is based on the resolution of two separated set of equations for the non-coexisting phases. These sets of the local instantaneous equations can be directly solved in the context of DNS. The position of the interface and associated discontinuous properties across the interface must be precisely solved to impose satisfactory boundary conditions for both fluid domains. The resolution of this interface can be done using Lagrangian methods, such as front tracking (*Hirt et al. 1974; Popinet and Zaleski 1994*) and marker-and-cell (MAC) (*Harlow and Welch 1965*), or Eulerian methods based on interface capturing and reconstruction, such as level set (LS) (*Osher and Fedkiw 2001; Herrmann 2005; Tanguy and Berlemont 2005; Arienti and Sussman 2014*), volume-of-fluid VOF (*Hirt and Nichols 1981; Aulisa et al. 2003; Fuster et al. 2009; Herrmann 2008*) and hybrid methods VOF/LS (*Vu et al. 2016; Menard et al. 2007; Shinjo and Umemura 2010; Shinjo and Umemura 2011*).

These techniques have been improved through the years (*Popinet and Zaleski 1994; Desjardins et al. 2013; le Chenadec and Pitsch 2013*). In addition, reduced order models were used for the modeling of the diffuse interface such as averaging process (*Drew and Passman 1999*). This is done to decrease the cost of these methods (*Pai and Subramaniam 2012*). In this case, the interface is treated as a mixing zone since at the same macroscopic position, both of the phases coexist and each occupies a fraction of the volume. *Baer and Nunziato (1986)* derived models based on fluid mechanics and thermodynamics of reversible processes. Another strategy is based on the principle of least action (*Drui et al. 2016*). However, these models cannot predict precisely the atomization process. To avoid this limitation, a transport equation for interface area density can be added (*Vallet et al. 2001; Jay et al. 2006; Lebas et al. 2009*), but the problem of describing the size dispersion of the disperse phase remains an open problem for these models (*Essadki et al. 2016*).

When choosing to simulate the liquid jet from the beginning of the injection, a challenge is faced for the atomization process since one should accurately describe both the separated phases and the spray. This transition between the separated phases and the disperse phase is critical, especially when the desired final state is the disperse phase which is the case in the combustion domain (*Emre 2014*).

The modeling of this transition is a building block for future complete simulations. For more information one can refer to the work of *Reveillon et al. (2013); Le Touze (2015); Zuzio et al. (2016)*. This subject is also an on-going work by *Drui et al. (2016); Essadki et al. (2016)*.

Since the simulation of the full liquid jet faces many challenges, especially for the accurate transition between the separated phases regime and the spray regime, not all the scales can be simulated in the combustion chamber. The injection process itself is not simulated with the primary atomization and the separated phases are not resolved. Based on the conclusion of section 1.1, one can focus on the description of the disperse phase for predictive simulations in the combustion chamber.

1.2 Levels of resolution of the disperse phase

1.2.1 Microscopic resolution

The most detailed modeling level is the full direct numerical simulation (DNS), which provides a model for the dynamics of the interface between the disperse phase and the continuous phase, as well as the exchanges between these two phases.

Two big families of models deals with this detailed level of description.

The first one is the sharp interface tracking methods that are usually used for separated phases and was presented in subsection 1.1.1. An example of the VOF method for DNS of droplet-laden incompressible turbulence is shown in figure 1.3(a), illustrating the normalized curvature (colored) and the vorticity magnitude contours (grey scale) (*Baraldi and Ferrante 2012*).

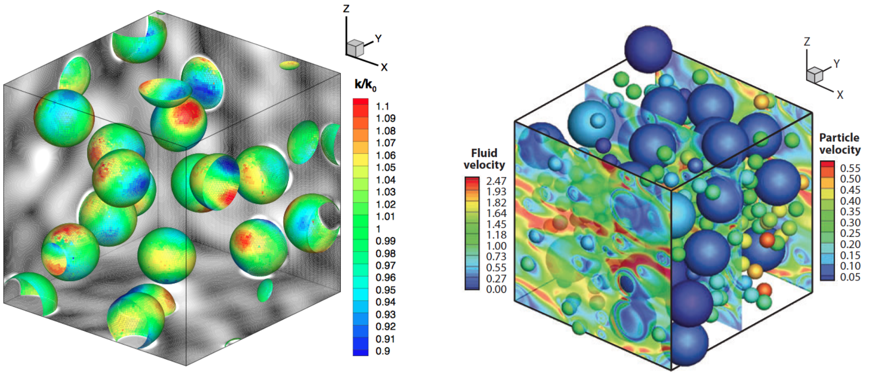

(a) DNS of droplet laden decaying isotropic turbulence by *Baraldi and Ferrante (2012)*

(b) PR-DNS of a dense bidisperse gas-solid suspension(done by Subramaniam and Tenneti)

Figure 1.3: *Fully resolved simulation examples*

The second family is the particle resolved direct numerical simulation where the exact Navier Stokes equations are solved by fully resolving the particles using imposed boundary conditions at the surface of each particle (*Xu and Subramaniam 2010*; *Tryggvason et al. 2010*; *Subramaniam 2013*). This full resolution at the microscopic level is very rich in information for each particle but is therefore computationally very expensive. In fact, the cost of this method is proportional to the number of particles. For this reason, its usage is limited to the academic field, but it is helpful to extract closure laws for the velocity fluctuations, the drag and the heat transfer. For the time being, a limited number of particles can be simulated with this method. For instance, particle resolved direct numerical simulation (PR-DNS) has been used in the literature to extract closure laws for drag, velocity fluctuations, and heat transfer for particle laden flow (*Tenneti et al. 2011; Tenneti and Subramaniam 2014*). Another result for a dense bidisperse gas-solid suspension with a total solid volume fraction of 0.4 and mean slip Reynolds number of 50, performed by Subramaniam et al. is shown in figure 1.3(b), where the particles are colored by the magnitude of their velocity. These approaches are still on going research topic (*Brändle De Motta et al. 2016; Rosso et al. 2016; Richter et al. 2016*).

Even if these two families are capable of studying complex detailed phenomena, their application are limited to specific cases where the resolution of the flow around the particles is mandatory for capturing the underlying physics. This is the case for example for the sedimentation and group combustion. However when the local resolution of the flow around and inside the droplet or the particle does not affect the physics, a more general level of resolution can be adopted based on coherent assumptions.

1.2.2 Scales separation

The disperse phase flows have a multi-scale nature. Several scales can be distinguished as it was illustrated in Figure 5 of the introduction:

- Microscopic: this level considers the atoms and molecules. But usually when talking about the microscopic level in the domain of disperse phase model, one refers to the vision where the particles size defines the scale. The microscopic description is essential when the smallest scales of the flow (Kolmogorov length scale) is smaller that the droplet size. In this case, the flow around and in the droplet should be resolved in order to capture all the dynamics. The resolution at this level was presented in the previous paragraph.
- Mesoscopic: this denotes intermediate scales where the variations of the flow are limited. In this case, the level of the resolution of the disperse phase is reduced; fewer details are resolved in comparison with the microscopic resolution. This level is accessible whenever the local microscopic interaction of fuel droplets with the surrounding gas is a short-range interaction that is quickly dissipated by viscosity. Practically, this is the case where the droplets are smaller than the Kolmogorov length scale of the undisturbed gas flow. Thus, one can neglect these microscopic interactions. More generally, if the microscopic interaction does not affect the general flow, the separation of scales is valid. Thus, the droplets are

described based on a point-particle assumption by neglecting the volume that they occupy. The conservation laws of the gas phase can be written everywhere in the domain.

- Macroscopic: defined by the control volume of the combustion chamber and by the macroscopic variables that one need to retrieve. Once the separation is set between the microscopic and mesoscopic scales, the mesoscopic equation can then be solved at the mesoscopic level or at the macroscopic level. The latter can be done by reduced models such as the two-fluid models already discussed in subsection 1.1.1, or by moment methods that are the subject of this thesis.

The separation between scales is influenced by all the underlying phenomena that the multiphase flow faces. For example, the interaction between the particles and the turbulent eddies generates a separation between the length scales of the motion of particles influenced by the energetic eddies and those influenced by dissipation. Through the scale separation assumption, the droplet modeled by a point-particle interacts locally with the gas through exchanges terms that are assumed to be localized in physical and phase space. These terms are modeled based on the scale separation by using the models of single droplet. This approach is valid only if short range interactions occur between the inclusions (*Crowe et al. 1998*). Thus, the scale separation assumption is not valid if rare events condition the observable dynamics (*Doisneau 2013*).

1.2.3 Boundary conditions

In order to be able to simulate the disperse phase without having the details of the description of the separated phase and of the transition region between the separated regime and the disperse phase, boundary conditions should be imposed at the beginning of the disperse regime. These boundary conditions chosen for the simulation of the disperse phase play a key role and can affect the type of the obtained disperse phase and, as a result, the dynamics of this phase. They are obtained based on the inlet conditions of the injector tip. This is sought as a modeling of the injection system and is devised based on phenomenological models and appropriate volume balances. Out of the existing models, we briefly present hereafter two models:

- The Downstream Inflow Turbulent Boundary Condition (DiTurBC) (*Martinez et al. 2010*), which is used to deduce the velocities of gas and liquid, the volume fraction and the droplet size profiles on a plane perpendicular to the spray axis, located downstream from the nozzle exit, at a distance nearly equal to ten times the exit diameter of the nozzle. This is represented in Figure 1.4. This is based on a first estimate of the properties of the flow at the nozzle exit. This model was developed and validated in the context of 3D simulations of diesel sprays.
- The Fuel Injection Method by Upstream Reconstruction (FIM-UR) (*San-*

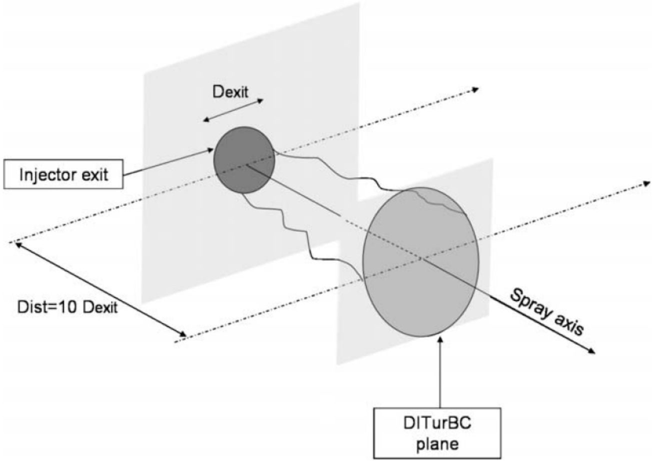

Figure 1.4: *Schematic representation of the DiTurBC model. (Source: Martinez et al. (2010))*

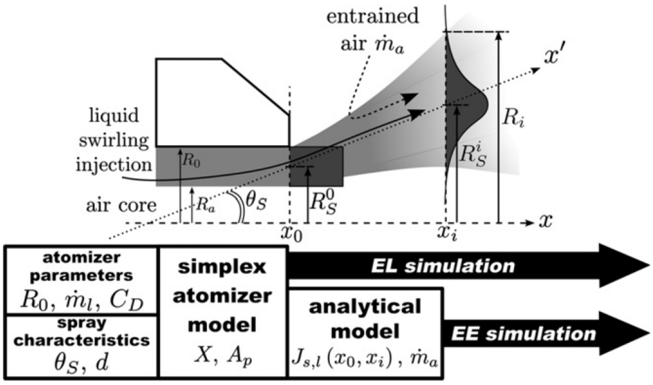

Figure 1.5: *Schematic representation of the FIM-UR methodology. (Source: Sanjosé et al. (2011))*

josé et al. 2011) is based on an autosimilarity assumption, as illustrated in Figure 1.5 (*Martinez et al. 2010*). It was initially designed for injection of one size droplets, and extended afterward to account for the dispersion in size by distributing the liquid volume fraction and droplet number density over all diameters (*Vié et al. 2013*).

One of the disadvantages of these models is that they rely on experimental data to adjust parameters such as the droplet diameters. As a consequence, even if these models are for now helpful to run computations, a long-term solution is still needed. This highlights to importance of the on-going work of modeling the transition between the separated and disperse regimes.

1.3 Physics of the disperse phase

The dynamics of the disperse phase depends on various phenomena and interactions whether between the droplets themselves or between the droplets and the carrier phase as it was illustrated in Figure 3 in the introduction. Since the focus of this thesis is on the spray/turbulence interaction, the other phenomena will not be taken into account.

Under this assumption, the forces that will define the dynamics of the disperse phase are the inter-droplets collisions and the drag whose intensities are measured through respectively two non-dimensional numbers: the Knudsen number (Kn) and the Stokes number (St).

1.3.1 Knudsen number

The Knudsen number depicts an estimate of the relative strength of the droplet-droplet collisions compared to the free transport or streaming operator (*Struchtrup 2005*). It is the ratio of the mean free path of the droplets λ_0 to a representative length scale of the flow L_0:

$$\mathrm{Kn} = \frac{\lambda_0}{L_0}. \tag{1.3}$$

For dense spray, the Knudsen number is small and the inter-droplet collisions are significant. In this case, the velocity relaxes toward an hydrodynamic equilibrium (such as the Maxwell-Boltzmann distribution for the local thermodynamical equilibrium in the kinetic theory of gas).

On the other hand, for dilute spray, the collision rate is negligible and does not affect the flow dynamics. Therefore, the Knudsen number is high and the underlying physics is more complex.

A dilute spray is studied in this thesis, thus the case of infinite Kn is chosen all along this thesis. It is essential to note that this collisionless condition is not by any means imposed by the modeling approach and it does not present any limitation of the models presented in this work.

A review of the collisional regimes can be found for example in *Crowe et al. (1998); Sirignano (1999)*.

1.3.2 Stokes number

The Stokes number quantifies the intensity of the droplets inertia. It is the ratio of the droplets relaxation time τ_p to a characteristic time scale of the carrier flow τ_G:

$$\mathrm{St} = \frac{\tau_p}{\tau_G}. \tag{1.4}$$

This number is a good indicator for the effect of droplets inertia (*Wells and Stock 1983; Maxey and Riley 1983*) in a way that different regimes for the droplets advection can be distinguished according to the various levels of St.

1.3.2.1 Size polydispersion

The particles in the disperse phase can have different sizes. This size dispersion is called polydispersity in opposition with monodispersity, where only one size is treated.

Since the mass, momentum and heat exchanges between the disperse and the carrier phase depends on the size, it is important to correctly model the polydispersion in order to be able to capture the size-conditioned underlying physics. In the literature, many references study the general behavior of the disperse phase with a monodisperse model based on an average size. One of the most used choices is the Sauter Mean Diameter. However, this assumption may be very limiting when size-coupling is important and the particle response is non-linear and when the polydispersity highly affect the macroscopic physical behavior. This is for example the case for the cold flow of MERCATO, the aeronautical configuration test rig of ONERA, within which *Vié et al. (2013)* and *Senoner et al. (2009)* presented the influence of the polydispersion on the evaporation time, the mean and RMS properties of the disperse phase and the spatial dispersion induced by the size conditioned dynamics. One of the interesting results in this work is the comparison of the vapor fuel mass fraction using a monodisperse model and a polydisperse one as seen in Figure 1.6.

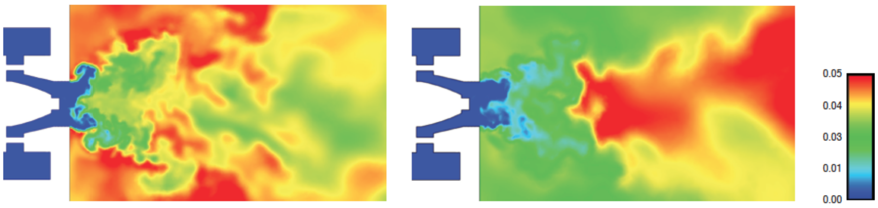

Figure 1.6: *Comparison of the fuel vapor mass fraction on the MERCATO test rig: monodisperse case (left) and polydisperse case (right) (Source: Vié et al. (2013))*

In this work, the inclusion is called particle even if it refers physically to a droplet since the presented methods can be applied to both particles and droplets.

1.3.3 Effect of the turbulence on the disperse phase

The interaction of particles with turbulent eddies leads to different behaviors according to the particles inertia. This can be seen as a dependence on the Stokes number, as mentioned earlier in this section.

For small St, the droplets will have nearly the same velocity as the gas. The neighbouring velocities will not have velocity dispersion since they interact with the same carrier dynamics (*Laurent and Massot 2001; Simonin et al. 2002*). In this case, the interaction between the particles and the turbulent eddies

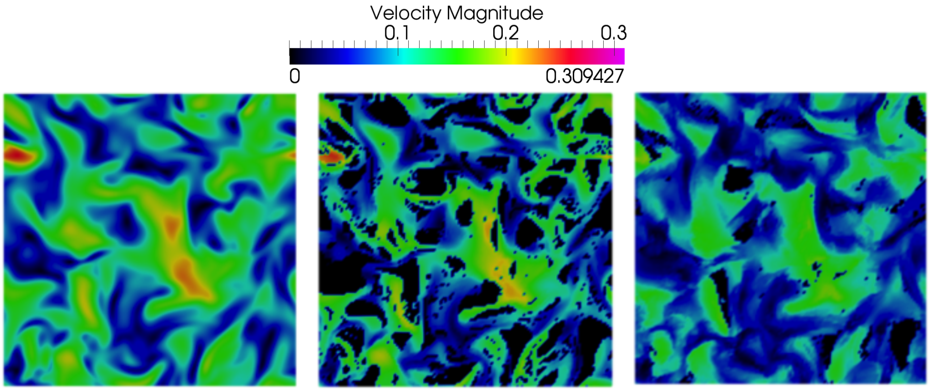

Figure 1.7: *2D view of the magnitude of the velocity field for the gas phase (left) and for two cases of disperse phase with low inertial particles (center) and with inertial particles (right). The disperse phase simulations are done with a Lagrangian method, the black regions referring to the regions of vacuum. This configuration is presented in Part III.*

generate small scale preferential concentration effects since the compressibility effect brings the particles together to the high strain/low vorticity zones (*Maxey 1987*).

On the other hand, with increasing St the particles are less influenced by the carrier phase motion. The neighbouring particles might have uncorrelated velocities since they are influenced by the memory of their interactions with very distant, independent carrier turbulence eddies (*Doisneau 2013; Février et al. 2005*). As a consequence, a particle will have its own motion driven by its inertia. In this case, multi-scale clustering is generated by a sweep-stick mechanism where the inertial particles stick to zero-acceleration points (*Coleman and Vassilicos 2009; Obligado et al. 2014*).

The different levels of segregation depending on St (*Zimmer et al. 2003*) can change the local mixture fraction and the evaporation rate (*Reveillon and Demoulin 2007*). The difference between these two cases is illustrated in Figure 1.7 showing the magnitude of the velocity field for the gas phase and for two cases of disperse phase the first with low inertial particles and the second with inertial particles.

1.3.4 Coupling with the carrier phase

Elghobashi (1991; 1994) classified the regimes of particle-laden turbulent flows according to the interaction between the particles and the turbulence. This classification is done as a function of the volume fraction φ_v and the Stokes number St as illustrated in Figure 1.8.

- For $\varphi_v < 10^{-6}$, the particles motion depends on the state of turbulence without inducing a feedback on the turbulent carrier phase. Due to this negligible effect of the particles on turbulence, the interaction between

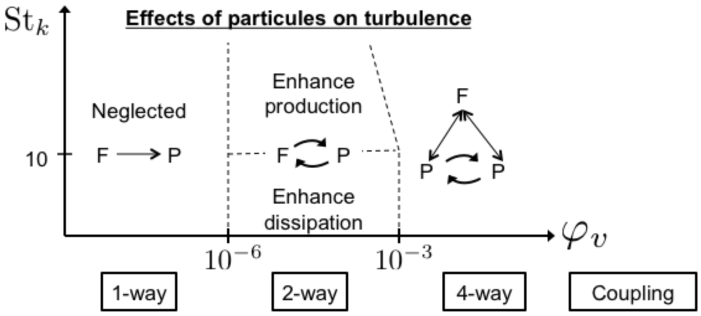

Figure 1.8: *Diagram illustrating the regimes of interactions of the disperse phase with the turbulence, adapted from Elghobashi (1991; 1994)*

the particles and turbulence is a one-way coupling.

- For $10^{-6} < \varphi_v < 10^{-3}$, a second regime is obtained where the volumetric particle loading is large enough to alter the turbulence structure. In this case, one should account for the two-way coupling between the phases. For small Stokes number, the particles increase the dissipation rate of turbulence energy. On the other hand, for large St, vortex shedding starts to take place resulting in enhanced production of turbulence energy (*Elghobashi 1991*).
  Below the $\varphi_v = 10^{-3}$ limit, the particulate phase is considered to be dilute.
- For $\varphi_v > 10^{-3}$, the particulate phase is dense and particle/particle collisions appear and should be accounted for in the modeling along with the two-way coupling between the two phases. The resulting regime is the four-way coupling regime.

This classification was proposed earlier in the thesis of *O'Rourke (1981)*, when the three regimes corresponded respectively to very thin, thin and thick sprays. In the combustion chamber the spray is in the dilute regime, since $\varphi_v < 10^{-3}$. Only one-way coupling or two-way coupling with the carrier should be taken into account. In this thesis, the study is restricted to one-way coupling. Nonetheless, we keep in mind that the vision of using methods that can be extended to two-way coupling.

1.4 Description of the disperse phase

Due to the complex and multi-scale nature of the disperse phase, many modeling approaches can be found in the literature. Actually, this phase can be described from different points of view, leading to various models having each a given level of details. These approaches range from the most detailed models at the microscopic level to the most general continuum models at the macroscopic level.

The microscopic models give detailed description of the interface between the

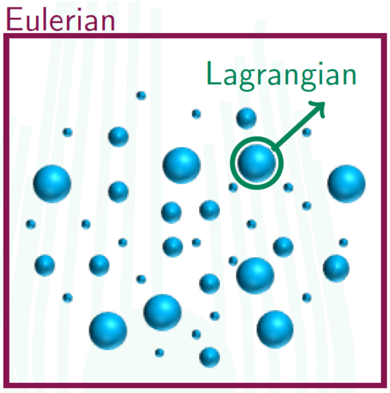

Figure 1.9: *Simplified illustration of the modeling strategies for disperse phase flows.*

two phases. This level contains all the variables needed to completely describe the two-phase flow, when coupled with a DNS description of the carrier phase. These type of models will not be used since they are very expensive and are not based on the scale separation assumption, as mentioned in the subsection 1.2.2.

A less detailed strategy at the mesoscopic level is the Discrete Particle Simulation (DPS), which is a deterministic Lagrangian approach, where the particles are tracked.

At this mesoscopic level, a probabilistic description of the disperse phase in the phase space is obtained through the kinetic approach. This intermediate model is formulated in terms of the Population Balance Equation (PBE) or the Generalized Population Balance Equation (GPBE), also called the Williams-Boltzmann equation (WBE), that gives a statistical description of the Number Density Function.

In comparison with the microscopic description, the number of variables used in this case is reduced but the number of degrees of freedom in this high dimensional phase space is still very high. Thus, directly solving the WBE is very expensive. Instead, it can be solved using Lagrangian approaches: the direct simulation Monte-Carlo method (DSMC) or the stochastic parcel. The former consists in tracking several computational particles representing one physical particle whereas the latter tracks a group of physical particles by a computational particle.

On the other hand, Eulerian approaches also exist in the literature to develop macroscopic models based on the conservation laws of the moment of the NDF[1].

A simplified illustration of the Lagrangian DPS and Eulerian approaches is shown in Figure 1.9 for a given grid element of the carrier phase mesh. It de-

---

[1] Other macroscopic models can be obtained directly from the microscopic model through ensemble or volume averaging. For more information about the two-fluid method one can refer to the article of *Drui et al. (2016)* and the references therein.

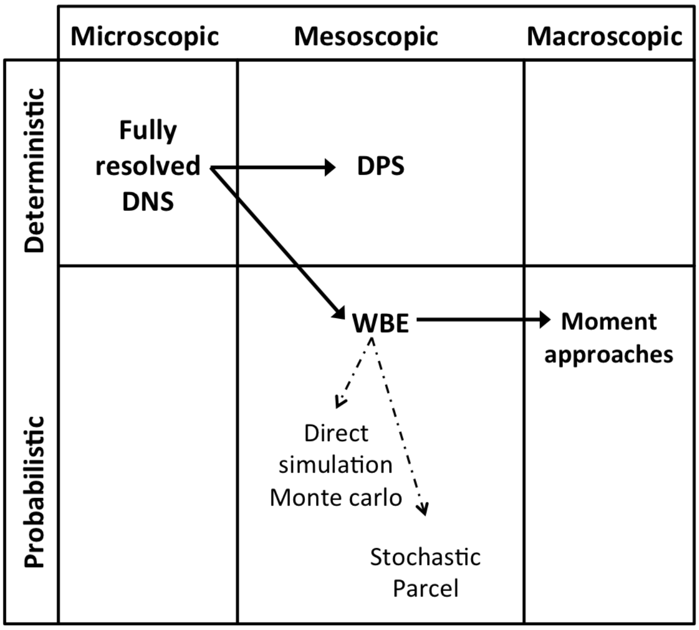

Figure 1.10: *Modeling strategies for disperse phase flows: from the microscopic scale to the macroscopic scale.*

picts the tracking nature of the Lagrangian method and the macroscopic nature of the Eulerian method. However, this representation does not delineate the statistical description obtained with the Eulerian approach.
These various modeling strategies are classified according to the nature of the underlying description whether deterministic or probabilistic and to the level of this description (see Figure 1.10). Each one of these approaches is introduced briefly in the following sections.

1.5 Mesoscopic level

Instead of adopting a microscopic approach, and suffering from its high cost and its impracticality for real applications, one can use a mesoscopic description for the disperse phase. This description is possible due to the scale separation assumption presented in subsection 1.2.2. This is done by using mesoscopic closure for which the forces and the collisions are localized in physical and phase space (*Massot 2007*; *Fox 2007*).

1.5.1 Discrete Particle Simulation

Actually, in some relatively dilute cases each physical droplet can be tracked as a Lagrangian numerical particle in the carrier flow. These individual droplets evolve through a system of Ordinary Differential Equations (ODE) of the

droplet parameters at its center of mass namely: the k^{th} droplet size S_k, its position x_k, velocity $\vec{\boldsymbol{c}}_k$ and temperature T_k (*Riley and Paterson 1974; Squires and Eaton 1991b; Zhu et al. 2007*).
These ODEs read:

$$\mathrm{d}_t\vec{\boldsymbol{x}}_k = \vec{\boldsymbol{c}}_k, \quad \mathrm{d}_t\vec{\boldsymbol{c}}_k = \overrightarrow{\mathbf{F}}_k, \quad \mathrm{d}_t S_k = R_{Sk}, \quad \mathrm{d}_t T_k = H_{Tk}, \tag{1.5}$$

where $\overrightarrow{\mathbf{F}}_k$, R_{Sk} and H_{Tk} are respectively the local external forces per unit mass on the droplet, the rate of change of its size and the heating rate. These source terms are functions of the droplet variables and the local gas properties.
This approach is the Discrete Particle Simulation (DPS), where the particles are treated in a point-wise manner, neglecting the effect of particle volume occupation. It was first introduced by *Riley and Paterson (1974)*. This method is also called point-particle DNS (*Pai and Subramaniam 2012*). The different phenomena such as collisions and coalescence are treated deterministically. For more information on this subject, one can refer to the work of *Fede and Simonin (2006); Wunsch (2009); Fede and Simonin (2010); Thomine (2011)*.
The accuracy of this method is directly dependent on the accuracy of the mesoscopic closures, but ends up being highly intuitive and easy to implement, at least for sequential codes. For this reason, this method is highly used in the literature, whether for example for solid particle dispersion (*Squires and Eaton 1991b; Squires and Eaton 1991a; Elghobashi and Truesdell 1992*) or for droplets in the combustion application (*Mashayek et al. 1997; Miller and Bellan 2000; Reveillon and Vervish 2005; Fréret et al. 2008*).
This Eulerian-Lagrangian approach with retro-coupling to the carrier is applied for example by Capecelatro et al. to turbulent liquid-solid slurries in horizontal pipes (2013b) and to cluster-induced turbulence (2014; 2015), where the approach accounts for the momentum coupling with finite-size inertial particles. Another example of an application for this two-way coupled Eulerian-Lagrangian approach is the radiation induced turbulence carried by Zamansky et al. (2014; 2016) for particle-laden flows. The projection step for the coupling is done by *Capecelatro and Desjardins (2013a); Zamansky et al. (2014)*, using Gaussian projection with a mesh-independent width. This decreases the error induced by the classical projection strategies which does not ensure mesh convergence.
It is important to note that when it comes to complex simulations involving a large number of droplets and High Performance Computing (HPC), this type of approach could have to deal with an intractable number of particles that are not homogeneously distributed in the combustion chamber for example. This leads to strong constraints in terms of computational time, either because of the number of particles to be solved or because of the load balancing issues inherent to the inhomogeneity of the disperse phase.
An example of the speedup of this Lagrangian method for a monodisperse simulation of nearly 560,000 particles in comparison with the speedup of a single

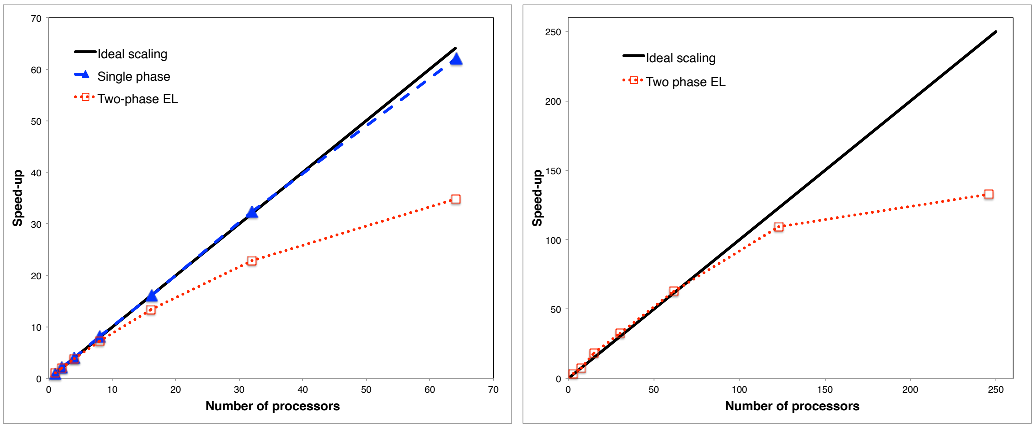

(a) by *Garcia (2009)* using 0.56 million particles on 3.1 million cells, compared with the speedup of the Eulerian simulation for the carrier phase

(b) by *Sun and Xiao (2016)* using 5.3 million particles on 1.3 million cells

Figure 1.11: *Speedup for Eulerian-Lagrangian simulation for two-phase flow based on a stong scaling*

phase carried out by *Garcia (2009)* is shown in Figure 1.11(a). This is done on a tetrahedron-based grid containing 3,115,898 cells and 549,369 nodes. The drop of the parallel performance observed for the Lagrangian simulation is mainly due to the parallel load imbalance generated by the partitioning algorithm which is a recursive inertial bisection (RIB) partitioning algorithm in this case. Thus, the dynamic load balancing is helpful for an efficient parallelization since if the domain is decomposed in the same way for the entire computation, some processors will have to compute a high number of particles while other does not have an important load (*Riber et al. 2009*).

It is important to note that for this same configuration the speedup was improved when the simulation was carried out on a hexahedron based grid (with 3,207,960 cells and 3,255,085 nodes) instead of the tetrahedron-based one (*Riber et al. 2009*; *Garcia 2009*).

Since the parallel implementation is one of the most challenging issue in the Lagrangian simulation, it is still studied in the literature (*Kaludercic 2004*; *Darmana et al. 2006*; *Kafui et al. 2011*; *Dubey et al. 2011*; *Guedot 2015*; *Sitaraman and Grout 2016*) in order to improve the partitioning algorithm and the load balancing strategies to be able to handle cases where the workload on each processor is severely skewed due to an uneven distribution of particles (*Pankajakshan et al. 2011*).

A recent example is shown in Figure 1.11(b) for a fluidized bed configuration. This test is performed by *Sun and Xiao (2016)* using 5.3 million particles on 1.3 million cells. In this case, the speedup is close to ideal for less than 100 processors but drops above this limit.

Knowing that the speedup is higher in this second example in comparison with the one shown in Figure 1.11(a), one should keep in mind that such a comparison is not very conclusive since the studied configurations and the number of particles per cell are different.

Apart from the HPC issues, there is also the problem of statistical convergence. Actually, when one wants to investigate the statistics of the disperse phase, many realizations must be performed, leading to a great increase of the overall computational cost.

In addition, the initial and boundary conditions necessary for such spray computations can be given statistically so that the unclear deterministic knowledge of these conditions adds some challenges to this method. This is the case for example when the injection and primary atomization of the spray are not solved and simplified models are used instead to deduce the mean and fluctuating values or even the PDF for the interesting parameters as mentioned in subsection 1.2.3.

1.5.2 Williams-Boltzmann equation

To avoid the resolution of every N physical droplets in the computational domain, one should retain a statistical point of view, which is based on the evolution of a Number Density Function (NDF). This NDF is obtained by ensemble averaging over a large number $\mathscr{N}_{f,p}$ of two-phase flow realizations $\mathscr{H}_{f,p}$ (*Février et al. 2005*):

$$f(t,\vec{\boldsymbol{x}},\boldsymbol{\xi}) = \lim_{\mathscr{N}_{f,p}\to\infty}\left[\frac{1}{\mathscr{N}_{f,p}}\sum_{\mathscr{N}_{f,p}}\sum_{m=1}^{N} P_m(t,\vec{\boldsymbol{x}},\boldsymbol{\xi},\mathscr{H}_{f,p})\right], \tag{1.6}$$

where t is the time, $\vec{\boldsymbol{x}}$ the position and $\boldsymbol{\xi}$ the internal phase space. The "fine grained" PDF, as called by *O'Brien (1980); Pope (1985)* in the context of reacting turbulent flows, is one realization of position and internal phase variables in time of any given particle (*Simonin et al. 2002*)
$P_m(t,\vec{\boldsymbol{x}},\boldsymbol{\xi},\mathscr{H}_{f,p}) = \delta(\vec{\boldsymbol{x}}-\vec{\boldsymbol{x}}_p^m(t))\delta(\boldsymbol{\xi}-\boldsymbol{\xi}_p^m(t))$.

As a consequence, the NDF is defined such that $f(t,\vec{\boldsymbol{x}},\boldsymbol{\xi})\mathrm{d}\vec{\boldsymbol{x}}\mathrm{d}\boldsymbol{\xi}$ is the probable number of particles that are located in the volume $[\vec{\boldsymbol{x}},\vec{\boldsymbol{x}}+\mathrm{d}\vec{\boldsymbol{x}}]$, at time t and whose internal phase space is in the interval $[\boldsymbol{\xi},\boldsymbol{\xi}+\mathrm{d}\boldsymbol{\xi}]$ (*Sainsaulieu 1995; Simonin 1996*).

Thus, the obtained mesoscale model is an average of many realizations that may include different behaviors on the microscopic scale but have the same mesoscale behavior. In this case, instead of solving N systems for the particles, each including a number of equations depending on the degree of freedom (DoF) considered for a particle, a statistical point of view is retained where the information on the DoF is included in the NDF. To do so, the droplets or particles are then represented as point particles by considering that the volume occupied by these particles is negligible compared to the one occupied by the carrier phase.

The dimension of the phase space is related to the number of internal coordinates necessary to describe the physics of one particle. The sole choice of the phase space is strongly related to the physics one wants to describe.
The NDF satisfies the WBE (*Williams 1958; Williams 1985; de Chaisemartin 2009; Laurent and Massot 2001*). If we consider, for example, that the particles are spherical, the phase space $\boldsymbol{\xi} = (\vec{\boldsymbol{c}}, S, T)$ is then composed of the velocity, size and temperature variables. In this case, the WBE reads:

$$\partial_t f + \partial_{\vec{\boldsymbol{x}}} \cdot (\vec{\boldsymbol{c}} f) + \partial_{\boldsymbol{\xi}} \cdot (\mathbf{R}_{\boldsymbol{\xi}} f) = \Gamma + Q. \tag{1.7}$$

The first two terms are the free transport of the disperse phase. The last term of the left hand side is the evolution of the NDF in the phase space and the source terms Γ, Q are the collision/coalescence and secondary break-up operators.
This mesoscopic formalism is also referred to as the kinetic approach, since it was inspired by the kinetic theory of gases (*Boltzmann 1872; Chapman 1918*). However, it is important to note the difference of the modeling level between the microscopic nature of the kinetic theory of gases and the mesoscopic nature of the, so-called, kinetic approach for the description of the disperse phase that is based on the scale separation.
In this work the coalescence and fragmentation terms are not accounted for. For more information on this subject one can refer to the thesis of *Doisneau (2013)* and the references therein. Under this condition and when the Knudsen number is infinite, the WBE becomes:

$$\partial_t f + \partial_{\vec{\boldsymbol{x}}} \cdot (\vec{\boldsymbol{c}} f) + \partial_{\vec{\boldsymbol{c}}} \cdot (\overrightarrow{\mathbf{F}} f) + \partial_S (R_S f) + \partial_T (H_T f) = 0, \tag{1.8}$$

where $\overrightarrow{\mathbf{F}}$ is the acceleration of the droplets due to external force (drag force, gravity), R_S is the evaporation rate (rate of change of the droplet size due to evaporation), H_T is the rate of change of the droplet temperature due to heat transfer.

It is important to note that even though simple droplet models are adopted in this work, the kinetic approach and the modeling procedure used can be extended to refined droplets laws if these closures do not include any history terms. For example, the Basset forces can not be modeled through the kinetic equation since they include history terms (*Laurent and Massot 2001*).

For tracers such as aerosols, the particles follow the carrier phase since their inertia does not have an important effect on the underlying physics. In this case there is no need to account for the velocity in the internal phase space. A Population Balance Equation is obtained that is also called General Dynamic

Equation (*Friedlander 2000; Nguyen et al. 2016*).

The main consequence of the high dimensional phase space is that solving the WBE using for instance a finite volume discretisation is hardly tractable, especially for 3D computations. However, such a work is done for plasmas simulation through the Vlasov solvers (*Filbet and Sonnendrücker 2003*).
Since the WBE is well defined and closed, its resolution techniques available in the literature are presented hereafter. These methods are divided into two families: the Lagrangian statistical approaches and the Eulerian methods.

1.5.3 Lagrangian Particle Tracking

In this subsection, the Lagrangian approach is depicted through two possible methods having different resolution level and accuracy compared to the deterministic Lagrangian technique DPS.

1.5.3.1 Direct Simulation Monte-Carlo method

The most accurate method for solving the WBE is the Lagrangian-Monte-Carlo method (*Subramaniam 2001*), especially in the field of DNS. It is also called direct simulation Monte-Carlo method (DSMC) by *Bird (1994)* in the context of rarefied gas and developed further by *Alexander and Garcia (1997)*. It approximates the NDF by a sample of discrete statistical particles representing a droplet. For this reason a high number of numerical particles is needed. The NDF is discretized into a sum of Dirac's δ-functions in the phase space:

$$f(t, \vec{\boldsymbol{x}}, \boldsymbol{\xi}) \approx \sum_{k=1}^{N_s} w_{pk} \delta(\boldsymbol{\xi} - \boldsymbol{\xi}_{pk}), \tag{1.9}$$

where N_s is the number of samples, w_{pk} is a weight and $\boldsymbol{\xi}_{pk}$ is the coordinate of each sample in the phase space. The weight is added to the numerical particles to adapt them to the needed refinement (*Doisneau 2013*). Since the weight is a real number, the numerical particle may represent a fraction of the physical particle or droplet. Each sample is tracked by using a system of ODE:

$$\frac{d\vec{\boldsymbol{x}}_{pk}}{dt} = \vec{\boldsymbol{c}}_{pk}, \tag{1.10}$$

$$\frac{d\vec{\boldsymbol{c}}_{pk}}{dt} = \vec{\mathbf{F}}(\boldsymbol{\xi}_{pk}), \tag{1.11}$$

$$\frac{dS_{pk}}{dt} = R_S(\boldsymbol{\xi}_{pk}), \tag{1.12}$$

$$\frac{dT_{pk}}{dt} = H(\boldsymbol{\xi}_{pk}), \tag{1.13}$$

where all the terms in the Right Hand Side (RHS) except the droplet velocity shall depend on the carrier gas phase properties (such as gas density, velocity

or temperature) localized at the particle position.
This method is not to be mixed up with the particle method applied for the fluid phase also called the weighted particle method (*Raviart 1985; Mas-Gallic and Raviart 1987; Degond and Niclot 1989*).
The DSMC gives the statistical result through the ensemble average of the different numerical particles. However, its accuracy is highly linked to the number of particles, since a large number of numerical particles is needed to reduce the noise and reach statistical convergence. In addition, a projection step is needed in order to couple this Lagrangian approach with the Eulerian resolution for the carrier phase. Another disadvantage of this method is the difficulty of load balancing (*Sitaraman and Grout 2016*) and efficient parallel implementation, as already explained for the DPS. These disadvantages are common to the three Lagrangian techniques presented in this section. In addition, the two-way coupling with the carrier phase is a stumbling block for this method. A possibility to overcome this challenge is through the particle-in-cell (PIC) method (*Filbet and Rodriges 2016; Dawson 1983*) used for Vlasov-Poisson system in plasma simulations.
It should be noticed that the above system does not take into account collisions, coalescence or break-up effects. Actually, since these terms imply creation/destruction of droplets, they are not included in the ODE system and usually require an additional step in the resolution of the disperse phase. A three-step split technique is developed in *Hylkema (1999); Laurent et al. (2004)*. This technique is compared to a Eulerian model for the simulation of the dynamics and the coalescence of particles in solid propellant combustion by *Doisneau et al. (2013)*. *Fede et al. (2015)* introduced a two-step splitting taking into account collisions and coalescence for particles transported by a turbulent flow in the framework of a joint fluid-particle PDF approach.
For now, even if DSMC is used for academic DNS configurations, it is still considered to be expensive for real applications when statistical convergence is required.
Compared to DPS, this method directly gives statistical results of several realizations, whereas for the DPS several simulations should be carried out to access this type of information. The open question here is which one of these two methods should be used? The answer is governed by the full understanding of these two methods and their peculiarities, which can be case-dependent. In the cases where the ensemble average is not enough to describe the disperse phase dynamic the DPS is preferred, as for example in the work of Zamansky et al. (2014; 2016). In the case of our study, the statistical results are useful and the DSMC is preferred.

1.5.3.2 Stochastic Parcel method

In realistic configurations where the number of physical particles is very large, associating a single numerical particle for each physical droplet becomes very

expensive. In this case, a statistical Lagrangian description can be applied by representing several physical droplets by a numerical particle. This computational particle is also called "parcel", to refer to the grouping of the particles assumed to have identical properties. This method was first introduced by *Crowe and Willoughby (1977)*. It was called Stochastic Parcel method (SP) by *O'Rourke (1981)* in the context of fuel sprays as an extension of the work of *Dukowicz (1980)*. It was also named the discrete parcel method (*Crowe et al. 1998*).
When changing the number of parcels, this method can lead to various dynamics when the two-way coupling is responsible for the destabilization of a spray jet such as in *Emre (2014)*.
This approach gives a coarser description level in comparison with the DPS. Indeed, if the effect of the disperse phase on the gas is neglected, the result using SP converges to the one with DPS when the number of physical particles per parcel is decreased and thus the number of statistical parcels increased. However the number of numerical particles is limited by the computational cost since the cost is proportional to the number of the tracked parcels. Thus, the cost can be controlled by choosing a limited number of parcels which make this method attractive for industrial applications but one should keep in mind that the result are not precise and can not be considered as a resolution method for the WBE.

The two stochastic Lagrangian methods presented above are not to be confound with the stochastic modeling that is used in some Lagrangian-Eulerian methods to add some random process to the resolved equation (*Subramaniam (2013); Balthasar and Kraft (2003); Ahmadi (2009)* and references therein). In the literature we can find many improvement for such stochastic modeling for the Lagrangian techniques for example in *Goodson and Kraft (2002); Sander and Kraft (2009)*. In addition, other types of stochastic models can be used for particle motion in turbulent flow (*Minier and Peirano 2001; Chibbaro and Minier 2011; Zamansky et al. 2011; Volkov 2007; Vinkovic et al. 2005; Vinkovic et al. 2006*).

1.6 Macroscopic level: Eulerian Moment Methods

Another way of solving the WBE is the macroscopic Eulerian method for which, instead of solving the WBE directly or tracking stochastically the droplets, one solves for some moments of the NDF. The moments are integrated quantities over the phase space, such as the droplet volume fraction or the overall momentum, and live in the physical space only. As a consequence, this approach decreases the dimensionality of the space to be discretized.

The moments which are only functions of time t and position $\vec{\boldsymbol{x}}$ are given by:

$$ {}^{l}M^{m}_{i,j,k}(t,\vec{\boldsymbol{x}}) = \int {}^{l}\boldsymbol{\xi}^{m}_{i,j,k} f(t,\vec{\boldsymbol{x}},\boldsymbol{\xi})\mathrm{d}\boldsymbol{\xi}, \tag{1.14}$$

where ${}^{l}\boldsymbol{\xi}^{m}_{i,j,k} = c_1^i c_2^j c_3^k S^l T^m$ and c_1, c_2 and c_3 are respectively the x, y and z components of the velocity $\vec{\boldsymbol{c}}$. For example, the total number density of the disperse phase is the zeroth order moment:

$$ n(t,\vec{\boldsymbol{x}}) = {}^{0}M^{0}_{0,0,0}(t,\vec{\boldsymbol{x}}) = \int f(t,\vec{\boldsymbol{x}},\boldsymbol{\xi})\mathrm{d}\boldsymbol{\xi}. \tag{1.15}$$

1.6.1 General system of moment equations

The general moment equation is obtained by multiplying the WBE by ${}^{l}\boldsymbol{\xi}^{m}_{i,j,k}$ and integrating the result over the phase space $\boldsymbol{\xi}$:

$$ \partial_t\, {}^{l}M^{m}_{i,j,k} + \partial_{\vec{\boldsymbol{x}}} \cdot \begin{pmatrix} {}^{l}M^{m}_{i+1,j,k} \\ {}^{l}M^{m}_{i,j+1,k} \\ {}^{l}M^{m}_{i,j,k+1} \end{pmatrix} = \mathbf{S}_F + S_S + S_T, \tag{1.16}$$

where $\mathbf{S}_F$, S_S and S_T are source terms resulting from the integration over the phase space of the drag, evaporation rate and heat exchange rate parts in the WBE. These terms read:

$$ \mathbf{S}_F = \int {}^{l}\boldsymbol{\xi}^{m}_{i,j,k} \partial_{\vec{\boldsymbol{c}}} \cdot \left(\vec{\mathbf{F}} f(t,\vec{\boldsymbol{x}},\boldsymbol{\xi})\right) \mathrm{d}\boldsymbol{\xi}, \tag{1.17}$$

$$ S_S = \int {}^{l}\boldsymbol{\xi}^{m}_{i,j,k} \partial_S \left(R_S f(t,\vec{\boldsymbol{x}},\boldsymbol{\xi})\right) \mathrm{d}\boldsymbol{\xi}, \tag{1.18}$$

$$ S_T = \int {}^{l}\boldsymbol{\xi}^{m}_{i,j,k} \partial_T \left(H_T f(t,\vec{\boldsymbol{x}},\boldsymbol{\xi})\right) \mathrm{d}\boldsymbol{\xi}. \tag{1.19}$$

The main advantages of this approach are:

- its intrinsic statistical convergence,
- its ease of coupling with the carrier phase since they are both modeled at the same macroscopic Eulerian level, which results in continua equations for both phases.
- the ease of parallel computing.

The main objectives that will govern the choice of the moment method in this work are:

- a realizable moment set: this realizability condition means that every set of moments is associated with a positive NDF. It is an essential condition to make sure that the link between the kinetic and the macroscopic level is maintained.

- accessible closures for the source terms: the terms $\mathbf{S}_F$, S_S and S_T can be in the simplest case function of the closed moment set. Otherwise, the closure of these source terms would be based on the reconstructed distribution obtained through the realizable moment set.
- mathematically well-posed system of equations resulting from the moment method. These equations are characterized by the hyperbolicity and entropic structure. This is helpful to devising accurate and robust numerical methods for the resolution of the obtained differential equations that can deal with the singularities.

These methods will not be detailed here since they are the subjects of the next two chapters.

1.7 Classification of the disperse phase and of the modeling approaches

1.7.1 Velocity and temperature dispersion

The Particle Trajectory Crossing (PTC) is captured through a velocity dispersion in the Eulerian models, this is called polykineticity. It refers to the coexistence of several velocities in a given vicinity. In the case where all the particles sharing the same location have the same velocity, a monokinetic spray is obtained.

The degree of polykineticity depends on the particle size and inertia and thus on the Stokes numbers St since low-inertial particles roughly follow the gas and can be described by a monokinetic model (*Jabin 2002; de Chaisemartin 2009*). On the other hand, the motion of inertial particles is conditioned by their history and different degrees of polykinetic complexity can be found according to the size of the particles.

These categories differ by the rate at which the droplets correlate their velocities with the gas one:

- for very small Stokes numbers St: the disperse phase velocity at a given position and time is equal to the carrier velocity in question;
- for small Stokes numbers: the droplets velocities are highly correlated to the carrier velocity;
- for moderate Stokes numbers: the droplets velocities are dispersed around a mean velocity that can significantly drift from the gas velocity;
- for large Stokes numbers: the dependence of the droplets dynamics on the carrier phase motion is complex this is included the interaction between the two as well as the droplets own motion driven by their inertia.

Thus, for the moderate to large Stokes numbers, the probability of having two particles at the same location having different velocity is high. This implies the probable occurrence Particle Trajectory Crossing which is the subject of the

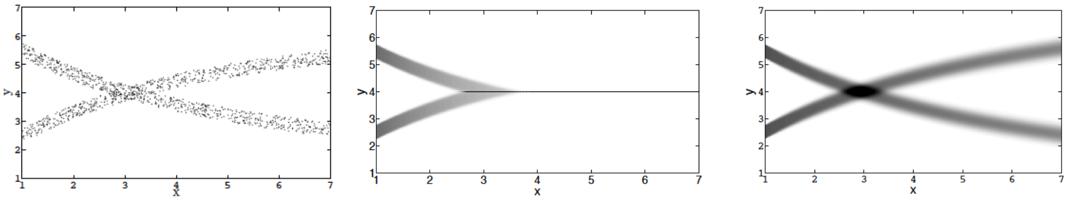

Figure 1.12: *Comparison of the mass density for simulation of two crossing jets using a Lagrangian approach, a monokinetic approach (center) and a polykinetic one (right) at the infinite Knudsen limit for* St = 5.29 *(adapted from Fréret et al. (2008))*

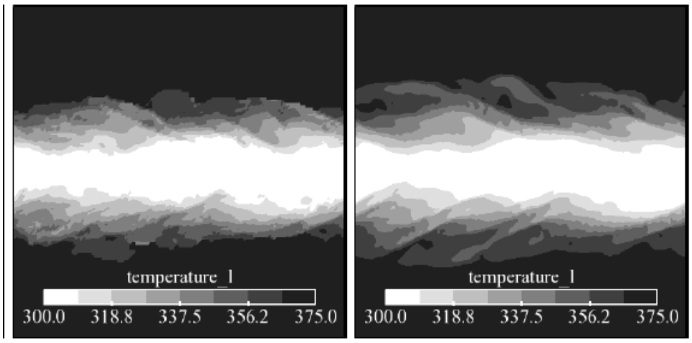

Figure 1.13: *Comparison of the particle mesoscopic temperature for the Lagrangian reference simulation (left) and the eulerian one (right). (Source: Dombard (2011))*

following subsection.

The simulation of the crossing of non-colliding jets for a Stokes number St = 5.29, shown in Figure 1.12, highlights the important of polykinetic model since the monokinetic one is incapable of capturing the crossing event.

In addition to the size and velocity dispersion, we can have also temperature dispersion. This is the case where in the same vicinity different particles have different temperatures. This depends on the thermal Stokes number St_T similar to the dynamic one St. The treatment of this dispersion is gaining more and more importance nowadays. It will not be treated in this thesis, for the interested readers this subject is studied in the work of Masi and Simonin (2014; 2012) and in the theses of *Masi (2010)*; *Dombard (2011)*; *Sierra (2012)* .

As an example, the comparison between the Lagrangian results and the Eulerian results using the Mesoscopic Eulerian Formalism that takes into account the temperature dispersion, is depicted in Figure 1.13. The temperature is plotted on a plane cut of a three-dimensional cold planar turbulent jet, loaded with solid particles and surrounded by a hot decaying turbulent flow. This comparison shows the importance of modeling the temperature dispersion for the non-isothermal configurations.

1.7.2 Types of Particles Trajectories Crossing

For high Knudsen numbers and high Stokes numbers, spray clusters may cross each other, so droplets might have different velocities at the same position and same time. This behavior is called particles trajectory crossing (PTC) and can be of two different natures (*Doisneau 2013*):

- the first one is the crossing of droplets having significantly different sizes and is called hetero-PTC. This PTC can occur between droplets belonging to the various Stokes categories as long as their inertia are not nearly the same.
- the second type is the homo-PTC defined as the crossing of the trajectories of equally sized droplets. This class of PTC start taking place for a moderately inertial to inertial particles. For moderate Stokes numbers, a small crossing scale, compared to the scale of the simulated geometry, characterizes the homo-PTC, whereas for high Stokes numbers the crossing is of large size.

The hetero-PTC should be accounted for in the polydisperse description of the spray. In fact, not all the modeling approach for polydispersion found in the literature are able to render hetero-PTC, but some of the models presented in chapter 3 consider size-conditioned velocities and temperatures and thus have the ability to intrinsically describe hetero-PTC. The polydisperse models found in the literature are based on the monokinetic assumption. These models are presented in chapter 3.

For the description of homo-PTC the challenge is different since the physics is more complex and the out-of-equilibrium state adds a big challenge in finding suitable closures for the velocity moment equations. In fact, when having this kind of PTC, the velocity distribution function is locally multi-modal with different velocities resulting from the various characteristics. This multiple velocity dynamics is referred to as polykineticity as mentioned in the previous subsection and must be treated correctly in order to understand the spray dynamics.

In addition, homo-PTC must be taken into consideration in modeling both monodisperse and polydisperse spray.

In chapter 2, the different polykinetic modeling approaches are presented for a monodisperse spray.

In addition, the extension of the chosen polykinetic model, subject of this thesis, to the polydisperse cases is also presented in chapter 3.

The treatment of velocity and size dispersion presented in chapters 2 and 3 is illustrated in Figure 1.14.

It is important to note that the PTC in the temperature space can also be classified according to these two types and one will a similar challenge of describing both homo and hetero PTC. The first should be accounted for through a temperature dispersion and the second has to be described in the polydisperse model.

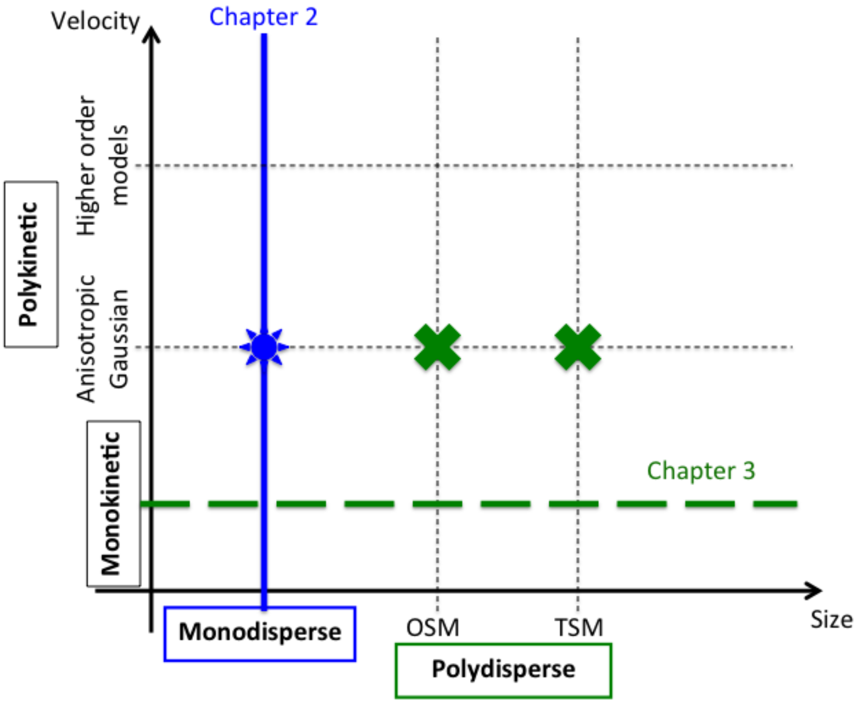

Figure 1.14: *Organization of the disperse phase modeling chapters according to the treatment of size and velocity dispersion: Chapter 2 for the treatment of velocity dispersion (bleu), Chapter 3 for the treatment of size dispersion (green), the symbols showing the focus of this thesis.*

1.7.3 Modeling approaches classification for turbulent dispersed multiphase flow

The above approaches were classified by *Balachandar and Eaton (2010)* according to their applicability in terms of timescales and volume fraction.

The appropriate choice of the full DNS is for high Stokes numbers where the particle diameter is greater than 0.1 times the Kolmogorov length scale (*Balachandar and Eaton 2010*). The Lagrangian approach was found to be the most suitable for moderately inertial particles. The Eulerian approach was limited to a small range of Stokes number going from 0.2 to 1. And the Equilibrium Eulerian is limited to small particles St < 0.2. This classification is illustrated in Figure 1.15 and it is proposed for the dilute case.

The objective of this thesis is to extend the range of applicability of the Eulerian approach to higher Stokes number. The challenge is that we want to meet this objective while solving the minimum number of moment required, guaranteeing the realizability of the moment set and obtaining a system of equation on the moment, that is well-posed mathematically, and allows to handle the inherent singularities. The obtained model should also be capable of treating polydispersion and can be extended in future work to take into account temperature dispersion.

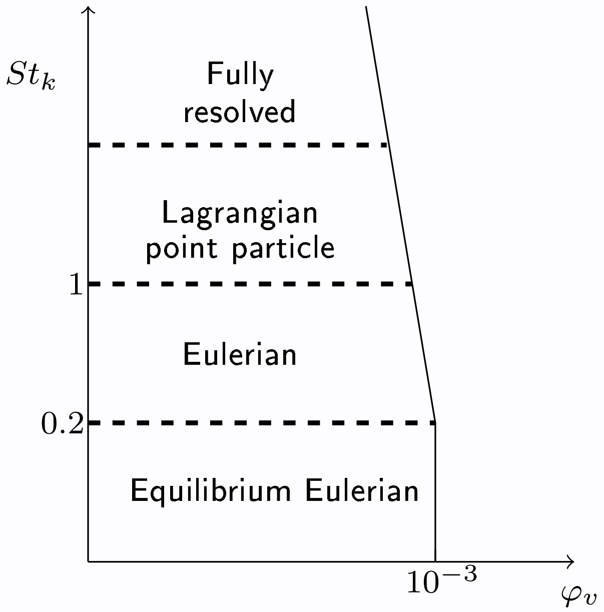

Figure 1.15: *Applicability of the different approaches to disperse phase modeling as a function of the fractional volume occupied by the disperse phase and the Stokes number. (Adapted from Balachandar and Eaton (2010))*

The proposed AG model, which is presented in chapter 2 along with its polydisperse extension in chapter 3, is a choice that meets all the mentioned requirements and it is a compromise between the detailed level of treatment of PTC and the cost of the model.

Chapter 2

Polykinetic moment methods

The available polykinetic approaches found in the literature are briefly presented in this chapter. The necessity of polykinetic modeling is highlighted for the description of PTC between particles of the same size also called homo-PTC. In fact providing polykinetic model is of paramount importance when dealing with moderately inertial to inertial particles. These methods are classified into two families according to the chosen nature of the closures: the Algebraic-Closure-Based Moment Methods and the Kinetic Based Moment Methods. Here, the focus is on the KBMM for its well-posed mathematical structure and its inherent link with the kinetic level that helps guaranteeing the realizability of the set of moments. From this family, the Anisotropic Gaussian model is chosen as a compromise between its ability to statistically capture the homo-PTC and the cost of the method compared to the higher order polykinetic methods. The polykinetic methods are presented in this chapter in a monodisperse context in order to decouple the homo-PTC from hetero-PTC and to concentrate on the description of homo-PTC. This is done to focus on evaluating and finding an efficient technique to statistically treat the polykineticity. The choice does not impede the model from handling the polydispersion and therefore the hetero-PTC; this extension is presented in the next chapter.

2.1 General Velocity Moments Equations

In the literature, one can find different models developed recently to treat polykineticity. Different levels of complexity, robustness and cost characterize these models.

The resulting simplified William Boltzmann equation for the case of infinite

Kn, reads:

$$\partial_t f + \partial_{\vec{x}} \cdot (\vec{\mathbf{c}} f) + \partial_{\vec{\mathbf{c}}} \cdot \left(\frac{\vec{\mathbf{u}_g} - \vec{\mathbf{c}}}{\tau_p} f \right) = 0, \tag{2.1}$$

where the Stokes law is chosen for the drag force for clarity, assuming that the studied particle Reynolds number is less than 1.

Knowing that the collisional case can be treated with the proposed approach (*Vié et al. 2015; Levermore and Morokoff 1998*), the infinite Kn limit is considered in this context and it is the most complex case.

In fact, for the disperse phase in dilute regime, the collisions are negligible. This is the case of infinite Kn where a relaxation towards an equilibrium distribution as in the collisional regimes in gas dynamics is not valid. However, in the disperse phase the drag acceleration makes the hydrodynamic equilibrium valid for small Stokes numbers by adding a dissipation phenomenon.

For the sake of simplicity and since our focus is on the free transport and drag terms, we will only consider these two terms in order to derive the general moment equations in velocity.

2.1.1 The Eulerian Approach and the Method of Moments

After multiplying equation (2.1) by $c_1^i c_2^j c_3^k$ and integrating the result over the phase space, one gets a system of moment equations. In a three-dimensional physical space, the general equation on the velocity moments is:

$$\partial_t M_{i,j,k} + \partial_{\vec{x}} \cdot \begin{pmatrix} M_{i+1,j,k} \\ M_{i,j+1,k} \\ M_{i,j,k+1} \end{pmatrix} = \frac{1}{\tau_p} \left(\vec{\mathbf{u}_g} \cdot \begin{pmatrix} iM_{i-1,j,k} \\ jM_{i,j-1,k} \\ kM_{i,j,k-1} \end{pmatrix} - (i+j+k) M_{i,j,k} \right), \tag{2.2}$$

where the general $(i+j+k)^{th}$ order moment in velocity is:

$$M_{i,j,k} = \int c_1^i c_2^j c_3^k f \mathrm{d}c_1 \mathrm{d}c_2 \mathrm{d}c_3. \tag{2.3}$$

For example, the 0^{th} order moment, common to all the phase variables, is equal to the number density n and the 1^{st} order moment is the velocity momentum. This system is not closed: actually for every set of moments of order N which contains the moments of order $(i+j+k) \leq N$, moments of order $N+1$ are needed to describe the higher order fluxes in physical space: $M_{i,j,k}$ where $i+j+k = N+1$.

It should be remarked that due to the linear drag law used in equation (2.1), the drag force terms in the moment equation do not require additional closures. For a more complex drag law, the drag force can be given for example with a

convective correction such as the Schiller-Naumann correction. In this case, the drag force is a function of the Stokes drag force and the particle Reynolds number Re_p. Here, the challenge is that the complex drag law can result in unclosed moments. A solution is proposed in section 2.3. However, as mentioned in chapter 1, this force should always be localized in physical and phase space and should rely on the assumption of point-particles, otherwise the kinetic approach would cease to be valid.
A particular example of the system of velocity moments (Equation (2.2)) is given up to the moments of first order ($i + j + k = 1$):

$$\begin{cases} \partial_t n + \partial_{\overrightarrow{\mathbf{x}}} \cdot (n\overrightarrow{\mathbf{u}}) = 0, \\ \\ \partial_t (n\overrightarrow{\mathbf{u}}) + \partial_{\overrightarrow{\mathbf{x}}} \cdot (n\overrightarrow{\mathbf{u}} \otimes \overrightarrow{\mathbf{u}} + \mathbf{\Sigma}) = \dfrac{n(\overrightarrow{\mathbf{u}_g} - \overrightarrow{\mathbf{u}})}{\tau_p}, \end{cases} \tag{2.4}$$

the closure problem can be interpreted as closing the covariance matrix $\mathbf{\Sigma}$ in the highest order flux which is the moment of second order ($n(\overrightarrow{\mathbf{u}} \otimes \overrightarrow{\mathbf{u}} + \mathbf{\Sigma})$). This is somehow similar to closing the Reynolds stress for RANS simulation or the subgrid scale tensor for LES: one needs to use the information in the flow and a reasonable set of assumptions to be able to prescribe the right closure. The main criterion that will drive the choice of the closure in DNS is the Stokes number relative to the Kolmogorov time scale.

$$\mathrm{St}_K = \frac{\tau_p}{\tau_K}. \tag{2.5}$$

When the Stokes number of the droplets is below one, the occurrence of homo-PTC is not frequent since the droplet are trapped into low vorticity regions. In this case, the closure is as simple as considering a zero covariance matrix: all the droplets in the same vicinity have the same velocity, which is characterized by a Dirac's δ-distribution in the velocity phase space.
For higher Stokes numbers, the problem becomes more complex since the homo-PTC becomes significant. In this case, the accuracy of the model to reproduce the right dynamics depends on its capacity to capture the homo-PTC.

The closure choice is a very important step in the Eulerian modeling since it should recover as much of the information lost due the resolution of a finite number of moments, as possible.
From the different Eulerian models developed for describing polykineticity, two families of approaches are discussed hereafter with a highlight on the chosen family and more specifically the selected model:

- Algebraic Closure Based Moment Methods (ACBMM): the unknown velocity moments are closed at the macroscopic level by considering physical and mathematical assumptions on the moments.
- Kinetic Based Moment Methods (KBMM): the closure is based on the choice of reconstruction of an underlying kinetic distribution. A class

of this family, which can be considered as a family of approaches on its own, is the quadrature-based moment methods (QMOM), where the NDF is represented by a finite sum of weighted delta-functions centered at discrete velocities. In this case, the resulting equations are written on the quadrature nodes: the weights and velocity abscissas. The velocity moments and the integrals are evaluated using these quadratures.

2.2 Algebraic-Closure-Based Moment Methods

A possible strategy to close the covariance matrix in the Algebraic-Closure-Based Moments methods (ACBMM) is to impose assumptions on the behavior of the covariance matrix, with respect to resolved variables, like the liquid phase velocity gradients.

The team of Olivier Simonin at IMFT proposed many possible closures, as found in the work of *Kaufmann et al. (2008); Masi and Simonin (2012); Masi et al. (2014)*, for example. Most of the proposed closures are based on a constitutive closure for the covariance, also called the random uncorrelated-motion particle kinetic stress tensor in Mesoscopic Eulerian Formalism (*Février et al. 2005*). These closures include the kinetic energy of the random uncorrelated-motion (RUE) $\delta\Theta_p$ that is solved by an additional transport equation.
For the closure, the covariance is first decomposed into an isotropic part and a deviatoric one. A simpler version of this closure takes into account only the isotropic part of the covariance. The decomposition of the RUM reads:

$$\sigma_{ij} = \sigma_{ij,iso} + \sigma^*_{ij} \quad \text{with the pressure term } \sigma_{ij,iso} = 2\delta\Theta_p/N_{dim}\delta_{ij}, \tag{2.6}$$

where $\delta\Theta_p$ is the kinetic energy of the random uncorrelated motion and the deviatoric part is modeled by:

$$\sigma^*_{ij} = \nu_{PTC}\left(\frac{\partial u_i}{\partial x_j} + \frac{\partial u_j}{\partial x_i} - \frac{2}{3}\delta_{ij}\frac{\partial u_k}{\partial x_k}\right) = -2\nu_{PTC}S^*_{ij}, \tag{2.7}$$

having $\nu_{PTC} = \tau_p\delta\Theta_p/N_{dim}$.
This model assumes a linear relationship between the deviatoric RUM and the rate-of-strain tensor through an eddy-viscosity, which uses the particle relaxation time as a typical timescale. It is based on a local equilibrium assumption on the stress tensor including a light anisotropy. It is called the VISCO model since it is based on a viscosity-type closure. It has been derived by *Simonin et al. (2002)* and used later on by *Kaufmann et al. (2008)* for inertial particles suspended in decaying isotropic turbulence. Its failure in the presence of mean shear was highlighted by *Riber (2007)*.
In the recent work of *Masi (2010); Masi et al. (2014); Masi and Simonin (2014)*, a more complex closure was developed based on a self-similarity assumption for the RUM stress tensor. The resulting model is called 2Φ-EASM.

This non-linear algebraic closure gives an implicit model for the Random Uncorrelated Motion of the particles able to take into account the anisotropy caused by PTC.

$$\sigma^*/2\delta\Theta_p = G_1\mathbf{S}^* + G_2\left(\mathbf{S}^* - \boldsymbol{\Omega}\mathbf{S}^*\right) + G_3(\mathbf{S}^{*2} - \frac{1}{N_{dim}}\left\{\mathbf{S}^{*2}\right\}\mathbf{I}),$$

where G_k are modeled using invariants of the particle rate of strain and vorticity, and $\boldsymbol{\Omega}$ is the particle vorticity tensor

$$\Omega_{ij} = 1/2(\partial_{x_j} u_{p,i} - \partial_{x_i} u_{p,j}). \tag{2.8}$$

The 2Φ-EASM was compared to the VISCO model by *Sierra (2012)* and was found to be more predictive, since it can render PTC at moderate Stokes numbers. This model has been validated in configurations with a mean shear by *Dombard (2011)*.
The ACBMM is included in the AVBP code and was used to simulate complex configurations (*Sanjosé et al. 2011*; *Riber 2007*; *Vié et al. 2013*; *Jaegle 2009*). In addition to these models, there is also the full second-order Eulerian model (*Le Lostec et al. 2008*; *Le Lostec et al. 2009*) where the components of the covariance matrix are solved. In this case the closure of the equations is based on a gradient-diffusion assumption for the triple correlations found in the governing equations of the covariance matrix components.
By using this family of closures, the link between the macroscopic conservation equations and the kinetic description at the mesoscopic level becomes complex and indirect. Thus the realizability is complicated and not guaranteed. However, in order to have physical results, conditions based on the Schwarz's inequality and the positiveness of the RUE should be imposed (*Vié et al. 2012*; *Schumann 1977*). In addition the resulting system of equations is not well-posed mathematically. These points are not helpful to devise adapted realizability-preserving numerical methods that guarantee that the results are physical and do not include for example negative number density, mass fractions or energy. Due to these limitations the second family of Eulerian approach is preferred in this context.

2.3 Kinetic Based Moment Approach and hierarchy

In order to close the moment system (2.2), one needs to provide:

- the moment set of order N containing the $N+1$ moments $\{M_{i,j,k}\}\,\forall\,(i+j+k) = 0...N$ and
- a closure relationship which allows to find the unknown fluxes (assumptions on the velocity distribution for example). In the KBMM, this is done by keeping the link between the kinetic level and the macroscopic level by reconstructing the NDF, which is supposed to have a given shape.

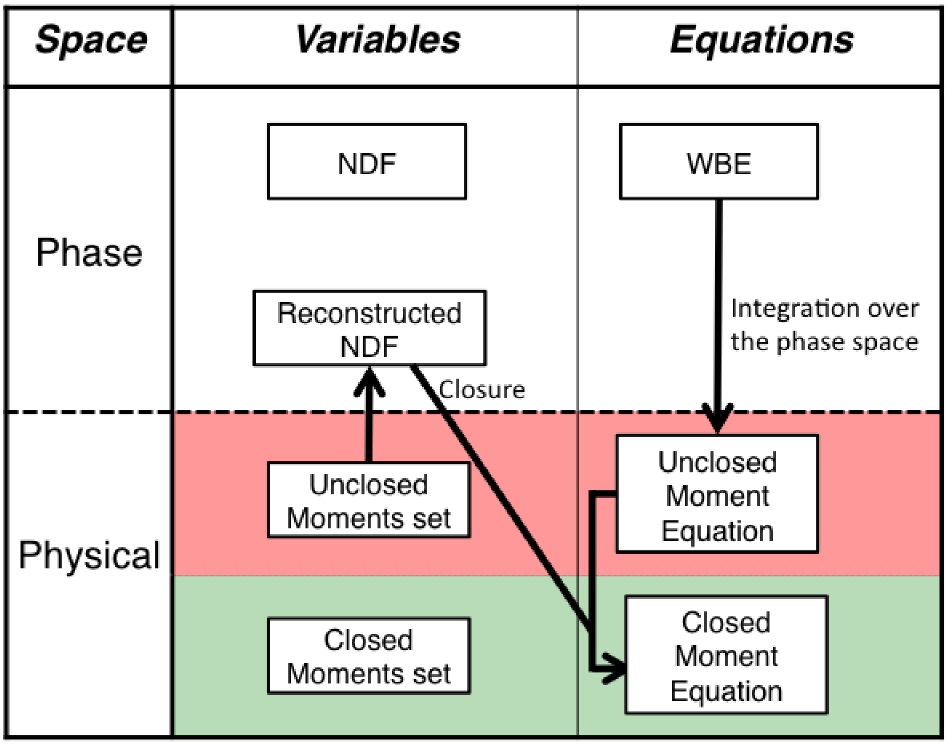

Figure 2.1: *NDF reconstruction and moment equation closure*

The shape of the NDF has as many parameters as the number of moments one needs to control. It should be chosen based on the physics one needs to describe and it should lead to simple algorithms in order to reconstruct the NDF from the moments set. This methodology is represented in figure 2.1.
Several models belonging to the KBMM family can be found in the literature based on different closures (*Laurent et al. 2012*), such as the monokinetic MK (*Laurent and Massot 2001*), the Gaussian divided into isotropic Gaussian (Iso) (*Massot 2007*) and anisotropic Gaussian AG (*Vié et al. 2015*), the QMOM (*Fox 2012; Yuan and Fox 2011; Kah et al. 2010; Chalons et al. 2012*) that includes for example conditional QMOM and extended QMOM and finally the multi-Gaussian MG (*Chalons et al. 2010; Chalons et al. 2016*). The moments used for this hierarchy are presented in 2D for the sake of simplicity in figure 2.2.

The choice of the closure is based on the physics one needs to describe and the obtained characteristics of the model.
It is important to note that the reconstruction can be helpful to derive a quadrature approximation for the moments resulting from the drag term whenever an arbitrary drag law is used (*Laurent et al. 2012*).
In the following, we study two models based on the MK and the Gaussian closures. Theses two distributions are also the basis quadratures for respectively

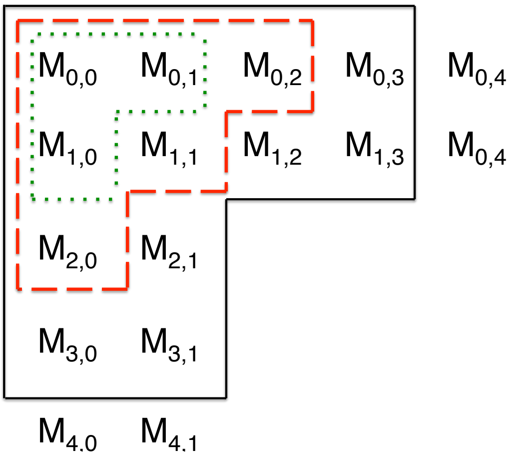

Figure 2.2: *2D moment set controlled by MG (all), CQMOM with 4 nodes (solid line), AG (dashed line) and MK (dotted line)*

the *QMOM* and *MG* models and we refer to the literature (*Fox 2012; Yuan and Fox 2011; Chalons et al. 2016*) for higher order methods.

2.3.1 Monokinetic model

As already mentioned within the framework of infinite Kn, the dissipative phenomenon is related to drag and drives the distribution towards a monokinetic one. Besides, the class of monokinetic distribution is stable by Equation (2.1) when St is below a critical value, making such an approach ideal for DNS of low inertia particles (*Laurent and Massot 2001*).
In this case, high segregation effects occur which lead to stiff accumulation regions along with vacuum generation in their vicinity.
These effects can be reproduced by the MK closure (*Laurent and Massot 2001*).
This assumption is known as the hydrodynamical equilibrium velocity (*de Chaisemartin 2009; Sainsaulieu 1995*) by analogy with the local thermodynamic equilibrium in the kinetic theory for the gas limit, yielding a hydrodynamic limit. The NDF is sought as a generalized Maxwell-Boltzmann distribution at zero temperature that means also zero velocity dispersion around the mean. It is assumed to write $f(t, \overrightarrow{\mathbf{x}}, \overrightarrow{\mathbf{c}}) = n(t, \overrightarrow{\mathbf{x}})\delta(\overrightarrow{\mathbf{c}} - \overrightarrow{\mathbf{u}}(t, \overrightarrow{\mathbf{x}}))$, where $\overrightarrow{\mathbf{u}}(t, \overrightarrow{\mathbf{x}})$ is the mean velocity of the disperse phase. The system of moments closes at first order in moments since the pressure is set to zero and we get therefore the following system:

$$\begin{cases} \partial_t n + \partial_{\overrightarrow{\mathbf{x}}} \cdot (n\overrightarrow{\mathbf{u}}) = 0, \\ \\ \partial_t (n\overrightarrow{\mathbf{u}}) + \partial_{\overrightarrow{\mathbf{x}}} \cdot (n\overrightarrow{\mathbf{u}} \otimes \overrightarrow{\mathbf{u}}) = \dfrac{n(\overrightarrow{\mathbf{u}_g} - \overrightarrow{\mathbf{u}})}{\tau_p}. \end{cases} \tag{2.9}$$

This model is for example used in the field of spray dynamics for combustion applications (*Cheneau et al. 2015; Franzelli et al. 2015; de Chaisemartin 2009; Fréret et al. 2010*) and in the field of solid propellant combustion (*Dupays 1996; Laurent et al. 2004; Doisneau et al. 2013; Sibra 2015*).

The MK model correctly reproduces the formation of depletion zones and accumulation regions obtained for small Stokes numbers but it does not take into consideration PTC. PTC that occurs for moderate to high inertial particles, cannot be capture by the single Dirac δ-function used for the velocity distribution in MK model. Instead, at each PTC location, unphysical δ-shocks is generated by this model. Another constraint of this model is that it does not preserve the kinetic energy of the disperse phase (*Bouchut 1994; Brenier and Grenier 1998*).

From a mathematical point of view, the free transport part of systems (2.9) is identical to the Pressureless Gas Dynamics system (PGD) (*Bouchut 1994; Marble 1970*). This system is used in astronomy where it is referred to as the sticky particles equations. The PGD system is weakly hyperbolic (in the sense that the Jacobian matrix is triangulable but non-diagonalizable) and can generate δ-shocks. Dedicated numerical methods have to face the challenging combination of being accurate (potentially high order) and handle the presence of singularities.

2.3.2 Gaussian model

The next closure in the KBMM family is the Gaussian closure (*Vié et al. 2015*). This closure controls the set of moment up to the second order. It was inspired by the work of *Levermore and Morokoff (1998)* in the context of out-of-equilibrium rarefied gas dynamics and was called the 10-moments closure. In the rarefied gases context, the good mathematical properties of this model at the kinetic and the moment levels was highlighted in *Holway Jr. (1966); Andries et al. (2000)* and a numerical approximation was proposed by *Brown et al. (1995)* and *Berthon (2006b)*. In fact, in the kinetic theory for rarefied gases, it was obtained using the ES-BGK collision operator to correct the prediction of Prandtl number which was equal to 1 in the classical BGK model of (*Holway Jr. 1966*). The Anisotropic Gaussian distribution was chosen based on the maximization of the Shannon entropy. The resulting system is hyperbolic and admits entropies (*Berthon 2006a*).

2.3.2.1 Isotropic Gaussian model

The simplest form of the Gaussian models is obtained when isotropic pressure is considered. In this case, the NDF is assumed to be an isotropic Gaussian distribution centered at $\vec{u}$ and with an isotropic dispersion σ:

$$f(t,\vec{x},\vec{c}) = \frac{n(t,\vec{x})}{\sqrt{\sigma}(2\pi)^{N_d/2}} \exp\left(-\frac{1}{2}\frac{(\vec{\mathbf{c}}-\vec{\mathbf{u}})^2}{\sigma}\right). \tag{2.10}$$

The resulting simplified system reads:

$$\begin{cases} \partial_t n + \partial_{\vec{\mathbf{x}}} \cdot (n\vec{\mathbf{u}}) = 0, \\ \partial_t(n\vec{\mathbf{u}}) + \partial_{\vec{\mathbf{x}}} \cdot (n\vec{\mathbf{u}} \otimes \vec{\mathbf{u}} + \mathbf{P}) = \dfrac{n(\vec{\mathbf{u}_g} - \vec{\mathbf{u}})}{\tau_p}, \\ \partial_t(n\mathcal{E}) + \partial_{\vec{\mathbf{x}}} \cdot ((n\mathcal{E} + \mathcal{P}) \cdot \vec{\mathbf{u}}) = \dfrac{n(\vec{\mathbf{u}_g} \cdot \vec{\mathbf{u}} - 2\mathcal{E})}{\tau_p}, \end{cases} \tag{2.11}$$

with,

$$\mathcal{E} = \frac{1}{2}\left|\vec{\mathbf{u}}\right|^2 + \sigma, \tag{2.12}$$

$$\mathbf{P} = \mathcal{P}\mathbf{I} = n\sigma\mathbf{I}. \tag{2.13}$$

The free transport part of system (2.11) is hyperbolic and identical to the Euler system of equations.

2.3.2.2 Anisotropic Gaussian model

This model was introduced for the first time for the modeling of the disperse phase in the work of *Vié et al. (2015)* in order to describe small-scale PTC for moderately inertial particle through a velocity variance described by an internal agitation energy.

Under the assumption of anisotropic Gaussian closure (AG), the NDF is assumed to write:

$$f(t,\vec{\mathbf{x}},\vec{\mathbf{c}}) = n(t,\vec{\mathbf{x}})\mathcal{N}(\vec{\mathbf{c}} - \vec{\mathbf{u}}(t,\vec{\mathbf{x}}), \mathbf{\Sigma}(t,\vec{\mathbf{x}})), \tag{2.14}$$

where $\mathcal{N}$ is a joint Gaussian distribution of center $\vec{\mathbf{u}}$ and covariance matrix $\mathbf{\Sigma} = (\sigma_{ij})$ in the space of dimension N_d:

$$\mathcal{N}(\vec{\mathbf{c}} - \vec{\mathbf{u}}, \mathbf{\Sigma}) = \frac{|\mathbf{\Sigma}|^{-1/2}}{(2\pi)^{N_d/2}} \exp\left(-\frac{1}{2}(\vec{\mathbf{c}} - \vec{\mathbf{u}})^T \mathbf{\Sigma}^{-1} (\vec{\mathbf{c}} - \vec{\mathbf{u}})\right). \tag{2.15}$$

The resulting system reads:

$$\begin{cases} \partial_t n + \partial_{\vec{\mathbf{x}}} \cdot (n\vec{\mathbf{u}}) = 0, \\ \partial_t(n\vec{\mathbf{u}}) + \partial_{\vec{\mathbf{x}}} \cdot (n\vec{\mathbf{u}} \otimes \vec{\mathbf{u}} + \mathbf{P}) = \dfrac{n(\vec{\mathbf{u}_g} - \vec{\mathbf{u}})}{\tau_p}, \\ \partial_t(n\mathbf{E}) + \partial_{\vec{\mathbf{x}}} \cdot ((n\mathbf{E} + \mathbf{P}) \vee \vec{\mathbf{u}}) = \dfrac{n(\vec{\mathbf{u}_g} \vee \vec{\mathbf{u}} - 2\mathbf{E})}{\tau_p}, \end{cases} \tag{2.16}$$

where $\vee$ denotes the symmetric tensor outer product[1], the total energy tensor $\mathbf{E}$ is given by the equation of state $\mathbf{E} = \frac{1}{2}\overrightarrow{\mathbf{u}} \otimes \overrightarrow{\mathbf{u}} + \frac{\mathbf{P}}{2n}$ and the anisotropic pressure tensor is $\mathbf{P} = n\mathbf{\Sigma}$.
In the case of isotropic pressure, a scalar conservation of energy is obtained by applying the trace operator on the last equation of system (2.16). In this case, the scalar energy is the trace of the energy matrix $\mathcal{E} = \mathrm{Tr}(\mathbf{E})$ and the isotropic Gaussian model can be obtained from the anisotropic one by assuming an isotropic pressure tensor.
For a 2D homogeneous configuration, the AG system as stated in *Berthon (2006a); Vié et al. (2015)*, has six eigenvalues: u has two orders of multiplicity and is associated to a linearly degenerated field. The eigenvalues $u \pm \sqrt{\frac{3p_{11}}{n}}$ are associated to genuinely nonlinear fields and the eigenvalues $u \pm \sqrt{\frac{p_{11}}{n}}$ are associated to linearly degenerate fields. Each of these last four eigenvalues have one order of multiplicity.
When it comes to the entropic structure, the two entropy families in 2D are:

$$s_{11} = \frac{p_{11}}{n^3}, \qquad s_{12} = \frac{p_{11}p_{22} - p_{12}^2}{n^4}. \tag{2.17}$$

The AG model is the lowest order model capable to statistically reproduce the PTC. This is done through the anisotropic pressure and thus through the anisotropic tensorial energy. For this reason, it is already expected that with the isotropic simplification, the main advantage of the Gaussian closure will be lost. For this reason the isotropic Gaussian model will only be studied for the evaluation of the numerics in 1D and 2D. The evaluation of the KBMM in more realistic 3D cases is performed only for the MK and AG models in part IV.
The free transport part of system (2.16) is similar to the Euler equations but with a tensorial form for the energy equation. This system is hyperbolic.

It is important to note that the QMOM which is based on the sum of Dirac δ-functions to account for the multi-modal velocity distribution at the crossing event suffers from the same drawbacks of the MK model. It leads to a weakly hyperbolic system and it generates unphysical δ-shocks when more than two trajectories cross (*Chalons et al. 2012*).
To avoid the drawbacks of the QMOM, the MG quadrature was proposed by (*Chalons et al. 2010*). Instead of using a point distribution for the quadrature, a continuous function is used; this function is the Gaussian function. The MG can describe small and large scale PTC. The small-scale PTC is represented by the dispersion of each Gaussian whereas the large-scale PTC is rendered by the dispersion of the centers of the Gaussian distribution (*Laurent et al. 2012; Chalons et al. 2016*). This highlights the importance of the detailed

---

[1] The symmetric tensor outer product acts on a symmetric k-tensor and a symmetric l-tensor by symmetrizing the $(k+l)$-tensor that is their usual tensor outer product (*Levermore and Morokoff 1998*).

study of the Gaussian model as a closure on its own or as a step towards the understanding of the MG model.

2.4 Comparison and objectives

2.4.1 Two crossing jet configuration

A fundamental comparative case for the crossing of two jets in the context of infinite Knudsen number and infinite Stokes number is presented hereafter. This test problem developed by *Doisneau (2013)* is chosen here to illustrate the behavior of the models: MK, Iso, AG and QMOM. It is based on two symmetrical jets with respect to the x-axis, having the same velocity cross each other at the origin.

For all the models in question, the velocity component in the x-direction is accurately described since it is equal for the two jets before and after the crossing (figure 2.3). In this particular case, the challenging point is the right description of the velocity along the y-direction. The exact solution is captured by the QMOM, since it is based on an underlying velocity distribution of two Dirac-δ functions at the kinetic level. It is able to reproduce the bimodal behavior at the crossing point. When it comes to the AG result, entropy is created at the crossing location, which makes the process irreversible: after the crossing it is impossible to know the repartition of droplets coming from each jet. This is completely expected since the AG is not based on a multimodal assumption of the velocity distribution. Instead, it has a unique maximum with a dispersion that has different values in the different directions. Since the closure has a single peak, the kinetic energy at the crossing is transferred to internal energy through energy conservation. The advantage of this model is that it reproduces the right spatial dispersion σ_y which is equal to the dispersion obtained by QMOM, since the energy is redistributed in the direction of the crossing. Similarly, for the Iso closure, the macroscopic kinetic energy is transferred uniformly to internal energy but this time, the energy is transferred in all the direction without taking into account the specific direction of the PTC. Actually, the conservation of the scalar energy impedes the directional transfer of information. When it comes to the MK result, an artificial spatial averaging for the momentum takes place at the crossing location and breaks the link between the mesoscopic level and the macroscopic one. A Dirac δ-shock is created and the macroscopic kinetic energy is lost. Again, it is expected that this equilibrium assumption is unable to account for out-of-equilibrium conduct.

Keeping in mind that the AG is not designed for capturing such deterministic PTC, this case underlines its ability to capture the right length scale of the crossing. Then, in the real case where the drag adds dissipation to the PTC, the AG should be able to statistically reproduce the underlying physics.

It is important to note that in this theoretical test case the numerical dissipation is not accounted for.

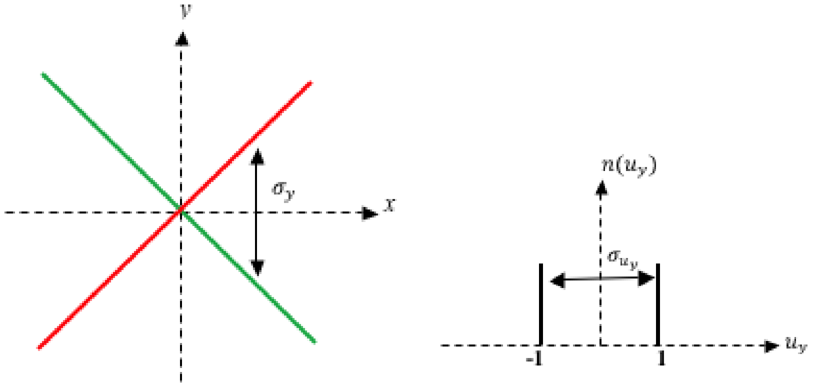

(a) Trajectories with QMOM (b) Distribution function double Dirac

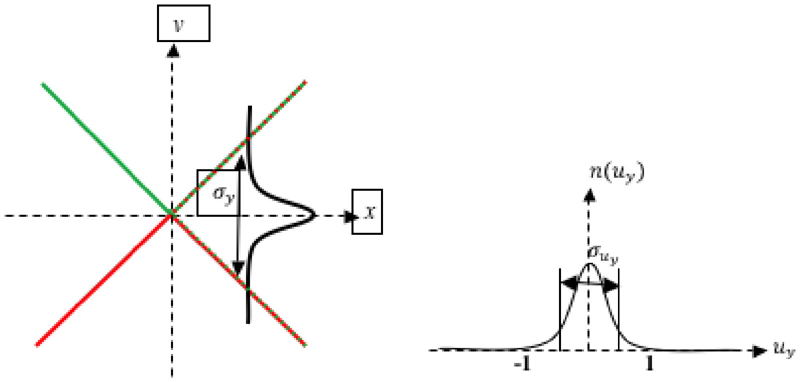

(c) Trajectories with AG (d) Distribution function Anisotropic Gaussian

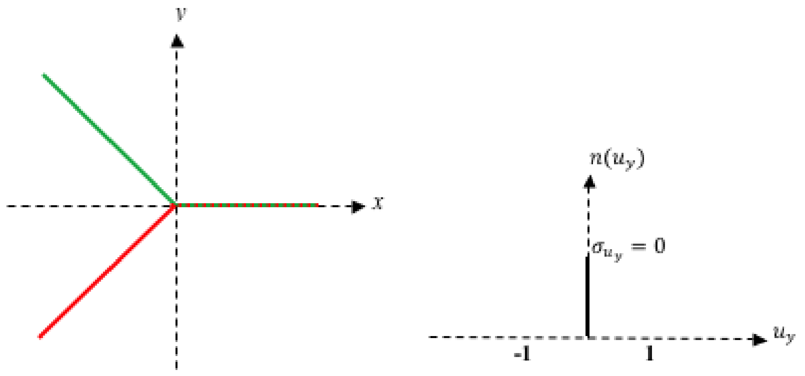

(e) Trajectories with MK (f) Distribution function Dirac

Figure 2.3: *To the left two crossing jets trajectories, to the right distribution function of the velocity in the y-direction*

Knowing that the large-scale PTC can be treated deterministically with QMOM and both small and large scale PTC can be treated with MG, the AG model is chosen here since it is the least expensive model in the KBMM capable of treating statistically the PTC. It is a compromise between the details of the PTC one can recover and the cost of the method. And as mentioned before, this can be sought as an important step to understand the treatment of small-scale PTC with the MG quadrature model in the hierarchy.

2.4.2 Summary of the properties of AG

The obtained system is well posed: it is hyperbolic with entropic structure. Its solution is well-defined. In addition, for all the above KBMM models, the link between the kinetic level and the macroscopic level can be kept by ensuring the realizability of the chosen moment set. The AG model is intrinsically realizable since it relies on a non-negative NDF for the closure. It does not have problems at the border of the moment space, unlike the higher order moment methods QMOM, MG or any other entropy based-closure that suffer from this limitation (*Chalons et al. 2016*). This subject is discussed in a more general context in the work of *Hauck et al. (2008)*.

For the numerical resolution of this system, the realizable space in question defines the constraints of the numerical scheme that should preserve this realizability. In addition, the large variations that might be encountered in the density field (going from vacuum zones to high concentration regions for small St for example) require high order robust numerical methods.
In order to find a numerical method capable to meet all these constraints, different numerical schemes are presented in Part II along with a comparison on 1D and 2D test cases.

Chapter 3

Polydisperse modeling

In this chapter, the existing methods that handle polydispersion in size are presented. These methods are the size sampling method, the pivot method, the method of moments with interpolative closure, the multi-fluid method, the quadrature-based moment method and the Eulerian multi-size moment model. Among these methods, we focus on the multi-fluid method, since it is well suited for evaporating sprays and was proven to be efficient in industrial codes and has been validated on academic and industrial configurations. The extension of this method to higher order is also presented. This method was originally based on the monokinetic closure and thus is unable to reproduce the homo-PTC. However, it is extended to treat polykinetic cases based on the Anisotropic Gaussian closure for the velocity distribution. This AG multi-fluid method is presented based on the one size moment and affine two-size moments multi-fluid model.

3.1 Eulerian polydisperse models

In this thesis, the assumption of spherical particles is made. Thus, only one size variable is needed to parametrize the polydispersity. This variable can be the radius, the surface or the volume depending on the physical phenomena one wants to treat.

In the literature, several types of Eulerian models handling polydispersion can be found:

- The size sampling method (*Laurent and Massot 2001*; *BenDakhlia 2001*), also referred to as Multi-Class method at ONERA (*Murrone and Villedieu 2011*; *Sibra 2015*). In this method, the distribution is sampled into N classes, as shown in Figure 3.1, each having its own mean size, velocity and temperature. For each sample, the shapes of the velocity, temperature and size distribution are assumed to be Dirac-delta functions. Therefore, the sampling can be directly applied to the semi-kinetic system

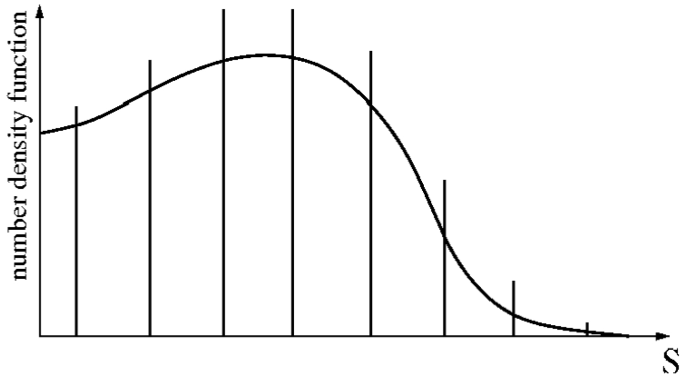

Figure 3.1: *Dirac discretization of the size phase space for sampling models.*

based on monokinetic mono-temperature assumption. In fact, the NDF is approximated by:

$$f(t,\vec{\boldsymbol{x}},S,\vec{\boldsymbol{c}},T) \approx \sum_{i=1}^{N} n_i(t,\vec{\boldsymbol{x}})\delta(S-S_i(t,\vec{\boldsymbol{x}}))\delta(\vec{\boldsymbol{c}}-\vec{\boldsymbol{u}}_i(t,\vec{\boldsymbol{x}}))\delta(T-T_i(t,\vec{\boldsymbol{x}})). \tag{3.1}$$

Each sample acts, then, as an isolated fluid having its number density n_i, size S_i, velocity $\vec{\boldsymbol{u}}_i$ and temperature T_i. This method is also called Lagrangian-in-size approach since the quantities in question are function of time and space only. A drawback of this approach is that it does not take into account any interaction between the different samples. In addition, a great care should be devoted to avoid the singularities that can be faced due the delta distribution for all the internal phase space variables (*Laurent and Massot 2001*). Thus, no crossing can be treated in size, velocity nor temperature. Moreover, coalescence and break-up cannot be easily modeled with this method.
For more information on this method, one can refer to the theses of *Doisneau (2013)*; *Sibra (2015)* and the references therein.

- The presumed PDF method for the size consists in supposing a form for the size distribution (*Babinsky and Sojka 2002*). This form is characterized by a set of parameters whose evolution is solved. The choice of the presumed PDF shape should be based on a given physics and can be experimentally justified or should result of some model simplifications. In the work of *Mossa (2005)*, this method was used and evaluated in the context of reactive evaporation flows. This method suffers from limited accuracy and stability and it faces sever singularities when treating the evaporation, since it forces the shape of the NDF throughout the evaporation process.
- The pivot methods assess the integral source terms based on the choice

of discrete sizes called the pivots (*Kostoglou and Karabelas 1994; Kumar and Ramkrishna 1996b*). This is done by casting these terms into moment evolution equations at the pivots while conserving a given number of moments of the NDF. In an early version of these methods, the integral terms were evaluated pointwise with a correction to ensure the conservation of mass. These zero order methods, as named by *Kostoglou and Karabelas (1994)*, are unable to describe the details of the NDF. In the fixed pivot techniques (*Kumar and Ramkrishna 1996b*), these terms are computed at the pivot locations but they are not linked to the kinetic level. *Kumar and Ramkrishna (1996a)* extended these methods to moving pivot techniques to increase the accuracy while preserving some moments of the global size distribution. A main drawback of this method is the assumption of an identical temperature and velocity for all the sizes. These methods are usually used in 0D or homogeneous contexts to solve the PBE (*Gelbard et al. 1980*). They have some ad-hoc continuous aspects that differentiate them from the sampling methods, and since they do not rely on a NDF reconstruction they also differ from the Multi-Fluid methods (*Doisneau 2013*).

- The method of moments with interpolative closure (MOMIC) was introduced by *Frenklach and Harris (1987)* and was further developed to describe various aspects of the dynamics of particles (*Frenklach 2002; Frenklach 2009*). The closures of the fractional-order moments are obtained by interpolation among whole order moments at each integration step by separating the positive order and negative order fractional moments. They are both evaluated by Lagrangian interpolation: the former using the whole order moments while the latter using normalized moments.
  Balthasar and Frenklach (2005) extended this method to particles of non-spherical shapes. The main disadvantage of this method is the realizability problem. Another difficulty is faced when a certain change of particles size is at the verge of removing all particle material (*Frenklach 2002*). This method was used for both laminar and turbulent sooting flames, for some examples one can check the work of *Roy et al. (2014)* and the references therein.
  This method was coupled by *Mueller et al. (2009)* to the Direct Quadrature Method of Moments and the obtained method is called the Hybrid Method of Moments (HMOM). This method captures the bimodal soot NDF and the result was validated with experimental data.
- The Multi-Fluid method: this technique consists in discretizing the size phase space into N_S intervals called "sections". It is based on the sectional method by *Tambour (1980); Greenberg et al. (1993)* and was characterized with the kinetic point of view and underlying assumptions in *Laurent and Massot (2001)*. It is assessed on different configuration of increasing complexity for example in *de Chaisemartin (2009)*. The classical MF approach is based on the semi-kinetic system based a presumed Dirac-delta

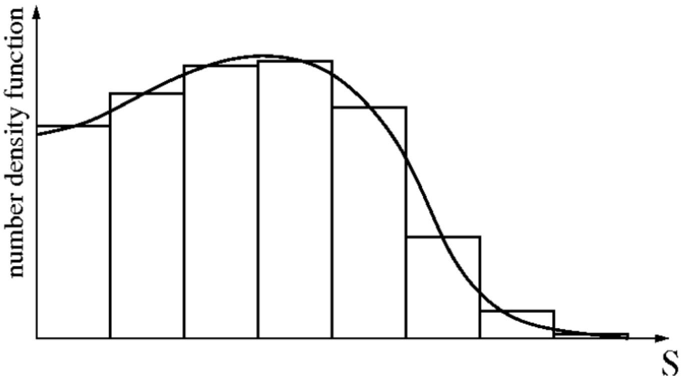

Figure 3.2: *Discretization of the size phase space for the classical Multi-Fluid method.*

distributions for the velocity and temperature conditioned by size. The resulting semi-kinetic system is averaged based on a finite volume approach which leads to conservation equations for mass, momentum and energy of droplets in each section having a fixed mean size. The size distribution is assumed to be a piecewise constant function. This method is expensive since a high number of sections (ten to twenty) is needed and a system of conservation equation has to be resolved for each section (*Laurent 2006*).

This classical MF method also known as the one-size moment method OSM was extended to higher order using more complex forms for the size distribution function. In this case, more size moments per section are solved. For example the two-size moment method (TSM) consists in solving two size moments per section. The reconstruction in size can also be exponential (*Dufour 2005; Doisneau 2013; Sibra 2015*) or affine (*Laurent et al. 2016; Doisneau et al. 2013*), as represented in Figure 3.2. In this way, the number of sections needed to precisely describe the evaporation is decreased. This method is of great interest in this work since it already accounts for hetero-PTC and can be relatively easily extended to treat polykineticity and capture homo-PTC. This method was used to treat polydispersion with the MEF in the work of *Vié et al. (2013)*.

- The quadrature-based moment methods: in this case the system of moment equations is closed using quadrature formula to compute the unknown high order moments as a function of low order ones. In Quadrature Method of Moment QMOM (*McGraw 1997; Mead and Papanicolaou 1984; Marchisio et al. 2003; Wright et al. 2001*) which is based on moment methods derived from Population Balance Equations (*Ramkrishna and Fredrickson 2000*), the closed moment equations are resolved thanks to the quadrature closure. This method, which is uni-variate and deals with unique velocity, was extended to multivariate QMOM methods. This later has been developed to account for the size velocity correlations

(*Marchisio and Fox 2005*). However these approaches might face realizability, stability, accuracy and cost issues.
Another method based on quadrature is the Direct Quadrature Method of Moment (DQMOM). It writes directly the equations on the quadrature weights and abscissae (*Fox et al. 2008*). DQMOM is more attractive than QMOM from a computational cost point of view, since the reconstruction is done less often. In the work of *Belt and Simonin (2009)*, DQMOM was combined to the joint fluid-particle PDF approach of *Simonin (1996)* to account for the coalescence of droplets in turbulent two-phase flows through the transport equations of the velocity, agitation and fluid-particle covariance.
The DQMOM method suffers from predicting the evaporating flux at zero droplet size. This drawback was improved with using the Extended Quadrature Method of Moment (EQMOM) (*Yuan et al. 2012*). The bivariate extension of the EQMOM is recently developed by combining the features of EQMOM and CQMOM, and it was applied to soot formation in premixed flames (*Salenbauch et al. 2015*) and coupled droplet evaporation and heat-up (*Pollack et al. 2016*). A robust algorithm is developed for the reconstruction step of EQMOM in the work of *Nguyen et al. (2016)* where the method is also compared to TSM and to the sampling method in the context of fine particles.

- Eulerian Multi-Size Moment model (EMSM) was introduced by *Massot et al. (2010)* and developed in the thesis of *Kah (2010)*. This model is based on the continuous description of the size distribution to treat the disappearing droplets and to evaluate the shift in size due to evaporation. This is done by combining a flux/quadrature approach. The NDF reconstruction is done based on the moments through Entropy Maximization (*Mead and Papanicolaou 1984*). An example using the first four moments of the NDF is shown in Figure 3.3.
  Compared to MF methods, this approach is less time consuming when looking at an equivalent accuracy (*Kah et al. 2012*). It was applied to realistic internal-combustion-engine configuration by *Emre et al. (2014)*. The main drawback of this method is that it accounts for a single velocity for all the droplets. Thus, the hetero-PTC cannot be captured by this method. To deal with this issue, a Coupled Size Velocity Moments method was developed. CSVM takes into account the size velocity correlations by transporting additional size-velocity moment in each space dimension (*Vié et al. 2013*). The EMSM is extended in the work of *Essadki et al. (2016)* to fractional moments in surface, linked with geometrical variables of the interface between the two phases. The resulting geometrical moment model is a first step towards the description of the transition between the separated and the disperse phase.

In the following, the focus is on the Multi-Fluid Method. The OSM and TSM are presented based on the MonoKinetic closure for the velocity. Then, their

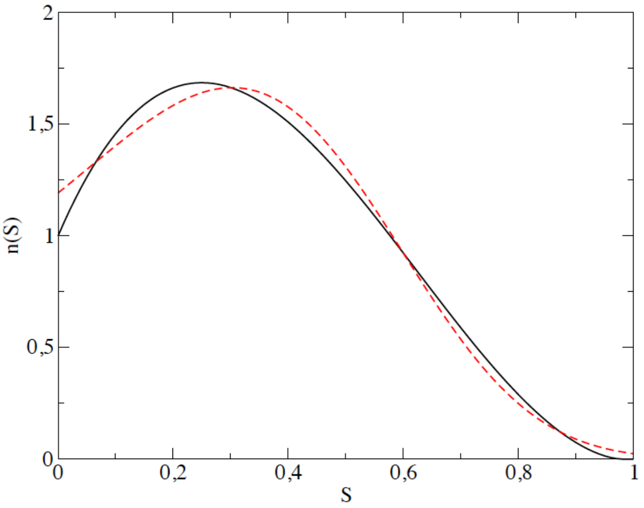

Figure 3.3: *Discretization of the size phase space with the EMSM using its 4 first moments (in dashed red)*

extension to Anisotropic Gaussian closure is presented.

3.2 Multi-Fluid model

The first step of this method is the semi-kinetic formalism that was introduced with the associated assumption in the work of *Laurent and Massot (2001)*. The key idea is to consider that the degrees of freedom of the NDF are all conditioned by the size. As a consequence, the phase space is reduced to a 1D sub-manifold where the size-conditioned variables are governed by conservation laws.

3.2.1 Semi-kinetic system

The semi-kinetic system of conservation laws is derived by assuming that the droplets at $(t, \vec{\boldsymbol{x}})$ having the same size are characterized by a given average velocity $\vec{\boldsymbol{u}}(t, \vec{\boldsymbol{x}}|S)$ and a temperature $T(t, \vec{\boldsymbol{x}}|S)$. The dispersion around these mean values is assumed to be zero in all directions. Thus, the NDFs for the velocity and the temperature are Dirac-delta functions in velocity and temperature respectively. These NDFs are conditioned by the droplet size.

$$f(t, \vec{\boldsymbol{x}}, S, \vec{\boldsymbol{c}}, T) = n(t, \vec{\boldsymbol{x}}, S)\delta(\vec{\boldsymbol{c}} - \vec{\boldsymbol{u}}(t, \vec{\boldsymbol{x}}|S))\delta(T - T_d(t, \vec{\boldsymbol{x}}|S)). \tag{3.2}$$

When it comes to the velocity, this is the monokinetic closure presented in the previous chapter in subsection 2.3.1.
The size of the phase space is reduce to the moments of order zero and one in the velocity variable at a given time, position and for a given droplet size.

Under these assumptions, the semi-kinetic system is closed in velocity and temperature and reads:

$$\begin{aligned}
&\partial_t n + \partial_{\vec{\boldsymbol{x}}} \cdot (n\vec{\boldsymbol{u}}) = -\partial_S(nR_{S,d}),\\
&\partial_t n\vec{\boldsymbol{u}} + \partial_{\vec{\boldsymbol{x}}} \cdot (n\vec{\boldsymbol{u}} \otimes \vec{\boldsymbol{u}}) = -\partial_S(nR_{S,d}\vec{\boldsymbol{u}}) + n\overrightarrow{\mathbf{F}}_d,\\
&\partial_t nh_l + \partial_{\vec{\boldsymbol{x}}} \cdot (nh_l\vec{\boldsymbol{u}}) = -\partial_S(nR_{S,d}h_l) + nC_{p,l}H_{T,d},
\end{aligned} \tag{3.3}$$

where $R_{S,d} = R_S(\vec{\boldsymbol{u}}, T_d)$, $\overrightarrow{\mathbf{F}}_d = \overrightarrow{\mathbf{F}}(\vec{\boldsymbol{u}}, T_d)$ and $H_{T,d} = H_T(\vec{\boldsymbol{u}}, T_d)$ are modeled in Appendix A and h_l is defined as $h_l = h(\vec{\boldsymbol{u}}, T_l)$. In this case the Stokes law is used to model the drag force per unit mass.

3.2.2 Classical Multi-Fluid method

To account for polydispersion, the size phase space is discretized into N_S sections. In each section or interval $[S_p, S_{p+1}[$, the evolution of the moments is derived based on the semi-kinetic system (3.3). Thus, N_S systems of conservation equations are obtained for N_S "fluids". These fluids exchange mass, momentum and heat.

In the classical MF method, only one moment in size is considered to obtain the averaged equations in each section. This moment is the surface moment of order $\frac{3}{2}$. In this case one gets in a given section a system of equations of evolution of:

- mass $\left({}^{\frac{3}{2}}M^0_{0,0,0}\right)$
- momentum $\left({}^{\frac{3}{2}}M^0_{i,j,k}\right)$ where $i + j + k = 1$
- heat $\left({}^{\frac{3}{2}}M^1_{0,0,0}.\right)$

This system is closed by assuming that the size distribution, which is a function of the surface for a given section, is independent of time and position. This means that the repartition of sizes in a given section $[S_p, S_{p+1}]$ is decoupled from the evolution of the mass concentration: $n(t, \vec{\boldsymbol{x}}, S) = m^{(p)}(t, \vec{\boldsymbol{x}})\varphi_S^{(p)}$. Based on these assumptions, the mass concentration, the momentum and the heat in this section reads:

$$m^{(p)}(t, \vec{\boldsymbol{x}}) = \int_{S_p}^{S_{p+1}} \frac{\rho_l S^{3/2}}{6\sqrt{\pi}} n(t, \vec{\boldsymbol{x}}, S)\mathrm{d}S, \tag{3.4}$$

$$m^{(p)}(t, \vec{\boldsymbol{x}})\vec{\boldsymbol{u}}^{(p)}(t, \vec{\boldsymbol{x}}) = \int_{S_p}^{S_{p+1}} \frac{\rho_l S^{3/2}}{6\sqrt{\pi}} n(t, \vec{\boldsymbol{x}}, S)\vec{\boldsymbol{u}}\mathrm{d}S, \tag{3.5}$$

$$m^{(p)}(t, \vec{\boldsymbol{x}})h_d^{(p)}(t, \vec{\boldsymbol{x}}) = \int_{S_p}^{S_{p+1}} \frac{\rho_l S^{3/2}}{6\sqrt{\pi}} n(t, \vec{\boldsymbol{x}}, S)h_l\mathrm{d}S. \tag{3.6}$$

Then, the above assumption leads to:

$$\int_{S_p}^{S_{p+1}} \frac{\rho_l S^{3/2}}{6\sqrt{\pi}} \varphi_S^{(p)} \mathrm{d}S = 1. \tag{3.7}$$

In the classical MF, $\varphi_S^{(p)}$ is a constant that may be chosen constant in radius, volume or surface. Since the size variable chosen here is the surface, $\varphi_S^{(p)}$ is then set to be a constant in surface given by:

$$\varphi_S^{(p)} = \frac{15\sqrt{\pi}}{\rho_l \left(S_{p+1}^{5/2} - S_p^{5/2} \right)}. \tag{3.8}$$

In addition, the average velocity and temperature in the p^{th} section are supposed to be independent of the droplets size.
Based on the above hypotheses, the system of conservation laws in the p^{th} section is obtained by integrating the semi-kinetic system over the size phase space of the considered section:

$$\int_{S_p}^{S_{p+1}} \frac{\rho_l S^{3/2}}{6\sqrt{\pi}} \text{Eq.(3.3)} \mathrm{d}S, \tag{3.9}$$

and this system reads:

$$\partial_t m^{(p)} + \partial_{\vec{\boldsymbol{x}}} \cdot (m^{(p)} \vec{\boldsymbol{u}}^{(p)}) = S_1, \tag{3.10}$$

$$\partial_t m^{(p)} \vec{\boldsymbol{u}}^{(p)} + \partial_{\vec{\boldsymbol{x}}} \cdot (m^{(p)} \vec{\boldsymbol{u}}^{(p)} \otimes \vec{\boldsymbol{u}}^{(p)}) = \overrightarrow{\mathbf{S}}_2 + m^{(p)} \overrightarrow{\mathbf{F}}_d^{(p)}, \tag{3.11}$$

$$\partial_t m^{(p)} h_d^{(p)} + \partial_{\vec{\boldsymbol{x}}} \cdot (m^{(p)} h_d^{(p)} \vec{\boldsymbol{u}}^{(p)}) = S_3 + m^{(p)} C_{p,l} H_{T,d}^{(p)}, \tag{3.12}$$

where the source terms read:

$$S_1 = m^{(p)} (E_1^{(p)} + E_2^{(p)}) - m^{(p+1)} E_1^{(p+1)}, \tag{3.13}$$

$$\overrightarrow{\mathbf{S}}_2 = m^{(p)} \vec{\boldsymbol{u}}^{(p)} (E_1^{(p)} + E_2^{(p)}) - m^{(p+1)} \vec{\boldsymbol{u}}^{(p+1)} E_1^{(p+1)}, \tag{3.14}$$

$$S_3 = m^{(p)} h_d^{(p)} (E_1^{(p)} + E_2^{(p)}) - m^{(p+1)} h_d^{(p+1)} E_1^{(p+1)}. \tag{3.15}$$

The averaged drag and heat exchange source terms are given by:

$$\overrightarrow{\mathbf{F}}_d^{(p)}(t, \vec{\boldsymbol{x}}) = \frac{1}{m^{(p)}} \int_{S_p}^{S_{p+1}} \frac{\rho_l S^{3/2}}{6\sqrt{\pi}} \overrightarrow{\mathbf{F}}_d(t, \vec{\boldsymbol{x}}, S, \vec{\boldsymbol{u}}) n(t, \vec{\boldsymbol{x}}, S) \mathrm{d}S, \tag{3.16}$$

$$H_{T,d}^{(p)}(t, \vec{\boldsymbol{x}}) = \frac{1}{m^{(p)}} \int_{S_p}^{S_{p+1}} \frac{\rho_l S^{3/2}}{6\sqrt{\pi}} H_{T,d}(t, \vec{\boldsymbol{x}}, S, \vec{\boldsymbol{u}}, T_d) n(t, \vec{\boldsymbol{x}}, S) \mathrm{d}S. \tag{3.17}$$

For simple models of the drag and heat transfer terms where their dependence on the size can be supposed to be $1/S$, these terms read:

$$\overrightarrow{\mathbf{F}}_d^{(p)}(t, \vec{\boldsymbol{x}}) = \overrightarrow{\mathbf{F}}_d(t, \vec{\boldsymbol{x}}, S_d^{(p)}, \vec{\boldsymbol{u}}^{(p)}), \tag{3.18}$$

$$H_{T,d}^{(p)}(t, \vec{\boldsymbol{x}}) = H_{T,d}(t, \vec{\boldsymbol{x}}, S_d^{(p)}, \vec{\boldsymbol{u}}^{(p)}, T_d^{(p)}), \tag{3.19}$$

where the characteristic droplet surface in the p^{th} section based on the constant surface recontruction is:

$$S_d^{(p)} = \frac{3\left(S_{p+1}^{5/2} - S_p^{5/2}\right)}{5\left(S_{p+1}^{3/2} - S_p^{3/2}\right)}. \tag{3.20}$$

For example, in section p, the drag per unit mass modeled by the Stokes law has the following form:

$$\overrightarrow{\mathbf{F}}_d^{(p)}(t,\vec{\boldsymbol{x}}) = \frac{\overrightarrow{\mathbf{U_g}}(t,\vec{\boldsymbol{x}}) - \vec{\boldsymbol{u}}^{(p)}(t,\vec{\boldsymbol{x}})}{\tau_p^{(p)}}, \tag{3.21}$$

where the characteristic time in section p is given by:

$$\frac{1}{\tau_p^{(p)}} = \int_{S_p}^{S_{p+1}} \frac{\rho_l S^{3/2}}{6\sqrt{\pi}} \frac{\varphi_S}{\tau_p} \mathrm{d}S = \frac{1}{C_{St} S_d^{(p)}}, \tag{3.22}$$

with $C_{St} = \dfrac{\rho_l}{18\pi\mu_g}$.

The evaporation source term is divided into two exchange terms. The first one is between successive sections ($E_1^{(p)}$ and $E_1^{(p+1)}$) and the second is the exchange between the disperse phase and the underlying gas ($E_2^{(p)}$), see Figure 3.4. This separation is done through an integration by parts and leads to:

$$E_1^{(p)} = \rho_l \frac{S^{3/2}}{6\sqrt{\pi}} R_S^{(p)} \varphi_S^{(p)}, \tag{3.23}$$

$$E_2^{(p)} = \int_{S_p}^{S_{p+1}} \rho_l \frac{\mathrm{d}_S(S^{3/2})}{6\sqrt{\pi}} R_S^{(p)} \varphi_S^{(p)} \mathrm{d}S. \tag{3.24}$$

By replacing $\varphi_S^{(p)}$ by its value and integrating we get:

$$\begin{aligned} E_1^{(p)} &= 5\frac{S_p^{3/2}}{2\left(S_{p+1}^{5/2} - S_p^{5/2}\right)} R_S^{(p)}, \\ E_2^{(p)} &= \frac{5\left(S_{p+1}^{3/2} - S_p^{3/2}\right)}{2\left(S_{p+1}^{5/2} - S_p^{5/2}\right)} R_S^{(p)} = \frac{15 R_S^{(p)}}{10 S_d^{(p)}}. \end{aligned} \tag{3.25}$$

For more information on this method and its two-way coupling with the carrier, one can refer to the thesis of *Laurent (2002)*. This model was evaluated on different configurations of increasing complexity, for example from Taylor Green vortices to 3D frozen HIT in *de Chaisemartin (2009)*. The ability of this model to precisely discribe polydispersion and hetero-PTC was proven. However, the MK MF model is expensive since a high number of sections must be considered in order to have a precise description of the polydispersion and thus of the evaporation. This is due to the fact that this model is of low order in evaporation description (*Laurent 2006*). To overcome this limitation, high order MF models can be used.

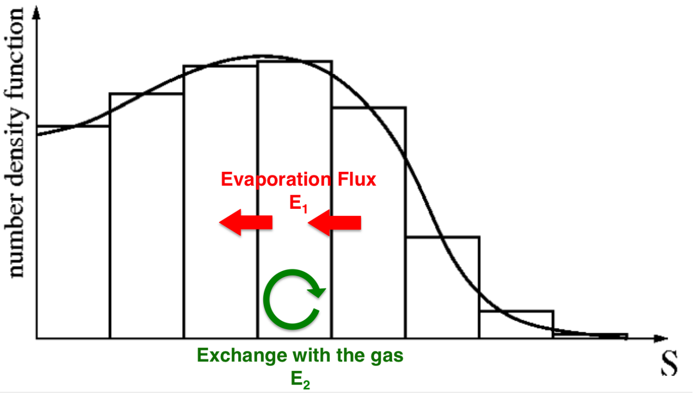

Figure 3.4: *Evaporation source term separated into two contributions between two successive sections and between the disperse phase in each section and the gas phase*

3.2.3 High order Multi-Fluid method

Instead of assuming a piecewise constant distribution in size and solving only for one moment in size, higher order MF methods suppose complex forms for $n(t, \vec{x}, S)$ with additional parameters. In this case, for each parameter an additional moment in size should be accounted for in order to close the system. For example, in *Dufour (2005)*, a piecewise exponential size distribution was chosen:

$$n(t, \vec{x}, S) = a_1^{(p)}(t, \vec{x}) \exp(-a_2^{(p)}(t, \vec{x})S) \quad \text{for } S \in [S_p, S_{p+1}[. \tag{3.26}$$

Since this distribution depends on two parameters $a_1^{(p)}$ and $a_2^{(p)}$, two moments in size should be accounted for, namely the moment of order 0 and 3/2 in surface which are respectively the number density and the mass. This method was validated for polydisperse and evaporating test cases in *Dufour (2005); Laurent (2006); Doisneau (2013); Sibra (2015)* where the derivation of this method can be found.

Instead of having an exponential form for the size distribution, a piecewise affine reconstruction can be used, where once again the moment of order 0 and 3/2 in surface are transported or the moments of order 0 and 1. For more details, one may refer to *Laurent (2006); Doisneau (2013); Laurent et al. (2016)*. In the cases where the studied moments are of order 0 and 3/2 in surface, the resulting system of conservation laws in section p which is obtained from the integration of the semi-kinetic system (3.3) gives the evolution of the number density $n^{(p)}$, the mass $m^{(p)}$ and the momentum $m^{(p)}\vec{u}^{(p)}$.

These two methods are both two size moments MF methods, examples of these TSM and of the classical one size MF method are illustrated in Figure 3.5.

In general, according to the choice of the size variable, the order of the method in size and therefore the form of the size distribution, the moments to be solved are chosen. The link between the number density, radius, surface, mass and the

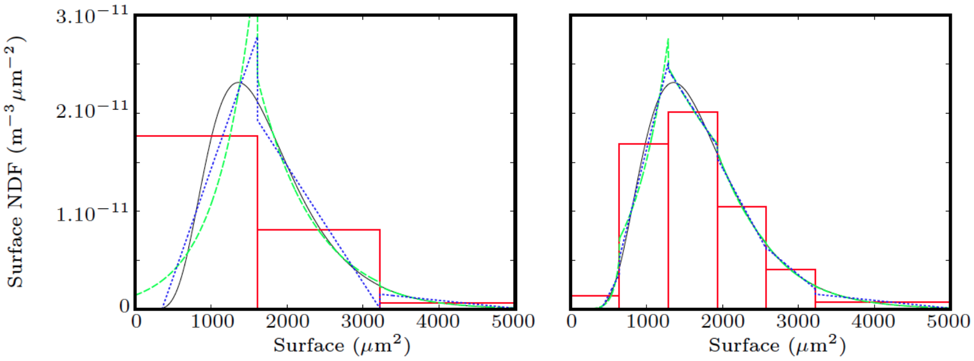

Figure 3.5: *Size distribution: reference NDF in black full line, OSM in read boxes, exponential TSM in dashed green line, affine TSM in dotted bleu line: 13 sections (left), 6 sections (right). (Source: Doisneau (2013))*

Choice of the size variable	Radius		Surface		Volume	
	power	coef.	power	coef.	power	coef.
Number	0	1	0	1	0	1
Radius	1	1	1/2	$1/\sqrt{4\pi}$	1/3	$(3/(4\pi))^{\frac{1}{3}}$
Surface	2	4π	1	1	2/3	$(6\sqrt{\pi})^{\frac{2}{3}}$
Mass	3	$\rho_l 4\pi/3$	3/2	$\rho_l/(6\sqrt{\pi})$	1	ρ_l

Table 3.1: *The link between different order moments and physical quantities such as the number density, radius, surface and mass (adapted from Doisneau (2013)).*

moments is shown in Table 3.1. Now that the Multi-fluid method is presented for the monokinetic closure, the extension of this method to the Anisotropic Gaussian velocity closure in presented in the next section in order to statistically account for homo-PTC.

3.3 Multi-Fluid Anisotropic Gaussian model

The Multi-Fluid Anisotropic Gaussian model was first introduced in the thesis of *Doisneau (2013)* using a TSM formalism to treat coalescence.
In this section, the classical MF method is derived based on an Anisotropic Gaussian distribution for the velocity.
In the following, we consider the size-velocity moments of the NDF in the section p given in equations (3.4), (3.5), (3.6) and (3.27).

$$m^{(p)}\mathbf{E}^{(p)} = \int_{S_{p-1}}^{S_p} \frac{\rho_l}{6\sqrt{\pi}} S^{3/2} n(S) \boldsymbol{E}(S) \mathrm{d}S. \tag{3.27}$$

Moreover, $\mathbf{\Sigma}_p$ is also defined by: $\mathbf{E}^{(p)} = \frac{1}{2}\left(\vec{\boldsymbol{u}}_p \otimes \vec{\boldsymbol{u}}_p + \mathbf{\Sigma}_p\right)$.

3.3.1 Semi-kinetic system

First, the semi-kinetic system is derived by assuming that the droplets at $(t, \vec{\boldsymbol{x}})$ having the same size are characterized by a given average velocity $\vec{\boldsymbol{u}}(t, \vec{\boldsymbol{x}}|S)$ and a temperature $T(t, \vec{\boldsymbol{x}}|S)$. The dispersion around the mean velocity is of paramount important for this model since it is responsible of statistically capturing the PTC and it has different values for the different directions. For the temperature the dispersion around the mean value is set to be zero in all directions. Thus, the distribution function for the temperature is a Dirac-delta function, whereas the velocity distribution function is the Anisotropic Gaussian function presented in the previous chapter. The NDF is then given as the velocity and temperature distributions, conditioned by the droplet size:

$$f(t, \vec{\boldsymbol{x}}, S, \vec{\boldsymbol{c}}, T) = n(t, \vec{\boldsymbol{x}}, S)\mathcal{N}(\overrightarrow{\mathbf{c}} - \overrightarrow{\mathbf{u}}(t, \overrightarrow{\mathbf{x}}), \mathbf{\Sigma}(t, \overrightarrow{\mathbf{x}}))\delta(T - T_d(t, \vec{\boldsymbol{x}}|S)). \tag{3.28}$$

Under these assumption the semi-kinetic system is closed in velocity and temperature and reads:

$$\begin{aligned}
&\partial_t n + \partial_{\vec{\boldsymbol{x}}} \cdot (n\vec{\boldsymbol{u}}) = -\partial_S(nR_{S,d}),\\
&\partial_t n\vec{\boldsymbol{u}} + \partial_{\vec{\boldsymbol{x}}} \cdot (n(\vec{\boldsymbol{u}} \otimes \vec{\boldsymbol{u}} + \mathbf{\Sigma})) = \frac{n(\overrightarrow{\mathbf{U_g}} - \vec{\boldsymbol{u}})}{\tau_p} - \partial_S(nR_{S,d}\vec{\boldsymbol{u}}),\\
&\partial_t n\mathbf{E} + \partial_x \cdot (n(\mathbf{E} + \mathbf{\Sigma}) \vee \vec{\boldsymbol{u}}) = \frac{n(\overrightarrow{\mathbf{U_g}} \vee \vec{\boldsymbol{u}} - 2\mathbf{E})}{\tau_p} - \partial_S(nR_{S,d}\mathbf{E}),\\
&\partial_t nh_l + \partial_{\vec{\boldsymbol{x}}} \cdot (nh_l\vec{\boldsymbol{u}}) = -\partial_S(nR_{S,d}h_l) + nC_{p,l}H_{T,d}.
\end{aligned} \tag{3.29}$$

3.3.2 OSM-AG model

Using the same classical Multi-Fluid method presented in section 3.2, the MF-AG system is derived based on the integration of the semi-kinetic AG system over the size of a given section p. This is done by accounting for the surface moment of order 3/2:

$$\int_{S_p}^{S_{p+1}} \frac{\rho_l S^{3/2}}{6\sqrt{\pi}} \text{Eq.}(3.29)\mathrm{d}S. \tag{3.30}$$

The form of the velocity distribution function is supposed to be an Anisotropic Gaussian function $\mathcal{N}$ in the section p. The resulting MF-AG system of conservation equations reads:

$$\partial_t m^{(p)} + \partial_{\vec{\boldsymbol{x}}} \cdot (m^{(p)}\vec{\boldsymbol{u}}^{(p)}) = S_1, \tag{3.31}$$

$$\partial_t m^{(p)}\vec{\boldsymbol{u}}^{(p)} + \partial_{\vec{\boldsymbol{x}}} \cdot (m^{(p)}(\vec{\boldsymbol{u}}^{(p)} \otimes \vec{\boldsymbol{u}}^{(p)} + \mathbf{\Sigma}^{(p)})) = \overrightarrow{\mathbf{S}}_2 + m^{(p)}\overrightarrow{\mathbf{F}}_d^{(p)}, \tag{3.32}$$

$$\partial_t m^{(p)}\mathbf{E}^{(p)} + \partial_x \cdot (m^{(p)}(\mathbf{E}^{(p)} + \mathbf{\Sigma}^{(p)}) \vee \vec{\boldsymbol{u}}^{(p)}) = \mathbf{S_E} + \mathbf{S}_g^{(p)}, \tag{3.33}$$

$$\partial_t m^{(p)}h_{ld}^{(p)} + \partial_{\vec{\boldsymbol{x}}} \cdot (m^{(p)}h_{ld}^{(p)}\vec{\boldsymbol{u}}^{(p)}) = S_3 + m^{(p)}C_{p,l}H_{T,d}^{(p)}, \tag{3.34}$$

where the source terms S_1 and $\overrightarrow{\mathbf{S}}_2$, S_3 and $\overrightarrow{\mathbf{F}}_d^{(p)}$ are given by equations (3.13) and (3.21), and $\mathbf{S}_{\mathbf{E}}$ and $\mathbf{S}_g^{(p)}$ read:

$$\mathbf{S}_{\mathbf{E}} = m^{(p)}\mathbf{E}^{(p)}\left(E_1^{(p)} + E_2^{(p)}\right) - m^{(p+1)}\mathbf{E}^{(p+1)}E_1^{(p+1)}, \tag{3.35}$$

$$\mathbf{S}_g^{(p)} = \frac{m^{(p)}(\overrightarrow{\mathbf{U}_{\mathbf{g}}} \vee \vec{\boldsymbol{u}}^{(p)} - 2\mathbf{E}^{(p)})}{\tau_p^{(p)}}. \tag{3.36}$$

The resulting system for OSM-AG is capable to accurately describe the polydispersion by using nearly 10 sections, and to capture the velocity dispersion. Therefore, it captures hetero-PTC and reproduces statistically the homo-PTC.

3.3.3 TSM-AG

Instead of using the classical MF method to derive a polydisperse AG model, one can use high order MF such as the TSM that gives accurate results with less sections than with OSM.

In this case, in addition to the size-velocity moments defined in the begining of this section, an additional moment is defined, it is the moment of order 0 in all variable, ${}^0M^0_{0,0,0}$. This is the number density, which, for a given section p, reads:

$$n^{(p)} = \int_{S_{p-1}}^{S_p} n(S)\mathrm{d}S. \tag{3.37}$$

To close the equations on the moments, the NDF is reconstructed from the controlled moments. This means that $n(S)$, $\vec{\boldsymbol{u}}(S)$ and $\boldsymbol{\Sigma}(S)$ from Equation (3.28) are presumed in each section p: $\vec{\boldsymbol{u}}(S)$ and $\boldsymbol{\Sigma}(S)$ are assumed to be constant, equal to $\vec{\boldsymbol{u}}$ and Σ, and an affine by part reconstruction $\kappa_p(S)$ is used for $n(S)$, which was shown to be accurate and stable (*Laurent et al. 2016*). As in the case of OSM, the repartition of sizes in a given section $[S_p, S_{p+1}]$ is decoupled from the evolution of the mass concentration $n^{(p)} = m^{(p)}(t, \vec{\boldsymbol{x}})\kappa_p(S)$.

Three types of reconstruction are used for $\kappa_p(S)$, depending on the value of $m^{(p)}/n^{(p)}$. They are represented in Figure 3.6 (see *Laurent et al. (2016)* for more details).

With this presumed NDF, the equations are written:

$$\partial_t n^{(p)} + \partial_{\vec{\boldsymbol{x}}} \cdot (n^{(p)}\vec{\boldsymbol{u}}^{(p)}) = S_0, \tag{3.38}$$

$$\partial_t m^{(p)} + \partial_{\vec{\boldsymbol{x}}} \cdot (m^{(p)}\vec{\boldsymbol{u}}^{(p)}) = S_1, \tag{3.39}$$

$$\partial_t m^{(p)}\vec{\boldsymbol{u}}^{(p)} + \partial_{\vec{\boldsymbol{x}}} \cdot (m^{(p)}(\vec{\boldsymbol{u}}^{(p)} \otimes \vec{\boldsymbol{u}}^{(p)} + \boldsymbol{\Sigma}^{(p)})) = \overrightarrow{\mathbf{S}}_2 + m^{(p)}\overrightarrow{\mathbf{F}}_d^{(p)}, \tag{3.40}$$

$$\partial_t m^{(p)}\mathbf{E}^{(p)} + \partial_x \cdot (m^{(p)}(\mathbf{E}^{(p)} + \boldsymbol{\Sigma}^{(p)}) \vee \vec{\boldsymbol{u}}^{(p)}) = \mathbf{S}_{\mathbf{E}} + \mathbf{S}_g^{(p)}, \tag{3.41}$$

$$\partial_t m^{(p)}h_{ld}^{(p)} + \partial_{\vec{\boldsymbol{x}}} \cdot (m^{(p)}h_{ld}^{(p)}\vec{\boldsymbol{u}}^{(p)}) = S_3 + m^{(p)}C_{p,l}H_{T,d}^{(p)}, \tag{3.42}$$

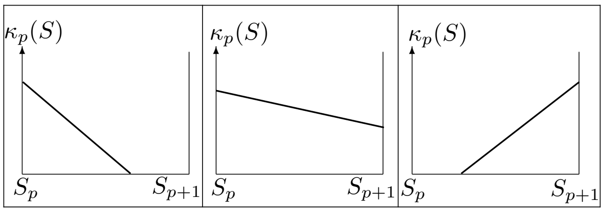

Figure 3.6: *The three types of affine reconstructions.*

where the source terms S_1 and $\overrightarrow{\mathbf{S}}_2$, S_3, $\overrightarrow{\mathbf{F}}_d^{(p)}$, $\mathbf{S_E}$ and $\mathbf{S}_g^{(p)}$ are given by equations (3.13), (3.21) and (3.35) , where $E_1^{(p)}$ and $E_2^{(p)}$ are expressed through the general formula to take into account the affine reconstruction in size $\kappa_p(S)$ instead of assuming constant $\varphi_S^{(p)}$ as for OSM:

$$E_1^{(p)} = \rho_l \frac{(S_p)^{3/2}}{6\sqrt{\pi}} R_S^{(p)} \kappa_p(S_p), \tag{3.43}$$

$$E_2^{(p)} = \int_{S_p}^{S_{p+1}} \rho_l \frac{S^{1/2}}{4\sqrt{\pi}} R_S^{(p)} \kappa_p(S) \mathrm{d}S. \tag{3.44}$$

In addition the source terms S_0 reads:

$$S_0 = R_S^{(p)} \kappa_p(S_p) - R_S^{p+1} \kappa_p(S_{p+1}), \tag{3.45}$$

with $\tau_p^{(p)} = \frac{\rho_l}{18\pi\mu_g} S_p^{mean}$ and

$$S_p^{mean} = \frac{\int_{S_p}^{S_{p+1}} S^{3/2} \kappa_p(S) \mathrm{d}S}{\int_{S_p}^{S_{p+1}} S^{1/2} \kappa_p(S) \mathrm{d}S}. \tag{3.46}$$

This high order moment method in size and velocity is able to reproduce the two types of PTC and to describe polydispersion in an efficient and accurate way. This model however does not account for the temperature dispersion and further developement should be done in the future to obtain a high order moment method is size, velocity and temperature. Even without this extension, the TSM-AG is a promising model to describe the spray combustion especially since it represents a compromise between the cost and the level of details. Thus, the direct perspective of this work is to validate this model in academic and industrial combustion applications.

Part II

Numerical methods

In this part, the numerical strategy used to solve the systems of equations obtained in Part I is presented. Chapter 4 starts with a non exhaustive overview of the classical families of discretization, followed by the meshing techniques and the system of equations to be solved. In addition, a summary of few academic, semi-industrial and industrial codes is used to depict the use of the numerical schemes in computational fluid dynamics for the transport solvers. Finally, the objectives and challenges for the choice of the numerical scheme are specified. Based on these objectives, several numerical schemes are chosen and presented in chapter 5, namely the third order finite element Two-Steps Taylor-Galerkin (TTGC) scheme, the second order finite volume kinetic scheme (FVKS), a realizability-preserving second order finite volume MUSCL/HLL scheme and a realizability-preserving second order Discontinuous Galerkin method (DG). These schemes are compared on 1D and 2D test cases in Chapter 6.

Chapter 4

Numerical schemes: overview and objectives

This chapter is an introduction to some numerical methods for the resolution of the partial differential equations (PDE) resulting from the modeling procedure. First, a non-exhaustive overview of some classical discretizations is presented, namely the finite difference (FD), the finite volume (FV), the finite element (FE), and the discontinuous Galerkin methods (DG). This brief review is found in section 4.1, where the general advantages and disadvantages of each family is discussed. The meshing techniques are exhibited is section 4.2. The system of PDE to be resolved is then presented along with the splitting strategy leading to the separate resolution of the hyperbolic system of equations and source terms.
Then, few academic, semi-industrial and industrial codes are presented to illustrate the use of the numerical schemes covered in section 4.1 in computational fluid dynamics for the transport part.
Finally, the characteristics and properties of the numerical scheme that are required for the resolution of the resulting hyperbolic PDE are presented.

4.1 Introduction to numerical methods

In the literature, one can find various numerical schemes for the resolution of systems of partial differential equations. Most of these schemes belong to one of the three families: the finite difference (FD), the finite volume (FV) and the finite element (FE) methods. These families differ by their spatial discretization. Thus, the spatial derivative operators are represented differently according to the chosen family.
In the following, the discrete versions of a PDE are compared to show the differences between these strategies.

For clarity, this is done for a 1D conservation law (Equation (4.1)) of the variable u. It writes:

$$u_t + (f(u))_x = 0, \tag{4.1}$$

where $f : \mathbb{R} \to \mathbb{R}$ is the flux function for $x \in \mathbb{R}$.

4.1.1 Finite difference methods

This family is considered to be the simplest approach. It is based on the strong or differential form of the governing equation (Equation (4.1)). A grid x_i for $i = 1, ..., N$ is laid down in space, as represented in Figure 4.1. The local grid size is Δx_i.

The main idea is to evaluate the solution of the PDE as a pointwise approximation at the grid points. By doing so, the issue is the evaluations of the space derivatives, which is done using a Taylor expansion. This leads to the semi-discretized equation (4.2) when considering for example the forward discretization. u_h and f_h are the numerical approximations of respectively the solution and the flux. Under certain conditions, the numerical solution $u_h(x_i, t)$ may converge toward an approximation of the solution of the PDE.

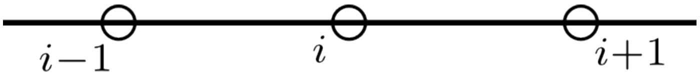

Figure 4.1: *Finite difference discretization in 1D*

$$\frac{\mathrm{d}u_h(x_i,t)}{\mathrm{d}t} + \frac{f_h(x_{i+1},t) - f_h(x_i,t)}{\Delta x_i} = 0. \tag{4.2}$$

For example, for the linear advection equation where $f(u) = au$ and a is constant, using a first order forward Euler time integration, Equation (4.2) becomes:

$$\frac{u_h(x_i,t+1) - u_h(x_i,t)}{\Delta t} + a\frac{u_h(x_{i+1},t) - u_h(x_i,t)}{\Delta x_i} = 0, \tag{4.3}$$

that is only stable if $a < 0$ under the Courant-Friedrichs-Lewy condition (CFL) $\frac{|a|\Delta t}{\Delta x} \leq 1$. Here comes the importance of the upwind differencing, where the difference direction is adapted according to the direction of propagation of the information: forward difference is chosen for $a < 0$ and backward difference selected for positive values of a.

One of the oldest and most fundamental theoretical reference for the finite difference technique is by *Courant et al. (1928)*. Then, after the second world war, this technique gained popularity and progress especially for its use in large scale practical applications with the aid of increasingly efficient computers (*Thomée 2001*). The finite difference method was then used for the resolution of hyperbolic equations, starting with the work of *Lax and Wendroff (1964); Courant*

et al. (1952). For these equations, the information is expected to propagate as waves moving along characteristics (*LeVeque 2002*). Thus, upwind differencing, which is a one-sided approximation where the side depends on the direction of propagation of the information for each characteristic (*LeVeque 2002; Toro 2009*), gained popularity for convection-dominated problems (*Courant et al. 1952; Godunov 1959; Fromm 1968; van Leer 1986; van Leer 2006*).
Another interest is that high order finite difference can be easily obtained since the accuracy of the method is determined by the order of approximation of the discrete derivatives. This unfortunately leads to very large stencils making the method complex and unattractive for unstructured grids (*Visbal and Gaitonde 2002; Liu et al. 2006*) and parallel computing.
An alternative approach to deriving high order finite differences is to use compact finite differences (*Lele 1992; Yee 1997*), where a Padé approximation is used to approximate the derivatives.
The advantages of the finite difference methods lay in their simplicity and the flexibility to choose a given expansion in time. This makes them easy in programing and efficient in terms of computational cost. Owing to these strong points, this approach was traditionally used for computationally costly problems, such as laminar-turbulent transition (*Kloker 1997*).
However, the bottleneck of this method is due to its discretization based on topologically square network of lines, making the approach itself impractical for handling complex geometries in multiple dimensions (*Peiro and Sherwin 2005*). In addition, this classical approach can break down near discontinuities where the differential equation does not hold in the classical sense (*LeVeque 2002*).

4.1.2 Finite volume method

The use of the integral form of the PDEs has great advantages, since it is not limited to a special mesh structure. For example, we can see the integral form of Equation (4.1) in Equation (4.4):

$$\frac{\partial}{\partial t}\left(\int_V u(x,t)\mathrm{d}V\right) + \int_V (f(u))_x\,\mathrm{d}V = 0. \tag{4.4}$$

This is the starting point of the finite volume and finite element techniques.
In the finite volume methods, the domain is tessellated into non-overlapping control volumes (CV) organized in a structured or unstructured way to cover the whole geometry. The 1D FV discretization is shown in Figure 4.2 where the i^{th} grid cell or CV is $I_i = [x_{i-1/2}, x_{i+1/2}]$.
Once the meshing is done, an integral conservation law is then written on each CV, I_i where f^* is the numerical flux:

$$\int_{I_i} \frac{\partial u}{\partial t}\mathrm{d}V + \int_{I_i} (f(u))_x\,\mathrm{d}V = \left(\frac{\partial}{\partial t}\int_{I_i} u\mathrm{d}x\right) + (f^*(u(x_{i+1/2})) - f^*(u(x_{i-1/2}))) = 0.$$

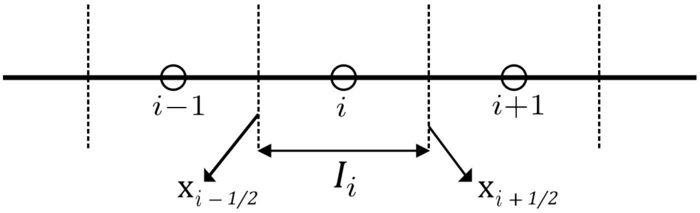

Figure 4.2: *Finite volume discretization in 1D*

(4.5)

At this point, it can be seen that Equation (4.5) requires the knowledge of the fluxes at each cell interface. These fluxes depend on the state on each side of the interface. In fact, if a first order approximation (piecewise constant) is considered, a Riemann problem (RP) is obtained at each interface. *Godunov (1959)* proposed to solve the two Riemann problems found at the interfaces: RP($\overline{u}_{i-1}, \overline{u}_i$) and RP($\overline{u}_i, \overline{u}_{i+1}$) as seen in Figure 4.3. The updated value of the cell averaged solution in the i^{th} CV is then obtained by taking the integral average in I_i of the combined solutions of these two local RP.

The solution of the RP is not always mathematically straightforward and is most of the time computationally expensive. Consequently, a number of alternative numerical fluxes called approximate Riemann solver have been proposed in the literature. Among the various numerical fluxes available in the literature, we here name Roe flux (*Roe 1981*), Osher flux (*Osher and Solomon 1982*), Lax-Friedrichs flux, HLL flux (*Harten et al. 1983*) and HLLC flux (*Toro et al. 1994*). For more details, the reader may refer for example to one of the following references: *Toro (2009); LeVeque (2002)*.

To extend this approach to higher order schemes, a generalized Riemann problem (GRP) is obtained instead of RP that does not have a self-similar analytical solution as the case of RP.

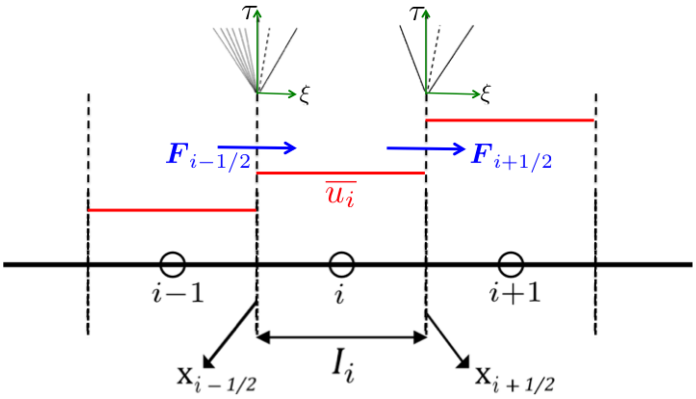

Figure 4.3: *Finite volume discretization in 1D*

A second challenge is faced through the theorem of Godunov stating that all linear schemes that preserve solution monotonicity are at most first order accurate (*Godunov 1959*). Thus, high order schemes should add nonlinearity to simultaneously be able to monotonously resolve the discontinuities and keep the global precision (*Barth and Ohlberger 2004*).
In the 1970s, two high order FV methods were proposed and they were both based on the idea of adding nonlinearity to avoid spurious oscillations in the vicinity of strongly varying gradients (*van Leer 2006*). These schemes are the Flux-Corrected Transport method (FCT) by *Boris and Book (1973)*, where the higher order extension is included in the flux and the Monotone Upstream Scheme for Conservation Laws (MUSCL) by *van Leer (1974)*, where the higher order extension is based on a reconstruction step. The state of the art of these two schemes along with the limiting technique is briefly presented in the next paragraphs.

4.1.2.1 Flux-Corrected Transport

The FCT is based on a predictor-corrector methodology. First, the solution is estimated through a first order nonoscillatory scheme, and then it is corrected by removing the dissipative errors to get a solution of high order accuracy using corrective fluxes. This method was then used and evolved by many researcher and it still finds its way in today's research world (*Zalesak 1979; Boris et al. 1993; Zalesak 1997; Cheng-cai and Jun 2010; Patnaik and Boris 2010; Kuzmin et al. 2012*).

4.1.2.2 Monotone Upstream Scheme for Conservation Laws

The MUSCL by van Leer (1974; 1979) uses linear interpolation and preserves the monotonicity by a slope limiting procedure. This scheme combines the Godunov's method where the fluxes are derived from the solution of the RP at the interfaces with a high order reconstruction leading to upwind-based scheme (*van Leer 2006*). It is important to note that *Kolgan (1972)* devised a high order extension of the Godunov's method that was very similar to MUSCL (*van Leer 2006; Toro 2009*).
An advanced version of MUSCL was later developed by *Colella and Woodward (1984)*. It is the piecewise-parabolic method (PPM) where the basic interpolation functions are parabolae and additional dissipation is introduced. *Colella (1984)* presented also a comparison between the PPM scheme, the classical MUSCL and other schemes such as FCT scheme and Godunov's scheme for the simulation of two-dimensional fluid flow with strong shocks.
Lately, Berthon (2005; 2006b; 2014) analyzed the stability of the MUSCL scheme for the Euler equations, its robustness on unstructured meshes and introduced a new version of the MUSCL scheme based on Dual Mesh Gradient Reconstruction.

Ever since its publication, the MUSCL method has been the subject of many studies and advances, its usage was extended for example to 2D shallow water equations (*Hou et al. 2015*) and two-phase flows (*Vié et al. 2013; Vié et al. 2015*). Another improvement is the Multislope MUSCL method for unstructured meshes (*Buffard and Clain 2010; Le Touze et al. 2015; Dupif 2017*).

If this scheme is applied without the limiting procedure, it will generate spurious oscillations and wiggles especially near discontinuities. For many cases, these oscillations are also generated even for smooth solution due to the dispersive nature of the schemes. For this reason, the use of limiters is of paramount importance and it should:

- keep the high order accuracy where possible but degenerate to lower order near discontinuities,
- eliminate or minimize phase error.

Actually, a slope limiter is used in many high order FV and FD methods. It is a very widely used way to preserve the monotonicity and thus it is presented in appendix C.

These limiters suffer from the risk of degenerating to lower order of accuracy in smooth regions. In fact, *Osher (1984)* proved that the total variation diminishing (TVD) discretizations reduce to at most first order accuracy at non-sonic critical points. Thus, the need for devising schemes with weaker constraints emerged and this was one of the main reasons for the development of the Essentially Non-Oscillatory schemes that is the subject of the next paragraph.

4.1.2.3 Essentially Non-Oscillatory schemes

In the late 1980s, a new non-linear technique was introduced for the development of oscillation-free higher order FV methods based on the non-oscillatory interpolation theory.

The Essentially Non-Oscillatory schemes by *Harten et al. (1986)* is based on a piecewise polynomial interpolation where a nonlinear procedure of selection of the discrete stencil whose data will give the smoothest interpolant is applied. The resulting ENO scheme is total variation bounded (TVB) (*Harten et al. 1987*). Following this work, Shu and Osher (1988; 1989) worked on the efficient implementation of these schemes. Then, an advanced version of this scheme was developed: the Weighted Essentially Non-Oscillatory schemes (*Liu et al. 1994; Jiang and Shu 1996*). WENO has higher accuracy in smooth solution regions than the classical ENO scheme. Also, the differentiability in WENO is improved leading to higher robustness for steady state calculations (*Barth and Ohlberger 2004*).

In the literature, we can find many research directions for the advancement of WENO schemes, whether by improving the accuracy or the efficiency by tuning the linear and nonlinear weights or the smoothness indicators (*Shu 2016*). For example, an improved version of WENO from the accuracy point of view can be found in the work of *Castro and Toro (2008)* called WENO-Z scheme. Other examples are the ADER WENO (*Dumbser et al. 2014; Balsara and Kim 2016*) and the adaptive mesh WENO (*Hu et al. 2015*). The main disadvantages of these methods is their high computational cost and the fact that they are TVB which may cause problems of negative densities near vacuum regions.

4.1.3 Finite element methods

Similar to the FV, the finite element methods do not use the differential form of the PDEs but they use its integral form instead. In fact, the FE method does not use exactly the integral form shown in Equation (4.4) but an alternative integral form called the weak or variational form, which is the first step in a weighted residual formulation leading to the finite element discretization (*Donea and Huerta 2003*).

Before presenting the historical review of the FE method itself, we will go further back in time to the late 1890s, when *Lord Rayleigh (1894)* used for the first time the variational formulation. Few years later, *Ritz (1909)* presented an approach where the approximate solution based on the variational formulation is a finite linear combination of polynomials.

One of the earlier developments were made by *Hrennikoff (1941)* who named the approach the framework method. At the same time, *Courant (1943)* proposed a discrete solution based on continuous piecewise linear functions over triangulations adapted to the studied geometry. This article is considered to be the starting point of the FE method, knowing that this method is indebted to the work of *Galerkin (1915)* especially for the orthogonality condition and for the used of test and trial functions that belong to the same class. For a historical survey on the finite element methods, one may refer for example to the articles of *Clough (1990); Donea and Quartapelle (1992); Thomée (2001)*. Here only a brief summary of the history of the FE methods is presented.

The FE method was first introduced as a computational method in the domain of solid mechanics in civil and aeronautical engineering to solve for structural analysis and complex elasticity problems (*Argyris 1955; Turner et al. 1956*). And it is due to this engineering work that the word finite element came to life during a presentation entitled "the finite element method in plane stress analysis" by *Clough (1960)*.

Another independent article for the launching of FE method is by *Feng (1965)* who named the method "FD method based on variation principle". Actually, *Feng (1965)* and *Friedrichs (1962)* both worked on the construction and analysis of the Rayleigh-Ritz procedure.

More advancements were carried out by *Hinton and Irons (1968); Baker (1975); Ciarlet (1978)*. Also in this period, mathematical analysis of the FE method were conducted by (*Birkhoff et al. 1968; Strang and Fix 1973*).

The success of the FE method in structural mechanics was not directly trans-

lated to the fluid dynamics field. This is due to the generation of spurious node-to-node oscillations by the standard Galerkin FE method. Thus, stabilization techniques were developed and were considered a major breakthrough back then in FE methods for fluid dynamics such as the Streamline-Upwind Petrov-Galerkin (SUPG) and the Galerkin/Least-squares methods (*Donea and Huerta 2003*). *Brooks and Hughes (1982)* proposed an artificial diffusion operator that acts only in the flow direction and not transversely, which was the basic idea of SUPG (*Bonhaus 1998*).
Then, the Taylor-Galerkin method was devised for time-dependent advection dominated PDE, were the time discretization is taken as the first step of the discretization process and is prearranged to match the high spatial accuracy achieved by linear elements (*Donea and Huerta 2003*). This family of methods was published in several papers by Donea and collaborators (*Donea 1984; Donea et al. 1987; Donea and Quartapelle 1992; Quartapelle and Selmin 1993*) and more recently by *Colin and Rudgyard (2000)*.

This weak integral form is obtained by multiplying the differential form by the weighting or test function ψ, integrating it over the whole domain V and finally applying the Green-Gauss divergence theorem to the flux term:

$$\int_V \left(u_t + \nabla \cdot f(u)\right)\psi \mathrm{d}V = \int_V u_t \psi \mathrm{d}V - \int_V \left(\nabla\psi \cdot f(u)\right)\mathrm{d}V + \int_A \psi\left(f(u)\cdot n\right)\mathrm{d}A = 0, \tag{4.6}$$

where A is the boundary of the domain V and n is the unit normal vector pointing outward.
After the variational formulation, the discretization strategy follows. The first step is to discretize the domain V into N elements, $I_i = [x_i, x_{i+1}]$ as seen in Figure 4.4. Based on this spatial discretization the discretized version of the weak form of the PDE is obtained as the sum over the whole domain of the weak formation on the elements:

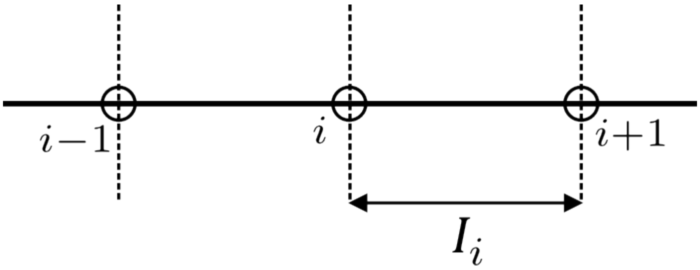

Figure 4.4: *Finite element discretization in 1D*

$$\sum_i \left[\int_{I_i} u_t \psi \mathrm{d}V - \int_{I_i} \left(\nabla\psi \cdot f(u)\right)\mathrm{d}V + \int_{\delta I_i} \psi\left(f(u)\cdot n\right)\mathrm{d}A\right] = 0. \tag{4.7}$$

The local approximate solution is then defined through trial functions also called admissible solutions. This leads to the discrete approximate solution u_h obtained as a linear combination of these basis functions $\varphi_i(x)$:

$$u_h(x,t) = \sum_{i=1}^{N+1} u_i(t)\varphi_i(x). \tag{4.8}$$

An example of basis functions as piecewise continuous polynomials is shown in Figure 4.5. The choices of the test and trial function spaces are two very important ingredients of the FE discretization strategy and govern the type of the obtained FE scheme. For example, in Galerkin FE methods, the weighting functions and the basis functions belong to the same space.

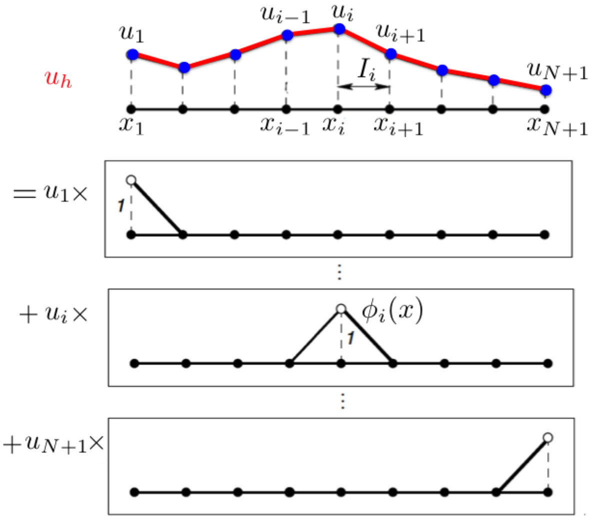

Figure 4.5: *A piecewise linear approximation (adapted from Peiro and Sherwin (2005))*

The advantages of the FE method is its geometric flexibility due to the use of the variational approach, the compact stencil of the high order schemes since this can be achieved by increasing the degree of the trial function and the straightforward error analysis.
The main disadvantage is the coupling of the degrees of freedom at the nodes. This is faced in the continuous FE method and leads to coupled system of equations to be solved every time step.

All the FE methods mentioned so far are continuous methods where the elements are conforming meaning that continuity is required for the test and trial functions at the nodes. Another class is the discontinuous Galerkin method for which a brief history is presented in the following subsection and a new scheme belonging to this family is presented in details in the next chapter.

4.1.4 Discontinuous Galerkin methods

The Discontinuous Galerkin methods gain more and more popularity each day since this approach couples the advantages of the finite volume and finite elements method.
Knowing that this method is usually classified as a FE method, here it is presented as an independent family since it has hybrid finite element and finite volume methodologies. A brief history of the development of the DG method is presented hereafter. For a more comprehensive survey one may refer to the work of Shu (2013; 2016), *Landmann (2012)* or *Larat (2016)*, as well as the books of *Kanshat (2007)* and *Hestaven and Warburton (2008)* for example.
The first discontinuous Galerkin method for steady state linear scalar conservation laws was introduced by *Reed and Hill (1973)* to solve the neutron transport equations. A year later, LeSaint and Raviart carried the first error estimated for the DG method of Reed and Hill and studied its rates of convergence. This work evolved further in (1986) by Johnson and Pitkaranta.
From year (1989) to (1998b), Cockburn and Shu published a series of five papers considered to be a keystone in the DG history. In this work, linear and nonlinear time dependent hyperbolic systems were solved by the DG method. The time discretization was done with Strong Stability Preserving (SSP) Runge-Kutta methods (*Gottlieb and Shu 1998; Gottlieb et al. 2001; Gottlieb et al. 2009; Shu 2001*).
Another reference for DG schemes for hyperbolic problems is by *Johnson (1993)*. *Jiang and Shu (1994)* proved the cell entropy inequality for DG for nonlinear conservation laws. Then, DG methods were designed for convection-diffusion problems by Bassi and Rebay in (1997) , Cockburn and Shu in (1998a) and Baumann and Oden in (1999b).
Atkins and Shu (1998) analyzed the stability limitations and introduced quadrature-free implementation of DG for hyperbolic equations. In this same year, the local grid refinement method for DG was introduced (*van der Vegt and van der Ven 1998*). This hp-refined DG methodology was used later on by several researchers and engineers (*Eskilsson and Sherwin 2004; Hartmann 2006*). In this domain various superconvergence results can be found in the literature, one of the first article is by (*Cheng and Shu 2008*).
In (2004), Cockburn et al. formulated a locally divergence-free discontinuous Galerkin methods for the resolution of Maxwell equations.
For elliptic equations, the interior penalty discontinuous FE methods were developed by *Arnold et al. (2001)* in a DG framework. Further advances for DG for solving elliptic equations can be found in *Ortner and Süli (2007); Rivière (2008)*.
Dumbser and collaborators also worked on DG (*Dumbser and Munz 2005; Dumbser et al. 2008*). Two of their main contributions are the use of WENO limiter to achieve non-oscillatory properties (*Zhu et al. 2008; Zhu et al. 2011; Dumbser et al. 2014*) and the space-time adaptive ADER-DG (*Zanotti et al.*

2015).

If limiter introduced in the FV method is applied to the DG method the order of accuracy might be degenerated, for this reason another methodology was developed by *Zhang and Shu (2010)*. This methodology is formulated for maximum-principle-satisfying and positivity-preserving high order schemes (*Zhang 2011*) for DG and FV. Its application on DG was then carried out (*Zhang and Shu 2011*) as well as its application to 3D on unstructured mesh (*Zhang et al. 2012*; *Chen et al. 2016*).

These techniques were extended to the DG scheme for the Pressureless Gas Dynamics system (resulting from the MK model presented in the previous part) by *Larat et al. (2012)*, for Krause's consensus models by *Yang et al. (2013)*, for entropy-based moment closures for linear kinetic equations by *Alldredge and Schneider (2015)* and for the chemotaxis model by *Zhang et al. (2016)*.

One of the most recent advances is for curved boundary treatment with DG by *Zhang (2016)*.

In addition, different numerical schemes from the DG family were recently used for many other domains such as the shallow water model (*Kesserwani and Liang 2012*), the Lagrangian hydrodynamics (*Vilar et al. 2011*), the front tracking ghost fluid method (*Lu et al. 2016*),the level set method (*Fechter and Munz 2015*; *Hitz et al. 2016*; *Ta et al. 2016*), the relativistic astrophysics (*Teukolsky 2016*) and the coupled Navier-Stokes/Cahn-Hilliard equations (*Pigeonneau and Saramito 2016*).

In DG, first the computational domain is divided into $N = \frac{1}{h}$ sub-intervals I_i, see Figure 4.6.

$$I_i =]x_{i-\frac{1}{2}}, x_{i+\frac{1}{2}}[, \tag{4.9}$$

where,

$$x_{i-\frac{1}{2}} = \frac{(i-1)}{N}, \quad x_i = \frac{(i-1/2)}{N}, \quad x_{i+\frac{1}{2}} = \frac{i}{N}, \quad i = 1, ..., N. \tag{4.10}$$

The spatial discretization is based on the weak formulation and uses trial function spaces for approximating the solution similar to the FE methods. However, unlike the classical FE methods, DG allows discontinuity across the element interfaces as illustrated in Figure 4.6 . The treatment of these discontinuities is done with the FV technique of solving general RP at the interfaces. Also the

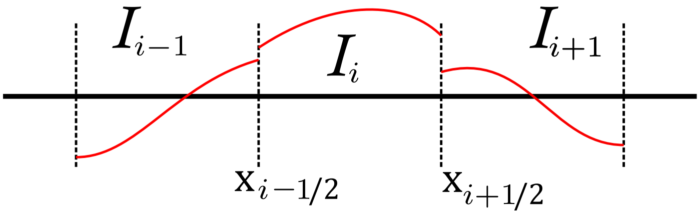

Figure 4.6: *Discontinuous space discretization for DG*

nonlinear limiting technique already introduced for the FV methods may be used in DG to avoid spurious oscillations near discontinuities.

4.2 Meshing

Meshes can be classified based on the type of the elements used, the connectivity between the elements and the control volumes on which the equations are discretized.
Various elements exist: the most used ones are the triangles or rectangles in 2D and hexahedra and tetrahedra in 3D.
In addition there exist various ways to define the Control Volume for a cell in the domain, for example in Figure 4.7 one can see the 2D triangular mesh for cell centered CV and vertex centered CV (*Barth and Ohlberger 2004*).

The connectivity based classification is considered as a classification of the grids. Three types can be distinguished:

- structured meshes where the connectivity between the elements is simple and regular. It allows a storage arrangement for the relationships between the neighboring cells. This type is limited by the used of quadrilateral elements in 2D and hexahedra in 3D.
- unstructured meshes where irregular connectivity is found in the grid. The advantage of this method is that a greater flexibility for the choice of the elements type. However, it is not very efficient when it comes to the storage, since one needs to store all the information needed about the connectivity between the cells.
- hybrid meshes that contains both meshes types.

Even if the structured mesh that have been traditionally used to discretize the computational domain are very useful for devising efficient high order numerical schemes, they are inherently difficult and time consuming when dealing with complex geometries. On the other hand, unstructured meshes can be

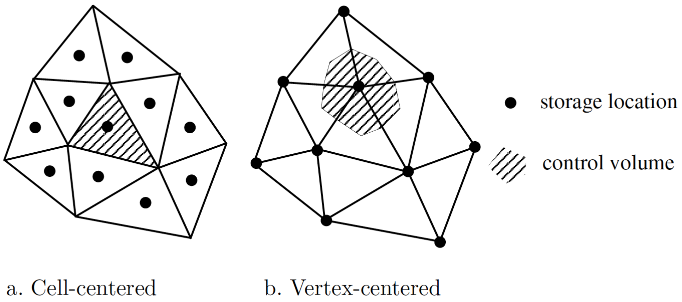

Figure 4.7: *2D triangular tesselation with control volume variants, source Barth and Ohlberger (2004)*

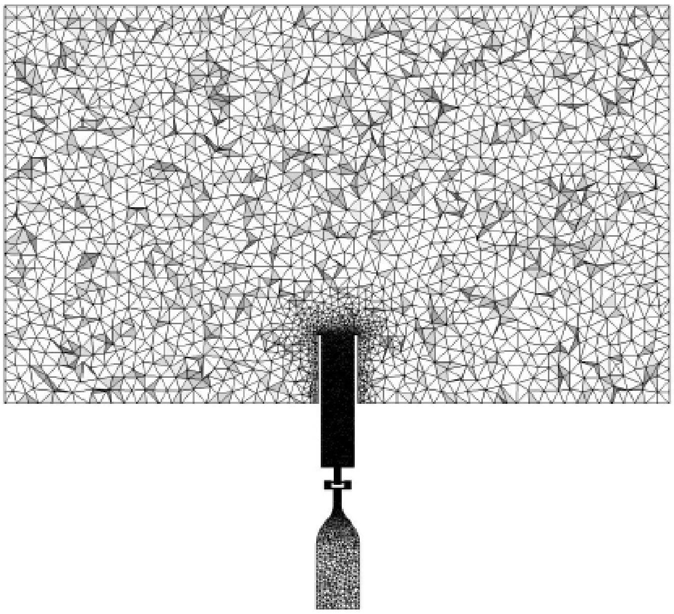

Figure 4.8: *Axial view of a mono-injector 3D unstructured mesh with tetrahedra, source Philip (2016)*

highly automated and time efficient. In addition, for the complex geometries the unstructured technique offers a great flexibility compared to the structured one where the domain should be divided into different blocks to obtain a convenient structured mesh in each of these subdomains. An example of unstructured meshes is illustrated in Figure 4.8. Finally, the unstructured meshes are more easily used for the adaptive techniques and in case where topological alteration of the mesh is needed. On the other hand, unstructured mesh may demand a larger memory that the structured one.

Finally, in complex application where the geometries are complex and large what is usually done to optimize the cost of a simulation is to used a coarse mesh in the regions of low interest while refining locally the mesh in a optimal manner near the regions of interest. This is known as the adaptive mesh refinement (AMR) and was a revolution in the computational domain since it provides accurate solutions at lower costs. It was introduced by *Berger and Oliger (1984)* on structured grids. In general, the adaptation method can be done by redistributing the grid (r-refinement) or by enriching the grid (h-refinement). The h-refinement method is particularly attractive to industrial applications due to its flexibility, especially when used with unstructured grids. The AMR can be done through a block-based method where the block structures are uniformly refined or a cell-based method that allows high rate of compression (*Essadki et al. 2016*; *Drui et al. 2016*).

The complete strategy of AMR can be divided into three steps:

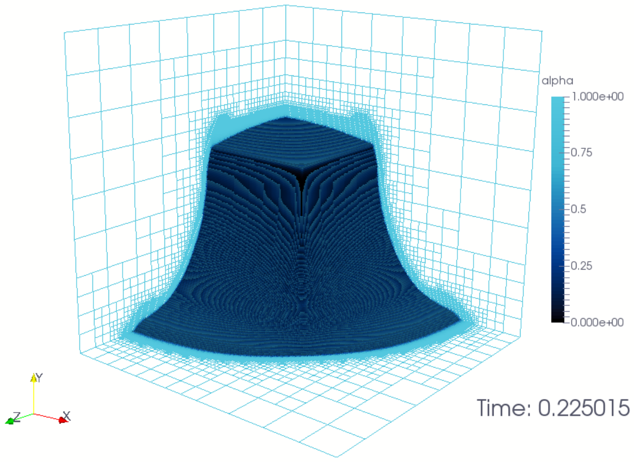

Figure 4.9: *AMR on structured grid for a 3D dam-break configuration, source Drui et al. (2016)*

- compute the solution at time t^n
- estimate the local error
- adapt the mesh according to the error estimate

An example of AMR for a dam break is shown in Figure 4.9 on structured grid (*Drui et al. 2016*).

These techniques will not be used in this work but the proposed method should have the flexibility of application with AMR.

4.3 System of equations

4.3.1 Operator splitting methods

In order to numerically solve the resulting system of the MK and Gaussian model presented in part I. For simplicity, the source terms are splitted from the free transport terms by the operator splitting technique proposed by *Strang (1968)*. This technique is of second order in time, if the time step is smaller than all the physical scales and the solution is regular (*Descombes and Massot 2004*; *Descombes et al. 2016*).
The ODE source term resulting from the splitting is afterward solved exactly, thanks to its simple form. Nevertheless, one should note that in a very high order context, it is also possible to solve the entire system including source terms. For example, in the discontinuous Galerkin framework, one can refer to the work of *Zhang and Shu (2011)*.

4.3.2 Specific hyperbolic PDE for the disperse phase conservation laws

The general form of the system of conservation laws in one dimension is:

$$\partial_t \mathbf{W} + \partial_x \boldsymbol{\mathcal{F}}(\mathbf{W}) = 0, \quad x \in [0,1]; t \in [0, T_s], \tag{4.11}$$

where $\mathbf{W}(x,t)$ is the unknown set of moments and $\boldsymbol{\mathcal{F}}(\mathbf{W})$ the conservative flux. This system of conservation laws is hyperbolic whenever the Jacobian $J(\mathbf{W}) = \partial_{\mathbf{W}} \boldsymbol{\mathcal{F}}$ is diagonalizable with real eigenvalues.
For the PGD and Euler systems we have respectively:

$$\mathbf{W}_{PGD} = (n, nu), \quad \boldsymbol{\mathcal{F}}_{PGD} = (nu, nu^2); \tag{4.12}$$

$$\mathbf{W}_{Euler} = (n, nu, n\mathcal{E}), \quad \boldsymbol{\mathcal{F}}_{Euler} = (nu, nu^2 + P, (n\mathcal{E} + \mathcal{P})u). \tag{4.13}$$

In this part the number density is noted n.
The Euler system is hyperbolic whereas the PGD system is weakly hyperbolic and more challenging for the numerical scheme.
We consider an initial boundary value problem (IBVP) with initial condition $\mathbf{W}_0$ and periodic boundary conditions:

$$\mathbf{W}(x,0) = \mathbf{W}_0(x), \quad \forall\, x \in [0,1], \tag{4.14}$$

$$\mathbf{W}(0,t) = \mathbf{W}(1,t), \quad \forall\, t \in [0, T_s]. \tag{4.15}$$

Boundary conditions are not a matter in this part. Unless specfied otherwise, periodic boundary conditions will be considered.

4.4 Academic, semi-industrial and industrial codes

The numerical schemes mentioned in section 4.1, among others, can be found as one of the main elements of the transport solvers. Whether these codes are academic, semi-industrial or industrial, their main goal is to numerically solve some PDEs in order to simulate and understand the dynamics in questions. Some of these solvers representing a sample of the available codes based on FD, FV, continuous and discontinuous FE discretization are classified and illustrated in Figure 4.10. More details of this list can be found in appendix B. One can notice from this sample that three of the mostly used high order FV schemes are MUSCL and ENO (or WENO). Whereas the most used FE scheme are TTGC and DG. Actually, DG is being recently used more than before since it is one of the most studied high-order schemes with compact stencils. Other scheme can be found in the literature with compact stencils, namely the Spectral Difference (*Liu et al. 2006*), and Spectral Volume (*Wang 2002*) methods.
In the last decade, the Flux Reconstruction (FR) approach and more generally the Correction Procedure using Reconstruction (CPR) were proposed. These methods started gaining popularity nowadays. The FR scheme was implemented for example in the PyFR code (*Witherden et al. 2014*) for solving the

advection-diffusion problems and it is under development in the Vincent Lab at the Imperial College London. Another example is the High Fidelity Large Eddy Simulation code (HiFiLES) (*López-Morales et al. 2014*) for the simulation of compressible NS and Euler equations, which is under active development in the Aerospace Computing Laboratory at Stanford University.
The CPR is based on the differential formulation and provides a unifying framework for the compact stencils high-order schemes. The CPR methods will not be addressed in this work. For the interested readers a review on these schemes can be found in the work of *Huynh et al. (2014)*.
In the literature, there is no numerical solver that can at the same time deal with zero densities in vacuum regions, solve the singularities in the case of the weakly hyperbolic system, and solve the different model in the KBMM hierarchy while preserving the realizability.

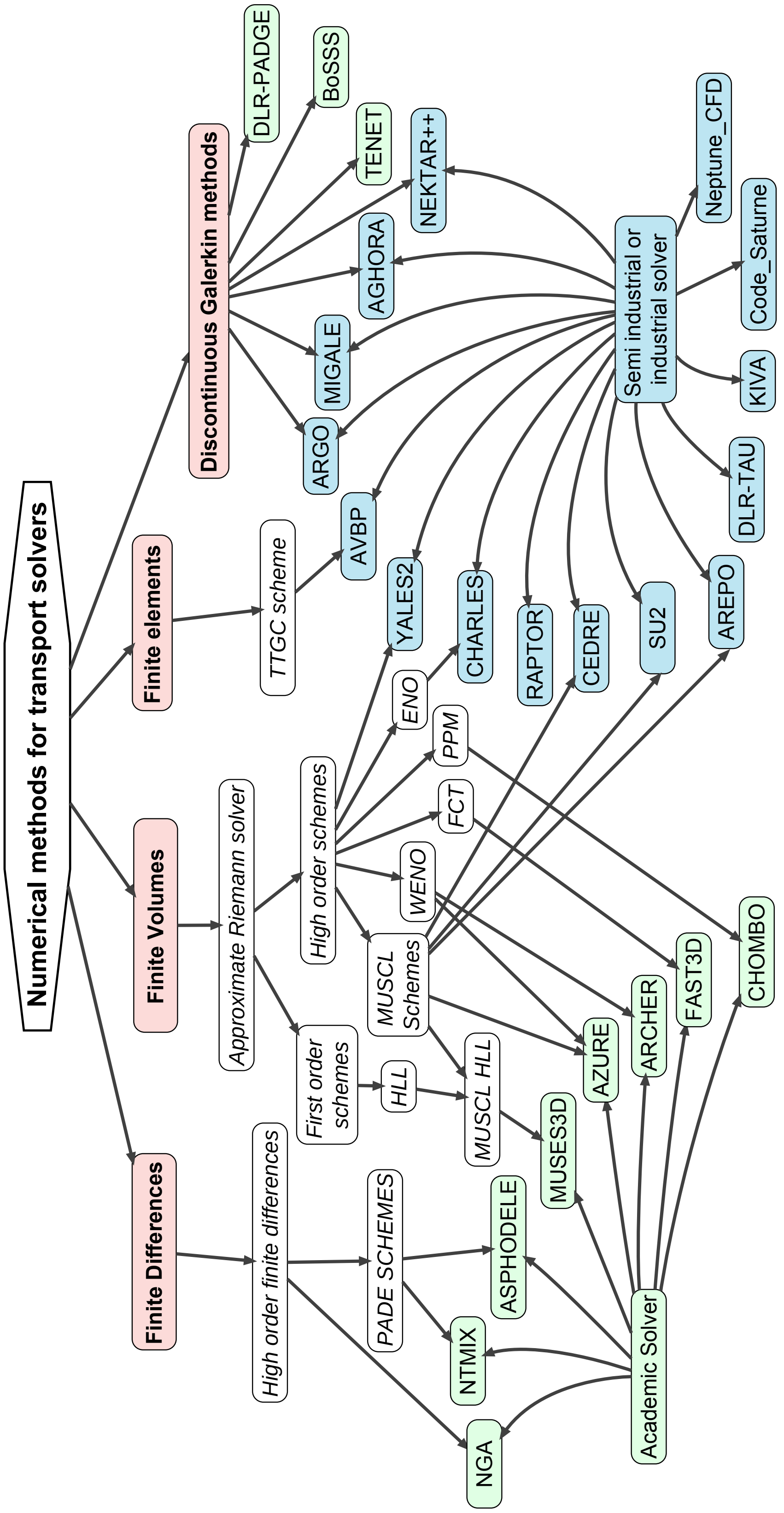

Figure 4.10: *Numerical methods for transport solvers*

4.5 Objectives and challenges

In general, with the rapid growth of computers, in terms of FLOPS and available memory, and with the increasing study and understanding of numerical schemes, the computational methods are expected to give more accurate solutions for more complex realistic configurations and at lower computational cost.

In the domain of combustion, the unstructured meshes are widely used to cope with the complex geometries. With all the advantages that unstructured meshes can provide, it is important to keep in mind that structured grids are still used for many academic and some industrial applications.

In addition to these objectives, we have more objectives that are specific for the simulation of spray. In fact, the realizability conditions presented in Chapter 2 should be preserved by the numerical schemes. Even if the moment method itself is realizable (for every set of moment a non negative NDF can be associated), the numerical scheme can update the moment set in a wrong way that leads to irrealizability. Thus, the numerical scheme should be realizability-preserving. It should respect the physical constraints coming from the underlying kinetic representation.
In addition, a high order robust numerical method is needed to minimize the numerical diffusion, which may be of the same order of magnitude as some underlying physical phenomena. In this way, the numerical scheme will be able to capture the fine structures appearing in the solution and to reproduce the large variations that might be encountered in the density field (going from vacuum zones to high concentration regions) without inducing spurious oscillations.
To sum up, the numerical scheme should be:

- **accurate** to be able to reproduce the large variations of the density,
- **preserve the realizability** in order to maintain a physical sense to the solution. For example, the solution should not include any negative density, nor negative pressure,
- applicable to **unstructured mesh** computations needed to simulate disperse phase flows in real configurations including complex geometries,
- as **cost effective** as possible, otherwise it would not be suitable for industrial use,
- **parameter free**: no need for example for artificial viscosities to stabilize the scheme and suppress spurious oscillations that can result near high gradients.

To achieve these goals of accuracy, robustness and realizability preserving on unstructured, the Discontinuous Galerkin method (DG) is a promising numerical approach. In this work DG is used for the simulation of disperse phase based of the MK and Iso model. It is compared to different schemes from the FV and FE family on 1D and 2D configurations (*Sabat et al. 2014*; *Sabat et al. 2014*).

Chapter 5

Numerical Schemes for Euler/Euler simulations

In the Eulerian/Eulerian framework, the most used three schemes are the third order finite element Two-steps Taylor-Galerkin (TTGC) scheme (Colin and Rudgyard 2000), the second order finite volume kinetic scheme (FVKS) (Bouchut et al. 2003) and the finite volume MUSCL scheme (van Leer 1979). In the case of our study, realizability-preserving schemes are required. The FVKS meets this requirement but it can only be used for closure based on the mono-kinetic quadrature. Since the models to be solved numerically are the monokinetic (MK) (Laurent and Massot 2001) and the Gaussian model (Massot 2007; Vié et al. 2015), other schemes that are able to solve these systems should be proposed. A proposed structured finite volume scheme was derived by (Vié et al. 2015). This MUSCL/HLL scheme is of second order and it preserves the realizability. However the classical version of this scheme cannot be naturally applied to the unstructured meshes for the complex application spray combustion.

To achieve the goals of accuracy, robustness and realizability, the Discontinuous Galerkin method (DG) is a promising numerical approach (Larat et al. 2012; Zhang et al. 2012; Zhang and Shu 2010; Zhang 2011). Based on the recent work of Zhang et al. (2012), the DG method used is associated to a convex projection strategy, which imposes the realizability constraints without affecting the accuracy. The main contribution of this work is to apply one of the latest developments in the field of numerical methods (DG) to physical models, taking into account the free transport and drag terms of the disperse phase flow, which are the building blocks for the Eulerian modeling based on moment methods. In this chapter these four schemes: TTGC, FVKS, MUSCL/HLL and DG are presented in 1D.

5.1 Two-steps Taylor-Galerkin

From the different numerical schemes used in industrial or semi-industrial codes, the Two-steps Taylor-Galerkin scheme (TTGC) is chosen here. In fact this scheme is the most used one in AVBP, and the one that is recommended for the simulation of disperse phase flow computations. The numerical strategy involves two ingredients: the convection scheme itself, and the artificial viscosity. The former solves the equation while the latter stabilizes the solution.

5.1.1 Centered Cell-Vertex Numerical Schemes: TTGC

To present this scheme, we restrict the analysis to scalar problems, since this scheme will only be used on the linear advection test cases in the next chapter. In fact, this scheme is used here as a reference of a third order scheme.

The TTGC version extended to m-component vector variable $\mathbf{W}$ given by Equation (4.11) can be found in (*Colin and Rudgyard 2000*) for the Euler equations for LES.

The following general 1D conservation law is then considered:

$$u_t + (f(u))_x = 0. \tag{5.1}$$

In this section, we present the scalar version of this scheme for simplicity and since in Chapter 6 the TTGC scheme is only used for 1D test cases on the linear advection equation.

Partial derivatives in space and time are denoted by $(.)_x$ and $(.)_t$ respectively. Then, by deriving Equation (5.1) with respect to time, one gets:

$$u_{tt} = -\left((f(u))_x\right)_t = -\left(f'(u).u_t\right)_x = \left(f'(u).\left(f(u)\right)_x\right)_x. \tag{5.2}$$

This formula will be useful later.

5.1.2 Taylor expansion in time

First, a time discretization is performed based on the family of two-step Taylor-Galerkin time schemes that reads:

$$\tilde{u}^n = u^n + \alpha\Delta t u_t^n + \beta\Delta t^2 u_{tt}^n + (\Delta t^3), \tag{5.3a}$$

$$u^{n+1} = u^n + \Delta t\left(\theta_1 u_t^n + \theta_2 \tilde{u}_t^n\right) + \Delta t^2\left(\varepsilon_1 u_{tt}^n + \varepsilon_2 \tilde{u}_{tt}^n\right) + (\Delta t^3). \tag{5.3b}$$

This family depends on six parameters. It was developed as an extension of the Euler Taylor Galerkin (ETG) (*Donea 1984*; *Donea et al. 1987*) and two-step Taylor-Galerkin (TTG) schemes (*Quartapelle and Selmin 1993*) that were found to be very dissipative at intermediate to high frequencies (*Colin and Rudgyard 2000*). Then, by using Equations (5.1) and (5.2), one obtains:

$$\tilde{u}^n = u^n - \alpha\Delta t\left(f(u^n)\right)_x + \beta\Delta t^2\left(f'(u^n).\left(f(u^n)\right)_x\right)_x + (\Delta t^3), \tag{5.4a}$$

$$\begin{aligned} u^{n+1} = {} & u^n - \Delta t\left(\theta_1\left(f(u^n)\right)_x - \theta_2\tilde{u}_t^n\right) \\ & + \Delta t^2\left(\varepsilon_1\left(f'(u^n).\left(f(u^n)\right)_x\right)_x + \varepsilon_2\tilde{u}_{tt}^n\right) + (\Delta t^3). \end{aligned} \tag{5.4b}$$

Now a space discretization is needed.

5.1.3 Approximation in space: Galerkin method

The domain is cut into N intervals (regular or not) and the numerical solution is sought as a piecewise continuous polynomial. Then, the set of possible solutions is spanned at the nodes of the mesh by Lagrange basis functions $(\varphi_i)_{i=1,\dots,N}$:

$$u^n(x) = \sum_i u_i^n \varphi_i(x) \quad \text{and} \quad \tilde{u}^n(x) = \sum_i \tilde{u}_i^n \varphi_i(x). \tag{5.5}$$

The numerical solution is now searched such that the residuals obtained by its injection in Equations (5.4a) and (5.4b) are orthogonal to every piecewise linear and continuous function on the considered cell. Then, for all piecewise polynomial continuous function ψ, one should have:

$$\langle (5.4a), \psi \rangle = 0 \quad \text{and} \quad \langle (5.4b), \psi \rangle = 0, \tag{5.6}$$

where $\langle ., . \rangle$ denotes the standard scalar product on $\mathcal{L}^2([0;1])$.

Since φ_i span the considered functional space, relations (5.6) still stand true if they are verified for every φ_i.
Now, the flux functions $f(u^n)$ and $f(\tilde{u}^n)$ are also considered to be spanned by the φ_is and take at each degree of freedom i the values $f(u_i^n)$ and $f(\tilde{u}_i^n)$ respectively. Furthermore, the flux jacobian $f'(u)$ is supposed to be constant. These are standard hypothesis in the field of Finite Elements.

If $\mathbf{U}^n$, $\tilde{\mathbf{U}}^n$, $\mathbf{U}^{n+1}$, $f(\mathbf{U}^n)$, $f(\tilde{\mathbf{U}}^n)$, $f'(\mathbf{U}^n)$ and $f'(\tilde{\mathbf{U}}^n)$ now represent the coordinates of u^n, $\tilde{u}^n$, u^{n+1}, $f(u^n)$, $f(\tilde{u}^n)$, $f'(u^n)$ and $f'(\tilde{u}^n)$ in the basis of Lagrange functions $(\varphi_i)_{i=1,\dots,N}$, the following double linear problem is obtained:

$$\mathcal{M}\tilde{\mathbf{U}}^n = \mathcal{M}\mathbf{U}^n - \alpha\Delta t \mathbb{T} f(\mathbf{U}^n) - \beta \Delta t^2 \mathbb{D} \left(f'(\mathbf{U}^n).f(\mathbf{U}^n) \right), \tag{5.7a}$$

$$\begin{aligned} \mathcal{M}\mathbf{U}^{n+1} &= \mathcal{M}\mathbf{U}^n - \Delta t \mathbb{T} \left(\theta_1 f(\mathbf{U}^n) + \theta_2 f(\tilde{\mathbf{U}}^n) \right) \\ &\quad - \Delta t^2 \mathbb{D} \left(\varepsilon_1 f'(\mathbf{U}^n).f(\mathbf{U}^n) + \varepsilon_2 f'(\tilde{\mathbf{U}}^n).f(\tilde{\mathbf{U}}^n) \right), \end{aligned} \tag{5.7b}$$

where matrices $\mathcal{M}$ (mass), $\mathbb{T}$ (stiffness) and $\mathbb{D}$ (dissipation) are given by:

$$\mathcal{M} = (\langle \varphi_i, \varphi_j \rangle)_{i,j} = \frac{\Delta x}{6} \begin{pmatrix} 4 & 1 & & & 0 \\ 1 & 4 & \ddots & & \\ & \ddots & \ddots & \ddots & \\ & & \ddots & 4 & 1 \\ 0 & & & 1 & 4 \end{pmatrix}, \tag{5.8}$$

$$\mathbb{T} = (\langle \varphi_i, (\varphi_j)_x \rangle)_{i,j} = \begin{pmatrix} 0 & 1/2 & (0) \\ -1/2 & \ddots & 1/2 \\ (0) & -1/2 & 0 \end{pmatrix}, \tag{5.9}$$

$$\mathbb{D} = (\langle(\varphi_i)_x, (\varphi_j)_x\rangle)_{i,j} = \frac{1}{\Delta x}\begin{pmatrix} 2 & -1 & & 0 \\ -1 & 2 & \ddots & \\ & \ddots & 2 & -1 \\ 0 & & -1 & 2 \end{pmatrix}. \tag{5.10}$$

Within the general family of the Two-step Taylor-Galerkin scheme, a particular choice is made for the TTGC scheme that depends on only one parameter $\gamma = \varepsilon_1$. This choice is made to keep the scheme the least expensive and less dissipative than the ETG and TTG schemes. For the other five parameters, *Colin and Rudgyard (2000)* suggested: $\theta_1 = \varepsilon_1 = 0$, $\beta = \frac{1}{6}$ and $\alpha = 0.5 - \gamma$. And Equations (5.3) simplify to:

$$\tilde{u}^n = u^n + \left(\frac{1}{2} - \gamma\right)\Delta t u_t^n + \frac{1}{6}\Delta t^2 u_{tt}^n + (\Delta t^3), \tag{5.11a}$$

$$u^{n+1} = u^n + \Delta t u_t^n + \Delta t^2 \gamma u_{tt}^n + (\Delta t^3). \tag{5.11b}$$

The TTGC scheme is then a family of schemes parametrized by γ.

One of the main constraints of TTGC is its dispersive character, since it can lead to spurious oscillation that can highly affect the results. Thus, this imposes the use of empirical artificial viscosity. This latter needs to be tuned manually, decreasing as a result the order of convergence without eventually ensuring the generic robustness.

5.1.4 Artificial viscosity

The artificial viscosity in AVBP has been introduced in the first place for the gaseous phase, and was later adapted to the liquid phase (*Kaufmann 2004; Riber 2007; Martinez 2010*). The goal of the artificial viscosity is to stabilize the convection scheme in non-linear region, where the scheme is subject to oscillations and/or overshoots/undershoots. The difficulty with this kind of approach is to find the right parameters that ensure the stabilization of the computation with the minimal impact on the accuracy.

The artificial viscosity is applied in two ways:

- A second order operator that acts like a viscosity and diffuses the strong gradients.
- A fourth order operator that acts like a bi-Laplacian and removes the high frequencies from the solution. It is also called hyper diffusion. This type of artificial viscosity is usually only applied where the first type is not.

A sensor controls the application of the artificial viscosity. The design of such a sensor is highly important as it will govern the accuracy of the solution as well as the robustness of the scheme. For instance, if the artificial viscosity is applied everywhere at any time, the solution will be stable but not accurate. On the contrary no artificial viscosity can lead to unstable solution, even if the theoretical order is maintained. For the disperse phase flow, the design of the sensor is highly important and can drastically modify the solution. In this case stabilizing the solution could be highly time-consuming in order to reach a trade-off between stability and accuracy. The analysis of the sensor design is detailed in the work of *Vié (2010)* and will not be treated here.

This scheme is extensively used in the literature for various academic and industrial simulations. One of the recent simulation carried out using the TTGC scheme in AVBP is the LES of the ignition sequence of an full annular multiple-injector burner by *Philip et al. (2015)*, shown in Figure 5.1. This simulation was conducted for the gaseous combustion without accounting for the spray combustion. Other two phase simulations carried out using this scheme can be found in the literature for example in the work of *Sanjosé et al. (2011); Boileau (2007); Riber et al. (2009); Vié (2010)*. This scheme faces difficulties in the resolution of the MK and Gaussian models near vacuum regions and it cannot deal with the singularities faced in the PGD equations.

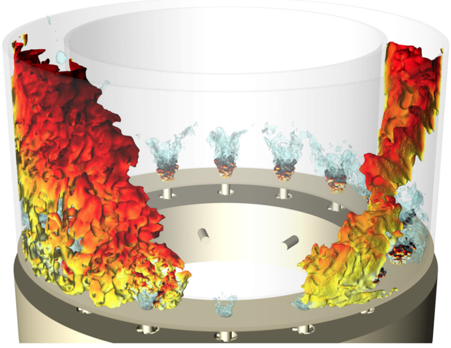

Figure 5.1: *Simulation of MICCA, the annular multiple-injector combustor using the AVBP code (Philip et al. 2015).*

5.2 Finite Volume Kinetic Scheme

The finite volume kinetic scheme (FVKS) (*Bouchut et al. 2003; de Chaisemartin 2009*) was developed in order to capture the singularities faced during the resolution of the PGD system. This is done in a robust way while preserving the realizability of the moments. It is based on the equivalence between the macroscopic and the mesoscopic descriptions for the PGD system, as illustrated in Figure 5.2. Instead of using the macroscopic equation to derive an approximate solution of the updated moments, the moments are linked to the underlying NDF whose update in time can be analytically solved through the kinetic equation, which is linear.

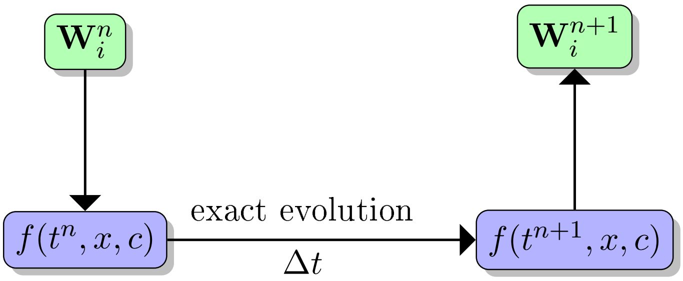

Figure 5.2: *Time advancement of the kinetic based transport scheme*

5.2.1 General kinetic schemes in $1-\mathrm{D}$

The transport kinetic equation is simplified as follows in 1-D by taking account of the convection term only:

$$\partial_t f + \partial_x (cf) = 0. \tag{5.12}$$

Under the MK assumption $f(t,x,c) = n(t,x)\delta(c-u(t,x))$, this equation has the exact solution $f(t,x,c) = f(t_n, x - c(t-t_n), c)$ (*Bouchut et al. 2003; de Chaisemartin 2009; Massot 2007*).
By integrating Equation (5.12) over $(t,x,c) \in (t_n,t_{n+1})\times(x_{i-1/2},x_{i+1/2})\times\mathbb{R}\times\mathbb{R}$ over a mesh of constant size Δx , the discretized system is obtained in its conservative form:

$$\mathbf{W}_i^{n+1} = \mathbf{W}_i^n - \frac{\Delta t}{\Delta x}(\boldsymbol{F}_{i+1/2} - \boldsymbol{F}_{i-1/2}), \tag{5.13}$$

where the average $\mathbf{W}_i^n = (n_i^n, n_i^n u_i^n)$ is defined by Equation (5.14) and the fluxes $\boldsymbol{F}_{i+1/2}$ are decomposed in $\boldsymbol{F}_{i+1/2} = \boldsymbol{F}_{i+1/2}^{+} + \boldsymbol{F}_{i+1/2}^{-}$ as shown in Equation (5.15).

$$\mathbf{W}_i^n = \frac{1}{\Delta x}\int_{x_{i-1/2}}^{x_{i+1/2}} \mathbf{W}(t_n,x)\mathrm{d}x, \tag{5.14}$$

$$\boldsymbol{F}_{i+1/2}^{\pm} = \frac{1}{\Delta t}\int_{t_n}^{t_{n+1}} \int_{\pm c\geq 0} \begin{pmatrix} 1 \\ c \end{pmatrix} c\, f(t, x_{i+1/2}, c)\, \mathrm{d}c\mathrm{d}t. \tag{5.15}$$

Finally, the exact solution of the kinetic scheme is used to evaluate the fluxes update. Here, a reconstruction in space is needed. For a constant reconstruction, one obtains the first order kinetic scheme, stable under the CFL condition $|u_i|\Delta t \leq \Delta x$:

$$\boldsymbol{F}_{i+1/2}^{+} = \begin{pmatrix} n_i(u_i)_+ \\ n_i u_i (u_i)_+ \end{pmatrix} \quad , \quad \boldsymbol{F}_{i+1/2}^{-} = \begin{pmatrix} n_{i+1}(u_{i+1})_- \\ n_{i+1}u_{i+1}(u_{i+1})_- \end{pmatrix}, \tag{5.16}$$

with the convention $(y)_+ = \max\{0,y\}$, $(y)_- = \min\{0,y\}$.

5.2.2 Second order kinetic scheme

For the second order scheme, piecewise linear reconstructions are considered for n and u:

$$\text{for} \quad x_{i-1/2} < x < x_{i+1/2} \qquad \begin{cases} n(x) = n_i^n + D_{n_i}(x - x_i), \\ u(x) = \overline{u_i} + D_{u_i}(x - x_i), \end{cases} \tag{5.17}$$

where $x_i = (x_{i+1/2} + x_{i-1/2})/2$ is the center of the i^{th} cell and where, to simplify the notation, the t_n dependence of each function is implicit.
In order to have the conservation property in each cells, the velocity reconstruction is not based on the velocity average value u_i^n but on the corresponding corrected average. This step is essential to guarantee that the cell average of the momentum $q(x) = n(x)u(x)$ at time t_n is indeed $q_i^n = n_i^n u_i^n$ as shown in Equation (5.18). Based on this condition the corrected velocity average $\overline{u_i}$ is obtained (Equation (5.19)).

$$n_i^n u_i^n = \frac{1}{\Delta x} \int_{x_{i-1/2}}^{x_{i+1/2}} n(x)u(x)\,\mathrm{d}x, \tag{5.18}$$

$$\overline{u_i} = u_i^n - \frac{D_{n_i} D_{u_i}}{n_i^n} \frac{\Delta x^2}{12}. \tag{5.19}$$

Now that the conservativity of the reconstruction is guaranteed, the slopes should be computed in order to finish the reconstruction step. The slopes should be limited to ensure that the reconstructed velocities respect the maximum principle and the reconstructed number density at the interface is always non-negative.
The slope limiter used in the first two methods is either a minmod or a MC limiter (*LeVeque 2002; de Chaisemartin 2009*). These limiters are obtained from Equation (5.20) by respectively taking $\alpha = 1$ or $\alpha = 2$ with $\Delta^+ n = n_{i+1}^n - n_i^n, \quad \Delta^- n = n_i^n - n_{i-1}^n, \quad \chi = \Delta x(1 + \Delta x D_{n_i}/6n_i^n)$

$$\begin{aligned} D_{n_i} &= \frac{(sgn(\Delta^+ n) + sgn(\Delta^- n))}{2} \min\left(\frac{|\Delta^+ n + \Delta^- n|}{2\Delta x}, \frac{\alpha|\Delta^- n|}{\Delta x}, \frac{\alpha|\Delta^+ n|}{\Delta x}\right), \\ D_{u_i} &= \frac{(sgn(\Delta^+ u) + sgn(\Delta^- u))}{2} \min\left(\frac{|\Delta^+ u + \Delta^- u|}{2\chi}, \frac{\alpha|\Delta^+ u|}{2\Delta x - \chi}, \frac{\alpha|\Delta^- u|}{\chi}, \frac{1}{\Delta t}\right). \end{aligned} \tag{5.20}$$

5.2.3 Flux evaluation

Finally, the fluxes can then be evaluated from $n_{i-1/2}^L$, $n_{i-1/2}^R$, $u_{i-1/2}^L$, $u_{i-1/2}^R$, the corresponding values of $n(t_n, x)$ and $u(t_n, x)$ at the left and the right of interface $x_{i-1/2}$ between the cells $i-1$ and i:

$$\begin{aligned} n_{i-1/2}^L &= n_{i-1}^n + \tfrac{\mathbf{dx}}{2} D_{n_{i-1}}, & n_{i-1/2}^R &= n_i^n - \tfrac{\mathbf{dx}}{2} D_{n_i}, \\ u_{i-1/2}^L &= \overline{u_{i-1}} + \tfrac{\mathbf{dx}}{2} D_{u_{i-1}}, & u_{i-1/2}^R &= \overline{u_i} - \tfrac{\mathbf{dx}}{2} D_{u_i}, \end{aligned} \tag{5.21}$$

so that the decomposed fluxes are (*de Chaisemartin 2009*):

$$\begin{aligned} \boldsymbol{F}^{+}_{i-1/2} &= \mathbf{U}^{L}_{i-1/2}\alpha^{L}_{i-1/2} - \tfrac{\Delta t}{2}(\alpha^{L}_{i-1/2})^2\,\Gamma^{+}_{i-1/2}, \\ \boldsymbol{F}^{-}_{i-1/2} &= \mathbf{U}^{R}_{i-1/2}\alpha^{R}_{i-1/2} - \tfrac{\Delta t}{2}(\alpha^{R}_{i-1/2})^2\,\Gamma^{-}_{i-1/2}, \end{aligned} \tag{5.22}$$

with the following definitions:

$$\mathbf{U}^{L}_{i-1/2} = n^{L}_{i-1/2}\begin{pmatrix} 1 \\ \alpha^{L}_{i-1/2} \end{pmatrix}, \qquad \mathbf{U}^{R}_{i-1/2} = n^{R}_{i-1/2}\begin{pmatrix} 1 \\ \alpha^{R}_{i-1/2} \end{pmatrix}, \tag{5.23}$$

$$\alpha^{L}_{i-1/2} = \frac{(u^{L}_{i-1/2})_{+}}{1+\Delta t D_{u_{i-1}}}, \qquad \alpha^{R}_{i-1/2} = \frac{(u^{R}_{i-1/2})_{-}}{1+\Delta t D_{u_{i}}}, \tag{5.24}$$

with:

$$\Gamma^{+}_{i-1/2} = \begin{pmatrix} D_{n_{i-1}} \\ -n^{L}_{i-1/2}D_{u_{i-1}} + \alpha^{L}_{i-1/2}D_{n_{i-1}} + \tfrac{\Delta t}{3}D_{n_{i-1}}D_{u_{i-1}}\alpha^{L}_{i-1/2} \end{pmatrix}, \tag{5.25}$$

$$\Gamma^{-}_{i-1/2} = \begin{pmatrix} D_{n_{i}} \\ -n^{R}_{i-1/2}D_{u_{i}} + \alpha^{R}_{i-1/2}D_{n_{i}} + \tfrac{\Delta t}{3}D_{n_{i}}D_{u_{i}}\alpha^{R}_{i-1/2} \end{pmatrix}. \tag{5.26}$$

The resulting second order scheme in space and time is capable of treating the delta-shocks and vacuum. It also ensures that the number density is non-negative and the velocity respects a maximum principle.

5.2.4 Extension to multi-dimensions

Several types for the extension of the FVKS to multi-dimensions are possible (*de Chaisemartin 2009*). For the academic tests in the present work, the most suitable technique to the higher dimensions extension is the directional splitting technique (Alternating Direction Technique (*LeVeque 2002*)) on quadrilateral meshes. This technique is efficient and easily implemented on structured grids.

The 1-D procedure presented in section 5.2.1 is repeated for each direction with the addition each time of an equation corresponding to the velocity component in the other directions. For example, in 2-D, one will consider the following piecewise linear reconstruction for the second order scheme for the x-direction (for simplicity the j subscript for the y-direction is dropped):

$$\text{for} \quad x_{i-1/2} < x < x_{i+1/2} \qquad \begin{cases} n(x) = n_i^n + D_{n_i}(x - x_i), \\ u(x) = \overline{u_i} + D_{u_i}(x - x_i), \\ v(x) = \overline{v_i} + D_{v_i}(x - x_i), \end{cases} \tag{5.27}$$

with $\overline{v_i} = v_i^n - \frac{D_{n_i} D_{v_i}}{n_i^n} \frac{\Delta x^2}{12}$ and the slope limiter for v in the x-direction:

$$\begin{aligned} D_{v_i} = {} & \frac{1}{2}(sgn(v_{i+1}^n - v_i^n) + sgn(v_i^n - v_{i-1}^n)) \\ & \min\left(\frac{|v_{i+1}^n - v_i^n|}{\Delta x(1 - \Delta x D_{n_i}/6n_i^n)}, \frac{|v_i^n - v_{i-1}^n|}{\Delta x(1 + \Delta x D_{n_i}/6n_i^n)}, \frac{1}{\Delta t} \right). \end{aligned} \tag{5.28}$$

Each of the decomposed fluxes given by Equation (5.22) has in this case an additional term for v. The values at the left and right of the interface $x_{i-1/2}$ are:

$$\mathbf{U}_{i-1/2}^L = n_{i-1/2}^L \begin{pmatrix} 1 \\ \alpha_{i-1/2}^L \\ v_{i-1/2}^L \end{pmatrix}, \qquad \mathbf{U}_{i-1/2}^R = n_{i-1/2}^R \begin{pmatrix} 1 \\ \alpha_{i-1/2}^R \\ v_{i-1/2}^R \end{pmatrix}, \tag{5.29}$$

where, $v_{i-1/2}^L = \overline{v_{i-1}} + \frac{\mathbf{dx}}{2} D_{v_{i-1}}$, $\qquad v_{i-1/2}^R = \overline{v_i} - \frac{\mathbf{dx}}{2} D_{v_i}$ and

$$\Gamma_{i-1/2}^+ = \begin{pmatrix} D_{n_{i-1}} \\ \\ -n_{i-1/2}^L D_{u_{i-1}} + \alpha_{i-1/2}^L D_{n_{i-1}} + \frac{\Delta t}{3} D_{n_{i-1}} D_{u_{i-1}} \alpha_{i-1/2}^L \\ \\ n_{i-1/2}^L D_{v_{i-1}} + v_{i-1/2}^L D_{n_{i-1}} - \frac{2\Delta t}{3} D_{n_{i-1}} D_{v_{i-1}} \alpha_{i-1/2}^L \end{pmatrix}, \tag{5.30}$$

$$\Gamma_{i-1/2}^- = \begin{pmatrix} D_{n_i} \\ \\ -n_{i-1/2}^R D_{u_i} + \alpha_{i-1/2}^R D_{n_i} + \frac{\Delta t}{3} D_{n_i} D_{u_i} \alpha_{i-1/2}^R \\ \\ n_{i-1/2}^R D_{v_i} + v_{i-1/2}^R D_{n_i} - \frac{2\Delta t}{3} D_{n_i} D_{v_i} \alpha_{i-1/2}^R \end{pmatrix}. \tag{5.31}$$

For the second order scheme, piecewise linear reconstructions are considered for the density and velocity.

This scheme was previously used to solve 3D HIT and other combustion applications in the thesis of *de Chaisemartin (2009)*. For example, *Fréret et al. (2012)* carried a comparison between the Lagrangian and multi-fluid MK simulation on a spray jet configuration. The liquid mass of this spray jet is shown in Figure 5.3.

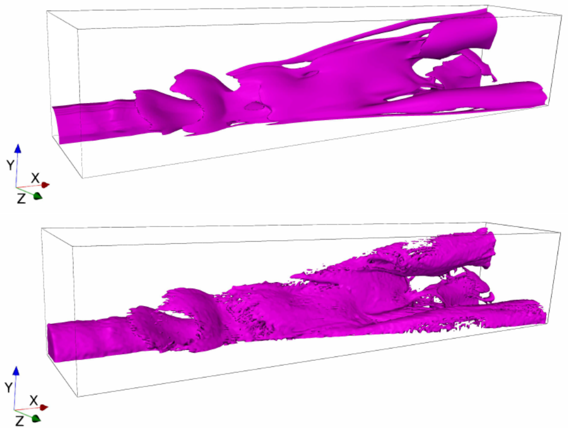

Figure 5.3: *Qualitative comparison of the liquid mass obtained with the MF model (top) and the Lagrangian one (bottom) based on the stoichiometric iso-contour 0.0625 of the liquid phase. (Source (Fréret et al. 2012))*

5.3 Finite Volume MUSCL/HLL Scheme

In this section, a realizable second order MUSCL/HLL (*Vié et al. 2015*) is presented. This scheme was developed because the FVKS cannot be applied to models that are not based on a Dirac δ-function for the NDF (*Chalons et al. 2012; Kah et al. 2010*).

It is obtained using the MUSCL strategy (*van Leer 1979*) with a linear conservative reconstruction of the primitive variables ($\boldsymbol{\mathcal{U}} = \left(n, \overrightarrow{\mathbf{u}}\right)$ for the PGD system and $\boldsymbol{\mathcal{U}} = \left(n, \overrightarrow{\mathbf{u}}, \sigma\right)^T$ for the Euler system) within each cell, in order to calculate the interface values. Similar to the FVKS, the conservation property should be respected and this is done through the corrected cell average quantites. Then, the fluxes are evaluated with the reconstructed values at the interface. Multi-dimensional problems are solved by a dimensional splitting strategy. The time integration is done by means of a 2nd order Runge-Kutta method.

In the following, the reconstruction, the slope limitation and the flux evaluation strategies are shown for the 2-D scheme in the x-direction. For more details, one may refer to the work of *Vié et al. (2013); Vié et al. (2015)*.

5.3.1 Conservative Reconstruction

Similar to the kinetic scheme, the linear reconstruction proposed in *Vié et al. (2015)* is based on primitive variables. The main objective of this reconstruction strategy is to ensure the realizability of the moment set. The cell reconstructed variables $\widetilde{\boldsymbol{\mathcal{U}}}$ are obtained by the limited linear reconstruction based on the corrected cell value $\overline{\boldsymbol{\mathcal{U}}}$ for each reconstructed variable:

$$\tilde{\boldsymbol{\mathcal{U}}}_i(x) = \overline{\boldsymbol{\mathcal{U}}}_i + \mathcal{D}_{\boldsymbol{\mathcal{U}}}(x - x_i), \tag{5.32}$$

where for the PGD and Euler systems, we have respectively:

$$\overline{\boldsymbol{\mathcal{U}}}_{i,PGD} = (\overline{n}_i, \overline{u}_i, \overline{v}_i)^T, \quad \mathcal{D}_{\boldsymbol{\mathcal{U}},PGD} = (D_{n_i}, D_{u_i}, D_{v_i})^T, \tag{5.33}$$

$$\overline{\boldsymbol{\mathcal{U}}}_{i,Euler} = (\overline{n}_i, \overline{u}_i, \overline{v}_i, \overline{\sigma}_i)^T, \quad \mathcal{D}_{\boldsymbol{\mathcal{U}},Euler} = (D_{n_i}, D_{u_i}, D_{v_i}, D_{\sigma_i})^T, \tag{5.34}$$

The corrected cell values are one of the main differences between the scheme used in this work and the classical reconstruction strategies of MUSCL schemes (*Berthon 2005*). These corrected cell values are imposed by the conservation of the cell value for each moment in order to ensure that the fluxes will not affect the realizability (*Vié et al. 2013*):

$$W_{kl} = \frac{1}{\Delta x} \int_{x_{i-1/2}}^{x_{i+1/2}} \tilde{W}_{kl,i}(x)\mathrm{d}x, \tag{5.35}$$

where $k+l \leq 1$ for the PGD system and $k+l \leq 2$ for the Euler system. Finally the corrected cell values are:

$$\overline{n}_i = n_i, \qquad \overline{u}_i = u_i - \frac{D_{n_i} D_{u_i}}{n_i}\frac{\Delta x^2}{12}, \qquad \overline{v}_i = v_i - \frac{D_{n_i} D_{v_i}}{n_i}\frac{\Delta x^2}{12}, \tag{5.36}$$

$$\overline{\sigma}_i = \sigma_i - \frac{\Delta x^2}{12}\left(\frac{D_{u_i}^2 + D_{v_i}^2}{2}\right)\left(1 + \frac{\Delta x^2}{12}\frac{D_{n_i}^2}{n_i^2}\right) - \frac{\Delta x^2}{12}\frac{D_{n_i} D_{\sigma_i}}{n_i}. \tag{5.37}$$

The last step of this reconstruction is the slope evaluation and limitation.

5.3.2 Slope Limitation

Since the slopes can generate unrealizable corrected cell values, the slope evaluation is complex but mandatory to ensure the positivity of the density, the variance (in case of Euler system) and to force a maximum principle of the variables to guarantee robustness. A minmod or MC limiter with a positivity constraint is first applied to the density. This limiter is the same as the one used for the FVKS. For the PGD system, also the same limiter used in the slope limiting procedure in the FVKS is applied to the velocities (see Equation (5.20)).

On the other hand, for the Euler system, a limiter with a constraint to ensure the positivity of the energy is applied to the velocities:

$$\begin{aligned} D_{u_i,Euler} = {} & \frac{1}{2}\left(\mathrm{sign}(u_{i+1} - u_i) + \mathrm{sign}(u_i - u_{i-1})\right) \\ & \min\left(\frac{|u_{i+1} - u_i|}{\Delta x\left(1 - \frac{D_{n_i}}{n_i}\frac{\Delta x}{6}\right)}, \frac{|u_i - u_{i-1}|}{\Delta x\left(1 + \frac{D_{n_i}}{n_i}\frac{\Delta x}{6}\right)}, D_{u_i}^{\max,\sigma_i}, \frac{1}{\Delta t}\right), \end{aligned} \tag{5.38}$$

where:

$$D_{u_i}^{\max,\sigma_i} = \sqrt{\frac{\sigma_i}{\frac{\Delta x^2}{12}\left(1 + \frac{\Delta x^2}{12}\frac{D_{n_i}^2}{n_i^2}\right)}}. \tag{5.39}$$

Finally, for the Euler system a similar slope limitation is applied to the variance:

$$D_{\sigma_i} = \frac{1}{2}\left(\operatorname{sign}(\sigma_{i+1}-\sigma_i) + \operatorname{sign}(\sigma_i - \sigma_{i-1})\right) \min\left(\frac{|\sigma_{i+1}-\sigma_i|}{\Delta x\left(1-\frac{D_{n_i}}{n_i}\frac{\Delta x}{6}\right)}, \frac{|\sigma_i-\sigma_{i-1}|}{\Delta x\left(1+\frac{D_{n_i}}{n_i}\frac{\Delta x}{6}\right)}\right). \quad (5.40)$$

The extension of this method to the AG model is developed and evaluated in the work of *Vié et al. (2015)*.

5.3.3 Flux evaluation

After the reconstruction, an approximate Riemann solver is used for the flux evaluation, for which the right and left states at the interface result from the reconstruction procedure.

In fact, a realizability-preserving numerical flux is needed to guarantee that the update will not move the moment set out of the space of realizability $\mathcal{S}$.

Now, we define what we mean by realizability-preserving numerical flux. A realizability-preserving numerical flux $\boldsymbol{\mathcal{F}}^{num}(\mathbf{W}_L, \mathbf{W}_R)$ for a first order finite volume scheme is defined such that for any three neighboring realizable states $\mathbf{W}_{i-1}^n, \mathbf{W}_i^n, \mathbf{W}_{i+1}^n \in \mathcal{S}$ at time step n, the explicit first order Euler update $\mathbf{W}_i^{n+1}$ in cell I_i also belongs to $\mathcal{S}$ under the classical CFL condition for first order finite volume schemes and is thus realizable.

In the case of the PGD system or the Euler system, there exist already such realizability-preserving fluxes. Among them one can cite the family of HLL solvers or even the Godunov solvers.

For the scheme in question, a HLL approximate Riemann solver is chosen (*Harten et al. 1983*). Thus, given the initial states of each side of the interface $\mathbf{W}_L$ and $\mathbf{W}_R$ as illustrated in Figure 5.4 with fluxes $\boldsymbol{\mathcal{F}}(\mathbf{W}_L)$ and $\boldsymbol{\mathcal{F}}(\mathbf{W}_R)$ respectively, the intermediate state is found by integrating Equation (4.11):

$$\mathbf{W}^* = \frac{\lambda_{min}\mathbf{W}_L - \lambda_{max}\mathbf{W}_R}{\lambda_{min}-\lambda_{max}} - \frac{\boldsymbol{\mathcal{F}}(\mathbf{W}_L) - \boldsymbol{\mathcal{F}}(\mathbf{W}_R)}{\lambda_{min}-\lambda_{max}}, \quad (5.41)$$

where R and L stand respectively for the right and left side of the interface. λ_{min} and λ_{max} are respectively the slowest and fastest characteristic waves of the states on the left and right side of the interface.

Then, the fluxes at the interface are:

$$\boldsymbol{\mathcal{F}}^{HLL}(\mathbf{W}_L, \mathbf{W}_R) = \frac{1}{2}\left(\boldsymbol{\mathcal{F}}(\mathbf{W}_L) + \boldsymbol{\mathcal{F}}(\mathbf{W}_R)\right) - \frac{1}{2}|\lambda_{min}|\left(\mathbf{W}^* - \mathbf{W}_L\right) - \frac{1}{2}|\lambda_{max}|\left(\mathbf{W}_R - \mathbf{W}^*\right). \quad (5.42)$$

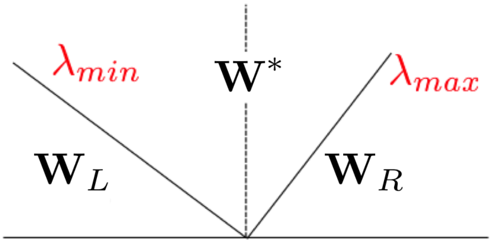

Figure 5.4: *Schematic view of Riemann fan adopted for the HLL solver*

Finally, using a strong stability preserving (SSP), 2-step Runge-Kutta method for the integration in time (*Gottlieb et al. 2001*), one gets:

$$\begin{aligned}\tilde{\mathbf{W}}_i &= \mathbf{W}_i^n - \frac{\Delta t}{\Delta x}\left(\boldsymbol{\mathcal{F}}_{i+1/2}^n - \boldsymbol{\mathcal{F}}_{i-1/2}^n\right),\\ \tilde{\tilde{\mathbf{W}}}_i &= \tilde{\mathbf{W}}_i - \frac{\Delta t}{\Delta x}\left(\tilde{\boldsymbol{\mathcal{F}}}_{i+1/2}^{n+1/2} - \tilde{\boldsymbol{\mathcal{F}}}_{i-1/2}^{n+1/2}\right),\\ \mathbf{W}_i^{n+1} &= \frac{\mathbf{W}_i + \tilde{\tilde{\mathbf{W}}}_i}{2}.\end{aligned} \tag{5.43}$$

In fact, the 2-step Runge-Kutta method can be performed in another way that is not SSP and is usually used more frequently since it does not require to store $\mathbf{W}_i$ and is thus less memory consuming. However, here in order to preserve the realizability of the moments, the time update should also be realizability preserving, thus SSP.

The resulting scheme is at second order in time and space and it preserves the realizability of the moments. It is an accurate, stable and realizable scheme on structured meshes. However, as all MUSCL formulation, it degenerates to first order near discontinuities and the choice of the slope limiting procedure crucially affects the amount of numerical dissipation.

This scheme was used for 1D and 2D configurations in *Vié et al. (2012)*; *Vié et al. (2015)* such as the 2D configuration that mimics the injection of particles in a turbulent flow illustrated in Figure 5.5.

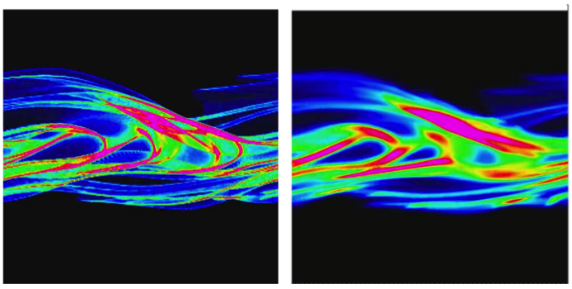

Figure 5.5: *Snapshot of the number density: Lagrangian reference (left), Anisotropic Gaussian model solved by MUSCL/HLL(right) ; adapted from (Vié et al. 2012)*

5.4 Convex state preserving discontinuous Galerkin scheme

The method presented here is based on the classical DG formulation of *Cockburn and Shu (1998b)* and evolved to satisfy the realizability constraints by the application of the maximum principle and a positivity preservation technique (*Zhang and Shu 2010; Zhang et al. 2012*). The extension of this framework to the case of weakly hyperbolic equations (PGD system) was initiated by *Larat et al. (2012)*. A similar work can be found in the article of *Yang et al. (2013)*.

In this first subsection, the general framework of the realizability constraints preservation is introduced in one dimension of space. Extension to two-dimensional computations is then explained in the second subsection. Furthermore, this extension to 2-D problems can be generalized to any higher number of spatial dimensions.

5.4.1 Scheme in one dimension of space

For the sake of clarity, a structured mesh is used, but a similar work can be done for an unstructured discretization in a more general context. Then, for a method of order $k+1 \in \mathbb{N}^*$, $\varphi_i^j(x)$ are $k+1$ basis functions, polynomials of order k in I_i, for $j = 1, ..., k+1$. The L^2 scalar products of the φ_i^js over I_i give the mass matrix $\mathcal{M}$:

$$(\mathcal{M})_{jl} = \int_{I_i} \varphi_i^j(x)\varphi_i^l(x)\mathrm{d}x,$$

which becomes diagonal under the choice of a suitable orthogonal basis. This mass matrix involves only the local degrees of freedom compared to TTGC where the mass matrix is a general matrix over the whole domain.

Next, according to classical DG formulation, the numerical solution $\mathbf{W}_h$ is the unique solution within the functional space spanned by the φ_i^js of the variational formulation of Equation (4.11) on this functional space.

$$\mathbf{W}_h(x,t) = \sum_i^N \chi_{I_i}(x) \sum_j^{k+1} \mathbf{W}_i^j(t)\varphi_i^j(x), \tag{5.44}$$

where χ_{I_i} is the characteristic function of I_i equals to 1 in I_i and 0 elsewhere. $\mathbf{W}_h$ is a piecewise polynomial solution such that:

$$\int_{I_i} \left(\partial_t \mathbf{W}_h + \partial_x \boldsymbol{\mathcal{F}}(\mathbf{W}_h)\right) \varphi_i^j(x)\mathrm{d}x = 0, \quad \forall i = 1,\dots,N, \forall j = 1,\dots,k+1. \tag{5.45}$$

By combining the two last equations and integrating by part, we get the following DG semi-discretization in space:

$$\begin{aligned} |I_i|(\boldsymbol{\mathcal{M}}_{jl})d_t\mathbf{W}_i^l + \left(\boldsymbol{\mathcal{F}}^*_{i+\frac{1}{2}}\varphi_i^j(x_{i+\frac{1}{2}}) - \boldsymbol{\mathcal{F}}^*_{i-\frac{1}{2}}\varphi_i^j(x_{i-\frac{1}{2}})\right) = \\ \int_{I_i} \boldsymbol{\mathcal{F}}(\mathbf{W}_h(x,t))\partial_x\varphi_i^j \mathrm{d}x; \forall i = 1,...,N; \forall j = 1,...,k, \end{aligned} \tag{5.46}$$

where $\boldsymbol{\mathcal{F}}^*_{i+\frac{1}{2}}$ is a chosen numerical flux at cell interface $x_{i+\frac{1}{2}}$.
Once this is done, one obtains a set of ordinary differential equations (ODE) for the degrees of freedom (DoF) $\mathbf{W}_i^j(t)$ which need to be solved in time. This should be done using the family of Strong Stability Preserving (SSP) (*Gottlieb et al. 2009*) time integrators, which respect the realizability constraint. The following explains the realizability preservation within the context of a first order forward Euler time integration, having in mind the obvious generalization to any SSP method.
Let us now explain the preservation of the convex constraint of realizability by the DG scheme. By summing Equation (5.46) over all the DoFs j of a given cell I_i, one obtains the equation of evolution of the cell mean value:

$$\overline{\mathbf{W}}_i^{n+1} = \overline{\mathbf{W}}_i^n - \frac{\Delta t}{|I_i|}\left(\boldsymbol{\mathcal{F}}^*_{i+\frac{1}{2}} - \boldsymbol{\mathcal{F}}^*_{i-\frac{1}{2}}\right). \tag{5.47}$$

Now, because $\mathbf{W}_h$ is a k^{th} order polynomial in I_i, the following Gauss-Lobatto quadrature is exact, when m is such that $k \leq 2m-3$:

$$\overline{\mathbf{W}}_i = \frac{1}{|I_i|}\int_{I_i} \mathbf{W}_h(x,t^n)\mathrm{d}x = \sum_{q=1}^m \omega_q \mathbf{W}_h(x_q,t^n). \tag{5.48}$$

In 1D, the m Gauss-Lobatto quadrature points x_q, $q = 1,...,m$ have strictly positive weights ω_q.
Next, the balance of the numerical fluxes $\boldsymbol{\mathcal{F}}^*_{i+\frac{1}{2}} = \boldsymbol{\mathcal{F}}^*(\mathbf{W}_{i+1}^n, \mathbf{W}_i^n)$ and $\boldsymbol{\mathcal{F}}^*_{i-\frac{1}{2}} = \boldsymbol{\mathcal{F}}^*(\mathbf{W}_i^n, \mathbf{W}_{i-1}^n)$ entering the cell I_i is split into a sum of balances of numerical fluxes at two neighboring quadrature points:

$$\boldsymbol{\mathcal{F}}^*_{i+\frac{1}{2}} - \boldsymbol{\mathcal{F}}^*_{i-\frac{1}{2}} = \sum_{q=0}^m \left(\boldsymbol{\mathcal{F}}^*(\mathbf{W}_{i,q+1}, \mathbf{W}_{i,q}) - \boldsymbol{\mathcal{F}}^*(\mathbf{W}_{i,q}, \mathbf{W}_{i,q-1})\right). \tag{5.49}$$

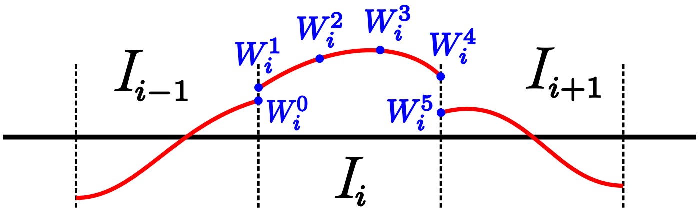

Figure 5.6: *Quadrature points on the cell I_i, $m = 4$.*

The set of m quadrature points has been implicitly extended to $q = 0, ..., m + 1$ where x_0 and x_{m+1} are respectively the coordinates of the right and left quadrature points on the left and right neighboring cells, see Figure 5.6.
Finally, by combining the three above equations, one obtains the update equation:

$$\overline{\mathbf{W}}_i^{n+1} = \sum_{q=0}^{m} \omega_q \left(\mathbf{W}_h(x_q, t^n) - \frac{\Delta t}{\omega_q |I_i|} \left(\boldsymbol{\mathcal{F}}^*(\mathbf{W}_{i,q+1}, \mathbf{W}_{i,q}) - \boldsymbol{\mathcal{F}}^*(\mathbf{W}_{i,q}, \mathbf{W}_{i,q-1}) \right) \right), \tag{5.50}$$

which is a convex combination of abstract first order updates, because $\omega_q > 0, \forall q$ and $\sum\limits_q \omega_q = 1$.
The numerical flux selected is the Lax-Friedrichs flux:

$$\boldsymbol{\mathcal{F}}^{LF}(\mathbf{W}_L, \mathbf{W}_R) = \frac{1}{2} \left(\boldsymbol{\mathcal{F}}(\mathbf{W}_L) + \boldsymbol{\mathcal{F}}(\mathbf{W}_R) \right) - \frac{1}{2} |\lambda| \left(\mathbf{W}_R - \mathbf{W}_L \right), \tag{5.51}$$

which can be viewed as a particular HLL approximate Riemann solver where$|\lambda| = max(|\lambda_{min}|, |\lambda_{max}|)$ in Equation (5.42).
Then, the higher order update in Equation (5.50) is also realizability-preserving when:

- the numerical flux $\boldsymbol{\mathcal{F}}^*$ is realizability preserving,
- the quadrature states $\mathbf{W}_q^n = \mathbf{W}_h^n(x_q)$ are realizable,
- the following constrained CFL condition is provided:

  $$\frac{\Delta t . \alpha_i}{|I_i|} \leq \min_q \omega_q, \tag{5.52}$$

  where α_i is greater than the spectral radius (the absolute value of eigenvalues) of the Jacobian of the flux at all the quadrature points x_q, $q = 0, \ldots, m+1$. Since the smallest weights of the Gauss-Lobatto quadrature are on the borders of the interval then $\min_q \omega_q = \omega_1 = \omega_Q$.

For the second order in 1D, this last CFL constraint is $\frac{1}{2}$, which is exactly the same CFL constraint as for second order finite volume schemes. It is also important to notice that the Gauss-Lobatto quadrature does not have to be necessarily used in the evaluation of the overall updates in Equation (5.46).

One can use any accurate enough quadrature to estimate the right hand side integral. However, realizability at the Gauss-Lobatto quadrature points will certainly ensure realizability of the mean value at next time step.

A delicate point still needs to be addressed to finish our proof. The initial condition is supposed to be physical and thus realizable everywhere, in particular at the quadrature points. By using a realizability-preserving numerical flux and keeping the restricted CFL condition (Equation (5.52)), we obtain realizable mean values in each cell I_i for the first time step. But nothing ensures the solution to be now realizable at every quadrature point. Fortunately, because the space of realizable moments $\mathcal{S}$ is convex, for each non-realizable quadrature state $\mathbf{W}_i^q = \mathbf{W}_h(x_q)$ there exist a unique $\theta_q \in [0,1]$ such that $\widetilde{\mathbf{W}}_i^q = \theta_q \mathbf{W}_i^q + (1-\theta_q)\overline{\mathbf{W}}_i$ lies on the boundary of $\mathcal{S}$, see Figure 5.7. The numerical solution is then redefined as:

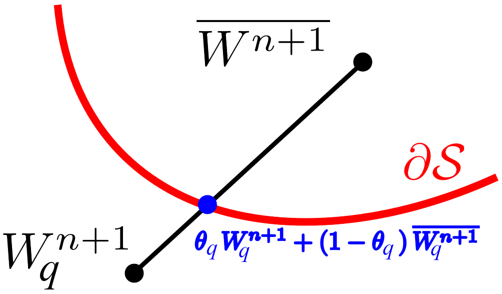

Figure 5.7: *A space projection in cell I_i, associating for any quadrature state $\mathbf{W}_q^{n+1}$ lying outside the space of constraints, a state $\widetilde{\mathbf{W}}_q^{n+1}$ at the boundary $\partial\mathcal{S}$ of this space*

$$\widetilde{\mathbf{W}}_h(x,t^{n+1}) = \theta_i(\mathbf{W}_h(x,t^{n+1}) - \overline{\mathbf{W}}_i^{n+1}) + \overline{\mathbf{W}}_i^{n+1}, \quad \theta_i = \min_{q=1,..,m} \theta_q. \tag{5.53}$$

This space projection has the following properties:

- the cell mean value is obviously conserved,
- it is shown in *Zhang (2011)* that the accuracy of the scheme is preserved for regular solutions.

$\widetilde{\mathbf{W}}_h$ is finally a $(k+1)^{th}$ order approximation of $\mathbf{W}_h$ which respects the convex constraints at all quadrature points, which can be used for the next time step and the scheme can go on.

5.4.2 Extension to $2-\mathrm{D}$

The 2-D domain is tessellated into triangles. Let T_i be a triangle of the mesh and j a DoF of T_i with its associated k^{th} order basis function $\varphi_{T_i}^j$. The conservative flux is $\boldsymbol{\mathcal{F}}(\mathbf{W}) = (\mathbf{f}(\mathbf{W}), \mathbf{g}(\mathbf{W}))$ where for the PGD and Euler system we have respectively:

$$\mathbf{W}_{PGD} = n\begin{pmatrix} 1 \\ u \\ v \end{pmatrix}, \quad \boldsymbol{\mathcal{F}}_{PGD} = n\left(\begin{pmatrix} u \\ u^2 \\ uv \end{pmatrix}, \begin{pmatrix} v \\ uv \\ v^2 \end{pmatrix}\right); \tag{5.54}$$

$$\mathbf{W}_{Euler} = n \begin{pmatrix} 1 \\ u \\ v \\ \mathcal{E} \end{pmatrix}, \quad \boldsymbol{\mathcal{F}}_{Euler} = \left(\begin{pmatrix} nu \\ nu^2 + \mathcal{P} \\ nuv \\ (n\mathcal{E} + \mathcal{P})u \end{pmatrix}, \begin{pmatrix} nv \\ nuv \\ nv^2 + \mathcal{P} \\ (n\mathcal{E} + \mathcal{P})v \end{pmatrix} \right). \tag{5.55}$$

The numerical flux $\boldsymbol{\mathcal{F}}^*(\mathbf{W}_{ext}, \mathbf{W}_{int}, \overrightarrow{\mathbf{n}})$ is supposed to be realizability preserving. $\mathbf{W}_{ext}$ and $\mathbf{W}_{int}$ denote states on both sides of the considered edge of normal $\overrightarrow{\mathbf{n}}$. Then the differential system reads:

$$|T_i|(\boldsymbol{\mathcal{M}}_{jl})d_t\mathbf{W}^l_{T_i} + \int_{\partial T} \boldsymbol{\mathcal{F}}^* \left(\mathbf{W}_{ext}(s), \mathbf{W}_{int}(s), \vec{\mathbf{n}}(s)\right) \varphi^j_{T_i}(s) ds = \int_{T_i} \boldsymbol{\mathcal{F}}(\mathbf{W}(x,t)) \cdot \overrightarrow{\nabla\varphi^j_{T_i}} \mathrm{d}x. \tag{5.56}$$

After summing over all the degrees of freedom j of T_i and discretizing in time, we get the equation of the evolution of the mean value in T_i:

$$\overline{\mathbf{W}}^{n+1}_{T_i} = \overline{\mathbf{W}}^{n}_{T_i} - \int_{\partial T} \boldsymbol{\mathcal{F}}^* \left(\mathbf{W}_{ext}(s), \mathbf{W}_{int}(s), \vec{\mathbf{n}}(s)\right) ds, \tag{5.57}$$

where the right contour integral is estimated using the appropriate Gauss quadrature. The main difficulty in the extension of the 1-D scheme to two dimensions is to find a quadrature rule which is exact for polynomials of order k, has strictly positive quadrature weights and includes in its quadrature points the Gauss quadrature points used to integrate the numerical fluxes on

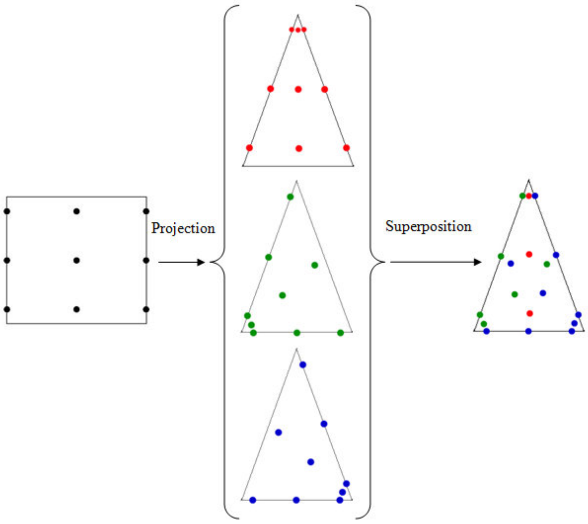

Figure 5.8: *The quadrature points on the triangle for k=2 resulting from the superposition of the three projections (inspired by Zhang el al. 2012)*

∂T. If such a quadrature exists, in a similar way to the 1D case the mean value update (see Equation (5.57)) can be recast into a convex combination of states at interior quadrature points and formal first order updates at edges Gauss quadrature points (*Zhang et al. 2012*). Under a certain CFL condition, $\overline{\mathbf{W}}_{T_i}^{n+1}$ is then realizable if $\mathbf{W}_h$ is realizable at all the quadrature points, which can be ensured in the same way as in the one dimensional case. A quadrature with such properties exists naturally on quadrangles through a tensor product of the considered Gauss quadrature for the edges in one direction and an accurate enough ($2m-3 \geq k$) Gauss-Lobatto quadrature in the other direction. A projection mapping the top edge of the quadrangle onto one vertex of the triangle and the other edges onto the three edges of the triangle will then give a set of quadrature points at desired accuracy, with strictly positive quadrature weights and which coincide with the Gauss quadrature points on two of the three edges. By this mean, three projections are defined and by superimposing the three resulting sets we obtain the sought quadrature. Figure 5.8 illustrates the construction of such a set of quadrature points in a very high order framework. The represented set of quadrature points works for polynomials of order 2 and 3: it allows for third and fourth order numerical methods in space and eventually involves 18 quadrature points. However, in the second order case, *ie.* linear representation of the solution, only 6 quadrature points are required: 2 per edges. Finally, it can be shown that for this special quadrature-point construction, the realizability constraint is

$$\frac{\alpha_{T_i} \Delta t \, |\partial T_i|}{|T_i|} \leq \frac{2}{3} \omega_1^{G-L}, \tag{5.58}$$

where α_{T_i} is still an overestimation of the eigenvalues of the Jacobian of the flux at all the considered quadrature points for a given triangle T_i, $|\partial T_i|$ is the perimeter of T_i and ω_1^{G-L} is the smallest weight (always on the edges of the interval) of the considered Gauss-Lobatto quadrature. At second order, we will use 2 points with weights $\frac{1}{2}$, which means a global CFL constraint equal to $\frac{1}{3}$. This scheme was already evaluated on 1D and 2D test cases for solving the MK model by *Larat et al. (2012)*. An example on a 2D HIT on unstructured mesh is shown in Figure 5.9.

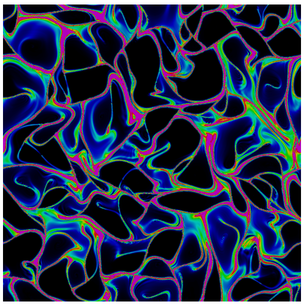

Figure 5.9: *2D frozen HIT coupled with the MK model solved by DG on unstructured mesh*

Chapter 6

Evaluation and Comparisons

A comparison between the different schemes presented in the previous chapter, is conducted here. Even though numerical computations have already been led in 2D and 3D with the MK model using the FVKS, the present contribution focuses on 1D results for a full understanding of the trade-off between robustness and accuracy and of the impact of the limitation procedures on the numerical dissipation. For the simplest 1D case studies, the linear advection, the TTGC scheme is compared with the other schemes as well, showing the constraints of such a scheme when no artificial viscosity is added as stated in subsection 5.1.4. In a second part, 2D results of a frozen HIT are presented for the evaluation of the realizable MUSCL/HLL finite volume scheme, and the convex state preserving RKDG scheme. Comparison with the Lagrangian simulations, considered as the reference, is led both qualitatively and quantitatively. Advantages and drawbacks of each of these schemes are finally discussed.

6.1 1D comparison

Four 1D test cases of increasing complexity are presented in this section. For all these tests, periodic boundary conditions are considered. The results are obtained for a CFL=0.5 and a mesh of 100 cells (except for convergence study where the mesh varies in the range between 20 and 500 grid points).

First, we want to assess the numerical method implemented with the most simplified version of the PGD system where the velocity is everywhere equal to unity. In this case, the linear advection equation is obtained. For this configuration the TTGC result is presented along with the FV results and the RKDG results.

6.1.1 Linear advection of a Gaussian profile

We consider a Gaussian-like initial condition given by Equation (6.1) with a velocity $u(x) = 1$. After a complete period the exact solution is translated back to its initial position.

$$n(x,0) = \begin{cases} [\cos(\pi(2x-1))]^4 & \text{if } 0.25 < x < 0.75 \\ 0 & \text{otherwise} \end{cases} \tag{6.1}$$

In Figure 6.1, the solutions of the different schemes are represented after 10 cycles. The solutions of the schemes with the minmod limiter are clearly smeared out.

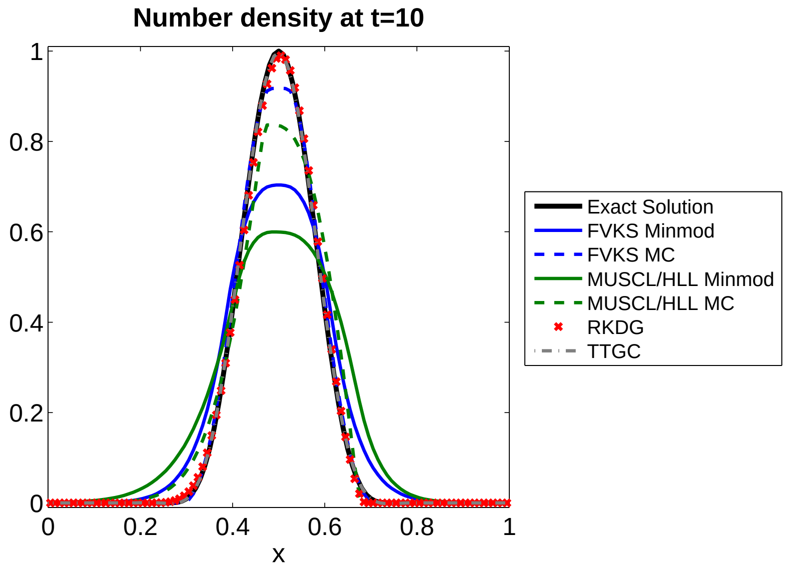

(a) Full window

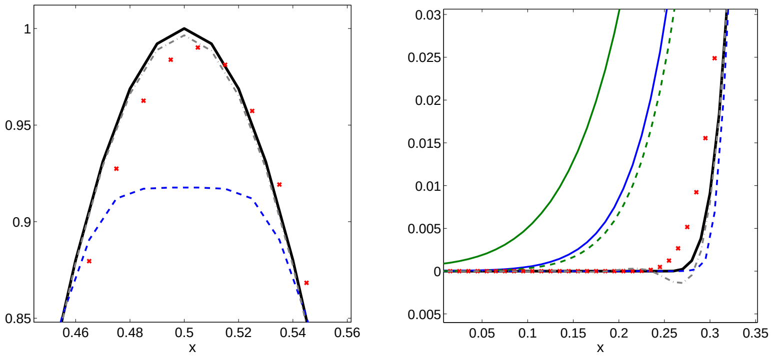

(b) Zoom at the maximum (c) Zoom near zero number density

Figure 6.1: *Number density results of the linear advection equation having a Gaussian-like initial solution, at t=10 using RKDG, FVKS, MUSCL/HLL and TTGC.*

Table 6.1: *Errors of the different schemes for the linear advection of the Gaussian at t=1*

Errors	TTGC	RKDG	FVKS MC	MUSCL MC	FVKS Minmod	MUSCL Minmod
1-norm	9.837×10^{-5}	7.705×10^{-4}	1.702×10^{-3}	8.317×10^{-3}	8.387×10^{-3}	1.541×10^{-2}
2-norm	1.523×10^{-4}	1.277×10^{-3}	4.464×10^{-3}	1.451×10^{-2}	1.729×10^{-2}	2.976×10^{-2}
∞-norm	3.677×10^{-4}	2.957×10^{-3}	2.532×10^{-2}	4.087×10^{-2}	7.368×10^{-2}	1.137×10^{-1}

Table 6.2: *Exact order of the different schemes at t=1*

Orders	TTGC	RKDG	FVKS MC	MUSCL MC	FVKS Minmod	MUSCL Minmod
1-norm	3.1757	2.0198	2.2511	1.5936	1.5939	1.5024
2-norm	3.1440	2.0381	1.9257	1.5375	1.4337	1.3458
∞-norm	3.1317	2.0659	1.4949	1.1978	1.1254	1.0819

We can also observe the leading phase error for the RKDG and MUSCL/HLL solutions, which is a sign of numerical dispersion. The solution of the third order TTGC is the least dissipated; no dispersion is noticed in this case. For the FVKS MC solution we notice a minor flattening of the bump due to slope limitation. According to these results, the list of the schemes arranged in increasing order of numerical diffusion is: TTGC, RKDG, FVKS MC, MUSCL/HLL MC, FVKS Minmod and MUSCL/HLL Minmod.

We next perform a convergence study at $t = 1$. The numerical errors of the different schemes are found in Table 6.1 using a mesh of 100 points. Based on this table, we can quantitatively compare the dissipation of the different schemes and obtain the same conclusion as before concerning the order of numerical diffusion.

The convergence curves in the 2-norm are plotted in Figure 6.2 for the different schemes. In addition, Table 6.2 provides the orders of convergence for each norm of error. Second order is obtained for RKDG and FVKS with MC limiter, which is not the case for MUSCL/HLL particularly for coarse meshes. When it comes to TTGC we recover third order accuracy for this smooth initial condition. When using the minmod limiter instead of MC, the slopes are respectively reduced by 13% and 26% for MUSCL/HLL and FVKS. Also an interesting feature is that RKDG and TTGC maintains respectively the exact second and third order of convergence in the 1-norm and in the ∞-norm, which is not the case for the two other FV schemes.

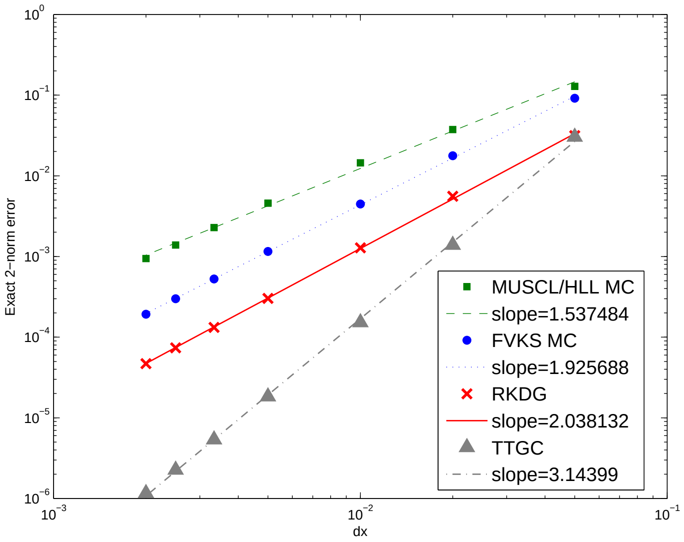

Figure 6.2: *Convergence study in the 2-norm of the linear advection equation having a Gaussian-like initial solution, at t=1, using FVKS, MUSCL/HLL, TTGC and RKDG.*

6.1.2 Linear advection of a rectangular hat

The initial condition for the **second test** case is a rectangular hat:

$$n(x,0) = \begin{cases} 1 & \text{if } 0.25 < x < 0.75 \\ 0 & \text{otherwise} \end{cases} \tag{6.2}$$

The solution at t=10 is shown in Figure 6.3. TTGC creates spurious oscillations near the sharp discontinuities and leads to unphysical results, which is expected since this is the only scheme that is not limited. All the other scheme are robust. Using the Minmod limiter the discontinuities are smeared out, whereas the MC limiter provides a sharper reconstruction. The RKDG result matches the exact solution a little better than the FVKS MC one. As already mentioned in the chapter 6, the TTGC generates oscillations and leads to unphysical solutions containing negative number density for example. Thus, in order to stabilize the scheme, artificial viscosity is essential. Since the scheme is not parameter free, it does not meet our objectives and it will no more be used in the following numerical comparisons.

The remaining 1D test cases solve for the PGD system with two different initial conditions.

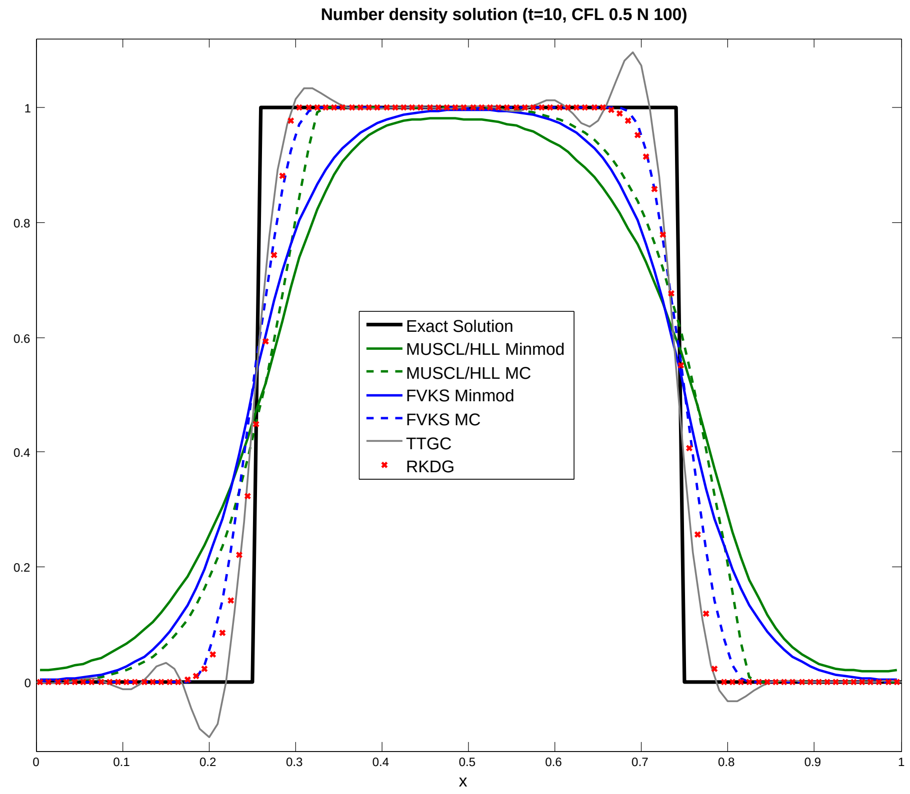

Figure 6.3: *Linear advection equation with a rectangular hat initial condition at t=10 (CFL=0.5, 100 cells)*

6.1.3 PGD system with initial data generating vacuum states, shocks and rarefaction waves.

The **third test** is similar to numerical test I in *Bouchut et al. (2003)*. This later can be considered as a reference test to evaluate the performance of the numerical schemes for the resolution of the PGD system (*Boileau et al. 2010*; *Yang et al. 2013*; *Sabat et al. 2014*; *Boileau et al. 2015*) since it creates accumulation zones and vacuum states. The initial condition for the density and the velocity is given by Equation (6.3).

$$\left\{\begin{array}{lcl} n(x,0) & = & 0.5 \qquad\qquad\qquad 0 \le x \le 2, \\ u(x,0) & = & \left\{\begin{array}{rcrcl} -0.4 & x < 0.5 & \text{or} & & x > 1.8, \\ 0.4 & 0.5 < & x & < 1, & \\ 1.4 - x & 1 < & x & < 1.8. & \end{array}\right. \end{array}\right. \tag{6.3}$$

This initial velocity is depicted in Figure 6.4.

The exact solution for $t < 1$ is given for the density and the velocity respec-

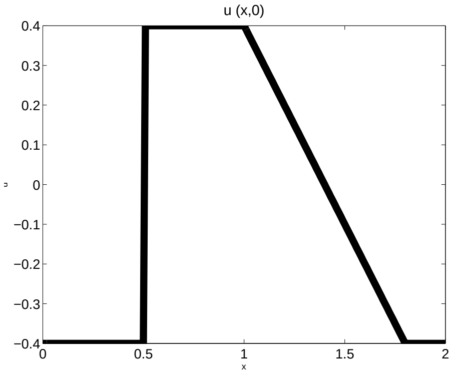

Figure 6.4: *Initial velocity for the third test case*

tively by the following equations:

$$n(x,t) = \begin{cases} 0.5 & x < 0.5 - 0.4t \quad \text{or} \quad 0.5 + 0.4t < x < 1 + 0.4t \quad \text{or} \quad x > 1.8 - 0.4t, \\ 0 & 0.5 - 0.4t < x < 0.5 + 0.4t, \\ \dfrac{0.5}{1-t} & 1 + 0.4t < x < 1.8 - 0.4t \end{cases} \tag{6.4}$$

$$u(x,t) = \begin{cases} -0.4 & x < 0.5 - 0.4t \quad \text{or} \quad x > 1.8 - 0.4t, \\ \text{undefined} & 0.5 - 0.4t < x < 0.5 + 0.4t, \\ 0.4 & 0.5 + 0.4t < x < 1 + 0.4t, \\ \dfrac{1.4 - x}{1-t} & 1 + 0.4t < x < 1.8 - 0.4t \end{cases} \tag{6.5}$$

The density is plotted in Figure 6.5 for the three schemes at $t = 0.5$. The RKDG solution is obtained by guaranteeing the positivity of the density and by applying a maximum principle on the absolute value of the velocity. These two conditions define the convex state for this method. We can notice that all the schemes create small overshoots near the discontinuities (after $x = 1.2$ and before $x = 1.6$), these being already observed in *Bouchut et al. (2003)*. These overshoots have the highest amplitude for the MUSCL/HLL (4.5% above 1.0), are a little bit smaller for RKDG and reduce to only 1% for the FVKS results. It is important to note that these overshoots are replaced by a spike at $x = 0.4$ when a scheme of first order is used, since such a scheme is inconsistent at sonic points (*Bouchut 1994*).

In addition, RKDG creates overshoots before $x = 0.3$ and after $x = 0.7$ since no limiter is used at these points and the scheme does not ensure local monotonicity. When FVKS gives the most satisfactory solution compared to the exact, RKDG also shows the sharpest resolution of the discontinuities. Finally, the velocity component is not shown, since it is nearly the same for all the schemes.

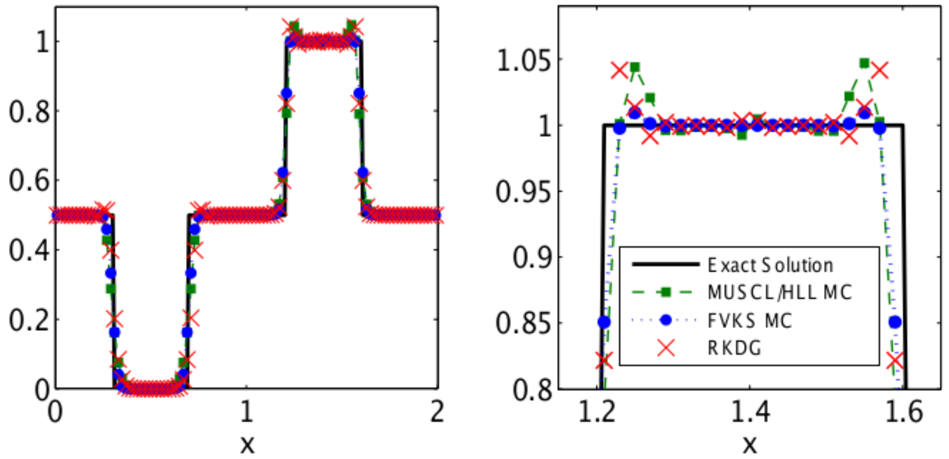

Figure 6.5: *Third test case: density results for the different schemes at t=0.5*

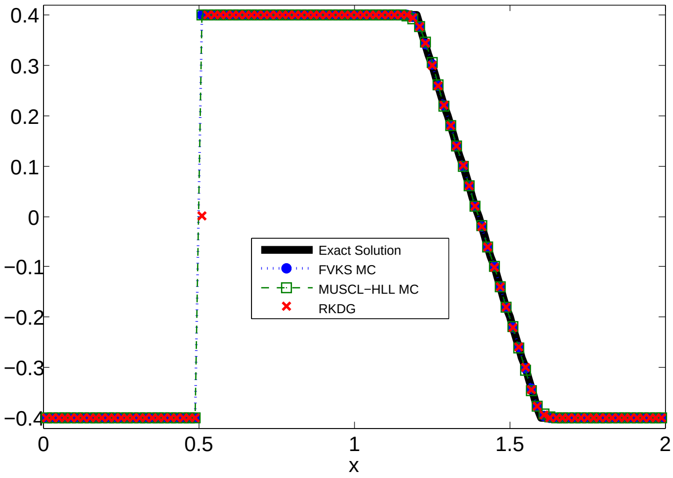

Figure 6.6: *Third test case: velocity results for the different schemes at t=0.5*

6.1.4 PGD system with initial data generating singularities

The **last test** is a more complex problem. It is a replicate, under the MK model, of two packets of particles approaching each other with opposite velocities. For $0 \leq x \leq 1$, the initial condition is given in Equation (6.6) and plotted in Figure 6.7

$$\begin{cases} n(x,0) & = & [\sin(2\pi x)]^4 \\ u(x,0) & = & \begin{cases} -1 & \text{if } x > 0.5 \\ 1 & \text{otherwise} \end{cases} \end{cases} \tag{6.6}$$

At t=0.5, the density exact solution is a Dirac measure at x=0.5 containing all the initial mass. Therefore, we should have all the matter concentrated in one cell at x=0.5. RKDG result is obtained using an additional modified min-mod limiter (*Cockburn and Shu 1989*) and the convex constraint is defined as positive density and absolute velocity limited to 1.0.

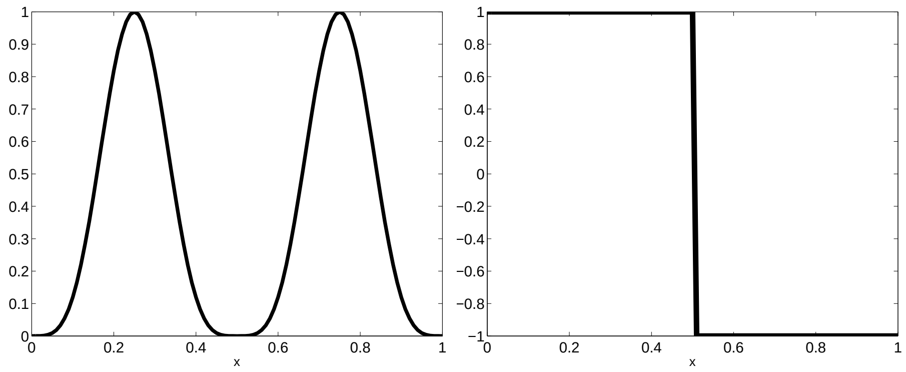

(a) Initial number density (b) Initial velocity

Figure 6.7: *Initial conditions for the last 1D test case*

For this test case, we consider a mesh of 101 cells in order to have a cell center at 0.5 to check if the schemes capture the right position of the Dirac. The numerical results are shown in Figures 6.8 and 6.9. All the schemes are able to physically capture the singularity. The major part of the matter is concentrated in three cells for RKDG ([0.4802, 0.5198]: the mid-cell and its two neighboring cells), in two cells for MUSCL/HLL ([0.4901, 0.5198]: the mid-cell and its right neighbor) but it is concentrated in only one cell for the FVKS result ([0.4901, 0.5099]). The FVKS gives the highest density at x=0.5 (37.87).

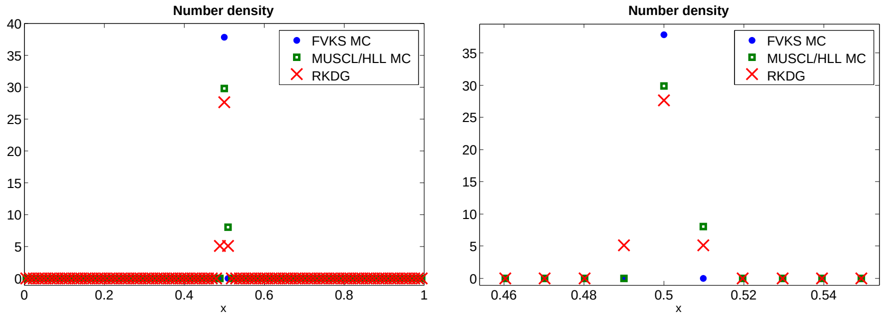

(a) Full window (b) Zoom in

Figure 6.8: *Last test case: number density results for the different schemes at t=0.5*

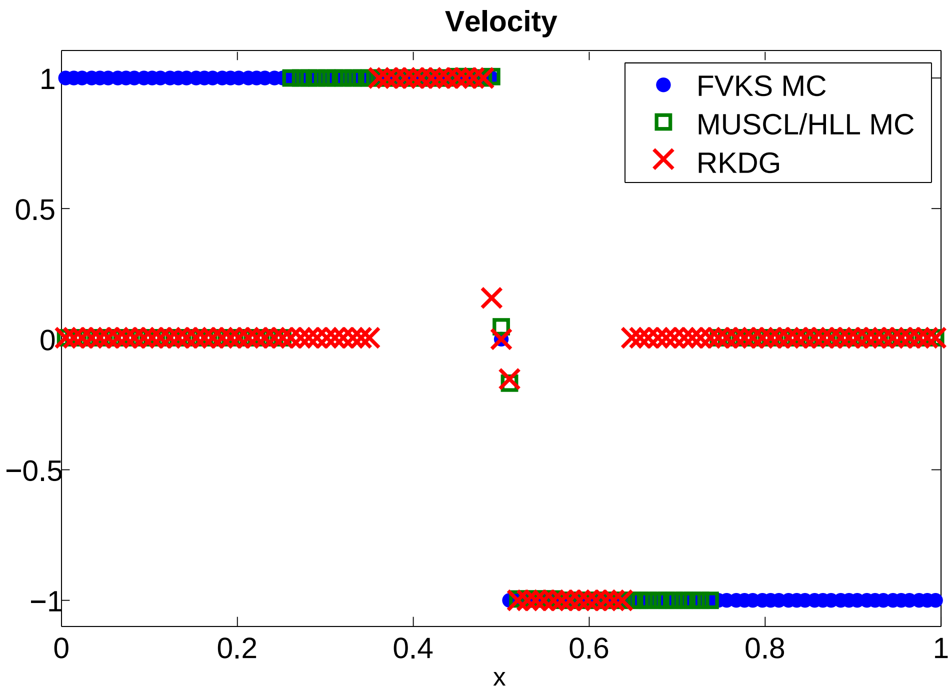

Figure 6.9: *Last test case: velocity results for the different schemes at t=0.5*

At this point the density using MUSCL/HLL and RKDG is reduced respectively by 21% and 27%. For a density less than 10^{-12} we consider void and set the velocity to zero. From the velocity results, it is seen that vacuum is not generated using FVKS. We have void outside the interval $[0.2525, 0.7475]$ for MUSCL/HLL and $[0.3515, 0.6485]$ for RKDG. The RKDG has the largest interval of vacuum but the FVKS gives the sharpest profile near the velocity discontinuity. According to the performance of RKDG in the previous problems, a better result is expected. For this reason, same test case is repeated with a CFL number small enough to run RKDG without adding a slope limiter. In this case the results of the FVKS and MUSCL/HLL were not greatly affected, whereas the RKDG gives a sharper profile for the velocity discontinuity and therefore a localization of the density in two cells. The final RKDG result is however not totally satisfactory because mass accretion in the mid-cell is not as good as FVKS.

For the presented test cases, the RKDG and the FVKS are competitive with each other and overpass the MUSCL/HLL. The FVKS provides slightly better results than RKDG and we believe this is due to the exact update in time for the former.

6.2 2D comparison

6.2.1 Test Cases: Homogeneous Isotropic Turbulence

In order to further assess the DG method, a two-dimensional test case is investigated. It represents a one-way interaction between a 2D periodic frozen homogeneous isotropic turbulent velocity field (HIT) of size 3x3 and a spray which is homogeneously distributed in density and at rest at $t = 0$.
The HIT has been generated with the ASPHODELE code of CORIA, which resolves the three-dimensional Navier-Stokes equations for the gas phase under the low-Mach number assumption (*Guichard et al. 2004*). The Kolmogorov time scale of the turbulence is 0.36.
This fundamental test case is chosen not only to conduct a general comparison between the results of different schemes, but also to be able to examine the segregation and to assess the diffusivity and robustness of the numerical methods.[1]

The study is conducted for the two models based on the monokinetic and the isotropic Gaussian closure, for two different Stokes numbers with respect to the Kolmogorov time scale of the turbulence, namely 0.8 and 4.2. For the sake of comparison and in order to have a physical reference, a Lagrangian Discrete Particle Simulation is conducted for each of these Stokes numbers. Ten million particles are used, ensuring a satisfactory statistical convergence. The Lagrangian results for the number density are computed after a time large enough with respect to the relaxation time of the particles τ_p in order to catch the real dynamic of the flow including any possible high concentration regions and vacuum zones (see Figure 6.10). At small Stokes number (St = 0.8), strong segregation effects occur: particles are gathered in low vorticity zones, and no or negligible PTC is encountered, so that the two considered models should provide suitable results. On the other hand, at a higher Stokes number St = 4.2, particles with greater inertia do not accumulate in the low vorticity zones. They start oscillating around equilibrium trajectories and generate PTC. In this context, the MK model will fail to predict this type of dynamics. Therefore we only investigate the Isotropic Gaussian model for this Stokes number.

---

[1] It is important to note that this 2D HIT field does not give an idea about turbulence in real configurations. The physical results are instead presented on 3D HIT in Part III

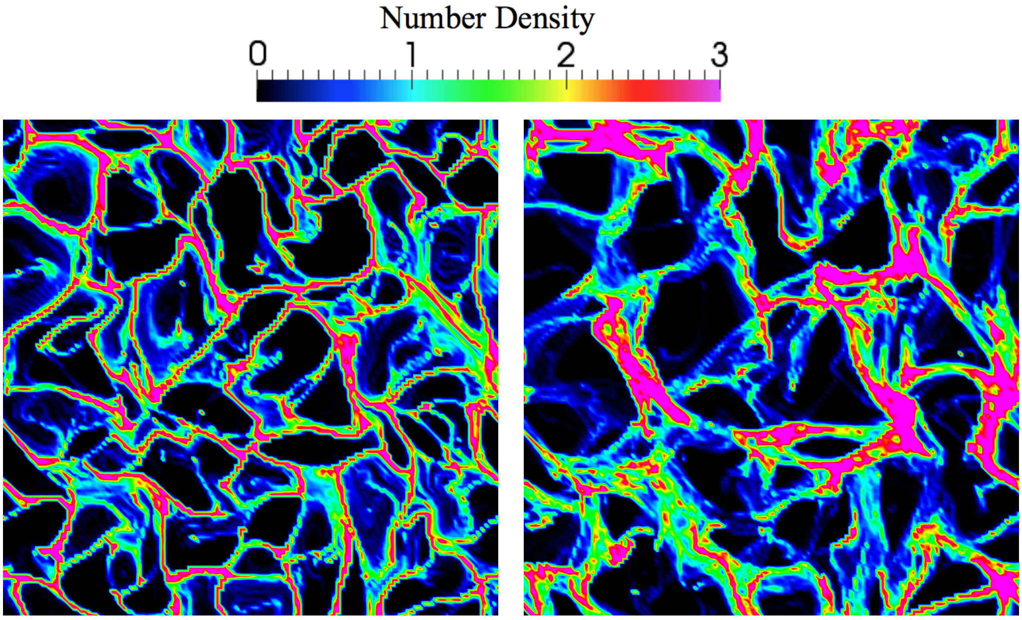

(a) Lagrangian results for St = 0.8 at t=4 (b) Lagrangian results for St = 4.2 at t=12

Figure 6.10: *Snapshots of the particle number density solved by the Lagrangian approach*

In order to compare the density of particles obtained by the two methods at a given time, we consider a 128^2 quadrangular mesh for the FV and the same mesh for DG where quadrangles have been cut into triangles (so if we refer to a 128^2-cell mesh for the DG results it means that we have triangular mesh based on the 128^2 quadrangular mesh). For the FV scheme we have four degrees of freedom per cell. Since this quadrangle is divided into two triangles in the case of DG having 3 DoFs each, for the same mesh DG has 1.5 times more DoFs. A snapshot of the number density is taken after a time long enough ($t \geq 4\tau_{int}$), this time is chosen to be t=4 and t=12 respectively for St = 0.8 and St = 4.2. Finally, the segregation of particles G_{pp}^{Δ} is investigated, which corresponds to the spatial correlation of the number density field at a given cell size length (*Simonin et al. 2006*):

$$G_{pp}^{\Delta} = \frac{\langle n^2 \rangle}{\langle n \rangle^2} \tag{6.7}$$

where $\langle . \rangle$ is the averaging operator over the whole domain. And, for the sake of comparison, the segregation is always calculated on a 64^2 quadrangular mesh, the result of the finer meshes being projected on this reference mesh. This projection is essential since the segregation depends on the length at which it is measured. In fact, it increases with the decrease of length. Thus, in order to compare the segregation of the results computed on different mesh, they should be projected on the coarsest mesh chosen here to be 64^2 cells. In this case, the segregation is measured based on a length scale of 0.0469.

The evolution of the segregation with time is analyzed. It quantifies the degree of accumulation of droplets in the high concentration regions, as well as the degree of depletion in the vacuum zones. Three different meshes are considered namely 64^2, 128^2 and 256^2 for both models and both numerical schemes. These results are compared with one another, but also with two references, namely the statistically converged Lagrangian simulation and a highly refined finite volume solution on a 1024^2-cell mesh. The Lagrangian result is the physical reference as it contains all the physics. The FV segregation on the 1024^2-cell mesh is the numerical reference, because it should encounter a significantly lower numerical diffusion, thus being closer to the solution of the considered model at mesh convergence.

6.2.2 First Test Case: Monokinetic-HIT

In Figure 6.11, the results of the MK model is shown for St $= 0.8$. The structure in these figures matches qualitatively the Lagrangian result given in Figure 6.10. This is expected since for the low inertia particles, we do not have considerable PTC. However, due to numerical diffusion, the solution is smeared out. This diffusivity affects particularly the solution of the FV scheme as seen in Figure 6.11(a). The fact that the DG method provides finer structures and more droplet clusters than the FV for the same mesh is pointed out here and is quantified through the segregation study, see Figure 6.12 and its analysis in the next paragraph. This case illustrates the low numerical diffusivity of the second order DG method compared to the FV one [2].

In Figure 6.12, we show the evolution with time of the segregation, for different meshes and for a particle Stokes number equal to 0.8. For a given mesh, the segregation of the DG results is higher than the one of the FV solutions and it is also closer to the Lagrangian segregation. The segregation rate of the DG solution for a given mesh (N^2) is quantitatively comparable to the one of the FV solution for a mesh which is at least twice as refined as the mesh used for the DG solution $(2N)^2$. In terms of DoFs, the segregation obtain with DG having a total of $6(N^2)$ DoFs is comparable to the result obtain with FV having $16(N^2)$ DoFs, which is more than twice the DoFs used for the result with DG. Now, if we compare the segregation of the DG solution for a refined mesh (256^2) with the one of the highly refined FV solution (1024^2), we note that the curve of the segregation of the DG solution is slightly beneath the refined FV segregation curve. Also, the segregations for the two numerical schemes tend to be asymptotic with the Lagrangian profile when refining the mesh. This proves

---

[2] It is important to note that a study on totally unstructured mesh with DG in 2-D was already done but will not be presented here; for more information one may refer to the CTR Annual Research Brief of *Larat et al. (2012)*.

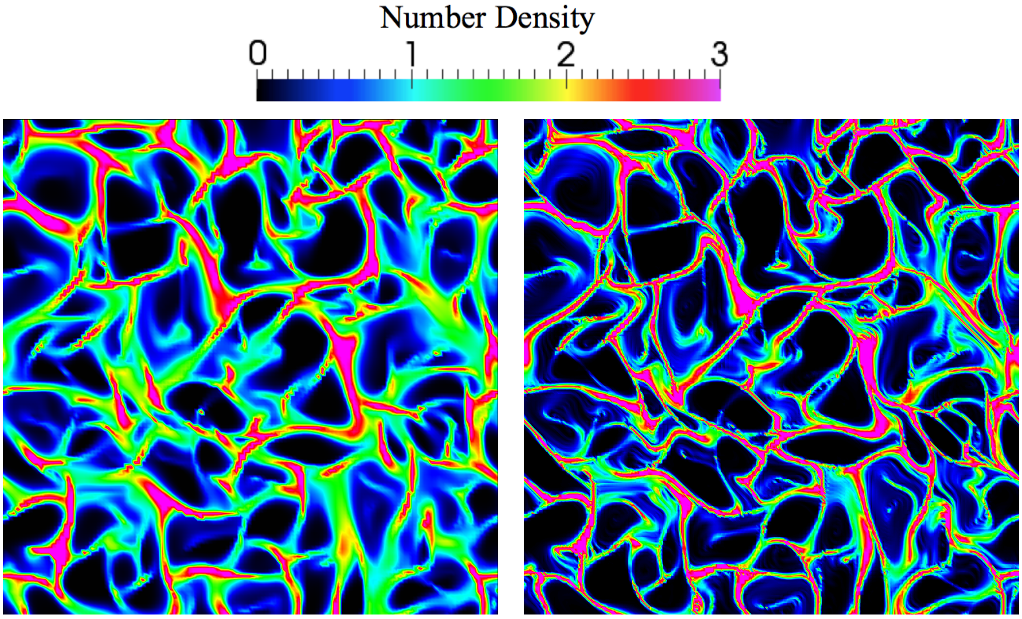

(a) 2^{nd} order FV solution (b) 2^{nd} order DG solution

Figure 6.11: *Particle number density at t=4 for the problem with MK closure for* St $= 0.8$ *and a* 128^2*-cell mesh*

two points:

- the MK model has the ability to reproduce the high segregation effects,
- the DG method is found to be less diffusive than the FV one.

In this section, we compare the DG results to the MUSCL/HLL results only without taking into account the results of the FVKS since both DG and MUSCL/HLL are suitable for solving both the PGD and Euler systems unlike the FVKS that is limited to the PGD resolution. However, we can note that from a qualitative point of view, the results of the MUSCL/HLL and FVKS were found to be very similar, but the FVKS is less expensive.

From a computational cost point of view, for a given mesh the FV method is cheaper than the DG method but it will give results of lower quality. The additional cost for DG method is caused mainly by the integration by quadrature, the realizability preservation and a higher number of DoFs per cell. However, one should keep in mind that these ingredients make the DG scheme more precise than the FV. For a given mesh, the ratio of time per DoF is nearly 10 times higher for the DG scheme. In order to assess the cost to quality ratio, one needs to compare the cost of the two methods for the same result accuracy. The DG solutions with 64^2 and 128^2-cell meshes are comparable to the FV results with 128^2 and 256^2-cell meshes respectively. In this case the DG results is two times more expensive than the FV results. On the other hand, if one considers

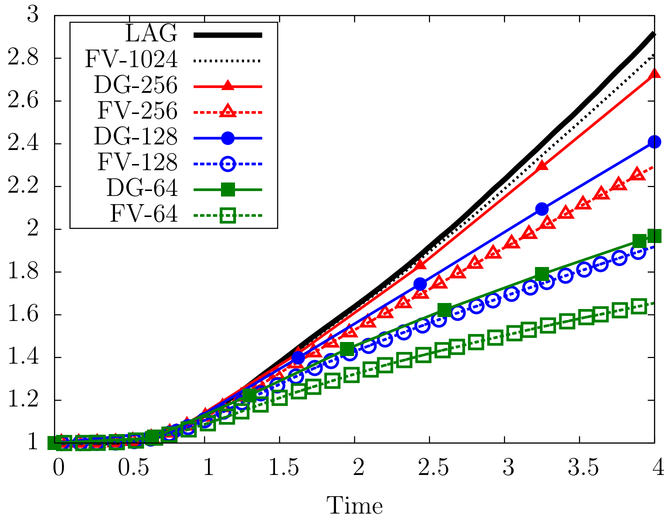

Figure 6.12: *Evolution of the segregation with time for the Lagrangian and MK model using FV and DG method with different meshes for a Stokes number of 0.8*

Table 6.3: *CPU computation time in seconds and Degrees Of Freedom for different meshes for DG and FV results with MK closure for a Stokes number of 0.8*

Mesh	**64^2**	**128^2**	**256^2**	**1024^2**
Time DG (s)	43.05	384.04	3130.05	–
Time FV (s)	2.84	24.45	180.02	13583.41
DoF DG	24576	98304	393216	–
DoF FV	16384	65536	262144	4194304
Time/DoF DG (s)	1.75×10^{-3}	3.91×10^{-3}	7.96×10^{-3}	–
Time/DoF FV (s)	1.7×10^{-4}	3.7×10^{-4}	6.9×10^{-4}	3.24×10^{-3}

the numerical solution given by the DG approach for 256^2-cell mesh which is qualitatively (see Figure 6.13) and quantitatively comparable to the FV result for the 1024^2-cell mesh, DG is found to be more than four times faster in this case.

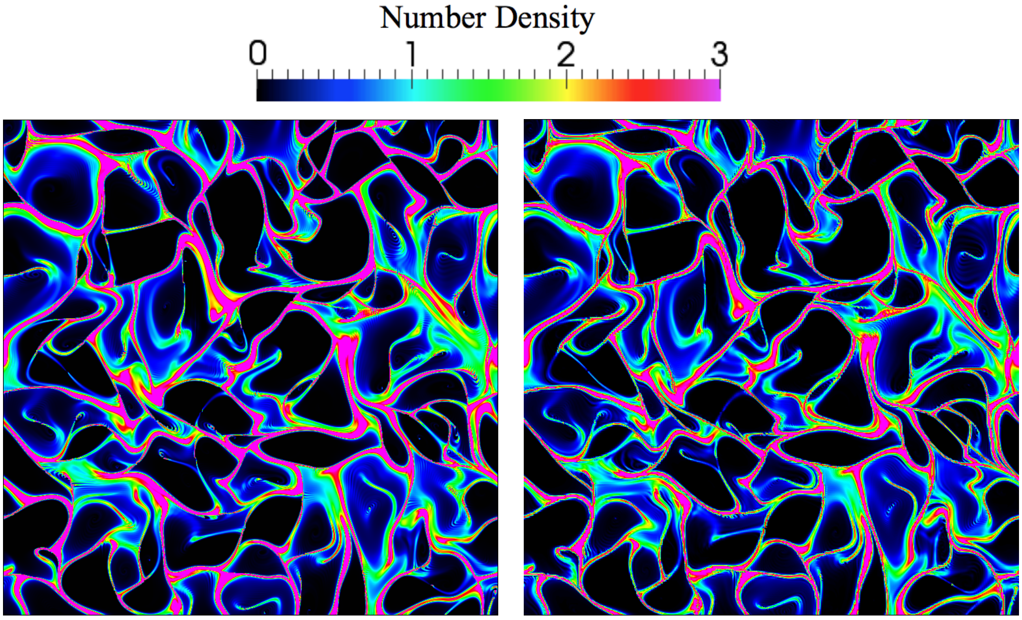

(a) FV solution on the 1024^2-cell mesh (b) DG solution on the 256^2-cell mesh

Figure 6.13: *Particle number density at t=4 for the problem with MK closure for a Stokes number of 0.8 with a* 1024^2*-cell mesh for the FV results and a* 256^2*-cell mesh for the DG results*

In fact, the segregation study with DG (refined mesh, 256^2) took around 52 minutes while nearly 4 hours of computation were spent for an equivalent result with FV (highly refined mesh 1024^2 cells) knowing that the degrees of freedom (DoF) in this case are greater for FV see Table 6.3.

6.2.3 Second Test Case: Isotropic Gaussian- HIT

In Figures 6.14 and 6.15, the results of the isotropic Gaussian model are shown respectively for St = 0.8 and St = 4.2.

At St = 0.8, the model reproduces the general Lagrangian structure but the result is more spread out than the one given by the Lagrangian method or by the MK model using DG. Some of the fine highly concentrated clusters are widened, and the stiff regions in the FV result are clearly more diffused than those of the DG solution. This is due to the numerical diffusion which is higher for the MUSCL/HLL than the DG scheme.

At St = 4.2, the isotropic Gaussian closure model captures the global structures of the Lagrangian reference solution. However, on the contrary to the results at lower Stokes number, it shows some finer ligaments than the Lagrangian solution.

In fact, by comparing the numerical results to the Lagrangian one (see Figures

6.10(b) and 6.15), the effect of the model on the results is observed. The model in question is limited by the isotropic assumption, so the preferential accumulations are overestimated using this model compared to the Lagrangian result.

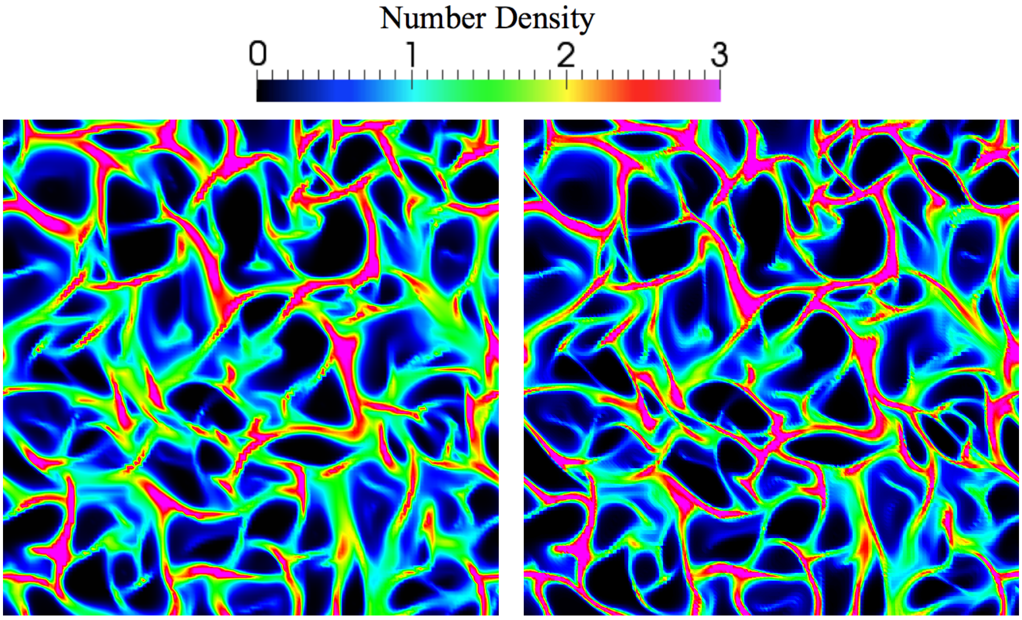

(a) 2^{nd} order FV solution (b) 2^{nd} order DG solution

Figure 6.14: *Particle number density at t=4 for the HIT problem with isotropic Gaussian closure for a Stokes number equal to 0.8 and a* 128^2*-cell mesh*

In addition, by comparing the numerical results for a given model, the effect of numerical diffusion[3] will be pointed out. Qualitative observations of the snapshot of figures 6.14 and 6.15, show once more a lower numerical diffusion by the DG approach compared to the FV technique.

---

[3] The numerical diffusion spreads out the structures, and lowers the segregation.

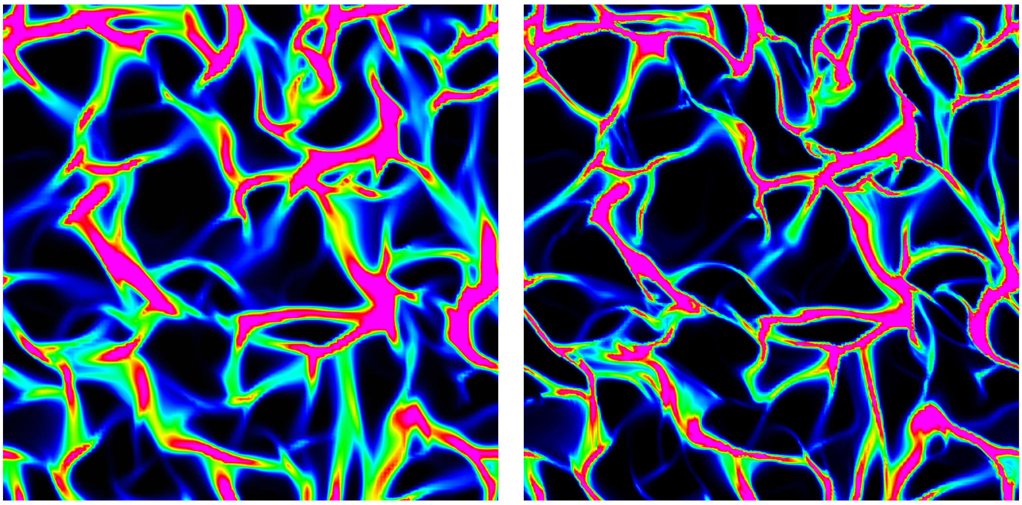

(a) 2^{nd} order FV solution (b) 2^{nd} order DG solution

Figure 6.15: *Particle number density at t=12 for the HIT problem with isotropic Gaussian closure for a Stokes number equal to 4.2 and a* 128^2*-cell mesh*

The latter conclusion needing to be quantitatively assessed, the evolution of the segregation with time for different meshes, for two Stokes numbers $\mathrm{St} = 0.8$ and $\mathrm{St} = 4.2$ is shown respectively in Figures 6.16 and 6.17.

For low inertia particles, $\mathrm{St} = 0.8$, the segregation profiles for the two schemes tend to converge to the Lagrangian one when the mesh is refined but for the same mesh the MK model provides a steeper profile than the isotropic Gaussian model. For a given mesh, the segregation of the DG results is higher than the segregation of the FV solutions.

In the case of moderate Stokes number, the segregation profile for this model is diverging from that of the Lagrangian; the model is no more capturing the correct physics of the flow. The difference between temporal evolution of segregation of the Lagrangian method and the numerical methods is due to the inappropriateness of the model as detailed by *Vié et al. (2015)*. From a numerical point of view, the segregation of the DG solution on the refined mesh (256^2) is nearly equivalent to the one of FV with a 1024^2-cell mesh. And in general the segregation of the DG solution is higher than the segregation of the FV result for the same mesh. Here DG also has a level of convergence significantly higher than FV. From a modeling point of view, this model is found to be unsuitable for describing the physics of moderately inertial particles because of the unphysical high segregation. In fact, the PTC are intrinsically anisotropic, so that the isotropic model is too restrictive and therefore overestimates the segregation since it underestimates the mean central energy (*Vié et al. 2015*).

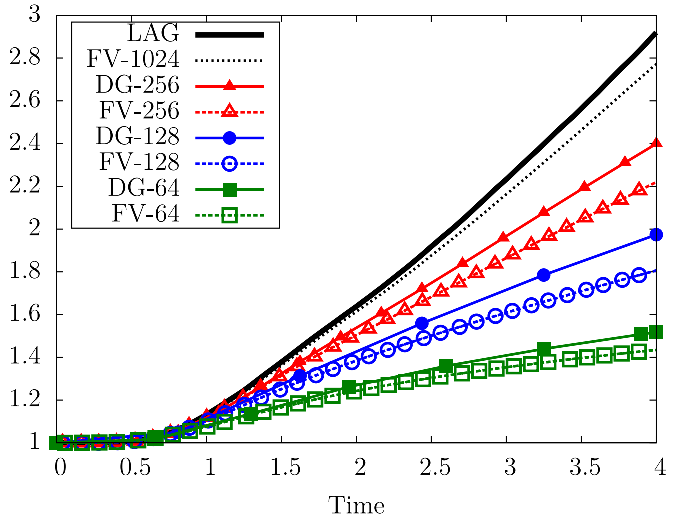

Figure 6.16: *Evolution of the segregation with time for the Lagrangian and isotropic Gaussian closure model using FV and DG method with different meshes for a Stokes number of 0.8*

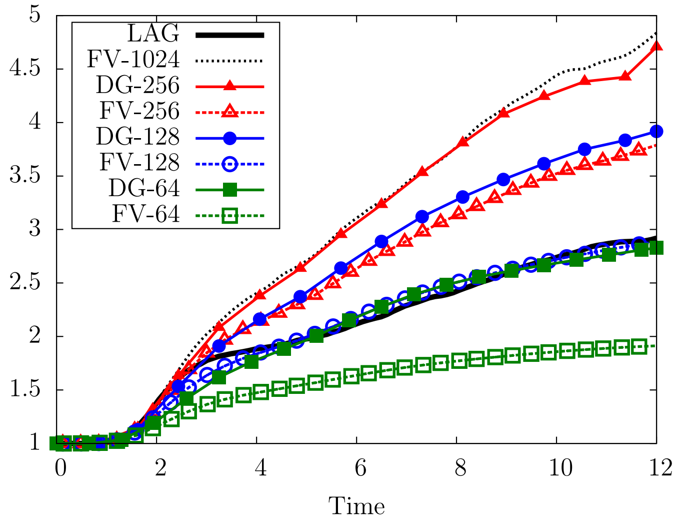

Figure 6.17: *Evolution of the segregation with time for the Lagrangian and isotropic Gaussian closure model using FV and DG method with different meshes for a Stokes number of 4.2*

6.2.4 Towards Predictive Simulations: Anisotropic Gaussian-HIT

The Gaussian closure is the first class of pressure-like models for capturing PTC. However, the isotropic assumption is too restrictive to reproduce crossings induced by the turbulence shear zones, which are intrinsically anisotropic (*Vié et al. 2015*). To highlight the potential of such a modeling approach, we compare the results at St=4.2 for the isotropic and Anisotropic Gaussian closure with the FV scheme. The MUSCL/HLL scheme used for the AG model is developed by *Vié et al. (2015)*.

On the one hand, the isotropic Gaussian closure results shown in Figure 6.15(a) differ significantly from the Lagrangian results (Figure 6.18(b)). Even if it actually captures some of the global structure of the solution, it clearly overestimates the preferential accumulation effects. On the other hand, the anisotropic Gaussian closure results (Figure 6.18(a)) using the same mesh (i.e. 128^2) qualitatively match the Lagrangian results with a slight underestimation of the preferential accumulation effects. In addition, for the segregation study we take three meshes, namely the 64^2, 128^2 and 256^2-cell meshes. The comparison of the segregations, in Figure 6.19, shows that the AG closure does not cre-

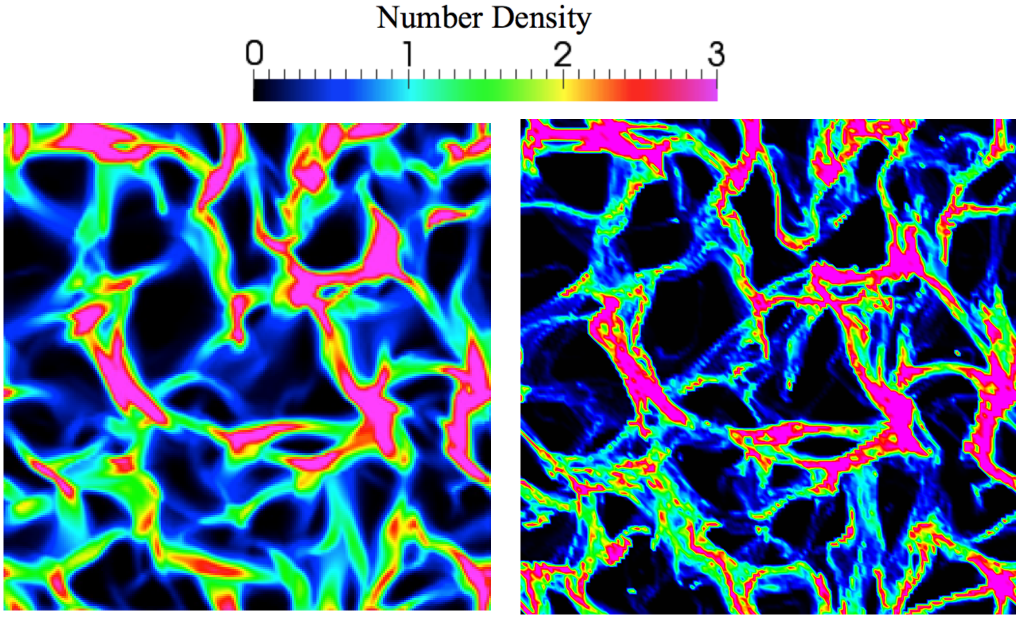

(a) Anisotropic Gaussian model using the 2nd order FV scheme for a 128^2-cell mesh, St=4.2 at t=12

(b) Lagrangian results for St=4.2 at t=12

Figure 6.18: *Particle number density at t=12 for the HIT problem with the Anisotropic Gaussian model using 2nd order FV scheme and the Lagrangian solution for a Stokes number equal to 4.2*

ate unphysical accumulations, as the segregation is still below the Lagrangian segregation, where the isotropic Gaussian closure leads to highly overestimated segregation for a moderate refinement. Finally, the segregation trend of the AG result tends to approach the Lagrangian one so that whenever the mesh is refined the profile will stay below the Lagrangian profile, whereas the Isotropic segregation curves diverges already for relatively coarse meshes. It is thus clear that more realistic simulations must rely on this new closure since it can account for the anisotropy of PTC. Thus, a detailed evaluation of this model in 3D is essential; this is the subject of part III.

From a numerical point of view, to complete this study, the DG scheme should be adapted to the AG model. A first result is presented here to prove once again the potential of the DG method in comparison with the MUSCL/HLL. The comparison of the segregation between the MUSCL/HLL results and the RKDG results for the anisotropic Gaussian model is depicted in Figure 6.20. This is done for a Stokes number St = 4.2 until a time $t = 6$. For a given mesh the segregation using DG is higher than the segregation using MUSCL/HLL. The DG result on a 128^2 mesh gives the same level of segregation as the MUSCL/HLL result with a 256^2 mesh. Thus, DG is less dissipative and more accurate than the MUSCL/HLL.

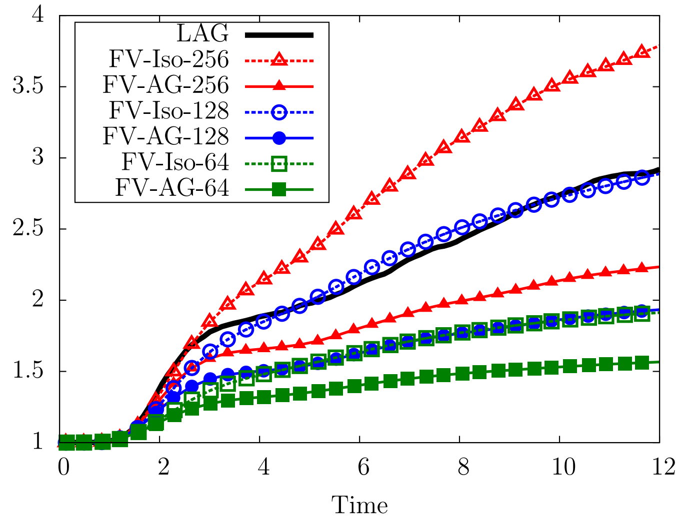

Figure 6.19: *Evolution of the segregation with time for the Lagrangian, isotropic Gaussian closure, and Anisotropic Gaussian closure model using FV for a Stokes number of 4.2*

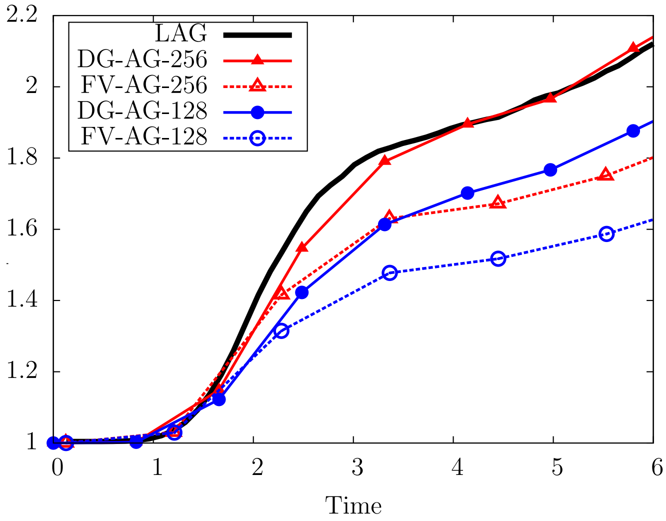

Figure 6.20: *Evolution of the segregation with time for the Lagrangian and Anisotropic Gaussian model using the MUSCL/HLL and RKDG scheme for a Stokes number of 4.2*

6.3 Conclusion

The 1D comparison of the different numerical schemes presented in this work is an essential step toward the ultimate goal of finding an accurate, realizable, cost effective and parameter-free numerical scheme on unstructured grids that can be applied to the KBMM hierarchy. The RKDG and the MUSCL/HLL were applied to higher order models such as the isotropic Gaussian and Anisotropic Gaussian closures KBMM while the application of the FVKS is limited to the Dirac distributions for the velocity. Therefore, even though it is remarkable that the FVKS usage is attractive for this model, we are interested in a numerical scheme applicable to all the KBMMs and the new class of RKDG is a promising choice. To ensure the monotonicity of the RKDG results the best method should be found to make sure that the local maximum principle is respected without degenerating to lower accuracy.

Further investigation of the PGD problem generating the δ-shock should be carried out to better understand the RKDG result deterioration.
When it comes to 2D comparison of the numerical methods, the proposed realizable DG scheme is proven to be robust and accurate. This scheme respects the realizability conditions and can be used on unstructured meshes, which are crucial for real complex geometries. It is less diffusive in comparison with the various second order FV scheme, and for the studied cases more competitive. For the sake of comparison, an algorithmic complexity analysis should be carried out for the two schemes.

From a modeling point of view, the MK closure is suitable for low Stokes number. Besides, for moderate Stokes number the Isotropic Gaussian closure model is not reproducing the physics of the problem accurately. Therefore, other Eulerian modeling methods of higher order in moments and higher level in the hierarchy of models have to be used. A first model is the Anisotropic Gaussian closure model and is shown to reproduce the physics of particle trajectory crossing for a relatively large range of Stokes numbers. More realistic 3D results using this model are thoroughly presented and discussed in the following part.

Therefore, further work should be done to extend the proposed realizable DG scheme to higher order models starting with the AG model. In addition, quality/cost comparisons between the DG and the MUSCL/HLL results still need to be carried out for this model.

One of the perspectives is also to extend this work to higher order DG schemes and to three-dimensional space. The extension to three-dimensional space of the comparison DG-FV is essential since the DG scheme is is often criticized for its high cost due to the high number of degrees of freedom belonging each element. This reputation made DG less attractive for industrial codes in the last decades, however with the increase of computational resources and the achievement done with DG, the latter is used more frequently. This highlights the importance of a cost/quality comparison (similar to the one presented in this work) between the 3-D results of the DG and the MUSCL/HLL schemes.

Part III

Computational dynamics of particle laden flows

In this part, the AG model is evaluated on a 3D Forced Homogeneous Isotropic Turbulence. First, the test case is presented in Chapter 7 along with the forcing scheme, the energy spectrum model and the properties of the resulting turbulent field. In addition, the statistical convergence of the Lagrangian simulations is evaluated and the Lagrangian qualitative results are presented for three St. *Then the AG results are compared to the Lagrangian ones and Eulerian results based on the MK closure. This comparison is carried out for a range of* St *going from particles of very small inertia (St* ~ 0.1*) to high inertia (St* ~ 15*). Depending on their nature, hese results are divided into two chapters. Chapter 8 includes:*

- *qualitative results for the number density field, the velocity field and the elements of the covariance matrix. A comparison between the different models (MK, AG and Lagrangian) is presented for four Stokes numbers, namely* $\mathrm{St} =$ *0.5, 1, 3 and 8 where the Eulerian results are simulated on a* 128^3 *mesh. For* $\mathrm{St} = 0.5$ *and* $\mathrm{St} = 3$ *the mesh refinement effect on the Eulerian results is also qualitatively evaluated on* 64^3, 128^3, 256^3 *and* 512^3 *grids.*
- *qualitative scatter plots for the one-point correlation of the velocity of the disperse phase to check how much the Eulerian velocity is similar to the Lagrangian one, and most importantly to check whether the disperse phase velocity is correlated to the carrier phase velocity or not. This is done for two Stokes numbers,* $\mathrm{St} = 0.5$ *and* 8.
- *quantitative mean statistical results including the segregation, the mean total energy and the mean internal energy. The evolution of these quantities with time is compared for the different models and for different Stokes numbers. In addition, these statistical quantities at a given time are plotted as a function of the Stokes number for the different models and meshes.*

In Chapter 9, we present:

- *quantitative results for the distribution functions of the number density, the velocity magnitude, the trace of the pressure tensor and finally the disperse phase Mach number.*
- *autocorrelation functions for the number density, velocity and internal energy. Based on these two-points correlations two length scale are computed. These scales are respectively: the characteristic size of the clusters and the longitudinal integral length scales of the disperse phase motion. The change of these length scales as a function of the particles inertia is then presented.*

Through all these qualitative and quantitative analysis, the Anisotopic Gaussian model is proven to be a good candidate for the simulation of moderately inertial to inertial particles in complex applications, when the MK model ceases to capture the underlying physics of the problem. Finally, the range of scales for which the AG model is suitable is identified.

Chapter 7

3D HIT test case

The subject of this chapter is to define the simulated configuration through the three dimensional gas field used as the source of the dynamics of the disperse phase. First, the energy model spectrum chosen for the Homogeneous Isotropic Turbulence (HIT) is presented. Then, the forcing scheme used to force the HIT is specified. The resulting Forced HIT used for the carrier phase is then described through its characteristics and properties. The understanding of this phase is of paramount importance, since it will govern the dynamics of the disperse phase through a one-way coupling. This classical academic test case is essential for the validation of the disperse phase models, since it represents one of the canonical samples of the physics faced in industrial applications.
The Lagrangian reference is also presented in this chapter along with the statistical convergence of the results and some examples of the qualitative results for different Stokes numbers. Finally, the perspective test cases that can be chosen for further evaluation and validation of the AG model are proposed.

7.1 Homogeneous Isotropic Turbulence

The three dimensional test case ran in this part is based on a 3D Forced Homogeneous Isotropic Turbulence (FHIT) for the carrier phase resolved in a cubic domain, with periodic boundary conditions.
This carrier phase is computed with a dimensionless DNS solver for low Mach number flow. This academic tool is the ASPHODELE code which was developed at CORIA (*Reveillon and Demoulin 2007*; *Péra 2005*; *Meftah 2008*; *Bouali 2011*; *Thomine 2011*).

The forcing scheme is based on an initial solution for a HIT that is obtained based on a model for the energy spectrum. In the following the selected model is introduced before presenting the spectral forcing scheme.

7.1.1 Model spectrum

The energy spectrum function introduced in *Pope (2000)* is used as the model spectrum:

$$E_m(\kappa) = C\langle\varepsilon\rangle^{2/3}\kappa^{-5/3}f_L(\kappa L)f_\eta(\kappa\eta), \tag{7.1}$$

with:

$$f_L(\kappa L) = \left(\frac{\kappa L}{[(\kappa L)^2 + c_L]^{1/2}}\right)^{5/3+p_0}, \tag{7.2}$$

$$f_\eta(\kappa\eta) = \exp\left(-\beta[((\kappa\eta)^4 + c_\eta^4)^{1/4} - c_\eta]\right), \tag{7.3}$$

where $\eta = \left(\frac{\nu^3}{\langle\varepsilon\rangle}\right)^{1/4}$ is the Kolmogorov length scale given as a function of the carrier phase viscosity ν and the mean dissipation rate of turbulent kinetic energy $\langle\varepsilon\rangle$. In addition, the length scale $L = \frac{\langle\mathrm{TKE}\rangle^{3/2}}{\langle\varepsilon\rangle}$ characterises the large eddies, where $\langle\mathrm{TKE}\rangle$ is the mean turbulent kinetic energy.

f_L is a non-dimensional function that governs the shape of the energy containing range. For large κL this function tends to 1. The shape of the dissipation range is determined by the non-dimensional function f_η. For small $\kappa\eta$ this function tends to 1.

Unless told otherwise the parameters of this model are set to: $C = 1.5$, $\beta = 5.2$ and $p_0 = 4$.

An example of the energy spectrum function normalized by the Kolmogorov scales $\frac{E_m(\kappa)}{\eta u_\eta^2}$ is shown in Figure 7.1. For small wavenumbers, the power law $E(\kappa) \sim \kappa^4$ is verified as seen in Figure 7.1 through the slope of the dashed-doted line; this is the von Kármán spectrum defined by Equation (7.2). This region of small wavenumbers is the energy containing range. In the inertial subrange, the Kolmogorov spectrum with a $-5/3$ slope is obtained since both $f_L(\kappa L)$ and $f_\eta(\kappa\eta)$ tend to unity. For large wavenumbers, the exponential decay region is also evident.

Knowing the energy spectrum function $E(\kappa)$, the turbulent kinetic energy and the dissipation rate can be calculated using the following equations:

$$\langle\mathrm{TKE}\rangle = \int_\kappa E(\kappa)\mathrm{d}\kappa, \tag{7.4}$$

$$\langle\varepsilon\rangle = \int_\kappa D(\kappa)\mathrm{d}\kappa = 2\nu\int_\kappa E(\kappa)\kappa^2\mathrm{d}\kappa. \tag{7.5}$$

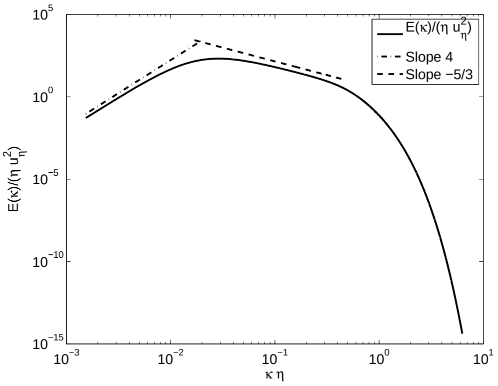

Figure 7.1: *An example of the energy model spectrum function*

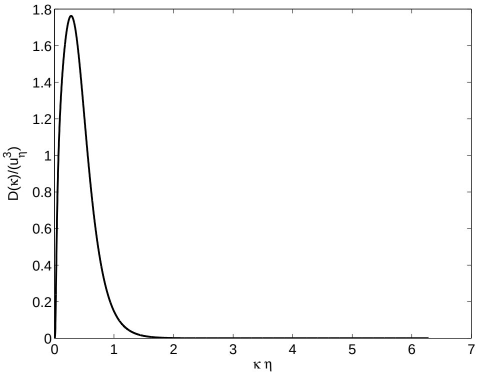

Figure 7.2: *An example of the dissipation spectrum*

Also the integral length scale can be determined based on the energy spectrum function. We distinguish here the two expressions for two dimensional HIT (*Guichard et al. 2004*) and three dimensional HIT (*Pope 2000; Guichard et al. 2004*):

$$L_{11} = \frac{2}{\langle \mathrm{TKE} \rangle} \int_\kappa \frac{E(\kappa)}{\kappa} \mathrm{d}\kappa \quad \text{(in 2-D)}, L_{11} = \frac{3\pi}{4\langle \mathrm{TKE} \rangle} \int_\kappa \frac{E(\kappa)}{\kappa} \mathrm{d}\kappa \quad \text{(in 3-D)}. \tag{7.6}$$

The dissipation spectrum $D_m(\kappa) = 2\nu\kappa^2 E_m(\kappa)$ normalized by the Kolmogorov scales $(D(\kappa)/u_\eta^3)$ is shown in Figure 7.2.

From this figure, one can notice that above a certain limit of $\kappa\eta$ the dissipation spectrum is very small (for the given example for $\kappa\eta > 2$ the dissipation spectrum is negligible). This limit is important since it is a criterion for the resolution of the smallest scales and therefore defines the maximum ratio of grid spacing Δx to the Kolmogorov lengthscale η for Direct Numerical Simulation.

7.2 Forcing scheme

To get a statistically stationary spectral turbulence, a fully controlled deterministic forcing scheme (FC-DFS) was developed in *Guichard et al. (2004)* as an extension of the work of *Overholt and Pope (1998)*. FC-DFS controls the turbulent kinetic energy and monitors the energy for low wave-number (no energy increase) by adding a "negative" energy to the simulated spectrum whenever needed.

The turbulence is forced by adding to the spectral velocity equations, a linear source term:

$$\partial_t \overrightarrow{\mathbf{U}_g^f} = A^f + \frac{f_\kappa}{\tau_f} + \overrightarrow{\mathbf{U}_g^f}, \tag{7.7}$$

where A^f is the contribution of the classical Navier-Stokes equation, $f_\kappa(\kappa_f, \Delta\kappa_f)$ is the forcing function and τ_f is a characteristic relaxation delay of the forcing. The main idea behind this scheme is to force the simulated spectrum to a model spectrum for the large scales ($\kappa < \kappa_f$). This can be seen through the equation of time evolution of the energy spectrum with the attraction parameter:

$$\frac{\mathrm{d}E_s}{\mathrm{d}t} = C_\kappa + F_\kappa \frac{\alpha_f(t) E_m(\kappa) - E_s(\kappa, t)}{\tau_f}, \tag{7.8}$$

where C_κ is the energy contribution without the forcing source terms, and F_κ is a filter function that sets the forcing amplitude for every wavenumber κ:

$$F_\kappa = \frac{1 - \exp\left(-\frac{(\kappa-\kappa_f)^2}{\Delta\kappa_f^2}\right)}{1 - \exp\left(-\frac{(-\kappa_f)^2}{\Delta\kappa_f^2}\right)} H(\kappa_f - \kappa), \tag{7.9}$$

with $H(\kappa_f - \kappa)$ being the Heaviside function.

For stability reasons, the relaxation time of the simulated spectrum to the modeled one should be smaller that the Kolmogorov time scale: $\tau_f = C_f \tau_k = C_f \sqrt{\frac{\nu}{\langle \varepsilon \rangle}}$ with C_f being a constant smaller than one. *Guichard et al. (2004); Reveillon and Demoulin (2007)* determined the forcing function by the following equation:

$$f_\kappa = \frac{F_\kappa}{2E_s(\kappa, t)} (\alpha_f(t) E_m(\kappa) - E_s(\kappa, t)), \tag{7.10}$$

where $\alpha_f(t)$ is a coefficient that controls the mean turbulent kinetic energy:

$$\alpha_f(t) = \frac{\langle \mathrm{TKE} \rangle_m - \langle\langle \mathrm{TKE} \rangle\rangle + \tau_f \langle \varepsilon \rangle + \int_\kappa F_\kappa E_s(\kappa, t) \mathrm{d}\kappa}{\int_\kappa F_\kappa E_m(\kappa, t) \mathrm{d}\kappa}, \tag{7.11}$$

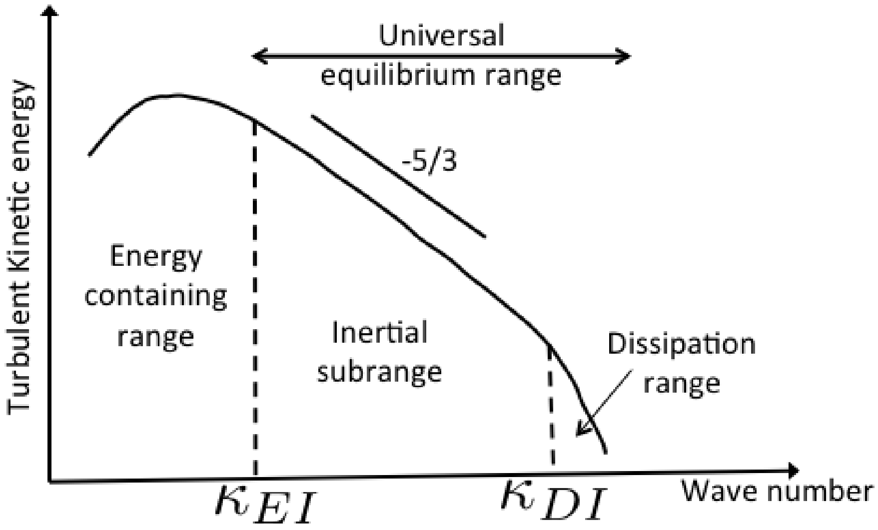

Figure 7.3: *Energy Cascase various eddy scales and ranges*

with $\langle \mathrm{TKE} \rangle_m = \int_\kappa E_m(\kappa) d\kappa$ the turbulent kinetic energy of the model spectrum. This forcing procedure will lead to a statistically stationary grid turbulence in the physical domain by stabilizing the major properties of the turbulence: the energy, the dissipation rate and the integral length scale.
Practically, if the goal is to get a simulated turbulent having an integral length scale nearly equal to the integral scale of the model spectrum, the cut-off wavenumber should be selected accordingly (*Guichard et al. 2004*). This means that κ_f should be set to $\kappa_{\mathrm{EI}} = \frac{2\pi}{l_{\mathrm{EI}}}$ separating the inertial subrange and the energy-containing range (see Figure 7.3 (*Pope 2000*)). In this case, the universal equilibrium range composed of the dissipation range and the inertial subrange evolves freely while the energy-containing range is forced to relax towards the energy containing range of the model spectrum.

7.3 Small Reynolds number HIT test case

The DNSs presented in this thesis are done for a low Reynolds number turbulence, knowing that the evaluation itself and the application of Anisotropic Gaussian model is not limited to low turbulence flow. All the values of the variables presented in this work are dimensionless, and the normalizing Reynolds number and viscosity are respectively 10^3 and 10^{-3}.

7.3.1 Velocity field and general properties

This turbulence is obtained for a cube of size 5^3 using a 128^3 mesh.
The evolution of the turbulent properties is shown in Figure 7.4. The different

characteristics in question are the mean turbulent kinetic energy ($\langle\text{TKE}\rangle$), the mean dissipation rate ($\langle\varepsilon\rangle$), the Kolmogorov time and length scales (time τ_K and length η). One can notice that after a time $t > 15$ the turbulence is statistically stationary. For this reason the different simulation of the disperse phase are all carried out until reaching a final time $t = 40$, which is approximately ten times the time scale of the large eddies. At $t = 40$, the magnitude of the velocity field is plotted in Figure 7.5 and the kinetic energy spectrum (E) along with the dissipation spectrum (D) are presented in Figure 7.6.

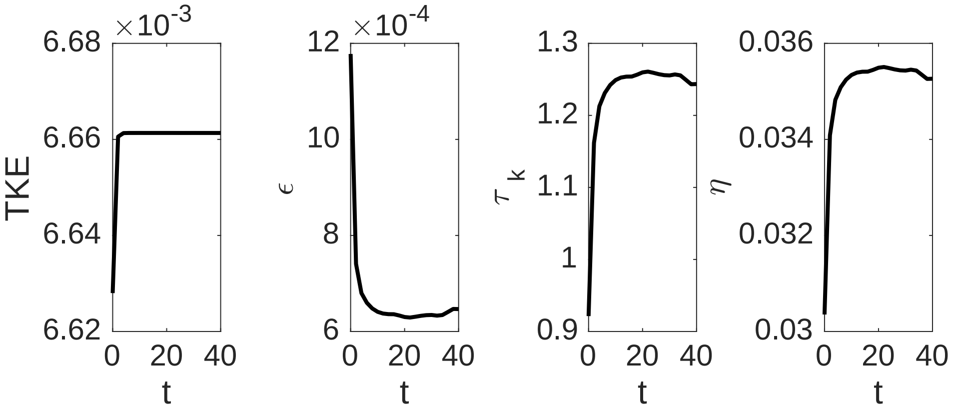

Figure 7.4: *Evolution of the characteristics of the forced HIT with time on a* 128^3 *mesh*

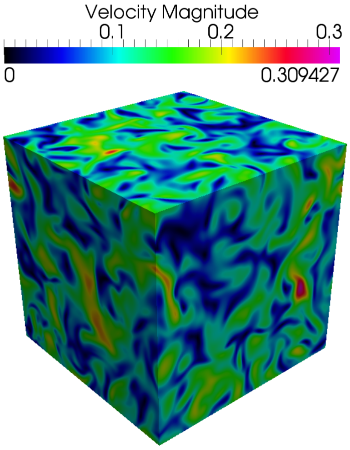

Figure 7.5: *Velocity magnitude of a forced HIT at final time* $t = 40$ *on a* 128^3 *mesh*

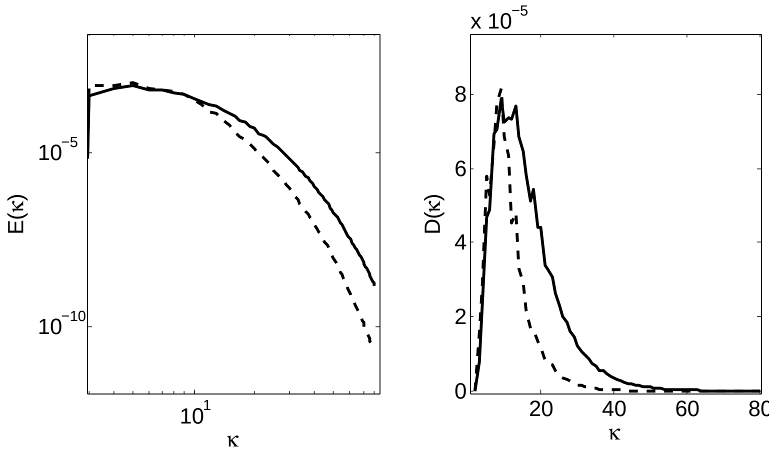

Figure 7.6: *Kinetic energy spectrum (left) and dissipation spectrum (right) for the forced HIT at initial time ($t = 0$ full line) and final time ($t = 40$ dashed line)*

7.3.2 Characterisitic time scale of the fluid

In order to estimate the inertia of the particles with respect to the carrying fluid, the Stokes number should be calculated. The smallest turbulent scale capable of generating the PTC is the Kolmogorov length scale. For this reason the Kolmogorov time scale is chosen here as the characteristic time of the fluid. This choice is very common in DNS. Since this time scale is not constant in time for our FHIT, the characteristic time of the gas is taken to be the average of the Kolmogorov time scale for $t > 10$ for simplicity. It is found to be equal to 1.2545 (see Figure 7.7).

The Kolmogorov time scale is calculated based on the kinematic viscosity ν and the mean dissipation rate $\langle \varepsilon \rangle$ as follows:

$$\tau_K = \sqrt{\frac{\nu}{\langle \varepsilon \rangle}}, \tag{7.12}$$

where the mean dissipation rate of the turbulent kinetic energy is given as a function of the kinematic viscosity and the strain rate tensor s_{ij}:

$$\langle \varepsilon \rangle = 2\nu \langle s_{ij} s_{ij} \rangle, \quad \text{where } s_{ij} = \frac{1}{2} \left(\frac{\partial u_{g_i}}{\partial x_j} + \frac{\partial u_{g_j}}{\partial x_i} \right). \tag{7.13}$$

Based on these definitions, the characteristic time scale chosen to calculate the Stokes number can be criticized as being a mean property of the fluid. In fact, within the domain, local times smaller than τ_k can be encountered, leading to higher "local" Stokes numbers. To illustrate this possibility, the distribution of the ratio of the local dissipation rate to two times the kinematic viscosity is

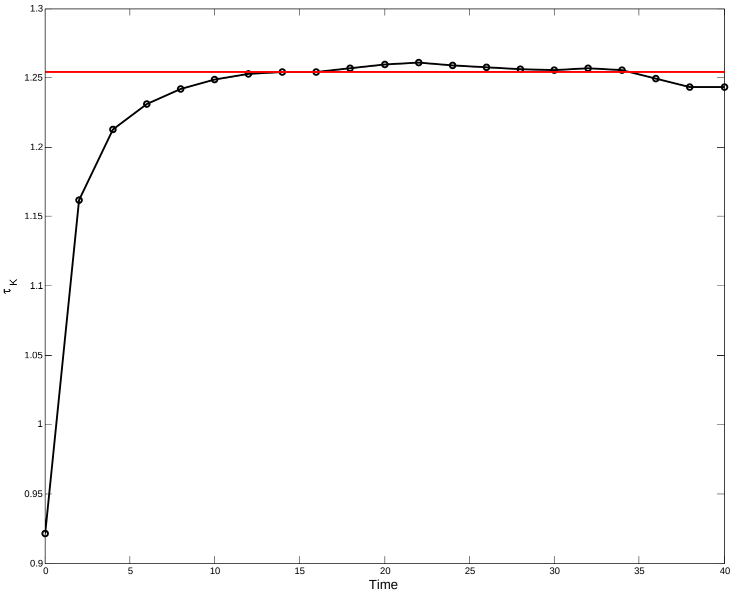

Figure 7.7: *Evolution of Kolmogorov time scale of the forced HIT with time (black) and chosen characteristic time scale for the gas (red)*

plotted in Figure 7.8.

In addition to this Stokes number based on the Kolmogorov scale St_K, another Stokes number relative to the integral scales St_E is also used when plotting the different quantitative results as a function of the Stokes numbers at final time. This is done in order to compare the behavior of the evolution of the AG results as a function of the particles inertia to the Lagrangian ones. The milestones chosen for this comparison are the particles having a relaxation time equal to the Kolmogorov time scale on one hand $\mathrm{St}_K = 1$, and the particles of relaxation time equal to the integral time scale $\mathrm{St}_E = 1$ on the other hand.

In the following, without specific notations, the Stokes number denotes the one based on the Kolmogorov scale. Otherwise, it is clearly mentioned that the Stokes number based on the integral scale is used.

For the integral scales, the computation was based on the two-point velocity correlation R_{ij} which reads (*Pope 2000*):

$$R_{ij}(r) = \langle u_i(\vec{\boldsymbol{x}}) u_j(\vec{\boldsymbol{x}} + r\vec{\boldsymbol{e}}) \rangle, \text{where } \vec{\boldsymbol{e}} \text{ is a given unit vector.} \tag{7.14}$$

In general, the longitudinal integral length scale is given as the area under the curve of the longitudinal velocity autocorrelation function $f_{long}(r)$ (*Pope 2000*)

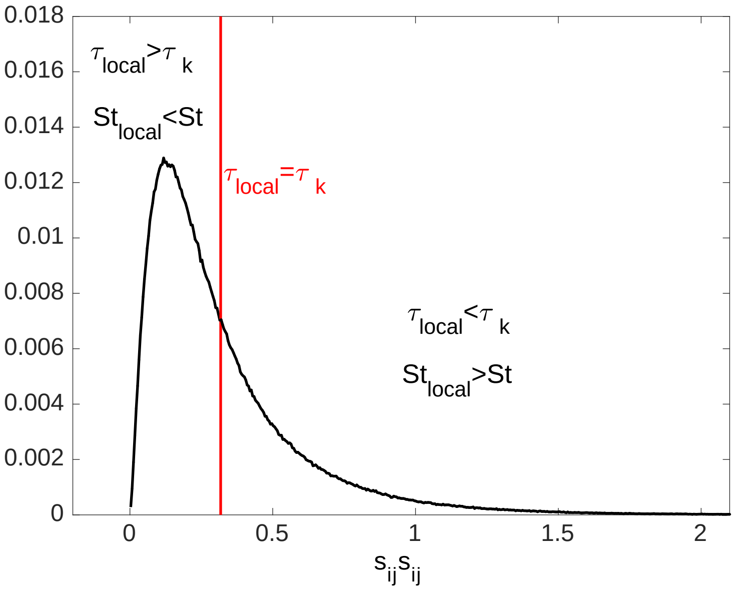

Figure 7.8: *The distribution function of $s_{ij}s_{ij}$ for the forced HIT at $t = 40$ in black and its mean value $\langle s_{ij}s_{ij}\rangle$ in red.*

(equation (7.15))

$$L_{11} = \int f_{long}(r)\mathrm{d}r, \tag{7.15}$$

where $f_{long}(r) = \dfrac{R_{ii}}{3U_{rms}^2}$.
Based on these formulae, we get at $t = 40$ the longitudinal integral length scale $L_{11} = 0.65217$, the Eulerian integral time scale $\tau_E = 9.7864$ and the Reynolds number $\mathrm{Re}_L = 43.46$.
In order to be able to compare the results presented in this part to other results in the litterature with different forcing methods, it is essential to calculate the Lagrangian integral time scale, τ_L ,based on the temporal velocity correlation function. Based on the velocity field in question the Lagrangian integral times scale is $\tau_L = 4.7905$.
Thus, in addition to the reference to the particles of relaxation time equal to the Kolmogorov time scale on one hand $\mathrm{St}_K = 1$, and to the particles of relaxation time equal to the Eulerian integral time scale $\mathrm{St}_E = 1$, one can also add a reference to the particles of relaxation time equal to the Lagrangian integral time scale $\mathrm{St}_L = 1$ whenever needed.
The turbulence properties of the FHIT is summarized in Table 7.1. Finally, this DNS is carried out with $\kappa_{max}\eta = 2.8428$ that provides sufficiently small grid spacing for the resolution of the smallest dissipative motions (*Pope 2000*).

Table 7.1: *Turbulence properties of the HIT*

$\langle\text{TKE}\rangle$	τ_K	η	τ_L	τ_E	L_{11}	Re_L
0.00667	1.2545	0.03535	4.7905	9.7864	0.65217	43.46

7.4 Codes

The ASPHODELE solver couples a Eulerian description of the gas phase with a Lagrangian description of the spray. It is based on high order finite differences schemes.

Since the gas phase and the Lagrangian approach for the disperse phase are not the subject of this theses, the details of this code as well as the equations solved and the numerical scheme used for the gas carrier and Lagrangian approach are not presented here. For more information, on this subject one may refer to the work of *Reveillon and Demoulin (2007); Péra (2005); Meftah (2008); Bouali (2011); Thomine (2011).*

The disperse phase simulations were done using the MUlti-fluid Solver for Eulerian Spray, MUSES3D. This latter was developed at EM2C during the thesis of *de Chaisemartin (2009)* as a solver for multi-fluid spray computations with a parallel optimization based on the domain decomposition for High Performance Computing. This code is written in Fortran90/95 language and it uses finite volume methods to solves the Multi-Fluid equations. This implemented MF model was based on the MK assumption. For more details about MUSES3D, one may refer to the thesis of *de Chaisemartin (2009)*.

These two codes are coupled, as shown in Figure 7.9, to allow the comparison between the Lagrangian and Eulerian simulations of the disperse phase. The structure of these codes was recently optimized by J.C. Brändle de Motta and

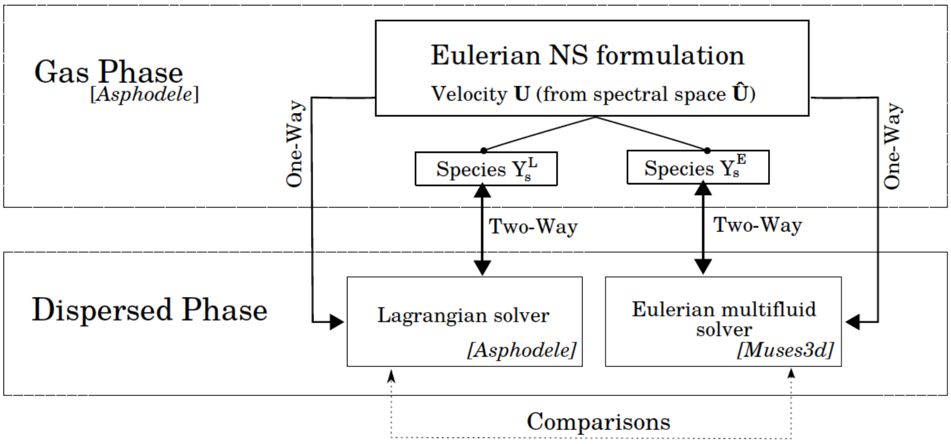

Figure 7.9: *Sketch of the coupling between ASPHODELE and MUSES3D codes. (Source Fréret et al. (2010))*

O. Thomine.
During this thesis, the AG model has been implemented in this optimized version of MUSES3D in order to evaluate the AG model on the 3D configuration in question.

7.5 Lagrangian results

For the Lagrangian simulations, the particles are initially distributed uniformly in the 128^3 mesh. These particles are initially at rest.

7.5.1 Projection

In order to compared the Eulerian results to the Lagrangian reference, the projection of the Lagrangian results on the Eulerian grid N_{eul}^3 is necessary. By doing so, the Lagrangian variables of N_p particles are transformed into Eulerian moments on the N_{eul}^3 grid elements. Whenever a Lagrangian particle p having a velocity $\vec{\boldsymbol{c}}_p(c_{p,x}, c_{p,y}, c_{p,z})$ is found in the grid element (x, y, z), the moment of order $i+j+k$ is augmented by the corresponding moment of the particle as shown in equation (7.16).

$$M_{i,j,k}(x,y,z) = \frac{N_{eul}^3}{N_p} \sum_{p=1}^{N_p} c_{p,x}^i c_{p,y}^j c_{p,z}^k \mathcal{H}(x-x_p, y-y_p, z-z_p), \tag{7.16}$$

where $\mathcal{H}(x-x_p, y-y_p, z-z_p)$ is a cubic top hat function centered at (x_p, y_p, z_p) and of characteristic width the Eulerian grid size $\Delta\vec{\boldsymbol{x}}$.
This projection is performed on the 128^3 Eulerian mesh to have the fields at the same level of refinement as the gas field which is simulated on a 128^3 mesh. This projection is also essential to qualitatively compare the Lagrangian results to the Eulerian results simulated on this same mesh.

7.5.2 Statistical convergence of the Lagrangian results

The Lagrangian results can be set as a reference as long as enough particles are used to achieve statistical convergence. In order to evaluate this statistical convergence, Lagrangian simulations were carried out for an increasing number of particles. The statistical results are presented and analyzed hereafter for three different total number of particles, nearly equal to twenty million, one hundred million and two hundred million particles. The comparison is based on two statistical quantities namely the segregation and the mean internal energy. The segregation, G_{pp}^{Δ}, represents the spatial correlation of the number density field at a given length scale (*Simonin et al. 2006*):

$$G_{pp}^{\Delta} = \frac{\langle n^2 \rangle}{\langle n \rangle^2}, \tag{7.17}$$

where $\langle . \rangle$ is the averaging operator over the whole domain. It is a measure of the degree of preferential accumulation and depletion. This quantity is of paramount importance in the domain of combustion since it could strongly affect the evolution of the mean vapor mixture fraction (*Reveillon and Demoulin 2007*).

The mean internal energy or mean central energy (MCE) is given by:

$$\mathrm{MCE} = \frac{\langle n(\sigma_{ii})^2 \rangle}{N_d \langle n \rangle}. \tag{7.18}$$

It is essential to study the evolution of the mean internal energy since it is through the velocity variance or the internal agitation energy that the AG model is capable of reproducing statistically the PTC. Since at each crossing an amount of the total kinetic energy is transformed into internal energy, the MCE is an evaluation of the occurrence of PTC.

These statistics are measured at the scale of the original mesh for the gas which means that a projection of the Lagrangian results on the 128^3 grid is done before computing these values.

For the small Stokes number $\mathrm{St} = 0.5$, the segregation does not change drastically when using 20 or 100 million particles, only a small shift is noticed as illustrated in Figure 7.10. When it comes to the mean internal energy, it is already supposed to be infinitesimal since the probability to have PTC is less than 1% based on the distribution of the ratio of the local dissipation rate to two times the kinematic viscosity of the carrier phase shown in Figure 7.8. The Lagrangian results with 20 million particles lead to a lower level of MCE compared to the other two simulations. From these measures, one can conclude that the statistical convergence for $\mathrm{St} = 0.5$ is obtained for 100 million particles. However, it can be argued, based on the minimal effect of the increase of the total number of particles, that one could only use 20 million particles and still obtain results that are accurate enough at lower computational cost. Thus, it is important to check whether the same behavior is obtained for moderately inertial and inertial particles too.

Figure 7.11 shows the statistical convergence for $\mathrm{St} = 3$. In this case, the simulation with the smallest number of particles in not statistically converges and the results cannot be used as a reference. However, when using 100 million particles, the evolution of the segregation in time is very similar to the case of 200 million particles. The same trend is observed with the MCE. As a consequence, one need to simulate 100 million particles in order to reach the convergence of the statistics.

The same conclusion can be drawn for a more inertial case, namely for $\mathrm{St} = 8$, as depicted in Figure 7.12. For this reason, all the Lagrangian results that are presented in this part are carried out with a total number of particles nearly equals to 100 million, in order to be able to consider the Lagrangian result as a physical reference for the comparison with the Eulerian models.

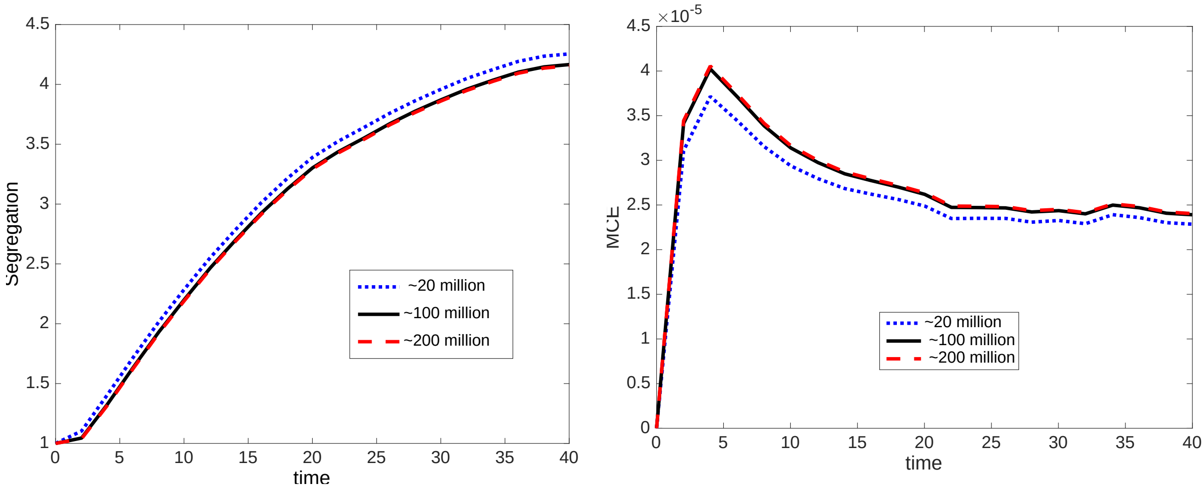

(a) Segregation

(b) Mean internal energy

Figure 7.10: *Statistical convergence of the Lagrangian results for* St $= 0.5$ *on the* 128^3 *mesh*

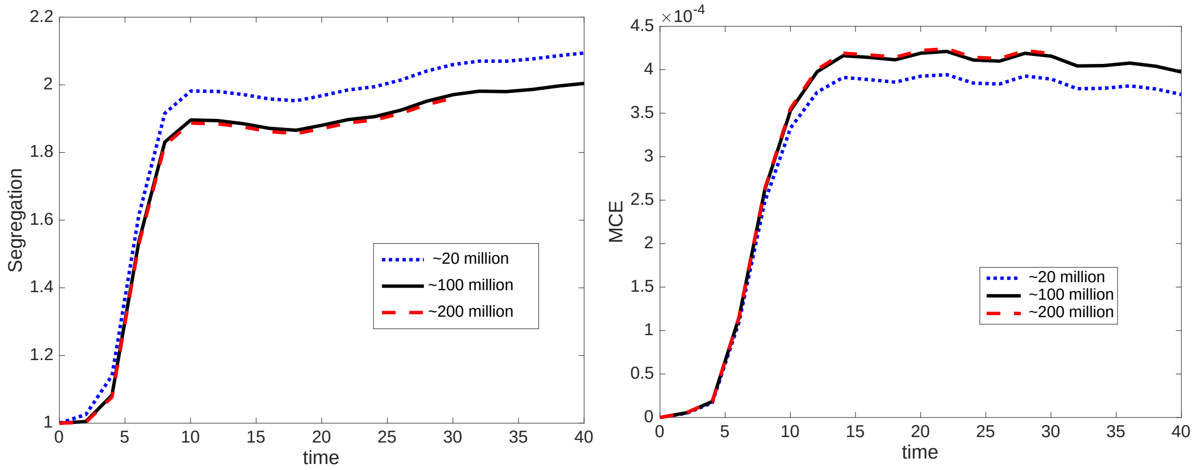

(a) Segregation

(b) Mean internal energy

Figure 7.11: *Statistical convergence of the Lagrangian results for* St $= 3$ *on the* 128^3 *mesh*

7.5.3 Qualitative results

The qualitative evaluation presented in this section is done for three different Stokes numbers: St $= 0.5$, 3 and 8.

For small Stokes numbers, the particles are gathered in low vorticity zones. In this case the occurrence of PTC is not significant and both Eulerian models are

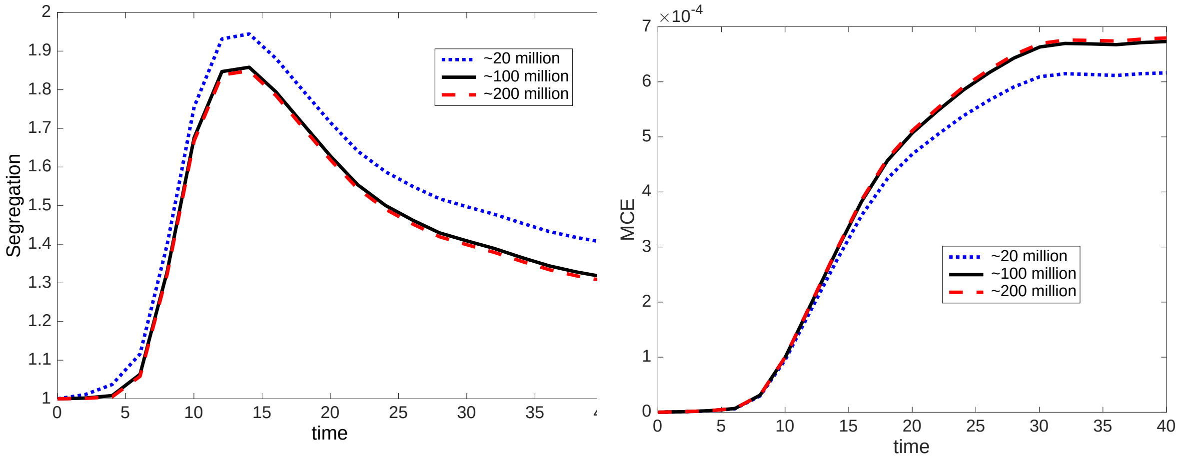

(a) Segregation (b) Mean internal energy

Figure 7.12: *Statistical convergence of the Lagrangian results for* St = 8 *on the* 128^3 *mesh*

expected to capture the structure of the number density field.

For St = 3, the vacuum zones become smaller and the particles are clustered into wider structures. This behavior should be captured by the AG models, whereas the MK is expected to overestimate the preferential concentrations at the PTC locations.

When it comes to the inertial case where St = 8, the structures found in the number density field are larger than in the other two cases but have lower number density. For this particle size, the dimension of the vacuum zones is tremendously decreased in comparison with the case of St = 1 (see figure 7.13). The velocity fields of the disperse phase for the three Stokes number in question are shown in Figure 7.14. The disperse phase velocity in the first case is very similar to the gas one, except in the vacuum regions where the velocity of the disperse phase is zero.

For the moderately inertial and inertial cases, the kinetic energy received from the gas is transformed in the disperse phase into internal energy created during the PTC. Thus, the velocity of the disperse phase for St = 3 and St = 8 is lower than that of the gas. Actually, this phenomena of energy transformation increases with the increase of the Stokes number and implies the decrease of the disperse phase velocity.

This energy conversion is also seen in Figure 7.15, where the velocity dispersion is very significant for St = 8 in comparison with the St = 0.5 case. In the latter cases, no significant PTC takes place. The generated internal energy is very low and only found in very thin regions as seen in Figure 7.15 for $St = 0.5$. This behavior is expected since the probability to have PTC is less than 1% based on the analysis presented in subsection 7.3.2. Nonetheless, in the range

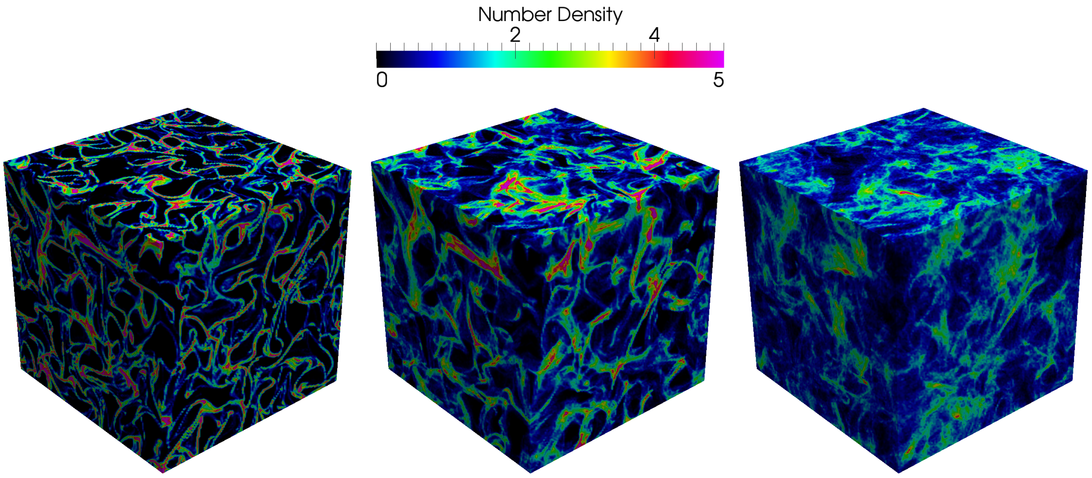

(a) $St = 0.5$ (b) $St = 3$ (c) $St = 8$

Figure 7.13: *Lagrangian number density field at* $t = 40$ *projected on a* 128^3 *mesh*

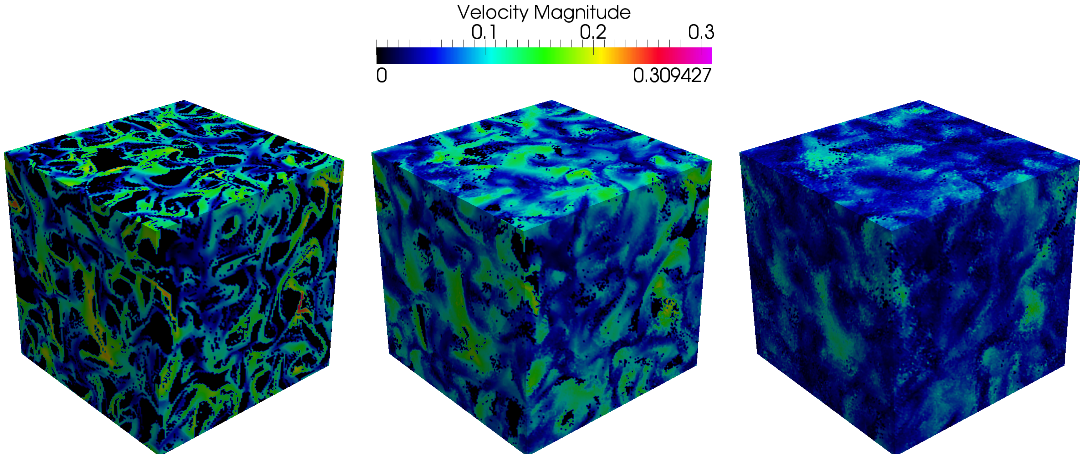

(a) $St = 0.5$ (b) $St = 3$ (c) $St = 8$

Figure 7.14: *Lagrangian velocity field at* $t = 40$ *projected on a* 128^3 *mesh*

of low Stokes number (St < 1), the probability of occurrence of these local PTC increases with St but does not highly affect the structure of the number density field.

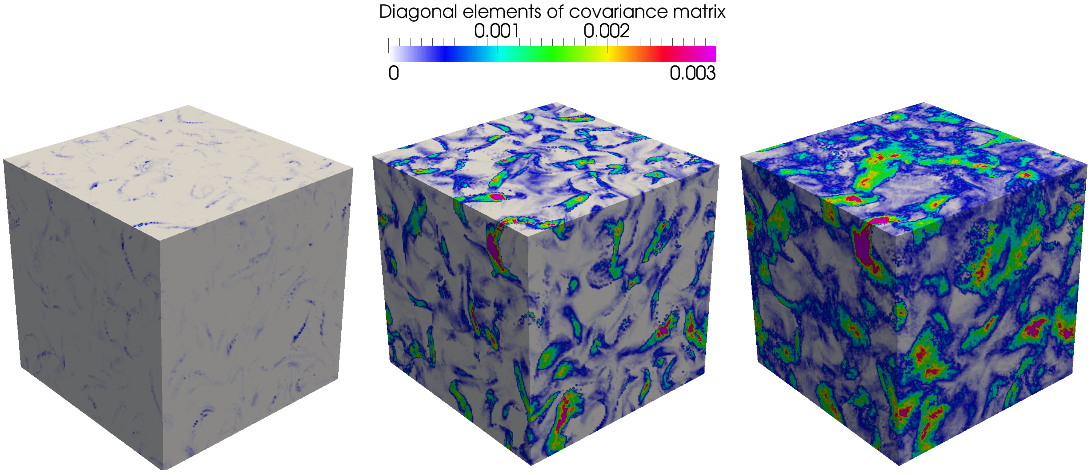

(a) $St = 0.5$ (b) $St = 3$ (c) $St = 8$

Figure 7.15: *Lagrangian Velocity dispersion field* σ_{11} *at* $t = 40$ *projected on a* 128^3 *mesh*

7.5.4 Evaluation of the third order moment

Now that the test case is well defined along with the reference solution, only one step is still essential before heading to the comparison between the AG results, MK results and the Lagrangian reference results. This last step checks to what extent the assumption of writing the third order moment as the third order moment of a Gaussian distribution as shown in equation (7.19) is valid. To do so, the third order moment computed from equation (7.19) is compared to the original one obtained directly from the Lagrangian result projected on the 128^3 Eulerian grid, as explained in subsection 7.5.1. This is done for the highest Stokes number in the studied range St =15.

$$M_{i,j,k} = ((n\mathbf{E} + \mathbf{P}) \vee \vec{\mathbf{u}}), \qquad \text{where } i + j + k = 3. \tag{7.19}$$

The distribution function of the Frobenius norm of the third order moment is also compared for the two ways of computation. As one can notice from Figure 7.16 the two results are nearly the same. The only two differences are the maximum value of the norm of the third order moment, which is higher when calculating this moment using equation (7.19), and the quantity close to the zero norm, which is also higher when the third order moment is calculated based on the Gaussian distribution. Since the differences between the two methods for computing the third order moment are small, one can conclude that the assumption of writing the third order moment by equation (7.19) is valid.

It is important to note that the current a posteriori tests should be extented to take into account the kurtosis, the skewness as well as the derivatives of the

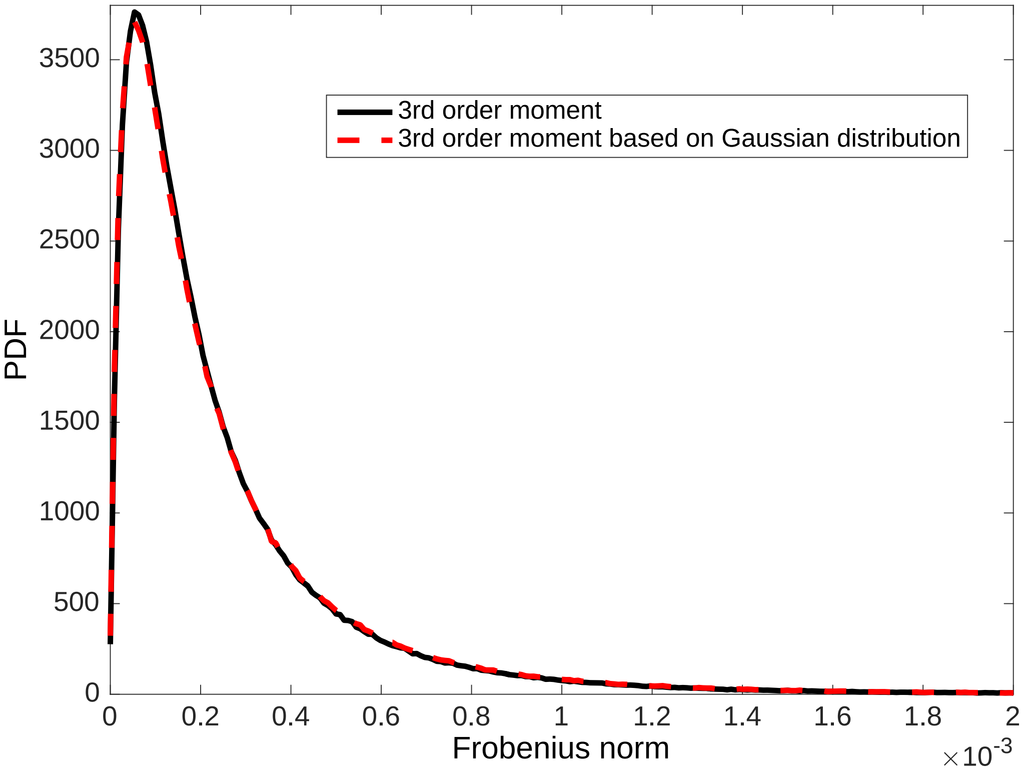

Figure 7.16: *Distribution function of the norm of third order moment and the one calculated based on the Gaussian distribution*

thrid order centered correlation to check whether the assumption of writing the third order moment based on Gaussian distribution is acceptable in the case of inhomogeneous flows such as turbulent channel flows (*Vance et al. 2006*).

Chapter 8

Qualitative visual results and quantitative mean statistics

In this chapter, the first part of the evaluation of the Anisotropic Gaussian model on a 3D Forced Homogeneous Isotropic Turbulence is presented. The AG results are compared to the Lagrangian ones and Eulerian results based on the Mono-Kinetic closure. This comparison is carried out for a range of Stokes numbers going from particles of very small inertia ($\mathrm{St} \sim 0.1$*) to high inertia (*$\mathrm{St} \sim 15$*). In this chapter three levels of evaluation are presented. First, qualitative visual results such as the number density field, the velocity magnitude and the elements of the covariant matrix are presented for four Stokes numbers:* $\mathrm{St} = 0.5, 1, 3$ *and* 8*. Second, the one-point correlation of the velocity is presented through scatter plots. These results show whether the disperse phase motion is highly correlated to the carrier phase velocity or not. Third, the quantitative mean statistical results are assessed, namely the segregation, the mean total energy and the mean central energy. The evolution of these results as a function of time for different Stokes numbers is presented, to check whether the AG model captures the change of the temporal evolution of the statistics with particles inertia. Finally, the statistical results at final time are plotted as a function of the Stokes number, for the different models and grids. These comparisons represent an important step showing the advantages of the AG model versus the MK one and a first step in defining the domain of validity of the AG model.*

8.1 Qualitative results

The qualitative evaluation presented in this section is based on the four different Stokes numbers: $\mathrm{St} = \{0.5, 1, 3, 8\}$. This choice is made to cover the various regimes that can be encountered in industrial applications:

- small particles that are characterized by a highly correlated motion to the carrier phase,
- particles at critical Stokes number leading to high concentrations and vacuum zones,
- moderately inertial particles where the two phenomena of high concentration and of particles trajectory crossing coexist,
- inertial particles where the occurrence of PTC governs the underlying dynamics.

Unless mentioned otherwise, the Eulerian simulations are done using the same level of mesh refinement as the gas, namely the 128^3 mesh. In fact, the native mesh of the gas carrier simulation is always kept unchanged and the Lagrangian results are projected on this Eulerian grid as mentioned in the previous chapter. When it comes to the Eulerian results, this mesh can be refined in order to decrease the numerical diffusion and to be able to evaluate the AG model based on more accurate results.

8.1.1 Small Stokes number: St $= 0.5$

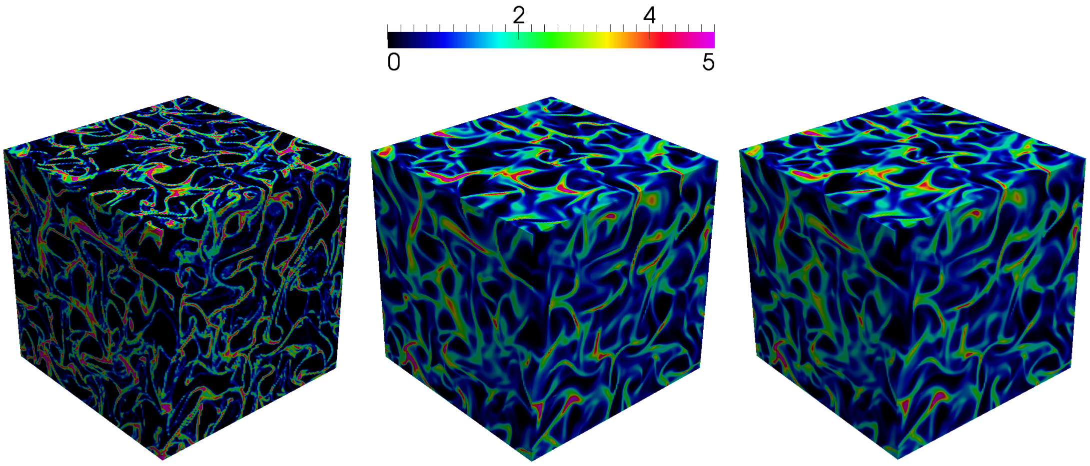

(a) Lagrangian (b) Mono-Kinetic (c) Anisotropic Gaussian

Figure 8.1: *Number density field at* $t = 40$ *on the* 128^3 *mesh for* St $= 0.5$

For small Stokes numbers, the particles are gathered in low vorticity and high strain zones driven by the hypercompressibility[1] effect (*Maxey 1987; Squires and Eaton 1991b*). In this case the occurrence of PTC is not significant, thus

---

[1] Since the local concentration of particles is modeled as a "fluid", the segregation can be interpreted as a hypercompressibility feature of this "fluid", this is when the concentration field becomes strongly non-uniform and faces rapid changes from vacuum to accumulation zones. For small St, the carrier phase dominates the behavior of the disperse phase through the drag force, so the gas velocity drives the compression of the particle phase into high strain/low vorticity zones.

the only energy of the disperse phase is the kinetic energy created by the particles advection. Therefore, both Eulerian models are capable of reproducing the real dynamics and capture the structure of the number density field including the zones of preferential accumulations and the vacuum zones (Figure 8.1). The difference between the Lagrangian and Eulerian results in this case is mainly due to numerical diffusion. In fact, the maximum value of the number density for the Lagrangian result is 70.28 compared to 24.97 for the MK and 21.75 for AG.

When comparing qualitatively the velocity fields in Figure 8.2, the structures as well as the maximum values are in a very good agreement, except for vacuum regions. Actually, for the Lagrangian simulation the velocity is intuitively set to zero in the vacuum regions. However for Eulerian cases, the velocity is defined everywhere since in the corresponding regions the number density might be very small but still simulated. In this case a velocity is associated to this small number density. Therefore, zero velocity magnitude is reached with Lagrangian simulations, but it is not the case for the MK and AG results. This difference decreases with mesh refinement.

In order to make sure that this difference is only found in the regions of vacuum or very low number density, the momentum magnitude is evaluated. The momentum is underestimated by both Eulerian simulations. This is due to numerical diffusion as mentioned before with the number density results. However, the Eulerian models reproduce well the zones of zero momentum depicted in white in Figure 8.3. This confirms the explanation of the difference between the minimum values of the velocity of the Lagrangian and Eulerian simulations. Numerically, this difference does not prevent from capturing the

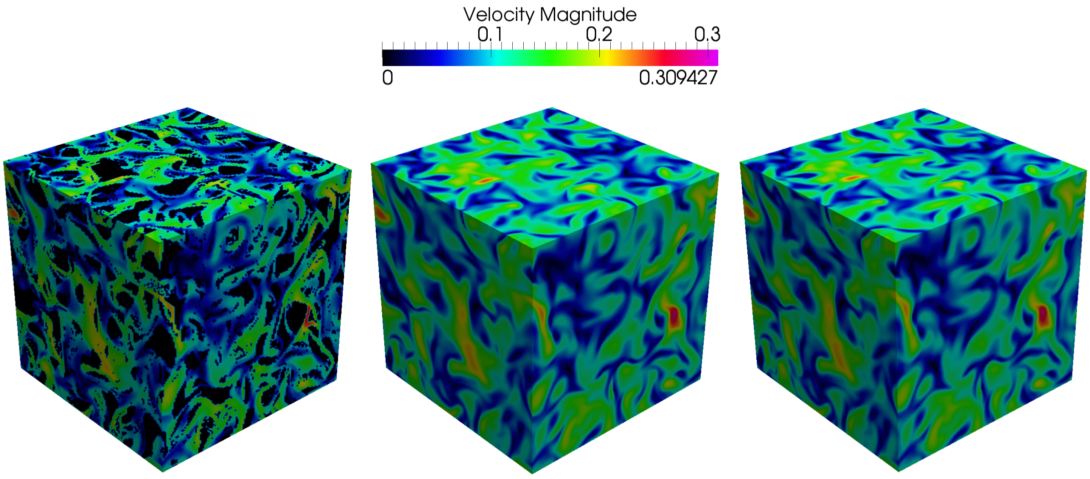

(a) Lagrangian (b) Mono-Kinetic (c) Anisotropic Gaussian

Figure 8.2: *Velocity magnitude field at* $t = 40$ *on the* 128^3 *mesh for* $\mathrm{St} = 0.5$

correct dynamics, since the solved equations are based on the conservative variables.

In the St = 0.5 case, no considerable PTC is taking place since the disperse phase relaxation time is smaller than the Kolmogorov time scale of the gas. In fact, based on the distribution of the local dissipation rate (Figure 7.8) only 0.04% of the carrier turbulent field has local Kolmogorov time scale smaller than or equal to the relaxation time of the particles. Thus, the velocity dispersion represented by its covariance matrix should be negligible if not zero. It is indeed the case as one can notice in Figure 8.4, for both the Lagrangian and AG results. Nevertheless, we observe that the AG model overestimates the velocity dispersion in comparison with the Lagrangian results. To avoid redundancy, the other elements of the covariance matrix are not presented for this particular Stokes number.

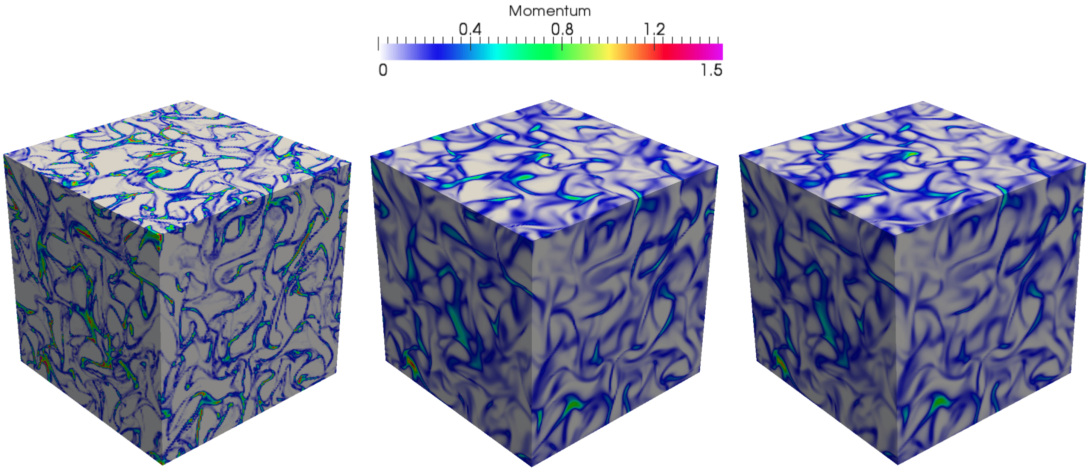

(a) Lagrangian (b) Mono-Kinetic (c) Anisotropic Gaussian

Figure 8.3: *Momentum magnitude at* $t = 40$ *on the* 128^3 *mesh for* $\mathrm{St} = 0.5$

The behavior of the disperse phase for this Stokes number is expected and already seen in the literature (*Maxey 1987; Squires and Eaton 1991b*). The particles do not have enough inertia to create their own path but follow the carrier phase instead.

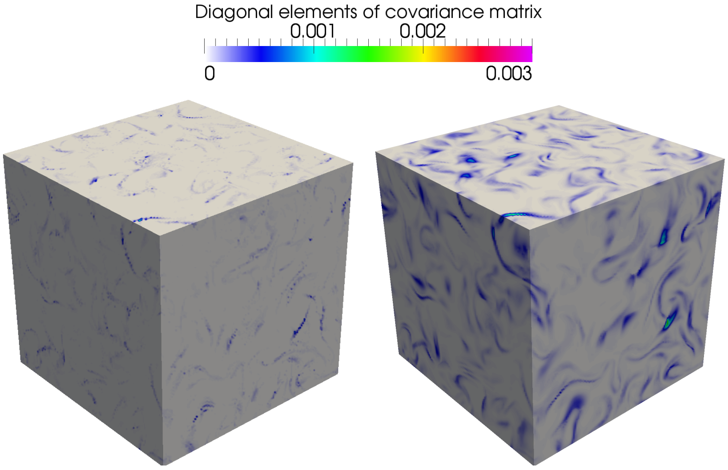

(a) Lagrangian σ_{11} (b) Anisotropic Gaussian σ_{11}

Figure 8.4: *Velocity dispersion fields* σ_{11} *at* $t = 40$ *on the* 128^3 *mesh for* $\mathrm{St} = 0.5$

8.1.1.1 Mesh refinement for the Eulerian results for $\mathrm{St} = 0.5$

In order to evaluate the Eulerian results while decreasing the numerical diffusion, the results for the MK are presented on the 64^3, 128^3, 256^3 and 512^3 meshes. This is done to decouple as much as possible the modeling effects from the numerical effects. The study is only shown for the MK results since for this Stokes number the results for both Eulerian models are nearly the same. This comparison is performed on the 2-D diagonal slice shown in Figures 8.5. From Figures 8.6(a), we observe that the number density field using MK tends to the Lagrangian number density. The result on the 512^3 grid captures globally the right structures, the correct vacuum zones and even the thin high concentration filaments.

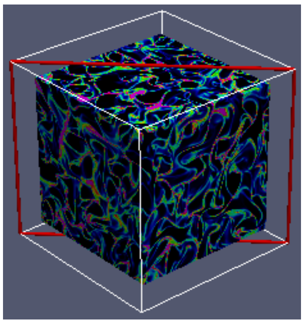

Figure 8.5: *The diagonal slice plan shown in red*

For the velocity, the results are not highly affected by the mesh refinement, as shown in Figure 8.6(b). For the coarsest mesh the right motion is already captured, except near the vacuum regions.

In order to check the differences found in the regions of vacuum or very low number density, the Eulerian velocity is set to zero in the regions of small number density, as shown in Figure 8.6(c). For a minimal value adapted to the diffusion of the numerical scheme, the first choice was selected to be equal to the grid size Δx. We observe that when decreasing the numerical errors,

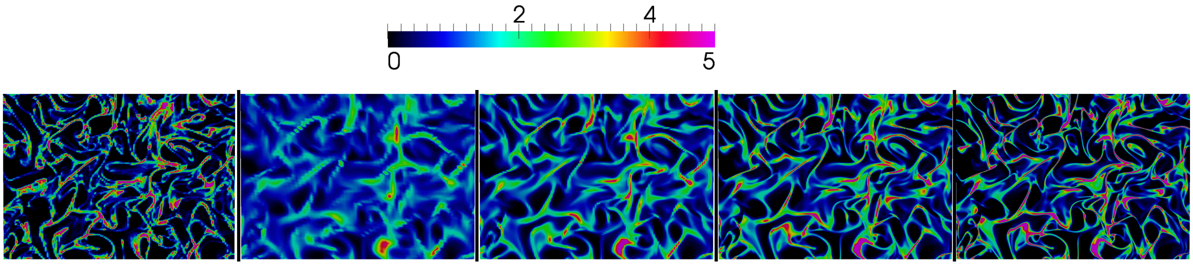

(a) Number density

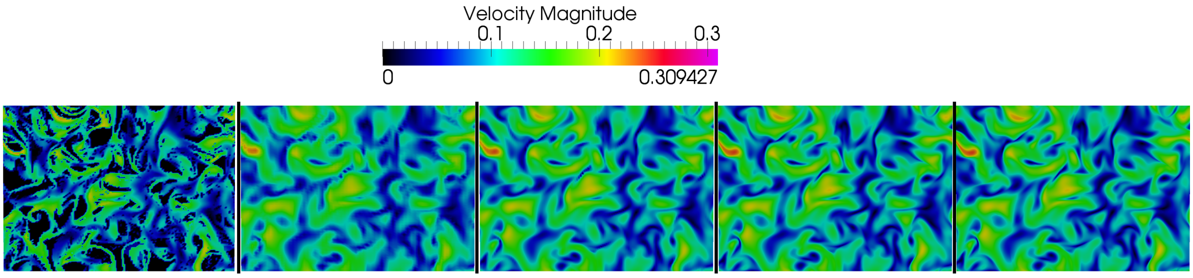

(b) Velocity

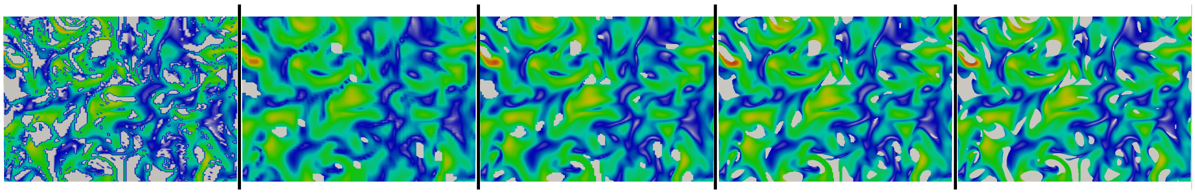

(c) Velocity fields where the velocity is set to 0 when $n < \Delta x$

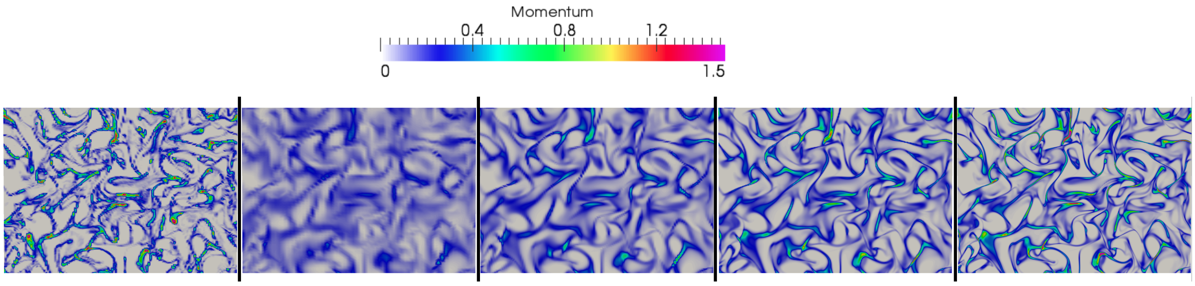

(d) Momentum

Figure 8.6: *From left to right: Lagrangian, MK on* 64^3, 128^3, 256^3 *and* 512^3 *meshes at* $t = 40$ *for* $\mathrm{St} = 0.5$

the vacuum zones match the Lagrangian ones. This behavior can also be depicted by the qualitative convergence of the momentum field of MK toward the Lagrangian one when refining the mesh (see Figure 8.6(d)).
Finally, a two-dimensional zoom in is shown for a small structure of the number density field containing a high concentration spot along with vacuum zones. The size of this zoom represents nearly 6% on the full box size as shown in Figure 8.7. The meshes are also shown for the different results in Figure 8.8. The MK result on the 64^3 mesh has dissipated the structure in a way that the preferential concentrations and vacuum spots are not reproduced. When refining the mesh, the structure begins to be clearer until reaching a well-defined shape similar to the Lagrangian one. This refined case captures the vacuum and the accumulation zones. One must however keep in mind the fact that this mesh is more refined that the native mesh (128^3) used for the carrier phase simulation.

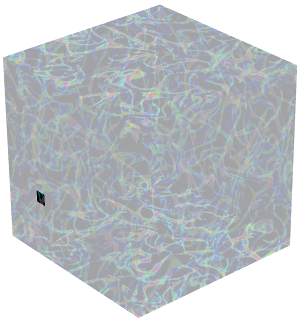

Figure 8.7: *Two dimensional zoom in for a structure of* 8x8x8 *hexahedrons within the native* 128^3 *grid.*

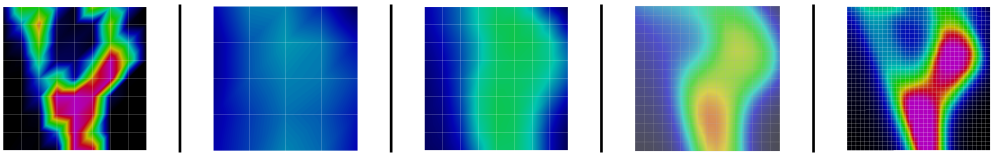

Figure 8.8: *Number density for the two-dimensional zoom in, from left to right: Lagrangian, MK on* 64^3, 128^3, 256^3 *and* 512^3 *meshes at* $t = 40$ *for* $\mathrm{St} = 0.5$

8.1.2 Critical Stokes number: $\mathrm{St} = 1$

For $\mathrm{St} = 1$, the physics to be captured is more challenging from the numerical point of view, since it has to deal with very high concentration in thin structures close to large depletion zones. In fact, the more we approach the critical Stokes number, the greater is the probability to have hypercompressibility zones and δ-shocks. The MK model deals naturally with these challenges, especially when solved with adapted numerical schemes similar to the Finite Volume Kinetic Scheme or the new RKDG class presented in part II. Such numerical schemes are able to capture δ-shocks and high gradients, with a minimum level of numerical diffusion.

When it comes to the number density (Figure 8.9), the Lagrangian results is providing finer structures and higher preferential concentration than the Eulerian results. Nevertheless, the global structure of the number density is captured by both the MK and AG models. Some structures in the MK results match more precisely the Lagrangian one than the AG results and some others are better captured by the AG model. The maximal value of the number density obtained in the Lagrangian results is higher than the one resulting from the Eulerian results: 56.35 for the Lagrangian compared to 33.50 for the MK and 12.78 for AG. This difference is due to the numerical diffusion effect. In addition, the MK model creates δ-shocks and leads to higher accumulations than the AG.

Through the comparison of the velocity fields plotted in Figure 8.10, the same behavior as for $\mathrm{St} = 0.5$ is found: a very good agreement between the Lagrangian and Eulerian results, except for vacuum regions shown as black spots in the Lagrangian velocity field. The analysis of this latter observation is the same as the one done for the lower St.

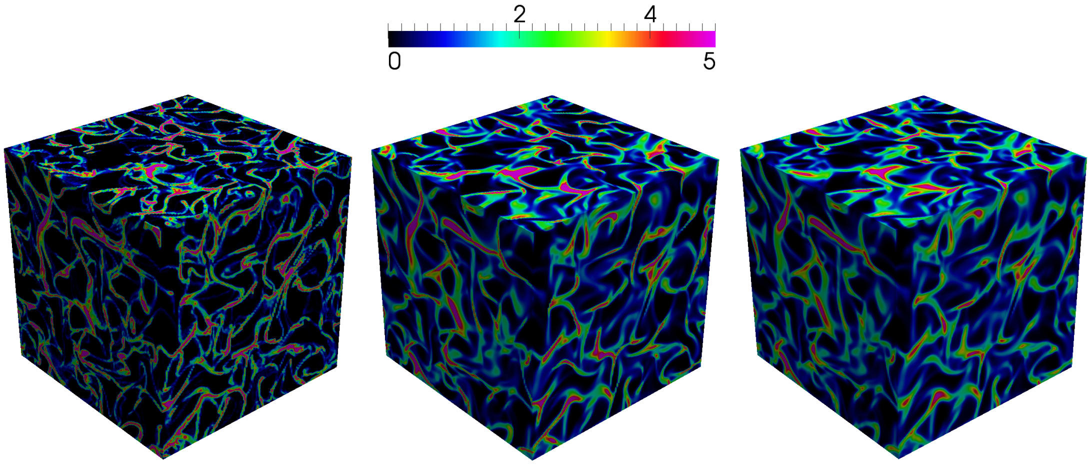

(a) Lagrangian (b) Mono-Kinetic (c) Anisotropic Gaussian

Figure 8.9: *Number density field at* $t = 40$ *on the* 128^3 *mesh for* $\mathrm{St} = 1$

The momentum magnitude depicted in Figure 8.11 shows that the difference of the velocity fields between the Lagrangian and Eulerian results are localized in the regions of very low number density or of vacuum. The Eulerian models underestimate the momentum. Nevertheless, the MK results have some structures of higher momentum than the AG ones and thus closer to the Lagrangian result.

From Figures 8.12, it is clear that for this Stokes number, the different ele-

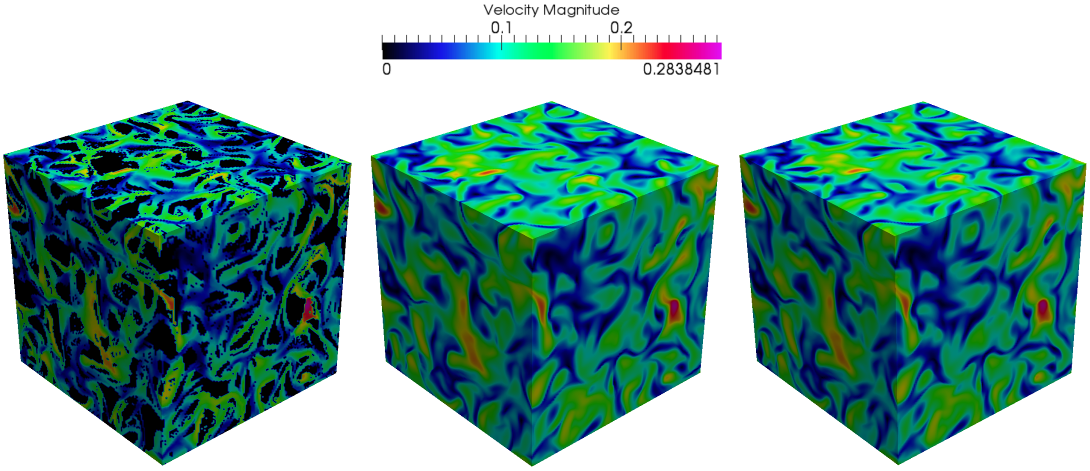

(a) Lagrangian (b) Mono-Kinetic (c) Anisotropic Gaussian

Figure 8.10: *Velocity magnitude field at* $t = 40$ *on the* 128^3 *mesh for* $\mathrm{St} = 1$

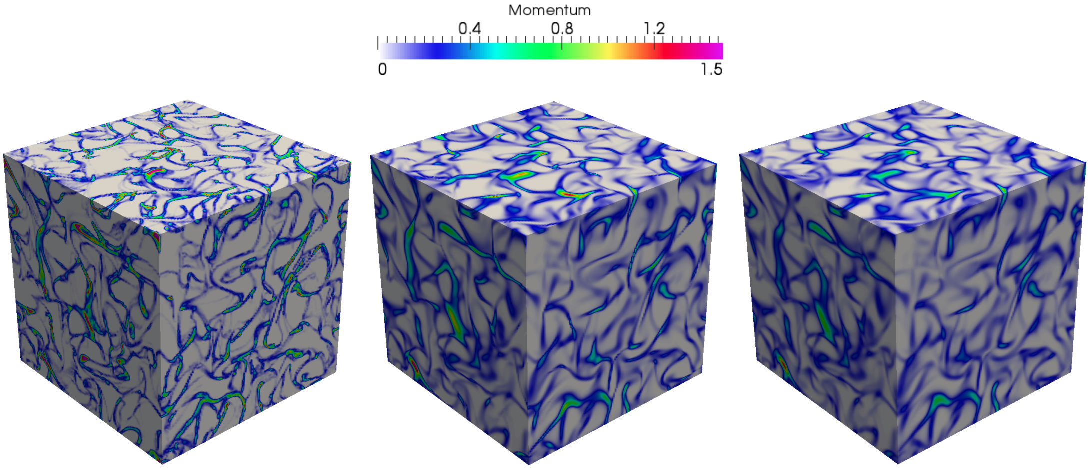

(a) Lagrangian (b) Mono-Kinetic (c) Anisotropic Gaussian

Figure 8.11: *Momentum magnitude at* $t = 40$ *on the* 128^3 *mesh for* $\mathrm{St} = 1$

ments of the covariance matrix have small values in most regions in the domain except where PTC begin to occur. In fact, the amount of local Kolmogorov time scales equal or smaller than the relaxation time of the particles is 11.22%. This percentage explains the occurrence of PTC in some regions of the domain. In this case the structures seem to be qualitatively the same for the Lagrangian and the AG solutions, with an overestimation by the AG model. At these PTC locations the MK model generates Dirac δ-shocks and an amount of the total kinetic energy is lost irreversibly whereas with the AG model when PTC occurs, an amount of the total kinetic energy is transformed into internal energy or energy of agitation.

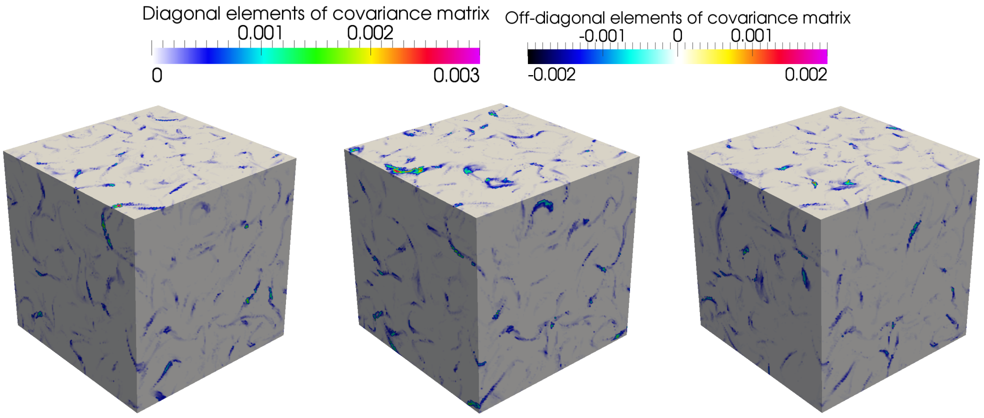

(a) Lagrangian σ_{11} (b) Lagrangian σ_{22} (c) Lagrangian σ_{33}

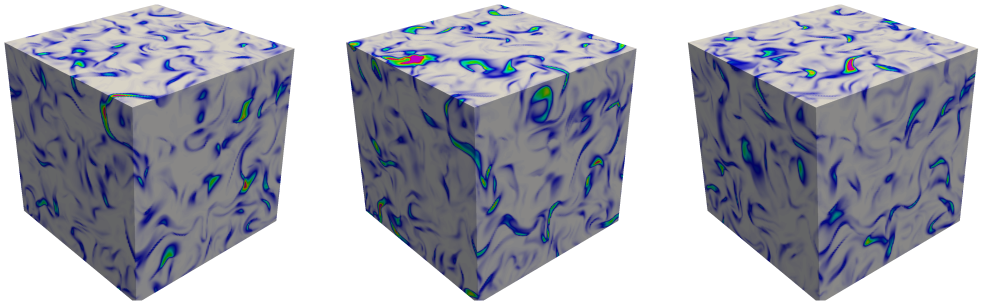

(d) AG σ_{11} (e) AG σ_{22} (f) AG σ_{33}

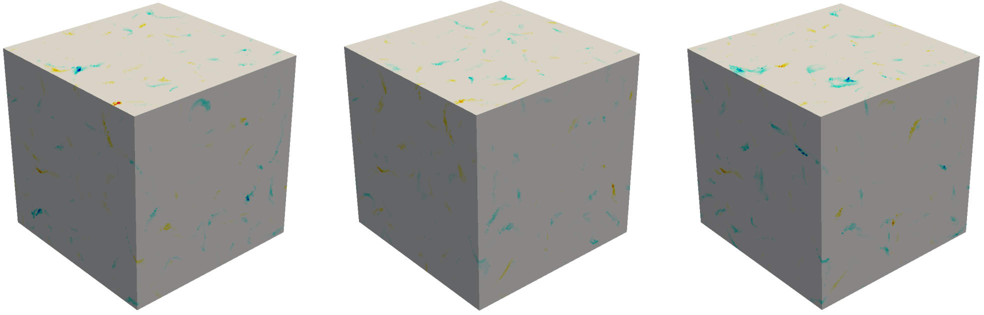

(g) Lagrangian σ_{12} (h) Lagrangian σ_{13} (i) Lagrangian σ_{23}

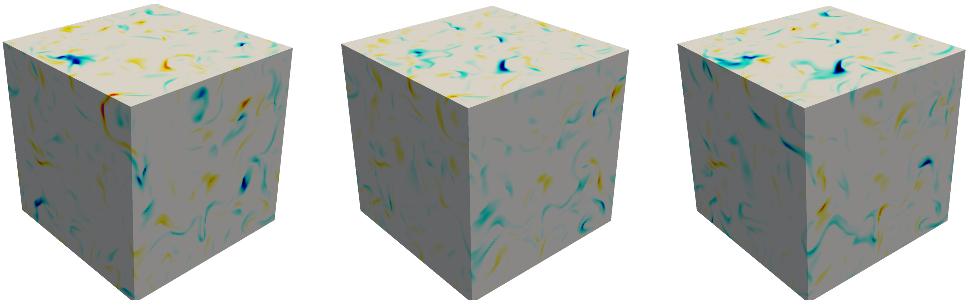

(j) AG σ_{12} (k) AG σ_{13} (l) AG σ_{23}

Figure 8.12: *Velocity dispersion fields at* $t = 40$ *on the* 128^3 *mesh for* $\mathrm{St} = 1$

In order to check whether the overestimation of the velocity dispersion by the AG model is localized in the vicinity of the vacuum regions, the pressure in the x-direction is shown in Figure 8.13. This possibility is refuted since the pressure is overestimated as well. This overestimation of the pressure accompanied with the underestimation of the number density surely means an amplified covariance. This overestimation is mainly due to the numerical dissipation that is included in the covariance terms. In future works, further evaluation of this numerical dissipation is needed to be able to extract the physical velocity dispersion created by the AG model along with the procedure of transforming the diffusion on the density into an increase in the internal energy by conservation of the total kinetic energy.

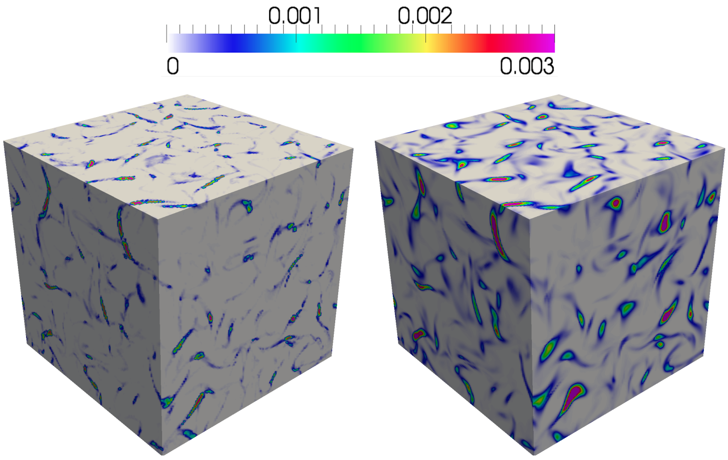

(a) Lagrangian (b) AG

Figure 8.13: *Pressure in the x direction, P_{11} at $t = 40$ for $\mathrm{St} = 1$ on the 128^3 mesh*

8.1.3 Moderate Stokes number: $\mathrm{St} = 3$

In this paragraph, the qualitative results are presented for a moderately inertial disperse phase having a Stokes number $\mathrm{St} = 3$. Based on the PDF of the local dissipation rate (Figure 7.8), 91.46% of the carrier field is characterized by a time scale smaller than the relaxation time of the moderately inertial particles. Thus, the underlying physics leads to significant PTC. In this case, the MK model is not expected to capture the right dynamics of the particle-laden flow. This is clearly seen through the number density fields plotted in Figure 8.14 where the preferential accumulations are highly overestimated using the MK model, compared to the Lagrangian and AG results. In addition, the structures are thinner with the MK model leading to vacuum zones larger than the Lagrangian ones. On the other hand, the AG model captures the global structures, their sizes and does not overestimate the accumulations. A maximum number density of 23.96 is reached with the Lagrangian, 58.82 with the MK and 7.06 with the AG. The difference between the maximal number density reached with the Lagrangian value and the AG is expected to decreases with mesh refinement, whereas the inverse trend is expected with the MK model. This analysis is the subject of the next section.

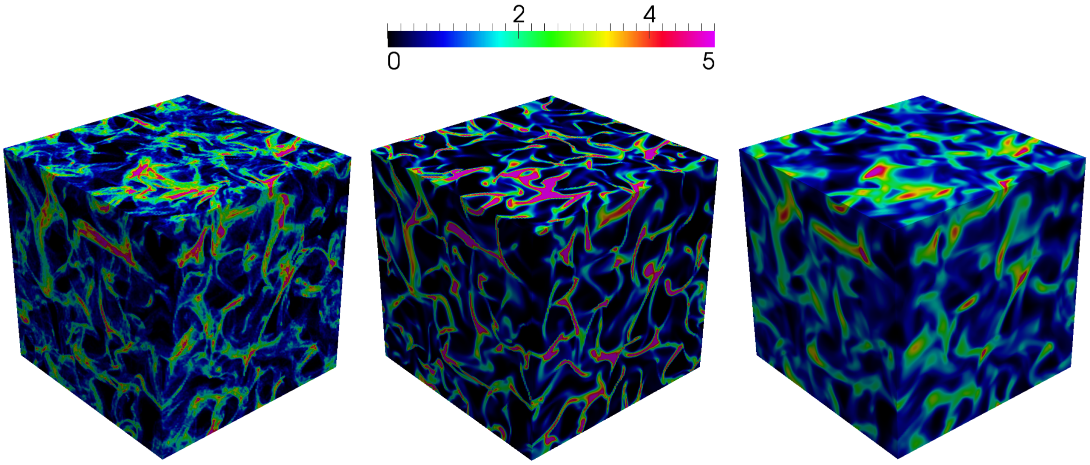

(a) Lagrangian (b) Mono-Kinetic (c) Anisotropic Gaussian

Figure 8.14: *Number density field at* $t = 40$ *on the* 128^3 *mesh for* $\mathrm{St} = 3$

From Figure 8.15, although globally both Eulerian results match the Lagrangian velocity, a slight overestimation of the velocity magnitude can be noticed in the MK result at some points. This overestimation is due to the fact that the disperse phase modeled by MK has a greater tendency to follow the gas. In addition Dirac δ-shocks are created at each PTC location with MK.

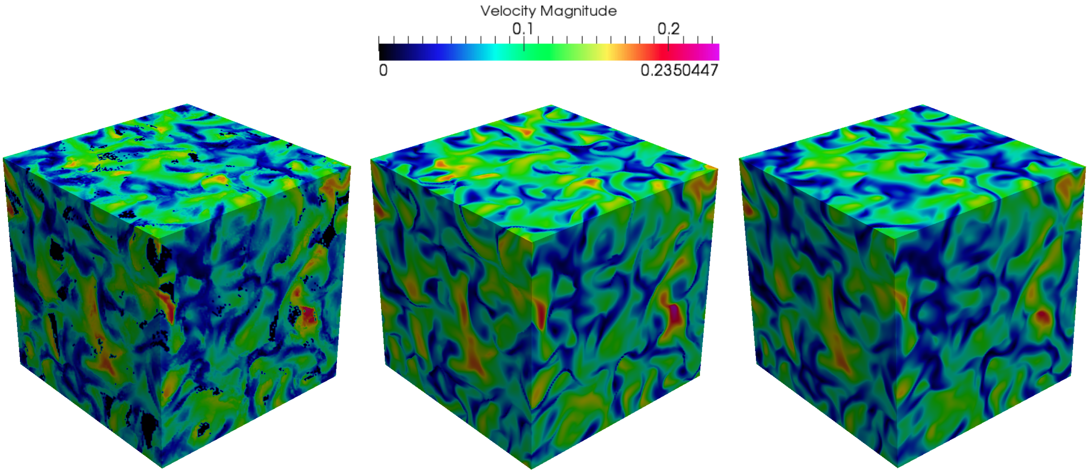

(a) Lagrangian (b) Mono-Kinetic (c) Anisotropic Gaussian

Figure 8.15: *Velocity magnitude field at* $t = 40$ *on the* 128^3 *mesh for* $\mathrm{St} = 3$

The diagonal elements of the covariance matrix are plotted in Figure 8.16 for the Lagrangian and AG results. This represents the one-dimensional velocity dispersions. The AG model in comparison with the Lagrangian captures the structure of the elements of this internal energy tensor. However, the AG model overestimates the value of the velocity dispersions in all the directions.
The off-diagonal elements can be seen in Figure 8.17, where once again the general structure is captured by the AG results but with an overestimation of the two-dimensional velocity dispersions. The effect of the mesh refinement is depicted later on for the case of high Stokes number.
For this moderate Stokes number the evaluation of the pressure in the x-direction (Figure 8.18) shows that the AG model does not overestimates the pressure. In fact the underestimation of the number density is the main reason for the overestimation of the velocity dispersion.

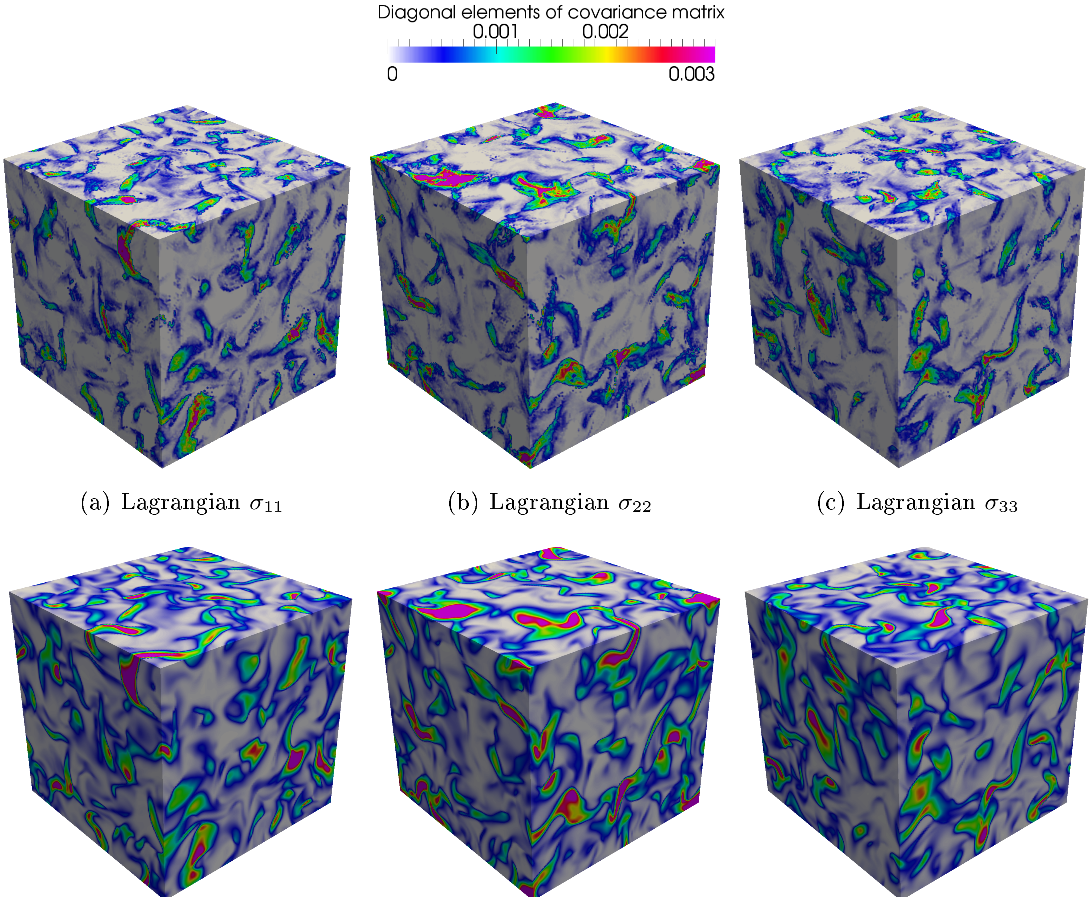

(a) Lagrangian σ_{11} (b) Lagrangian σ_{22} (c) Lagrangian σ_{33}

(d) Anisotropic Gaussian σ_{11} (e) Anisotropic Gaussian σ_{22} (f) Anisotropic Gaussian σ_{33}

Figure 8.16: *Velocity dispersion fields* σ_{ii} *at* $t = 40$ *on the* 128^3 *mesh for* $\mathrm{St} = 3$

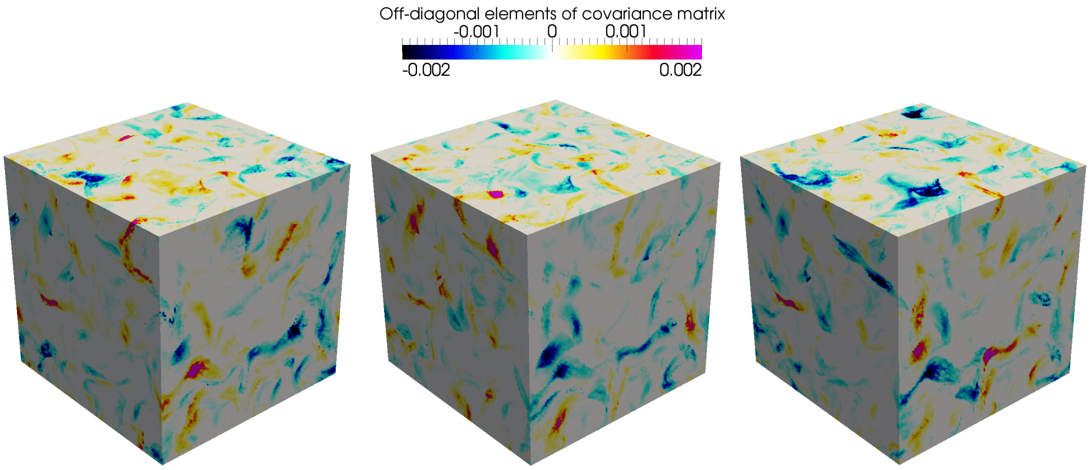

(a) Lagrangian σ_{12} (b) Lagrangian σ_{13} (c) Lagrangian σ_{23}

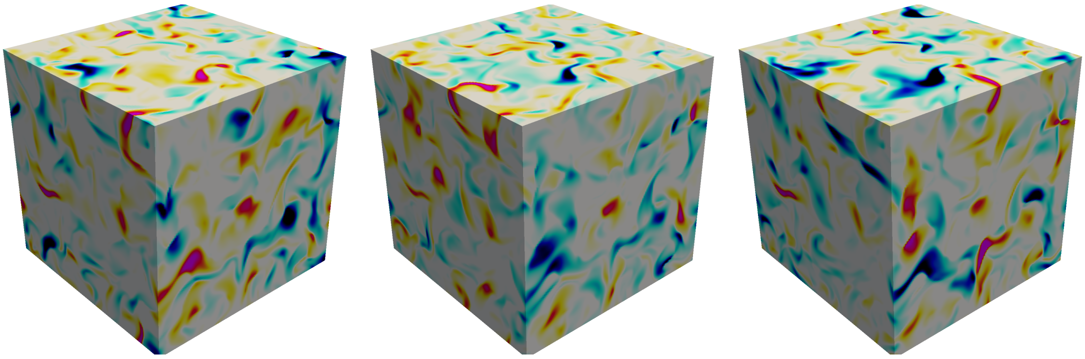

(d) Anisotropic Gaussian σ_{12} (e) Anisotropic Gaussian σ_{13} (f) Anisotropic Gaussian σ_{23}

Figure 8.17: *Velocity dispersion fields* σ_{ij} *for* $i \neq j$ *at* $t = 40$ *on the* 128^3 *mesh for* $\mathrm{St} = 3$

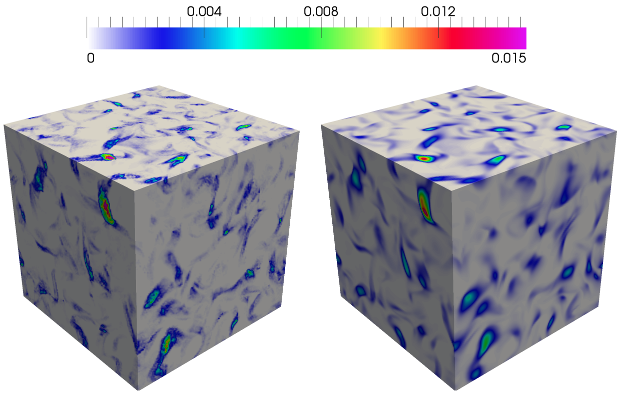

(a) Lagrangian (b) AG

Figure 8.18: *Pressure in the* x *direction,* P_{11} *at* $t = 40$ *for* $\mathrm{St} = 3$ *on the* 128^3 *mesh*

8.1.3.1 Mesh refinement for the Eulerian results for $\mathrm{St} = 3$

Contrary to the MK model, the AG model is found to capture the small-scale PTC and therefore to reproduce the right number density field for moderately inertial particles. It is now important to check the effect of the mesh refinement on the AG results, in comparison with the Lagrangian results. The effect of mesh refinement is also compared between the AG results and the MK ones. The results for the MK and AG are presented on the 64^3, 128^3 and 256^3 meshes. In addition, the AG results are also shown on the most refined mesh: 512^3 whereas the MK results are not shown on this mesh since it is clearly notice from the coarser meshes that the results of this model diverges from the Lagrangian results with mesh refinement. From Figures 8.19, we can conclude that number density field using AG matches the Lagrangian number density, while the MK results diverges from the Lagrangian one when refining the mesh.

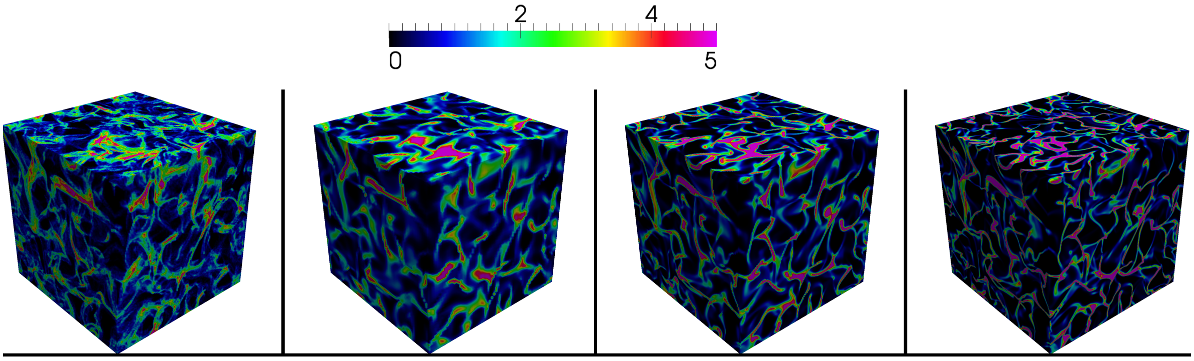

(a) from left to right, Lagrangian, MK on 64^3, 128^3, 256^3

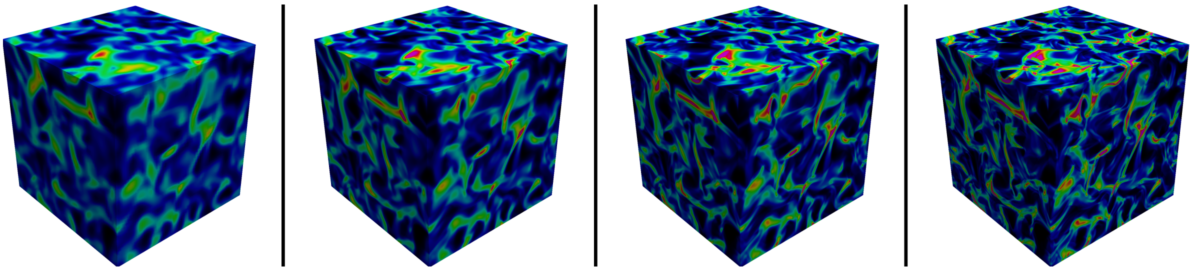

(b) from left to right: AG on 64^3, 128^3, 256^3 and 512^3

Figure 8.19: *Number density field at* $t = 40$ *for* $\mathrm{St} = 3$

For the velocity, the results are not highly affected by the mesh size. The MK model is always overestimating the velocity compared to the Lagrangian velocity, since it leads to unphysical δ-shocks at each PTC and generates hypercompressibility that is not related to the underlying physics at all. This is not the case with the AG model (Figures 8.20).

When it comes to the internal energy field calculated as the trace of the covari-

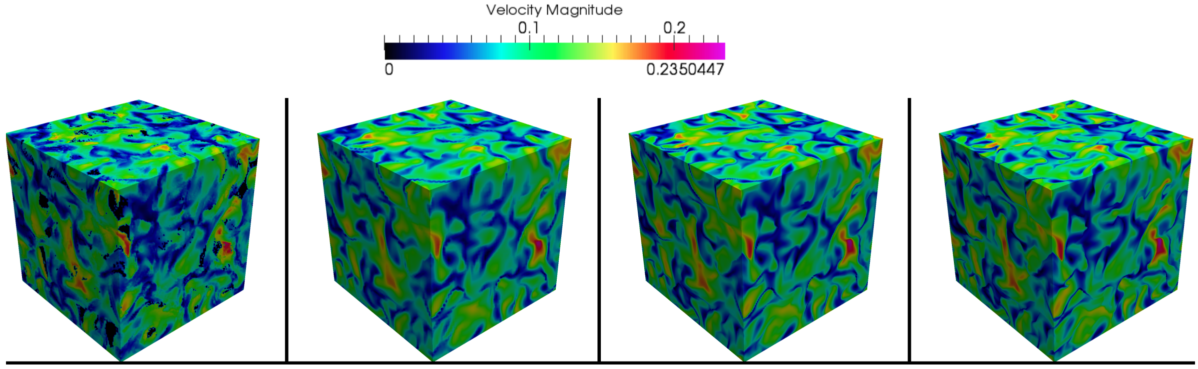

(a) from left to right, Lagrangian, MK on 64^3, 128^3, 256^3

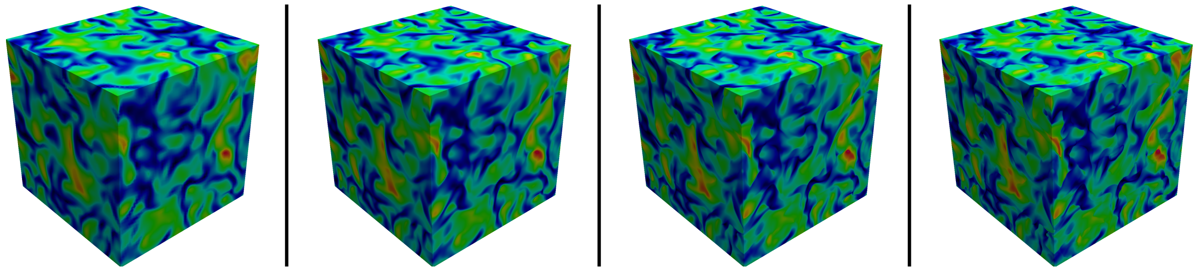

(b) from left to right: AG on 64^3, 128^3, 256^3 and 512^3

Figure 8.20: *Velocity field at* $t = 40$ *for* $\mathrm{St} = 3$

ance matrix divided by 3, the results from AG model present finer structures for finer mesh but still overestimate the central energy even though this overestimation decreases when refining the mesh (Figures 8.21).

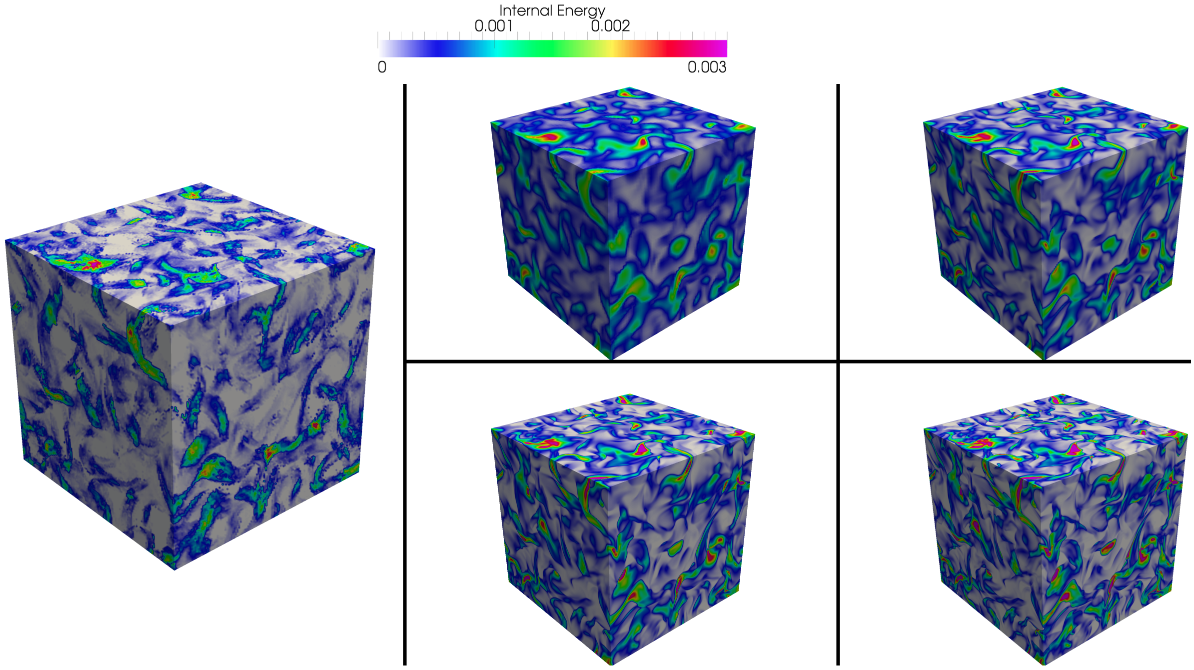

Figure 8.21: *Internal energy at* $t = 40$ *for* $\mathrm{St} = 3$*: from left to right, Lagrangian, AG on* 64^3, 128^3 *(top) ,* 256^3, 512^3 *(bottom)*

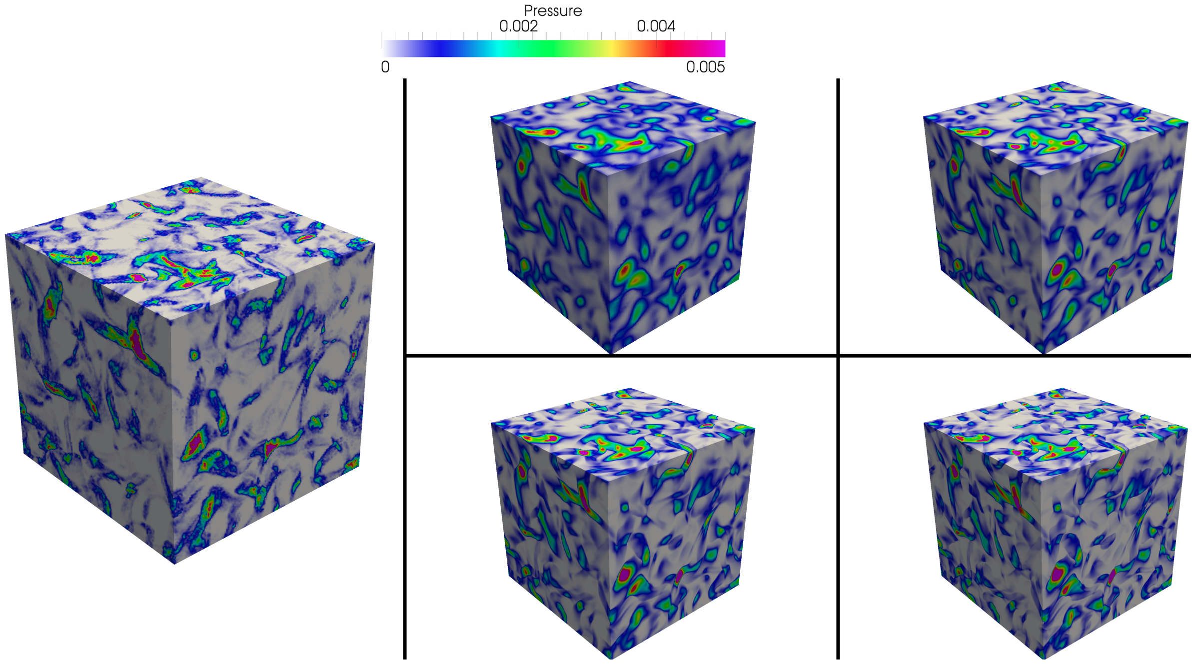

Figure 8.22: *Pressure at* $t = 40$ *for* $\mathrm{St} = 3$*: from left to right, Lagrangian, AG on* 64^3, 128^3 *(top) ,* 256^3, 512^3 *(bottom)*

8.1.4 High Stokes number: $\mathrm{St} = 8$

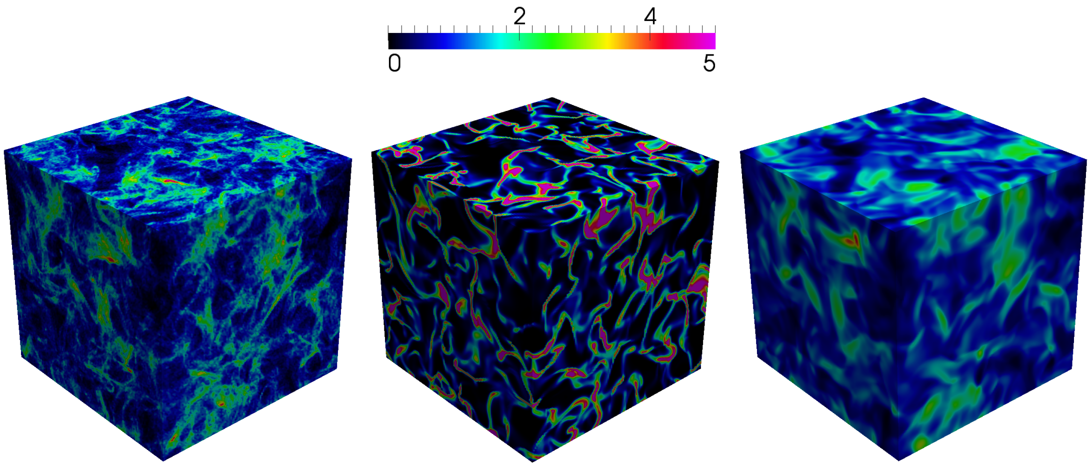

(a) Lagrangian (b) Mono-Kinetic (c) Anisotropic Gaussian

Figure 8.23: *Number density field at* $t = 40$ *on the* 128^3 *mesh for* $\mathrm{St} = 8$

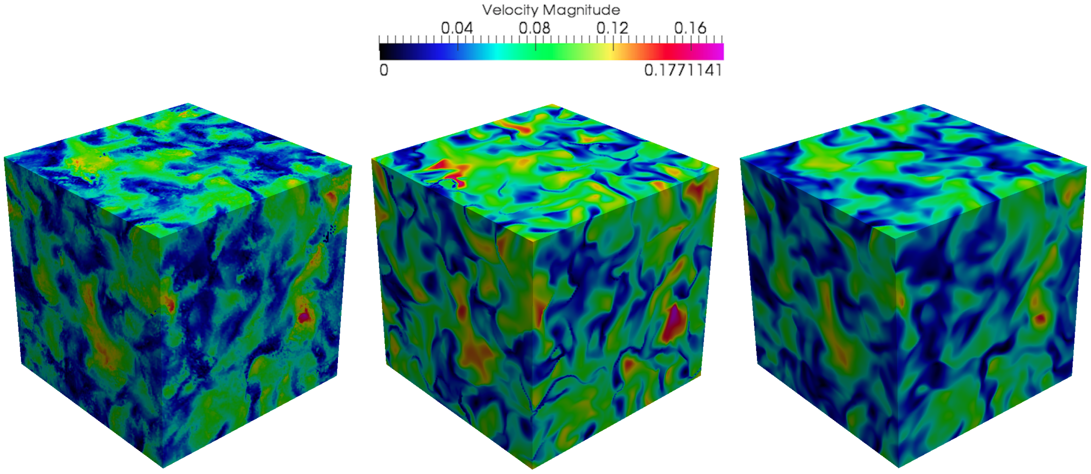

(a) Lagrangian (b) Mono-Kinetic (c) Anisotropic Gaussian

Figure 8.24: *Velocity magnitude field with the scale of the Lagrangian result at* $t = 40$ *on the* 128^3 *mesh for* $\mathrm{St} = 8$

In the following, the inertial disperse phase is simulated for a Stokes number $\mathrm{St} = 8$. In this case the local Stokes number is greater than 1 over nearly the whole domain since the percentage of the local time scale greater than $\tau_p = 10.036$ in the THI is 99.88%.
For the number density, unlike the MK model, the AG model captures the global structures and their sizes without excessive accumulation or enlarged

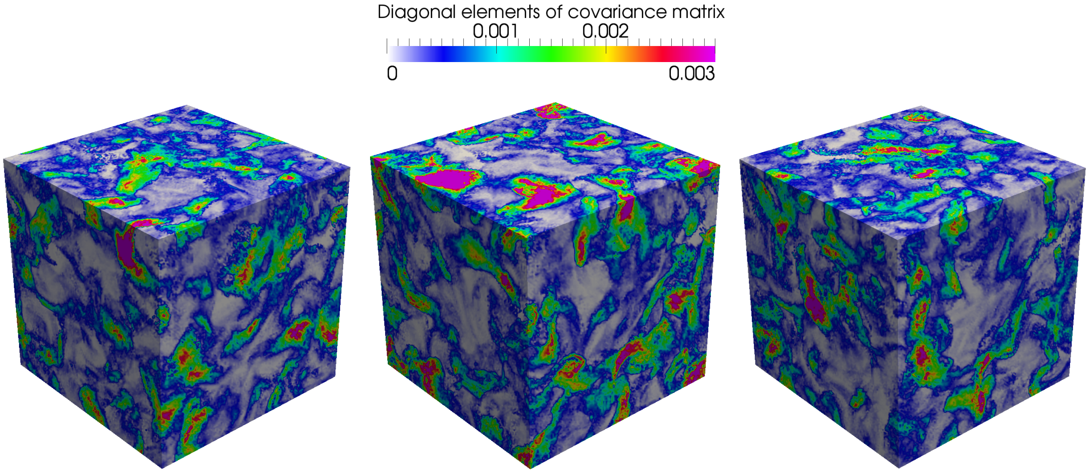

(a) Lagrangian σ_{11} (b) Lagrangian σ_{22} (c) Lagrangian σ_{33}

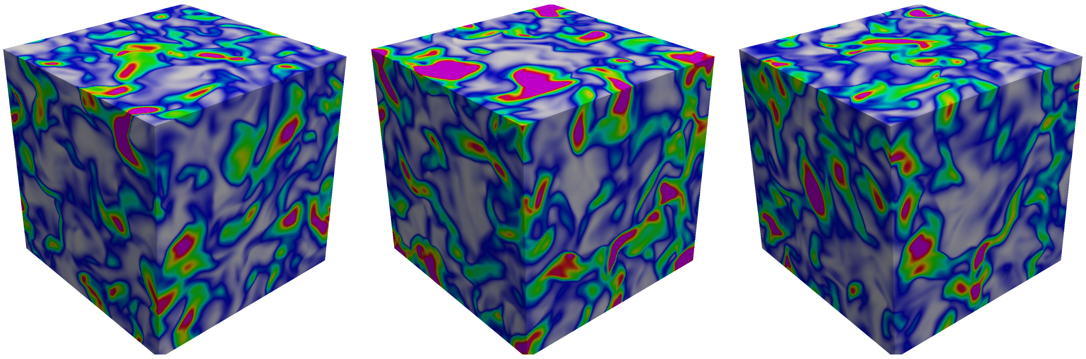

(d) Anisotropic Gaussian σ_{11} (e) Anisotropic Gaussian σ_{22} (f) Anisotropic Gaussian σ_{33}

Figure 8.25: *Velocity dispersion fields* σ_{ii} *at* $t = 40$ *on the* 128^3 *mesh for* $\mathrm{St} = 8$

vacuum region (Figure 8.23). In this case, the maximum values of the number density reached with of the Lagrangian, MK and AG are respectively 7.14, 105.87 and 4.36.

When it comes to the velocity shown in Figure 8.24, the AG result matches the Lagrangian velocity, whereas the MK model clearly overestimates the velocity magnitude.

The same conclusions and interpretations as for $\mathrm{St} = 3$ result from the velocity dispersion shown in Figures 8.25 and 8.26 where the AG model overestimates the covariance but captures the right structure.

Even though the AG model overestimates the velocity dispersion, it leads to an accurate estimation of the pressure as shown in Figure 8.27 through the trace of the pressure tensor, since the overestimation of the internal energy is balanced with the underestimation of the number density.

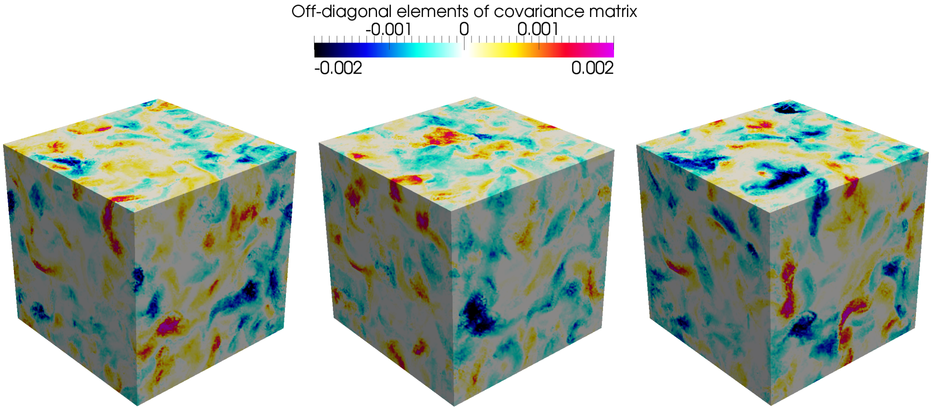

(a) Lagrangian σ_{12} (b) Lagrangian σ_{13} (c) Lagrangian σ_{23}

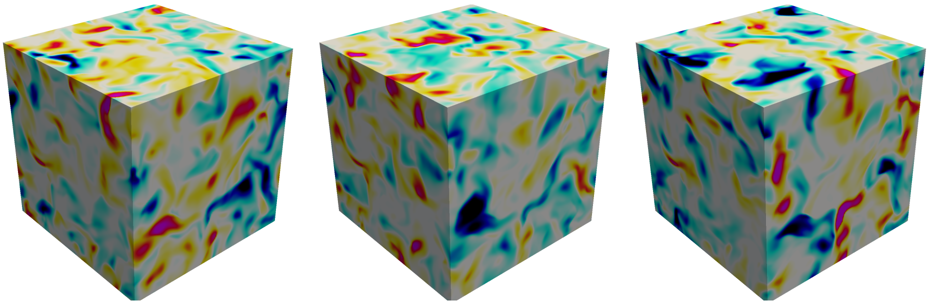

(d) AG σ_{12} (e) AG σ_{13} (f) AG σ_{23}

Figure 8.26: *Velocity dispersion fields* σ_{ij} *for* $i \neq j$ *at* $t = 40$ *on the* 128^3 *mesh for* $\mathrm{St} = 8$

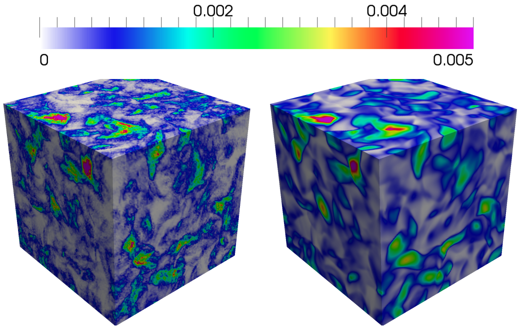

(a) Lagrangian (b) AG

Figure 8.27: *Pressure at* $t = 40$ *on the* 128^3 *mesh for* $\mathrm{St} = 8$

It is important to keep in mind that the results presented above give only general qualitative conclusions. Through these results, it is shown that the AG model is suitable for the description of a large range of Stokes numbers. It gives accurate results in comparison with the Lagrangian reference for moderate to inertial particles, where the MK model fails to predict the right dynamics. This is the first step of the comparison of the 3D results and it gives an idea about the potential of the AG model. However, it is not conclusive about the range of suitability, the quantitative convergence with mesh refinement and the limits of this model. Thus, a more detailed quantitative analysis is required for a complete validation of the AG model in 3D on the academic test case in question. This analysis starts with the statistical results conducted in section 8.3 and extends to the results on the distribution and autocorrelation function presented in Chapter 9.

8.2 One-point correlations

In this section the qualitative scatter plots are presented for the one-point velocity correlations. First, this is done to evaluate the correlation of the disperse phase motion with the gas motion. Second, the same type of results is performed to compare the velocities resulting from Eulerian simulations (AG and MK) to the one obtained with the Lagrangian reference. The more the scattered point are accumulated around the first bisector, the more the results are correlated.

Based on the analysis of the difference between the Lagrangian and the Eulerian velocities in the vacuum zones proposed in subsection 8.1.1, the points of zero velocity are not included in the Lagrangian scatter data.

8.2.1 Scatter plots of the disperse phase velocity versus the carrier phase velocity

The scatter plots for the disperse phase velocity as a function of the gas velocity for the small Stokes number St = 0.5 are similar, as shown in Figure 8.28. The disperse phase velocity is highly correlated to the gas velocity in this case. This is already expected from the qualitative results and since the particles are not inertial enough and follow the carrier phase.

For moderate to high Stokes number, for example St = 8, the disperse phase velocity is not totally correlated to the gas velocity anymore, since the particles are inertial enough to have their own motion as shown in Figure 8.28. In this case, the AG velocity scatter plot is qualitatively much similar to the Lagrangian than the MK one when looking at the percentage of scatter points crossed along the first bisector. For the Lagrangian and the AG, the first bisector only crosses the blue and cyan regions, whereas the MK crosses the blue, cyan, yellow and orange regions. This means that the correlation between the MK velocity and the carrier phase velocity is stronger than the correlation between the latter and the Lagrangian velocity. Thus, the MK model overestimates the velocity is this case.

Another comparison can be directly between the Eulerian velocities and the reference Lagrangian velocity in the following paragraph.

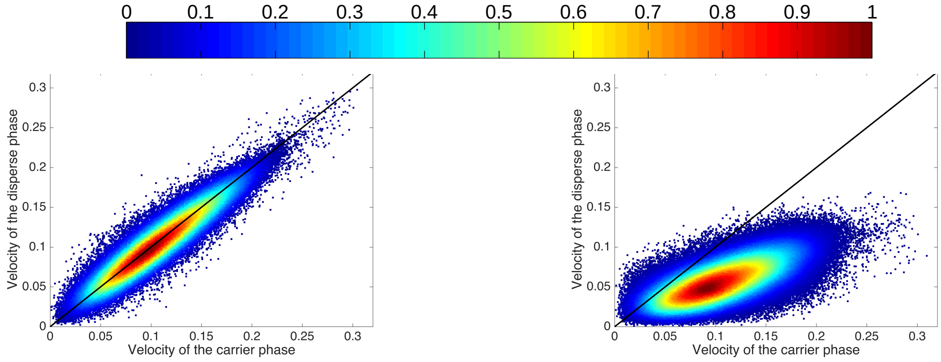

(a) Lagrangian, St = 0.5 (b) Lagrangian, St = 8

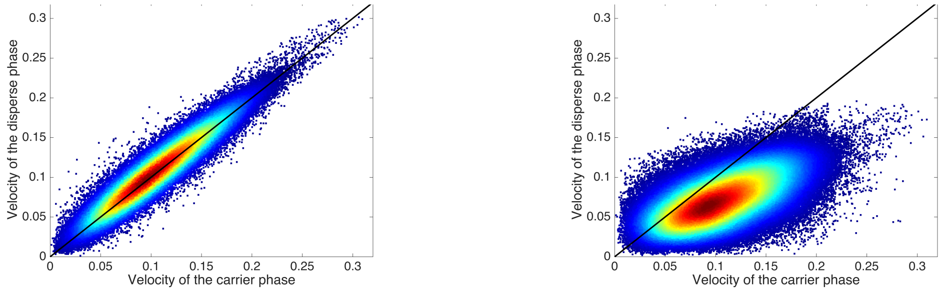

(c) Mono-Kinetic, St = 0.5 (d) Mono-Kinetic, St = 8

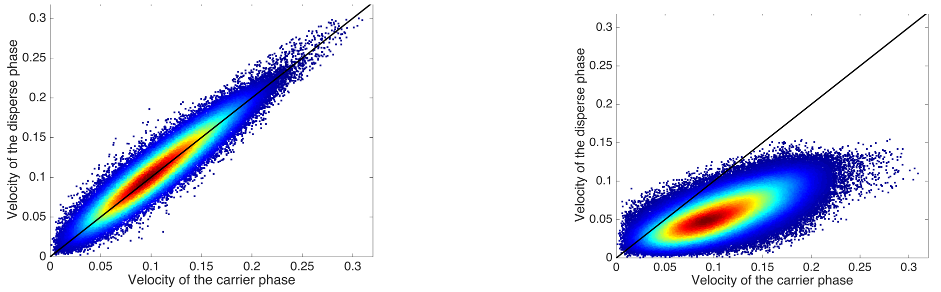

(e) Anisotropic Gaussian, St = 0.5 (f) Anisotropic Gaussian, St = 8

Figure 8.28: *Scatter plot of the disperse phase velocity magnitude as a function of the carrier phase velocity at* $t = 40$ *on the* 128^3 *mesh for* $\mathrm{St} = 0.5$

8.2.2 Scatter plots of the Eulerian velocity versus the Lagrangian one

The scatter plots for the velocity for St $= 0.5$ are nearly the same for both Eulerian results as shown in Figure 8.29. The Eulerian velocities are very similar to the Lagrangian results.

For St $= 8$, the scatter plots of the Eulerian velocity as a function of the Lagrangian velocity show that the AG are much more correlated to the Lagrangian result than the MK one. The latter overestimates the velocity since the one point correlation are distributed more to the left of the first bisector (Figure 8.30). This was expected based on the one-point correlation of the disperse phase velocity for the MK simulation and the carrier phase velocity where the former was found to be more correlated to the gas velocity in comparison with such correlation for the AG or Lagrangian results. It is important to note that this comparison is only qualitative, and in order to evaluate precisely the Eulerian velocities more quantitative measures are necessary such as the PDF and the autocorrelation function. This is the subject of the next chapter.

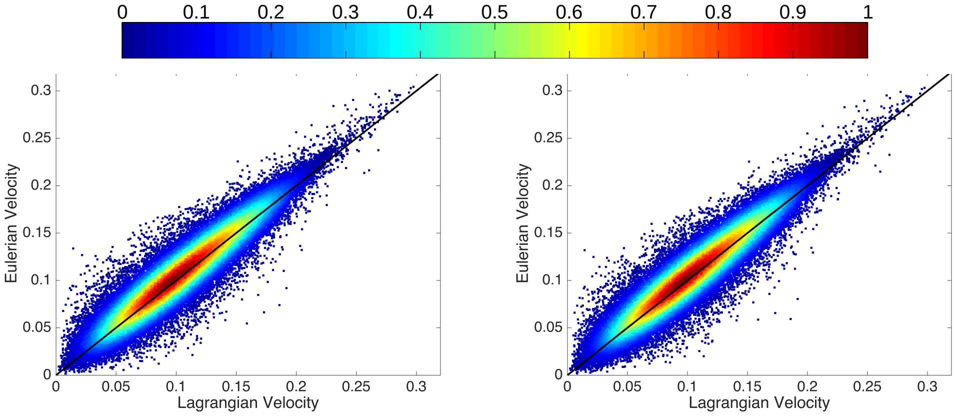

(a) Mono-Kinetic (b) Anisotropic Gaussian

Figure 8.29: *Scatter plot of the velocity of the Eulerian results as a function of the Lagrangian one at* $t = 40$ *on the* 128^3 *mesh for* St $= 0.5$

To conclude, on one hand, the domain of applicability of the MK model is found to be limited to critical Stokes number. This limitations is due to the Dirac δ distribution of the disperse phase velocity in the phase space, which limits the models from treating PTC. On the other hand, the AG visual qualitative results seem to be capturing the right dynamics of the disperse phase for the various Stokes numbers studied, ranging from small to high Stokes numbers. A more quantitative comparison is necessary to validate the AG model and define its domain of applicability of the scales that it is able to capture.

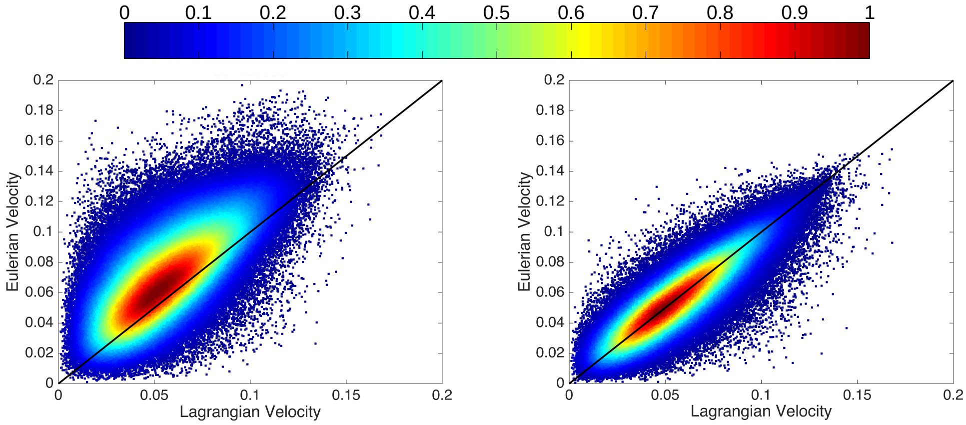

(a) Mono-Kinetic (b) Anisotropic Gaussian

Figure 8.30: *Scatter plot of the velocity of the Eulerian results as a function of the Lagrangian one at* $t = 40$ *on the* 128^3 *mesh for* $\mathrm{St} = 8$

8.3 Quantitative statistical results

Through the qualitative results the AG model is found to be a very promising method for the extension of the KBMM to moderately to high inertial particles, without tremendously increasing the cost of the method, as it is the case for the other polykinetic models (*Fox 2012*; *Yuan and Fox 2011*; *Kah et al. 2010*; *Chalons et al. 2010*; *Chalons et al. 2016*). To further understand the pros and cons of this model, the statistical results are essential, especially because the AG model is expected to statistically capture the PTC and not deterministically as shown in the two crossing jets configuration in the work of *Vié et al. (2015)*. For this reason, hereafter we present quantitative statistical results. The chosen quantities are the following:

- The segregation that was presented in the previous chapter and is given by Equation (7.17).
- The mean internal energy or mean central energy (MCE) also presented in the previous chapter (see Equation (7.18)).
- The mean total energy (MTE) is the spatial average of the actual energy over the whole domain. It evaluates the quantity of the overall momentum exchange in both mean and internal kinetic energies. It is given by the following equation:

$$\mathrm{MTE} = \frac{\langle n \sum_i^{N_d} ((u_i)^2 + (\sigma_{ii})^2) \rangle}{N_d \langle n \rangle}. \tag{8.1}$$

The evolution of these quantities with time is compared for the different models and for different Stokes numbers. In addition, these statistical quantities are plotted as a function of the Stokes number for the different models.

Before presenting the results, the general color code used in this section and through part III is defined. The statistical results for the simulation using the AG model are displayed using solid line, those using the MK model are drawn with dashed line. Concerning mesh refinement, the colors green, blue, red and gray correspond respectively to the 64^3, 128^3, 256^3 and 512^3 meshes. When the result is plotted over time for the different models and meshes, the lines are plain for the AG and Lagrangian and dashed for the MK, as illustrated in Figure 8.31(a). For a given time when the results are plotted as a function of the Stokes number, the lines have symbols as shown in Figure 8.31(b). Finally, for a given model, when a quantity is plotted as a function of time for different Stokes numbers the color code is a rainbow color map in the Stokes numbers as shown in the legend of Figure 8.32.

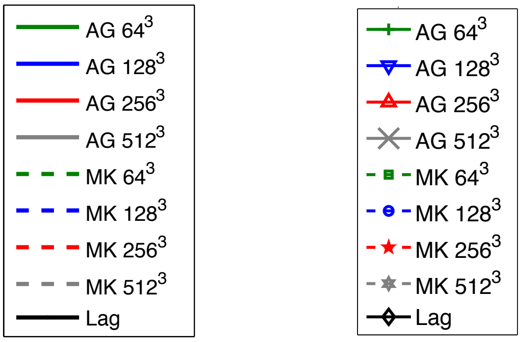

(a) when a variable is plotted as a function of time, for a given Stokes number

(b) when a variable is plotted as a function of the Stokes number, at a given time

Figure 8.31: *Legend for the Lagrangian result, AG and MK results on the* 64^3, 128^3, 256^3 *and* 512^3 *meshes*

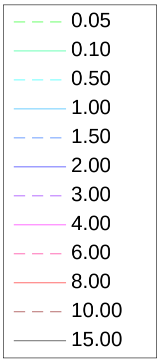

Figure 8.32: *Legend when a result is plotted as a function of time for different Stokes numbers*

8.3.1 Statistical quantities evolution with time for different Stokes numbers

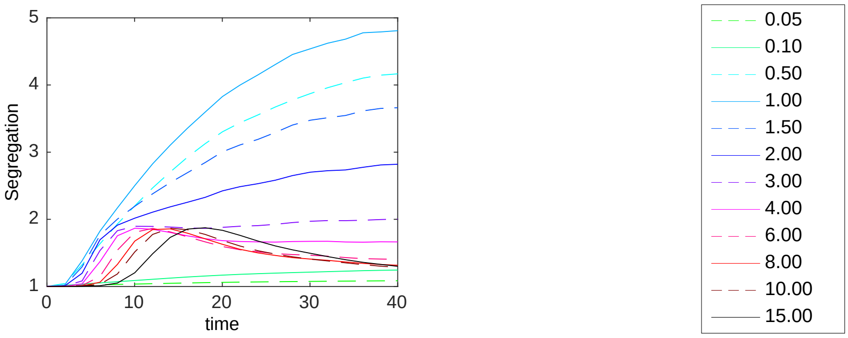

(a) Lagrangian

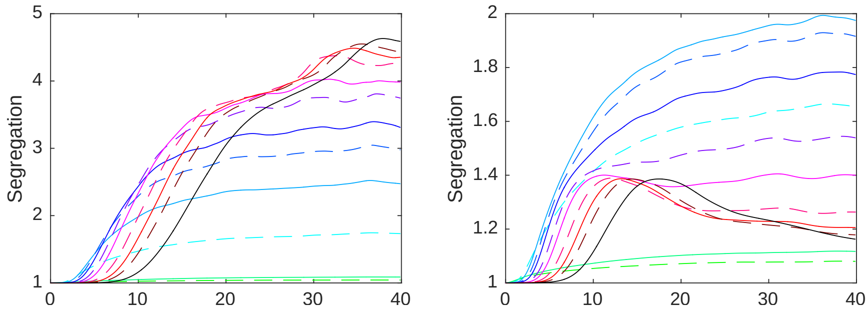

(b) MK on the 128^3 mesh (c) AG on the 128^3 mesh

Figure 8.33: *Evolution of the segregation with time for different Stokes numbers. The view windows is set to the maximum segregation reached by the simulation, i.e.* ~ 5 *for the Lagrangian and MK and* ~ 2 *for the AG.*

In this part, the time evolution profile of the different statistical quantities is evaluated for different Stokes numbers.
Starting with the segregation in Figure 8.33, the curves are monotonically increasing for Stokes numbers smaller than 1: in this range, the higher the Stokes, the greater the segregation. For $\mathrm{St} > 1$, the slope of the curves after $t = 10$ starts to decrease with increasing Stokes number, until, for a Stokes number of approximately 3, a maximum appears in the curve. Then, this behavior is the same for even higher Stokes number. The trend of the AG curves matches relatively well the Lagrangian one. However, we can notice a main difference for Stokes numbers near the critical one, where the AG does not reproduce the steep slope found in Lagrangian. This can be seen by comparing for the Lagrangian and AG the difference of the temporal evolution of the segregation for $\mathrm{St} = 1$ and $\mathrm{St} = 1.5$. In addition, the segregation is higher with the Lagrangian model for all the Stokes numbers. This was already seen in the qualitative results presented before and is mainly due to the numerical diffu-

sion. The MK results have the tendency to increase the segregation rate with the Stokes number, even beyond the critical Stokes number. So that for St > 1, the segregation is very overestimated with the MK model. This result was also expected from the qualitative results, since the MK model overestimated the preferential concentrations and resulted in large vacuum zones in comparison with the Lagrangian number density field.

For the mean agitation energy plotted in Figure 8.34, the trend of the AG curves matches the Lagrangian one, but only with slightly higher levels of the mean internal energy. This observation was already found through the qualitative results of the velocity dispersion, where the AG results lead to higher values for the covariance matrix elements in comparison with the Lagrangian results.

When it comes to the mean total energy, both the MK and AG curves meet the tendency of the Lagrangian ones (Figure 8.35).

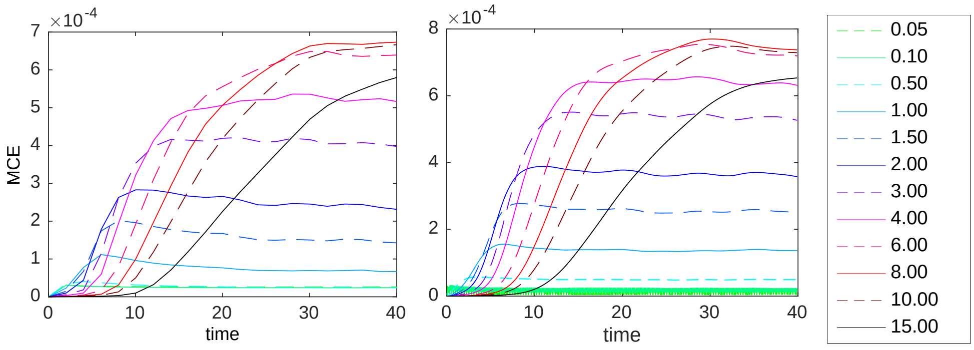

(a) Lagrangian (b) AG on the 128^3 mesh

Figure 8.34: *Mean internal energy evolution with time for different Stokes numbers*

Now that the trend of the time evolution over the range of Stokes numbers is assessed, the next goal is to evaluate for a given Stokes number the effect of mesh refinement on the time evolution of the statistics.

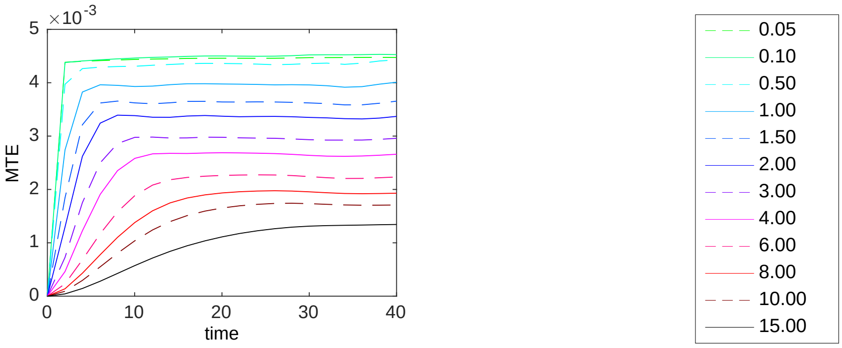

(a) Lagrangian

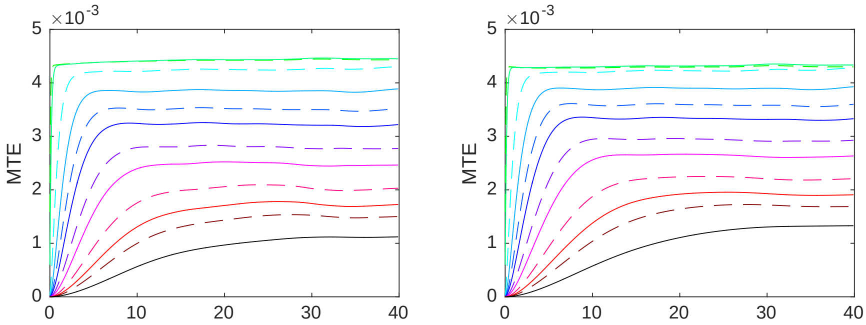

(b) MK on the 128^3 mesh (c) AG on the 128^3 mesh

Figure 8.35: *Mean total energy evolution with time for different Stokes numbers*

8.3.2 Statistical results comparison with mesh refinement

In order to compare the statistical results of the Lagrangian and Eulerian simulations on different meshes (64^3, 128^3, 256^3 and 512^3), the moments are projected on the coarsest mesh: in this case the 64^3 mesh. In fact, a unified projection is necessary since the measures of the segregation and the mean internal energy depend on the scale at which the spatial correlation is computed. It is important to note that the choice of this projection can bias the comparison, if it is not well suited. For example, in our case the ideal projection could have been on the native carrier phase grid, i.e. the 128^3 mesh. However, for the Eulerian results we have simulation on a coarser level and it is more appropriate to compare the different statistics on the scale of this coarsest mesh chosen (64^3). The exact value of the segregation and MCE is affected by the choice but the evolution of these quantities (as a function of time or Stokes number) is not altered. The proof of this assumption is presented in the next chapter, in subsection 9.2.1 based on the number density autocorrelations.
Before presenting the results for different Stokes numbers, the difference between the original results and the projected results is shown hereafter for a Stokes number equal to 3. It is important to note that if the statistics are not

computed at the same scale, then they are not really comparable. For example the Lagrangian result that is projected on a 128^3 Eulerian mesh (black curves in Figures 8.36 and 8.37) is only comparable to the Eulerian result simulated on the 128^3 mesh (blue curves), since it is already expected to have higher segregation for example when the results are projected on a finer mesh.
It is important to note that for the Lagrangian results, if the projection is not specified then it is done on the 128^3 mesh. This means that in the figures where the statistics are compared with and without projection, the Lagrangian results are projected on the native mesh of the gas phase.
From Figure 8.36, one can notice that the segregation level decreases when calculated on a 64^3 mesh and thus the differences between the different curves is smaller. The inverse is remarked for the mean internal energy (Figure 8.37), while the mean total energy is unaffected by this projection and can therefore be calculated on any given mesh, the total energy should be conserved (Figure 8.38).

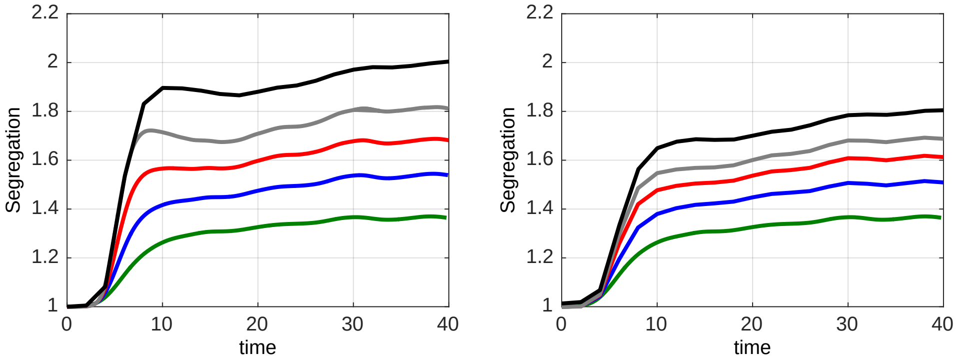

(a) Without projection

(b) With projection on the 64^3 mesh

Figure 8.36: *Segregation evolution with time for Lagrangian results and Eulerian AG results on the* 64^3, 128^3, 256^3 *and* 512^3 *meshes for* $\mathrm{St} = 3$

In the following, all the presented statistics are projected on a 64^3 mesh except for a couple of specific cases where also the projection on a 128^3 mesh in taken into account in order to provide a complete analysis that is mesh-dependent and that is not biased by the choice of the projection.

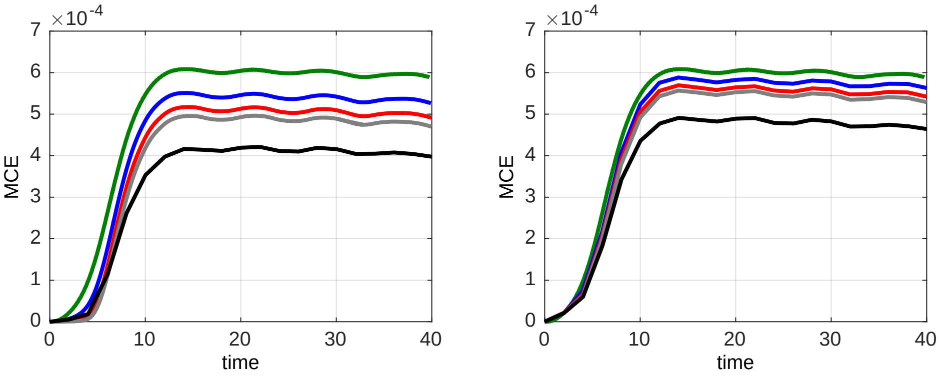

(a) Without projection (b) With projection on the 64^3 mesh

Figure 8.37: *Temporal evolution of the mean internal energy for Lagrangian results and Eulerian AG results on the* 64^3, 128^3, 256^3 *and* 512^3 *meshes for* $\mathrm{St} = 3$

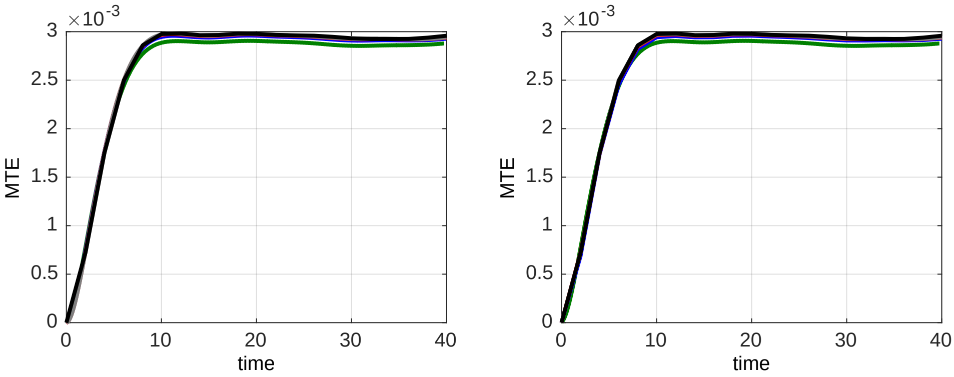

(a) Without projection (b) With projection on the 64^3 mesh

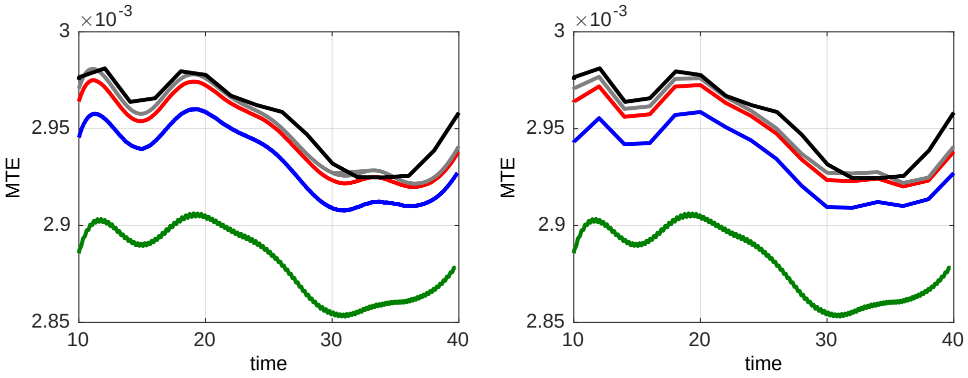

(c) Without projection (zoom in) (d) With projection on the 64^3 mesh (zoom in)

Figure 8.38: *Temporal evolution of the mean total energy for Lagrangian results and Eulerian AG results on the* 64^3, 128^3, 256^3 *and* 512^3 *meshes for* $\mathrm{St} = 3$

For the small Stokes number (St = 0.5), the time evolution of the statistics are plotted in Figure 8.39 for the Lagrangian and the Eulerian results. The MK and AG results lead to similar level of segregation and mean total energy. For this case, no significant difference is found between the Eulerian results. The carrier phase is followed by the disperse phase and both Eulerian models capture the underlying physics. For the segregation, it is clear that the Eulerian curves have lower segregation than the Lagrangian one but tend to reach this latter when refining the mesh.

In this case, no considerable mean internal energy is found. It is less than 3% of the MTE at $t = 40$ (see Figure 8.39). This is expected for this small St since the probability of having PTC is nearly 0.04%, as mentioned before.

It is important to keep in mind that the mean internal energy include mainly the effect of PTC but also the numerical diffusion for the Eulerian simulation. Thus, the highlighted importance of studying the mesh refinement effect on the results in order to be able to evaluate the model by minimizing the numerical errors. Also the projection affects the MCE as well as the segregation for all the simulations.

The mean total energy moves toward the Lagrangian mean total energy with mesh refinement.

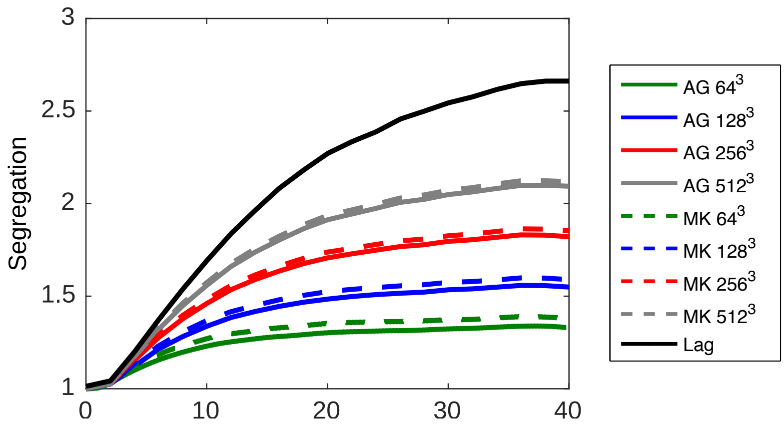

(a) Segregation

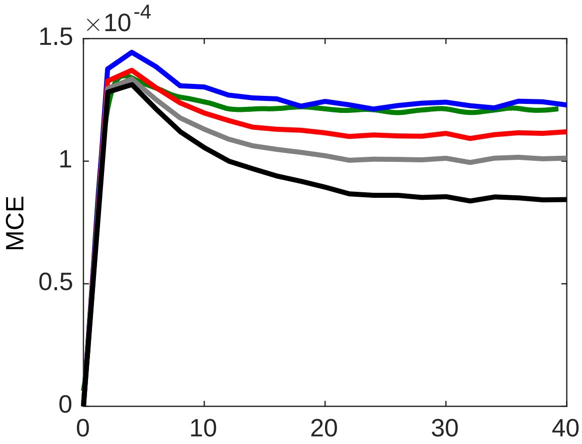

(b) Mean internal energy

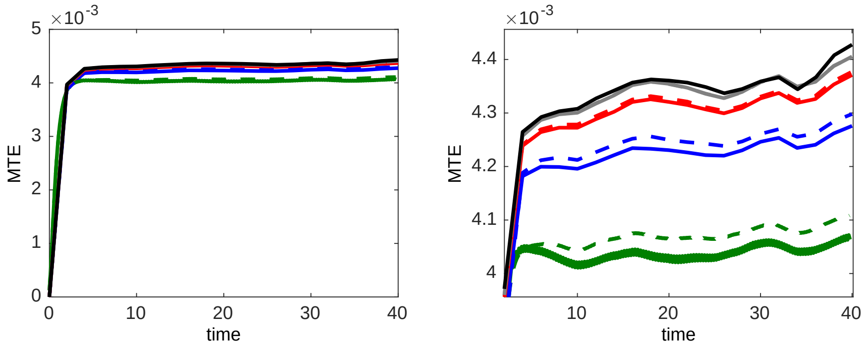

(c) Mean total energy (d) Mean total energy zoom

Figure 8.39: *Statistics evolution with time for Lagrangian results and Eulerian results on the* 64^3, 128^3, 256^3 *and* 512^3 *meshes with projection on the same* 64^3 *mesh for* St $= 0.5$

In Figure 8.40 the statistics are plotted for a Stokes number St =1. The segregation of the MK results is higher than the one of the AG results and is therefore closer to the Lagrangian segregation. When refining the mesh both Eulerian models generate higher segregation. However for the 512^3 mesh the MK segregation is slightly higher than the Lagrangian one for a time $t < 20$, which is due to the local PTC faced where the local Stokes number is higher than 1 as explained in the previous chapter (see section 7.3.2). These occurrences represent nearly 11% of the whole domain. The mean internal energy is higher with the AG model but tends to converge toward the Lagrangian level when the numerical diffusion is decreased through mesh refinement. The MCE is nearly 7% of the bulk MTE in this case at $t = 40$.

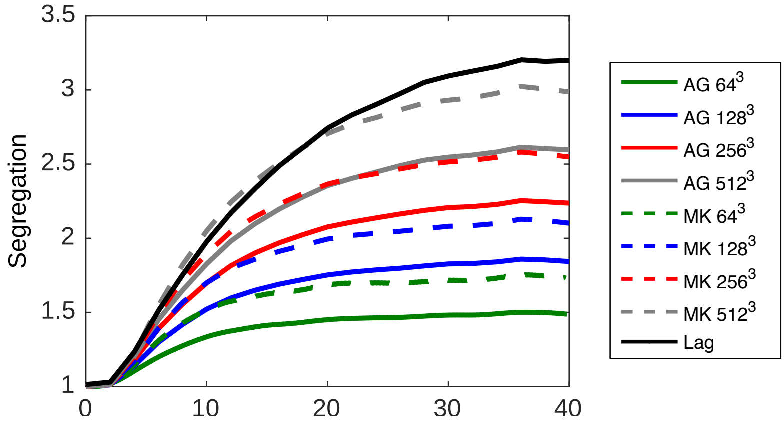

(a) Segregation

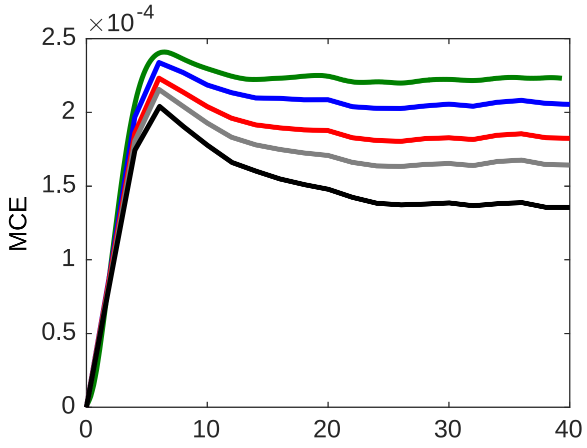

(b) Mean internal energy

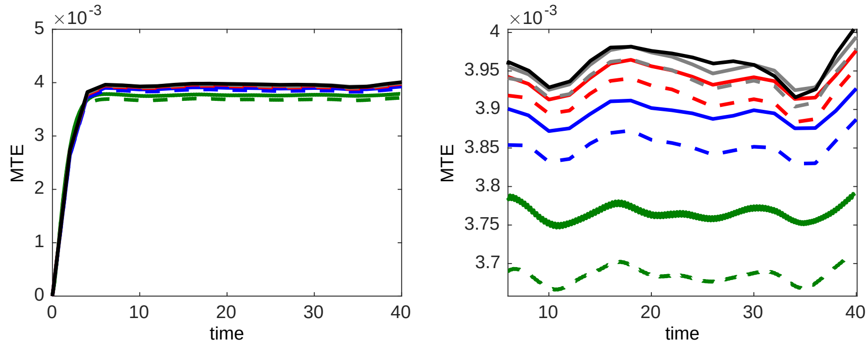

(c) Mean total energy (d) Mean total energy zoom

Figure 8.40: *Statistics evolution with time for Lagrangian results and Eulerian results using* 64^3, 128^3, 256^3 *and* 512^3 *meshes with projection on the same* 64^3 *mesh for* $\mathrm{St} = 1$

In addition, the segregation and the mean internal energy are presented for a projection on the DNS 128^3 mesh (Figure 8.41). At this length scale, the segregation of the AG model seems to be converging more slowly toward the Lagrangian one in comparison with the rate of convergence measured on the 64^3 mesh projection. In fact, the AG 512^3 result underestimates the Lagrangian segregation by 18.56% when measured on the 64^3 mesh projection and by 34.27% when measured on the 128^3 mesh projection. In addition, the mean internal energy is overestimated by the AG model on the 512^3 mesh by respectively 21.21% and 47.87%, when measured on the 64^3 and 128^3 meshes projections.

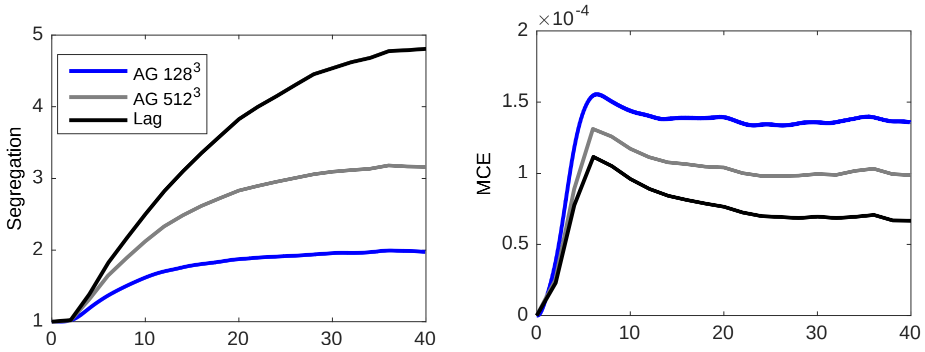

(a) Segregation (b) Mean internal energy

Figure 8.41: *Statistics evolution with time for Lagrangian results and AG results using* 128^3 *and* 512^3 *meshes with projection on the same* 128^3 *mesh for* $\mathrm{St} = 1$

In the case of moderately inertial particle $\mathrm{St} = 3$ (Figure 8.42), the segregation is overestimated by the MK model and diverges from the Lagrangian segregation curve when refining the mesh. On the other hand, the AG model captures the right physics and the segregation level approaches to the Lagrangian one when refining the mesh. This can be clearly seen in Figure 8.42b. The mean internal energy for the AG results is higher than the Lagrangian one. For the 512^3 mesh, the difference between the Lagrangian and AG levels has decreased but the convergence rate in this case is slow. The mean total energy for the refined AG result matches the Lagrangian one, where the MK model underestimates it.

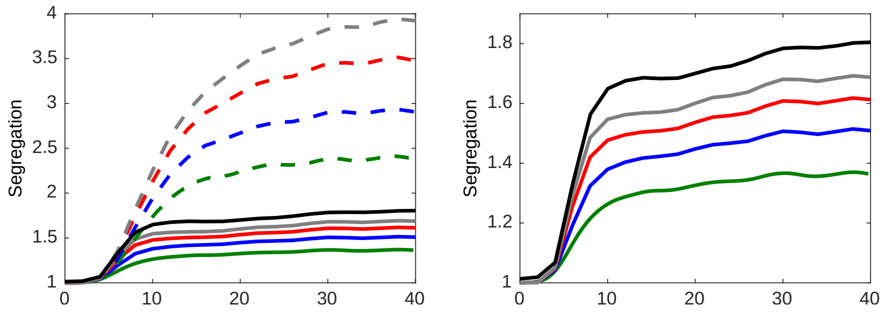

(a) Segregation (b) Segregation AG

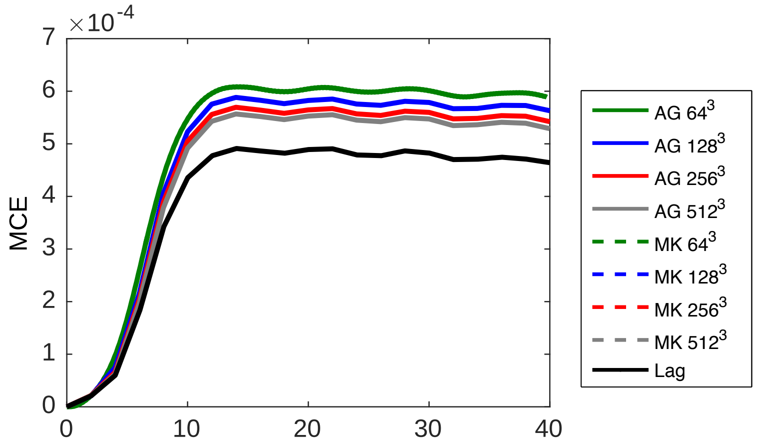

(c) Mean internal energy

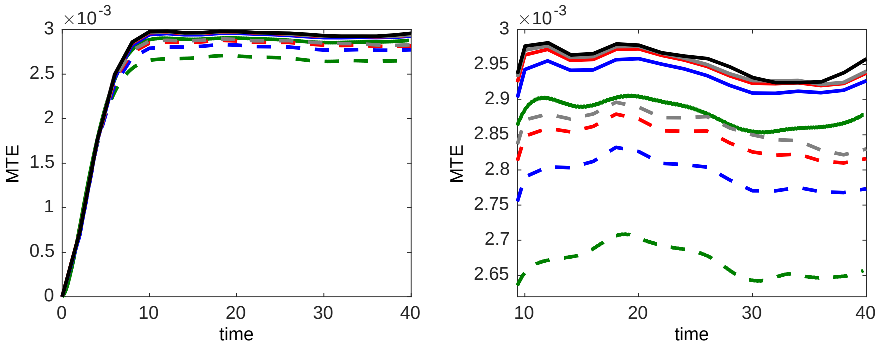

(d) Mean total energy (e) Mean total energy zoom

Figure 8.42: *Statistics evolution with time for Lagrangian results and Eulerian results on the* 64^3, 128^3, 256^3 *and* 512^3 *meshes with projection on the same* 64^3 *mesh for* $\mathrm{St} = 3$

When measured on the DNS scale, the segregation of the AG 512^3 results is underestimated by 11.62% (Figure 8.43) while it was underestimated by nearly half this percentage (5.94%) when measured on the 64^3 mesh. On the other hand, the mean internal energy is overestimated by 22.44% compared to 12.92% on the coarsest mesh scale. The rate of convergence of the AG results is nearly multiplied by two when the statistics are measured on the 64^3 mesh in comparison with the ones measured on the DNS scale, which is twice as refined as the 64^3 mesh.

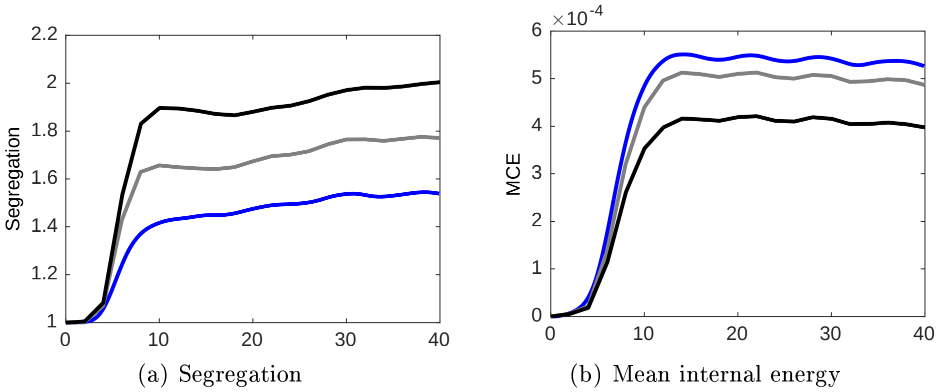

(a) Segregation (b) Mean internal energy

Figure 8.43: *Statistics evolution with time for Lagrangian results and AG results using* 128^3 *and* 512^3 *meshes with projection on the same* 128^3 *mesh for* St = 3

For inertial disperse phase, St = 8, the same analysis can be carried out as for St = 3. For this Stokes number, the rate of convergence of the AG results with mesh refinement towards the Lagrangian results is decelerated when it comes to the mean energies where the energy level are nearly stagnant (see Figure 8.44). This might mean that the percentage of large-scale PTC that cannot be statistically reproduced by the AG is high in this case and limits the performance of this model. This assumption is not confirmed yet since for the time range studied, the AG model seems to accurately estimate the mean total energy at t=40. In this case, the error between the most refined solution and the Lagrangian one is only 0.73%. On the other hand, the MK model underestimates the mean total energy by 8.32% on the 512^3 mesh.

The segregation on the 64^3 mesh scale is nearly the same for the Lagrangian result and the AG result on the 512^3 mesh, quantitatively the AG overestimates the segregation by 0.85%. Nevertheless, when measured on the carrier DNS scale, the segregation of the AG refined result underestimates the segregation by 0.79%. This means that the results are not conclusive in this case.

Actually, particular attention must be paid to the profile of the segregation results that seems to reach a plateau with the AG results but not yet with the Lagrangian. Thus, the final time chosen based on the carrier motion is not conclusive in this case, and the simulation should be carried for longer time until reaching a quasi-steady state.

The mean statistical results until t=80 which is nearly $8\tau_p$ are shown in Figure 8.46 for the Lagrangian simulation and the AG simulation on the 128^3 and 512^3

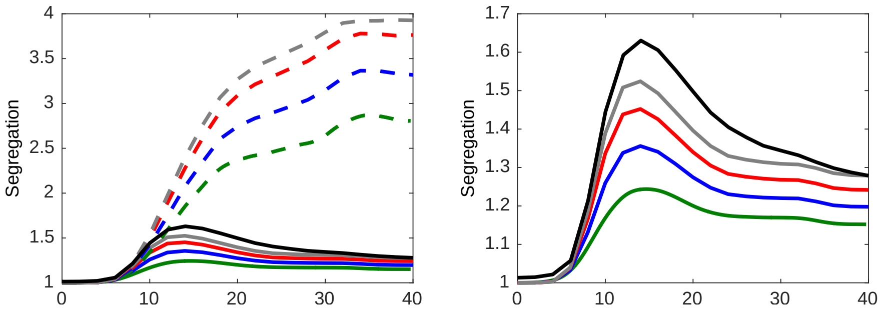

(a) Segregation (b) Segregation AG

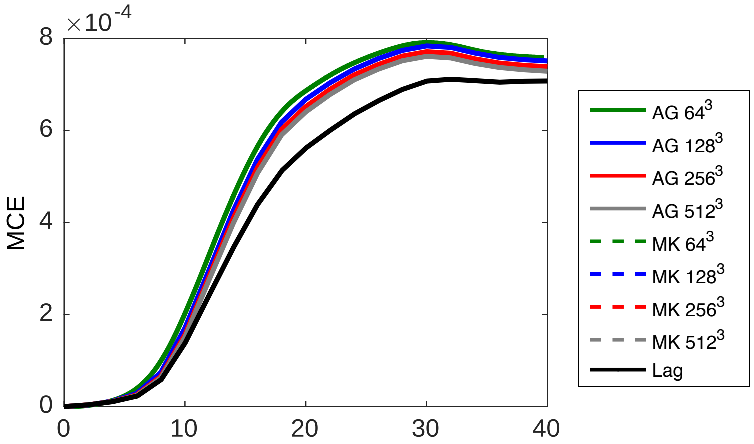

(c) Mean internal energy

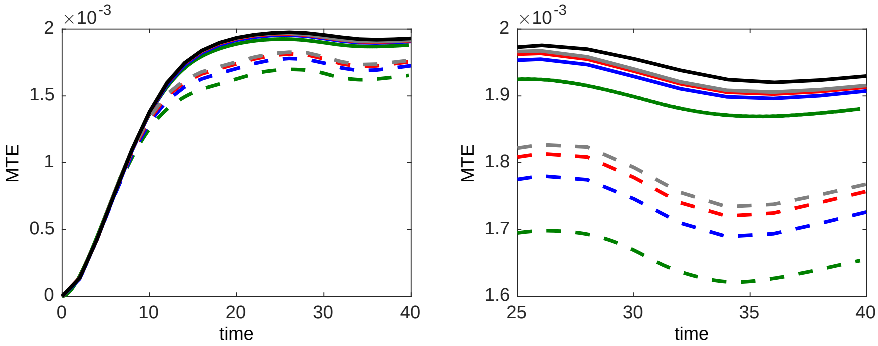

(d) Mean total energy (e) Mean total energy

Figure 8.44: *Statistics evolution with time for Lagrangian results and Eulerian results on the* 64^3, 128^3, 256^3 *and* 512^3 *meshes with projection on the same* 64^3 *mesh for* $\mathrm{St} = 8$

meshes. For a time higher than t=40, the AG results on the refined mesh starts to overestimate the segregation. The mean internal energy is underestimated for

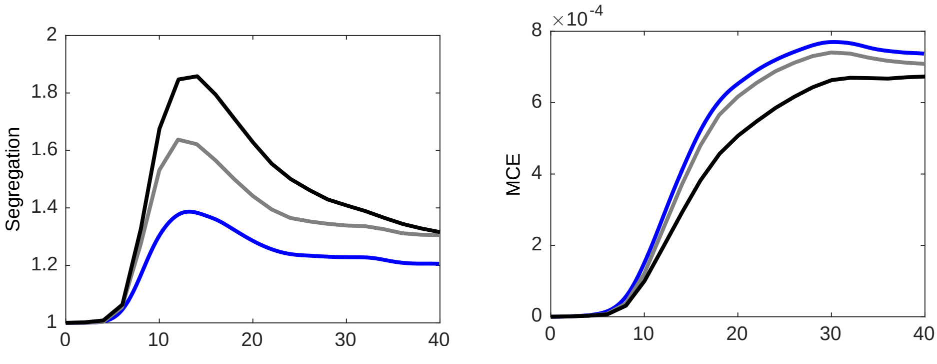

(a) Segregation (b) Mean internal energy

Figure 8.45: *Statistics evolution with time for Lagrangian results and AG results using* 128^3 *and* 512^3 *meshes with projection on the same* 128^3 *mesh for* $\mathrm{St} = 8$

t>45 on the 512^3 mesh. Based on these two measures, the AG solution diverges from the Lagrangian reference when refining the mesh (see Figure 8.46) . When it comes to the mean total energy, the difference between the refined AG result and the Lagrangian one increases with time. It is important to note that for the Stokes number in question the relaxation time of the disperse phase is 10.036 which is 2.55% higher than the integral time scale.

According to the results at this Stokes number, the AG model is not considered to be suitable for Stokes number higher than $\mathrm{St}_E = 1$, since the AG results on the refined mesh start to diverge from the Lagrangian reference. This is observed whenever the simulated time is long enough to start encountering large-scale crossing.

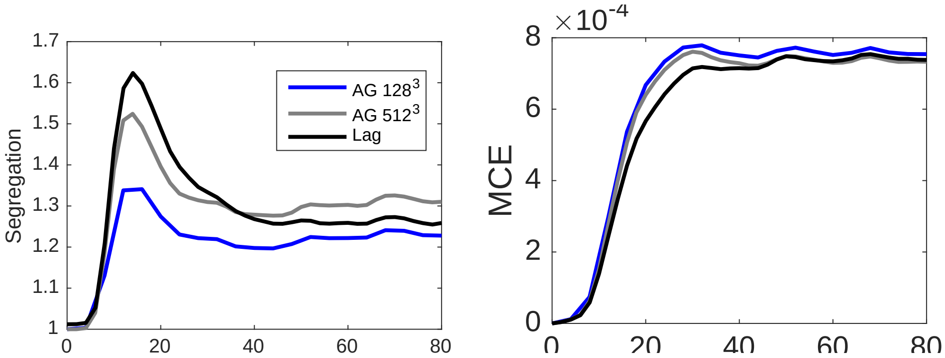

(a) Segregation (b) Mean internal energy

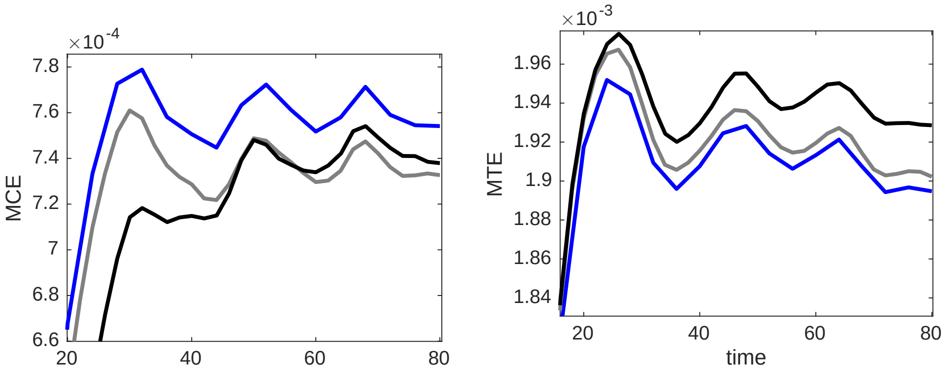

(c) Mean internal energy (zoom in) (d) Mean total energy (zoom in)

Figure 8.46: *Statistics evolution with time for Lagrangian results and AG results on the* 512^3 *mesh with projection on the same* 64^3 *mesh for* St = 8 *until t=80*

8.3.3 Statistical quantities evolution with Stokes number at final time t=40

Finally, the statistical results are plotted for the different models and meshes as a function of the Stokes number. Unless mentioned otherwise, this is done at time t=40 chosen after nearly four times the integral time scale.

The results are plotted as a function of the Stokes number based on the Kolmogorov time scale St_K (shown on the bottom x-axis) and of the Stokes number based on the large eddies St_E (shown on the top x-axis) as seen for example in Figure 8.47.

Based on the Lagrangian results, we can note that the segregation increases for small Stokes number until reaching its global maximum value for a Stokes number of $\mathrm{St}_K = 1$. After the unity critical Stokes numbers, the segregation decays progressively and tends to a plateau for Stokes number greater than $\mathrm{St}_E = 1$ (see Figure 8.47). Actually, since the small particles tend to follow the gas phase and segregate in the regions on low vorticities when increasing

the Stokes number below $\mathrm{St}_K = 1$, the segregation is increased. On the other hand, moderately inertial to high inertial particles will decorrelate from the gas phase and create PTC that may lower segregation.
This behavior was already observed in the literature (*Wang and Maxey 1993; Reveillon and Demoulin 2007*) where the preferential segregation was evaluated through different methods. For example, *Reveillon and Demoulin (2007)* computed the preferential segregation through the standard deviation of the density field on one hand and the maximum of the deviation of the density distribution from the Poisson distribution on the other hand. The latter way is actually the classical method to evaluate the segregation. They found that both methods lead to similar profiles for the evolution of the segregation with respect to the Stokes numbers, but the standard deviation of the density field is higher than the maximum of the deviation of the density distribution from the Poisson distribution for $\mathrm{St}_K > 3$.
Looking at the MK results, it is clear that this model does not reproduce this behavior for $\mathrm{St}_K > 1$. Instead, the segregation keeps increasing until reaching nearly a plateau for $\mathrm{St}_E > 1$, having a value much higher than the Lagrangian one. When refining the mesh the segregation of the MK results tends to the Lagrangian reference for a Stokes number $\mathrm{St}_K \leq 1$ but is overestimated for greater Stokes number and diverges from the Lagrangian reference. This behavior is due to the fact that this model is not capable of reproducing the PTC, and instead generates unphysical δ-shock and high concentrations and vacuum zones. It is important to note that all the classical QBMM that uses quadratures in the form of a sum of Dirac delta function lead to weakly hyperbolic conservation laws and face δ-shock singularities (*Chalons et al. 2012*).
For the AG model, the trend of the segregation dependence on particles inertia matches the Lagrangian one throughout the range of Stokes numbers studied. When refining the mesh, the AG curve tends to reach the Lagrangian. The rate of this convergence is higher for $\mathrm{St}_K > 1$ and is the lowest at $\mathrm{St}_K = 1$ where the underlying physics including hypercompressibility effects and depletion zones are very challenging for the numerical scheme.

To check the effect of the projection on the segregation evolution as a function of the Stokes number, the segregation is plotted for the Lagrangian and AG results and all the results are projected on the native DNS mesh. From Figure 8.48, one can notice that the rate of convergence of the segregation is nearly half the one obtained on the 64^3 mesh projection. The maximum difference between the AG refined results and the Lagrangian ones is obtained for the critical Stokes number. This difference decreases with the increase of the Stokes number in the range of $\mathrm{St}_K > 1$ and $\mathrm{St}_E < 1$ and then increase above this limit.

Another measure for the segregation as a function of the particles inertia is also presented here. It is the maximum value of the segregation along the studied time range. For small Stokes number, this value increases if the chosen final time is increased, since as shown in Figure 8.40 the segregation is mono-

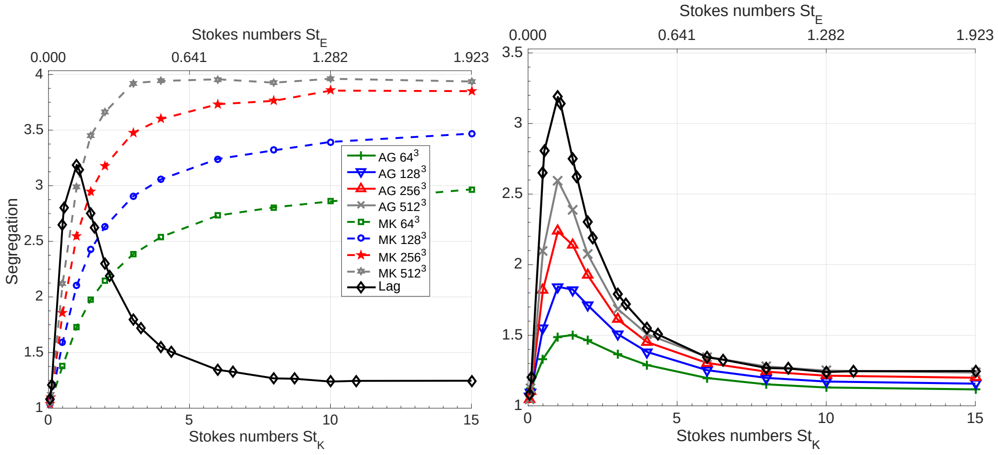

(a) Mono-Kinetic (b) Anisotropic Gaussian

Figure 8.47: *Segregation as a function of Stokes number for Lagrangian result and Eulerian results on the* 64^3, 128^3, 256^3 *and* 512^3 *meshes with projection on the same* 64^3 *mesh.*

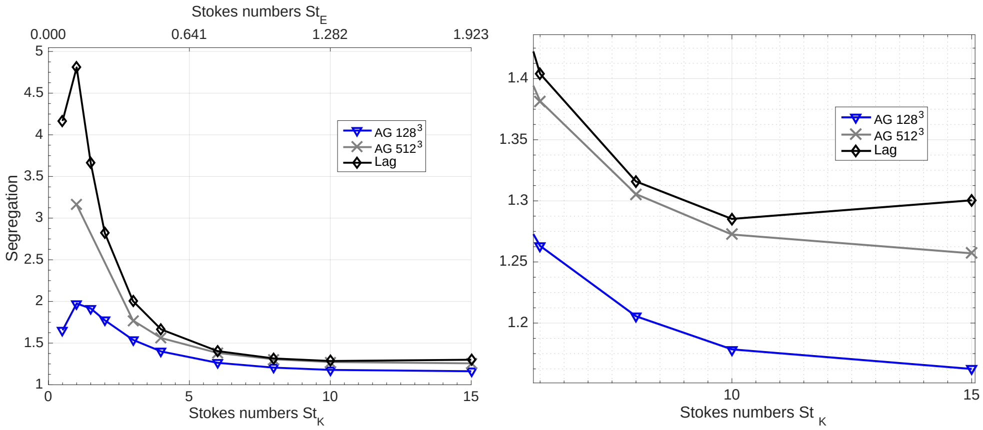

(a) Full scale (b) High Stokes numbers

Figure 8.48: *Segregation as a function of Stokes number for Lagrangian result and AG results on the* 128^3 *and* 512^3 *meshes with projection on the same* 128^3 *mesh.*

tonically increasing with time. However for high Stokes numbers (for example Figure 8.44), the segregation increases with time until reaching a maximum value and then decreases, thus, the maximum segregation in this case will not change for longer simulations. This means that for high Stokes numbers, the maximum measure is a stable way to evaluate the segregation independently from the final time of the simulation, under the condition to have a time long enough for the segregation to reach its maximal value. Therefore, this is a good way to evaluate the effect of mesh refinement and thus of the decrease of numerical diffusion on the results. This measure is plotted in Figure 8.49, where the results for small Stokes numbers are exactly the same as for the segregation at t=40 as it was already expected. Whereas for $\mathrm{St}_K \geq 3$ the maximum segregation is nearly constant for the Lagrangian result. This segregation is drastically overestimated with the MK model for which the results with mesh refinement diverge from the Lagrangian one. On the other hand, the AG model captures the right evolution of the maximum segregation with the particle inertia. For $\mathrm{St}_K \geq 3$ a nearly constant value is reached and this value tends to the Lagrangian one when refining the Eulerian mesh. This means that when the AG system is solved with a high order realizable scheme, it gives accurate values for that maximum segregation along the whole range of the Stokes numbers studied. These observations emphasize two main points. First, a quality of this model is highlighted, since independent of the final time of the simulation and of the limits of the AG model that are not defined yet, it leads always to the right value of the maximum segregation that has a great influence in the combustion domain since it governs the maximum fuel vapor mass fraction. Second, the importance of the development of new adapted high order numerical methods to solve the resulting AG system is asserted, which meets the perspective of the work presented in Part II of extending the convex state preserving Runge-Kutta discontinuous Galerkin method to the AG system.

For the mean internal energy, it increases with the Stokes number until reaching a nearly constant level with AG for Stokes numbers around $\mathrm{St}_E = 1$ and then decreases for $\mathrm{St}_K > 10$ (see Figure 8.50(a)). The increase of the mean internal energy with the Stokes number is due to the occurrence of PTC and is

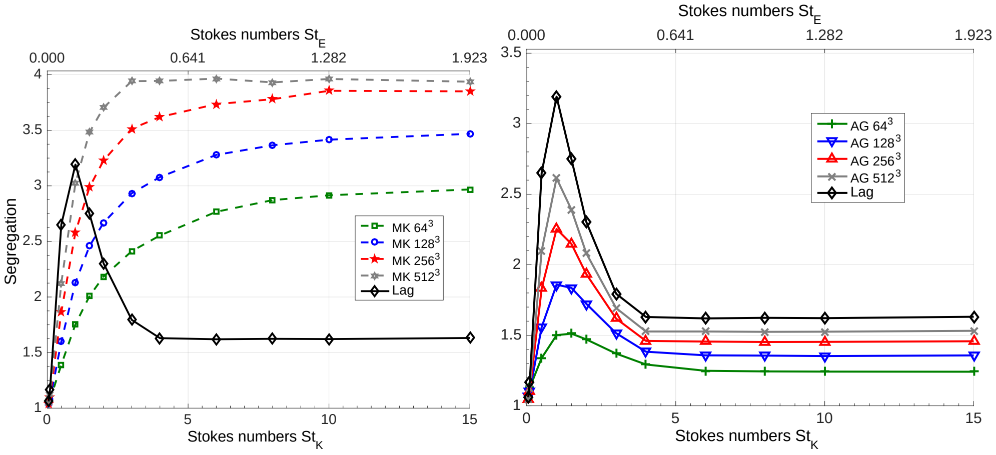

(a) Mono-Kinetic (b) Anisotropic Gaussian

Figure 8.49: *Maximum segregation as a function of Stokes number for Lagrangian result and Eulerian results on the* 64^3, 128^3, 256^3 *and* 512^3 *meshes with projection on the same* 64^3 *mesh.*

also noticed in the Lagrangian results.

By comparing the AG result to the Lagrangian one, we can conclude that the mean internal energy is slightly overestimated with the AG model and tends to the Lagrangian reference when refining the mesh. The profile of the evolution of the mean internal energy as a function of the particle inertia is captured accurately with the AG model. The same conclusion can be drawn based on the MCE computed on the DNS scale but in this case the rate of the convergence is slower. From Figure 8.51, the mean total kinetic energy is decreasing with increasing Stokes number.

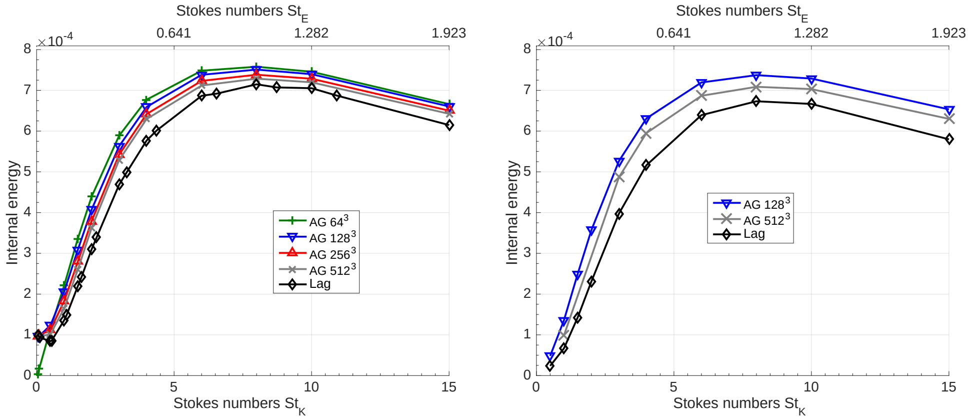

(a) Projection on the same 64^3 mesh. (b) Projection on the same 128^3 mesh.

Figure 8.50: *Mean internal energy as a function of Stokes number for Lagrangian result and Anisotropic Gaussian results with mesh refinement.*

For St $>$ 1, the MK model underestimates the MTE compared to the Lagrangian reference.

In this case, the AG model performs better and estimates accurately the MTE in comparison with the Lagrangian results. Furthermore, with mesh refinement the MTE of the AG solutions is less affected for St $>$ 1 than for the critical Stokes number. In fact, the difference between the MTE obtained on the coarsest mesh and the reference is 6% for St $=$ 1 and decreases to 3% for St $=$ 3. Thus, the MTE energy is already accurately reproduced by the AG model for moderately inertial to inertial particles even on the coarsest meshes.

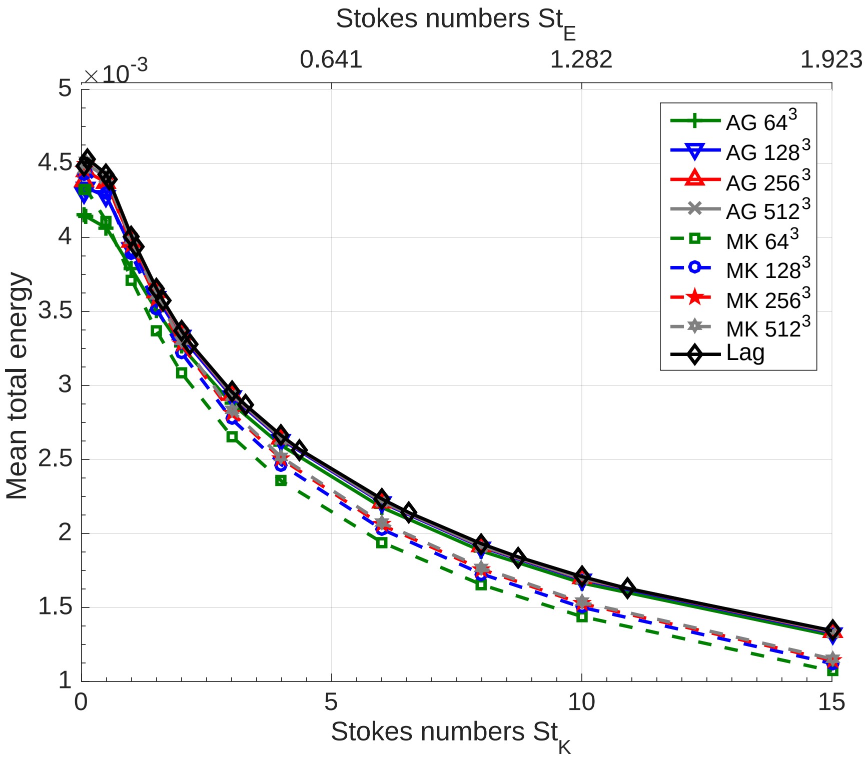

(a) Full scale

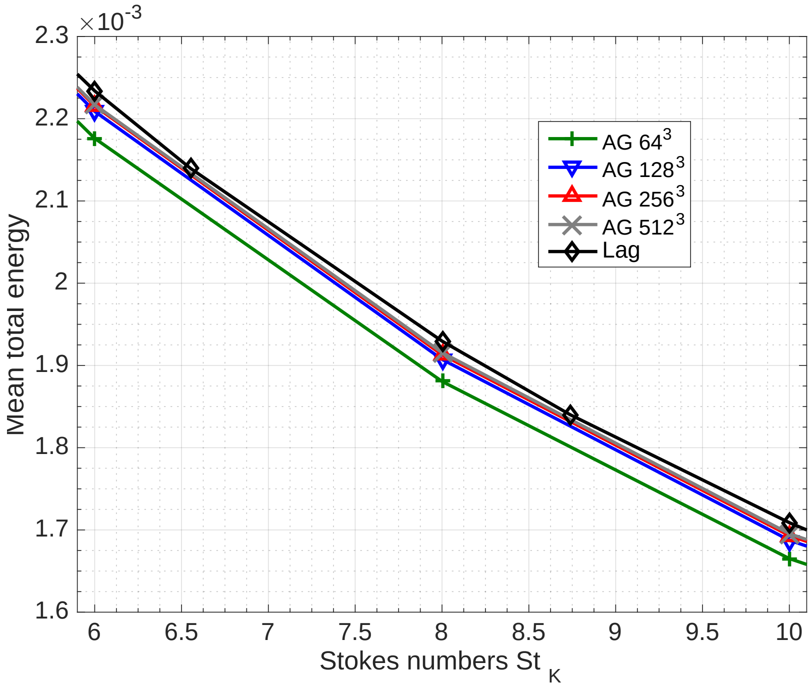

(b) Zoom in

Figure 8.51: *Mean total energy as a function of Stokes number for Lagrangian result and Eulerian results on the* 64^3, 128^3, 256^3 *and* 512^3 *meshes.*

Finally, the effect of the particle inertia on the ratio of the internal kinetic energy to the mean total kinetic energy and the ratio of the mean correlated kinetic energy to the mean total kinetic energy are plotted in Figure 8.52(a). The mean total energy is equal to the mean correlated kinetic energy for very small particles where the mean internal energy is negligeable. However for $\mathrm{St}_K > 1$ the mean internal energy increases significantly with the particle inertia and begins to constitute an important part of the mean total energy. The mean internal energy keeps rapidly increasing with the Stokes number until reaching $\mathrm{St}_E = 1$. Above this limit, the decrease of mean correlated energy and the increase of the mean internal energy is slowed down and the difference between the Lagrangian and AG results increases slightly for the highest Stokes number studied. With a 128^3 projection, the energy ratios behave in the same way as for the coarser projection, but the difference between the Lagrangian and the AG results is accentuated, especially for St = 15.

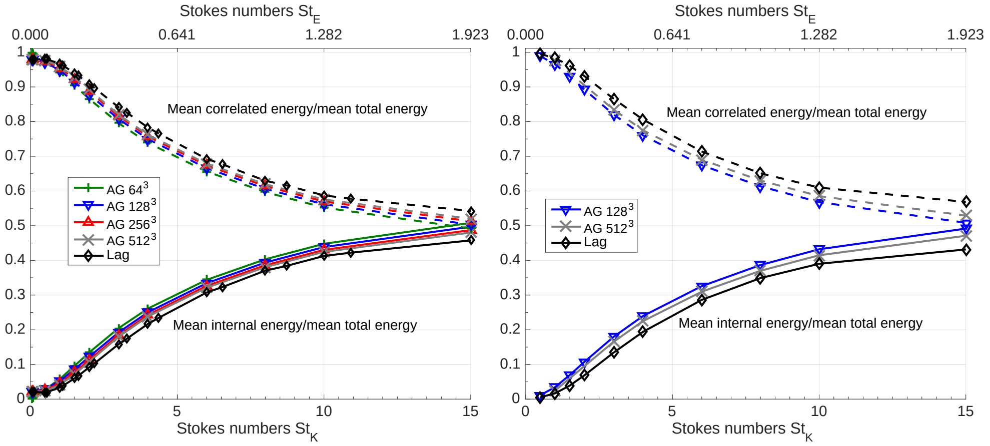

(a) Projection on the same 64^3 mesh. (b) Projection on the same 64^3 mesh.

Figure 8.52: *Mean energy ratios as a function of Stokes number for Lagrangian result and AG results with mesh refinement.*

It is important to note that the observations and analysis for $\mathrm{St}_E \geq 1$ presented in this subsection are not fully conclusive. For this reason, the same analysis is carried for the evolution of the mean statistics as a function of the particles inertia at time $t_f \geq 4\tau_p$ in the next subsection.

8.3.4 Statistical quantities evolution with Stokes number at time adapted to the particles relaxation time

In this paragraph, the comparison between the statistical results for the AG and the Lagrangian simulations as a function of the Stokes number is presented at final times adapted to the relaxation time of the disperse phase. The former is in general taken to be at least $4\tau_p$. In fact, for the small Stokes numbers, the chosen final time t_f is limited by the motion of the gas since it cannot be smaller than the time t_{FHIT} needed to reach a statistically steady state for the FHIT. Thus, the adapted final time is $t_f \geq \max(t_{FHIT}, 4\tau_p)$ and is plotted in Figure 8.53.

From Figure 8.54, it is clear that the AG model accurately estimates the segregation for $\mathrm{St}_E < 1$ and tends to the Lagrangian level when refining the mesh. On the other hand, an overestimation of the segregation by the AG results on the 512^3 mesh is observed for $\mathrm{St}_E \geq 1$. The overestimation itself is not an evidence of the limits of this model. The divergence of the AG segregation from the Lagrangian reference in this range is in fact the proof that the AG model is no more suitable to describe the underlying physics.

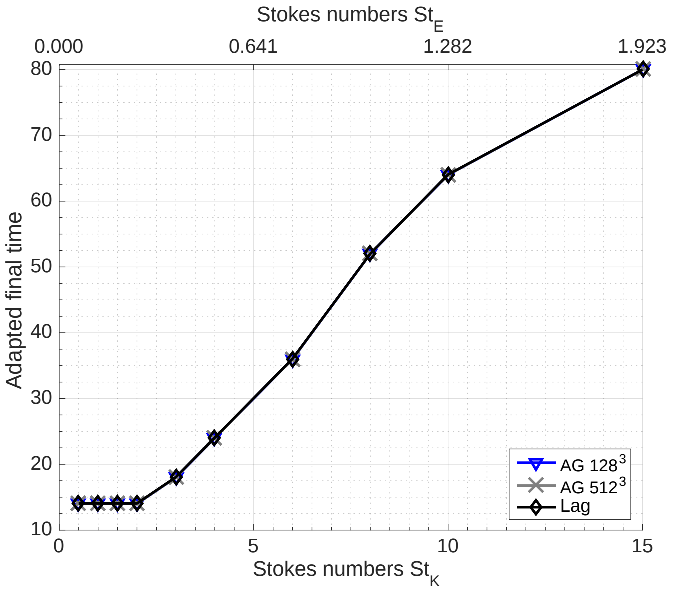

Figure 8.53: *The adapted final time t_f for different Stokes number*

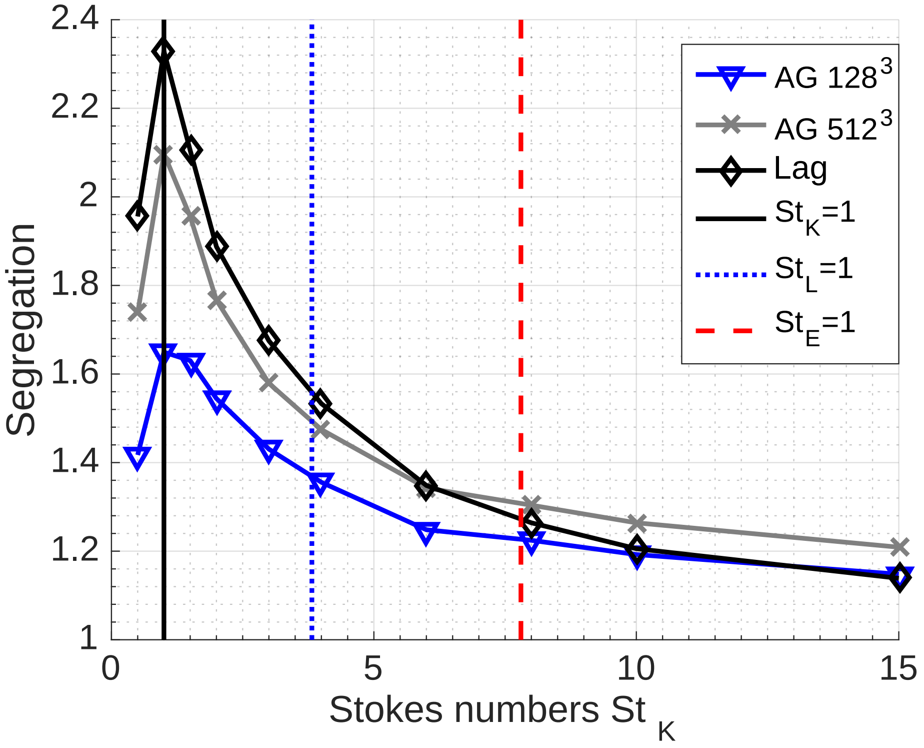

Figure 8.54: *Segregation as a function of Stokes number for Lagrangian result and Anisotropic Gaussian results on the* 128^3 *and* 512^3 *meshes with projection on the same* 64^3 *mesh at* t_f.

When it comes to the mean internal energy, the AG model overestimates this quantity for $\mathrm{St}_E < 1$ but tends to the Lagrangian limit even if the speed of this convergence is slower than in the segregation case. The overestimation for $\mathrm{St}_E < 1$, is due to the numerical dispersion included in the covariance matrix in the AG model as mentioned before.
Above this limit, the mean internal energy resulting from the AG simulations diverges from the Lagrangian reference when refining the mesh. In fact, as shown in Figure 8.55 the AG results on the 512^3 mesh underestimate the mean internal energy. This underestimation increases with the Stokes numbers and is expected to increase with the mesh refinement. A possible reason to this underestimation is that the statistical estimation of the internal energy through the AG model is not enough to capture the underlying physics for this range of Stokes numbers where the scale of the PTC is large and comparable to the integral length scale. This also implies that treating the PTC through a pressure tensor or a velocity dispersion around the mean value is only suitable for $\mathrm{St}_E < 1$ where the particles are not inertial enough to be completely decorre-

lated from the gas.

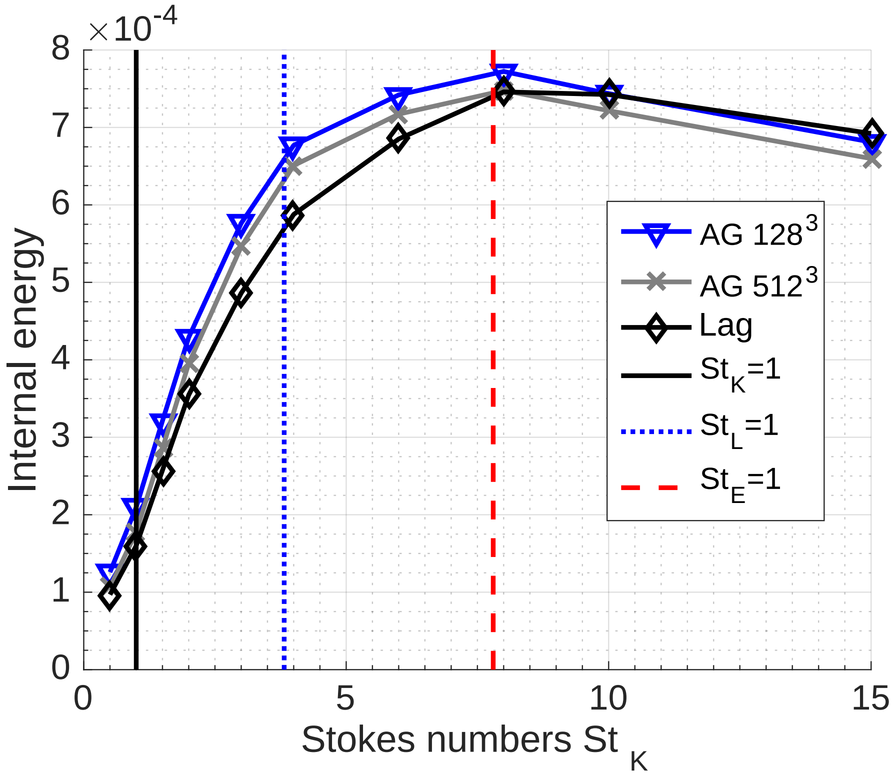

Figure 8.55: *Mean internal energy as a function of Stokes number for Lagrangian result and Anisotropic Gaussian results on the* 128^3 *and* 512^3 *meshes with projection on the same* 64^3 *mesh at* t_f.

At this range where the AG underestimates the mean internal energy, it is also noticed that the mean total energy is slightly underestimated as shown in Figure 8.56 and this underestimation become more pronounced with higher Stokes numbers.

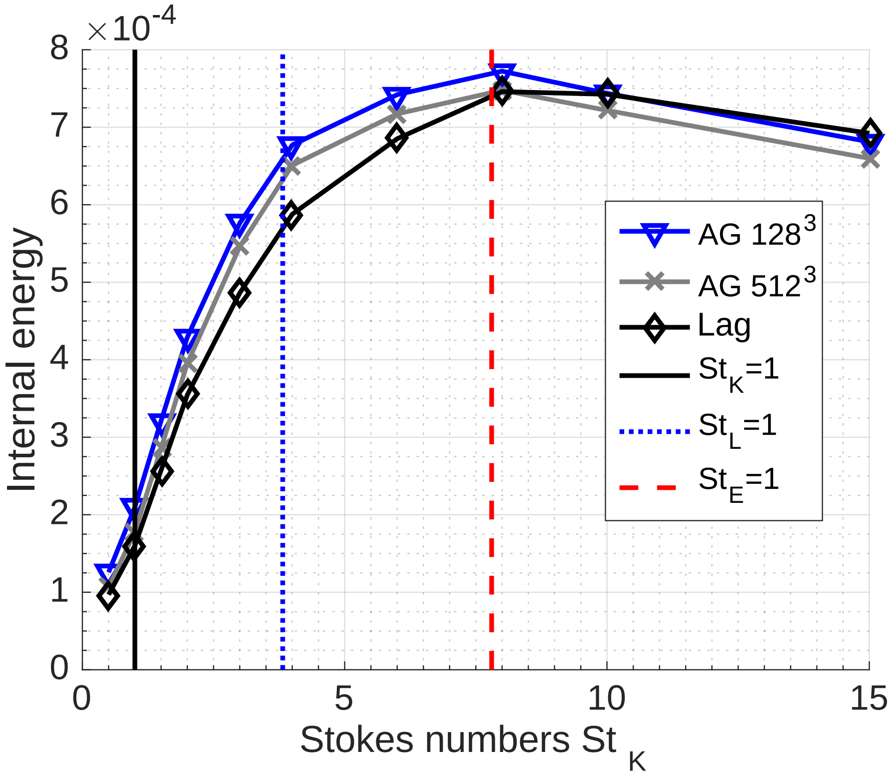

Figure 8.56: *Mean total energy as a function of Stokes number (zoom in) for Lagrangian result and Anisotropic Gaussian results on the* 128^3 *and* 512^3 *meshes at* t_f*.*

Finally, the profile for the energy ratio as a function of the particles inertia is also modified for high Stokes number when evaluated at t_f. Actually, the intersection between the ratio of the mean correlated energy and the mean internal energy to the mean total energy is observed with the Lagrangian results around $\mathrm{St}_K = 14$. Knowing that this behavior is reproduced by the AG results on the 128^3 mesh, but this measure diverges from the Lagrangian reference and the intersection is clearly not reached yet for the AG simulations on the 512^3 mesh.

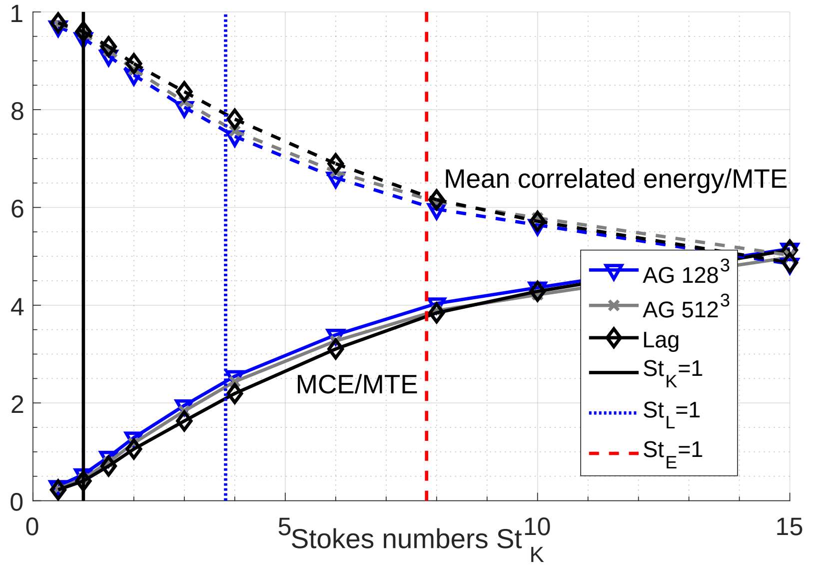

(a) Full scale

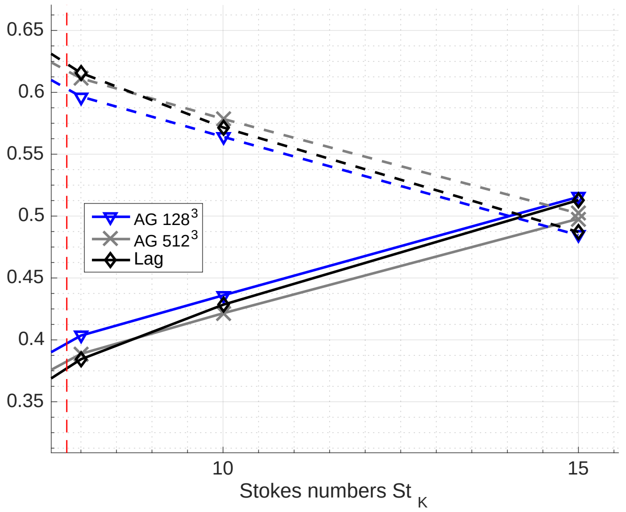

(b) Zoom in

Figure 8.57: *Mean energy ratios as a function of Stokes number for Lagrangian result and Anisotropic Gaussian results on the* 128^3 *and* 512^3 *meshes with projection on the same* 64^3 *mesh at* t_f*.*

In order to compare the effect of the particle inertia on the energy ratio found in this work with the results of *Février et al. (2005)*, the time scale ratio should be computed. This latter is equal to the ratio of the fluid integral time scale sampled along particle trajectories over the relaxation time of the particles.

Figure 8.58 illustrates the comparison between the energy ratio versus the time scale for the DNS Lagrangian results and the DNS Anisotropic Gaussian results on the 128^3 and 512^3 meshes along with the DNS Lagrangian results of particles inclusion in a fluid flow simulated using a grid of 128^3 and having a turbulent Reynolds number $\mathrm{Re}_L = 110$.
In *Février et al. (2005)*, these curves were plotted for various DNS and LES simulation having different turbulent Reynolds numbers and different parameters for the forcing schemes. The highlighted result is that the evolution of the energy ratios versus the time scale ratio were similar for all the carried simulations. Thus, in this work it is enough to compare this evolution with one of the results presented in *Février et al. (2005)*. It is important to note that in the work of *Février et al. (2005)*:

- the ratio of the mean correlated kinetic energy to the mean total kinetic energy is refered to as the mesoscopic Eulerian particle velocity field (MEPVF) contribution of the total turbulent kinetic energy;
- the ratio of the mean internal (or central) kinetic energy to the mean total kinetic energy (MCE/MTE) is refered to as the quasi-Brownian velocity distribution (QBVD) contribution of the total turbulent kinetic energy.

From Figure 8.58, one can conclude that the results of this work in terms of the evolution of the relative contribution of the mean internal energy and the mean correlated energy in the mean total kinetic energy as a function of the time scale ratio are similar to the results presented in *Février et al. (2005)*.

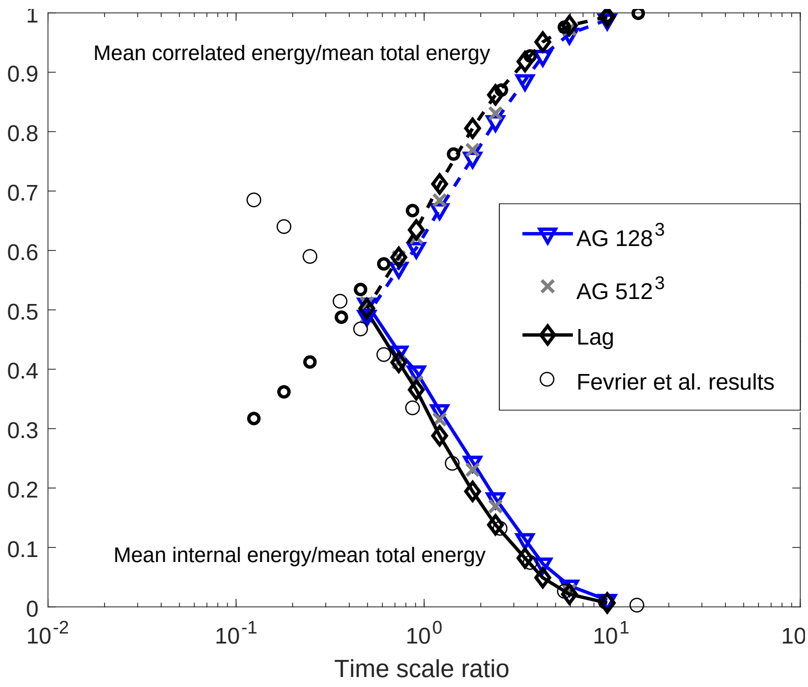

Figure 8.58: *Mean energy ratios versus the time scale for Lagrangian result and Anisotropic Gaussian results compared to the DNS results of Février et al. (2005)*

8.4 Conclusion

From the qualitative and statistical results presented in this chapter, several conclusion can be drawn.

First, for particle having small inertia $\mathrm{St}_K < 1$ both Eulerian models lead to accurate results. The qualitative results as well as the scatter plots for the one-point correlation and the quantitative statistical mean results highlight the inference that the MK and the AG reproduce the right physics in this case in comparison with the Lagrangian results. The MK model has the advantage of being less expensive than the AG model since in 3D the number of equations to be solved is only 4 for the MK model, versus 10 equations for the AG models. Thus, the MK is preferred over the AG model for the simulation of the disperse phase having a Stokes number based on the Kolmogorov scale less than 1. Also it can be more accurate whenever solved with adapted numerical methods such as the Finite Volume Kinetic Scheme or the new RKDG class presented in Part III. However, it is important to keep in mind the fact that the AG model has the advantage of capturing PTC that can locally occur when the local Stokes number overcomes the critical one. Here comes the importance of coupling these two models with adapted numerical methods based on relaxation schemes as in the work of *Boileau et al. (2015)*.

Second, for the moderately inertial to inertial disperse phase, the AG model gives the right qualitative behavior whereas the MK model ceases to reproduce the right dynamics of the disperse phase for Stokes numbers $St_K > 1$.

In addition, whenever the particle relaxation time is in the range between the Kolmogorov time scale and the Eulerian integral time scale characterizing the large eddies, the temporal evolution of the statistical mean variables is captured precisely with the AG model. The shape of the evolution of these quantities as a function of the particles inertia for a given time is also reproduced correctly in comparison with the Lagrangian reference.

For inertial to very inertial particles, $St_E \geq 1$, the AG model gives much better results than the MK model in comparison with the Lagrangian reference. The percentage of the error obtained with the 512^3 is no more than 10% for the segregation in the studied cases, whereas the error with MK model is large. Nevertheless, the AG model start diverging from this reference from the statistical point of view, when refining the mesh. For the studied fluid flow, the limits $St_E = 1$ corresponds to $St_L = 2.043$.

Finally, knowing that the comparisons presented in this chapter are very important steps towards the validation of the AG model, it is though not enough to clearly define the limits of this model and to fully understand its constraints. For this reason, quantitative results for the distribution function and the autocorrelations function are presented in the next chapter.

Chapter 9

Distribution functions and autocorrelations

In the previous chapter the AG model was found to give accurate results for $\mathrm{St}_E < 1$ *from a qualitative and mean statistical point of view. These conclusions are essential for the validation of the model in 3D but they are not sufficient for understanding the limits of this model and clearly defining its domain of applicability. For that purpose, further quantitative comparisons are presented in this chapter. Theses comparisons are more complicated than the quantitative mean statistics computed over the whole domain, presented in the previous chapter, and they lead to a more detailed analysis. The results are divided into two parts.*

First, the distribution functions of the number density, velocity and trace of the pressure matrix are presented for the different models for four St *belonging each to a different range of inertia, namely* $\mathrm{St} = 0.5, 1, 3$ *and* 8*. For the Eulerian results, the mesh refinement is also taken into account. In addition the distribution function of the disperse phase Mach number* $\mathrm{Ma_p}$ *is also presented. This is done for a classical measure for* $\mathrm{Ma_p}$ *and for another measure based on the ratio of the slip energy to the internal energy.*

Second, the autocorrelation of the number density and the autocorrelation of the velocity are shown for the different models and different Stokes numbers. Based on the number density autocorrelation, a characteristic size of the accumulation zones is defined and compared between the different models for the studied range of Stokes numbers. Similarly, the integral length scale based on the velocity autocorrelations is investigated. Based on the same method, a characteristic length scale of the PTC is also defined through an autocorrelation function for the trace of the internal energy.

Finally, the Stokes number range for which the use of the AG is mostly suitable is confirmed ($\mathrm{St}_K > 1$ *and* $\mathrm{St}_E < 1$*).*

9.1 Distribution functions

There exists several ways to evaluate the distribution of a given quantity. Numerically, they are all based on the idea of dividing the quantity in questions into bins and counting the number of elements found in each container or bin. For example, Figure 9.1 shows the distribution of the number density for the Lagrangian, AG and MK results on the 128^3 DNS mesh for $\mathrm{St} = 8$. On the left, we have the standard histogram plot displaying rectangles, with height proportional to the number of elements in the bin. On the right, the distribution function is plotted as the counts versus the location of the bin's center. In the following, this latter display is chosen for clarity. In addition, the resulting number of elements in each bin can be normalized by the area under the obtained curve. In this way, the resulting distribution function is a probability density function. Another possible way is to normalize the original distribution function by the total number of elements. We will use the first option to visualize the distribution.

In this section, the distribution function of the number density, the velocity, the trace of the pressure tensor and the PTC intensity are presented. For each of these quantities the results are divided into two parts. First, the distribution functions are plotted over the studied range of Stokes number. This is done for the Lagrangian, MK and AG model for a given mesh to check whether the Eulerian models have the same dependency of the distribution function on the Stokes numbers as the Lagrangian one. Second, for a given Stokes number, the distribution function of the Lagrangian result, AG and MK results on 64^3, 128^3, 256^3 and 512^3 meshes are plotted. This helps us to accurately evaluate the distribution function for the Eulerian results in comparison with the Lagrangian results and to examine the effect of mesh refinement.

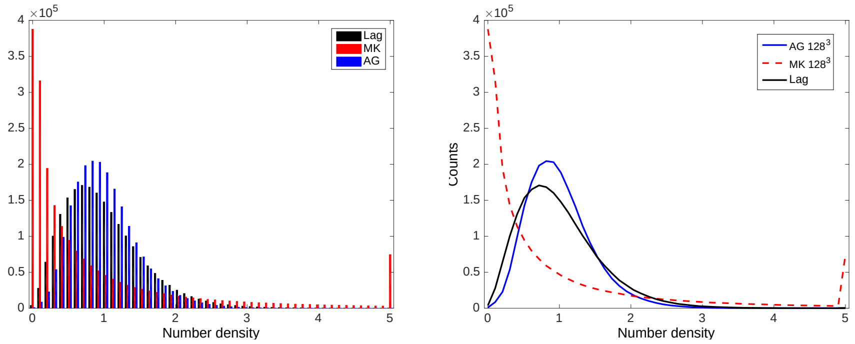

(a) Histogram (b) Distribution

Figure 9.1: *Distribution of the number density for the Lagrangian, AG and MK results on the* 128^3 *mesh for* $\mathrm{St} = 8$

9.1.1 Number density distribution function

In Figure 9.2, stacked plots of the distribution functions for the various Stokes numbers are shown. The trend of the curves as a function of the Stokes number obtained from the AG results matches the tendency observed for the Lagrangian results. Except for the degree of vacuum that is clearly underestimated for Stokes numbers around 1, the AG model captures the form of the distribution function. In the next paragraph this difference is found to be only due to the numerical diffusion. For the MK results, the distribution function of the number density does not change its form for St > 1. Actually when the Stokes number increases, the MK results have an increasing degree of void and a larger maximum number density due the singularities of the model such as the δ-shock generated at every crossing.

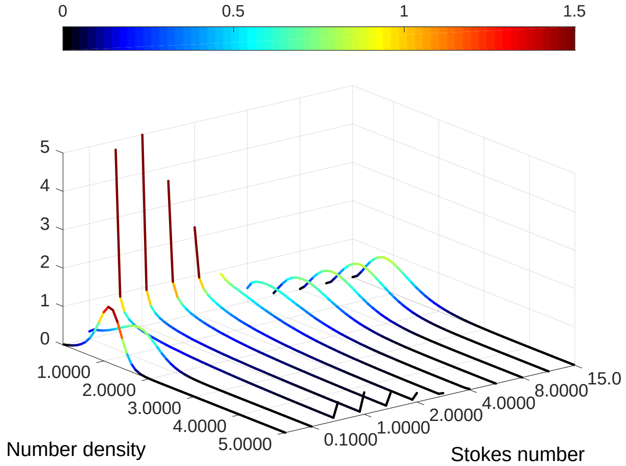

(a) Lagrangian

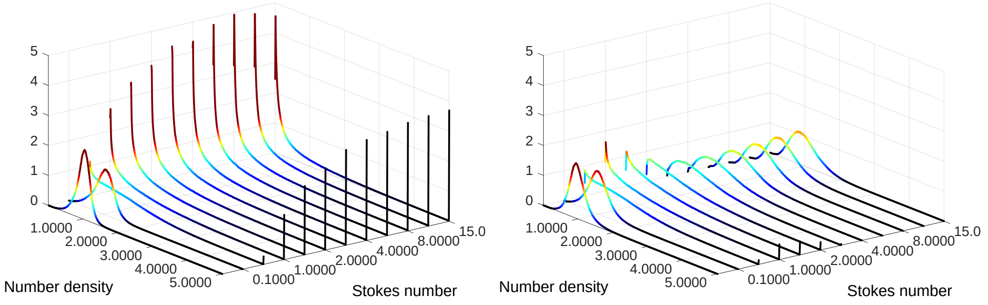

(b) MK on 128^3 mesh (c) AG on 128^3 mesh

Figure 9.2: *Distribution of the number density for different Stokes numbers*

For a Stokes number St $= 0.5$, in the case of a fine mesh, both Eulerian results match well the distribution function of the number density of the Lagrangian result (Figure 9.3). The Lagrangian results have however a greater degree of vacuum that is not reached yet with the most refined mesh studied due to the numerical diffusion. The number density PDFs obtained from the AG and MK results are very similar since the percentage of PTC occurrence is very low based on the distribution of the local dissipation rate shown in Figure 7.8.

For the critical Stokes number, St = 1, both Eulerian results tend to approach the number density PDF of the Lagrangian result (Figure 9.4) with mesh refinement. The PDF obtained from the MK result on the 512^3 mesh is however closer to the Lagrangian PDF than the AG one. The MK result might diverge from the Lagrangian with more mesh refinement since the amount of local Kolmogorov time scales equal or smaller than the relaxation time of the particles, is 11.22% and PTC might occur. This explains the difference between the MK and the AG results.

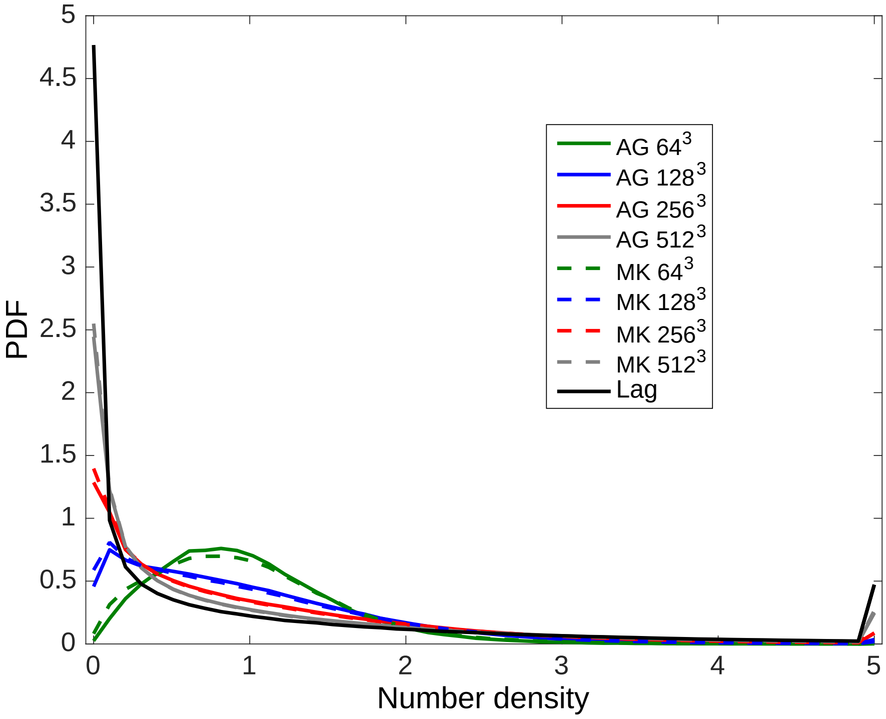

Figure 9.3: *Number density PDF for the Lagrangian, AG and MK results on* 64^3, 128^3, 256^3 *and* 512^3 *meshes for* $\mathrm{St} = 0.5$

For moderately inertial disperse phase, the number density PDF of the AG result approaches the Lagrangian one when refining the mesh, except for the underestimation of the vacuum zone. The MK number density distribution is clearly moving away from the Lagrangian one when refining the mesh and gives a higher number of elements where the number density is zero or very small (Figure 9.5) due to the singularities created by this model when PTC is occurring.

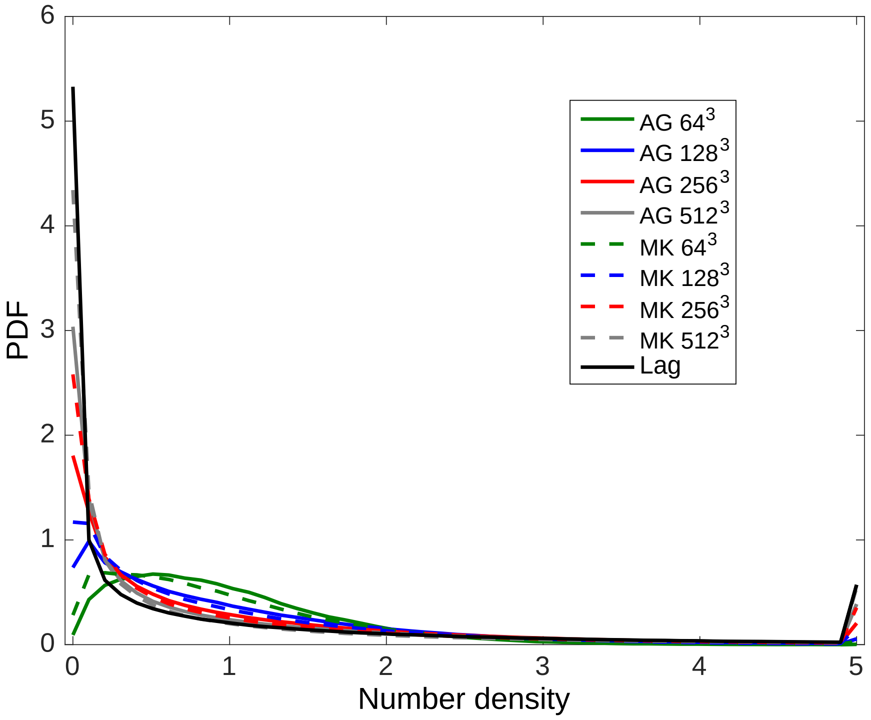

Figure 9.4: *Number density PDF for the Lagrangian, AG and MK results on* 64^3*,* 128^3*,* 256^3 *and* 512^3 *meshes for* $\mathrm{St} = 1$

For a high Stokes number, the distribution of the number density is plotted in Figure 9.6 at $t = 40$. In this case the curve of AG has the same form as the Lagrangian one, even for the coarsest meshes. This curve is however shifted to higher number densities: the maximum of the distribution is obtained for a higher number density. The MK result leads to the same shape for the number density PDF as for the smaller Stokes numbers. Nevertheless, for a longer time, $t = 80$, the number density distribution function resulting from the AG simulations start to digress from the Lagrangian reference with mesh refinement. This means that for the inertial particle, for a time long enough compared to the relaxation time of the particles, the AG model is no longer suitable for describing the underlying dynamics. Based on the nature of the model, this is expected since for high inertial particles, the PTC begins to happen at large scales and in this case the statistical description of the PTC through a velocity dispersion tensor is no longer sufficient. This possible explanation is still to be confirmed. It is important to note that this studied Stokes number $\mathrm{St}_K = 8$ corresponds to $\mathrm{St}_E = 1.026$.

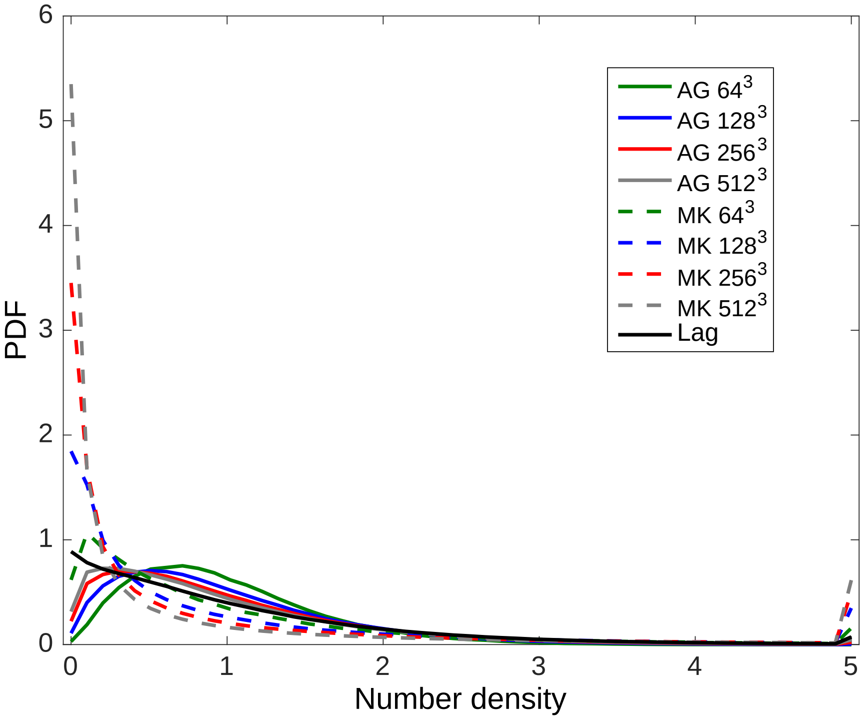

(a) MK and AG

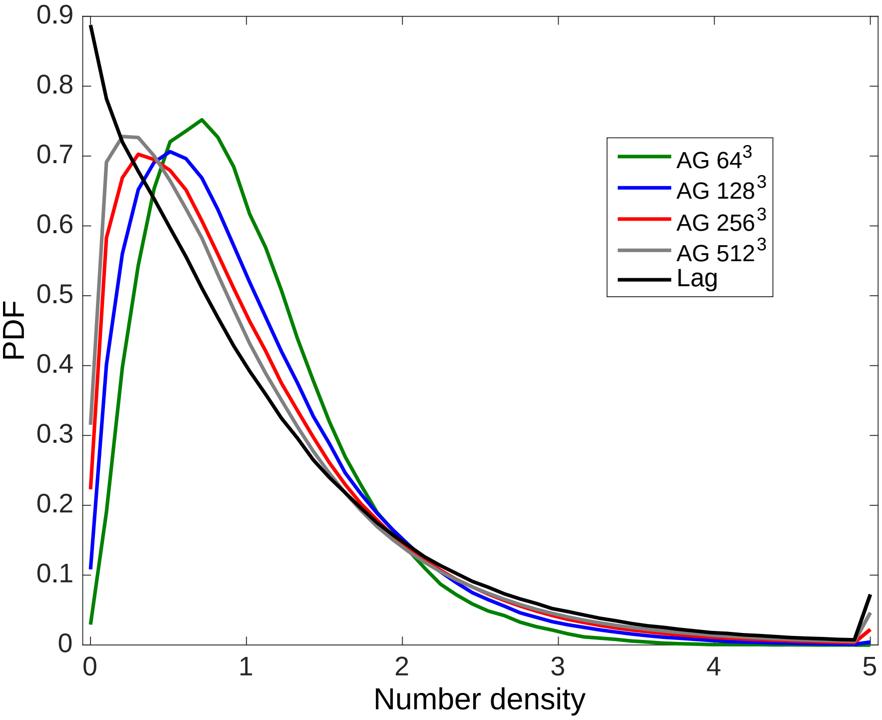

(b) AG

Figure 9.5: *Number density PDF for the Lagrangian, AG and MK results on* 64^3, 128^3, 256^3 *and* 512^3 *meshes for* $\mathrm{St} = 3$

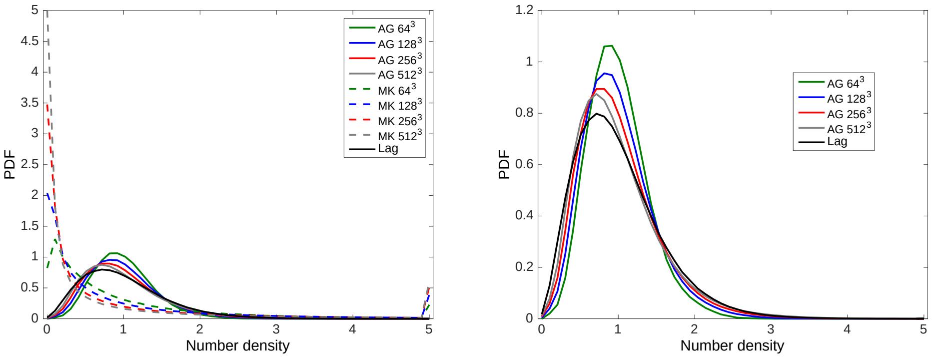

(a) MK and AG

(b) AG

Figure 9.6: *Number density PDF for the Lagrangian, AG and MK results on* 64^3, 128^3, 256^3 *and* 512^3 *meshes for* $\mathrm{St} = 8$ *at* $t = 40$

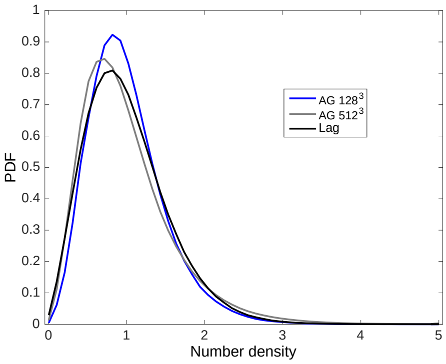

Figure 9.7: *Number density PDF for the Lagrangian, AG and MK results on* 128^3 *and* 512^3 *mesh for* $\mathrm{St} = 8$ *at* $t = 80$

9.1.2 Velocity distribution function

The distribution of the x-component of the velocity for different Stokes numbers shows that the more inertial the particles are, the narrower is the distribution function around 0, as depicted in Figure 9.8. This behavior is the same for all the models. Actually, for small Stokes numbers the distribution function is similar to that of the x-component of the gas velocity, as it will be shown in the next paragraph. It is important to note that the PDF of the velocity for the Lagrangian results is displayed without taking into account the vacuum zones where the velocity is zero. This is done to provide a better comparison of the velocity distribution between the different models, without including information about the vacuum zones that was already analyzed through the number density distribution in the previous subsection.

For a more detailed comparison, the distribution functions of the Lagrangian, AG and MK velocity in the x-direction are plotted.

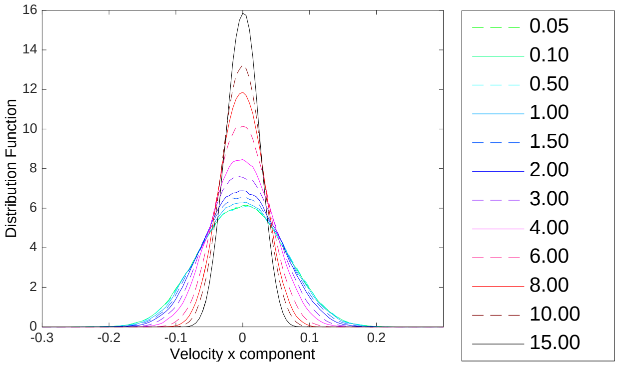

(a) Lagrangian

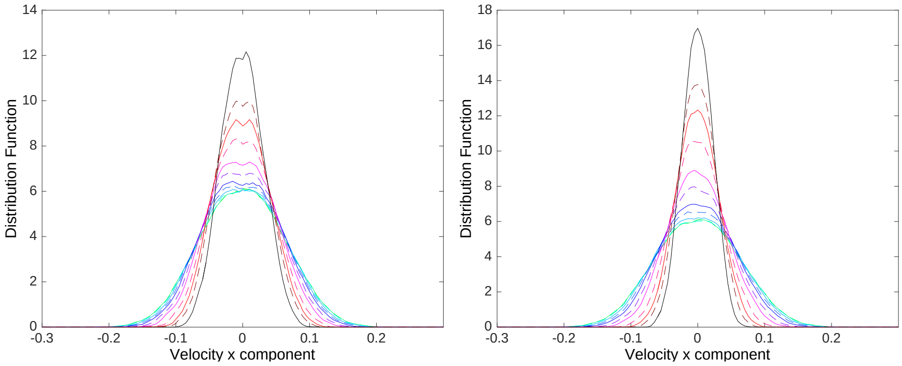

(b) MK on 128^3 mesh (c) AG on 128^3 mesh

Figure 9.8: *PDF of the x-component of velocity for different Stokes numbers*

First, for St $= 0.5$, the distribution functions for the disperse phase velocity in Figure 9.9 are much alike and they are similar to the gas velocity PDF. In this case, the motion of the disperse phase is totally governed by the carrier motion since the particles are small enough and thus are strongly correlated to the gas. For this Stokes number, the mesh refinement does not affect significantly the distribution function. The same behavior is obtained for $\mathrm{St} = 1$, where the only difference is depicted for very small velocities where the AG result on the refined mesh captures the information more accurately than the MK one (see Figure 9.10). For these near 0-velocities, we can observe a drift from the PDF of the gas that is caused by the possible local PTC occurrence which explains the ability of the AG to capture this difference when the MK model ceases to do so.

For $\mathrm{St} = 3$, the AG result matches the Lagrangian one except near zero velocity. For the MK results the velocity in the x-direction is less congregated near zero velocity and a bit more assembled near the maximum and minimum values (Figure 9.11). The velocity PDF of the MK result is not affected significantly by the mesh refinement and is closer to the carrier phase velocity PDF than the Lagrangian and the AG one. For the AG result, the distribution level of the AG velocity matches to the Lagrangian except near zero-velocity. In this case the difference with the carrier PDF is significant leading to an important slip velocity. In fact, in this case the PTC governs the motion of the disperse phase since 91.46% of the local Stokes number is higher than the critical one. Thus, at each crossing event the kinetic energy is transformed to internal energy, which explains the decrease in the disperse phase velocity. This behavior is accurately captured by the AG model. As for the MK model, first, it generates more total kinetic energy than the actual one since it does not transform any part of this energy to internal energy and second, a part of the total kinetic energy is lost irreversibly, as mentioned in the previous chapter. This irreversible energy loss, is due to the unphysical singularities that the MK model generates at PTC locations and to the fact that the conservation of the kinetic energy of the disperse phase is not taken into account.

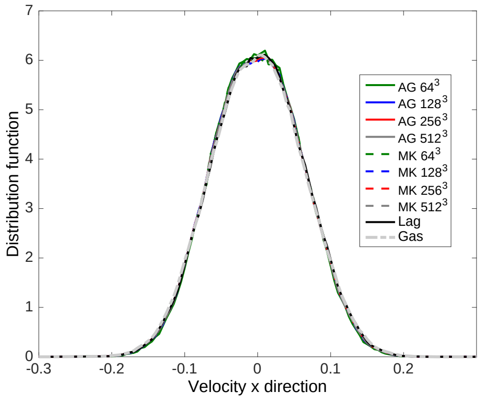

Figure 9.9: *PDF of the x-velocity for the Lagrangian, AG and MK results on* 64^3, 128^3, 256^3 *and* 512^3 *meshes for* $\mathrm{St} = 0.5$

The difference between the MK velocity distribution function and the La-

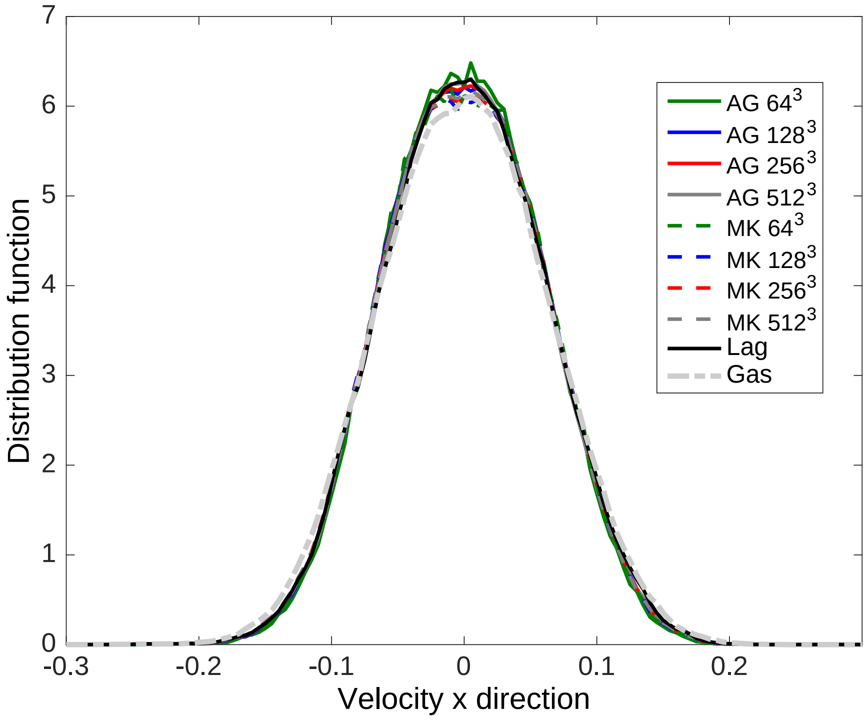

Figure 9.10: *PDF of the x-velocity for the Lagrangian, AG and MK results on* 64^3, 128^3, 256^3 *and* 512^3 *meshes for* $\mathrm{St} = 1$

grangian one is accentuated in the case of inertial particles (Figure 9.12). The degree near zero-velocity is underestimated with the MK model, and is scattered instead around the maximum and minimum values of the velocity in the x-direction. On the other hand, the velocity distribution with AG matches accurately the one obtained using the Lagrangian model at $t = 40$ and $t = 80$. The only effect of the mesh refinement is here noted around 0-velocity where for finer meshes at $t = 80$, the AG result starts to very slightly diverge from the Lagrangian one).

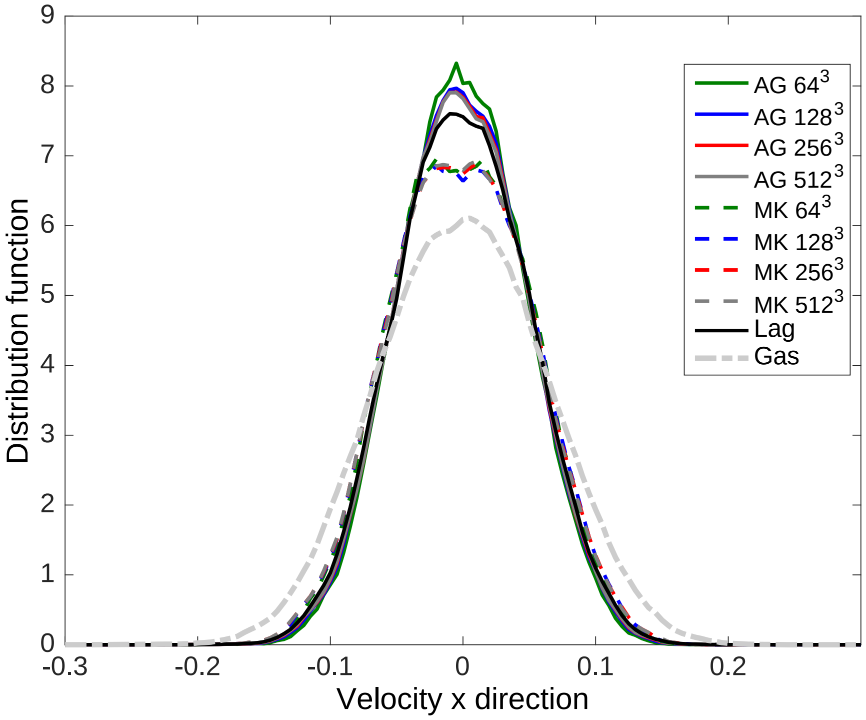

Figure 9.11: *PDF of the x-velocity for the Lagrangian, AG and MK results on* 64^3, 128^3, 256^3 *and* 512^3 *meshes for* $\mathrm{St} = 3$

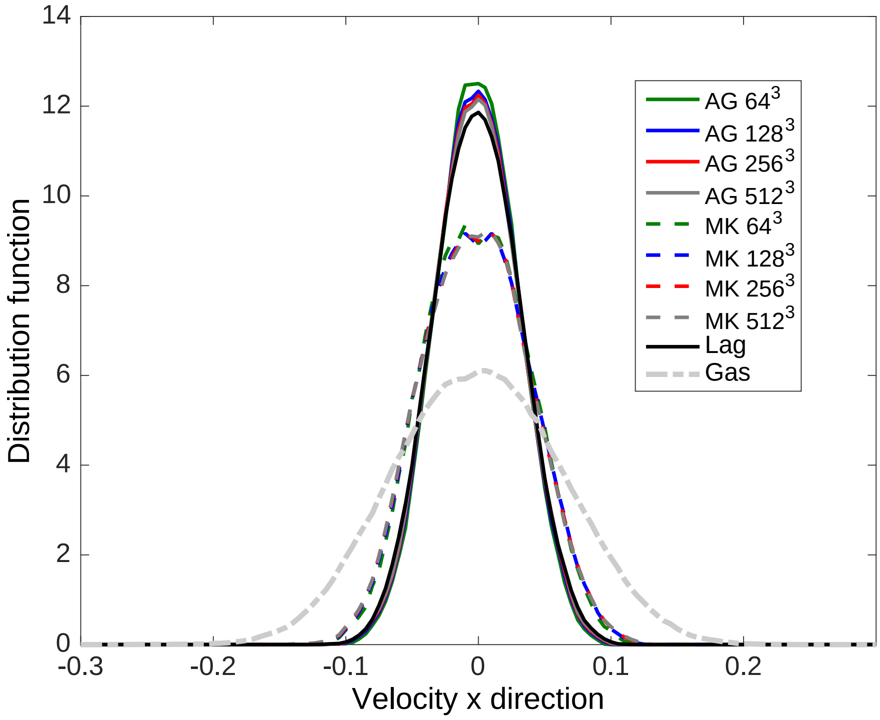

(a) $t = 40$

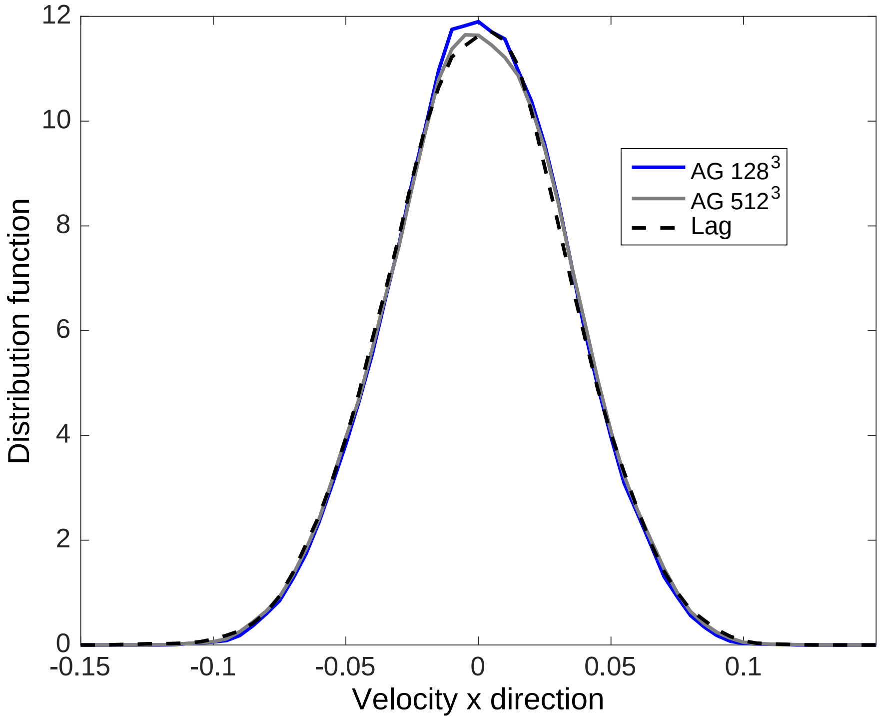

(b) $t = 80$

Figure 9.12: *PDF of the velocity in the x-direction for the Lagrangian, AG and MK results on* 64^3, 128^3, 256^3 *and* 512^3 *meshes for* $\mathrm{St} = 8$

9.1.3 PDF of the trace of the pressure tensor

The evolution of the distribution function of the pressure trace for different Stokes number can be evaluated (Figure 9.13). Actually, the higher the Stokes number, the lower the number of particles that have zero pressure and therefore zero internal energy. This was already expected from the mean energy ratio results versus Stokes number presented in the subsection 8.3.3 where it was found that low inertia particles have high mean correlated kinetic energy and very low mean internal energy. In addition, the number of particles having significant pressure increases with the Stokes number. Thus, the occurrence of PTC is more probable for higher Stokes numbers. This behavior can be noticed from both the Lagrangian and AG results.

To accurately evaluate the degree of PTC captured by the AG model, the distribution functions of the trace of the pressure tensor of the Lagrangian and AG simulations on different meshes are plotted.

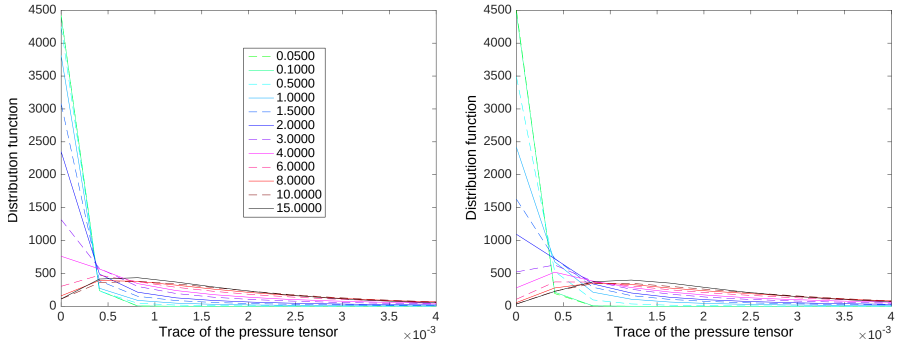

(a) Lagrangian zoom in (b) AG on 128^3 mesh zoom in

Figure 9.13: *Distribution of the pressure for different Stokes numbers*

For St = 0.5 and St = 1, the distribution function of the AG results tends to the Lagrangian one when refining the mesh (see Figures 9.14 and 9.15). In these two cases, the highest amount of particles have zero or very small pressure since, as explained previously, the probability of having local Stokes numbers higher than the critical one is less than 1% and 12% for St = 0.5 and St = 1 respectively.

For the moderately inertial particles, St = 3, the PDF of the pressure tensor is shown in Figure 9.16. The form of the PDF of the pressure trace for the AG result, on the different meshes, matches the Lagrangian one for high pressures. However, for zero pressure, the number of particles is underestimated by the AG results, especially on the coarse mesh. When refining the mesh, the difference between the distribution function of the internal energy resulting from the AG solution and the Lagrangian solution is decreased. Actually, the internal energy included two contributions, one is purely related to the model and is the reason

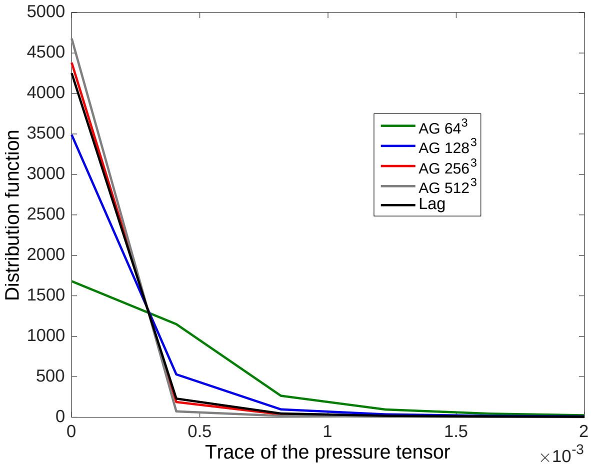

Figure 9.14: *PDF of the pressure for the Lagrangian and AG results on* 64^3, 128^3, 256^3 *and* 512^3 *meshes for* $\mathrm{St} = 0.5$

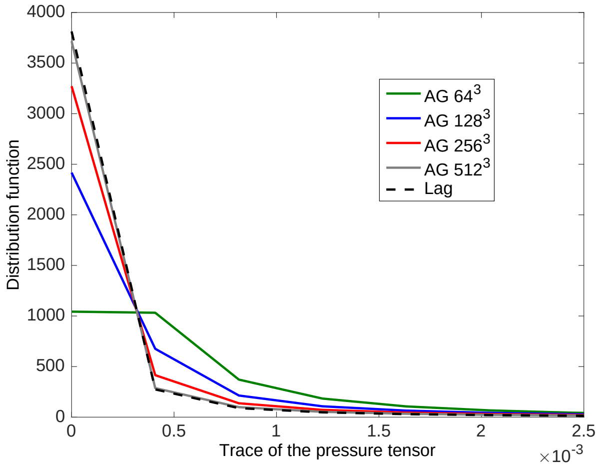

Figure 9.15: *PDF of the pressure for the Lagrangian and AG results on* 64^3, 128^3, 256^3 *and* 512^3 *meshes for* $\mathrm{St} = 1$

why the AG results are able to capture PTC and the other one is the effect of the numerical diffusion. This explains the convergence of the PDF of the internal energy using the AG model when refining the mesh, since by doing so, the second contribution is decreased and the physical behavior because preponderant; whereas for the coarsest mesh, the numerical diffusion part is overriding.

For the high Stokes number, $\mathrm{St} = 8$ (Figure 9.17), the PDF of the trace of the pressure tensor for the AG result tends to the Lagrangian one when refining the mesh at $t = 40$. However, at $t = 80$, the difference between the maximum of distribution function resulting from the AG simulations slightly diverges from the Lagrangian one, the same behavior is observed for the location of the

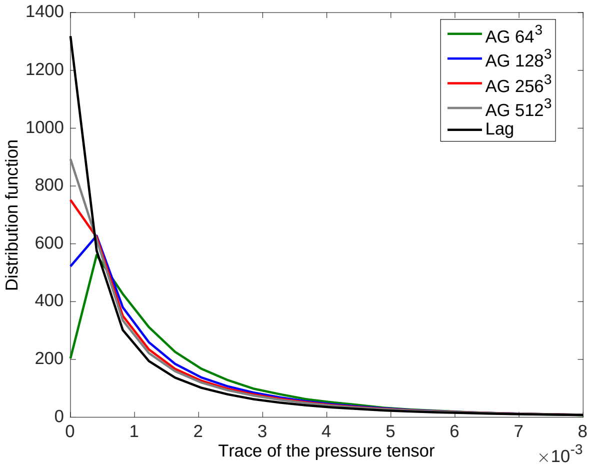

Figure 9.16: *PDF of the pressure for the Lagrangian and AG results on* 64^3, 128^3, 256^3 *and* 512^3 *meshes for* $\mathrm{St} = 3$

maximum.

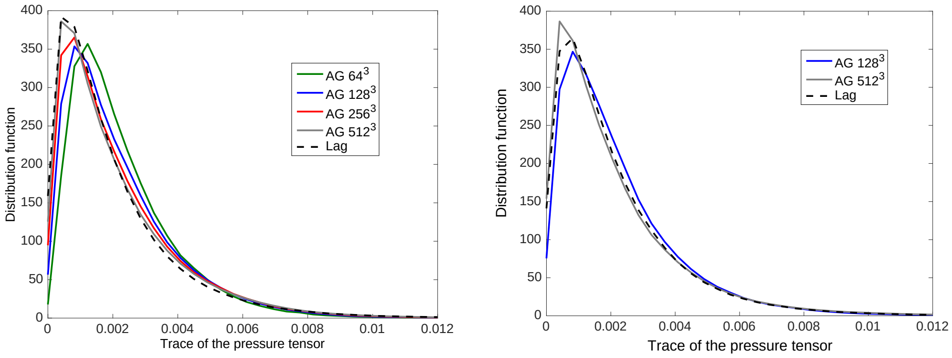

(a) $t = 40$ (b) $t = 80$

Figure 9.17: *PDF of the pressure for the Lagrangian and AG results on* 64^3, 128^3, 256^3 *and* 512^3 *meshes for* $\mathrm{St} = 8$

9.1.4 Disperse phase Mach number

9.1.4.1 Classical definition

A possible measure to evaluate the ratio of the mean motion to the velocity dispersion is the disperse phase Mach number $\mathrm{Ma_p}$. This Mach number is defined in analogy to the compressible gas dynamics as the ratio of the characteristic mean particle velocity and the speed of sound in the disperse phase (*Marchisio and Fox 2013*).

Based on this definition, it is directly obvious that for $\mathrm{Ma_p} > 1$ the mean advection is predominant, whereas for $\mathrm{Ma_p} < 1$, it is the velocity dispersion that overrides and governs the dynamics of the disperse phase through the internal energy.

$$\mathrm{Ma_p} = \frac{\|\vec{\boldsymbol{u}}\|}{\sqrt{\|\boldsymbol{\Sigma}\|}}. \tag{9.1}$$

This disperse phase Mach number is investigated for the different models and Stokes numbers.

For small Stokes number $\mathrm{St} = 0.5$, the PDF and cumulative distribution function (CDF) of $\mathrm{Ma_p}$ are plotted in Figure 9.18. In this case when refining the mesh, the AG does not seem to approach the Lagrangian PDF. This is not a very important difference since it is already known that in this case the particles are tracers and they do not have their own inertia but instead their motion is highly correlated to the underlying gas velocity. In fact, in this case the internal energy tends to zero and $\mathrm{Ma_p}$ tends to infinity. Thus, for computational purpose, a threshold was applied to the minimal value of the internal energy taken into account in $\mathrm{Ma_p}$ otherwise for this Stokes number we would have infinity $\mathrm{Ma_p}$ almost everywhere of the domain. Nevertheless, one can still see the very large $\mathrm{Ma_p}$ obtained through the CDF. In this case no significant PTC occur and the small velocity dispersion found through the Lagrangian result may be only due to the projection of the Lagrangian results on the Eulerian mesh. Once again, the predominant contribution of the numerical diffusion in the covariance matrix, for the AG result on the coarsest mesh, can be observed through the small value of $\mathrm{Ma_p}$ compared to the Lagrangian one.

For Stokes number $\mathrm{St} = 1$, the PDF and CDF of $\mathrm{Ma_p}$ for the AG results on the refined mesh have the same shape as the Lagrangian distributions (see

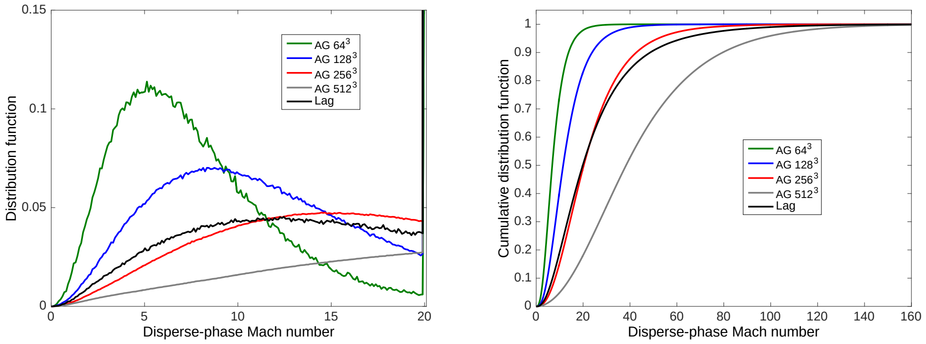

(a) PDF

(b) CDF

Figure 9.18: *Distribution function of the disperse phase Mach number for the Lagrangian and AG results on* 64^3, 128^3, 256^3 *and* 512^3 *meshes for* $\mathrm{St} = 0.5$

Figure 9.19). However, for the AG result on the 512^3 mesh, the maximum of the PDF is at a Mach number ${\rm Ma_p}^{max}$ lower than the one obtained with the Lagrangian result. For ${\rm Ma_p} > {\rm Ma_p}^{max}$, the Lagrangian simulation provides a higher level of matter than the one obtained through the 512^3 AG result. In this case, when refining the mesh, the AG results generates Mach numbers that are in accordance with the Lagrangian ones for ${\rm Ma_p} \leq 2$. Beyond this limit the ${\rm Ma_p}$ is underestimated by the AG model on the most refined mesh.
For the last two St, the hypercompressibility effect governs the dynamics of the disperse phase as we can see though the large ${\rm Ma_p}$ reached.

When it comes to the moderately inertial case for the Stokes number ${\rm St} = 3$, the shape of the distribution functions of ${\rm Ma_p}$ resulting from the AG simulation are similar to the Lagrangian one. They move toward the Lagrangian results with mesh refinement. The location of the maximum is however slightly underestimated with the AG model but this model leads to higher number of particles at this maximum as compared to the Lagrangian reference. For this intermediate St, a rich variety of phenomena coexist, the mean advection still has an important role but the PTC is as important as the mean advection if not predominant for governing the dynamics of the disperse phase. The AG model is able to accurately capture this variety as it is illustrated by the distribution functions of ${\rm Ma_p}$ in Figure 9.20.

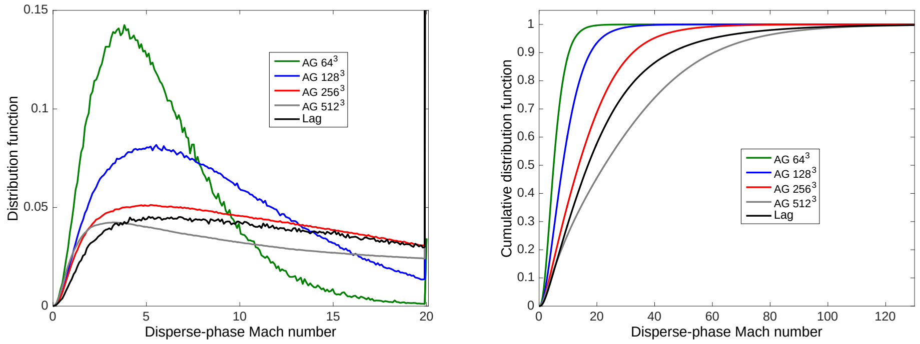

(a) PDF (b) CDF

Figure 9.19: *Distribution function of the disperse phase Mach number for the Lagrangian and AG results on* 64^3, 128^3, 256^3 *and* 512^3 *meshes for* ${\rm St} = 1$

A similar behavior is observed for ${\rm St} = 8$ at t=40 as for ${\rm St} = 3$, but in this case the difference between the Lagrangian and the AG result is increased as shown in Figure 9.21. Also, the convergence of the AG result to the Lagrangian one is clear through the CDF but is more questionable base on the PDF since in the range of $1 < {\rm Ma_p} \leq 2.3$ the level of distribution of ${\rm Ma_p}$ obtained with the AG model moves away from the Lagrangian one while refining the mesh. On the other hand, at $t = 80$ the AG result diverges from the Lagrangian one when refining the mesh. It is essential to note though, that right behavior is obtained

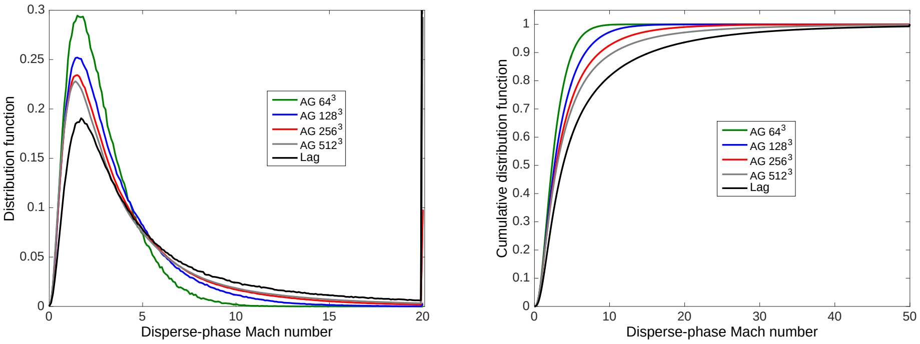

(a) PDF (b) CDF

Figure 9.20: *Distribution function of the disperse phase Mach number for the Lagrangian and AG results on* 64^3, 128^3, 256^3 *and* 512^3 *meshes for* $\mathrm{St} = 3$

for a $\mathrm{Ma_p} < 1$. This indicates that a comparison between the Lagrangian and AG results having $\mathrm{Ma_p}$ less or equal than a given limit might be an interesting way to better understand the limits of the AG model.

When comparing the percentage of the matter that has a $\mathrm{Ma_p} \leq 1$ and $\mathrm{Ma_p} \leq 2$ we notice that the AG gives better results for $\mathrm{Ma_p} \leq 2$ (see Figure 9.22). Nevertheless, this comparison is incomplete and should be also done at t=80, where the AG results where already found to sidetrack for high Stokes numbers ($\mathrm{St}_E > 1$).

For this reason, the percentage of the cumulative distribution having respectively $\mathrm{Ma_p} \leq 1$ and $\mathrm{Ma_p} \leq 2$ at $t = 80$ are presented in Figure 9.23. The quantity of particles having predominant velocity dispersion over the mean advection is estimated accurately by the AG model even for $\mathrm{St}_E > 1$ and this level tends to the Lagrangian one with mesh refinement. On the other hand, the AG model underestimates the quantity of particles having $\mathrm{Ma_p} \leq 2$ on the 512^3 mesh for $\mathrm{St}_E > 1$. When it comes to moderately inertial particles, the AG result is coherent with the Lagrangian reference independently on the time of the simulation and the limit chosen for the Mach number comparison.

The mean value of $\mathrm{Ma_p}$ over the domain is computed and plotted as a function of the Stokes numbers in Figure 9.24. For $\mathrm{St}_K > 1$, the mean value of $\mathrm{Ma_p}$ decreases with the increase of St. This behavior is capture by the AG model until $\mathrm{St}_E = 1$. Thus from an average value point of view, with the increase of the Stokes number, the transport due to the velocity dispersion becomes more prevailing in comparison to the mean advection.

Above this limit, as it is shown for t=80, the refined AG result overestimates the mean $\mathrm{Ma_p}$ for $\mathrm{St}_E > 1$.

When analyzing this measure of $\mathrm{Ma_p}$, the effect of drag is hidden in the mean advection part and can not be clearly compared to the velocity dispersion. Thus, in order to make sure that the analysis presented in this subsection is an

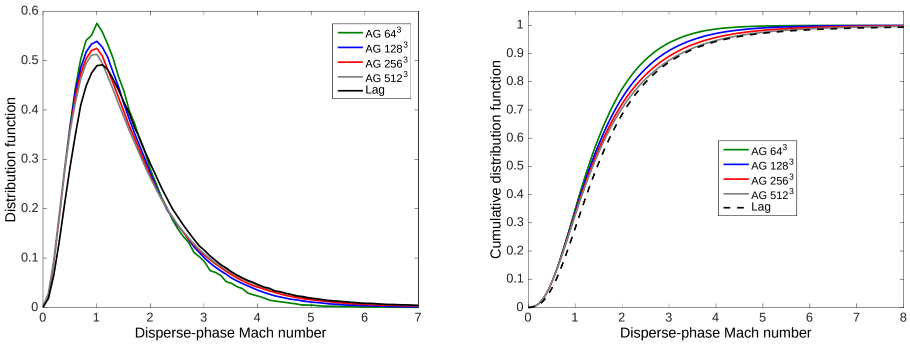

(a) PDF at $t = 40$ (b) CDF at $t = 40$

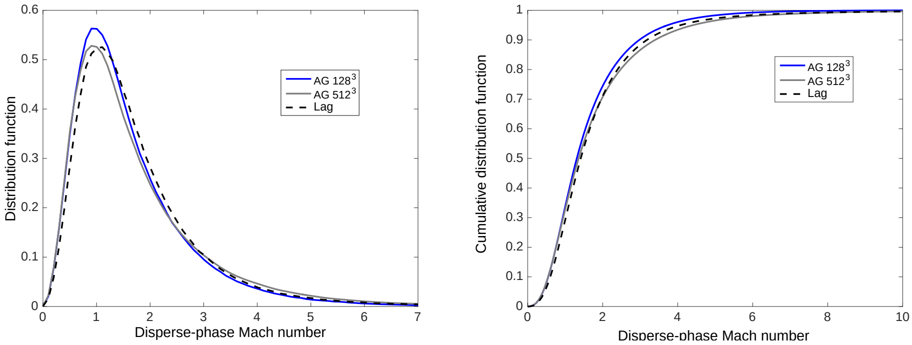

(c) PDF at $t = 80$ (d) CDF at $t = 80$

Figure 9.21: *Distribution function of the disperse phase Mach number for the Lagrangian and AG results with mesh refinement meshes for* $\mathrm{St} = 8$

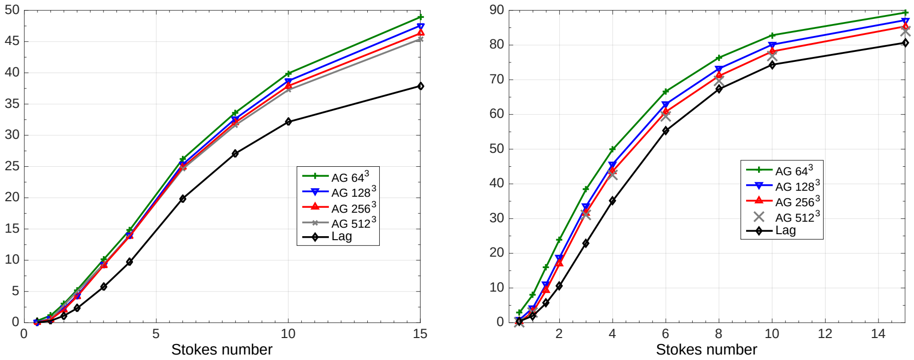

(a) $\mathrm{Ma_p} \leq 1$ (b) $\mathrm{Ma_p} \leq 2$

Figure 9.22: *Percentage of distribution for different* $\mathrm{Ma_p}$ *limits of the Lagrangian and the AG results on* 64^3, 128^3, 256^3 *and* 512^3 *meshes as a function of Stokes number at* $t = 40$

evidence that the AG model captures the event where the PTC is predominant

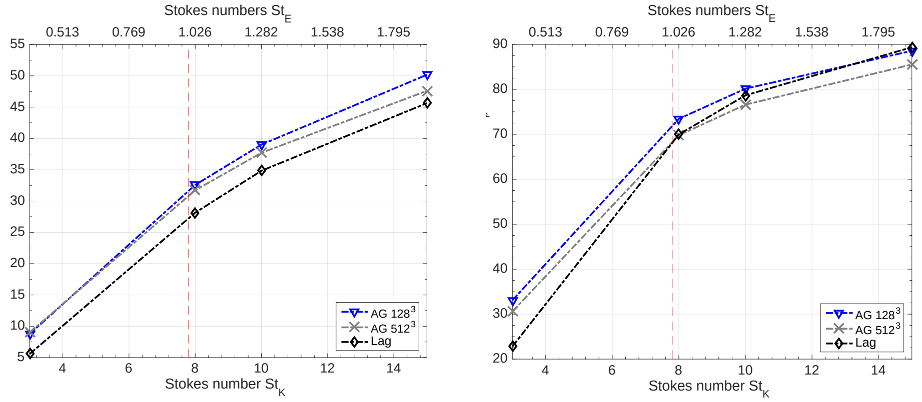

(a) $\mathrm{Ma_p} \leq 1$ (b) $\mathrm{Ma_p} \leq 2$

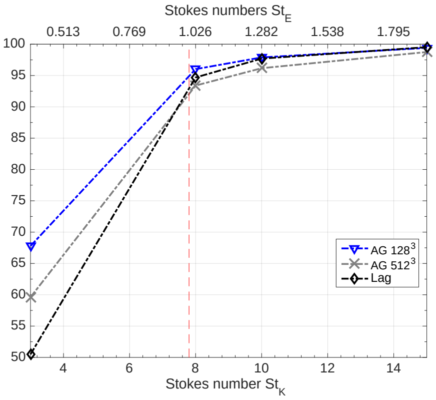

(c) $\mathrm{Ma_p} \leq 4$

Figure 9.23: *Percentage of distribution for different* $\mathrm{Ma_p}$ *limits of the Lagrangian and the AG results with mesh refinement as a function of Stokes number*

on the mean advection it is primordial to try to find another measure of the correlated to uncorrelated motion that clearly compares the dispersion to the relative motion.

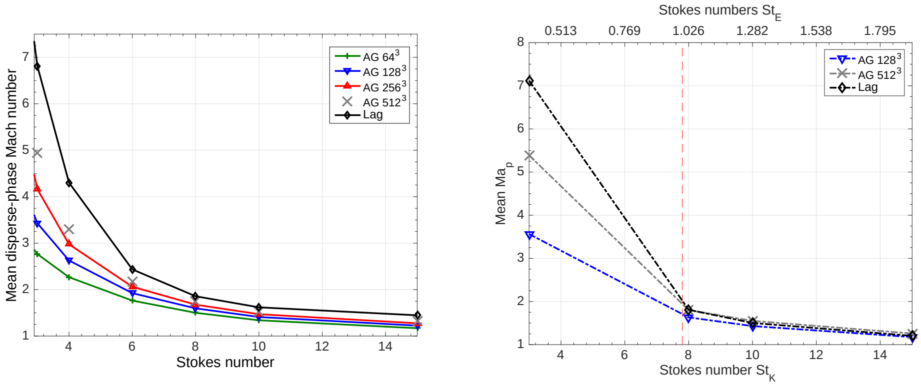

(a) t=40 (b) t=80

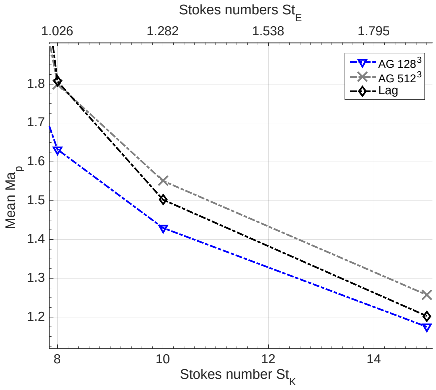

(c) t=80 (zoom in)

Figure 9.24: *Mean value of the disperse phase Mach number for the Lagrangian and AG results with mesh refinement as a function of Stokes number*

9.1.4.2 Definition based on energy ratios

In this paragraph a new definition for the disperse phase Mach number is derived. For simplicity this derivation is presented hereafter in 1D.

$$\partial_t(nV) + \partial_x(nV^2 + P) = \frac{n(U_g - V)}{\tau_p}. \tag{9.2}$$

First, the momentum equation in the AG model (Equation (9.2)) is non-dimensionalized. This equation can be writen using the material derivative notation as:

$$\mathrm{D}_t V = -\frac{\partial_x P}{n} + \frac{(U_g - V)}{\tau_p}. \tag{9.3}$$

In order to introduce the non-dimensional equation, the reference time τ_g and length scales L_0 are used and lead to a reference velocity $V_0 = L_0/\tau_g$. In addition a characteristic slip velocity V_{slp} and a typical pressure variation δP_0 are used. By using these reference variables, the non-dimensional variables are obtained:

$$x^* = \frac{x}{L_0}, \quad t^* = \frac{t}{\tau_g}, \quad V^* = \frac{V}{V_0}, \quad P^* = \frac{P}{\delta P_0}, \quad \text{and } (U_g - V)^* = \frac{(U_g - V)}{V_{slp}}. \tag{9.4}$$

The resulting dimensionless equation reads:

$$V_0^2 \mathrm{D}_{t^*} V^* = -\frac{\delta P_0}{n_0} \partial_{x^*} P^* + V_0 V_{slp} \frac{(U_g - V)^*}{\mathrm{St}}. \tag{9.5}$$

In the case of a specific PTC where V_0 is of the same order of V_{slp} and the two terms at the right hand side of Equation (9.5) balance out, we get:

$$\frac{\delta P_0}{n_0} \sim \frac{V_{slp}^2}{\mathrm{St}}. \tag{9.6}$$

Moreover, by combining the equation of the state $P = (\gamma - 1)ne$ where e is the internal energy, and the definition of the speed of sound C_0 we obtain that the internal energy is proportional to the square of the speed of sound as follows:

$$\frac{\gamma_0 \delta P_0}{n_0} = C_0^2 = \gamma_0(\gamma_0 - 1)e \sim e. \tag{9.7}$$

Finally the square of the Mach number is proportional to the square of the characteristic slip velocity and inversely proportional to the Stokes number and the internal energy.

$$\mathrm{Ma}^2 = \frac{\gamma_0 \delta P_0}{n_0 C_0^2} \sim \frac{V_{slp}^2}{e\ \mathrm{St}}. \tag{9.8}$$

By extending this result to the general AG equation, a new measure of the disperse phase Mach number $\mathrm{Ma_e}$ is obtained:

$$\mathrm{Ma_e} = \sqrt{\frac{n\left(\left\|\overrightarrow{\mathbf{U_g}} - \vec{\boldsymbol{u}}\right\|\right)^2}{\|\mathbf{P}\|\mathrm{St}}}, \tag{9.9}$$

where the norm of the pressure tensor is the trace of this tensor divided by 3:

$$\|\mathbf{P}\| = \frac{\mathrm{Tr}(\mathbf{P})}{3} = \frac{P_{ii}}{3}. \tag{9.10}$$

This definition takes into account the ratio of the slip energy to the dispersion energy with a dependency on the Stokes number.
The PDF of $\mathrm{Ma_e}$ is plotted in Figure 9.25 for different Stokes numbers at $t = 40$. In this case, as expected the Mach number is higher for small Stokes numbers

knowing that in this case the infinite Mach number is predominant over the whole domain due to the hypercompressibility effect. This infinite $\mathrm{Ma_e}$ is not shown in the PDF. The difference between the form of the $\mathrm{Ma_e}$ PDF of the AG and the Lagrangian results is big for small Stokes numbers where the maximum of the distribution is at smaller $\mathrm{Ma_e}$ for the AG results. For the moderately inertial to inertial cases, the form of the AG PDF matches the Lagrangian one and is expected to tend to the Lagrangian reference with mesh refinement.

For the inertial case at t=80, the PDF obtained from the AG simulation on the 128^3 mesh is very similar to the Lagrangian one, however it is expected to slightly diverge from this reference when refining the mesh.

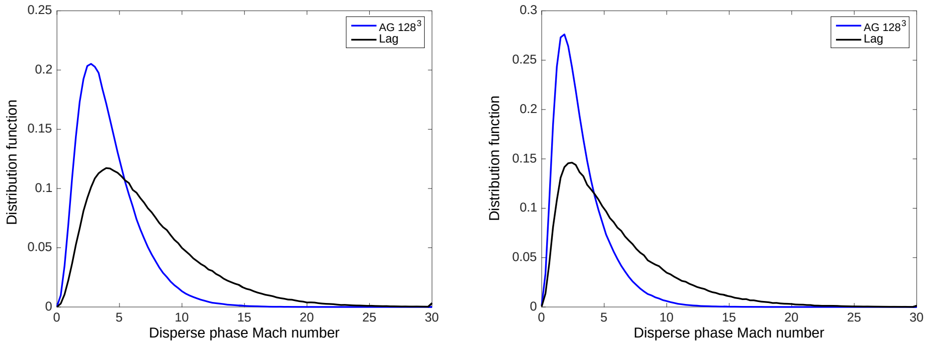

(a) St = 0.5 (b) St = 1

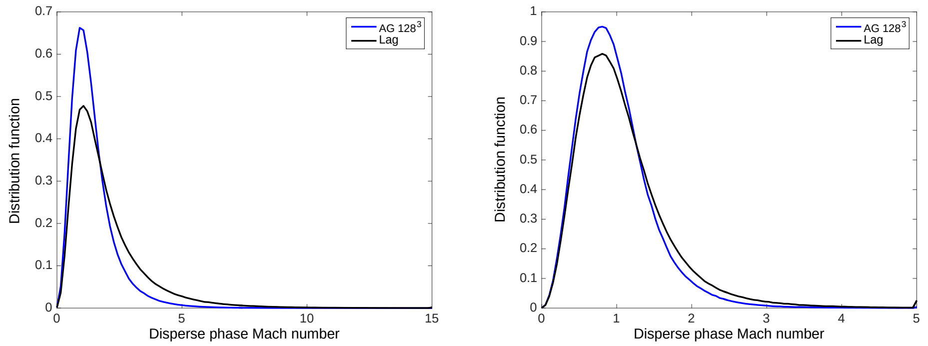

(c) St = 3 (d) St = 8

Figure 9.25: *Distribution function of the disperse phase Mach number* $\mathrm{Ma_e}$ *for the Lagrangian and AG results on the* 128^3 *mesh at* $t = 40$

Further investigations of the $\mathrm{Ma_e}$ results should be done on the refined 512^3 AG results to validate this possibility.

When it comes to the mean value of $\mathrm{Ma_e}$ over the whole domain, at t=40 the AG underestimates this Mach number but is expected to move towards the Lagrangian one when refining the mesh. As for the case of the inertial particles at $t = 80$ the AG results overestimate $\mathrm{Ma_e}$ for the highest St studied on the 128^3 mesh and is expected to moves away from the Lagrangian result for $\mathrm{St}_E > 1$

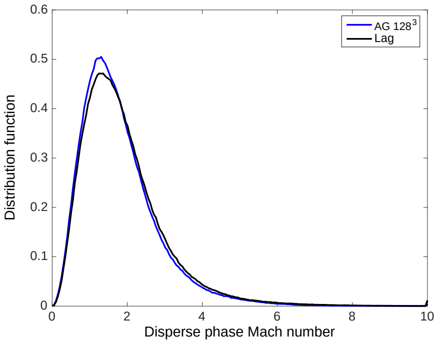

Figure 9.26: *Distribution function of the disperse phase Mach number for the Lagrangian and AG results on the* 128^3 *mesh for* $\mathrm{St} = 8$ *at* $t = 80$

on the 512^3 mesh.

Knowing that the results of both measures for the disperse phase Mach number lead to similar comparison between the Lagrangian and the AG results for moderate to high Stokes numbers, it is noted that it is easier to deal with this latter definition for the small Stokes number cases. First, the vacuum regions are automatically omitted from while computing $\mathrm{Ma_e}$ since the energy is weighted with the number density which is not the case for the classical definition. Second, when evaluating the Mach number in the PTC-free regions, using the first definition a threshold should be defined to avoid computing the infinite Mach numbers characterizing such regions. Whereas by using $\mathrm{Ma_e}$ instead of $\mathrm{Ma_p}$, these PTC-free regions can be excluded as being zones of negligible slip velocity solving by this the problem on computing infinite $\mathrm{Ma_e}$.

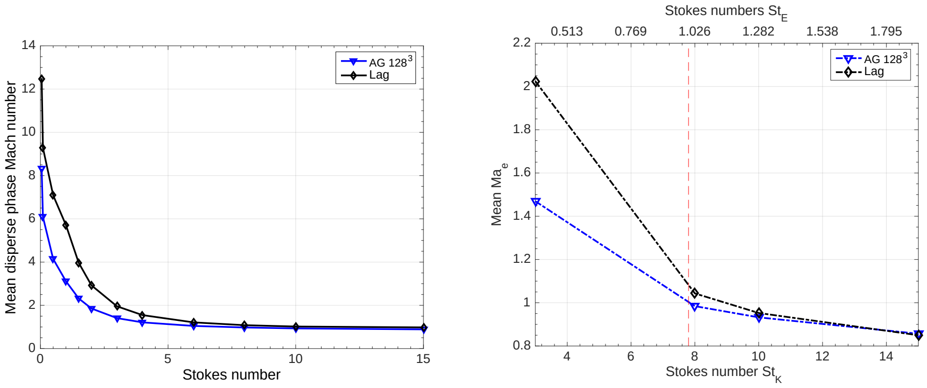

(a) $t = 40$ (b) $t = 80$

Figure 9.27: *Mean value of the disperse phase Mach number for the Lagrangian and AG results on the* 128^3 *mesh as a function of Stokes number*

9.2 Autocorrelation functions

The Eulerian two-points spatial autocorrelations are presented in this section for the number density, the velocity field and the trace of the energy tensor at $t = 40$ and $t = 80$. The effect of the particle inertia on these macroscopic two-points statistics is depicted. These results are compared for the different models, to check whether the AG model in comparison with the Lagrangian reference reproduces the form of the autocorrelation. Also, the capacity of the Eulerian models to capture the different characteristic scales based on these autocorrelation functions is studied. The advantages of the AG versus MK model is one more time underlined when it comes to these autocorrelations, the limits of the AG model are proved and the range of applicability of this model is clearly defined.

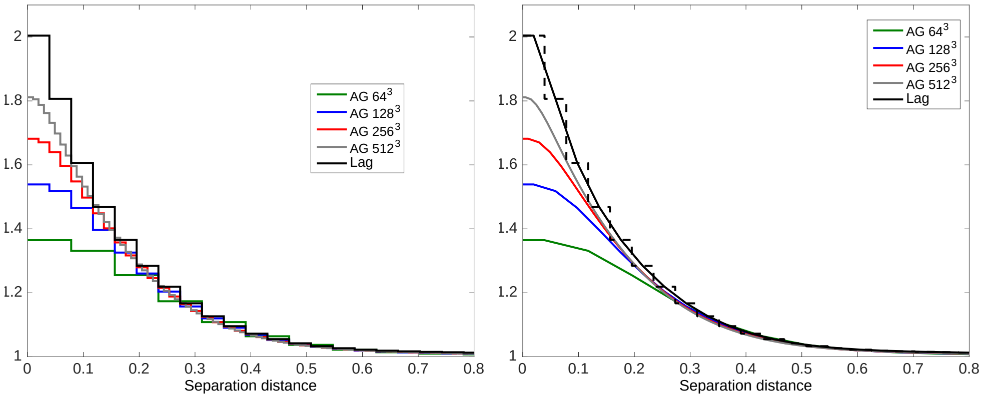

(a) Original result

(b) Modified presentation

Figure 9.28: *Illustration of the autocorrelation function*

Before presenting the results, the chosen way to display the Eulerian autocorrelation functions is first clarified. In fact, the minimum separation distance that one can deal with, based on a Eulerian mesh, is the element size Δx. Thus, the autocorrelation function is obtained as piecewise constant at intervals of size Δx unless if, depending on the numerical methods used, the quadrature values or the slope of the result is taken into account. For simplicity, the choice here is of first order, which means that the final result is taken constant per grid element. Thus, the autocorrelation is obtained as a piecewise constant function. However, for clarity, the stairs representation is transformed to a linear representation so that the value of the autocorrelation at a distance of i elements is drawn at $r = i\frac{\delta x}{2}$. As for a separation distance $0 \leq r \leq \frac{\delta x}{2}$ the value of the autocorrelation is set to be equal to its value in the original element which means that the linear curve is extended horizontally between $r = \frac{\delta x}{2}$ and $r = 0$ as shown in Figure 9.28.

9.2.1 Number Density

The number density autocorrelation gives the number of pair of particles separated by a distance r. This autocorrelation quantifies the accumulation of two particles. It is also called the radial distribution function and is given by Equation (9.11) (*Février et al. 2005; Sundaram and Collins 1997*):

$$g_{pp}(r) = \frac{\langle n(\vec{\boldsymbol{x}})n(\vec{\boldsymbol{x}}+r\vec{\boldsymbol{e}})\rangle}{\langle n(\vec{\boldsymbol{x}})\rangle\langle n(\vec{\boldsymbol{x}}+r\vec{\boldsymbol{e}})\rangle}, \text{where } \vec{\boldsymbol{e}} \text{ is a given unit vector.} \tag{9.11}$$

When the particles are distributed uniformly $g_{pp}(r)$ is constant and equal to 1. By taking $r = 0$, one obtains the segregation measured at the length scale defined by the mesh size.

In the following, the number density autocorrelation function is first plotted for the different Stokes numbers in Figure 9.29, in order to understand the effect of the particles inertia on the shape of the radial distribution function. Lagrangian and Eulerian results are compared to see whether they capture the same effects.

For all the Stokes numbers and models, g_{pp} is equal to the segregation at the origin and then decreases with increasing separation distance till reaching a nearly constant value $g_{pp}(\infty)$, very close to 1.

From the Lagrangian results at the origin, it is seen that the effect of the particle inertia on the segregation is recovered: it increases with increasing inertia for $\mathrm{St}_K < 1$, reaches its maximum at unity Stokes number and then decreases after this limit. A similar behavior is obtained along the different values of the separation distance. In fact, at a given separation distance r, the obtained number density autocorrelation is the segregation measured at a length scale equal to r. Nevertheless, the degree of change of the segregation with the particles inertia, decreases with increasing separation distance and the maximum segregation is obtained at higher St as shown in Figure 9.29(d). At the end, for large separation distance, the number density between two particles is no more correlated. This distance also depend on the Stokes number, it clearly increases for $\mathrm{St}_K < 1$ but its dependence on the particles inertia above this limit is not conclusive.

This evolution is captured by the AG model, knowing that segregation level is always underestimated due to the numerical diffusion. On the other hand, for the MK results, the segregation increases monotonously with the particle inertia no matter at what length scale it is measured.

Another important conclusion can be drawn from these results (see Figures 9.29(d) and 9.29(e)), it is actually a confirmation that the choice of measuring the segregation of the different results at the 64^3 mesh scale does not bias the study and analysis presented in section 8.3 of the previous chapter. In fact the dependency of the number density autocorrelation on St at the separation distance corresponding to the DNS mesh (128^3) or the coarsest mesh (64^3) that was chosen for the projection of the statistical results is the nearly the same. The only difference is that the segregation is lower.

Based on these finding, it is noted that the choice of the scale at which the segregation is measured can highly influence the results, leading to inaccurate analyses and conclusions. Thus, it is important to find a more general measure of the segregation effect independent of the scale. One possibility is the

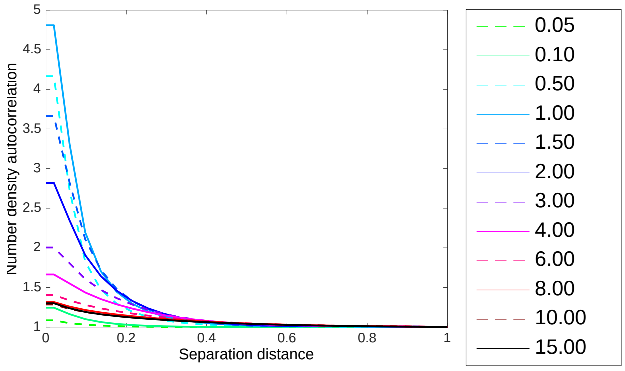

(a) Lagrangian

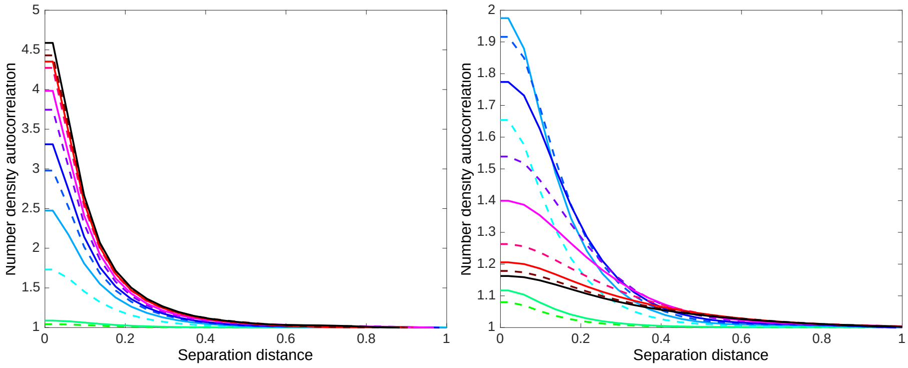

(b) MK on 128^3 mesh (c) AG on 128^3 mesh

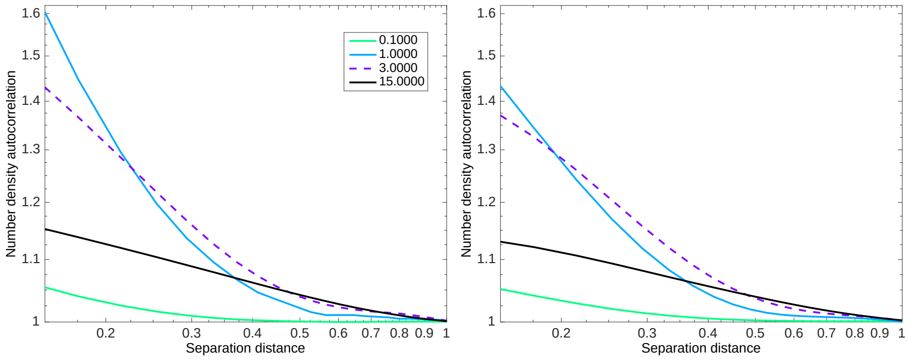

(d) Lagrangian, log scale (zoom in) (e) AG on 128^3 mesh, log scale (zoom in)

Figure 9.29: *Number density autocorrelations for different Stokes number*

area under the radial distribution function, which is plotted in Figure 9.30 as a function of the Stokes number. This measure leads to similar observations as for the effect of the particle inertia on the segregation presented in the previous chapter in Figures 8.47 and 8.48 based respectively on the original DNS mesh projection and on the 64^3 mesh. In fact, the area under the Lagrangian radial distribution function increases until reaching its maximum for a Stokes number $\mathrm{St}_K = 1$ and then decreases beyond this limit and tends to settle for Stokes numbers greater than $\mathrm{St}_E = 1$. This same behavior is reproduced with the AG model. However, for the MK results the area increases constantly until reaching nearly a plateau for $\mathrm{St}_E > 1$.

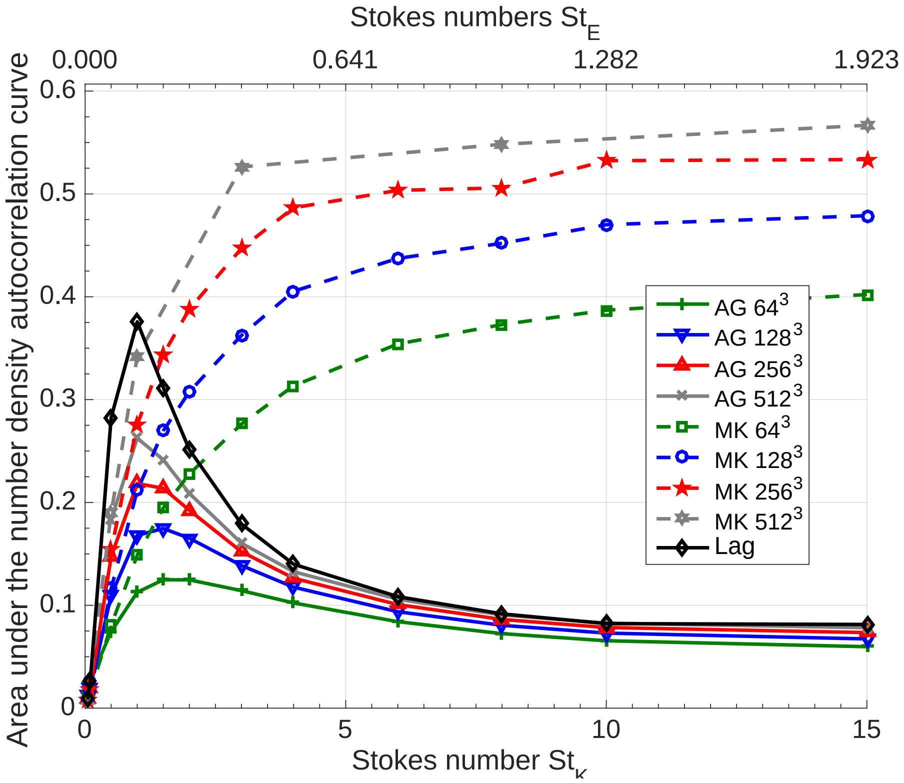

Figure 9.30: *Area under the number density autocorrelation function for the Lagrangian, Eulerian results on the* 64^3, 128^3, 256^3 *and* 512^3 *meshes as a function of Stokes number*

In the following, the number density autocorrelation function is compared for the different models and meshes at a given Stokes number.

First, for the small Stokes number $\mathrm{St} = 0.5$, both Eulerian models gives the right shape of the autocorrelation function and tend to the Lagrangian results when refining the mesh (Figure 9.31).

For St = 1, the MK model predicts a higher level of number density correlation in comparison to the AG on the same mesh for small separation distance. This level is closer to the Lagrangian one. However for the MK result on 512^3 mesh the two-point number density correlation is higher than the Lagrangian one for small separation distance (Figure 9.32). This is caused by the local PTC as explained in subsection 7.3.2.

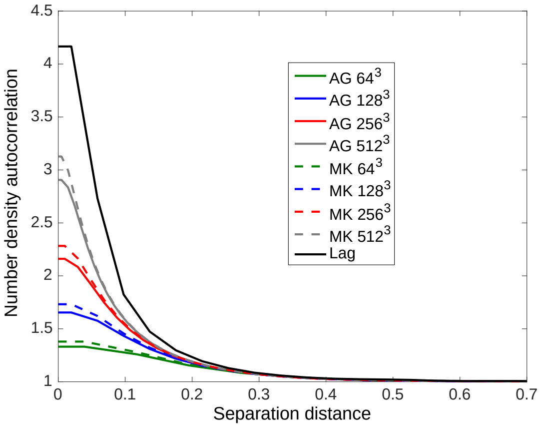

Figure 9.31: *Number density autocorrelations for the Lagrangian and Eulerian results on the* 64^3, 128^3, 256^3 *and* 512^3 *meshes for* St = 0.5

For moderately inertial to inertial particles, the MK result predict an overestimated number density autocorrelation as shown in Figure 9.33 for St = 3. On the other hand, the number density autocorrelation function obtained from the AG results tends to the one computed with the Lagrangian method for St = 3 as illustrated in Figures 9.33.

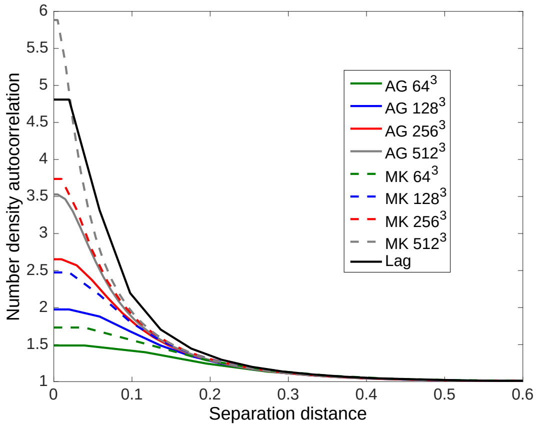

Figure 9.32: *Number density autocorrelations for the Lagrangian and Eulerian results on* 64^3, 128^3, 256^3 *and* 512^3 *meshes for* St = 1

When it comes to the inertial particles, St = 8 for example (Figure 9.34), the

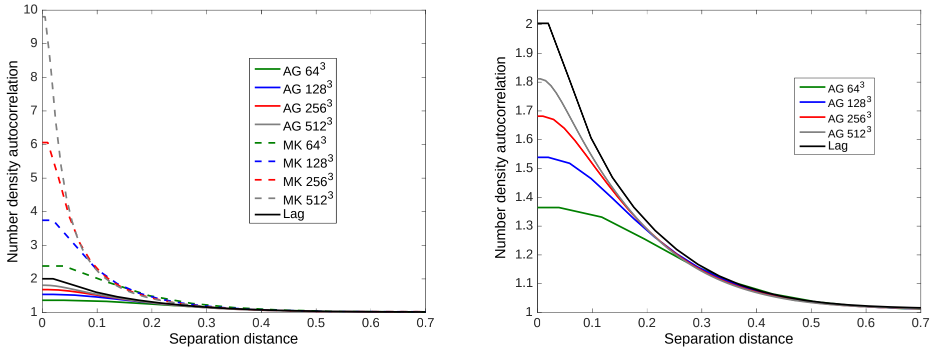

(a) MK and AG (b) AG

Figure 9.33: *Number density autocorrelations for the Lagrangian and Eulerian results on the* 64^3, 128^3, 256^3 *and* 512^3 *meshes for* $\mathrm{St} = 3$

AG result tend to the Lagrangian one at $t = 40$ but starts to move away from this reference at $t = 80$.

It is however important to note that along the studied range of the Stokes

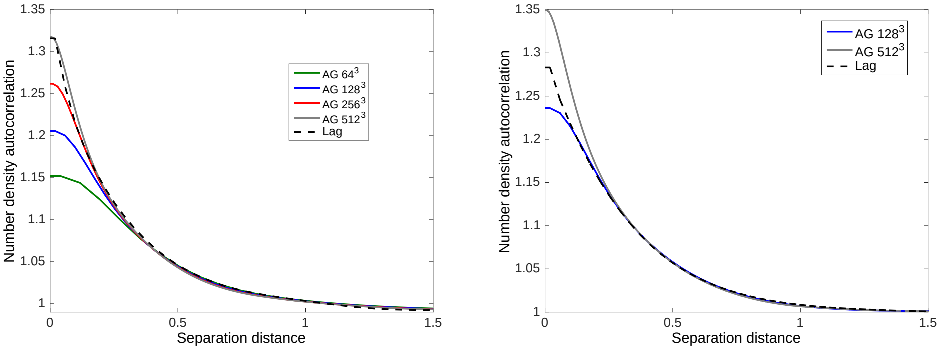

(a) $t = 40$ (b) $t = 80$

Figure 9.34: *Number density autocorrelations for the Lagrangian and Anisotropic Gaussian results with mesh refinement for* $\mathrm{St} = 8$

number, the AG model gives accurate results for the number density autocorrelation at long separation distances $r > 0.2$ even for $\mathrm{St}_E > 1$.

Now that the number density autocorrelation is evaluated and the AG model is proven to capture the right amount of correlation between two particles especially for moderately inertial to inertial particles, and for long separation distances over the whole range of St studied, the characteristic size of the accumulation zones is evaluated as a function of the particle inertia.

This characteristic size is obtained by evaluating the integral length scale of the number density autocorrelation function. This length scale represents the distance above which the number density is no more correlated. Practically, it renders a measure of the mean size of the clusters over the whole domain. The equation of this number density integral length scale (Equation (9.12)) is inspired from the work of *Moreau (2006)*:

$$L_p = \int \frac{(g_{pp}(r) - g_{pp}(\infty))}{(g_{pp}(0) - g_{pp}(\infty))} \mathrm{d}r. \tag{9.12}$$

The characteristic accumulation size, computed from the Lagrangian results at $t = 40$, increases with the particle inertia for $\mathrm{St}_K > 1$, until reaching a maximum for $\mathrm{St}_K = 8$ and then starts decreasing as shown in Figure 9.35(a). For the range of Stokes number between $\mathrm{St}_K = 1$ and $\mathrm{St}_E = 1$ the characteristic clusters size changes nearly linearly with the Stokes number. The MK model does not reproduce the right size of the clusters but leads to a nearly contant value of L_p for $\mathrm{St}_K > 1$ that diverges from the Lagrangian result. This was already expected based on the previous results and on the character of this model that generates unphysical δ-shock and hypercompressibility at each PTC event. Through these unphysical singularities the model predicts higher and higher concentrations and vacuum zones and tends to generate fine clusters which explains the underestimated clusters size for $\mathrm{St}_K > 1$. On the other hand, the AG results lead to the correct dimensions of the accumulations, especially for Stokes numbers ranging between $\mathrm{St}_K = 1$ and $\mathrm{St}_E = 1$.

In order to take into account the right dynamics of the inertial particles, the cluster size, obtained from the Lagrangian and AG simulation at $t = 80$, is represented in Figure 9.35(b) for the high Stokes numbers $\mathrm{St}_E > 1$ and for $\mathrm{St}_K = 3$ added only for the comparison purpose. It is noted that for the range of St studied, the resulting characteristic cluster size is larger than the Kolmogorov length scale and the integral length scale L_{11}. The AG results for $\mathrm{St}_E > 1$ diverges from the Lagrangian one when refining the mesh, and lead to smaller clusters sizes. The inability of the AG model to capture the right dynamics for $\mathrm{St}_E > 1$, leads us to inquire about the reason of such limits. This is related to the fact that the statistical description of the PTC through a velocity dispersion tensor in the energy equation is not capable of reproducing the physics. The question then arises: is there a maximum limit of the inertial energy that can be accurately reproduced statistically by the AG model? In order to try to answer this question, the computed characteristic scale is plotted as a function of the ratio of the mean internal energy to the mean total energy in Figures 9.36(a). From the curve of the Lagrangian result (in Figure 9.36(a)), the nearly linear rise of the cluster characteristic scale as a function of the ratio of the energy of the uncorrelated motion to the total energy is observed between $\mathrm{St}_K > 1$ and $\mathrm{St}_E < 1$ at $t = 40$. This behavior is captured by the AG result.

In order to check if this linear dependency is kept for the inertial particle the mean clusters size divided by the integral length scale of the gas L_{11}, for $\mathrm{St}_K > 1$ and $\mathrm{St}_E < 1$ at $t = 40$ and those for $\mathrm{St}_E > 1$ at $t = 80$, are plotted in the same graph (in Figure 9.37). For the Lagrangian clusters size, this dependency still

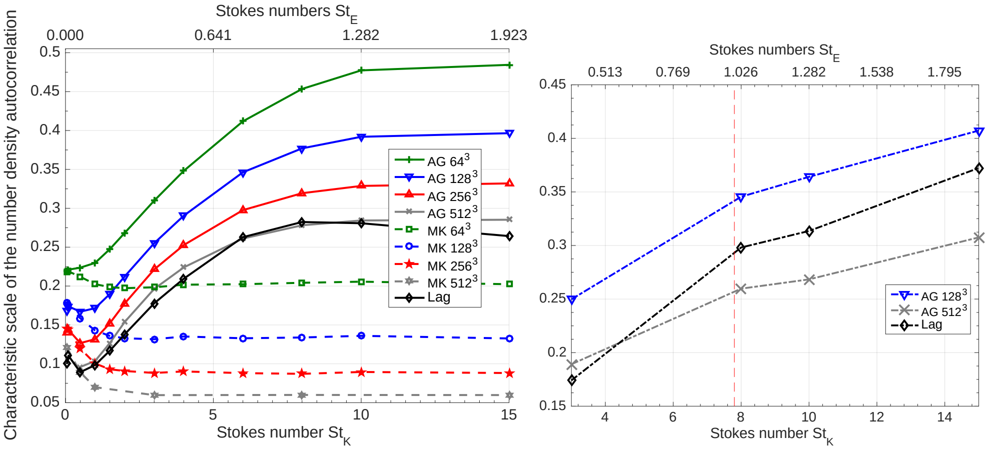

(a) $t = 40$ (b) $t = 80$

Figure 9.35: *Characteristic length scale based on the number density autocorrelations, for the Lagrangian and Eulerian results with mesh refinement as a function of Stokes number*

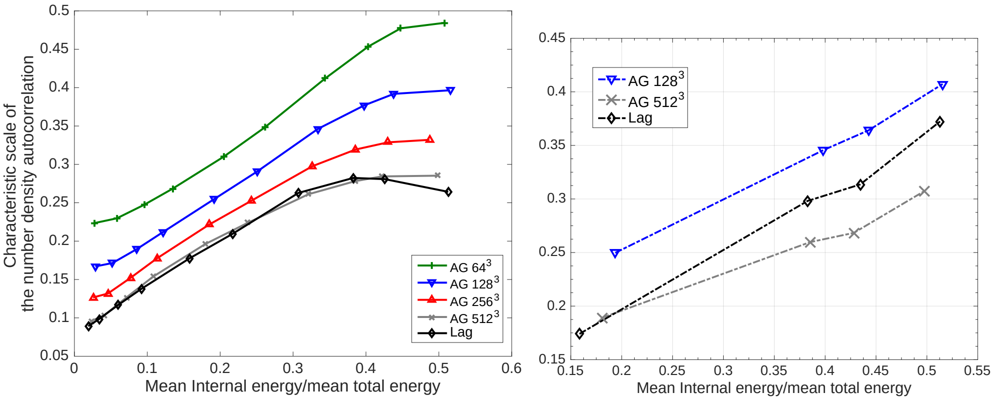

(a) $t = 40$ (b) $t = 80$

Figure 9.36: *Characteristic clusters size as a function of the ratio of the mean uncorrelated energy to the mean total energy for the Lagrangian and AG results with mesh refinement*

exists but it is broken with the AG model. Actually, the AG model ceases to capture the right dynamics when the uncorrelated energy is nearly 35% of the total energy. The slope obtained from the Lagrangian results is 0.9403 with a regression of 0.9962, whereas the slope from the AG results on the 512^3 mesh is 0.8683 with a regression of 0.9948.

In order to understand more the dynamics, the limits of the AG model and the meaning of the slope, further investigations of the linear dependence are

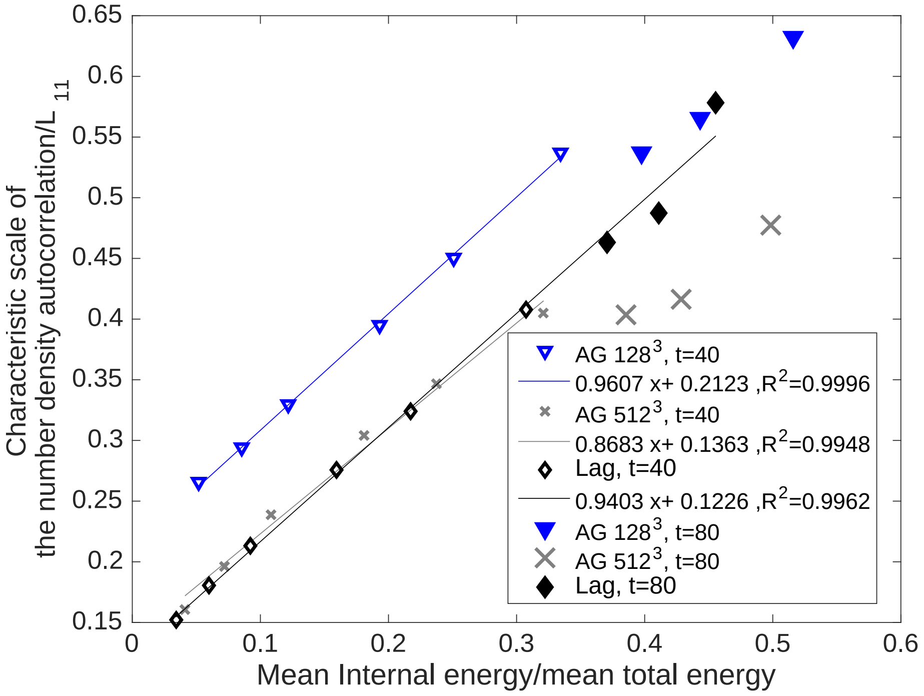

Figure 9.37: *Linear dependence of the mean clusters size on the ratio of the mean uncorrelated energy to the mean total energy for the Lagrangian and AG results with mesh refinement*

needed. This is essential to check whether the constraints of this model are indeed related to a given threshold of the energy ratio or not.

9.2.2 Velocity autocorrelation

The spatial two-points velocity autocorrelation is usually given by Equation (7.14) (*Pope 2000*) as presented in Chapter 7 for the FHIT.

$$R_{ij}(r) = \frac{\langle n(\vec{x})u_i(\vec{x})n(\vec{x}+r\vec{e})u_j(\vec{x}+r\vec{e})\rangle}{\langle n(\vec{x})n(\vec{x}+r\vec{e})\rangle}. \tag{9.13}$$

In this work, since there is a known difference between the zero-velocity of the Lagrangian results in the vacuum zone and the computed Eulerian velocity in the region of very low number density, and since the momentum is the conservative variable taken into account in the resolved system of equation, it is better to compute the velocity autocorrelation based on the momentum. Thus, the correlation of the velocity is then given by Equation (9.13) (*Février et al. 2005*).
The velocity correlations are plotted for different Stokes numbers in Figure 9.38.

The profile of the evolution of this function for increasing Stokes numbers is the same for Lagrangian and AG results whereas the MK result gives an unphysical peak for small separation distance in the case of all the Stokes numbers higher than 1.

For St = 0.5, the Eulerian results gives nearly the same velocity autocorrela-

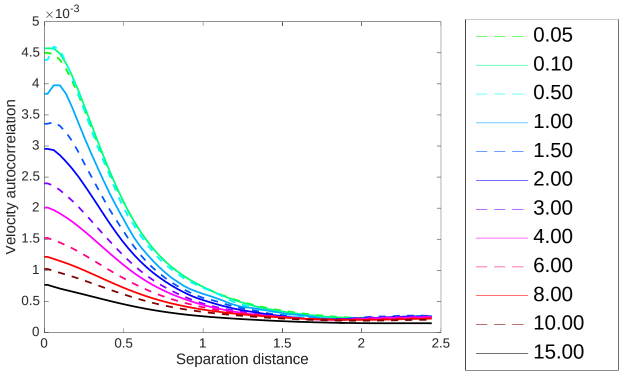

(a) Lagrangian

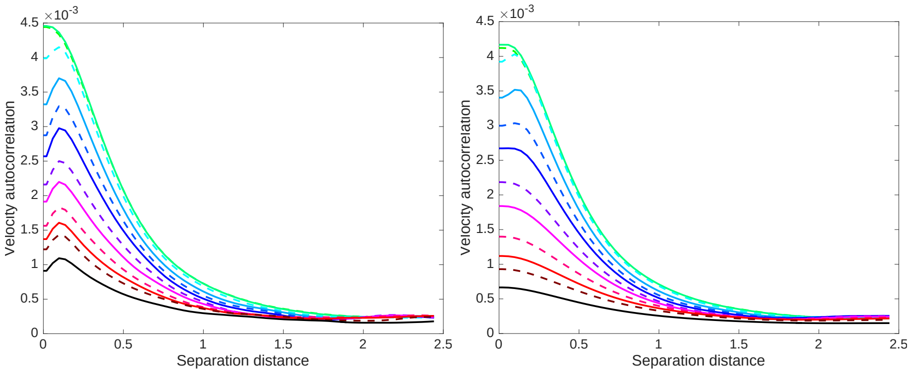

(b) MK on 128^3 mesh (c) AG on 128^3 mesh

Figure 9.38: *Velocity correlations for different Stokes number*

tion that tends to the Lagrangian one when refining the mesh (see Figure 9.39).

For unity Stokes number, the AG results lead to a more accurate velocity autocorrelation based on the Lagrangian reference at small separation distances. In fact, the result of the most refined MK simulation overestimates the peak in the autocorrelation at r=0.1 as shown in Figure 9.40. This is due to singularities generated by the MK model at the local PTC events which occur when the local Stokes number is higher than 1 (this occurrence is faced at 11% of the whole domain based on subsection 7.3.2). However both Eulerian results are very similar when it comes to the autocorrelation of the velocity for long separation distance $r > 0.25$

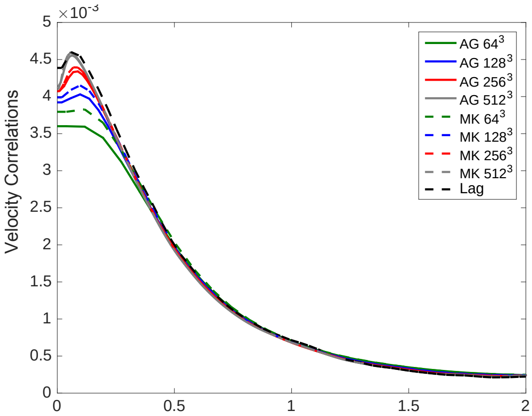

Figure 9.39: *Velocity correlations for the Lagrangian and Eulerian results on the* 64^3, 128^3, 256^3 *and* 512^3 *meshes for* $\mathrm{St} = 0.5$

For moderately inertial particles ($\mathrm{St} = 3$), the autocorrelation function resulting from the AG simulation has the same shape as the Lagrangian one, unlike the MK result that depicts an unphysical peak locate at small separation distance (Figure 9.41) and overestimates the velocity autocorrelation at a large range of r.

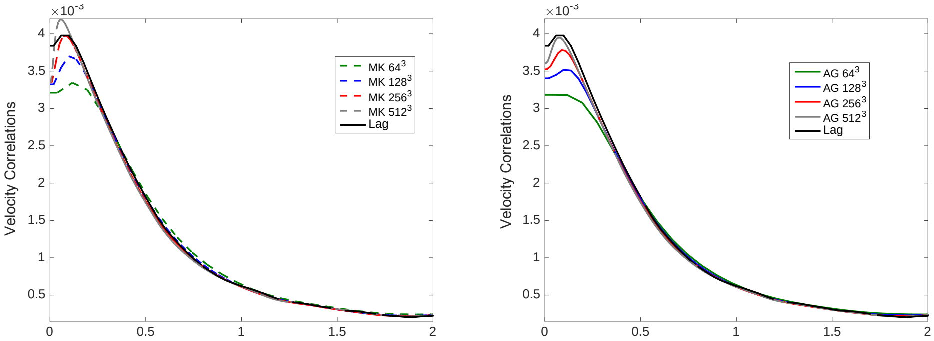

(a) MK (b) AG

Figure 9.40: *Velocity correlations for the Lagrangian and Eulerian results on the* 64^3, 128^3, 256^3 *and* 512^3 *meshes for* $\mathrm{St} = 1$

For $\mathrm{St} = 8$ at $t = 40$, the velocity correlation resulting from the MK simulations is totally different from the Lagrangian one, even for large separation distance with an important overestimation at small r. On the other hand, the AG model estimates well the velocity correlation for a separation distance greater than 0.1 but underestimates the velocity correlation between two particles separated by a distance smaller than 0.1. In this case, the results for the Lagrangian and the AG simulations at $t = 80$ lead to the same interpretation as at $t = 40$.

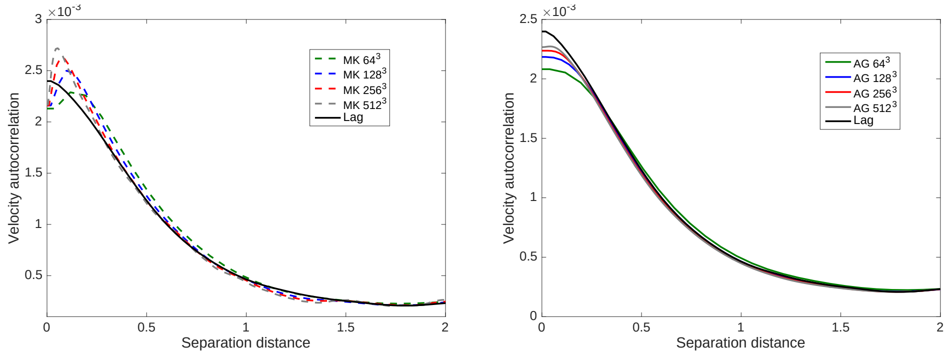

(a) MK (b) AG

Figure 9.41: *Velocity correlations for the Lagrangian and Eulerian results on the* 64^3, 128^3, 256^3 *and* 512^3 *meshes for* $\mathrm{St} = 3$

As presented for the FHIT, the longitudinal integral length scale L_{long} is usually given as the area under the curve of the longitudinal velocity correlation $f_{long}(r)$ (*Pope 2000*) (Equation (7.15)). This length scale is plotted for the different models as a function of the Stokes number at $t = 40$ in Figure 9.43(a). The AG simulation leads to a length scale bigger than the Lagrangian one but tends to this reference with mesh refinement. On the other hand, the MK model underestimates this length scale for $\mathrm{St}_K > 1$ and diverges from the reference. It is noticed that for $\mathrm{St}_K \geq 10$, the difference between the AG results on the 512^3 mesh and the Lagrangian one is higher than the case for $\mathrm{St}_K < 10$. However at $t = 80$, it is clearly seen that the AG results diverge from the Lagrangian for $\mathrm{St}_E > 1$ which means that the model is not accurately reproducing the correlated motion anymore but instead it is overestimating the correlation between the particles.

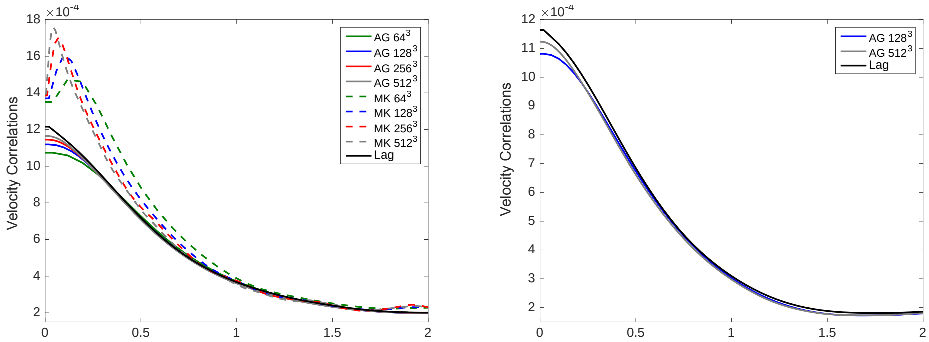

(a) $t = 40$ (b) $t = 80$

Figure 9.42: *Velocity correlations for the Lagrangian and Eulerian results with mesh refinement for* $\mathrm{St} = 8$

In this case, the resulting length scale is not always smaller than the longitudinal integral length scale of the gas L_{11}. One can wonder whether the AG model ceases to capture the right dynamics for the cases where $L_{long} > L_{11}$. To evaluate this possibility, the normalized integral length scale $\frac{L_{long}}{L_{11}}$ is plotted in Figure 9.44. Through these results the latter statement is denied.

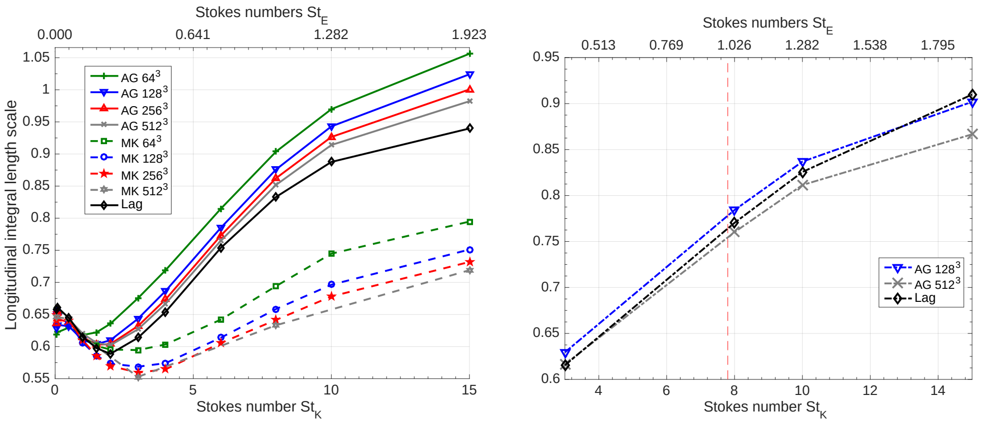

(a) $t = 40$ (b) $t = 80$

Figure 9.43: *Integral length scale based on the velocity autocorrelations, for the Lagrangian and AG results with mesh refinement as a function of Stokes number*

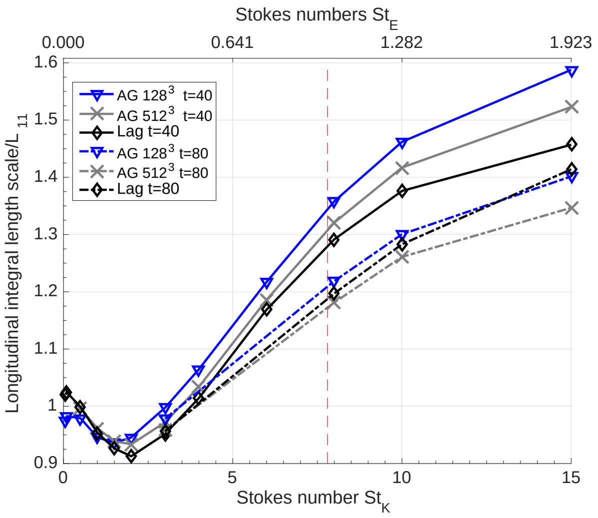

Figure 9.44: *Integral length scale based on the velocity autocorrelations of the disperse phase normalized by the longitudinal integral length scale of the carrier phase*

9.2.3 Internal energy autocorrelation

In a similar way to the number density and the velocity autocorrelation, the autocorrelation R_Σ of the trace of the internal energy $(\mathrm{Tr}(\boldsymbol{\Sigma}))$ is evaluated hereafter and plotted for different Stokes numbers. These correlations are added in order to quantify the mean PTC length scales based the characteristic length scale of the internal energy trace autocorrelation function.

$$R_\Sigma = \frac{\langle n(\vec{\boldsymbol{x}})\mathrm{Tr}(\boldsymbol{\Sigma})\,(\vec{\boldsymbol{x}})n(\vec{\boldsymbol{x}}+r\vec{\boldsymbol{e}})\mathrm{Tr}(\boldsymbol{\Sigma})\,(\vec{\boldsymbol{x}}+r\vec{\boldsymbol{e}})\rangle}{\langle n(\vec{\boldsymbol{x}})n(\vec{\boldsymbol{x}}+r\vec{\boldsymbol{e}})\rangle}. \tag{9.14}$$

For $\mathrm{St}=1$, the AG results tends to the Lagrangian one with mesh refinement as shown in Figure 9.45.

For moderately inertial particles ($\mathrm{St}=3$), the autocorrelation function resulting from the AG simulation have the same shape as the Lagrangian one (Figure 9.46). The AG model underestimates this autocorrelation even on the refined mesh for $r<0.4$.

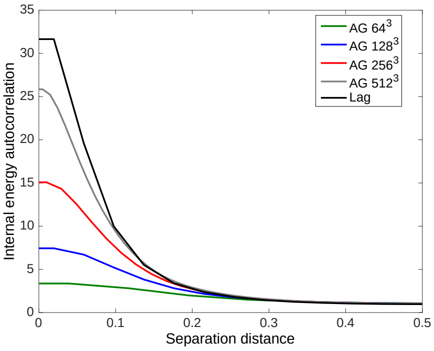

Figure 9.45: *Autocorrelations of the trace of internal energy for the Lagrangian and AG results on the* 64^3, 128^3, 256^3 *and* 512^3 *meshes for* $\mathrm{St}=1$

For $\mathrm{St}=8$ at $t=40$, the correlation resulting from the AG simulations tends to the Lagrangian one with a degree of underestimation for $r<0.4$. Nevertheless, the AG results diverges from the Lagrangian reference at $t=80$.

$$L_\Sigma = \int \frac{(f_\Sigma(r)-g_{pp}(\infty))}{(f_\Sigma(0)-f_\Sigma(\infty))}\mathrm{d}r, \text{ where } f_\Sigma(r) = \frac{R_\Sigma}{\langle \mathrm{Tr}(\boldsymbol{\Sigma})\,(\vec{\boldsymbol{x}})\rangle}. \tag{9.15}$$

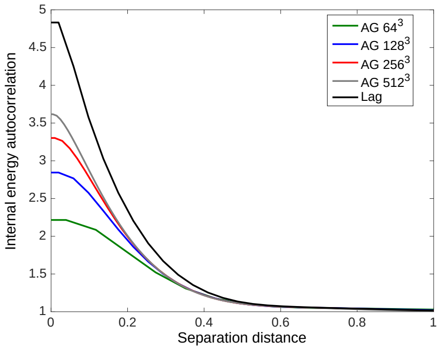

Figure 9.46: *Autocorrelations of the trace of internal energy for the Lagrangian and AG results on the* 64^3, 128^3, 256^3 *and* 512^3 *meshes for* $\mathrm{St} = 3$

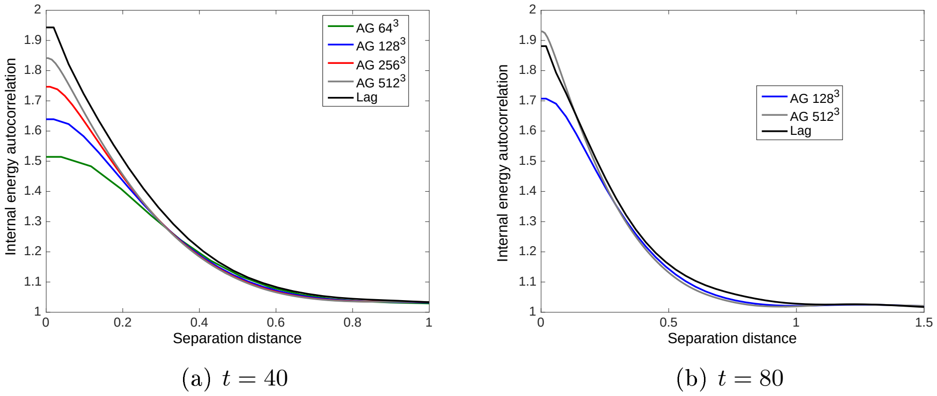

(a) $t = 40$ (b) $t = 80$

Figure 9.47: *Autocorrelations of the trace of internal energy for the Lagrangian and AG results with mesh refinement for* $\mathrm{St} = 8$

The mean characteristic size of this autocorrelation is given by Equation (9.15) and plotted as a function of the Stokes numbers in Figure 9.48(a) and 9.48(b) at $t = 40$ and $t = 80$ respectively. The AG results converges to the Lagrangian ones for $\mathrm{St}_K > 1$ and $\mathrm{St}_E < 1$ and diverges beyond this range.

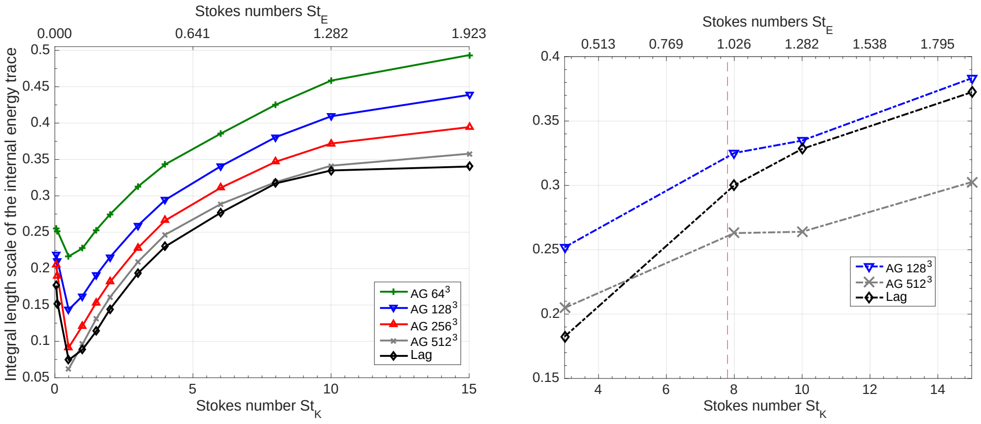

(a) $t = 40$

(b) $t = 80$

Figure 9.48: *Characteristic scale of the PTC based on the autocorrelation function of the trace of internal energy, for the Lagrangian and AG results with mesh refinement as a function of Stokes number*

9.3 Conclusion

Since the PDF and the autocorrelation function take into account the different points of the domain instead of dealing with averaged values over the domain as it was the case for the mean statistics presented in the previous chapter, one can say that the evaluation of the AG model through these functions was necessary in order to validate the model. Thus the results presented in the last two chapters represent a complete validation of the AG model on the FHIT academic test case. Based on the different results, the AG model is found to be a useful model for an accurate description of the disperse phase motion for $\mathrm{St}_E < 1$. Below this limit, it matches to the Lagrangian results when it comes to the PDF of the number density, the velocity, the pressure trace and the Mach number. This model also gives the right amount of the two-points correlations of the number density, the velocity and the internal energy trace. In the studied case, the maximum percentage of the mean internal energy below which the AG model captures the underlying dynamics is 35% of the mean total energy. In this range, the Stokes number based on the Eulerian integral scale is less than 1, $\mathrm{St}_E < 1$, and the corresponding Stokes number based on the Lagrangian integral scale is less than nearly 2.

In addition, the linear dependence of mean clusters size on the ratio of the mean uncorrelated energy to the mean total energy is highlighted through the Lagrangian number density autocorrelations. The AG model capture this linear dependence for $\mathrm{St}_E < 1$ where $\frac{\mathrm{MCE}}{\mathrm{MTE}} < 0.35$.

On the other hand, the MK model overestimated the correlated motion and the number density for $\mathrm{St}_K > 1$ and diverges from the Lagrangian reference. This behavior is due to the fact that this model is not capable of reproducing the PTC, and instead generate unphysical δ-shock and high concentrations and vacuum zones. It is important to note that all the classical QBMM that uses quadratures in the form of a sum of Dirac delta function lead to weakly hyperbolic conservation laws and face δ-shock singularities (see *Chalons et al. (2012)*).

When comparing the PDF of the disperse phase Mach number, a new measure for the Mach number is introduced. It is based on the ratio of the slip energy to the uncorrelated energy inspired from the momentum equation. This latter is found to be more adapted to the understanding of the underlying dynamics of the particulate phase. Finally, from all the results and analyses presented in these last two chapters, the domain of relevance of the use of the AG model extends from the unity Stokes number based on the Kolmogorov scale to the unity Stokes number based on the Eulerian integral scale, as shown in the diagram in Figure 9.49.

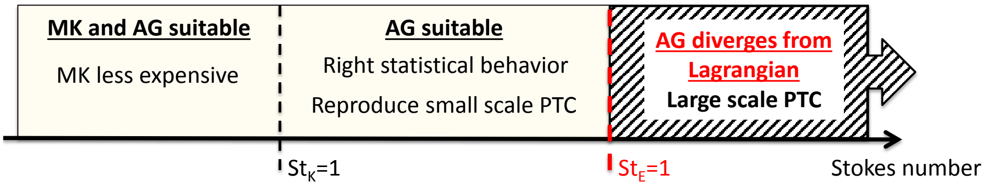

Figure 9.49: *Domain of validity of the AG model based on the qualitative and the statistical results.*

Part IV

Towards LES modeling of the disperse phase

In this part, the objective is to propose a first extension to Large Eddy Simulation (LES) of the AG model with the same level of potentials as the one obtained in DNS. In Chapter 10, the classical LES framework is presented and a brief review of existing models for single phase gaseous flow, and two-phase flows using Lagrangian Particle Tracking or Eulerian Moment Methods. We then concentrate on LES moment methods and suggest a first classification of the available methods depending on the way they are derived and on the transported moments. In particular, asymptotic limits for small Stokes number are exhibited, showing that moment methods derived from a filtered kinetic equation could ensure the correct behaviour in this limit. An emphasis is made on the fact that even if taking moments of the NDF and filtering can be done in any order, as they acts on different parts of the phase space, imposing a closure on the moment breaks this interchangeability, thus leading to different methods depending on the order of filtering and moment operations. In this chapter the derivation of the AG-LES model based on the filtering at the kinetic level is introduced. Finally, in Chapter 11, a first evaluation of the AG-LES model in a 2D frozen turbulence is performed, in order to investigate the behaviour of this model with respect to a subgrid parameter. This evaluation can not be seen as a complete validation because of the 2D character of our carrier phase, but can still provide information about the model and is a first step toward 3D cases. Results demonstrates a good sensitivity to Stokes number. The sensitivity of the LES result on the subgrid closures in general and on the estimation of the Lagrangian characteristic time of the particles interactions with the residual fluid velocity is also observed. It was noticed that the error of the LES subgrid model increase with decreasing Stokes number. Finally, the energy budget is analysed with a comparison between the filtered central energy of the DNS results and the central energy of the filtered.

Chapter 10

Large Eddy Simulation of particle laden flows

The objective of this chapter is to give an overview of the existing LES models in the literature. First, an introduction to the Large Eddy Simulation in the perspective of other methods is briefly presented, with the fundamental steps of a LES. Then, the filtering operation is detailed, along with the associated potential bias. As particle-laden flows are necessary based on a description of the carrier phase, classical models for gaseous flows are detailed with an emphasis on actual progresses and on-going developments. Finally, existing LES strategies for particle-laden flows are reviewed with a focus on Eulerian methods.

10.1 Introduction to Large Eddy Simulation

In realistic configurations, the multi-scale character of the physics prevents from simulating the whole range of scales of the problem. For instance, to fully resolve an aeronautical test rigs which size of about 10 cm with injection holes of about 100 μm with at least 10 points, one would need about $(10^{-1}/10^{-5})^3 = 10^{12}$ cells, where high-end up-to-date simulations use about 10^9 cells.
To circumvent this issue, averaged methods are generally used. There are two types of methods, which differ by the range of scales to be modeled (see Figure 10.1):

- Reynolds-Averaged Navier-Stokes (RANS): RANS methods are based on a statistical averaging of the equations to be solved. By doing so, the turbulent structures are completely modeled, and the only remaining part to be resolved is the mean flow. This kind of approach has been widely used in the literature because it does not require a fine mesh, since the statistical averaging smears out the small details. However, as all the turbulence is embedded into a model, the accuracy of the simulation

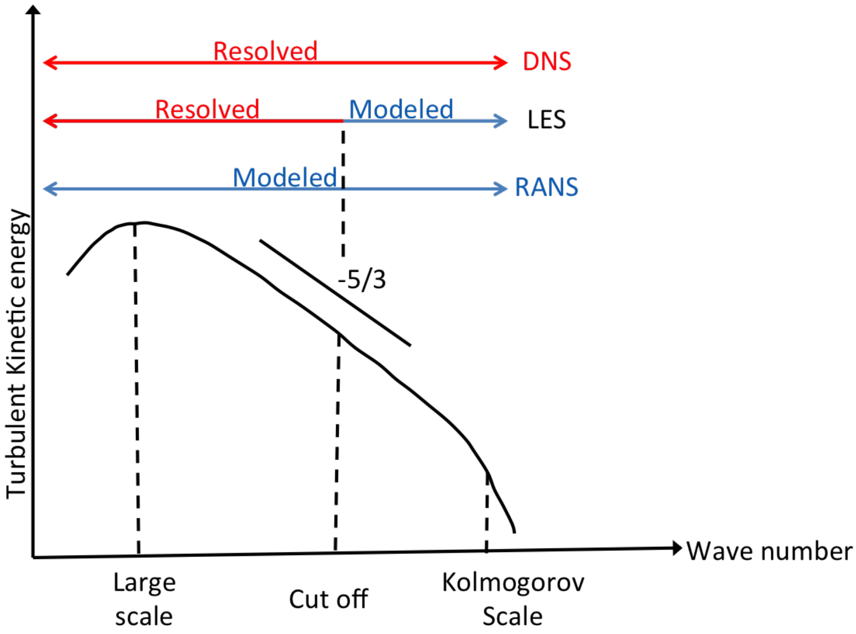

Figure 10.1: *Different techniques to simulate turbulence*

is highly dependent on the closure quality. Moreover, because of the statistical averaging, unsteady phenomenon cannot be captured.

- Large Eddy Simulation (LES): in LES, the equations are filtered using a filtering function that is characterized by a specific width. By doing so, the resulting set of equations only needs models for the scale smaller than the filter width, the larger one being resolved. LES is thus able to capture a wide range of turbulent scales depending on the filter width, and also to reproduce unsteady phenomena.

Nowadays, LES is considered to be an important technique to simulate multiphase turbulent flows since the Direct Numerical Simulation is very expensive and unaffordable for complicated industrial applications and the RANS techniques cannot capture all the important effects caused by the unsteadiness and instabilities since it models an averaged field.

Pope (2000) delineate the four following steps for defining a LES strategy:

- the definition of the filter and its width,
- the application of the filter to the equations of interest,
- the closure of the filtered equations,
- the numerical resolution of the final system.

In the following, we first detail the filtering step and the potential issues arising from this filtering. We then present the application of the filtering along with available closures in the literature for gas phase, Lagrangian particle tracking and Eulerian moment methods for particulate flows. The last point is not discussed here since the numerical schemes presented in Part II in the context of DNS can be used.

10.2 The choice of the filtering operator

In LES, the fundamental procedure is the filtering operation. Its objective is to avoid the resolution of length scales below a certain cut-off limit. This way, it will reduce the computational effort required for simulating the problem of interest. The filter is thus necessarily a low-pass one.

For a given quantity φ, the filtering is a convolution operation between φ and the filter G_Δ:

$$\overline{\varphi}(\vec{\boldsymbol{x}}) = \iiint G_\Delta(\vec{\boldsymbol{x}} - \vec{\boldsymbol{x}}_1)\varphi(\vec{\boldsymbol{x}}_1, t)\mathrm{d}\vec{\boldsymbol{x}}_1, \tag{10.1}$$

where $\overline{}$ denotes a filtered quantity. The unfiltered field can be decomposed into filtered and residual parts:

$$\varphi = \overline{\varphi} + \varphi', \tag{10.2}$$

where φ' is the residual part of the quantity φ.

The other residual terms are designated with the superscrit r. In addition, the subgrid correlation between two variables φ_1 and φ_2 are noted using the operator $(\ )^r$:

$$(\varphi_1\varphi_2)^r = \overline{\varphi_1\varphi_2} - \overline{\varphi_1}\,\overline{\varphi_2}, \tag{10.3}$$

The filter has the following properties:

- Normalization condition:
$$\iiint G_\Delta(\vec{\boldsymbol{x}} - \vec{\boldsymbol{x}}_1)\mathrm{d}\vec{\boldsymbol{x}}_1 = 1; \tag{10.4}$$
- Linearity:
$$\overline{\varphi_1 + \varphi_2} = \overline{\varphi_1} + \overline{\varphi_2}; \tag{10.5}$$
- Commutation with space and time derivatives (only for constant width filter):
$$\overline{\frac{\partial \varphi}{\partial t}} = \frac{\partial \overline{\varphi}}{\partial t}, \quad \overline{\frac{\partial \varphi}{\partial x_i}} = \frac{\partial \overline{\varphi}}{\partial x_i}. \tag{10.6}$$

Multiple filter definitions exist in the literature, in order to extract LES data from DNS simulations. The most used ones are the box filter, the Gaussian filter and the sharp cutoff filter also called spectral cutoff filter (*Sagaut 1998*). Other less famous filters can be found, such as the Cauchy and the Pao filter (*Pope 2000*).

A discussion about the choice of this filter to construct LES fields is available in (*Pope 2000*), where it is mentioned that the most compact filter in both physical and spectral spaces is the Gaussian filter, whereas the box filter is the most compact in physical space.
In the context of variable density flows, another important definition is the notion of Favre-averaged quantities:

$$\overline{\rho}\tilde{\varphi} = \iiint G_{\Delta}(\vec{\boldsymbol{x}} - \vec{\boldsymbol{x}}_1)\rho(\vec{\boldsymbol{x}})\varphi(\vec{\boldsymbol{x}}_1, t)\mathrm{d}\vec{\boldsymbol{x}}_1 = \overline{\rho\varphi}. \tag{10.7}$$

The main interest of this decomposition is that by using it, the closure of the correlations between velocity and density fields are no more needed. Nevertheless, the Favre-averaging is not necessarily performed by mean of the gaseous density, but can also be done using another weighting function, such as the number density of the disperse phase, as it will be shown in the following (*Fox 2014*).

10.3 LES closures in the literature

10.3.1 Gaseous flows

Gaseous flows can be potentially solved using the full system containing mass, momentum, energy and species equations. Each equation may raise its proper modeling issues. For example, in the case of combustion, source terms must account for subgrid scale composition in order to accurately reproduce the chemical evolution.
As we are interested in the dynamics of particles, we focus on the momentum equation, which gives the velocity field required to close the force term in the particle momentum equation. Moreover, as constant-density constant-viscosity flows with one-way coupling are investigated in this work, we focus on this regime. The filtered conservation equations for the velocity field $\vec{\boldsymbol{u}}_{\mathrm{g}}$ is then:

$$\frac{\partial \overline{u}_{g,i}}{\partial t} + \frac{\partial \overline{u}_{g,i}\overline{u}_{g,j}}{\partial x_j} = -\frac{1}{\rho}\frac{\partial}{\partial x_j}\overline{p}\delta_{ij} - \nu\frac{\partial^2}{\partial x_j^2}\overline{u}_{g,i} - \frac{\partial}{\partial x_j}\tau^r_{g,ij}. \tag{10.8}$$

Three closures are required for this equation:

- the filtered pressure $\overline{p}$: even though this term should be modeled, in general turbulent high-order correlations are neglected. As a consequence, it has the same form as in laminar conditions, except that it is evaluated using filtered quantities.
- the subgrid stress tensor $\boldsymbol{\tau}^r_g$: this is the main term to be modeled. It contains the primary effects of the turbulent subgrid scales onto the resolved scales.

To close the subgrid scale tensor, three types of approach can be found in the literature (*Sagaut 1998*):

- the functional approach: the closure aims at reproducing a specific "function" of the turbulent subgrid scale. The most used method is the subgrid scale viscosity closure, which reproduces the dissipative character of turbulent eddies. The most commonly used model is the Smagorinsky model (*Smagorinsky 1963*) that models the deviatoric part of the stress tensor:

  $$\boldsymbol{\tau}_g^{r,*} = -2\left(C_s \Delta\right)^2 |S|\, \boldsymbol{S}, \tag{10.9}$$

  where $\boldsymbol{S}$ is the shear stress tensor, C_s the Smagorinsky constant and Δ the filter width.
- the structural approach: the goal of such method is to give the best approximation of the SGS tensor by using the resolved velocity field structure. This method permits to consider the tensor anisotropy as well as backscatter effects. An example of such model is the one of *Bardina et al. (1980)*, which assumes a similar transfer between large to small resolved scales and between small resolved to unresolved scales:

  $$\boldsymbol{\tau}_g^{r} = \overline{\overline{\vec{\boldsymbol{u}}_{\mathrm{g}}} \otimes \overline{\vec{\boldsymbol{u}}_{\mathrm{g}}}} - \overline{\overline{\vec{\boldsymbol{u}}_{\mathrm{g}}}} \otimes \overline{\overline{\vec{\boldsymbol{u}}_{\mathrm{g}}}}, \tag{10.10}$$

- the MILES and ILES approaches: in such methods, the main idea is to consider that the numerical dissipation can be used as a surrogate to the turbulent subgrid scale physics. This is a pragmatic way to alleviate two issues at the same time, the numerical dissipation and the LES modeling.

Apart from that, many strategies also exist to improve the models for specific conditions. For example, damping functions can be used to adapt the model in wall-bounded flows. Another important improvement can be achieved by dynamically adapting the constant of the model using the Germano identity (*Germano et al. 1991*). Among this list of closing strategies, the most used in industrial computations, especially in the combustion community, is the functional approach through the use of eddy-viscosity models.

10.3.2 Lagrangian Particle tracking

Whereas, a wide literature concerning LES can be found and is largely diffused into CFD community for gaseous flows, this is not the case for disperse phase flows. Even if a lot of contributions can be found in the literature, in general, the impact of subgrid scales on particle dynamics is simply neglected, assuming that their impact in complex industrial applications is limited. Such an assumption may be accurate in the case of moderate to large Stokes number particles, or in specific cases where the subgrid phenomena do not really have an impact on the results compared to the resolved scales. But in general, subgrid scale effects have to be taken into account (*Kuerten 2006*; *Marchioli et al. 2008*).

To determine exactly where the closure is required, we write the equation of motion of a particle:

$$\mathrm{d}_t \vec{\boldsymbol{x}}_p = \vec{\boldsymbol{c}}_p \tag{10.11}$$

$$\mathrm{d}_t \vec{\boldsymbol{c}}_p = \frac{\vec{\boldsymbol{u}}_{\mathrm{g}}(\vec{\boldsymbol{x}}_p) - \vec{\boldsymbol{c}}_p}{\tau_p} = \frac{\overline{\vec{\boldsymbol{u}}_{\mathrm{g}}}(\vec{\boldsymbol{x}}_p) + \vec{\boldsymbol{u}}'_{\mathrm{g}}(\vec{\boldsymbol{x}}_p) - \vec{\boldsymbol{c}}_p}{\tau_p}, \tag{10.12}$$

where $\vec{\boldsymbol{x}}_p$ and $\vec{\boldsymbol{c}}_p$ are the position and velocity of the particle, respectively. In this equation, the issue is to determine the gas velocity along the particle trajectory, which is in fact decomposed into a mean field $\overline{\vec{\boldsymbol{u}}_{\mathrm{g}}(\vec{\boldsymbol{x}}_p)}$ and a random field $\vec{\boldsymbol{u}}'_{\mathrm{g}}(\vec{\boldsymbol{x}}_p)$, see *Minier and Peirano (2001); Chibbaro and Minier (2008); Pozorski and Apte (2009)* for example.

To recover this information, three types of methods are found in the literature:

- modeling the fluid velocity increment along the particle path (*Simonin et al. 1993; Fede et al. 2006; Shotorban and Mashayek 2006; Minier 2015*): in such approaches, the evolution of the fluid is written in the particle referential,
- reconstructing the velocity field at the subgrid level by deconvolution (*Shotorban et al. 2007; Kuerten 2006*),
- adding a random fluctuation to the resolved gas velocity (*Wang and Squires 1996; Vinkovic et al. 2006; Bini and Jones 2008; Gorokhovski and Zamansky 2014*).

10.3.3 Eulerian moment methods

When it comes to macroscopic Eulerian approaches, filtering Equation (2.2) yields to:

$$\begin{aligned}\partial_t \overline{M}_{i,j,k} + \partial_{\vec{\boldsymbol{x}}} \cdot \begin{pmatrix} \overline{M}_{i+1,j,k} \\ \overline{M}_{i,j+1,k} \\ \overline{M}_{i,j,k+1} \end{pmatrix} &= -\frac{1}{\tau_p}\left((i+j+k)\overline{M}_{i,j,k} - \overline{\vec{\boldsymbol{u}}}_{\mathrm{g}} \cdot \begin{pmatrix} i\overline{M}_{i-1,j,k} \\ j\overline{M}_{i,j-1,k} \\ k\overline{M}_{i,j,k-1} \end{pmatrix} \right), \\ &\quad - \frac{1}{\tau_p} \begin{pmatrix} i u_{g,1} M_{i-1,j,k} \\ j u_{g,2} M_{i,j-1,k} \\ k u_{g,3} M_{i,j,k-1} \end{pmatrix}^{r} . \end{aligned} \tag{10.13}$$

The final system of equations needs closures for the fluxes on the left hand side as well as for the velocity fluctuations-particulate phase moments correlations on the right hand side. To address the resolution of Equation (10.13), several approaches have been proposed (*Shotorban and Balachandar 2007; Moreau et al. 2010; Pandya and Mashayek 2002; Zaichik et al. 2009*).

They differ by:

- the range of application: depending on the closure assumptions, some methods are only suitable for low Stokes numbers (*Shotorban and Balachandar 2007*) or high Stokes numbers (*Moreau et al. 2010*), or can cover all ranges (*Pandya and Mashayek 2002; Zaichik et al. 2009*),

- the way the unknown terms are closed: unknown terms can be either closed by algebraic closures (*Moreau et al. 2010; Zaichik et al. 2009*) or assumptions on the NDF (*Pandya and Mashayek 2002*),
- the transported quantities: either full (*Pandya and Mashayek 2002*) or central moments (*Moreau et al. 2010; Zaichik et al. 2009*) can be transported and may generate different modeling strategies about the nature of internal energies.

10.3.3.1 A low Stokes number approach: the filtered Equilibrium Eulerian model

In *Shotorban and Balachandar (2007)*, the authors derive a LES strategy by filtering the Equilibrium Eulerian model of *Ferry and Balachandar (2001); Ferry and Balachandar (2002)*. Consequently, this approach is limited to low Stokes number, as it is for the Equilibrium Eulerian model. This model is developed in the context of two-way coupling and gravity, but here we focus on the one-way coupling, with the drag force as the only external force acting on the particles. We also neglect the Brownian motion that could arise for sufficiently small particles. The filtered equations read:

$$\partial_t \bar{n} + \partial_{\vec{\boldsymbol{x}}} \bar{n} \overline{\vec{\boldsymbol{u}}} = -\partial_{\vec{\boldsymbol{x}}} \vec{\boldsymbol{q}} \tag{10.14}$$

$$\overline{\vec{\boldsymbol{u}}} = \overline{\vec{\boldsymbol{u}}_\mathrm{g}} - \tau_p \left(\partial_t \overline{\vec{\boldsymbol{u}}_\mathrm{g}} + \overline{\vec{\boldsymbol{u}}_\mathrm{g}} \partial_{\vec{\boldsymbol{x}}} \overline{\vec{\boldsymbol{u}}_\mathrm{g}} \right) - \tau_p \partial_{\vec{\boldsymbol{x}}} \boldsymbol{\tau}^r_g, \tag{10.15}$$

where $\vec{\boldsymbol{q}} = \overline{n \vec{\boldsymbol{u}}} - \bar{n} \overline{\vec{\boldsymbol{u}}}$. Both terms need modeling, but here we focus on the modeling of the disperse phase, so that the subgrid stress of the gas phase $\boldsymbol{\tau}^r_g$ is supposed to be given. The particulate phase number density-velocity correlation is:

$$q_i = -C_s \frac{\Delta^2 |\bar{s}|}{\mathrm{Sc}_t} \partial_{x_i} \bar{n}. \tag{10.16}$$

where Sc_t is the turbulence Schmidt number, C_s a model constant and $|\bar{s}|$ the filtered rate of strain.

10.3.3.2 From moderate to high Stokes number: the filtered MEF with ACBMM

In *Moreau et al. (2010)*, the authors develop a LES method based on the Mesoscopic Eulerian Formalism (*Février et al. 2005*) and the ACBMM. In fact, they filter the moment equations (Equation (2.2)), but they also use Favre averaging based on the disperse phase:

$$\bar{n} \widetilde{\varphi} = \iiint n G_\Delta(\vec{\boldsymbol{x}} - \vec{\boldsymbol{x}}_1) \varphi(\vec{\boldsymbol{x}}_1, t) \mathrm{d}\vec{\boldsymbol{x}}_1. \tag{10.17}$$

It leads to the following equations:

$$\begin{cases} \partial_t \bar{n} + \partial_{\vec{\boldsymbol{x}}} \cdot (\bar{n}\widetilde{\vec{\boldsymbol{u}}}) = 0, \\ \\ \partial_t (\bar{n}\widetilde{\vec{\boldsymbol{u}}}) + \partial_{\vec{\boldsymbol{x}}} \cdot (\bar{n}\widetilde{\vec{\boldsymbol{u}}} \otimes \widetilde{\vec{\boldsymbol{u}}} + \bar{\mathbf{P}} + \bar{n}\mathbf{T}) = \dfrac{\bar{n}(\widetilde{\vec{\boldsymbol{u}}_{\mathrm{g}}} - \widetilde{\vec{\boldsymbol{u}}})}{\tau_p}, \\ \\ \partial_t \overline{\mathcal{P}} + \partial_{\vec{\boldsymbol{x}}} \cdot (\overline{\mathcal{P}}\widetilde{\vec{\boldsymbol{u}}} + \overrightarrow{\widetilde{\mathbf{Q}}} + \overrightarrow{\mathbf{R}}) = -\bar{\mathbf{P}}\partial_{\vec{\boldsymbol{x}}}\widetilde{\vec{\boldsymbol{u}}} - \dfrac{-2\overline{\mathcal{P}}}{\tau_p} + \bar{n}\Pi, \end{cases} , \tag{10.18}$$

where:

$$T_{ij} = \widetilde{u_i u_j} - \widetilde{u}_i \widetilde{u}_j, \tag{10.19}$$

$$\Pi = -\widetilde{\boldsymbol{\Sigma}\partial_{\vec{\boldsymbol{x}}}\vec{\boldsymbol{u}}} - \widetilde{\boldsymbol{\Sigma}}\partial_{\vec{\boldsymbol{x}}}\widetilde{\vec{\boldsymbol{u}}}, \tag{10.20}$$

$$\overrightarrow{\mathbf{R}} = \overline{\mathcal{P}\vec{\boldsymbol{u}}} - \overline{\mathcal{P}}\widetilde{\vec{\boldsymbol{u}}}. \tag{10.21}$$

In this work, the authors address the closure of $\mathbf{T}$ by mean of a Smagorinski-Yoshizawa model:

$$T_{ij} = T^*_{ij} + q_{p,r}, \tag{10.22}$$

$$T^*_{ij} = -C_S \Delta^2 |\tilde{S}^*| \tilde{S}^*_{ij}, \tag{10.23}$$

$$q_{p,r} = C_Y \Delta_F^2 |\tilde{S}^*|^2. \tag{10.24}$$

In opposite to the equilibrium model, this one considers particle-Favre-averaged quantities only.

10.3.3.3 Filtering the kinetic equation directly

Kinetic-Based LES models are based on the filtering of the kinetic equation:

$$\partial_t \overline{f} + \partial_{\vec{\boldsymbol{x}}} \cdot (\vec{\boldsymbol{c}}\overline{f}) + \partial_{\vec{\boldsymbol{c}}} \cdot \left(\frac{\overline{\vec{\boldsymbol{u}}}_{\mathrm{g}} - \vec{\boldsymbol{c}}}{\tau_p} \overline{f} \right) = -\frac{1}{\tau_p} \partial_{\vec{\boldsymbol{c}}} \cdot (\vec{\boldsymbol{u}}_{\mathrm{g}} f)^r, \tag{10.25}$$

where $(\vec{\boldsymbol{u}}_{\mathrm{g}} f)^r = \overline{\vec{\boldsymbol{u}}_{\mathrm{g}} f} - \overline{\vec{\boldsymbol{u}}}_{\mathrm{g}} \bar{f}$ is the subgrid correlations between the disperse phase NDF and the gas velocity.
In the literature, two works have been devoted to this strategy. In *Pandya and Mashayek (2002)*, the authors derive the kinetic equation in direct analogy with the work of Reeks (1991; 1992) who uses the Lagrangian History Direct Interaction (LHDI):

$$-\frac{1}{\tau_p} \partial_{\vec{\boldsymbol{c}}} \cdot (\vec{\boldsymbol{u}}_{\mathrm{g}} f)^r = \partial_{\vec{\boldsymbol{c}}} \cdot \left(\boldsymbol{\mu} \partial_{\vec{\boldsymbol{c}}} \overline{f} + \boldsymbol{\lambda} \partial_{\vec{\boldsymbol{x}}} \overline{f} - \vec{\boldsymbol{\gamma}} \overline{f} \right). \tag{10.26}$$

The expressions of these coefficients depend on the history of the particles and especially on the gas velocity seen by the particles along their trajectories:

$$\lambda_{ki} = \frac{1}{\tau_p^2} \int_0^t (u_{g,i}(\vec{\boldsymbol{x}}, t), u_{g,i}(\vec{\boldsymbol{x}}, \vec{\boldsymbol{c}}, t|t_1))^r G_{jk} \mathrm{d}t_1, \tag{10.27}$$

$$\mu_{ki} = \frac{1}{\tau_p^2} \int_0^t (u_{g,i}(\vec{\boldsymbol{x}}, t), u_{g,i}(\vec{\boldsymbol{x}}, \vec{\boldsymbol{c}}, t|t_1))^r \frac{\mathrm{d}G_{jk}}{\mathrm{d}t} \mathrm{d}t_1, \tag{10.28}$$

$$\gamma_i = \frac{1}{\tau_p^2} \int_0^t (\partial_{x_k} u_{g,i}(\vec{\boldsymbol{x}}, t), u_{g,i}(\vec{\boldsymbol{x}}, \vec{\boldsymbol{c}}, t|t_1))^r G_{jk} \mathrm{d}t_1, \tag{10.29}$$

where G_{jk} is the Green function.

These parameters represent the impact of the subgrid turbulence on the particle. $\boldsymbol{\mu}$ models the fact that the particle agitation energy tends towards the one of the gas subgrid scales because of the drag force, and acts as a white-noise. $\boldsymbol{\lambda}$ is due to the correlations of the turbulence: contrary to white-noise process, the turbulence is not δ-correlated in time and this coefficient is here to represent these correlations. $\vec{\boldsymbol{\gamma}}$ is an additional correction needed to account for the inhomogeneity of the flow into the drag force.

After defining these coefficients, *Pandya and Mashayek (2002)* propose a Dynamic filtering procedure applied to both gas and disperse phase, to derive a fully consistent LES approach, keeping the same form for the kinetic equation, but with different expression for the coefficients.

After obtaining the kinetic equation, one has to go up to the moment level. In *Pandya and Mashayek (2002)*, the authors derive equations for zero-to-second order moments and close the fluxes by using a zero third-order central moments assumption. Contrary to the model of *Moreau et al. (2010)*, where the sole filtered random uncorrelated energy (RUE) is solved, the total energy of the particles is solved here. The contribution of RUE as well as subgrid scale correlated energy is accounted for, without any direct access to the former or the latter. In fact, this model does not need do have access to each of them separately, and it is fully closed. Despite the full derivation of a consistent model, the authors do not propose any evaluation of the quality of this modeling approach.

In *Zaichik et al. (2009)*, the authors follow the same strategy but based on the work of *Zaichik (1999)*, which considers the impact of the gas phase on the disperse phase to be a Gaussian process, and thus make use of the Furutsu-Donsker-Novikov Formula (*Novikov 1964*). Eventually, they obtain a close shape for the subgrid term, without γ_i:

$$-\frac{1}{\tau_p} \partial_{\vec{\boldsymbol{c}}} \cdot (\vec{\boldsymbol{u}}_{\mathrm{g}} f)^r = \partial_{\vec{\boldsymbol{c}}} \cdot \left(\boldsymbol{\mu} \partial_{\vec{\boldsymbol{c}}} \overline{f} + \boldsymbol{\lambda} \partial_{\vec{\boldsymbol{x}}} \overline{f} \right). \tag{10.30}$$

The authors also derive moment equations, and they propose to close the unknown fluxes using a Chapman-Enskog expansion around the Maxwellian distribution, and to consider the isotropic assumption for the gas subgrid stresses.

Like in the model of Moreau et al. (2010), they derive a transport equation for the trace of the central second order moments.
They rewrite the subgrid terms in the kinetic equation:

$$\lambda_{ij} = g_u^r \tau_{g,ij}^r, \quad \mu_{ij} = \tau_{g,ik}^r \left(\frac{f_u^r}{\tau_p} + l_u^r \partial_{x_k} \overline{u}_j \right), \tag{10.31}$$

$$\tag{10.32}$$

where f_u^r, g_u^r and l_u^r are response coefficients which measure the coupling between the particles and the unresolved small scale turbulent eddies.
If the autocorrelation function of the continuous phase velocity fluctuations determined along the particle trajectory is assumed to be an exponential function ($\boldsymbol{\Psi}_{Lp} = \exp(-\frac{\tau}{T_L^r})$, where T_L^r is the Lagrangian integral timescale of residual velocity viewed by a particle Zaichik et al. (2008)), the long-time values of response coefficients are obtained (see Zaichik et al. (2009) for details):

$$f_u^r = \frac{1}{1 + \mathrm{St}_L^r}, \quad g_u^r = \frac{1}{\mathrm{St}_L^r (1 + \mathrm{St}_L^r)}, \quad l_u^r = \frac{1}{\mathrm{St}_L^r (1 + \mathrm{St}_L^r)^2}, \tag{10.33}$$

where $\mathrm{St}_L^r = \tau_p / T_L^r$ is the Stokes number relative to the Lagrangian integral timescale of the residual gas field velocity T_L^r. This Stokes number describes the inertia of a particle in terms of its interaction with energy carrying eddies at the subgrid scales.

10.4 Low St limits in LES moment models

The modeling of the dynamics of particles has to reproduce the evolution of two kinds of energy: the uncorrelated central energy of the unfiltered motion (UCE) and the subgrid correlated energy (SCE). As stated in Zaichik et al. (2009), these two energies have different behaviors with respect to the Stokes number and the filter size. On the one side, the UCE is insensitive to the filter size, and is purely related to the description of the PTC, which is a large scale effect Moreau et al. (2010) that appears for large Stokes numbers with respect to the Kolmogorov length scale. On the other side, the SCE is directly related to the filter size, and tends to zero for zero filter size (DNS limit). Moreover, the SCE decreases while increasing the Stokes number, as particles become more and more insensitive to the subgrid scales. Consequently, the low Stokes number limit of a LES model is of primary importance, as the dynamics of particles will be primary driven by this model in this limit. Here, a brief analysis of this limit is given for each model.

10.4.0.1 Equilibrium model

For the LES model of *Shotorban and Balachandar (2007)*, the limit system is:

$$\partial_t \overline{n} + \partial_{\vec{\boldsymbol{x}}} \overline{n}\overline{\vec{\boldsymbol{u}}} = \partial_{x_i} \left(C_s \frac{\overline{\Delta}^2 |\overline{s}|}{Sc_t} \partial_{x_i} n \right). \tag{10.34}$$

Equation (10.34) is an advection-diffusion equation with an isotropic diffusion coefficient. In the case of zero filter-width, the model recovers the zero Stokes number limit of the DNS system, that is a passive scalar equation for the number density field. There is no direct link between the limiting diffusion coefficient of the particulate phase and the subgrid tensor of the gas phase in the context of the dynamic procedure that is used in *Shotorban and Balachandar (2007)*.

10.4.0.2 Moreau et al.

In this model, the authors do not propose solutions to close the particle-gas velocity correlations that are included in the particle-Favre-averaged gas velocity. Actually, in a real computation, $\widetilde{\vec{\boldsymbol{u}}_{\mathrm{g}}}$ is not available, as you can have Reynolds-averaged gas velocity only in the case of incompressible gas velocity field. If the user uses the available gas velocity without modeling this term, it implies that:

$$\overline{n}\widetilde{\vec{\boldsymbol{u}}_{\mathrm{g}}} = \overline{n}\overline{\vec{\boldsymbol{u}}_{\mathrm{g}}}, \tag{10.35}$$

$$\begin{split}\iiint n\vec{\boldsymbol{u}}_{\mathrm{g}} G_\Delta(\vec{\boldsymbol{x}} - \vec{\boldsymbol{x}}_1)\varphi(\vec{\boldsymbol{x}}_1, t)\mathrm{d}\vec{\boldsymbol{x}}_1 = \\ \iiint nG_\Delta(\vec{\boldsymbol{x}} - \vec{\boldsymbol{x}}_1)\varphi(\vec{\boldsymbol{x}}_1, t)\mathrm{d}\vec{\boldsymbol{x}}_1 \iiint \vec{\boldsymbol{u}}_{\mathrm{g}} G_\Delta(\vec{\boldsymbol{x}} - \vec{\boldsymbol{x}}_1)\varphi(\vec{\boldsymbol{x}}_1, t)\mathrm{d}\vec{\boldsymbol{x}}_1,\end{split} \tag{10.36}$$

which can be true only in the case of a constant density field or a constant gas velocity field. In fact, the missing term can be mandatory for very small Stokes numbers. It is still an open subject to check if a transposed gradient model like the one used in the work of *Simonin et al. (1993)* is suitable for very small Stokes numbers.
For the model of Moreau et al. *Moreau et al. (2010)*, the limit system is:

$$\partial_t \overline{n} + \partial_{\vec{\boldsymbol{x}}} \overline{n}\widetilde{\mathbf{u}}_g = 0. \tag{10.37}$$

This equation involves the particle-Favre-averaged gas velocity, which needs a model to be closed. The low Stokes number limit is then not clearly determined. However, as the work of *Moreau et al. (2010)* focuses on Stokes number higher than 1, the impact of the low Stokes number limit was not investigated and requires an additional study. In the work of *Riber (2007)*, this velocity was replaced by the available gas velocity in the computation. The latter is the Reynolds averaged velocity or gas density-Favre averaged velocity, which can be considered as a model for high Stokes number, and for which the asymptotic limit is a passive scalar equation for the number density field advected with the resolved gas velocity:

$$\partial_t \overline{n} + \partial_{\vec{\boldsymbol{x}}} \overline{n} \overline{\vec{\boldsymbol{u}}}_g = 0. \tag{10.38}$$

It is important to note that the subgrid correlation between the fluid turbulent velocity and the particles distribution can have an important effect when dealing with dense inclusions such as fluidized beds due to the two way coupling and need to be modeled as shown in the a posteriori test in the work of *Parmentier et al. (2012)*.

10.4.0.3 Kinetic-Based LES models

For kinetic-based model, an asymptotic limit can be determined either at the kinetic or at the moment level. For the sake of simplicity, we only consider the asymptotic limit of Zaichik's system of equations, as the main features of the low Stokes number flows are contained in λ and μ, the γ term of Pandya and Mashayek being of interest for inhomogeneous flow only. The non-dimensional form of the kinetic equation is used and the reference time scale is the Lagrangian Integral one of the turbulence:

$$\partial_{t^*} \overline{f} + \vec{\boldsymbol{c}}^* \cdot \partial_{\vec{\boldsymbol{x}}^*} \overline{f} + \partial_{\vec{\boldsymbol{c}}^*} \cdot \left(\frac{\overline{\vec{\boldsymbol{u}}}_g^* - \vec{\boldsymbol{c}}^*}{\mathrm{St}} \overline{f} \right) = \partial_{\vec{\boldsymbol{c}}^*} \cdot \left(\boldsymbol{\mu}^* \partial_{\vec{\boldsymbol{c}}^*} \overline{f} + \boldsymbol{\lambda}^* \partial_{\vec{\boldsymbol{x}}^*} \overline{f} \right), \tag{10.39}$$

where:

$$\mu^*_{ij} = \tau^*_{g,ik} \left(\frac{f^r_u}{\mathrm{St}} \delta_{kj} + l^r_u \frac{\partial \overline{u}^*_{g,j}}{\partial x^*_k} \right), \quad \lambda^*_{ij} = g^r_u \tau^*_{g,ij}. \tag{10.40}$$

In the following, star exponents implying nondimensionalization are dropped for the sake of clarity.

To determine the equilibrium state and the asymptotic limit of the filtered kinetic equation Equation (10.39), The Chapman-Enskog expansion is used *Chapman and Cowling (1939)*. Contrary to the one proposed in *Alipchenkov and Zaichik (2007)*, it is performed in the classical way, assuming a decomposition of the solution into power of St, one gets:

$$\overline{f} = \overline{f}^0 + \mathrm{St} \overline{f}^0 \varphi^1 + \mathcal{O}\left(\mathrm{St}^2\right). \tag{10.41}$$

Rewriting Equation (10.39)

$$\partial_t \overline{f} + \vec{\boldsymbol{c}}.\partial_{\vec{\boldsymbol{x}}} \overline{f} = \frac{1}{\mathrm{St}} \mathcal{J}(\overline{f}), \tag{10.42}$$

where $\mathcal{J}(f)$ is the relaxation operator:

$$\mathcal{J}(\overline{f}) = \partial_{\vec{c}} \cdot \left[(\vec{c} - \overline{\vec{u}}_g)\overline{f} + \mathrm{St}\boldsymbol{\mu}\partial_{\vec{c}}\overline{f} + \mathrm{St}\boldsymbol{\lambda}\partial_{\vec{x}}\overline{f} \right]. \tag{10.43}$$

Inserting Equation (10.41) into Equation (10.42), and grouping terms by powers of St:

$$\partial_t \overline{f}^0 + \vec{c} \cdot \partial_{\vec{x}} \overline{f}^0 + \mathrm{St}\left(\partial_t \overline{f}^0 \varphi^1 + \vec{c} \cdot \partial_{\vec{x}} \overline{f}^0 \varphi^1 \right) = \frac{1}{\mathrm{St}} \mathcal{J}(\overline{f}^0) + \mathcal{J}(\overline{f}^0 \varphi^1) + \mathcal{O}(\mathrm{St}). \tag{10.44}$$

For small Stokes number, the zeroth order of Equation (10.44) is:

$$\mathcal{J}(\overline{f}^0) = \mathrm{St}\boldsymbol{\lambda}\partial_{\vec{x}}\overline{f}^0 + \mathrm{St}\boldsymbol{\mu}\partial_{\vec{c}}\overline{f}^0 - \left(\overline{\vec{u}}_g - \vec{c} \right) \overline{f}^0 = 0. \tag{10.45}$$

The solution of such an equation has the form:

$$\overline{f}^0(x,u) = \Gamma(\vec{x},\vec{c}) \frac{n}{(2\pi)^{3/2}\sqrt{|\boldsymbol{\tau}_g|}} \exp\left(-(\vec{c} - \overline{\vec{u}}_g)^t \boldsymbol{\tau}_g^{-1} (\vec{c} - \overline{\vec{u}}_g) \right), \tag{10.46}$$

where $\Gamma(\vec{x},\vec{c})$ is an unknown function that tends to 1 in the case of an homogenous NDF in space. The zeroth order distribution leads to the following equation on the density:

$$\partial_t n + \partial_{\vec{x}} \cdot n\vec{u}^0 = 0, \tag{10.47}$$

where $u^0 = \int u f^0 dv$. To find u^0, the zeroth order moment of Equation (10.45) is taken and leads to:

$$\vec{u}^0 = \overline{\vec{u}}_g - \frac{\boldsymbol{\tau}_g}{n} \partial_{\vec{x}} n, \tag{10.48}$$

so that the asymptotic limit at the kinetic level leads to the following asymptotic limit at the moment level:

$$\partial_t n + \partial_{\vec{x}} \cdot n\overline{\vec{u}}_g = \partial_{\vec{x}} \cdot (\boldsymbol{\tau}_g \partial_{\vec{x}} n). \tag{10.49}$$

Like the model of *Shotorban and Balachandar (2007)*, the asymptotic limit is an advection-diffusion equation. Here this diffusion coefficient is the subgrid tensor of the gaseous velocity field, so that, comparing to *Shotorban and Balachandar (2007)*, this diffusion coefficient could be anisotropic and could be definitely an improvement in the low Stokes number limit. It is also worth noticing that the resulting moment system does not depend on any closure at the moment level. To achieve the description of the low Stokes number limit, taken the first order moment of Equation (10.45), the asymptotic limit of the internal energy is recovered (*Chalons et al. 2015*):

$$\boldsymbol{\sigma}^0 = \boldsymbol{\tau}_g \left(1 - \partial_{\vec{x}} \cdot \overline{\vec{u}}_g - \partial_{\vec{x}} \cdot \left(\frac{\boldsymbol{\tau}_g}{n} \partial_{\vec{x}} n \right) \right). \tag{10.50}$$

10.5 Physical contents of the transported moments

Looking at the literature, several ways are available to derive and to close a LES model. This strategies differ by the level at which the filtering is operated, the moments that are transported and the way the moment equations are closed. The possible derivation strategies are summarized in Figure 10.2.
Theoretically, there is equivalence between filtering at the kinetic level and filtering at the moment level:

$$\begin{aligned}\overline{M}_{i,j,k}(t,\vec{x}) &= \int G_{\Delta}(\vec{x}-\vec{x}_1)\left(\int c_1^i c_2^j c_3^k f(t,\vec{x}_1,\vec{c})\mathrm{d}\vec{c}\right)\mathrm{d}\vec{x}_1 && (10.51)\\ &= \int c_1^i c_2^j c_3^k \left(\int G_{\Delta}(\vec{x}-\vec{x}_1) f(t,\vec{x}_1,\vec{c})\mathrm{d}\vec{x}_1\right)\mathrm{d}\vec{c} && (10.52)\\ &= M^{\overline{f}}_{i,j,k}(t,\vec{x}). && (10.53)\end{aligned}$$

This means that, if full moments are used, methods based on moment filtering and kinetic equation filtering are equivalent, the sole remaining issue being the closure of the equations. However, this equivalence does not hold when centered moments are considered instead of full moments because of the space dependence of the velocity used in the centering procedure (time dependence is omitted for the sake of clarity):

$$\begin{aligned}&\overline{C}_{i,j,k}(\vec{x}) = \\ &\int G_{\Delta}(\vec{x}-\vec{x}_1)\left(\int (c_1-u_1(\vec{x}_1))^i(c_2-u_2(\vec{x}_1))^j(c_3-u_3(\vec{x}_1))^k f(\vec{x}_1\vec{c})\mathrm{d}\vec{c}\right)\mathrm{d}\vec{x}_1\\ &\neq \int G_{\Delta}(\vec{x}-\vec{x}_1)\int (c_1-\widetilde{u}_1(\vec{x}_1))^i(c_2-\widetilde{u}_2(\vec{x}_1))^j(c_3-\widetilde{u}_3(\vec{x}_1))^k \overline{f}(\vec{x}_1,\vec{c})\\ &= C^{\overline{f}}_{i,j,k}(\vec{x}) && (10.54)\end{aligned}$$

The main consequence is that the content of the LES models may differ: if central moment equations are first derived and are then filtered, the central moments will not contain the contribution of the subgrid motion, whereas the other strategy will generate moments which contain both the subgrid motion and the agitation motion contributions. To illustrate this statement, we can have a look to the trace of the pressure tensor:

$$\overline{n}\mathrm{Tr}\left(\widetilde{\boldsymbol{\Sigma}}(\vec{\boldsymbol{x}})\right) = \int G(\vec{\boldsymbol{x}}-\vec{\boldsymbol{x}}_1)\left(\int \sum_{i=1,3}(c_i - u_i(\vec{\boldsymbol{x}}_1))^2 f(\vec{\boldsymbol{x}}_1,\vec{\boldsymbol{c}})\mathrm{d}\vec{\boldsymbol{c}}\right)\mathrm{d}\vec{\boldsymbol{x}}_1 \tag{10.55}$$

$$= \int G(\vec{\boldsymbol{x}}-\vec{\boldsymbol{x}}_1)\left(\int \sum_{i=1,3}(c_i^2 - 2c_iu_i(\vec{\boldsymbol{x}}_1) + u_i(\vec{\boldsymbol{x}}_1)^2) f(\vec{\boldsymbol{x}}_1,\vec{\boldsymbol{c}})\mathrm{d}\vec{\boldsymbol{c}}\right)\mathrm{d}\vec{\boldsymbol{x}}_1 \tag{10.56}$$

$$= \int \sum_{i=1,3} c_i^2\overline{f}(\vec{\boldsymbol{x}},\vec{\boldsymbol{c}})\mathrm{d}\vec{\boldsymbol{c}} - \overline{n}\sum_{i=1,3}\widetilde{u_i^2} \tag{10.57}$$

$$\neq \overline{n}\mathrm{Tr}\left(\boldsymbol{\Sigma}^{\overline{f}}(\vec{\boldsymbol{x}})\right) = \int \sum_{i=1,3} c_i^2\overline{f}(\vec{\boldsymbol{x}},\vec{\boldsymbol{c}})\mathrm{d}\vec{\boldsymbol{c}} - \overline{n}\sum_{i=1,3}\widetilde{u}_i^2. \tag{10.58}$$

The difference between the filtered second order central moment, $\overline{n}\widetilde{\boldsymbol{\Sigma}}(\vec{\boldsymbol{x}})$, and the second order central moment of the filtered NDF, $\overline{n}\boldsymbol{\Sigma}^{\overline{f}}(\vec{\boldsymbol{x}})$, is the subgrid contribution $\overline{n}\boldsymbol{\Sigma}_r$:

$$\overline{n}\widetilde{\vec{\boldsymbol{u}}\otimes\vec{\boldsymbol{u}}} = \overline{n}\widetilde{\vec{\boldsymbol{u}}}\otimes\widetilde{\vec{\boldsymbol{u}}} + \overline{n}\left(\widetilde{\vec{\boldsymbol{u}}\otimes\vec{\boldsymbol{u}}} - \widetilde{\vec{\boldsymbol{u}}}\otimes\widetilde{\vec{\boldsymbol{u}}}\right) = \overline{n}\left(\widetilde{\vec{\boldsymbol{u}}}\otimes\widetilde{\vec{\boldsymbol{u}}} + \boldsymbol{\Sigma}_r\right), \tag{10.59}$$

$$\overline{n}\widetilde{\boldsymbol{\Sigma}}(\vec{\boldsymbol{x}}) = \overline{n}\boldsymbol{\Sigma}^{\overline{f}}(\vec{\boldsymbol{x}}) - \overline{n}\boldsymbol{\Sigma}_r. \tag{10.60}$$

$$\begin{tikzcd}
f \arrow[r, "\text{filtering}"] \arrow[d, dashed, "\text{moments}"'] & \overline{f} \arrow[r, dashed, "\text{moments}"] & \overline{\mathbf{M}} \\
\mathbf{M} \arrow[r, "\text{filtering}"] \arrow[d, dotted, "\text{centered moments}"'] & \overline{\mathbf{M}} \arrow[r, dotted, "\text{centered moments}"] & \overline{\mathbf{C}}_{\tilde{u}} \\
\mathbf{C}_u \arrow[r, "\text{filtering}"] & \overline{\mathbf{C}_u} &
\end{tikzcd}$$

Figure 10.2: *Derivation strategies for a LES moment method for disperse phase flows.*

At the end, depending on the way the LES moment method is derived, we can end up with a different content in the transported moments, containing either the full velocity variance due to filtering and PTC, or the PTC contribution only. Getting the sole contribution of the filtering on the velocity distribution is only possible if the unfiltered field is monokinetic.

10.6 Commutativity breaking in the presence of moment closure

As suggested in *Vié et al. (2015)*, for a chosen moment method, we can cast the associated kinetic equation using a notional collision operator that leads to the closed moment system:

$$\partial_t f + \partial_{\vec{\boldsymbol{x}}} \cdot (\vec{\boldsymbol{c}} f) + \partial_{\vec{\boldsymbol{c}}} \cdot \left(\frac{\overrightarrow{\mathbf{u}_g} - \vec{\boldsymbol{c}}}{\tau_p} f \right) = \frac{f - f_{eq}}{\tau_c}, \tag{10.61}$$

where τ_c is the fictive collision time scale and f_{eq} is the expected kinetic closure for the moment equations. In the limit of infinitely small collision time τ_c, this kinetic equation leads to the following kinetic equation:

$$\partial_t f_{eq} + \partial_{\vec{\boldsymbol{x}}} \cdot (\vec{\boldsymbol{c}} f_{eq}) + \partial_{\vec{\boldsymbol{c}}} \cdot \left(\frac{\overrightarrow{\mathbf{u}_g} - \vec{\boldsymbol{c}}}{\tau_p} f_{eq} \right) = 0, \tag{10.62}$$

which corresponds to the appropriate moment equations. This collision term exhibits the effect of the closure choice, which leads to a first level of approximation of the real kinetic equation.
Through filtering Eq. 10.62, we get:

$$\partial_t \overline{f}_{eq} + \partial_{\vec{\boldsymbol{x}}} \cdot (\vec{\boldsymbol{c}} \overline{f}_{eq}) + \partial_{\vec{\boldsymbol{c}}} \cdot \left(\frac{\overline{\vec{\boldsymbol{u}}_{\mathrm{g}}} - \vec{\boldsymbol{c}}}{\tau_p} \overline{f}_{eq} \right) = -\frac{1}{\tau_p} \partial_{\vec{\boldsymbol{c}}} \cdot (\vec{\boldsymbol{u}}_{\mathrm{g}} f_{eq})^r, \tag{10.63}$$

where the filtered equilibrium distribution $\overline{f}_{eq}$ is:

$$\overline{f}_{eq}(t, \vec{\boldsymbol{x}}, \vec{\boldsymbol{c}}) = \int G(\vec{\boldsymbol{x}} - \vec{\boldsymbol{x}}', \Delta) f_{eq}(t, \vec{\boldsymbol{x}}', \vec{\boldsymbol{c}}) \mathrm{d}\vec{\boldsymbol{x}}'. \tag{10.64}$$

In the limit of zero filter width, the equilibrium distribution is not modified:

$$\lim_{\Delta \to 0} \overline{f}_{eq}(\vec{\boldsymbol{x}}, \vec{\boldsymbol{c}}) = \int \delta(\vec{\boldsymbol{x}} - \vec{\boldsymbol{x}}') f_{eq}(t, \vec{\boldsymbol{x}}', \vec{\boldsymbol{c}}) \mathrm{d}\vec{\boldsymbol{x}}' = f_{eq}(\vec{\boldsymbol{x}}, \vec{\boldsymbol{c}}). \tag{10.65}$$

The important point here is that even the filtered equilibrium distribution has not necessarily the same shape as the unfiltered one. As a result, in the presence of a closure assumption, the commutativity between the filtering and the moment operations is broken.
A pathological example is when considering a monokinetic closure for the unfiltered problem, i.e. $f_{eq}^{MK} = n(t, \vec{\boldsymbol{x}}) \delta\left(\vec{\boldsymbol{c}} - \mathbf{u}(t, \vec{\boldsymbol{x}})\right)$. As already stated, this distribution is a fairly accurate approximation for small Stokes number in turbulent flows. However, involving a filtering operation necessarily leads to a velocity dispersion, incompatible with the zero dispersion assumption of the MK closure. The main consequence is that the MK closure is not adequate for LES moment methods.

The same reasoning can be made using ISO and AG closures. In these cases, a Gaussian (isotropic or not) distribution is spatially filtered. In this case, even if the Gaussian distribution can capture velocity variances, summing over Gaussian distribution does not necessarily lead to a new Gaussian distribution. As a consequence, the Gaussian closure for the LES moment method is not a direct filtering of the DNS Gaussian moment method; it is another approximation by itself. This approximation is however consistent with the DNS method in the limit of zero filter-width.

10.7 The kinetic-based AG-LES moment

The closure on the kinetic level is done based on the Kraichnan's Lagrangian history direct interaction (LHDI) used by (*Reeks 1991; Reeks 1992*) in the context of RANS modeling. Then the correlation between the carrier phase velocity fluctuation and the number density is given in function of the diffusivity tensors, $\boldsymbol{\lambda}$ and $\boldsymbol{\mu}$:

$$(\vec{\boldsymbol{u}}_{\mathrm{g}} f)^{r} = \overline{\vec{\boldsymbol{u}}_{\mathrm{g}} f} - \overline{\vec{\boldsymbol{u}}_{\mathrm{g}}}\,\overline{f} = -\tau_p \left(\partial_{\vec{\boldsymbol{x}}} \cdot \boldsymbol{\lambda} \overline{f} + \partial_{\vec{\boldsymbol{c}}} \cdot \boldsymbol{\mu} \overline{f} \right). \tag{10.66}$$

By multiplying the filtered WB equation by power the i^{th}, j^{th} and k^{th} power of the component of $\vec{\boldsymbol{c}}$ and integrating the result over the phase space, the general filtered moment equation is obtained:

$$\partial_t \overline{M}_{i,j,k} + \partial_{\vec{\boldsymbol{x}}} \cdot \begin{pmatrix} \overline{M}_{i+1,j,k} \\ \overline{M}_{i,j+1,k} \\ \overline{M}_{i,j,k+1} \end{pmatrix} + \partial_{x_k} \begin{pmatrix} i\overline{M}_{i-1,j,k} \\ j\overline{M}_{i,j-1,k} \\ l\overline{M}_{i,j,k-1} \end{pmatrix} \vee \overrightarrow{\lambda_{k*}} =$$
$$\frac{1}{\tau_p} \left(\vec{\boldsymbol{u}}_g \cdot \begin{pmatrix} i\overline{M}_{i-1,j,l} \\ j\overline{M}_{i,j-1,k} \\ k\overline{M}_{i,j,k-1} \end{pmatrix} - (i+j+k)\overline{M}_{i,j,k} + \tau_p \begin{pmatrix} i(i-1)\overline{M}_{i-2,j,l} \\ j(j-2)\overline{M}_{i,j-2,k} \\ l(l-2)\overline{M}_{i,j,k-2} \end{pmatrix} \vee \boldsymbol{\mu} \right). \tag{10.67}$$

The filtered number density function is assumed to read: $\overline{f}_{eq}(t, \overrightarrow{\mathbf{x}}, \vec{\boldsymbol{c}}) = \overline{\rho}(t, \overrightarrow{\mathbf{x}})\mathcal{N}(\vec{\boldsymbol{c}} - \overrightarrow{\widetilde{\mathbf{u}}}(t, \overrightarrow{\mathbf{x}}), \boldsymbol{\Sigma}(t, \overrightarrow{\mathbf{x}}))$ where $\mathcal{N}$ is a joint Gaussian distribution of center $\overrightarrow{\widetilde{\mathbf{u}}}$ and covariance matrix $\boldsymbol{\Sigma} = (\sigma_{ij})$ in the space of dimension N_d:

$$\mathcal{N}(\vec{\boldsymbol{c}} - \overrightarrow{\widetilde{\mathbf{u}}}, \boldsymbol{\Sigma}) = \frac{|\boldsymbol{\Sigma}|^{-1/2}}{(2\pi)^{N_d/2}} \exp\left(-\frac{1}{2} (\vec{\boldsymbol{c}} - \overrightarrow{\widetilde{\mathbf{u}}})^T \boldsymbol{\Sigma}^{-1} (\vec{\boldsymbol{c}} - \overrightarrow{\widetilde{\mathbf{u}}}) \right). \tag{10.68}$$

where superscript $\overline{f}$ is omitted on $\boldsymbol{\Sigma}$ for the sake of clarity. Using this closure, the solved filtered kinetic equation is the following:

$$\partial_t \overline{f}_{eq} + \partial_{\vec{\boldsymbol{x}}} \cdot (\vec{\boldsymbol{c}} \overline{f}_{eq}) + \partial_{\vec{\boldsymbol{c}}} \cdot \left(\frac{\overline{\vec{\boldsymbol{u}}_{\mathrm{g}}} - \vec{\boldsymbol{c}}}{\tau_p} \overline{f}_{eq} \right) = -\frac{1}{\tau_p} \partial_{\vec{\boldsymbol{c}}} \cdot (\vec{\boldsymbol{u}}_{\mathrm{g}} f)^{r}, \tag{10.69}$$

for which no Equilibrium assumption is made for the subgrid scale. As a result, the equilibrium distribution will contain the subgrid contribution as well as the PTC part, without any access to the partitioning between the two, but with a closed system of equations at the moment level. The LES model based on the Anisotropic Gaussian distribution on the kinetic level is presented hereafter. The resulting system of equations is then:

$$\begin{aligned}
&\partial_t \overline{\rho} + \partial_{\vec{\boldsymbol{x}}} \cdot (\overline{\rho}\, \overrightarrow{\widetilde{\mathbf{u}}}\,) = 0, \\
&\partial_t (\overline{\rho}\, \overrightarrow{\widetilde{\mathbf{u}}}\,) + \partial_{\vec{\boldsymbol{x}}} \cdot (\overline{\rho}\, \overrightarrow{\widetilde{\mathbf{u}}} \otimes \overrightarrow{\widetilde{\mathbf{u}}} + \mathbf{P}) + \partial_{x_k} (\overline{\rho} \vee \overrightarrow{\lambda_{k*}}) = \frac{\overline{\rho}(\overrightarrow{\overline{\mathbf{u}}_g} - \overrightarrow{\widetilde{\mathbf{u}}}\,)}{\tau_p}, \\
&\partial_t (\overline{\rho}\mathbf{E}) + \partial_{\vec{\boldsymbol{x}}} \cdot ((\overline{\rho}\mathbf{E} + \mathbf{P}) \vee \overrightarrow{\widetilde{\mathbf{u}}}\,) + \partial_{x_k} (\overline{\rho}\, \overrightarrow{\widetilde{\mathbf{u}}} \vee \overrightarrow{\lambda_{k*}}) = \frac{\overline{\rho}(\overrightarrow{\overline{\mathbf{u}}_g} \vee \overrightarrow{\widetilde{\mathbf{u}}} - 2\mathbf{E}) + \tau_p \overline{\rho} \vee \boldsymbol{\mu}}{\tau_p}, \\
&\text{where } \mathbf{E} = \tfrac{1}{2} \overrightarrow{\widetilde{\mathbf{u}}} \otimes \overrightarrow{\widetilde{\mathbf{u}}} + \mathbf{P}/(2\overline{\rho}) \text{ and } \mathbf{P} = \overline{\rho}\boldsymbol{\Sigma}.
\end{aligned} \tag{10.70}$$

Models for $\boldsymbol{\lambda}$ and $\boldsymbol{\mu}$ are needed in order to have a closed system. Here the models based on the work of (*Zaichik et al. 2009*) are used.

It would be intresting in the continuiation of this work to compare the final system of equations with other LES models from the litterature to clarify the physical meaning of the terms found in this equation and compare the closures at the macroscopique level.

By coupling this formalism with the high order Multi-fluid method (TSM), the TSM AG LES can be obtained. This manipulation is straightforward.

Chapter 11

AG LES preliminary results

In this chapter preliminary results using the AG LES model are conducted and compared to the AG DNS results coupled with the DNS field for the gas velocity and with the filtered gas velocity. First, the used subgrid closures are presented in section 11.1 along with the filtering procedure. Then, in section 11.2 the qualitative results for the number density and the velocity are compared for various Stokes numbers, namely $\mathrm{St} = \{0.1, 1, 5, 15\}$. *Finally, the statistical results for the segregation and the mean total energy are presented in section 11.3 as a function of time for a given* St *as well as for fixed times as a function of the Stokes numbers. The test case presented is a 2D frozen HIT therefore one should keep in mind that the results give only a general idea of the dependence of the LES simulation on the subgrid terms but cannot be directly translated to realistic configurations.*

11.1 Subgrid closures and LES filtering

The DNS gas velocity field is a 2D box of a frozen homogeneous isotropic turbulence of size $\mathcal{L} = 4$ based on the energy spectrum of Pope. It has the following characteristics: the mean dissipation rate $\langle \varepsilon \rangle = 0.01678$, the mean turbulent kinetic energy $\langle \mathrm{TKE} \rangle = 0.04110$. The Kolmogorov length and time scales of this field are respectively $\eta = 0.01563$ and $\tau_K = 0.24414$. Based on the longitudinal velocity autocorrelation function $f_{long}(r)$ shown in Figure 11.1 the longitudinal integral scale is computed $L_{11} = 0.37843$. Thus the Reynolds numbers based on the integral length scale is $\mathrm{Re}_L = 76.7$. A geometric construction is then used to calculate the longitudinal Taylor microscale λ_f by plotting the parabola $p(r)$ osculating the longitudinal autocorrelation function at zero separation distance ($p(0) = f(0)$). This parabola reads (Pope 2000):

$$p(r) = 1 + \frac{f''_{long}(0) r^2}{2} = 1 - \frac{r^2}{\lambda_f}. \tag{11.1}$$

λ_f is obtained as the intersection point between the parabola and the axis of separation distance as shown in Figure 11.1.

Finally the longitudinal Taylor microscale is found to be equal to 0.2 and the corresponding Reynolds number based on the transverse microscale $\lambda_g = \frac{\lambda_f}{2}$ is $\mathrm{Re}_\lambda = 28.7$.

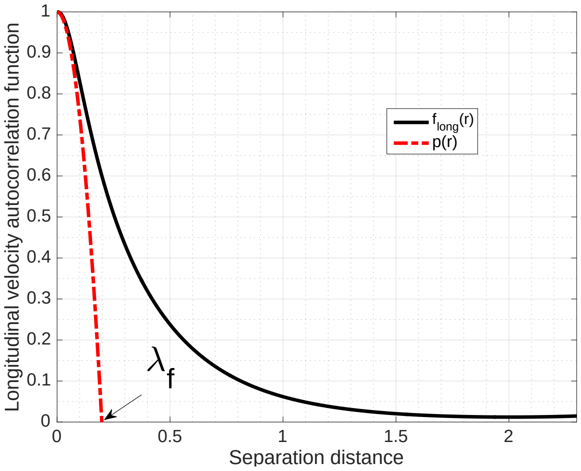

Figure 11.1: *Longitudinal velocity autocorrelation function along with the Taylor microscale geometric computation.*

These properties are summarized in Table 11.1.

Table 11.1: *Turbulence properties of the HIT*

$\langle\varepsilon\rangle$	$\langle\mathrm{TKE}\rangle$	η	τ_K	Re_L	Re_λ
0.01678	0.04110	0.01563	0.24414	76.7	28.7

11.1.1 Subgrid closure

For the models of $\boldsymbol{\lambda}$ and $\boldsymbol{\mu}$ presented earlier based on the work of *Zaichik et al. (2009)*, the subgrid stress tensor $\boldsymbol{\tau}_g^r$ should be modeled as well as the Lagrangian integral timescale of the residual gas field velocity T_L^r.

In this work the subgrid stress tensor is computed directly from the knoweledge of the DNS gas velocity field.

This timescale T_L^r is assumed to be given by the following equation in the work of *Zaichik et al. (2009)*; *Fede and Simonin (2006)* :

$$T_L^r = \alpha \frac{\langle \mathrm{TKE}^r \rangle}{\langle \varepsilon^r \rangle}, \quad \alpha = \frac{4}{3C_0}\left(1 + \frac{C_1}{\mathrm{Re}_\lambda}\right), \tag{11.2}$$

where $\langle\mathrm{TKE}^r\rangle$ is the averaged subgrid kinetic energy and $\langle\varepsilon^r\rangle$ is the averaged dissipation rate of the residual gas velocity field and the constants $C_0 = 7$ and $C_1 = 32$ for the case of isotropic turbulence (*Zaichik et al. 2003*).

In the case of high Re and whenever the filter size is in the inertial subrange, the subgrid dissipation rate is assumed to be equal to the dissipation rate of the original DNS velocity field.
Based on these assumption, this time scale is: $T_L^r = 0.1676$. In the case studied by *Zaichik et al. (2003)*, the turbulence is 3D and realistic, plus the Re is moderate so other estimation for the subgrid dissipation rate might be needed. Another choice is to estimate the subgrid dissipation rate based on the subgrid velocity field leading to $T_L^r = 0.6832$. Finally, in order to conduct a sensitivity study on this timescale, LES simulations are carried out for various values of T_L^r, namely 0.0500, 0.0800 and 0.2965, in addition to the two values computed based on Equation (11.2): 0.1676 and 0.6832.

11.1.2 Filtered velocity field with different filters

Multiple filter definitions exist in the literature, in order to extract the LES data from DNS simulations. The most used three are listed below:

- Box filter:

$$G_\Delta(\vec{\boldsymbol{x}} - \vec{\boldsymbol{x}}_1) = \begin{cases} \frac{1}{\Delta} & \text{for } |\vec{\boldsymbol{x}} - \vec{\boldsymbol{x}}_1| < \frac{\Delta}{2}, \\ 0 & \text{otherwize.} \end{cases} \tag{11.3}$$

- Gaussian filter:

$$G_\Delta(\vec{\boldsymbol{x}} - \vec{\boldsymbol{x}}_1) = \sqrt{\frac{6}{\pi \Delta^2}} \exp\left(\frac{-(\vec{\boldsymbol{x}} - \vec{\boldsymbol{x}}_1)^2}{\Delta^2} \right). \tag{11.4}$$

- Sharp-cut off filter where the transfer function $\widehat{G}_\Delta$ is defined in the wave space as:

$$\widehat{G}_\Delta(\boldsymbol{\kappa}) = \begin{cases} 1 & \text{for } |\boldsymbol{\kappa}| < \kappa_c = \frac{\pi}{\Delta}, \\ 0 & \text{otherwize.} \end{cases} \tag{11.5}$$

The energy spectra for the filtered velocity field obtained using these three filters for a filter width $\Delta = 0.046875$ are shown in Figure 11.2. Although the sharp-cut off filter is sharp in the spectral domain it is non-local in the physical space and can generate oscillations, the inverse is faced with the box filter (*Pope 2000*). As a consequence the Gaussian filter is preferred in this work.

11.1.3 Filtered velocity field with different filter size

For the selected Gaussian filter the energy spectra is plotted for various filter width in Figure 11.3. Because of the periodic boundary conditions used, one can notice the oscillatory behavior for the wavenumber greater than the

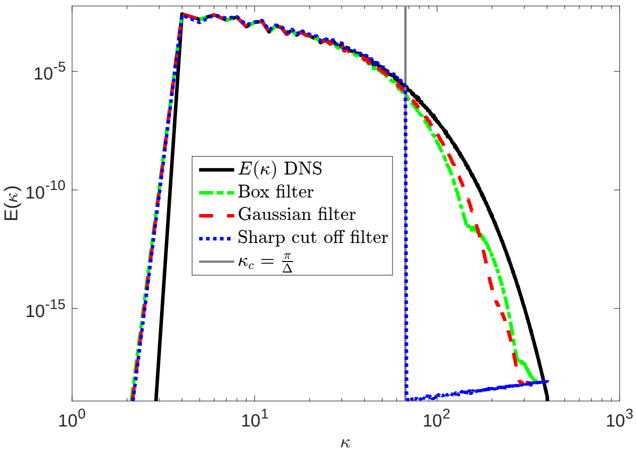

Figure 11.2: *Energy Spectrum filtered with box filter, Gaussian filter and sharp cut off filter with a filter size* $\Delta = 0.046875$

wavenumber of the filter width. These oscillations increase with the size of the filter and are amplified more with the box filter.

In addition, the mean value of the subgrid dissipation is plotted at the top left

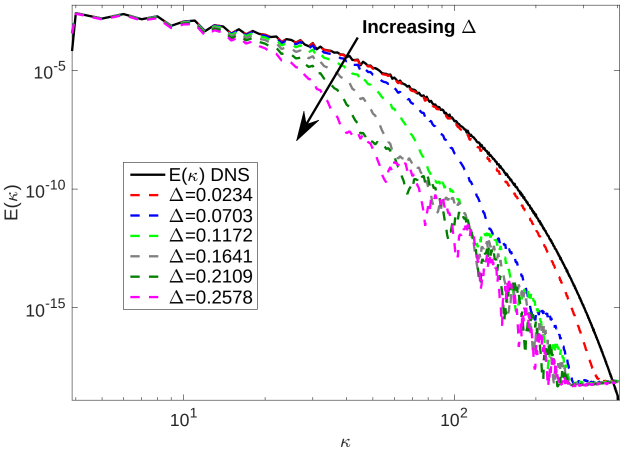

Figure 11.3: *Energy Spectrum filtered with Gaussian filter with various filter size*

of Figure 11.4 as a function of the filter size. The value based on the subgrid velocity field is shown in red with triangular symbols compared to the mean dissipation of the DNS velocity field in black. It is important to note that neither one of the two estimations is exact.

The mean subgrid kinetic energy, the Lagrangian integral timescale of the residual gas field velocity T_L^r using $\langle \varepsilon \rangle$, the mean value of the subgrid stress tensor and the percentage of resolved kinetic energy are also shown in Figure 11.4.

For a filter size $\Delta > 0.1$, the various quantities have a nearly linear dependence on the filter width. The subgrid terms increase with the filter width whereas the percentage of the resolved kinetic energy decrease with increasing Δ.

Finally, the values of T_L^r computed based on $\langle \varepsilon \rangle$ and $\langle \varepsilon^r \rangle$ are shown in Figure 11.5 for different filter sizes.

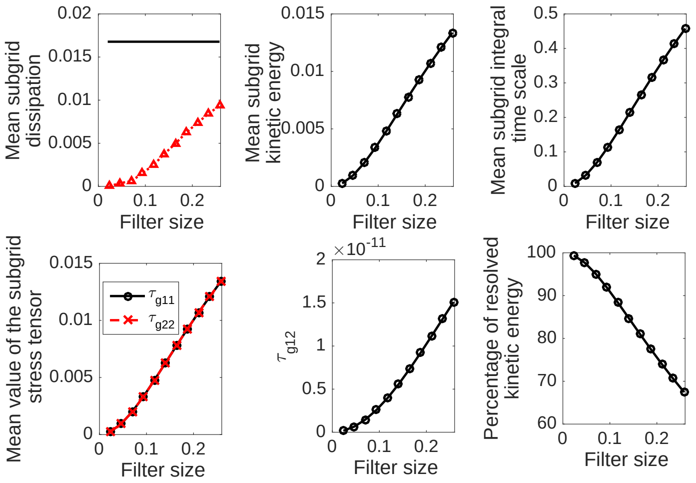

Figure 11.4: *Subgrid parameters and percentage of resolved kinetic energy as a function of the filter size*

In the following, the filter size is set to $\Delta = 0.14844$ where the percentage of the resolved turbulent kinetic energy is nearly 84%.

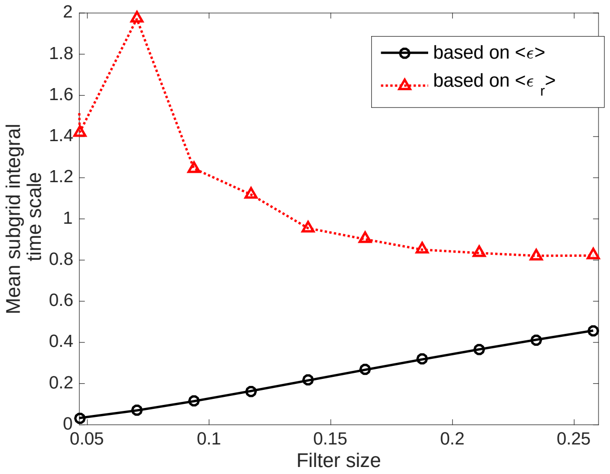

Figure 11.5: *Lagrangian integral timescale of the residual fluid velocity as a function of the filter size*

The selected filtered gas velocity field is now presented. The DNS velocity field of the gas along with the filtered velocity filter with a Gaussian filter of size $\Delta = 0.14844$ and the corresponding residual velocity field are illustrated in

Figure 11.6.

Using the same filter, the elements of the subgrid-scale stress tensor are computed and shown in Figure 11.6. This tensor highly influences the closure since it is included directly in the terms $\boldsymbol{\lambda}$ and $\boldsymbol{\mu}$ since the response coefficients are multiplied by this tensor and indirectly since the response coefficients depend on the value of the Stokes number St_L^r based on the Lagrangian integral timescale of the subgrid gas field velocity T_L^r that was assumed to be proportional to the subgrid turbulence kinetic energy $\langle \mathrm{TKE}^r \rangle = \frac{\sum_i \tau_{g,ii}}{2}$.

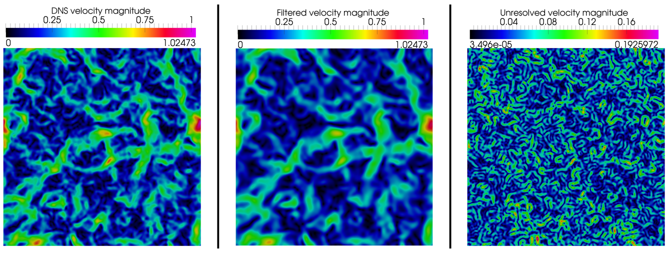

Figure 11.6: *DNS (left), filtered (center) and residual (right) fluid velocity*

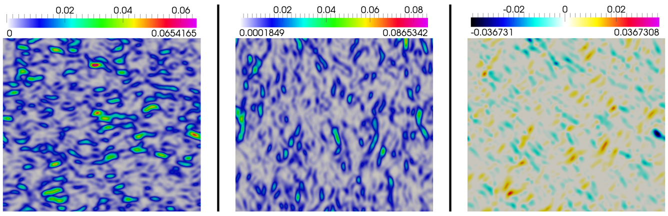

Figure 11.7: *Residual stress tensor* $\tau_{g,11}$ *(left),* $\tau_{g,22}$ *(center) and* $\tau_{g,12}$ *(right)*

11.2 Qualitative results

Now that the test case is defined along with the subgrid terms, the qualitative results are presented for the DNS, the DNS with filtered gas, the DNS results based on the filtered NDF and the LES with the most suitable value of the parameter T_L^r for each case of the studied Stokes numbers. It is important to note that for the number density and the velocity the filtered DNS result and the DNS results based on the filtered NDF are equivalent so in this case for simplicity the DNS results based on the filtered NDF are also called DNS filtered results. However, this is not the case for the energy.

The presented results are simulated using a first order HLL finite volume scheme on a 512^2 mesh for both DNS and LES results. The same mesh is chosen for the various simulations in order to concentrate on the model evaluation by isolating the differences due to numerical errors. In addition, the DNS in this case is based on the DNS AG simulation which presented itself some limitations in simulating high St cases. An alternative choice would have been to take the

Lagrangian simulation as reference. This choice is not retained in this study in order to compare the DNS and LES results based on the same level of numerical accuracy.

11.2.1 Stokes number = 0.1

The number density results at a time $t = 10\tau_p$ are shown in Figure 11.8 where qualitatively the LES result with $T_L^r = 0.05$ matched the filtered DNS number density while the DNS with filtered gas is more comparable to the DNS number density.

When it comes to the velocity, both LES results qualitatively match the DNS Favre filtered velocity as shown in Figure 11.9. In this case, the disperse phase velocity field of the LES is similar the filtered gas velocity illustrated in Figure 11.6. One can note that in this case even if the time is chosen large enough compared to the relaxation time of the particles but is it not long enough compared to the integral time of the DNS gas motion (with $\tau_L = 1.8667$ based on the velocity autocorrelation function). For this reason, the results are also

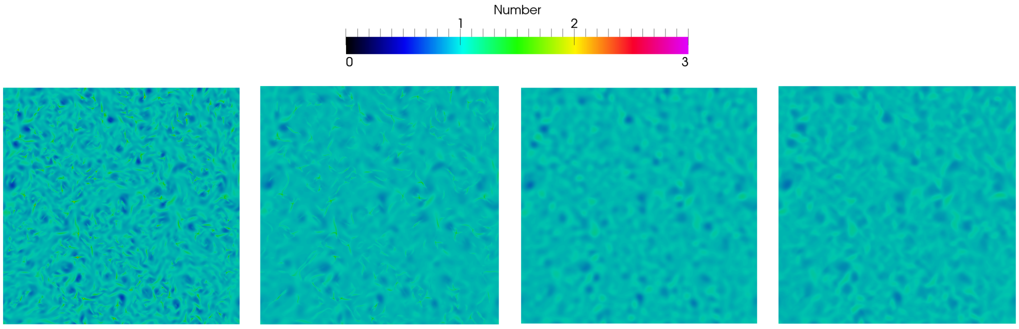

(a) DNS (b) DNS, filtered gas (c) DNS filtered (d) LES, $T_L^r = 0.05$

Figure 11.8: *Number density for* St $= 0.1$ *at* $t = 10\tau_p$

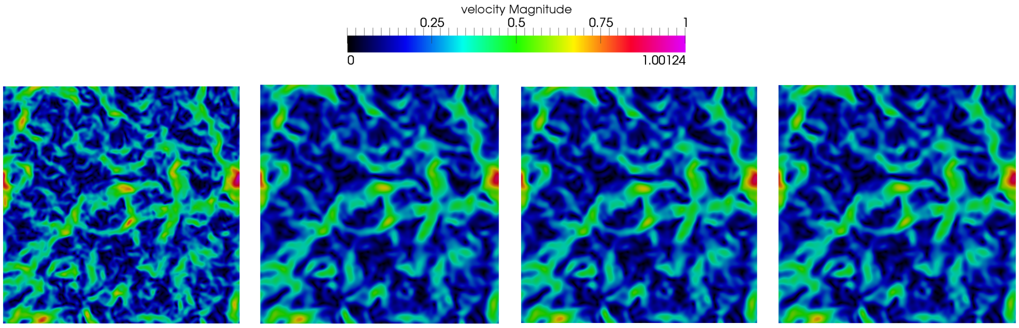

(a) DNS (b) DNS, filtered gas (c) DNS filtered (d) LES, $T_L^r = 0.05$

Figure 11.9: *Velocity for* St $= 0.1$ *at* $t = 10\tau_p$

shown for a final time $t = 36.62$ where the number density obtained through the LES with $T_L^\tau = 0.05$ is dissipated more than the filtered DNS leading to smaller vacuum zones as shown in Figure 11.10. As for the velocity, the results are kept nearly unchanged in comparison with those at $t = 10\tau_p$ (see Figure 11.11)

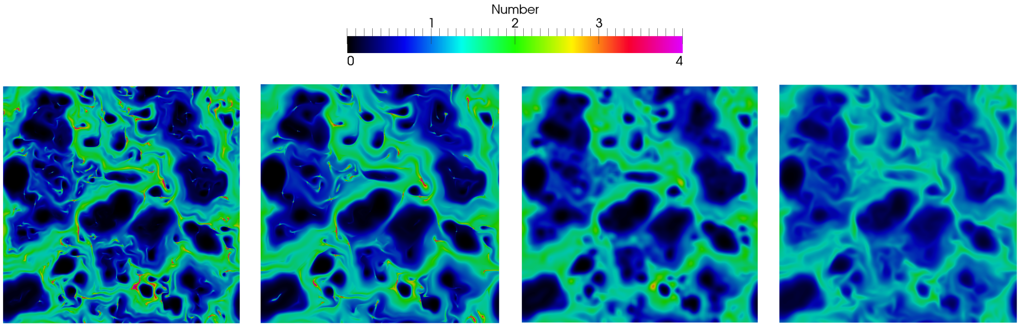

(a) DNS (b) DNS, filtered gas (c) DNS filtered (d) LES, $T_L^\tau = 0.05$

Figure 11.10: *Number density for* $\mathrm{St} = 0.1$ *at* $t = 36.62$

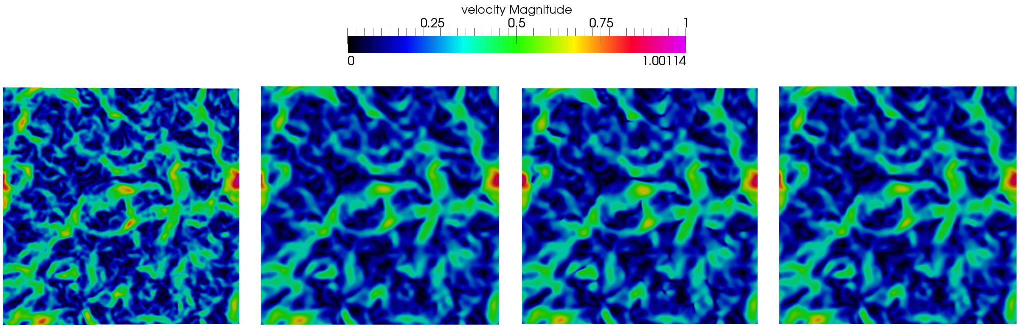

(a) DNS (b) DNS, filtered gas (c) DNS filtered (d) LES, $T_L^\tau = 0.05$

Figure 11.11: *Velocity for* $\mathrm{St} = 0.1$ *at* $t = 36.62$

11.2.2 Stokes number = 1

For the critical Stokes number, the number density results are shown in Figure 11.12 for $t = 36.62$. The LES number density with $T_L^\tau = 0.08$ is qualitatively similar to the filtered DNS number density whereas the DNS with filtered gas overestimates the number density compared to the filtered DNS and even compared to the DNS itself. In order to focus the attention on the differences between the various number density fields a zoom in view is shown in the bottom of Figure 11.12 where the overestimation of the number density by the DNS with filtered gas is clearly seen along with the similarities between the LES result and the filtered number density.

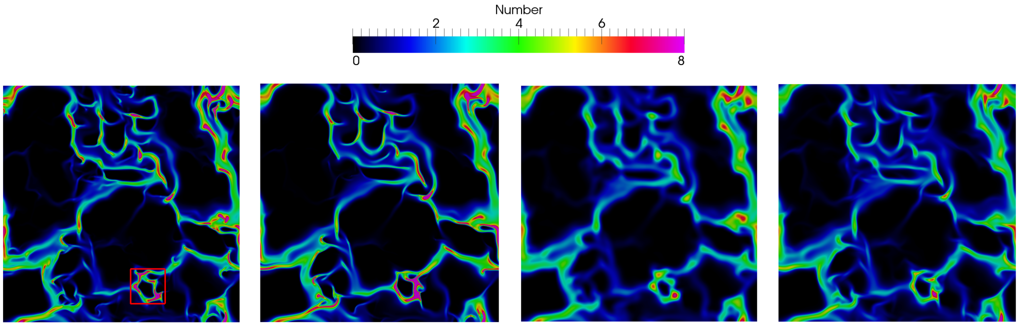

(a) DNS (b) DNS, filtered gas (c) DNS filtered (d) LES, $T_L^\tau = 0.08$

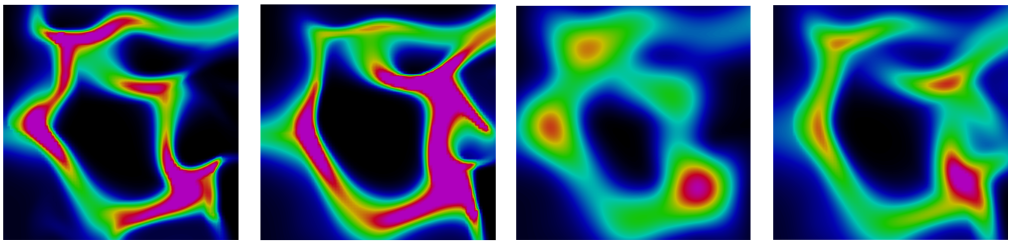

(e) DNS (f) DNS, filtered gas (g) DNS filtered (h) LES, $T_L^\tau = 0.08$

Figure 11.12: *Number density for* St $= 1$ *at* $t = 36.62$, *full scale (top) and zoom in (bottom)*

This result can also be seen through the velocity fields where the DNS with filtered gas overestimates some regions of vacuum (black spots) compared to the Favre filtered DNS velocity as shown in Figure 11.13. In spite of this difference globally both LES results are very similar.

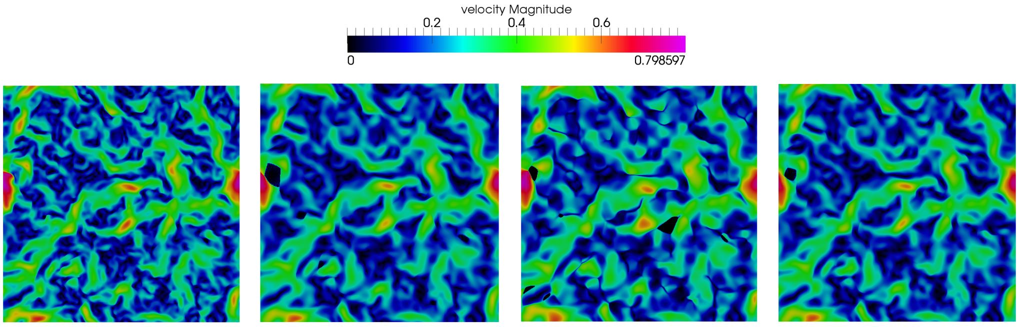

(a) DNS (b) DNS, filtered gas (c) DNS filtered (d) LES, $T_L^\tau = 0.08$

Figure 11.13: *Velocity for* St $= 1$ *at* $t = 36.62$

11.2.3 Stokes number = 5

For St $= 5$ and $t = 36.62$ the number density is overestimated with the DNS with filtered gas. This overestimation can be clearly seen in the zoom in window shown in Figure 11.14. On the other hand, the general structure of LES number density for $T_L^r = 0.1676$ qualitatively matches the number density of the filtered DNS number density without overestimations. This time scale is the estimate based on the assumptions of *Zaichik et al. (2009)*.

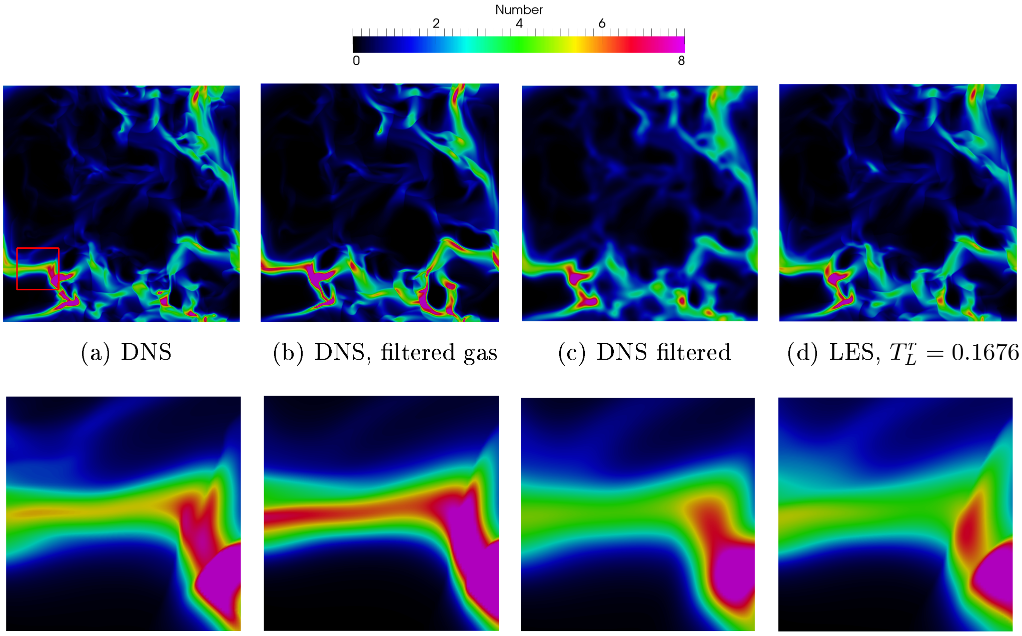

(a) DNS (b) DNS, filtered gas (c) DNS filtered (d) LES, $T_L^r = 0.1676$

(e) DNS (f) DNS, filtered gas (g) DNS filtered (h) LES, $T_L^r = 0.08$

Figure 11.14: *Number density for* St $= 5$ *at* $t = 36.62$, *full scale (top) and zoom in (bottom)*

Looking at the velocity fields in Figure 11.15, no noticeable differences are manifested between the different simulations.

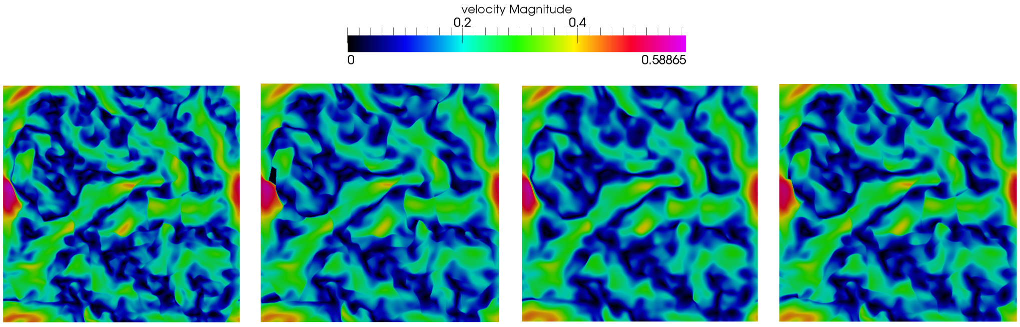

(a) DNS (b) DNS, filtered gas (c) DNS filtered (d) LES, $T_L^r = 0.1676$

Figure 11.15: *Velocity for* St $= 5$ *at* $t = 36.62$

11.2.4 Stokes number = 15

In the case of the highest Stokes number studied, St = 15, the LES number density with $T_L^r = 0.2965$ is more comparable to the filtered number density of the DNS then the DNS with filtered gas at $t = 36.62$. The latter overestimates the number density as shown in Figure 11.16.

It is important to note that for the cases of inertial particles, the reference DNS results selected is not the most accurate result since it is based on the AG model. This latter cannot accurately describe the large scale PTC that can be encountered for high St. As a consequence, the other qualitative and statistical results for this Stokes number will not be presented individually, they will only be shown for the evolution of a given statistical quantity in function of the particles inertia.

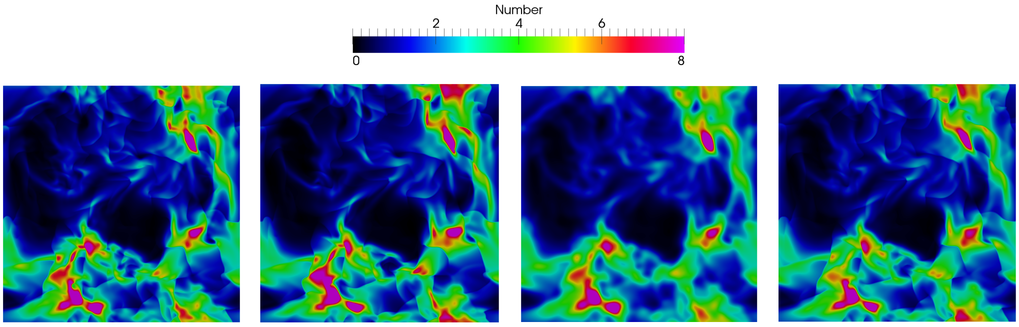

(a) DNS (b) DNS, filtered gas (c) DNS filtered (d) LES, $T_L^r = 0.2965$

Figure 11.16: *Number density for* St = 15 *at* $t = 36.62$

11.3 Statistical results

Even if the qualitative results are an evidence of the utility of the subgrid model, they are not enough and in some cases they are not conclusive. For a better comparison between the different LES subgrid models and a sensitivity study of the Lagrangian integral timescale of the residual gas field velocity T_L^r, statistical results for the segregation and the mean total energy are presented. This comparison is carried out for various Stokes numbers and the evolution of the statistics as a function of time is shown for the different LES results, DNS results and filtered DNS results. Finally, the energy budget analysis is presented for both the total and internal energy along with the comparison between the filtered DNS internal energy and the internal energy obtained based on the filtered NDF.

11.3.1 Stokes number = 0.1

For the smallest St studied, the statistics are presented for the full time range with a zoom on the range where $t < 10\tau_p$ in Figures 11.17 and 11.18 for the segregation and mean total kinetic energy respectively.

For $t < 10\tau_p$, the segregation of the LES results with $T_L^r = 0.05$ fits the filtered DNS segregation whereas all the other simulations overestimate it.

When investigating these results for a longer time, one can note that the right level of segregation is not obtained with any LES model. In comparison with the segregation level obtained with the DNS with filtered gas, all the subgrid model corresponding to the studied values of T_L^r do not present any advantage if one takes as a reference the filtered number density segregation.

On the other hand, for the mean total energy all the LES results lead to higher energy in comparison with the DNS with filtered gas. This level increases with the increase of T_L^r.

For the following comparisons, only the full time range is shown.

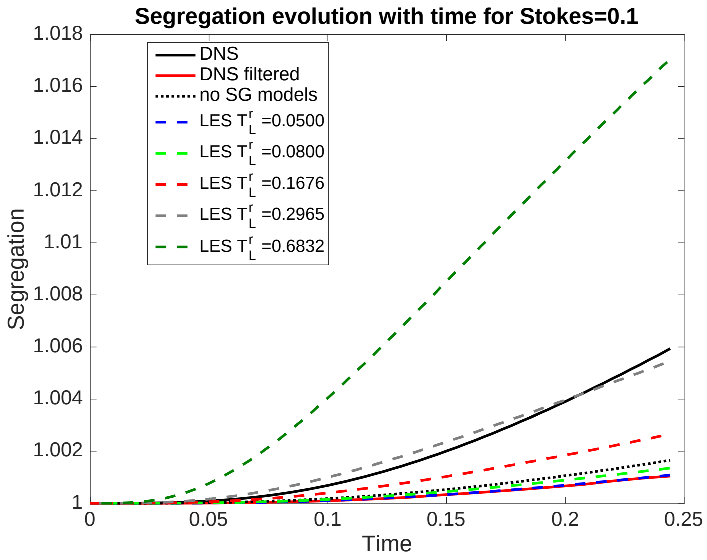

(a) Until $t = 10\tau_p$

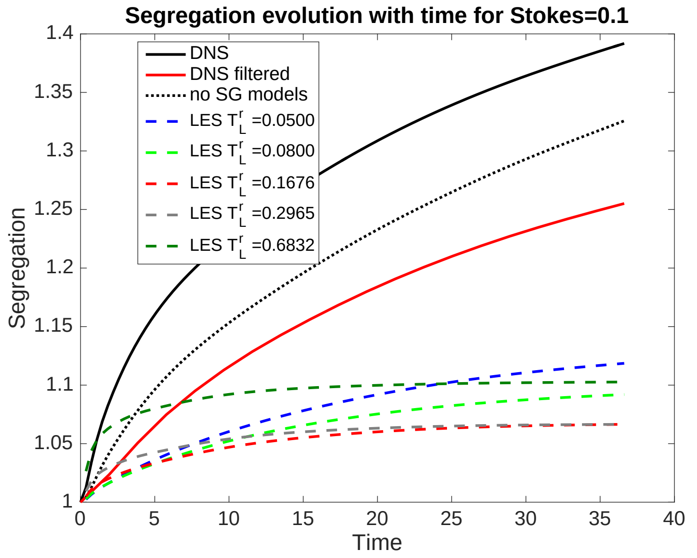

(b) Until $t = 36.62$

Figure 11.17: *Segregation for* $\mathrm{St} = 0.1$

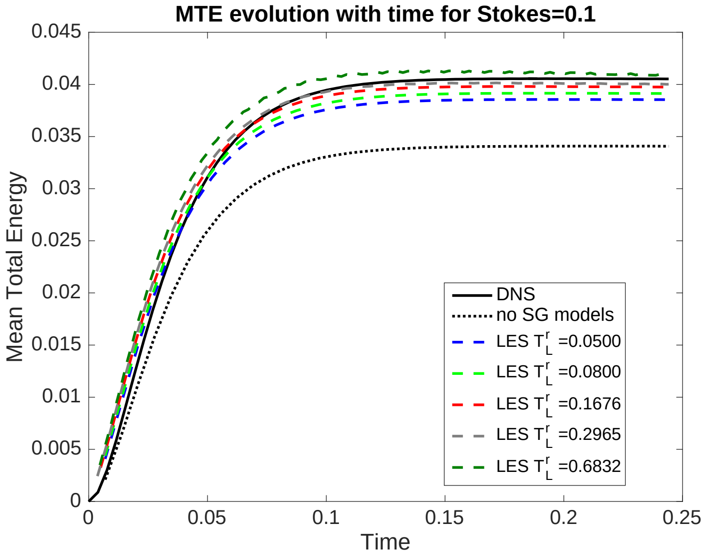

(a) Until $t = 10\tau_p$

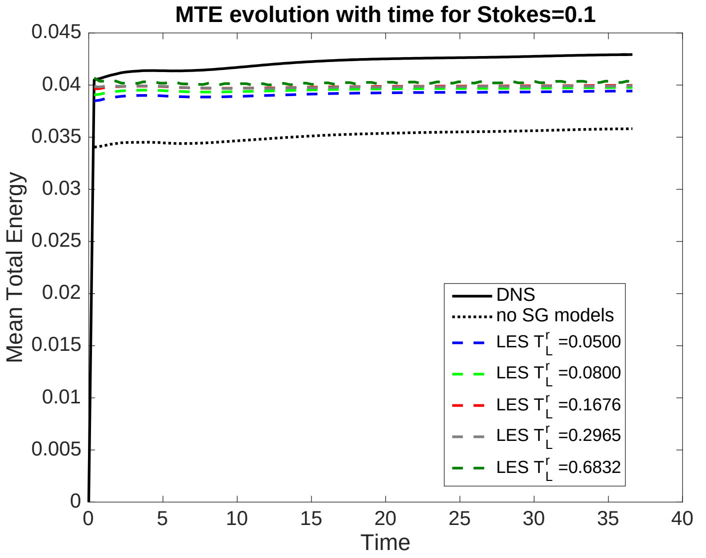

(b) Until $t = 36.62$

Figure 11.18: *Mean total energy for* $\mathrm{St} = 0.1$

11.3.2 Stokes number = 1

The temporal evolution of the segregation for St = 1 is shown in Figure 11.19. One obtains segregation levels comparable to the filtered DNS result when taking $0.05 < T_L^r < 0.08$. The segregation level increases with the decrease of the T_L^r until reaching the limit of no subgrid model.

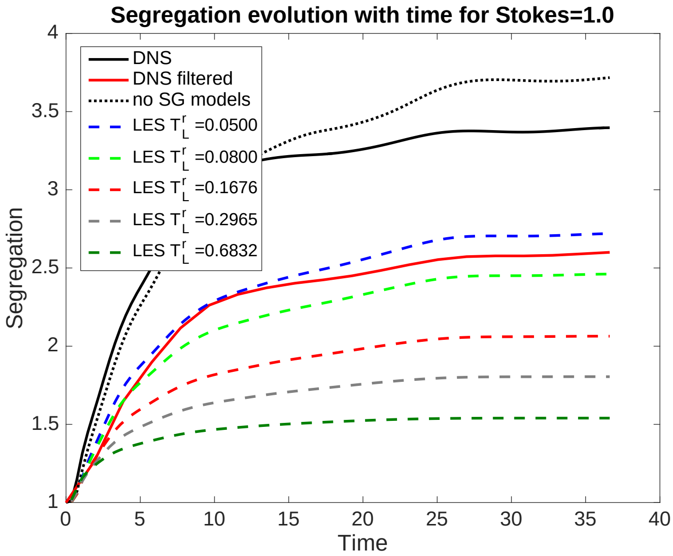

Figure 11.19: *Segregation for* St = 1 *at* $t = 36.62$

The mean total kinetic energy illustrated in Figure 11.20 shows that the level of energy increase with T_L^r and is more comparable to the DNS energy.

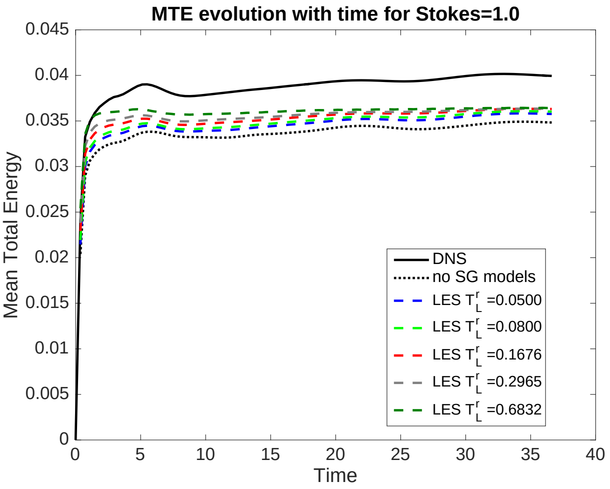

Figure 11.20: *Mean total energy for* St = 1 *at* $t = 36.62$

For any of the chosen values of T_L^r, the LES results with subgrid model are more accurate than the DNS with filtered gas. It is important to note that the filtered DNS is not shown in this case since the filter does not affect the mean total energy. Thus, the reference is the mean total energy of the DNS simulation.

11.3.3 Stokes number = 5

For St = 5, the segregation is well estimated by the LES when taking the Lagrangian integral timescale of the residual gas field velocity based on the estimation of *Zaichik et al. (2009)*: $T_L^r = 0.1676$ shown in dashed red lines in Figure 11.21. For higher T_L^r, the segregation is underestimated and vice versa.

The mean total energy is shown for this case in Figure 11.22 where the case of $T_L^r = 0.2965$ estimates the best this energy while above this limit the energy is overestimated as seen for example for $T_L^r = 0.6832$ (see Figure 11.22).

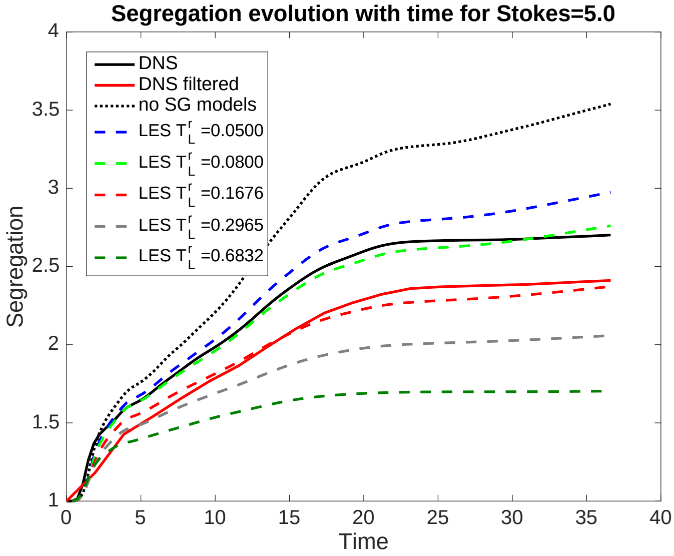

Figure 11.21: *Segregation for* St = 5 *at* $t = 36.62$

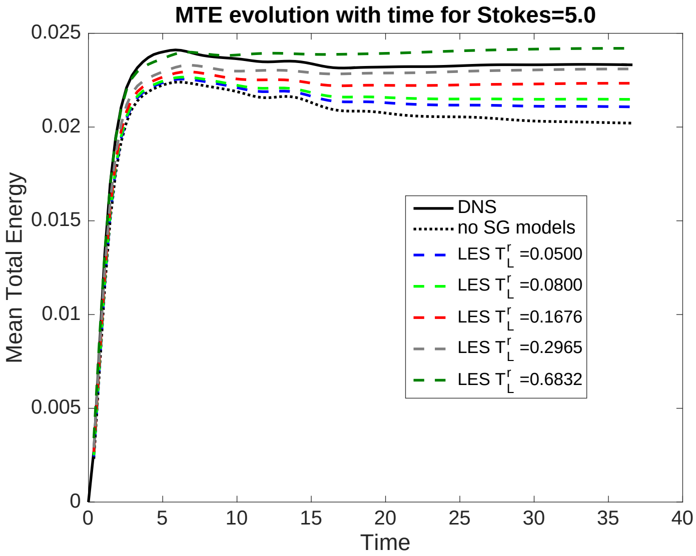

Figure 11.22: *Mean total energy for* St $= 5$ *at* $t = 36.62$

11.3.4 Statistics as a function of Stokes number

When comparing the segregation of the different simulation at $t = 10\tau_p$ as a function of the Stokes number, one can directly notice the sensitivity of the LES results on the estimation of the time scale T_L^r (see Figure 11.23). The segregation increases with the decrease of T_L^r. At this time, for $St \leq 5$ the most suitable value of T_L^r for the right segregation level compared to the filtered DNS results is the one estimated based on the assumption of *Zaichik et al. (2009)*: $T_L^r = 0.1676$. For higher Stokes number the results with $T_L^r = 0.2965$ are more comparable to the filtered results, but one should keep in mind that the DNS in this case in based on the AG model that generates itself errors in the case of inertial particles. For the case of small Stokes number, St < 0.5, the most suitable closure is obtained for $T_L^r = 0.05$ but this is only the case for short times.

The same results are plotted in Figure 11.24 at $t = 36.62$ where the most suitable closure is obtained with $T_L^r = 0.08$ for St ≤ 1, with $T_L^r = 0.1676$ for $1 <$ St < 8 and with $T_L^r = 0.2965$ for $8 \leq$ St < 15.

When it comes to the mean total kinetic energy the results are shown respectively for $t = 10\tau_p$ and $t = 36.62$ in Figures 11.25 and 11.26. Where the LES closures are shown to be advantageous compared to the DNS with filtered gas. For the levels of T_L^r studied, the mean total energy is better estimated when increasing T_L^r for St < 5. Above this limit, the case with $T_L^r = 0.2965$ recovers the energy level more precisely than all the other models.

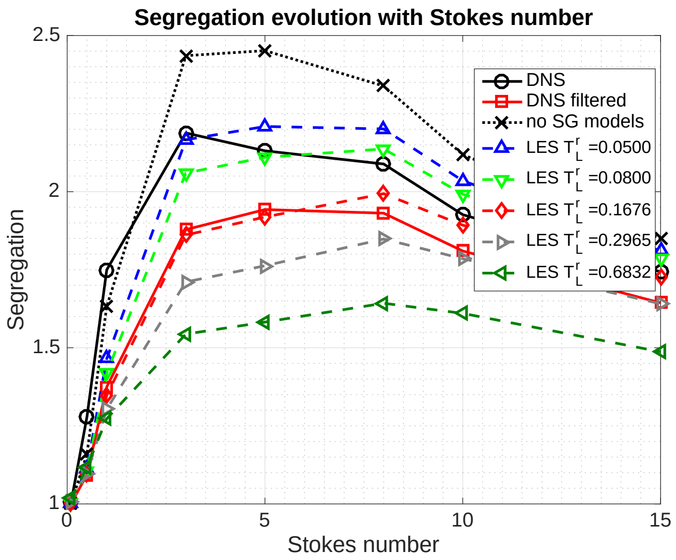

Figure 11.23: *Segregation as a function of the Stokes number at* $t = 10\tau_p$

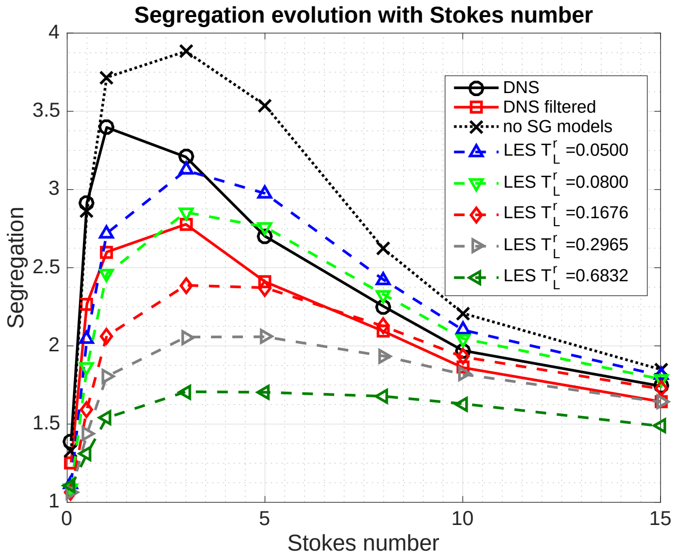

Figure 11.24: *Segregation as a function of the Stokes number at* $t = 36.62$

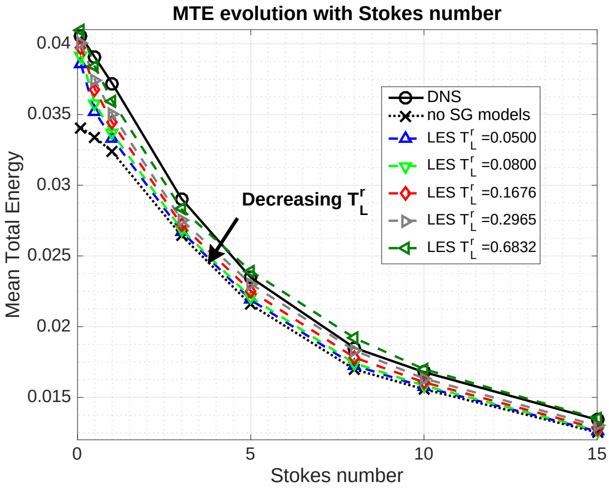

Figure 11.25: *Mean total energy as a function of the Stokes number at* $t = 10\tau_p$

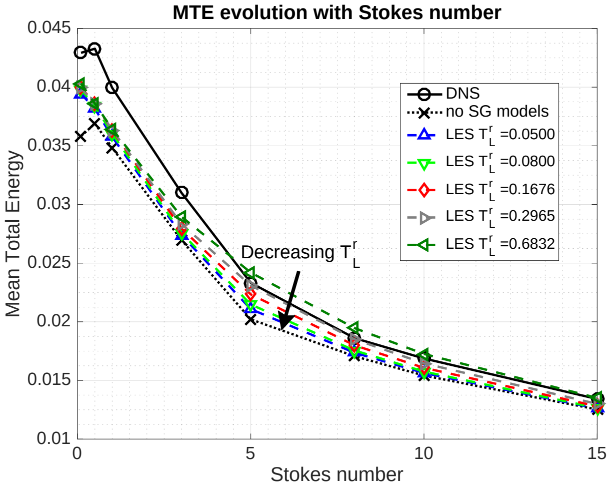

Figure 11.26: *Mean total energy as a function of the Stokes number at* $t = 36.62$

11.3.4.1 Energy budget analysis as a function of the Stokes numbers

The trace of the total kinetic energy tensor is shown in Figure 11.27 for the DNS simulation, the filtered DNS simulation and the computed results based on the sum of the filtered central energy and filtered correlated energy on the one hand, and based on the sum of central energy of the filtered NDF and the correlated energy of the filtered NDF on the other hand. The correlated part of this total energy is also depicted as a function of Stokes number. Based on these results, one can directly notice the difference between the filtered correlated energy $\widetilde{\vec{u} \otimes \vec{u}}$ and the correlated energy of the filtered NDF $\tilde{\vec{u}} \otimes \tilde{\vec{u}}$. This difference is the subgrid contribution $\overline{n}\Sigma_r$ as explained in the previous chapter, and it decreases with the increase of St. Another important observation is that the total energy is not sensitive to the filtering and is equivalent if computed based on the filtered DNS results or the results of the filtered NDF. The fact that the total energy is unaffected by the filtering is expected and it was discussed earlier in Part III.

The difference between the traces of the filtered central energy, $\overline{n}\widetilde{\Sigma}(\vec{\boldsymbol{x}})$, the central energy of the filtered NDF, $\overline{n}\Sigma^{\overline{f}}(\vec{\boldsymbol{x}})$, and the subgrid contribution $\overline{n}\Sigma_r$ is plotted in Figure 11.28. The decrease of the subgrid contribution already mentioned in the total energy analysis is verified. In addition, the computed filtered internal energy based on the internal energy of the filtered NDF minus the contribution of the subgrid scales is found to be identical to the directly filtered internal energy. The same can be said about the computed internal energy of the filtered NDF based on the filtered internal energy.

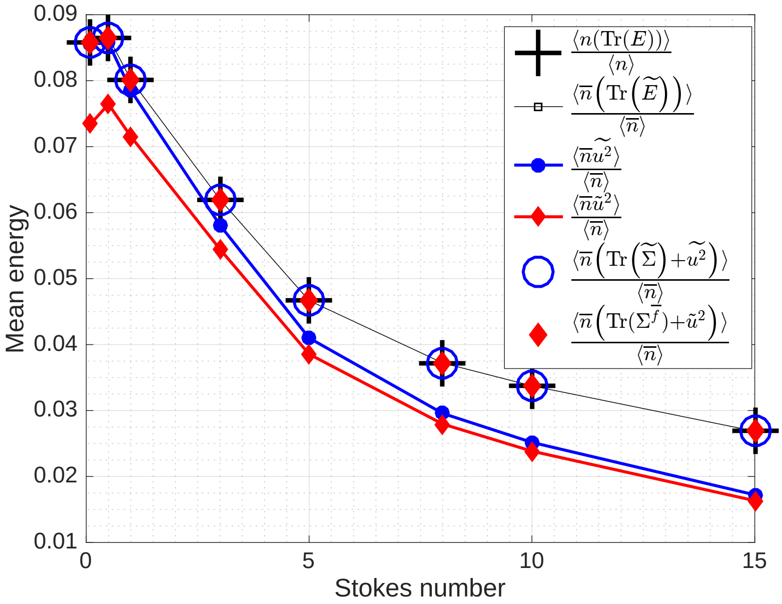

Figure 11.27: *Trace of the total energy as a function of Stokes number at* $t = 36.62$ *showing the DNS result (black plus sign) and the filtered results obtained by directly filtering the total energy (black line with rectangles) or computed based on the filtered central energy (blue circle) and central energy of the filtered NDF (red diamonds) along with the filtered correlated energy (blue line with circles) and the correlated energy of the filtered NDF (red line with diamonds).*

The filtered internal energy increases with St and is not sensitive to the filtering since this is solely based on the definition of spatially uncorrelated energy. However, the internal energy of the filtered NDF, which is used in this work, includes the contributions of both the uncorrelated energy and the subgrid energy. One can notice that the final dependence of this internal energy of the filtered NDF on St is the results of the competition of the increase of the filtered internal energy and the decrease of the subgrid internal energy.

Lastly, since the difference between the internal energy of the filtered NDF,

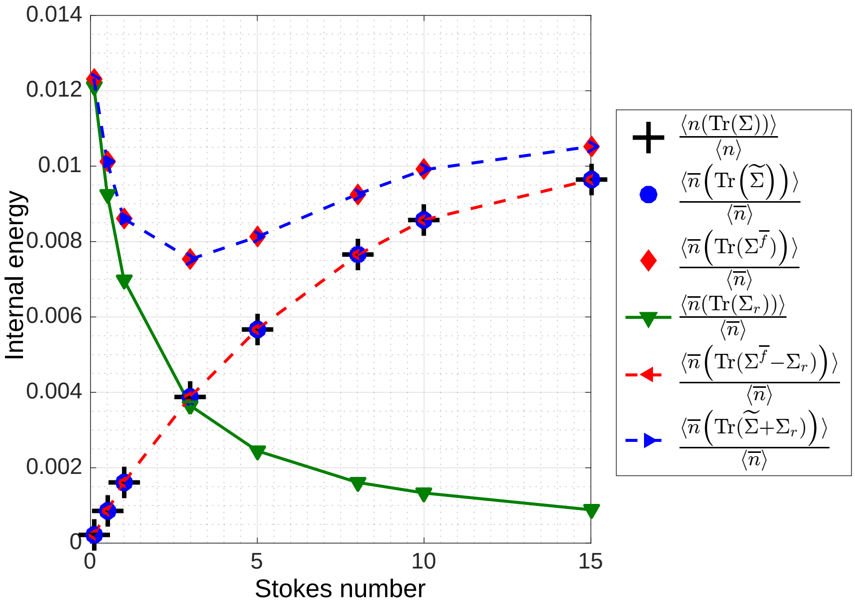

Figure 11.28: *Budget analysis of the trace of the internal energy tensor as a function of the Stokes number at* $t = 36.62$ *for the DNS based results: central energy (black plus sign) , filtered central energy (blue circle) and central energy of the filtered NDF (red diamond) and the subgrid central energy (green triangle).*

used in this work as a reference for the LES results, and the filtered internal energy classically used in the literature (*Moreau et al. 2010*) is clarified, the evolution of the mean internal energy for the LES results as a function of St can be addressed. These results are shown in Figure 11.29. The St dependence of the mean internal energy previously observed in the internal energy of the filtered NDF is recovered by all the LES results with the subgrid models unlike the case of DNS with filtered gas. This mean internal energy increase with T_L^r, and the point of minimum MCE is obtained for higher St when increasing T_L^r. The most comparable result to the mean internal energy of the filtered NDF is obtained for $T_L^r = 0.2965$.

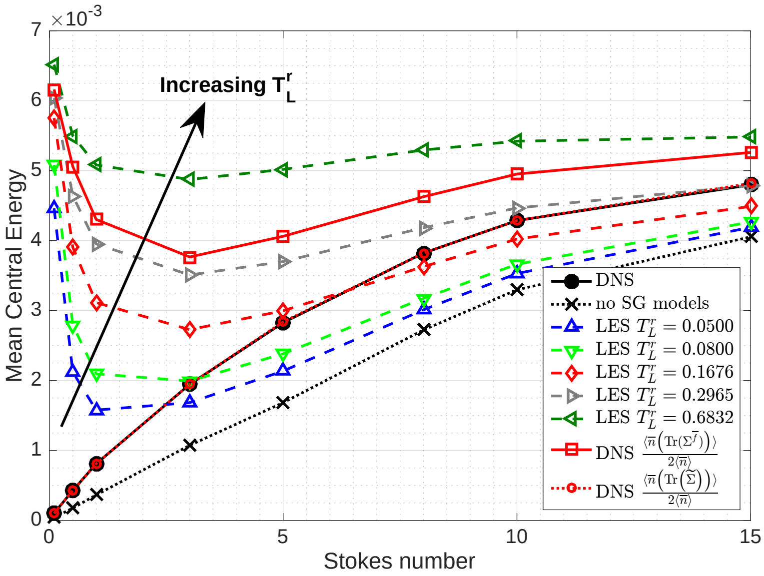

Figure 11.29: *Mean internal energy as a function of the Stokes number at* $t = 36.62$ *for the LES results compared to the mean internal energy of the DNS result (black line with circles), the filtered DNS (red dotted line with circles) and the results based on the filtered NDF (red line with rectangles).*

11.4 Conclusion

The results presented in this chapter are considered only preliminary results that show the sensitivity of the LES result on the subgrid closures in general and on the estimation of the Lagrangian characteristic time of the particles interactions with the residual fluid velocity. Through these results, it was noticed that the error of the LES subgrid model increase for small St, this is expected since while deriving these closures based on the Furustu-Donsker-Novikov formula for Gaussian random functions, *Zaichik et al. (2008)* neglected some terms that results in negligible errors for high St but the error is increased for low-inertial particles (Zaichik et al. (2008; 2009)).

In addition, the energy budget is analyzed with a comparison between the filtered central energy, $\widetilde{\Sigma}(\vec{\boldsymbol{x}})$, the central energy of the filtered NDF $\overline{\Sigma^f}(\vec{\boldsymbol{x}})$. The total kinetic energy in the case of the fully kinetic based LES was found to be composed of three contribution: the filtered correlated kinetic energy, the internal (or central) energy of the filtered NDF and the subgrid internal energy Σ_r.

Finally, in order to evaluate the AG LES model more realistic 3D simulations must be carried out, in the future, coupled with a dynamic turbulence. For these simulations, one can envision local values at the scale of the filter width of the time scale T_L^r. The present work proves the important for these prospect studies since the LES results were found to be very sensitive to the subgrid closure in general and to T_L^r more specifically.

Conclusions and future works

In the general framework of predictive simulations of two-phase combustion in aeronautical burners, various phenomena can be encountered. These latter belong to three main disciplines: the dynamics of the liquid fuel phase, the turbulence of the carrier gas phase and the combustion process. High-fidelity simulation of the combustion chamber should rely on the accurate description of these multi-scale multi-physics building blocks driving the two-phase combustion as well as the complex interactions between them.

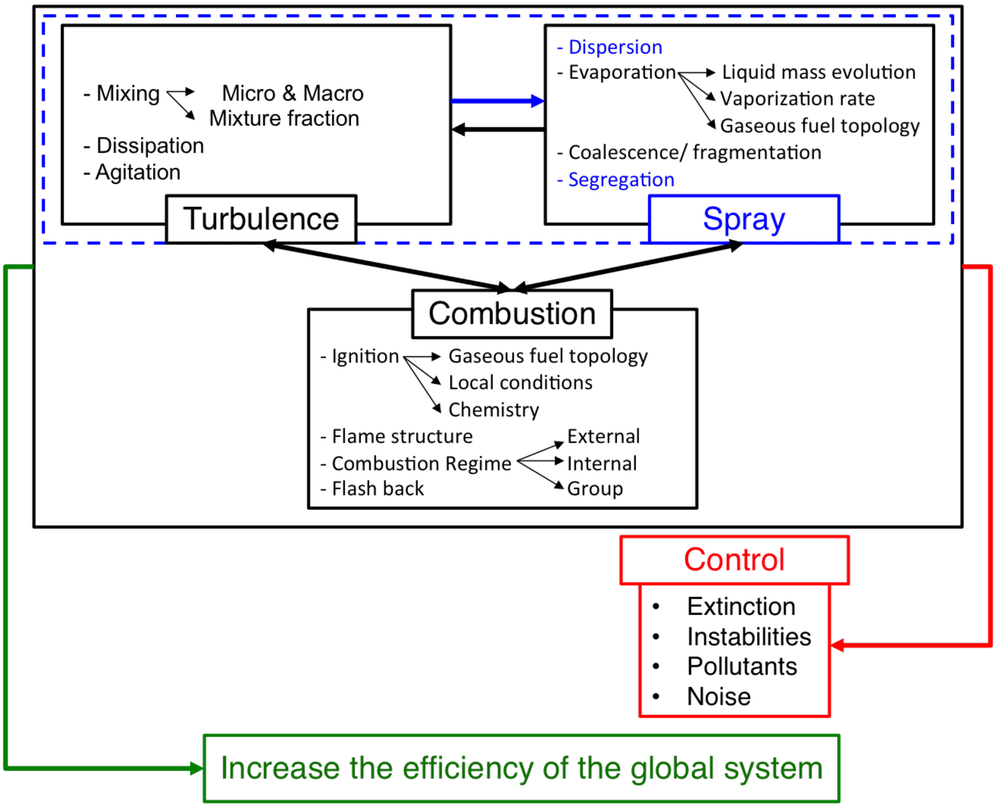

Figure 11.30: *The general liquid fuel dynamics, combustion and turbulence interactions along with the focus of the presented study in blue.*

In fact, the full understanding of these various phenomena and their reciprocal influence on each other is the main milestone towards designing new combustion chambers where the pollutants emission is controlled, the global efficiency of the system is increased, the noise is reduced and the combustion instabilities are monitored.

In this context, the focus of the work presented in this thesis was the modeling and the simulation of the spray in the turbulent region downstream of the injector. This center of attention is situated in the general context along with the various phenomena and the practical long-term objectives that drove this study in Figure 11.30.

The precise modeling of this disperse phase is necessary as well as the accurate and robust numerical strategy used for the resolution of the resulting systems of equation, thus these two axes constituted the different contributions of this thesis. These contributions along with short- and long-term prospects are presented in the following sections.

Results and achievements

The contributions of this thesis are divided into three major parts:

- Modeling and simulation of the disperse phase in the context of DNS

  The Anisotropic Gaussian model was chosen in this work based on the review of the models available in the literature that can treat polydispersion and polykineticity. This choice was based on the objectives of guaranteeing the realizability of the controlled moment set and the well-posedness of the resulting equations.

  The polydisperse extension of the AG model has also been proposed based on the OSM and TSM multi-fluid methods.

  The main goal of this work was a nearly extensive evaluation of the AG model on a 3D turbulent configuration, through a one-way coupling with a forced Homogeneous Isotropic Turbulence field for the gas. For this objective, the AG3D model was implemented in the parallel solver MUSES3D using a realizability-preserving second order MUSCL/HLL scheme. This evaluation was done for a wide range of Stokes number ranging from $\mathrm{St} = 0.05$ to $\mathrm{St} = 15$. The model was compared to a Lagrangian reference simulation and to the monokinetic model based on:
  - qualitative results such as the number density field, the velocity magnitude and the velocity dispersion;
  - quantitative mean statistical results .i.e. the segregation, the mean total energy and the mean internal energy;
  - quantitative results for the distribution functions of the number density, the velocity, the pressure and the disperse phase Mach number based on the classical definition and on a new definition proposed in this work;
  - quantitative results for the number density autocorrelation, the longitudinal velocity autocorrelation and the internal energy autocorrelation, as well as characteristic scales based on these autocorrelation functions.

  These qualitative and quantitative results were used to compare and assess the AG model. This latter was found to be a useful model for the accurate description of the disperse phase motion for $\mathrm{St}_E < 1$. This model gives a compromise between the level of details of the description of the PTC and the cost and complexity of the method and is thus, a good candidate for complex applications of spray combustion.

- Numerical resolution of the resulting systems

  In order to obtain accurate and robust results, the resulting systems of equations should be solved with realizability-preserving high order methods. In addition, the scheme should be applicable to unstructured mesh computations needed to simulate the spray in real configurations including complex geometries such as the combustion chamber. Based on these objectives, a new scheme for the resolution of weakly hyperbolic and hyperbolic systems on unstructured grids was used. This is the realizability-preserving DG scheme. The DG results were compared in 1D and 2D configurations to other third order and second order schemes. It was also evaluated and compared on a 2D test case qualitatively and quantitatively to the Lagrangian results and to the reference simulations provided by the second order structured realizability-preserving MUSCL/HLL finite volume scheme.

  This evaluation was carried out for the resolution of the PDG and Euler system resulting respectively from the MK and isotropic Gaussian models. This was done based on structured mesh. Through these comparisons, the DG method was shown to be competitive for the description of the spray dynamics and suitable for the spray combustion application. This parameter-free scheme stays robust even when facing the severe singularities created by the models, especially the MK model that generate dirac δ-shocks. It can accurately reproduce the high preferential concentration that characterizes the dynamics of low inertia particles as well as the right segregation level. These accurate description of these quantities is essential in the domain of spray combustion since they affect the local mixture fraction, the evaporation rate and the flame structure.
- Extension of the AG model to the LES

  The AG model was extended for LES in this work in order to be able to compute realistic configurations where high Reynolds flows make the simulation of the whole range of scales unreachable. In the aeronautical burners these scales range from the system size of about 10cm to the smallest turbulent eddies that can reach the order of 1μm.

  Classically, in the literature the extension of a DNS model for the disperse phase is usually done by directly filtering macroscopic conservation laws constituting the DNS model (*Moreau et al. 2010*). In this thesis, another approach was chosen by applying the filter at the mesoscopic kinetic level (*Zaichik et al. 2009*), in order to keep a direct link between the filtered moment equation and the filtered kinetic equation that helps guaranteeing the realizability of the moment set.

  Based on this strategy a LES formalism was developed using fully kinetic-based closure. Finally, the AG-LES model was assessed in a monodisperse configuration using the simplest form of the subgrid term on a 2D frozen HIT. These results constitute only a first preliminary example that shows the importance of the accurate description of the unresolved scales and the challenge faced to select the right subgrid closures.

These contributions represent a step forward toward the long objectives of the high fidelity simulation of the spray combustion. In fact, the studied AG model opens a new possibility for accounting for the moderate to inertial droplets (or particles) dynamics in industrial configurations. The implementation of this model in the CEDRE code is an on-going work in the thesis of *Dupif (2017)*. In addition, this realizable model along with the realizability-preserving parameter-free high order numerical schemes can offer great advantages in the AVBP code. This possibility comes in the continuity of the support of SNECMA SAFRAN for this work.

Finally, it is important to note that even if the general context of this study is oriented to spray combustion in aeronautical burners, the models and numerical methods studied in this thesis can be used in many other applications such as the alumina particles in rocket engines, aerosols and clouds in environmental applications and proto-planetary nebula in astronomical applications.

Future works

As far as the prospects of this work are concerned, several types of extensions can be envisioned whether in the general academic context or the industrial context of the spray combustion applications. Some of these future works can be fulfilled on the short term and others need further improvement in various domains in order for them to be reachable. Among the diverse possibilities, eight openings are considered:

- The evaluation of the AG model on other configurations should be conducted namely on the 3D turbulent sheared flows similar to the one studied in the work of *Dombard (2011); Masi and Simonin (2012)*. In addition, the AG model from the KBMM hierarchy should be compared on such a 3D configuration to the 2Φ-EASM model from the ACBMM family as an extension of the 2D comparison presented in the work of *Vié et al. (2012)*.
- The development of a comprehensive two-way coupled, polydisperse model based on the AG model to statistically treat the PTC and on a similar model to take into account the temperature dispersion. The two-way coupling itself for the AG model is treated in the theses of *Dupif (2017); Mercier (2018)*. In this model, one should also account for the coalescence and break-up (*Doisneau 2013*) of the particles. In this way, the different interactions between the particles themselves and between the disperse

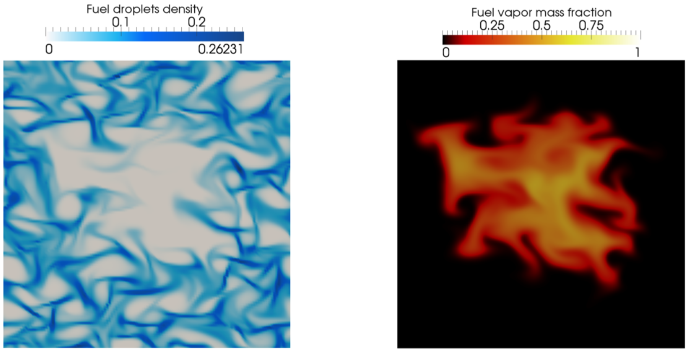

Figure 11.31: *Liquid fuel number density (left) and fuel vapor mass fraction (left) obtained with the multi-fluid MK simulations for a cold flame configuration on a 2D HIT.*

phase and the carrier phase would be represented.

- AG for spray combustion: the direct extension of the simulation presented in this work concerns the physical analysis of evaporating spray prior to the combustion. This can be done based on the TSM-AG that should be implemented in the MUSES3D code in order to simulate simplified cold flames configurations similar to the ones conducted in the work of *Fréret et al. (2010)*; *Fréret et al. (2012)* based on the OSM-MK model. An example of this configuration in 2D is illustrated in Figure 11.31.

  This test should be done first in the simplified framework of 3D HIT with two-way coupling that can lead to understand the interaction between the 3D turbulent eddies and the spray dynamics. This is possible based on the TSM-AG model presented in this thesis, since it was designed in a way to keep the genericity so that the two way coupling can be added and complex laws for evaporation and heat transfer can be used in order to accurately simulate the spray evaporation and combustion.

  Another application in this context belongs to the NEXTFLAME-ANR[1] that targets to compare experimental results against numerical simulations for laminar stationary and pulsated spray of heptane evaporating in a counterflow configuration. The first step of this comparison is done based on the multi-fluid MK model (*Brandle De Motta et al. 2016*) as shown in Figure 11.32. The next step comes as a prospect of this thesis by comparing the experimental and Lagrangian results with the Eulerian results based on the multi-fluid AG model for the cases where PTC occur. The importance of extending this study to include the AG model can be seen through the overestimated number density of the droplets by the MK models as shown in Figure 11.32(b). The 2D axisymmetric version of the AG model is studied in the thesis of *Dupif (2017)* and can be found

---

[1] supported by the ANR and the FRAE through the grant ANR-13-BS09-0023-01 and is a joint work between the EM2C laboratory and the CERFACS.

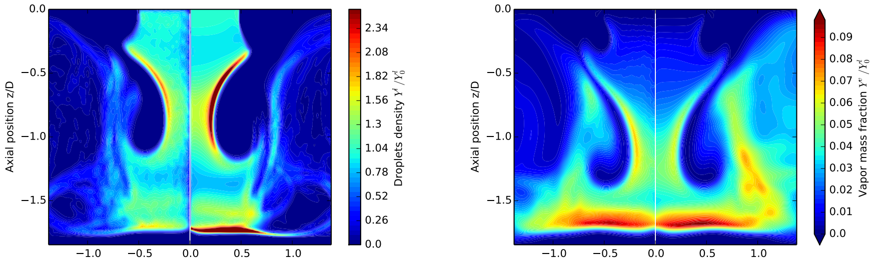

(a) The droplets density (b) The fuel vapor mass fraction

Figure 11.32: *Comparison between the Lagrangian (left on each subfigure) and OSM-MK (right on each subfigure) results for the axisymmetric counterflow configuration (Source Brandle De Motta et al. (2016))*

in the work of *Dupays et al. (2016)*.

- Extension of DG: the evaluation of the realizability preserving DG scheme was done in this thesis on 1D and 2D configurations for the resolution of the PDG and Euler system on structured mesh. Thus, a first extension can be sought by applying this scheme to the Anisotropic Gaussian closure model, a preliminary result for this case was presented in this thesis based on the work of Larat et al. . This should be followed by quality/cost comparisons between the DG and the MUSCL/HLL results for this model similar to the one carried on for MK model in this thesis. A second prospect is to extend the DG scheme to higher order and to three-dimensional space. This extension should be supported with a cost/quality comparison between DG and other FV (similar to the one presented in this work) on 3D configuration on unstructured meshes. To do so, the multi-slope version of the MUSCL/HLL scheme developed in the work of *Dupif (2017)* can be used. This comparison is essential to prove that the DG scheme is competitive with the FV scheme for the simulation of the spray in complex industrial configurations.
- Coupling between MK and AG: depending on the particles St and local flow regime one can prefer to choose between the MK or the AG. On the one hand, the MK model is cost effective and treats accurately the vacuum regions and the singularity faced for low inertia particles but is incapable of reproducing the PTC. On the other hand, the AG model can reproduced the right physics for low inertia to moderately-inertial particles but is more expensive than the MK model where compared for the same level of accuracy for small St. For this reason one tends to prefer the MK for small St and AG for moderately-inertial to inertial particles. For this reason, a relaxation scheme should be used similar to the one used in the work of *Boileau et al. (2015)* to treat both PGD and Euler system. This extension is a on-going work (*Boileau et al. 2016*).
- Subgrid models for AG LES: the extension of the AG model to the LES context that leads to a new fully kinetic based closure formalism for the

LES of spray is the first step toward the development of a realizable polydisperse/polykinetic model for the LES of the disperse phase. In future works, accurate subgrid models should be developed and evaluated on configurations of increasing complexity in order to reach the level faced in industrial applications. In addition the two-way coupling between the disperse and the carrier phases should be taken into account. These two subjects are on-going work in the thesis of *Mercier (2018)*.

- Higher order models can be used such as the quadrature based moment model based on a dirac distribution or a Anisotropic Gaussian for the velocity leading respectively to QMOM or MG. The former is studied in various configurations in the literature whereas the latter is still considered as a new model that is not fully assessed. The evaluation of the AG model can be seen as a first step in the evaluation of the MG model since this latter is based on the AG distribution for the quadratures choice, however further evaluation of the MG model should be conducted but one should keep in mind that the used on the MG is not considered for industrial applications for the time being to its unaffordable cost. In addition other higher order models can be sought based on the *Levermore (1996)* hierarchy of the rarified gas dynamics.
- High fidelity predictive simulation of the complete fuel injection in the aeronautical combustion chambers: this objective depends also the accurate simulation of the separated phase itself and more challengingly of the transition between the pure disperse phase and pure separated-phases and thus the accurate simulation of the atomization process. Thus, it is envisioned as an objective on the long run. The modeling of this transition is a building block for future complete simulations. For more information one can refer to the work of *Reveillon et al. (2013)*; *Le Touze (2015)*; *Zuzio et al. (2016)*, this subject in also an on-going work by *Drui et al. (2016)*; *Essadki et al. (2016)*.
- Industrial simulation of aeronautical combustion chambers using the AG model for the spray dynamics: in order to reach this objective, the AG model should be implemented in the AVBP code. In order to simplify this task, one can start by the implementation of this model along with the realizability-preserving parameter-free numerical method for a monodisperse phase. Once this first step is validated on industrial configurations, the extension to polydisperse evaporating cases can be then implemented.

Appendix A

Droplet models

The empirical correlations for the physical phenomena related to the unclosed terms in the WBE are presented hereafter. They are classical models for isolated droplets that are compatible with the deterministic and the kinetic description of the disperse phase. These laws are essential to be able to replace the physical droplet of mass m_p, surface $S = 4\pi r_p^2$, velocity $\vec{\boldsymbol{c}}$ and temperature T by a point-particle. The density of the liquid disperse phase ρ_l is considered to be constant.

A.1 External forces per unit mass

The external forces acting on a droplet can be divided into gravity, drag force, Basset force and lift force (*Crowe et al. 1998*). In the context of gas-liquid flow, the gas to liquid density ratio is of order 10^{-3} to 10^{-2}. In this case the external forces reduce to the gravity and drag (*Dufour 2005*). In the present work, the only external force that will be accounted for is the drag force. The gravity is neglected only for the sake of simplicity.
A general form of the drag force per unit mass is written as a function of the drag coefficient (*O'Rourke 1981*; *Sirignano 1999*):

$$m_p \overrightarrow{\mathbf{F}} = \frac{1}{8}\rho_g S(\overrightarrow{\mathbf{U_g}} - \vec{\boldsymbol{c}})\|\overrightarrow{\mathbf{U_g}} - \vec{\boldsymbol{c}}\| \tag{A.1}$$

where the drag coefficient depends on the turbulent regime and therefore on the droplet Reynolds number Re_p as shown in figure A.1 (*Clift et al. 1978*). The Reynolds number of the droplet is given by:

$$\mathrm{Re}_p = \frac{\rho_g \|\overrightarrow{\mathbf{U_g}} - \vec{\boldsymbol{c}}\|\sqrt{S}}{\mu_g \sqrt{\pi}} \tag{A.2}$$

The drag coefficient is then given by the Stokes law (*Stokes 1846*) for $Re_p < 1$, by the experimental correlation of *Schiller and Naumann (1935)* for $Re_p > 10^3$ or by many other relationships (*Clift et al. 1978*) such as the constant value

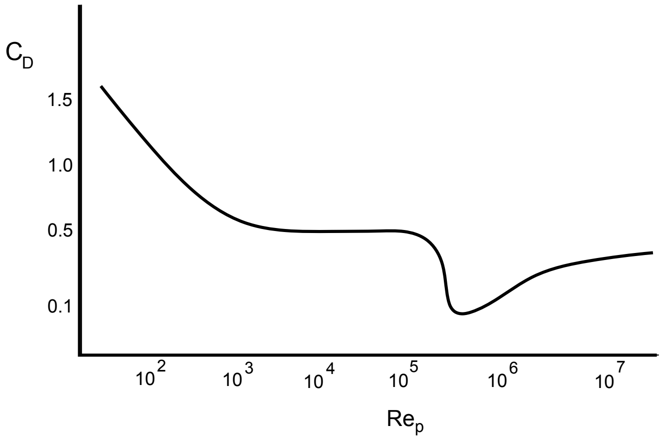

Figure A.1: *Drag coefficient of a sphere as a function of Reynolds number*

coefficient given by *Crowe et al. (1998)* for higher Re_p:

$$C_D = \begin{cases} 24Re_p^{-1} & \text{if } \mathrm{Re}_p < 1, \\ 24Re_p^{-1}(1 + 0.15Re_p^{0.687}) & \text{if } 1 < \mathrm{Re}_p < 10^3, \\ 0.445 & \text{if } 10^3 < \mathrm{Re}_p < 3.5x10^5 \end{cases} \tag{A.3}$$

The modeling approach presented in this thesis is valid for all the drag laws and correlations depicted above, however the simplest model is chosen here. This choice is acceptable when the droplets are small enough not to reach the turbulent regimes. The drag force per unit mass reads:

$$F = \frac{18\pi\mu_g}{S\rho_l}(\overrightarrow{\mathbf{U_g}} - \vec{c}) = \frac{(\overrightarrow{\mathbf{U_g}} - \vec{c})}{\tau_p} \tag{A.4}$$

where τ_p is the characteristic momentum transfer time of the droplets also called the velocity relaxation time:

$$\tau_p = \frac{S\rho_l}{18\pi\mu_g} \tag{A.5}$$

A.2 Evaporation rate

The rate of change of the size is here reduced to only the evaporation since the dilatation is not taking into account due to the assumption of constant disperse phase density. The evaporation rate is then implicitly written in relation with the mass variation of the droplet or the mass flux of vapor at the droplet surface:

$$[\dot{m}_p]_S = -\frac{\rho_l\sqrt{S}}{4\sqrt{\pi}}R_S \tag{A.6}$$

Then a diffusive mass boundary layer δ_m is defined to take into account the relative velocity between the droplet and the carrier phase. In this case the convective Sherwood number reads:

$$\mathrm{Sh}_c = 2\frac{\delta_m}{\delta_m - r_p} \tag{A.7}$$

Based on the spherical symmetry of the droplet, a unidimensional formulation is considered so that when no cheminal reaction takes place the conservation laws of the fuel vapor mass fraction Y_F and of the total mass give:

$$[\dot{m}_p]_S = 2\pi r_p \rho_g \mathrm{Sh}_c D_{Y_F} ln(1 + B_M) \tag{A.8}$$

where $B_M = \frac{[Y_F]_S - [Y_F]_\infty}{1 - [Y_F]_S}$ is the Spalding dimensionless mass transfer number and D_{Y_F} is the binary diffusion coefficient in the Fick's law.
Thus, the evaporation rate reads:

$$R_s = 4\pi r_p \frac{\rho_g}{\rho_l} \mathrm{Sh}_c D_{Y_F} ln(1 + B_M) \tag{A.9}$$

The details of the derivation of this model can be found in (*Abramzon and Sirignano 1989; Versaevel 1996; Reveillon and Demoulin 2007*).
In the special case where the droplet temperature is assumed to be constant, the d^2 law (*Godsave 1953; Spalding 1953*) is obtained. This law states that the rate of change of the square of the droplet diameter is equal to a coefficient φ independent from the droplet diameter and only depends on the local gas properties.

$$\mathrm{d}_t d^2 = -\varphi \tag{A.10}$$

In this case convective Sherwood number is equal to 2 and the evaporation rate reduces to:

$$R_s = 8\pi r_p \frac{\rho_g}{\rho_l} D_{Y_F} ln(1 + B_M) \tag{A.11}$$

where B_M is either found through a saturation law (*Reveillon and Demoulin 2007*) or it is assumed to be constant.

A.3 Temperature change rate

The heat absorbed by the liquid H_l is the source of the temperature change rate of the droplets:

$$H_l = m_p C_{p,l} H_T \tag{A.12}$$

In fact, this heat comes from the gas H_g so that the conductive heat balance on the droplet surface gives:

$$H_g = [\dot{m}_p]_S L_v + H_l \tag{A.13}$$

where L_v is the vaporization latent heat and $H_g = S\lambda_g \mathrm{d}_t T_g = Sh_c(T_\infty - [T]_S)$ with h_c being the convective modified heat transfer coefficient.
Similarly to the evaporation rate derivation, a thermal diffusive boundary layer δ_T is defined with the Nusselt number $\mathrm{Nu}_c = 2\frac{\delta_T}{\delta_T - r_p}$. Then through the energy conservation a new expression for the mass flux of fuel vapor at the droplet surface is obtained:

$$[\dot{m}_p]_S = 2\pi r_p C_{p,g}^{-1} \mathrm{Nu}_c \lambda_g ln(1 + B_T) \tag{A.14}$$

where $B_T = \frac{\rho_g U_g C_{p,g}}{h_c}$ is the dimensionless heat transfer number. Based on equations (A.8) and (A.14), the following expression for the temperature rate of change is obtained:

$$H_T = 6\pi \frac{\rho_g}{\rho_l S C_{p,l}} \mathrm{Sh}_c D_{Y_F} ln(1 + B_M) \left(\frac{C_{p,g}(T_g(\vec{\boldsymbol{x}}_p) - [T]_s)}{B_T} - L_v \right) \tag{A.15}$$

with

$$B_T = (B_M + 1)^{\frac{\mathrm{Sh}_c \mathrm{Sc}}{\mathrm{Nu}_c \mathrm{Pr}}} \tag{A.16}$$

and the dimentionless Prandtl and Schmidt number respectively equal to:

$$\mathrm{Pr} = \frac{C_{p,g}\mu_g}{\lambda_g} \quad \text{and } \mathrm{Sc} = \frac{\mu_g}{\rho_g D_k} \tag{A.17}$$

The above procedure can be found in details in *Reveillon and Demoulin (2007); de Chaisemartin (2009)*.
In general for given Sh_c, B_M and B_T the models for the evaporation and temperature change rate are obtained. As it was mentioned before the simplest case is for $\mathrm{Sh}_c = 2$ when the heat transfer is negligeable. For more realistic cases, many choices exist in the literature to take the convection into account (*Sirignano 1999*) such as the empirical expressions for Sh_c and Nu_c by *Faeth (1983)* or other methods found in *Abramzon and Sirignano (1989); Clift et al. (1978)*.

Appendix B

Academic, semi-industrial and industrial codes

B.1 Academic codes

NGA is a 3-D massively parallel, fully conservative, low mach CFD solver for both DNS and LES of reacting turbulent flows. The fluid mass, momentum and energy conservation laws are solved using a high accuracy variable density energy conserving finite difference scheme (*Desjardins et al. 2008*) on cartesian or cylindrical meshes. This code also includes a Lagrangian solver for the particle. The first version of this code have seen the light in 2005 at the Center for Turbulence Research. Currently, it is maintained and developed by the research group of Olivier Desjardins at Cornell University and Guillaume Blanquard at CalTech. An example of a simulation of cluster induced turbulence using NGA done by Capecelatro et al. (2014; 2015) is shown in figure B.1.

NTMIX is a 3D fully parallel, structured DNS and LES solver for reactif two phase flows. The compressible Navier Stokes equations for the gas phase are solved with a compact finite difference scheme of order 6 (*Lele 1992*) and a three stage Runge-Kutta scheme for the time evolution. The second part of this code is the Lagrangian disperse phase solver. NTMIX is developed by the CRCT (Centre de Recherche en Combustion Turbulente) including CERFACS, IFP, IMFT and EM2C (*Poinsot et al. 1993; Cuenot and Poinsot 1996; Vermorel et al. 2003; Riber 2007; Moreau 2006*).

ASPHODELE is a 3D DNS low mach number code for the turbulent gas phase with lagrangian tracking solver for the disperse phase. It is a structured cartesian and axisymmetric code with MPI parallelisation. It uses an implicit high-order compact finite-difference scheme (*Lele 1992*) for the gas, it is a generalization of the classical FD schemes of type Padé. A third-order explicit Runge-Kutta (RK) scheme with a minimal data storage method is used for the time resolution. It is developed at CORIA by Reveillon and collaborators (*Reveillon and Demoulin 2007; Thomine 2011*). At the time being, it is maintained and evolved by CORIA and EM2C.

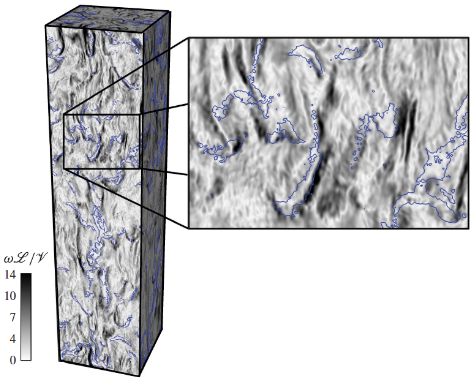

Figure B.1: *Fluid vorticity magnitude in gravity-driven Cluster Induced Turbulence (Capecelatro et al. 2015)*

ARCHER is a 3D code for liquid/gas interface simulations. For the gas phase, the convective terms are solved with a fifth order WENO scheme while the diffusive terms are solved with a second order centered scheme with Adams Bashforth or RK3 schemes in time. This code is developped at CORIA by the group of Demoulin, F.-X. and Réveillon, J. (*Tanguy and Berlemont 2005; Menard et al. 2007*).

FAST3D is a flow solver based on the SHASTA algorithm Sharp and Smooth Transport Algorithm (*Boris and Book 1973; Zalesak 1997*) that uses the Flux-Corrected Transpor scheme in the LCPFCT library by *Boris et al. (1993)*. It was developped more than 20 years ago at the Laboratories for Computational Physics and Fluid Dynamics of the US naval research laboratory. This code used for example for the LES of urban aerodynamics by contaminant transport (*Patnaik and Boris 2010*).

AZURE is a CFD software that includes an unstructured and structured grids modules. For the unstructured one, the compressible Navier-Stokes system is discretized using a cell-centered finite vol-ume formulation on mixed-element grids. The convective terms are solved by either second or third-order MUSCL that satisties the TVD condition or 3rd and 5th orders WENO schemes. It is developped at (*Antoniadis et al. 2015*).

MUSES3D is the the MUlti-fluid Solver for Eulerian Spray initially developed by *de Chaisemartin (2009)* at the EM2C. For the physical transport the

Finite Volume Kinetic Scheme (*Bouchut et al. 2003*) was implemented for the resolution of the PDG system. Since this scheme is limited to the resolution of the MK model, in this work, the implementation of second order MUSCL scheme was carried out for the treatment of PDG and AG systems. This code is massively parrallel and it includes both cartesian and axisymmetric discretization.

CHOMBO is a software for AMR solutions of partial differential equations. It is developped by the Applied Numerical Algorithms Group part of the Computational Research Division at Lawrence Berkeley National Laboratory. Few years ago, the PPM method was implemented in this code by *Sekora and Colella (2009)*.

TENET is astrophysical code that is an extension of the AREPO code of the Heidelberg Institute for Theoretical Studies that is presented in the following section. It is an MPI-parallel RKDG code that solves the Euler system on AMR grids (*Bauer et al. 2016; Schaal et al. 2015*). One of the simulation done recently on this code is the Kelvin-Helmholtz simulation shown in figure B.2 that was solved with fourth order DG scheme by *Schaal et al. (2015)*.

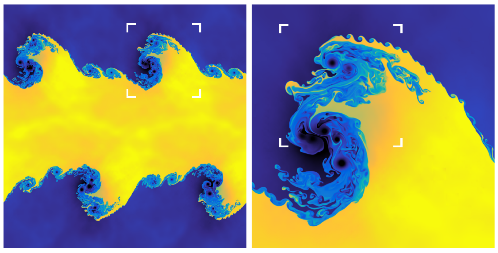

Figure B.2: *Kelvin-Helmholtz simulation with DG-4 and AMR using the TENET code (Schaal et al. 2015)*

BoSSS is the Bounded Support Spectral Solver which is a CFD code initiated by *Kummer (2012)*. It is based on the DG scheme ans is currently developped at the Technische Universitat Darmstadt.

DLR-PADGE is the Parallel Adaptive Discontinuous Galerkin Environment of the German aerospace center (DLR). It solves the RANS equations with high order adaptive DG methos on unstructured frids. Its main application is the aerospace engineering (*Hartmann et al. 2010; Schoenawa and Hartmann 2014; Hartmann and Leicht 2016*).

B.2 Semi-industrial and industrial codes

AVBP is is a parallel CFD code that solves the three-dimensional compressible Navier-Stokes on unstructured and hybrid grids based on a cell-vertex formulation. The associated numerical scheme is a Two-Step Taylor-Galerkin scheme called TTGC, which is a finite element scheme. This compact central scheme achieves third order in time and space, and is well-designed for Large Eddy Simulation (LES), especially in terms of dissipation and dispersion (*Colin and Rudgyard 2000*). Despite the good properties of such a scheme for turbulent reactive flows, it has a hard time to solve the Eulerian moment equations: because of the very stiff accumulations and gradients and vacuum zones, it requires stabilisation procedures such as artificial viscosity which end up to be a long iterative process for finding the stable set of parameters (*Lamarque 2007; Martinez 2010; Vié 2010; Dombard 2011*). This code started as a project in 1993 by Michael Rudgyard and Thilo Schönfeld. Currently, it represents one of the most advanced CFD tools for the simulation of unsteady turbulence for reacting flows.
The ownership of this code is shared with IFPEN and CERFACS under the leadership of Thierry Poinsot. It is used by multiple laboratories in Europe for example IMFT, EM2C, Von Karmann Institute and ETH Zurich and companies such as SNECMA, TURBOMECA and Airbus Safran Launchers.
One of the recent simulation carried out using this code is the LES of the ignition sequence of an full annular multiple-injector burner by *Philip et al. (2015)* shown in figure 5.1.

YALES2 is a massively parallel unstructured low-Mach number code for the DNS and LES of reacting two-phase flows. For the convective terms, it uses secons and fourth order finite volume scheme for the spatial descretization and fourth order explicit integration in time. It was developed by *Moureau et al. (2011a)*. One of the interesting simulation done using this code is the LES prediction of the PRECCINSTA burner shown in figure B.3 performed by *Moureau et al. (2011b)* at CORIA.

CharLES is an unstructured compressible flow solver for LES. It uses a novel FV scheme for the resolution of the spatially-filtered compressible Navier-Stokes equations (*Khalighi et al. 2010*). The shocks are handled with a hybrid second order central-ENO scheme along with the HLLC numerical flux (*Hu et al. 2009*). It is owner and developed by Cascade Technologies at Stanford.

RAPTOR is a turbulent combustion code developed at Combustion Research Facility of Sandia National Laboratories by *Oefelein et al. (2007)*. It uses LES to explore the chemical and physical processes of combustion LES using non-dissipative, discretely conservative, staggered, finite-volume differencing.

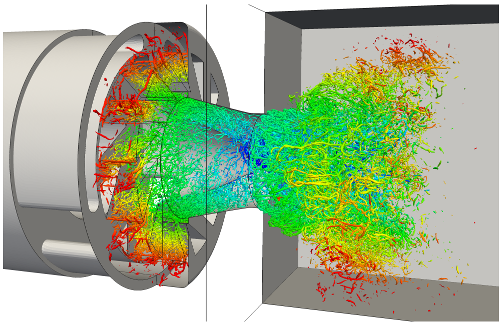

Figure B.3: *Turbulent structures resulting from the massively parallel LES predictions of the PRECCINSTA burner with YALES2 code (Moureau et al. 2011a)*

CEDRE is an unstructured multi-physics solver in the field of propulsion and energetics. It can treat many physical phenomena such as combustion, acoustics, compressibility and two-phase flow. Thus, several solver constiture the software; for example Charme solver for the fluid transport, SPIREE solver for the eulerian description of the disperse phase, and SPARTE solver for the Lagrangian description of this phase. It is developped at the ONERA and is used for research and industrial applications using Arbitrary Lagrangian-Eulerian (ALE) formalism. This software is presented by *Refloch et al. (2011)*. For the fluid solver called Charme, the equations are solved with a cell-centered finite volume approach where the interpolation is of type MUSCL. This method can be either monoslope or multislope (*Le Touze et al. 2015*); the latter is very useful on unstructured meshes. This scheme is also used in SPIREE along with kinetic schemes FVKS for the spatial discretization of the convective terms when the model is based on the MK closure (*Murrone and Villedieu 2011*).

SU2 is the Stanford University Unstructured tool suite. It solves complex multi-physics problems on arbitrary unstructured meshes based on both FV methods. The space discretization is a dual grid with control volumes constructed using a median-dual, vertex-based scheme. It also included FE methods. It is parallelized with MPI paradigm. This tool suite is is under development in the Aerospace Design Lab of the department of aeronautics and astronautics at Stanford university and has been released as an open-source software.
In the main transport solver SU2-CFD, the convective fluxes can be discretized using central or upwind methods at first order whereas for second order schemes MUSCL approach is used with gradient limitation (*Palacios et al. 2013*). Recently, single and multi-node optimizations of SU2 for implicit RANS calculations on unstructured grids is carried out by*Economon et al. (2016)*.

AREPO is a cosmological hydrodynamical simulation parallelized code on a fully dynamic unstructured mesh with adaptive mesh refinement. It uses a finite-volume approach , based on a second-order unsplit Godunov scheme with an exact Riemann solver. The FV scheme used is the MUSCL-Hancock scheme with the Voronoi cells as principle control volumes. This code is developped at Heidelberg Institute for Theoretical Studies by *Springel (2010)*. Figure B.4 illustrate an astrophysical simulation using AREPO; it shows the time evolution of the two galaxies falling together freely and undergoing a galaxy merger.

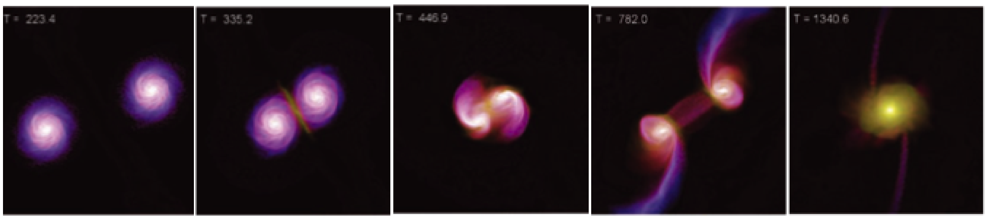

Figure B.4: *Simulation of the evolution of the projected gas density in a galaxy collision with non-radiative gas using the AREPO code (Springel 2010)*

DLR-TAU is a software that solves the RANS equations using second order finite volume scheme. It is used on complex geometries and simulate subsonic to hypersonic flow regime on hybric unstructured mesh. It is developped by the numerical methods department of the German aerospace center as both a research tool and production tool for the aircraft industry and research community (*Schwamborn et al. 2006*).

KIVA is a family of CFD software for the simulation of chemically reacting flows with sprays. It is a 3D, transient, multiphase, multicomponent code developed by Los Alamos National Laboratory since 1985 (*Amsden and Amsden 1993*). The current version is unstructured and parallel (*Torres and Trujillo 2006; Torres et al. 2010*). It uses a finite volume discretization technique with ALE approach. For the disperse phase, a stochastic method is used for Lagrangian particle dynamics. This software was used by many intustrial companies such as General Motors and Cummins. This software is still used for research in the combustion field for example the most recent simulation with KIVA is of compressed natural gas direct injection engine (*Choi and Park 2016*).

`Code_Saturne` is open-source CFD software that solves the Navier-Stokes equations in RANS or LES context for steady or unsteady flows, laminar or turbulent, incompressible or weakly dilatable, isothermal or not and with optional scalars transport. For the convective terms this code propose different finite volume solver with collocated arrangement for solution variables such as the first order upwind scheme and Second Order Linear Upwind (SOLU) Scheme. It also includes a Lagrangian particle-tracking method for the disperse phase with ALE technique.

In 1997, this code was initially developed by Electricité de France (EDF) (*Archambeau et al. 2004*). Some of recent advancement on this code is its optimization on Petascale systems by *Fournier et al. (2011)* and the implementation of adapted numerical scheme for the simulation of the presence of spacer grids with mixing vanes in nuclear reactors fuel assemblies by *Capone et al. (2016)*.

`Neptune_CFD` is a fully unstructured finite volume solver created by EDF and CEA and financially supported by AREVA and IRSN. It is developped for analysing and simulating thermal-hydraulics nuclear reactors. It is based on advanced physical models such as two-fluid or multi field model combined with interfacial area transport and two-phase turbulence (*Guelfi et al. 2007*). A version of this code is developped at the IMFT for the study of gas-particle flows in general and fluidized bed more specifically (*Neau et al. 2010*).

ARGO is massively parallel CFD code for compressible or incompressible flows. It includes several numerical scheme for example for the convective terms a second order finite volume scheme, a kinetic energy central scheme and also high order discontinuous Galerkin schemes (*de Wiart and Hillewaert 2015*). It is developped by Cenaero and included RANS and LES methodologies.

MIGALE is a parallel high-order accurate Discontinuous Galerkin code allowing to solve the RANS equations. The high-order DG is used for the unsteady simulation of turbulent flows by using high-order implicit time integration schemes (*Codenotti et al. 1998; Bassi et al. 2011; Bassi et al. 2015; Lorini et al. 2016*). An example of a simulation done using this code by *Bassi et al. (2014)* on a delta wing is shown in figure B.5.

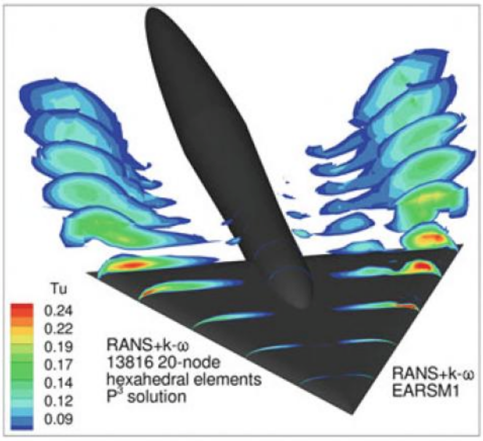

Figure B.5: *Turbulence intensity contours around VF2 medium radius delta wing simulated with MIGALE code (Bassi et al. 2014)*

AGHORA is a 3D massively parrallel, unstructured solver for the simulation of NS equations. It is based on the DG scheme where the numerical fluxes across the elements interfaces are based on Roe or Lax-Friedrichs approximations. Two parallel implementation are found in this code the first one is based on the MPI technique while the second is a hybrid MPI and OpenMP approach.

NEKTAR++ is an open-source software framework designed to support the development of high performance scalable solvers for partial differential equations on unstructured grids. It included both continuous and discontinuous Galerking FE schemes (*Cantwell et al. 2015*; *Bolis et al. 2016*) for the 3D simulation of both compression and incompressible NS or Euler equations. The software is currently maintained and developed by members of the SherwinLab at Imperial College London and Kirby's group at the University of Utah.

It is important to note that is the above list some of the widely used commercial codes are not mentionned such as ANSYS Fluent, ANSYS CFX, COMSOL Multiphysics, Gerris and `Star_CD`. A comparison of three of these software, namely Fluent, CFX and `Star_CD` was carried out by *Iaccarino (2001)* for simulation of the turbulent flow in an asymmetric two-dimensional diffuser.

Appendix C

Slope limiters

van Leer (2006) defined the limiter as "a nonlinear algorithm that reduces the high-derivative content of a subgrid interpolant in order to make it non-oscillatory".

In order to ensure that the solution does not contain any spurious oscillations and that a monotone advection is reproduced robustly using the finite volume methods, the limiter must satisty a Total Variation Diminishing (TVD) condition.

This property was first introduced by *Harten (1983)* inspired by the work of *Glimm and Lax (1967)*. The term TVD figured at the first time in *Harten (1984)*; *Sweby (1984)*.

The total variation TV is defined as the sum of the local variations:

$$\mathrm{TV}(u) = \sum_i |u_{i+1} - u_i| \tag{C.1}$$

In fact, if the scheme introduces oscillations then the total variation will increase. Thus, a numerical scheme is said to be TVD if its total variation does not increase with time. For this reason, this property was first called total variation nonincreasing (TVNI) (*Harten 1983*).

$$\mathrm{TV}(u^{n+1}) \leq \mathrm{TV}(u^n) \tag{C.2}$$

Based on these definition, *Harten (1983)* proved that:

- a monotone scheme is TVD,
- a TVD scheme is monotonicity preserving.

Through this TVD property the ability of a scheme to stay globally stable in the boundary variation space is evaluated.

In reality, a TVD scheme is used to capture the discontinuities without generating misleading spurious oscillations.

The theorem of *Godunov (1959)* presented earlier translates that TVD linear schemes are at most of first order. Therefore, as mentioned before, high order schemes require nonlinear techniques to stay TVD and the most famous method is based on the limiting procedure. The limiting technique was first used by *Boris and Book (1973); van Leer (1974)*. A detailed review of these limiters can be found for example in *Sanders and Bradford (2006); Toro (2009)*, however in the following only a summary of the most widely used limiters is presented.

The limiting functions defined by equation (C.3) is plotted in figure C.1 as a function of the smoothness monitor given by $r = \dfrac{u_{i+1} - u_i}{u_i - u_{i-1}}$ (*van Leer 1974*). This is done for the following limiters: van Leer, van Albada, minimum-modulus (minmod), Superbee and Double Minmod (also called monotonized central-difference limiter (MC)) that are respectively given by equations (C.5), (C.6), (C.7), (C.8) and (C.9).

$$\mathcal{R}(r) = \frac{2D_{u_i}}{u_{i+1} - u_{i-1}} \tag{C.3}$$

And, the TVD condition is translated by equation (C.4) (*Sanders and Bradford 2006*).

$$\mathcal{R}(r) \leqslant \min\left[\frac{4r}{r+1}, \frac{4}{r+1}\right] \quad \forall \quad r \geqslant 0 \tag{C.4}$$

As for the dissipation, if $\mathcal{R}(r) > 1$ the limiter is antidissipative whereas when $\mathcal{R}(r) < 1$ it is dissipative.

$$\mathcal{R}_{\text{van Leer}}(r) = \frac{2(r + |r|)}{(1+r)^2} \tag{C.5}$$

$$\mathcal{R}_{\text{van Albada}}(r) = \frac{2r}{1+r^2} \tag{C.6}$$

$$\mathcal{R}_{\text{Minmod}}(r) = \max\left[0, \min\left(\frac{2r}{1+r}, \frac{2}{1+r}\right)\right] \tag{C.7}$$

$$\mathcal{R}_{\text{Superbee}}(r) = \max\left[0, \min\left(\frac{4r}{1+r}, \frac{2}{1+r}\right), \min\left(\frac{2r}{1+r}, \frac{4}{1+r}\right)\right] \tag{C.8}$$

$$\mathcal{R}_{\text{MC}}(r) = \max\left[0, \min\left(1, \frac{4r}{1+r}, \frac{4}{1+r}\right)\right] \tag{C.9}$$

Thus, for $r \neq 1$, the minmod limiter is dissipative and smeares the discontinuities. On the other hand, the double minmod or MC limiter generates the least truncation error over the range of r, since for $1/3 < r < 3$, it is characterised by

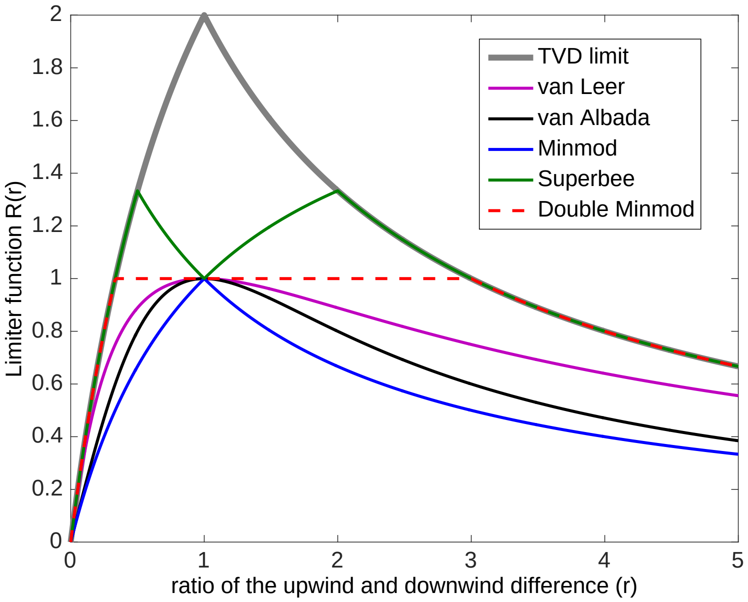

Figure C.1: *Van Leer diagram of slope limiters*

$\mathcal{R}(r) = 1$. In addition, the MC limiter has exactly the dissipation level required to garantee the TVD limit. Another choice may be the Superbee limiter which is anti-dissipative and therefore sharpens the edges.

Another way to represent these limiters is the Sweby diagram (*Sweby 1984*) where the limiters are interpreted as flux limiters. The limiter function φ is represented as a function of the consecutive gradient ratio $\theta = \dfrac{u_i - u_{i-1}}{u_{i+1} - u_i}$ which is a measure of the smoothness of the data near the interface. This plot is shown in figure C.2 where the region of second-order TVD methods is shaded in gray.

We can clearly notice that the Superbee limiter lies along the upper boundary of the TVD region. whereas the Minmod limiter lies along its lower boundary (*LeVeque 2002*) these two limiter are respectively the less and the most restrictive limiters in the TVD region. Both of these limiters are not smooth at $\theta = 1$ since at this point they are changing from the Beam-Warming to the Lax-Wendroff approximation. This problem is resolved with the MC limiter where the limiter function is smooth near $\theta = 1$.

For more information about this representation one may refer to the article of *Sweby (1984)* or the book of *LeVeque (2002)* for example.

It is important to note that the list of the limiter presented in the above paragraph is not complete for example a successful limiter that is not presented here is the Koren limiter *Koren (1993)*.

In the litterature several limiters were developped to attempt to remedy the problem of degenerating to lower order of accuracy faced with all the classical

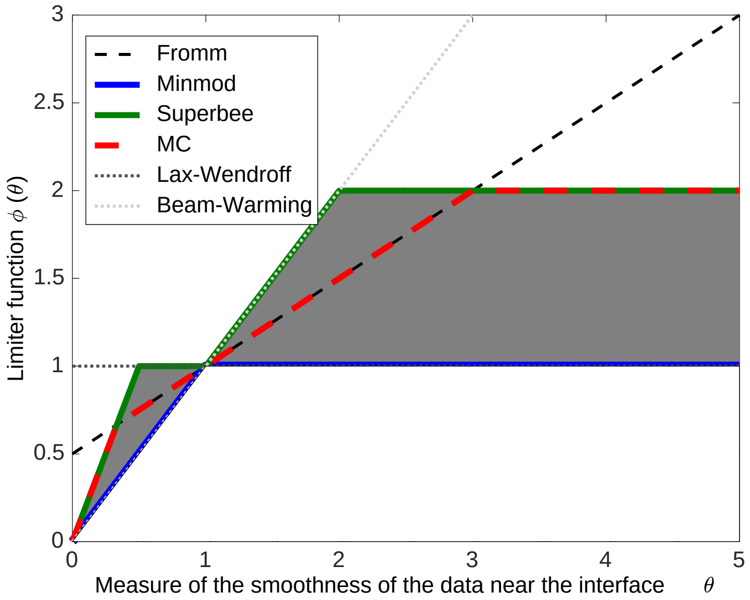

Figure C.2: *Sweby diagram of slope limiters*

limiters (*Cada and Torrilhon 2009*; *Sekora and Colella 2009*) but will not be adressed in this work.

References

Abramzon, B. and W. Sirignano (1989). Droplet vaporization model for spray combustion calculations. *Int. J. Heat Mass Transfer 32*, 1605–1618. *(p. 315, 316)*

Ahmadi, G. (2009). Lagrangian versus Eulerian method for nano-particles. In *Modeling and Computation of Nanoparticles in Fluid Flows, Lectures Notes of the von Karman Institute, NATO RTO- EN-AVT-169*, pp. 1–46. *(p. 43)*

Alexander, F. J. and A. L. Garcia (1997). The Direct Simulation Monte Carlo method. *Computers in Physics 11*(6), 588–593. *(p. 41)*

Alipchenkov, V. and L. Zaichik (2007). Differential and algebraic models for the second moments of particle velocity and temperature fluctuations in turbulent flows. *Fluid Dynamics 42*(2), 236–254. *(p. 276)*

Alldredge, G. and F. Schneider (2015). A realizability-preserving discontinuous Galerkin scheme for entropy-based moment closures for linear kinetic equations in one space dimension. *Journal of Computational Physics 295*, 665 – 684. *(p. 93)*

Amsden, D. C. and A. A. Amsden (1993). The KIVA story: a paradigm of technology transfer. *IEEE Transactions on Professional Communication 36*(4), 190–195. *(p. 322)*

Andries, P., P. Le Tallec, J. Perlat, and B. Perthame (2000). The Gaussian-BGK model of Boltzmann equation with small Prandtl number. *Eur. J. of Mech. B - Fluids 19*, 813–930. *(p. 58)*

Antoniadis, A., P. Tsoutsanis, Z. A. Rana, I. Kokkinakis, and D. Drikakis (2015). Azure: An Advanced CFD Software Suite Based on High-Resolution and High-Order Methods. In *53rd AIAA Aerospace Sciences Meeting, AIAA SciTech*, Kissimmee, Florida. *(p. 318)*

Archambeau, F., N. Méchitoua, and M. Sakiz (2004). Code Saturne: A Finite Volume Code for the computation of turbulent incompressible flows - Industrial Applications. *International Journal on Finite Volumes 1*(1), 1–62. *(p. 323)*

Argyris, J. (1955). Energy theorems and structural analysis: A generalized discourse with applications on energy principles of structural analysis including the effects of temperature and non-linear stress-strain relations Part I. general theory. *Aircraft Engineering and Aerospace Technology 27*(4), 125–134. *(p. 89)*

Arienti, M. and M. Sussman (2014). An embedded level set method for sharp-interface multiphase simulations of Diesel injectors. *International Journal of Multiphase Flow 59*(1), 1–14. *(p. 5, 26)*

Arnold, D. N., F. Brezzi, B. Cockburn, and L. D. Marini (2001). Unified analysis of Discontinuous Galerkin methods for elliptic problems. *SIAM J. Numer. Anal. 39*(5), 1749–1779. *(p. 92)*

Atkins, H. and C.-W. Shu (1998). Quadrature free implementation of Discontinuous Galerkin method for hyperbolic equations. *AIAA Journal 36*(5), 775–782. *(p. 92)*

Aulisa, E., S. Manservisi, R. Scardovelli, and S. Zaleski (2003). A geometrical area-preserving Volume-of-Fluid method. *Journal of Computational Physics 192*, 355–364. *(p. 5, 26)*

Babinsky, E. and P. Sojka (2002). Modeling drop size distributions. *Progress in energy and combustion science 28*(4), 303–329. *(p. 66)*

Baer, M. R. and J. W. Nunziato (1986). A two-phase mixture theory for the deflagration-to-detonation transition (DDT) in reactive granular materials. *International Journal of Multiphase Flow 12*(6), 861–889. *(p. 5, 26)*

Baker, G. A. (1975). A Finite Element method for first order hyperbolic equations. *Mathematics of Computation 29*(132), 995–1006. *(p. 89)*

Balachandar, S. and J. K. Eaton (2010). Turbulent dispersed multiphase flow. *Annual Review Fluid Mechanics 42*, 111–133. *(p. xx, 48, 49)*

Balsara, D. and J. Kim (2016). A subluminal relativistic magnetohydrodynamics scheme with ADER-WENO predictor and multidimensional Riemann solver-based corrector. *Journal of Computational Physics 312*, 357 – 384. *(p. 89)*

Balthasar, M. and M. Frenklach (2005). Detailed kinetic modeling of soot aggregate formation in laminar premixed flames. *Combustion and Flame 140*(1-2), 130 – 145. *(p. 67)*

Balthasar, M. and M. Kraft (2003). A stochastic approach to calculate the particle size distribution function of soot particles in laminar premixed flames. *Combustion and Flame 133*(3), 289 – 298. *(p. 43)*

Baraldi, A. and A. Ferrante (2012). A VoF method for DNS of droplet-laden incompressible turbulence . In *Seventh International conference on Computational Fluid Dynamics*. *(p. 27)*

Bardina, J., J. H. Ferziger, and W. C. Reynolds (1980). Improved subgrid scale models for Large Eddy Simulation. In *13th Fluid and Plasma Dynamics Conference*. AIAA Paper No. 80-1357. *(p. 269)*

Barth, T. and M. Ohlberger (2004). *Finite Volume Methods: Foundation and Analysis*, Volume 1, Chapter in "Encyclopedia of Computational Mechanics", pp. 1–57. John Wiley & Sons, Ltd. *(p. xxi, 87, 88, 94)*

Bassi, F., L. Botti, A. Colombo, A. Crivellini, A. Ghidoni, A. Nigro, and S. Rebay (2015). *Time Integration in the Discontinuous Galerkin Code MIGALE - Unsteady Problems*, pp. 205–230. Cham: Springer International Publishing. *(p. 323)*

Bassi, F., L. Botti, A. Colombo, A. Ghidoni, and S. Rebay (2011). *Discontinuous Galerkin for turbulent flows*, Chapter in "Adaptive High-Order Methods in Computational Fluid Dynamics", pp. 1–32. World Scientific.

(p. 323)

Bassi, F., L. Botti, A. Colombo, A. Ghidoni, and S. Rebay (2014). *Implementation of an Explicit Algebraic Reynolds Stress Model in an Implicit Very High-Order Discontinuous Galerkin Solver*, pp. 111–123. Cham: Springer International Publishing. *(p. xxx, 323)*

Bassi, F. and S. Rebay (1997). A high-order accurate discontinuous Finite Element method for the numerical solution of the compressible Navier-Stokes equations. *Journal of Computational Physics 131*, 267–279. *(p. 92)*

Bauer, A., K. Schaal, V. Springel, P. Chandrashekar, R. Pakmor, and C. Klingenberg (2016). Simulating turbulence using the astrophysical Discontinuous Galerkin Code TENET. In *to appear in Proceedings of the SPPEXA symposium, Lecture Notes in Computational Science and Engineering*. Springer International Publishing. *(p. 319)*

Baumann, C. and T. Oden (1999a). A discontinuous hp Finite Element method for convection diffusion problems. *Computer Methods in Applied Mechanics and Engineering 175*(3), 311 – 341. *(p. 92)*

Baumann, C. and T. Oden (1999b). A discontinuous hp Finite Element method for Euler and Navier-Stokes equations. *International Journal for Numerical Methods in Fluid 31*, 79 – 95. *(p. 92)*

Belt, R. and O. Simonin (2009). Quadrature Method of Moments for the PDF Modeling of Droplet Coalescence in Turbulent Two-Phase Flows. In *ASME Fluids Engineering Division Summer Meeting*, Volume 1. *(p. 69)*

BenDakhlia, R. (2001). *Combustion stationnaire et instationnaire de mï¿½langes diphasiques*. Ph. D. thesis, Ecole Centrale Paris. *(p. 65)*

Berger, M. and J. Oliger (1984). Adaptive mesh refinement for hyperbolic partial differential equations. *Journal of Computational Physics 53*(3), 484 – 512. *(p. 95)*

Berthon, C. (2005). Stability of the MUSCL schemes for the Euler equations. *Communications in Mathematical Sciences 3*(2), 133–157. *(p. 87, 111)*

Berthon, C. (2006a). Numerical approximations of the 10-moment Gaussian closure. *Mathematical Sciences 75*(256), 1809–1831. *(p. 58, 60)*

Berthon, C. (2006b). Robustness of MUSCL schemes for 2D unstructured meshes. *Journal of Computational Physics 218*(2), 495–509. *(p. 58, 87)*

Berthon, C., Y. Coudière, and V. Desveaux (2014). Second-order MUSCL schemes based on dual mesh gradient reconstruction. *ESAIM: Mathematical Modelling and Numerical Analysis 48*(2), 583–602. *(p. 87)*

Bini, M. and W. Jones (2008). Large-Eddy Simulation of particle-laden turbulent flows. *Journal of Fluid Mechanics 614*, 207–252. *(p. 270)*

Bird, G. (1994). *Molecular gas dynamics and the direct simulation of gas flows*. Oxford: Clarendon Press. *(p. 9, 41)*

Birkhoff, G., M. H. Schultz, and R. S. Varga (1968). Piecewise hermite interpolation in one and two variables with applications to partial differential equations. *Numerische Mathematik 11*(3), 232–256. *(p. 89)*

Boileau, M. (2007). *Simulation aux grandes échelles de l'allumage diphasique des foyers aéronautiques.* Ph. D. thesis, Institut National Polytechnique de Toulouse. *(p. 105)*

Boileau, M., C. Chalons, J.-F. Bourgouin, C. Terrier, F. Laurent, S. de Chaisemartin, and M. Massot (2010). Robust numerical schemes for Eulerian spray DNS and LES in two-phase turbulent flows. In *Proceedings of the 7th International Conference on Multiphase Flow, Tampa,FL, United States.* *(p. 125)*

Boileau, M., C. Chalons, and M. Massot (2015). Robust numerical coupling of pressure and pressureless gas dynamics equations for Eulerian spray DNS and LES. *SIAM J. Sci Comp 37*(1), 79–102. *(p. 125, 217, 310)*

Boileau, M., J. Lagarde, V. Dupif, F. Laurent, and M. Massot (2016). Two-size moment Eulerian multi-fluid method describing the statistical trajectory crossing, modeling and numerical scheme. In *9th International Conference on Multiphase Flow, Firenze, Italy.* *(p. 310)*

Boivin, M., O. Simonin, and K. D. Squies (1998). Direct numerical simulation of turbulence modulation by particles in isotropic turbulence. *Journal of Fluid Mechanics 375*, 235–263. *(p. 11)*

Bolis, A., C. Cantwell, D. Moxey, D. Serson, and S. Sherwin (2016). An adaptable parallel algorithm for the direct numerical simulation of incompressible turbulent flows using a fourier spectral/hp element method and MPI virtual topologies. *Computer Physics Communications 206*, 17 – 25. *(p. 324)*

Boltzmann, L. (1872). Weitere studien über das wärmegleichgewicht unter gasmolekülen. *Sitzungsberichte der Kaiserlichen Akademie der Wissenschaften, Wien II 66*, 275–370. *(p. 40)*

Bonhaus, D. L. (1998). *A High-Order Accurate Finite Element Method for Viscous Compressible Flow.* Ph. D. thesis, Virgina Tech University. *(p. 90)*

Borghi, R. (1988). Tubrbulent combustion modeling. *Prog. Energy Combust. Sci. 14*, 245 – 292. *(p. 6)*

Boris, J. and D. Book (1973). Flux-corrected transport. I. SHASTA, a fluid transport algorithm that works. *Journal of Computational Physics 11*(1), 38 – 69. *(p. 87, 318, 326)*

Boris, J., A. Landsberg, E. Oran, and J. Gardner (1993). LCPFCT - A Flux-Corrected Transport Algorithm for Solving Generalized Continuity Equations. NRL Memorandum Report 93-7192. *(p. 87, 318)*

Bouali, Z. (2011). *Impact d'une phase liquide dispersée sur le processus d'auto-inflammation : prise en compte d'une chimie détaillée.* Ph. D. thesis, Université de Rouen. *(p. 147, 156)*

Bouchut, F. (1994). On zero pressure gas dynamics. In *Advances in kinetic theory and computing*, Volume 22 of *Ser. Adv. Math. Appl. Sci.*, pp. 171–190. World Sci. Publ., River Edge, NJ. *(p. 58, 126)*

Bouchut, F., S. Jin, and X. Li (2003). Numerical approximations of pressureless and isothermal gas dynamics. *SIAM Journal on Numerical Analysis 41*, 135–158. *(p. 101, 105, 106, 125, 126, 319)*

Boudier, G., L. Gicquel, T. Poinsot, D. Bissières, and C. Bérat (2007). Comparison of LES, RANS and experiments in an aeronautical gas turbine combustion chamber. *Proceedings of the Combustion Institute 31*(2), 3075–3082. *(p. 6)*

Brändle De Motta, J., J. Estivalezes, E. Climent, and S. Vincent (2016). Local dissipation properties and collision dynamics in a sustained homogeneous turbulent suspension composed of finite size particles. *International Journal of Multiphase Flow 85*, 369–379. *(p. xix, 8, 13, 16, 28)*

Brandle De Motta, J., S. Robbes, F. Shum Kivan, M. Boileau, M. Massot, and E. Riber (2016). Experimental and numerical investigation of a pulsated evaporating spray. 9th International Conference on Multiphase Flow, ICMF. *(p. xxx, 309, 310)*

Brenier, Y. and E. Grenier (1998). Sticky particles and scalar conservation laws. *SIAM Journal of Numerical Analysis 35*, 2317–2328. *(p. 58)*

Brooks, A. and T. Hughes (1982). Streamline upwind/Petrov-Galerkin formulations for convection dominated flows with particular emphasis on the incompressible Navier-Stokes equations. *Computer Methods in Applied Mechanics and Engineering 32*(1), 199 – 259. *(p. 90)*

Brown, S., P. Roe, and C. Groth (1995). Numerical solution of a 10-moment model for non-equilibrium gas dynamics. *(p. 58)*

Buffard, T. and S. Clain (2010). Monoslope and multislope MUSCL methods for unstructured meshes. *Journal of Computational Physics 229*(10), 3745 – 3776. *(p. 88)*

Cada, M. and M. Torrilhon (2009). Compact third-order limiter functions for finite volume methods. *Journal of Computational Physics 228*(11), 4118 – 4145. *(p. 328)*

Cant, S. (2011). *RANS and LES Modelling of Premixed Turbulent Combustion*, pp. 63–90. Dordrecht: Springer Netherlands. *(p. 6)*

Cantwell, C., D. Moxey, A. Comerford, A. Bolis, G. Rocco, G. Mengaldo, D. De Grazia, S. Yakovlev, J.-E. Lombard, D. Ekelschot, B. Jordi, H. Xu, Y. Mohamied, C. Eskilsson, B. Nelson, P. Vos, C. Biotto, R. Kirby, and S. Sherwin (2015). Nektar++: An open-source spectral/ element framework. *Computer Physics Communications 192*, 205 – 219. *(p. 324)*

Capecelatro, J. and O. Desjardins (2013a). Eulerian-Lagrangian modeling of turbulent liquid-solid slurries in horizontal pipes. *Journal of Computational Physics 238*, 1–31. *(p. 11, 37)*

Capecelatro, J. and O. Desjardins (2013b). Eulerian-Lagrangian modeling of turbulent liquid-solid slurries in horizontal pipes. *International Journal of Multiphase Flow 55*, 64–79. *(p. 37)*

Capecelatro, J., O. Desjardins, and R. O. Fox (2014, 5). Numerical study of collisional particle dynamics in cluster-induced turbulence. *Journal of Fluid Mechanics 747*, R2 (1–13). *(p. 37, 317)*

Capecelatro, J., O. Desjardins, and R. O. Fox (2015, 10). On fluid-particle dynamics in fully developed cluster-induced turbulence. *Journal of Fluid Mechanics 780*, 578–635. *(p. xxx, 37, 317, 318)*

Capone, L., S. Benhamadouche, and Y. Hassan (2016). Source terms modeling for spacer grids with mixing vanes for CFD simulations in nuclear reactors. *Computers and Fluids 126*, 141 – 152. *(p. 323)*

Castro, C. and E. Toro (2008). Solvers for the high-order Riemann problem for hyperbolic balance laws. *Journal of Computational Physics 227*, 2481–2513. *(p. 89)*

Chalons, C., R. Fox, F. Laurent, M. Massot, and A. Vié (2016). A multi-Gaussian quadrature- based moment method for dispersed multiphase flows. *Submitted to SIAM Journal on Multiscale Modeling and Simulation*. *(p. 56, 57, 60, 63, 188)*

Chalons, C., R. O. Fox, and M. Massot (2010). A multi-Gaussian quadrature method of moments for gas-particle flows in a LES framework. In *Proceedings of the Summer Program 2010, Center for Turbulence Research, Stanford University*, Stanford, pp. 347–358. *(p. 56, 60, 188)*

Chalons, C., D. Kah, and M. Massot (2012). Beyond pressureless gas dynamics: quadrature-based velocity moment models. *Communication in Mathematical Sciences 10*(4), 1241–1272. *(p. 56, 60, 110, 205, 259)*

Chalons, C., M. Massot, and A. Vié (2015). On the Eulerian Large Eddy Simulation of disperse phase flows: an asymptotic preserving scheme for small stokes number flows. *SIAM Journal on Multiscale Modeling and Simulation 13*, 291–315. *(p. 277)*

Chapman, S. (1918). On the kinetic theory of a gas. Part II: A composite monoatomic gas: Diffusion, viscosity, and thermal conduction. *Phil. Trans. R Soc. A*(217), 115–197. *(p. 40)*

Chapman, S. and T. Cowling (1939). *The mathematical theory of non-uniform gazes* (third ed.). Cambridge Mathematical Library. Cambridge University Press. *(p. 276)*

Chen, Z., H. Huang, and J. Yan (2016). Third order maximum-principle-satisfying direct discontinuous Galerkin methods for time dependent convection diffusion equations on unstructured triangular meshes. *Journal of Computational Physics 308*, 198 – 217. *(p. 93)*

Cheneau, B., A. Vié, and S. Ducruix (2015). Large Eddy Simulations of a liquid fuel swirl burner: Flame characterization for pilot and multipoint injection strategies. In *ASME. Turbo Expo 2015: Turbine Technical Conference and Exposition*, Volume 4A: Combustion, Fuels and Emissions. *(p. 7, 58)*

Cheng, Y. and C.-W. Shu (2008). Superconvergence and time evolution of discontinuous Galerkin Finite Element solutions. *Journal of Computational Physics 227*(22), 9612 – 9627. *(p. 92)*

Cheng-cai, S. and L. Jun (2010). The SHASTA code modified by self-adaptive mesh and numerical experiment of magnetic reconnections. *Chinese As-*

tronomy and Astrophysics 34(3), 288 – 304. *(p. 87)*

Chibbaro, S. and J. P. Minier (2008). Langevin pdf simulation of particle deposition in a turbulent pipe flow. *Journal of Aerosol Science 39*, 555–71. *(p. 270)*

Chibbaro, S. and J. P. Minier (2011). A note on the consistency of hybrid Eulerian/Lagrangian approach to multiphase flows. *International Journal of Multiphase Flow 37*(3), 293–297. *(p. 43)*

Choi, M.and Song, J. and S. Park (2016). Modeling of the fuel injection and combustion process in a CNG direct injection engine. *Fuel 179*, 168 – 178. *(p. 322)*

Ciarlet, P. (1978). *The Finite Element Method for Elliptic Problems.* New York: Oxford. *(p. 89)*

Clift, R., J. R. Grace, and M. E. Weber (1978). *Bubbles, Drop and Particles.* New York: Academic Press. *(p. 313, 316)*

Clough, R. (1960). The Finite Element method in plane stress analysis. In *Proceedings of Second ASCE Conference on Electronic Computation*, Volume 8, Pittsburg, Pennsylvania, pp. 345–378. *(p. 89)*

Clough, R. (1990). Original formulation of the Finite Element method. *Finite Elements in Analysis and Design 7*, 89–101. *(p. 89)*

Cockburn, B., F. Li, and C.-W. Shu (2004). Locally divergence-free discontinuous Galerkin methods for the maxwell equations. *Journal of Computational Physics 194*(2), 588 – 610. *(p. 92)*

Cockburn, B. and C.-W. Shu (1989). TVB Runge-Kutta local projection discontinuous Galerkin finite element method for scalar conservation laws II: General framework. *Mathematics of Computation 52*(186), 411–435. *(p. 92, 128)*

Cockburn, B. and C.-W. Shu (1998a). The local discontinuous Galerkin method for time-dependent convection-diffusion systems. *SIAM Journal on Numerical Analalysis 35*, 2440–2463. *(p. 92)*

Cockburn, B. and C.-W. Shu (1998b). The Runge-Kutta discontinuous Galerkin method for conservation laws V - multidimensional systems. *Journal of Computational Physics 141*(2), 199–124. *(p. 92, 114)*

Codenotti, B., G. Mariotti, S. Pedinotti, and G. Resta (1998). Parallel implementation of a discontinuous finite element method for the solution of the Navier-Stokes equations. In D. Emerson, J. Periaux, A. Ecer, N. Satofuka, and P. Fox (Eds.), *Parallel Computational Fluid Dynamics 1997*, pp. 257 – 261. Amsterdam: North-Holland. *(p. 323)*

Colella, P. (1984). The numerical simulation of two-dimensional fluid flow with strong shocks. *Journal of Computational Physics 54*(1), 115–173. *(p. 87)*

Colella, P. and P. Woodward (1984). The Piecewise Parabolic Method (PPM) for gas-dynamical simulations. *Journal of Computational Physics 54*(1), 174 – 201. *(p. 87)*

Coleman, S. W. and J. C. Vassilicos (2009). A unified sweep-stick mechanism to explain particle clustering in two- and three-dimensional homogeneous, isotropic turbulence. *Physics of Fluids 21*(11), 1–10. *(p. 33)*

Colin, O. and M. Rudgyard (2000). Development of high-order Taylor-Galerkin schemes for LES. *Journal of Computational Physics 162*(2), 338–371. *(p. 90, 101, 102, 104, 320)*

Courant, R. (1943). Variational methods for the solution of problems of equilibrium and vibrations. *Bulletin of the American Mathematical Society 49*, 1–23. *(p. 89)*

Courant, R., K. Friedrichs, and H. Lewy (1928). Uber die partiellen dierenzengleichungen der mathematischen physik. *Math. Ann. 100*, 32–74. English translation, with commentaries by Lax, P.B., Widlund, O.B., Parter, S.V., in IBM J. Res. Develop. 11 (1967). *(p. 84)*

Courant, R., E. Isaacson, and M. Rees (1952). On the solution of nonlinear hyperbolic differential equations by finite differences. *Communications on Pure and Applied Mathematics 5*(3), 243–255. *(p. 85)*

Crowe, C., M. Sommerfeld, and Y. Tsuji (1998). *Multiphase flows with droplets and particles*. Boca Raton, Fla. CRC Press. *(p. 29, 31, 43, 313, 314)*

Crowe, C. and P. Willoughby (1977). A study of particle growth in a rocket nozzle. *AIAA Journal 5*(7), 1300–1304. *(p. 9, 43)*

Cuenot, B. and T. Poinsot (1996). Asymptotic and numerical study of diffusion flames with variable Lewis number and finite rate chemistry. *Combustion and Flame 104*(1), 111 – 137. *(p. 317)*

Darecki, M., C. Edelstenne, T. Enders, E. Fernandez, P. Hartman, J.-P. Herteman, M. Kerklosh, I. King, P. Ky, M. Mathieu, G. Orsi, G. Schotman, C. Smith, and J.-D. Wörner (2011). Flightpath 2050 europe's vision for aviation, report of the high level group on aviation research. *(p. 1)*

Darmana, D., N. Deen, and J. Kuipers (2006). Parallelization of an Euler-Lagrange model using mixed domain decomposition and a mirror domain technique: Application to dispersed gas-liquid two-phase flow. *Journal of Computational Physics 220*(1), 216 – 248. *(p. 38)*

Dawson, J. (1983). Particle simulation of plasmas. *Reviews of modern physics 55*(2), 403 – 447. *(p. 42)*

de Chaisemartin, S. (2009). *Eulerian models and numerical simulation of turbulent dispersion for polydisperse evaporation sprays*. Ph. D. thesis, Ecole Centrale Paris, France. Available on TEL : http://tel.archives-ouvertes.fr/tel-00443982/en/. *(p. 10, 40, 45, 57, 58, 67, 73, 105, 106, 107, 108, 109, 156, 316, 318)*

de Wiart, C. C. and K. Hillewaert (2015). *Development and Validation of a Massively Parallel High-Order Solver for DNS and LES of Industrial Flows*, pp. 251–292. Cham: Springer International Publishing. *(p. 323)*

Degond, P. and B. Niclot (1989). Numerical analysis of the weighted particle method applied to the semiconductor Boltzmann equation. *Numerische Mathematik 55*(5), 599–618. *(p. 42)*

Descombes, S., M. Duarte, and M. Massot (2016). *Operator Splitting Methods with Error Estimator and Adaptive Time-Stepping. Application to the Simulation of Combustion Phenomena*, Chapter in "Splitting Methods in Communication and Imaging, Science,and Engineering, Scientific Computation", pp. 537–551. Springer International Publishing Switzerland. Glowinski, R. at al. Editors. *(p. 11, 96)*

Descombes, S. and M. Massot (2004). Operator splitting for nonlinear reaction-diffusion systems with an entropic structure: singular perturbation and order reduction. *Numer. Math. 97*(4), 667–698. *(p. 96)*

Desjardins, O., G. Blanquart, G. Balarac, and H. Pitsch (2008). High order conservative finite difference scheme for variable density low mach number turbulent flows. *Journal of Computational Physics 227*(15), 7125 – 7159. *(p. 317)*

Desjardins, O., J. McCaslin, M. Owkes, and P. Brady (2013). Direct numerical and large-eddy simulation of primary atomization in complex geometries. *Atomization and Sprays 23*(11), 1001–1048. *(p. 5, 26)*

Doisneau, F. (2013). *Eulerian modeling and simulation of polydisperse moderately dense coalescing spray flows with nanometric-to-inertial droplets : application to Solid Rocket Motors*. Ph. D. thesis, Ecole Centrale Paris. *(p. xvii, xx, 29, 33, 40, 41, 47, 61, 66, 67, 68, 74, 75, 308)*

Doisneau, F., F. Laurent, A. Murrone, J. Dupays, and M. Massot (2013). Eulerian Multi-Fluid models for the simulation of dynamics and coalescence of particles in solid propellant combustion. *Journal of Computational Physics 234*, 230–262. *(p. 42, 58, 68)*

Doisneau, F., A. Sibra, J. Dupays, A. Murrone, F. Laurent, and M. Massot (2014). An efficient and accurate numerical strategy for two-way coupling in unsteady polydisperse moderately dense sprays: application to Solid Rocket Motor instabilities. *Journal of Propulsion and Power 20*(3), 727–748. *(p. 11)*

Dombard, J. (2011). *Direct Numerical Simulation of non-isothermal dilute sprays using the Mesoscopic Eulerian Formalism*. Ph. D. thesis, INP Toulouse. *(p. xx, 46, 55, 308, 320)*

Donea, J. (1984). A Taylor Galerkin method for convective transport problems. *International Journal for Numerical Methods in engineering 20*, 101–119. *(p. 90, 102)*

Donea, J. and A. Huerta (2003). *Finite Elements Methods for Flow Problem*. Wiley. *(p. 89, 90)*

Donea, J. and L. Quartapelle (1992). An introduction to finite element methods for transient advection problems. *Computer Methods in Applied Mechanics and Engineering 95*(2), 169 – 203. *(p. 89, 90)*

Donea, J., L. Quartapelle, and V. Selmin (1987). An analysis of time discretization in the finite element solution of hyperbolic problems. *Journal of Computational Physics 70*, 463. *(p. 90, 102)*

Drew, D. and S. Passman (1999). *Theory of multicomponent fluids*, Volume

135. Springer. *(p. 5, 26)*

Drui, F., A. Fikl, P. Kestener, S. Kokh, A. Larat, V. Le Chenadec, and M. Massot (2016). Experimenting with the p4est library for AMR simulations of two-phase flows. *ESAIM : Proceedings and Surveys 53*, 232–247. *(p. xxi, 95, 96)*

Drui, F., S. Kokh, A. Larat, and M. Massot (2016). A hierarchy of simple hyperbolic two-fluid models for bubbly flows. *submitted to Physics of Fluids*, 1–22. *(p. 5, 26, 35, 311)*

Duarte, M., S. Descombes, C. Tenaud, S. Candel, and M. Massot (2013). Time-space adaptive numerical methods for the simulation of combustion fronts. *Combustion and Flame 160*(6), 1083–1101. *(p. 11)*

Dubey, A., K. Antypas, and C. Daley (2011). Parallel algorithms for moving Lagrangian data on block structured Eulerian meshes. *Parallel Computing 37*(2), 101 – 113. *(p. 38)*

Dufour, G. (2005). *Modï¿½lisation multi-fluide eulï¿½rienne pour les ï¿½coulements diphasiques ï¿½ inclusions dispersï¿½es.* Ph. D. thesis, Universitï¿½ Paul Sabatier Toulouse III. *(p. 68, 74, 313)*

Dukowicz, J. (1980). A particle-fluid numerical model for liquid sprays. *Journal of Computational Physics 35*(2), 229–253. *(p. 43)*

Dumbser, M., D. Balsara, E. Toro, and C.-D. Munz (2008). A unified framework for the construction of one-step finite volume and discontinuous Galerkin schemes on unstructured meshes. *Journal of Computational Physics 227*, 8209–8253. *(p. 92)*

Dumbser, M., A. Hidalgo, and O. Zanotti (2014). High order space-time adaptive ADER-WENO finite volume schemes for non-conservative hyperbolic systems. *Computer Methods in Applied Mechanics and Engineering 268*, 359 – 387. *(p. 89)*

Dumbser, M. and C.-D. Munz (2005). Building blocks for arbitrary high order Discontinuous Galerkin schemes. *Journal of Scientific Computing 27*, 215–230. *(p. 92)*

Dumbser, M., O. Zanotti, R. Loubère, and S. Diot (2014). A posteriori subcell limiting of the discontinuous Galerkin finite element method for hyperbolic conservation laws. *Journal of Computational Physics 278*, 47–75. *(p. 92)*

Dupays, J. (1996). *Contribution ł'étude du role de la phase condensée dans la stabilité d'un propulseur à propergol solide pour lanceur spatial.* Ph. D. thesis, Institut National Polytechnique de Toulouse. *(p. 58)*

Dupays, J.and Dupif, V., A. Larat, and M. Massot (2016). Accurate and robust numerical strategy for axisymmetric Eulerian modeling of particle-laden and spray flows of moderate inertia with particle trajectory crossing. in preparation for Journal of Computational Mathematics. *(p. 310)*

Dupif, V. (2017). *Modélisation et simulation de l'écoulement diphasique dans les moteurs à propergol solide par une approche eulérienne polydispersée en taille et en vitesse.* Ph. D. thesis, Université Paris-Saclay, France.

(p. 88, 308, 309, 310)

Economon, T., D. Mudigere, G. Bansal, A. Heinecke, F. Palacios, J. Park, M. Smelyanskiy, and P. Alonso, J. J.and Dubey (2016). Performance optimizations for scalable implicit RANS calculations with SU2. *Computers and Fluids 129*, 146 – 158. *(p. 321)*

Elghobashi, S. (1991). Particle-laden turbulent flows: direct simulation and closure models. *Applied Scientific Research 48*(3), 301–314. *(p. xix, 11, 33, 34)*

Elghobashi, S. (1994). On predicting particle-laden turbulent flows. *Applied Scientific Research 52*(4), 309–329. *(p. xix, 33, 34)*

Elghobashi, S. and G. Truesdell (1992). Direct numerical simulation of particle dispersion in a decaying isotropic turbulence. *Journal of Fluid Mechanics 242*, 655–700. *(p. 9, 37)*

Emre, O. (2014). *Modélisation de la polydispersion des brouillards de gouttes sous l'effet des interactions two-way turbulentes pour l'injection directe à haute pression dans les moteurs*. Ph. D. thesis, Ecole Centrale Paris. Available at https://tel.archives-ouvertes.fr/tel-01089937. *(p. 10, 11, 26, 43)*

Emre, O., R. O. Fox, M. Massot, S. de Chaisemartin, S. Jay, and F. Laurent (2014). Towards Eulerian modeling of a polydisperse evaporating spray under realistic internal-combustion-engine conditions. *Flow Turbulence and Combustion 93*(4), 689–722. *(p. 69)*

Eskilsson, C. and S. J. Sherwin (2004). A triangular spectral/hp discontinuous Galerkin method for modelling 2d shallow water equation. *International Journal for Numerical Methods in Fluids 45*(6), 605–623. *(p. 92)*

Essadki, M., S. de Chaisemartin, F. Laurent, and M. Massot (2016). High order moment model for polydisperse evaporating sprays towards interfacial geometry desciption. *submitted to SIAM*. *(p. 5, 10, 26, 311)*

Essadki, M., S. de Chaisemartin, M. Massot, F. Laurent, A. Larat, and S. Jay (2016). High order moment methods and adaptive mesh refinement for polydisperse evaporating spray simulations. *Oil & Gas Science and Technology*, 1–25. In press, doi:10.2516/ogst/2016012. *(p. 10, 69, 95)*

Faeth, G. (1983). Evaporation and combustion of spray. *Progress in Energy and Combustion Science 9*, 1–76. *(p. 316)*

Fechter, S. and C.-D. Munz (2015). A discontinuous Galerkin based sharp-interface method to simulate three-dimensional compressible two-phase flow. *International Journal for Numerical Methods in Fluids 78*(7), 413–435. *(p. 93)*

Fede, P. and O. Simonin (2006). Numerical study of the subgrid fluid turbulence effects on the statistics of heavy colliding particles. *Physics of Fluids 18*(4), 045103, 1–17. *(p. 37, 284)*

Fede, P. and O. Simonin (2010). *Effect of Particle-Particle Collisions on the Spatial Distribution of Inertial Particles Suspended in Homogeneous Isotropic Turbulent Flows*, pp. 119–125. Berlin, Heidelberg: Springer

Berlin Heidelberg. *(p. 37)*

Fede, P., O. Simonin, and P. Villedieu (2015). Monte-Carlo simulation of colliding particles or coalescing droplets transported by a turbulent flow in the framework of a joint fluid-particle pdf approach. *International Journal of Multiphase Flow 74*, 165–183. *(p. 42)*

Fede, P., O. Simonin, P. Villedieu, and K. D. Squires (2006). Stochastic modeling of the turbulent subgrid fluid velocity along inertial particle trajectories. In *Proceedings of the Summer Program 2006, Center for Turbulence Research, Stanford University*, pp. 247–258. *(p. 270)*

Feng, K. (1965). Finite difference schemes based on variational principles (in chinese). *Appl. Math. Comput. Math. 2*, 238–262. *(p. 89)*

Ferry, J. and S. Balachandar (2001). A fast Eulerian method for disperse two-phase flow. *Int. J. Multiphase Flow 27*, 1199–1226. *(p. 271)*

Ferry, J. and S. Balachandar (2002). Equilibrium expansion for the Eulerian velocity of small particles. *Powder Technology 125*, 131–139. *(p. 271)*

Février, P., O. Simonin, and K. D. Squires (2005). Partitioning of particle velocities in gas-solid turbulent flow into a continuous field and a spatially uncorrelated random distribution: theoretical formalism and numerical study. *J. Fluid Mech. 533*, 1–46. *(p. xxvi, 10, 33, 39, 54, 215, 216, 244, 251, 271)*

Filbet, F. and L. Rodriges (2016). Asymptotically stable particle-in-cell methods for the vlasov/poisson system with a strong external magnetic field. *SIAM J. Numer. Anal. 54*(2), 1120 – 1146. *(p. 42)*

Filbet, F. and E. Sonnendrücker (2003). Comparison of Eulerian Vlasov solvers. *Computer Physics Communications 150*(3), 247 – 266. *(p. 41)*

Fiorina, B., D. Veynante, and S. Candel (2015). Modeling combustion chemistry in large eddy simulation of turbulent flames. *Flow, Turbulence and Combustion 94*, 3–42. *(p. 6)*

Fournier, Y., J. Bonelle, C. Moulinec, Z. Z. Shang, A. Sunderland, and J. Uribe (2011). Optimizing code saturne computations on petascale systems. *Computers and Fluids 45*(1), 103 – 108. 22nd International Conference on Parallel Computational Fluid Dynamics (ParCFD 2010)ParCFD. *(p. 323)*

Fox, R. (2007). *in "Computational Models for Turbulent Multiphase Reacting Flows",* Udine, July 2006, Chapter Fundamental of Polydisperse Multiphase Flows. CISM Courses and Lectures. Springer Verlag. D.L. Marchisio and R.O. Fox Editors. *(p. 36)*

Fox, R. (2014). On multiphase turbulence models for collisional fluid-particle flows. *Journal of Fluid Mechanics 742*, 356–424. *(p. 10, 268)*

Fox, R., F. Laurent, and M. Massot (2008). Numerical simulation of spray coalescence in an Eleurian framework: direct quadrature method of moments and multi - fluid method. *Journal of Computational Physics 227*(6), 3058–3088. *(p. 10, 69)*

Fox, R. O. (2012). *Quadrature- Based Moment Methods*, Chapter in "Stochastics Methods in Fluid Mechanics", *Udine, July 2012*, pp. 79–123. CISM Courses and Lectures. Springer Wien New York. *(p. 56, 57, 188)*

Franzelli, B., E. Riber, B. Cuenot, and M. Ihme (2015). Numerical modeling of soot production in aero-engine combustors using large eddy simulations. In *ASME. Turbo Expo 2015: Turbine Technical Conference and Exposition*, Volume 4B: Combustion, Fuels and Emissions. *(p. 58)*

Franzelli, B., E. Riber, L. Gicquel, and T. Poinsot (2012). Large eddy simulation of combustion instabilities in a lean partially premixed swirled flame. *Combustion and Flame 159*(2), 621–637. *(p. 6)*

Franzelli, B., A. Vié, B. Fiorina, and N. Darabiha (2013, June). Large eddy simulation of swirling kerosene/air spray flame using tabulated chemistry. In *Proceedings of ASME Turbo Expo 2013: Turbine Technical Conference and Exposition*, San Antonio, Texas. *(p. 7)*

Franzelli, B., A. Vié, and M. Ihme (2016). Large eddy simulation of combustion instabilities in a lean partially premixed swirled flame. *Combustion and Flame 163*, 100–114. *(p. 6)*

Frenklach, M. (2002). Method of moments with interpolative closure. *Chemical Engineering Science 57*(12), 2229 – 2239. *(p. 67)*

Frenklach, M. (2009). Modeling particle dynamics with MOMIC. In *Modeling and Computation of Nanoparticles in Fluid Flows, Lectures Notes of the von Karman Institute, NATO RTO- EN-AVT-169*, pp. 1–14. *(p. 67)*

Frenklach, M. and S. J. Harris (1987). Aerosol dynamics modeling using the method of moments. *Journal of Colloid and Interface Science 118*(1), 252 – 261. *(p. 67)*

Fréret, L., F. Laurent, S. de Chaisemartin, D. Kah, R. Fox, P. Vedula, J. Reveillon, O. Thomine, and M. Massot (2008). Turbulent combustion of polydisperse evaporating sprays with droplet crossing: Eulerian modeling of collisions at finite Knudsen and validation. In *Proceedings of the Summer Program 2008, Center for Turbulence Research, Stanford University*, pp. 277–288. *(p. xx, 37, 46)*

Fréret, L., O. Thomine, F. Laurent, J. Reveillon, and M. Massot (2012). Direct Numerical Simulation of polydisperse evaporating sprays in 3D jet configuration using Euler-Euler and Euler-Lagrange formalisms. In *Proceedings of the summer program 2012, Center for Turbulence Research, Stanford University*, pp. 345–354. *(p. xxi, 9, 109, 110, 309)*

Fréret, L., O. Thomine, J. Reveillon, S. de Chaisemartin, F. Laurent, and M. Massot (2010). On the role of preferential segregation in flame dynamics in polydisperse evaporating sprays. In *Proceedings of the Summer Program 2010, Center for Turbulence Research, Stanford University*, pp. 383–392. *(p. xxiii, 58, 156, 309)*

Friedlander, S. K. (2000). *Smoke, Dust, and Haze, Fundamental of Aerosol Dynamics* (second ed.). Topics in Chemical Engineering. Oxford University Press. *(p. 41)*

Friedrichs, K. (1962). A finite difference scheme for neumann and dirichlet problems. Technical report, AEC Comp. and Appl. Math. Center, Courant Inst., Math. Sci., New York Univ. Report No NYO-9760. *(p. 89)*

Fromm, J. E. (1968). A method for reducing dispersion in convective difference schemes. *Journal of Computational Physics 3*(2), 176 – 189. *(p. 85)*

Fujita, A., H. Watanabe, R. Kurose, and S. Komori (2013). Two-dimensional direct numerical simulation of spray flames - Part 1: Effects of equivalence ratio, fuel droplet size and radiation, and validity of flamelet model. *Fuel 104*, 515–525. *(p. 6)*

Fuster, D., A. Bagué, L. Boeck, T. ans Le Moyne, A. Leboissetier, S. Popinet, P. Ray, R. Scardovelli, and S. Zaleski (2009). Simulation of primary atomization with an octree adaptive mesh refinement and VOF method. *International Journal of Multiphase Flow 35*(6), 550 – 565. *(p. 5, 26)*

Galerkin, B. (1915). Series occurring in some problems of elastic stability of rods and plates. *Vestnik Insz. (Engineering Bulletin) 19*, 897–908. *(p. 89)*

Garcia, M. (2009). *Development and validation of the Euler-Lagrange formulation on a parallel and unstructured solver for Large-Eddy Dimulation*. Ph. D. thesis, Université Toulouse III. available online at http://ethesis.inp-toulouse.fr/archive/00000715/. *(p. 38)*

Garcia-Rosa, N. (2008). *Phénomènes d'allumage d'un foyer de turbomachine en conditions de haute altitude*. Ph. D. thesis, Université Toulouse III. *(p. 25)*

Gelbard, F., Y. Tambour, and J. Seinfeld (1980). Sectional representations for simulating aerosol dynamics. *Journal of Colloid and Interface Science 76*(2), 541 – 556. *(p. 67)*

Germano, M., U. Piomelli, P. Moin, and W. Cabot (1991). A dynamic subgrid-scale eddy viscosity model. *Physics of Fluids 3*, 1760–1765. *(p. 269)*

Gicquel, L., G. Staffelback, and T. Poinsot (2012). Large eddy simulations of gaseous flames in gas turbine combustion chambers. *Progress in Energy and Combustion Science 38*(6), 782 – 817. *(p. 6)*

Glimm, J. and P. D. Lax (1967). Decay of solutions of systems of hyperbolic conservation laws. *Bull. Amer. Math. Soc. 73*(1), 105. *(p. 325)*

Godsave, G. (1953). Studies of the combustion of drops in a fuel spray: the burning of single drops of fuel. In *4th Symposium (International) on Combustion*, The Combustion Institute, Baltimore, pp. 818–830. *(p. 315)*

Godunov, S. K. (1959). Difference method for the numerical computation of discontinuous solutions of fluid dynamics equations. *Math. Sbornik 47*, 271–306. translation, U.S. Joint Publ. Res. Service, JPRS 7226 (1969). *(p. 85, 86, 87, 325)*

Goodson, M. and M. Kraft (2002). An efficient stochastic algorithm for simulating nano-particle dynamics. *Journal of Computational Physics 183*(1), 210 – 232. *(p. 43)*

Gorokhovski, M. and R. Zamansky (2014). Lagrangian simulation of large and small inertial particles in a high reynolds number flow: Stochastic simulation of subgrid turbulence/particle interactions. In *Proceedings of the Summer Program 2014, Center for Turbulence Research, Stanford University*, pp. 37–46. *(p. 270)*

Gottlieb, S., D. I. Ketcheson, and C.-W. Shu (2009). High order strong stability preserving time discretizations. *J. Sci. Comput. 38*(3), 251–289. *(p. 92, 115)*

Gottlieb, S. and C.-W. Shu (1998). Total Variation Diminishing Runge-Kutta schemes. *Mathematics of computation 67*(221), 73–85. *(p. 92)*

Gottlieb, S., C.-W. Shu, and E. Tadmor (2001). Strong stability-preserving high-order time discretization methods. *SIAM Review 43*(1), 89–112. *(p. 92, 113)*

Greenberg, J., I. Silverman, and Y. Tambour (1993). On the origin of spray sectional conservation equations. *Combustion and Flame 93*, 90–96. *(p. 67)*

Guedot, L. (2015). *Development of numerical methods for the characterization of large scale structures in aeronautical swirl burners : application to multi-points injectors.* Ph. D. thesis, INSA de Rouen, France. *(p. 7, 38)*

Guelfi, A., M. Boucker, J. Herard, P. Peturaud, D. Bestion, P. Boudier, E. Hervieu, P. Fillion, and M. Grandotto (2007). A new software platform for advanced nuclear thermal hydraulics. *Nuclear Science and Engineering 156*(3), 281–324. *(p. 323)*

Guichard, L., J. Reveillon, and H. R. (2004). Direct numerical simulation of statistically stationary one- and two- phase turbulence combustion: a turbulent injection procedure. *Flow, Turbulence and Combustion 73*, 133–167. *(p. 130, 149, 150, 151)*

Hannebique, G., P. Sierra, E. Riber, and B. Cuenot (2013). Large eddy simulation of reactive two-phase flow in an aeronautical multipoint burner. *Flow, Turbulence and Combustion 90*(2), 449–469. *(p. 7)*

Harlow, F. and J. E. Welch (1965). Numerical calculation of time-dependent viscous incompressible flow of fluid with free surface. *Physics of Fluids 8*(12), 2182–2189. *(p. 26)*

Harten, A. (1983). High resolution schemes for hyperbolic conservation laws. *Journal of Computational Physics 49*, 357–393. *(p. 325)*

Harten, A. (1984). On a class of high resolution total variation stable Finite Difference schemes for hyperbolic. *SIAM J. Numer. Anal. 21*(1), 1–23. *(p. 325)*

Harten, A., B. Engquist, S. Osher, and S. Chakravarthy (1987). Uniformly high order accurate essentially non-oscillatory schemes, iii. *Journal of Computational Physics 71*(2), 231 – 303. *(p. 88)*

Harten, A., P. D. Lax, and B. van Leer (1983). On upstream differencing and Godunov-type schemes for hyperbolic conservation laws. *SIAM Review 25*(1), 35–61. *(p. 86, 112)*

Harten, A., S. Osher, B. Engquist, and S. Chakravarthy (1986). Special issue in honor of milt rose's sixtieth birthday some results on uniformly high-order accurate essentially nonoscillatory schemes. *Applied Numerical Mathematics 2*(3), 347 – 377. *(p. 88)*

Hartmann, R. (2006). Adaptive discontinuous Galerkin methods with shock-capturing for the compressible Navier-Stokes equations. *International Journal for Numerical Methods in Fluid 51*, 1131 – 1156. *(p. 92)*

Hartmann, R., J. Held, T. Leicht, and F. Prill (2010). Discontinuous Galerkin methods for computational aerodynamics: 3d adaptive flow simulation with the DLR PADGE code. *Aerospace Science and Technology 14*(7), 512 – 519. *(p. 319)*

Hartmann, R. and T. Leicht (2016). Generation of unstructured curvilinear grids and high-order discontinuous Galerkin discretization applied to a 3D high-lift configuration. *International Journal for Numerical Methods in Fluids*. published online. *(p. 319)*

Hauck, C. D., C. D. Levermore, and A. L. Tits (2008). Convex duality and entropy-based moment closures: Characterizing degenerate densities. *SIAM Journal on Control and Optimization 47*(4), 1977–2015. *(p. 63)*

Herrmann, M. (2005). A Eulerian level set / vortex sheet method for two - phase interface dynamics. *Journal of Computational Physics 203*, 539–571. *(p. 26)*

Herrmann, M. (2008). A balanced force refined level set grid method for two-phase flows on unstructured flow solver grids. *Journal of Computational Physics 227*(4), 2674 – 2706. *(p. 5, 26)*

Hestaven, J. and T. Warburton (2008). *Nodal Discontinuous Galerkin Methods*. Springer-Verlag. *(p. 92)*

Hinton, E. and B. Irons (1968). Least squares smoothing of experimental data using finite elements. *Strain 4*(3), 24–27. *(p. 89)*

Hirt, C., A. Amsden, and J. Cook (1974). An arbitrary Lagrangian-Eulerian computing method for all flow speeds. *Journal of Computational Physics 14*(3), 227–253. *(p. 5, 26)*

Hirt, C. and B. Nichols (1981). Volume of fluid (VOF) method for the dynamics of free boundaries. *Journal of Computational Physics 39*(1), 201–225. *(p. 26)*

Hitz, T., S. Fechter, and C.-D. Munz (2016). Simulation of evaporating droplets within a discontinuous Galerkin multi-scale framework. In *9th International Conference on Multiphase Flow*, Firenze, Italy. *(p. 93)*

Holway Jr., L. (1966). New statistical models for kinetic theory: methods of construction. *Physics of Fluids 9*(9), 1658–1673. *(p. 58)*

Hou, J., Q. Liang, H. Zhang, and R. Hinkelmann (2015). An efficient unstructured MUSCL scheme for solving the 2D shallow water equations. *Environmental Modelling and Software 66*, 131 – 152. *(p. 88)*

Hrennikoff, A. (1941). Solution of problems in elasticity by the framework method. *Journal of applied mechanics 8*, 169–175. *(p. 89)*

Hu, F., R. Wang, X. Chen, and H. Feng (2015). An adaptive mesh method for 1d hyperbolic conservation laws. *Applied Numerical Mathematics 91*, 11 – 25. *(p. 89)*

Hu, X., N. Adams, and G. Iaccarino (2009). On the HLLC riemann solver for interface interaction in compressible multi-fluid flow. *Journal of Computational Physics 228*(17), 6572 – 6589. *(p. 320)*

Huynh, H., Z. Wang, and P. Vincent (2014). High-order methods for computational fluid dynamics: A brief review of compact differential formulations on unstructured grids. *Computers and Fluids 98*, 209 – 220. 12th {USNCCM} mini-symposium of High-Order Methods for Computational Fluid Dynamics - A special issue dedicated to the 80th birthday of Professor Antony Jameson. *(p. 98)*

Hylkema, J. (1999). *Modélisation cinétique et simulation numérique dún brouillard dense de gouttelettes. Application aux propulseurs à poudre.* Ph. D. thesis, ENSAE. *(p. 42)*

Iaccarino, G. (2001). Predictions of a turbulent separated flow using commercial CFD codes. *ASME. J. Fluids Eng. 123*(4), 819–828. *(p. 324)*

Itani, L., G. Bruneaux, A. Di Lella, and C. Schulz (2015). Two-tracer LIF imaging of preferential evaporation of multi-component gasoline fuel sprays under engine conditions. *Proceedings of the Combustion Institute 35*(3), 2915 – 2922. *(p. 3)*

Jabin, P.-E. (2002). Various levels of models for aerosols. *Mathematical Models and Methods in Applied Sciences 12*(7), 903–919. *(p. 45)*

Jaegle, F. (2009). *Large Eddy Simulation of evaporating sprays in complex geometries using Eulerian and Lagrangian methods.* Ph. D. thesis, Institut National Polytechnique de Toulouse. *(p. 10, 55)*

Jay, S., F. Lacas, and S. Candel (2006). Combined surface density concepts for dense spray combustion. *Combustion and Flame 144*(3), 558–577. *(p. 26)*

Jenny, P., D. Roekaerts, and N. Beishuizen (2012). Modeling of turbulent dilute spray combustion. *Progress in Energy and Combustion Science 38*(6), 846 – 887. *(p. 6)*

Jiang, G. and C. Shu (1994). On a cell entropy inequality for discontinuous Galerkin methods. *Mathematics of Computation 62*, 531–538. *(p. 92)*

Jiang, G.-S. and C.-W. Shu (1996). Efficient implementation of weighted eno schemes. *Journal of Computational Physics 126*(1), 202 – 228. *(p. 88)*

Johnson, C. (1993). Discontinuous Galerkin finite element methods for second order hyperbolic problems. *Computer Methods in Applied Mechanics and Engineering 107*(1-2), 117 – 129. *(p. 92)*

Johnson, C. and J. Pitkaranta (1986). An analysis of the discontinuous Galerkin method for a scalar hyperbolic equation. *Mathematics of Computation 46*, 1–26. *(p. 92)*

Jones, W., A. Marquis, and K. Vogiatzaki (2014). Large-eddy simulation of spray combustion in a gas turbine combustor. *Combustion and Flame 161*(1), 222 – 239. *(p. 7)*

Kafui, D., S. Johnson, C. Thornton, and J. Seville (2011). Parallelization of a Lagrangian-Eulerian DEM/CFD code for application to fluidized beds. *Powder Technology 207*(1-3), 270–278. *(p. 38)*

Kah, D. (2010). *Taking into account polydispersity for the modeling of liquid fuel injection in internal combustion engines.* Ph. D. thesis, Ecole Centrale de Paris. available online at http://tel.archives-ouvertes.fr/tel-00618786/en/. *(p. 10, 69)*

Kah, D., F. Laurent, L. Fréret, S. De Chaisemartin, R. Fox, J. Reveillon, and M. Massot (2010). Eulerian quadrature-based moment models for dilute polydisperse evaporating sprays. *Flow Turbulence and Combustion 85*, 649–676. Special Issue dedicated to S. B. Pope. *(p. 56, 110, 188)*

Kah, D., F. Laurent, M. Massot, and S. Jay (2012). A high order moment method simulating evaporation and advection of a polydisperse spray. *Journal of Computational Physics 231*(2), 394–422. *(p. 69)*

Kaludercic, B. (2004). Parallelisation of the Lagrangian model in a mixed Eulerian-Lagrangian CFD algorithm. *Journal of Parallel and Distributed Computing 64*(2), 277–284. *(p. 38)*

Kanshat, G. (2007). *Discontinuous Galerkin Methods for Viscous Flow.* Wiesbaden Deutscher Universitatsverlag. *(p. 92)*

Kaufmann, A. (2004). *Vers la simulation des grandes échelles en formulation Euler - Euler des écoulements réactifs diphasiques.* Ph. D. thesis, Institut National Polytechnique de Toulouse. *(p. 104)*

Kaufmann, A., M. Moreau, O. Simonin, and J. Helie (2008). Comparison between Lagrangian and mesoscopic Eulerian modelling approaches for inertial particles suspended in decaying isotropic turbulence. *Journal of Computational Physics 227*, 6448–6472. *(p. 54)*

Kesserwani, G. and Q. Liang (2012). Dynamically adaptive grid based discontinuous Galerkin shallow water model. *Advances in Water Resources 37*, 23 – 39. *(p. 93)*

Khalighi, Y., J. W. Nichols, F. Ham, S. Lele, and P. Moin (2010). Unstructured large eddy simulation for prediction of noise issued from turbulent jets in various configurations. In *17th AIAA/CEAS Aeroacoustics Conference*, Portland, Oregon. *(p. 320)*

Kloker, M. J. (1997). A robust high-resolution split-type compact fd scheme for spatial direct numerical simulation of boundary-layer transition. *Applied Scientific Research 59*(4), 353–377. *(p. 85)*

Kolgan, V. (1972). Application of the minimum-derivative principle in the construction of finite-difference schemes for numerical analysis of discontinuous solutions in gas dynamics. *Uch. Zap. TsaGI (in Russian) 3*(6), 68–77. *(p. 87)*

Koren, B. (1993). *A robust upwind discretization method for advection, diffusion and source terms*, Chapter in "Numerical Methods for Advection-Diffusion Problems", pp. 117–138. Vieweg, Braunschweig, Germany. *(p. 327)*

Kostoglou, M. and A. Karabelas (1994). Evaluation of zero order methods for simulating particle coagulation. *Journal of Colloid and Interface Science 163*(2), 420–431. *(p. 67)*

Kuerten, J. G. M. (2006). Subgrid modeling in particle-laden channel flow. *Phys. Fluids 18*, 025108. *(p. 269, 270)*

Kumar, S. and D. Ramkrishna (1996a). On the solution of population balance equations by discretization–II. A moving pivot technique. *Chemical Engineering Science 51*(8), 1333–1342. *(p. 67)*

Kumar, S. and D. Ramkrishna (1996b). On the solution of population balance equations by discretization–III. Nucleation, growth and aggregation of particles. *Chemical Engineering Science 51*(8), 1311–1332. *(p. 67)*

Kummer, F. (2012). *The BoSSS Discontinuous Galerkin solver for incompressible fluid dynamics and an extension to singular equations*. Ph. D. thesis, Technische Universitï¿½t, Darmstadt. *(p. 319)*

Kuzmin, D., R. Lï¿½hner, and S. Turek (2012). *Flux-Corrected Transport: Principles, Algorithms, and Applications*. Springer Science and Business Media. *(p. 87)*

Lamarque, N. (2007). *Schémas numériques et conditions limites pour la simulation aux grandes échelles de la combustion diphasique dans les foyers d'hélicoptere*. Ph. D. thesis, Institut National Polytechnique de Toulouse, France. *(p. 320)*

Landmann, B. (2012). *A parallel discontinuous Galerkin code for the Navier-Stokes and Reynolds-averaged Navier-Stokes equations*. Ph. D. thesis, Universitï¿½t Stuttgart. *(p. 92)*

Larat, A. (2016). Notes on the Discontinuous Galerkin methods for the numerical simulation of hyperbolic equations. Research report, CNRS. *(p. 92)*

Larat, A., M. Massot, and A. Vié (2012). A stable, robust and high order accurate numerical method for Eulerian simulation of spray and particle transport on unstructured meshes. In *Annual Research Briefs 2012*, Center for Turbulence Research, Stanford University, USA, pp. 205–216. *(p. 93, 101, 114, 119, 132)*

Laurent, F. (2002). *Modélisation mathématique et numérique de la combustion de brouillards de gouttes polydispersés*. Ph. D. thesis, Université Claude Bernard, Lyon 1. *(p. 73)*

Laurent, F. (2006). Numerical analysis of eulerian multi-fluid models in the context of kinetic formulations for dilute evaporating sprays. *Mathematical Modeling and Numerical Analysis 3*, 431–468. *(p. 68, 73, 74)*

Laurent, F. and M. Massot (2001). Multi-fluid modeling of laminar polydispersed spray flames: origin, assumptions and comparison of the sectional and sampling methods. *Combustion Theory and Modelling 5*, 537–572. *(p. 6, 10, 32, 40, 56, 57, 65, 66, 67, 70, 101)*

Laurent, F., M. Massot, and P. Villedieu (2004). Eulerian multi-fluid modeling for the numerical simulation of coalescence in polydisperse dense liquid sprays. *Journal of Computational Physics 194*(2), 505–543. *(p. 42, 58)*

Laurent, F., A. Sibra, and F. Doisneau (2016). Two-size moment multi-fluid model: a robust and high-fidelity description of polydisperse moderately dense evaporating sprays. *Communications in Computational Physics*, 1–41. accepted, available online at https://hal.archives-ouvertes.fr/hal-01169730. *(p. 68, 74, 77)*

Laurent, F., A. Vié, C. Chalons, R. Fox, and M. Massot (2012). A hierarchy of Eulerian models for trajectory crossing in particle-laden turbulent flows over a wide range of stokes numbers. In *Annual Research Briefs 2012*, Center for Turbulence Research, Stanford University, USA, pp. 193–204. *(p. 10, 56, 60)*

Lax, P. and B. Wendroff (1964). Difference schemes for hyperbolic equations with high order of accuracy. *Comm. Pure Appl. Math. 17*, 381–398. *(p. 85)*

le Chenadec, V. and H. Pitsch (2013). A 3D unsplit forward/backward Volume-of-Fluid approach and coupling to the Level Set method. *Journal of Computational Physics 233*, 10 – 33. *(p. 5, 26)*

Le Lostec, N., R. O. Fox, O. Simonin, and P. Villedieu (2008). Numerical description of dilute particle-laden flows by a quadrature-based moment method. In *Proceedings of the Summer Program 2008, Center for Turbulence Research, Stanford University*, Stanford, pp. 209–221. *(p. 55)*

Le Lostec, N., P. Villedieu, and O. Simonin (2009, August). Comparison between Grad's and quadrature-based methods of moments for the numerical simulation of unsteady particle-laden flows. In *Proceedings of ASME 2009 Fluids Engineering Division Summer Meeting*, Colorado, USA. *(p. 55)*

Le Martelot, S., R. Saurel, and B. Nkonga (2014). Towards the direct numerical simulation of nucleate boiling flows. *International Journal of Multiphase Flow 66*, 62–78. *(p. 5)*

Le Touze, C. (2015). *Coupling between separated and dispersed two-phase flow models for the simulation of primary atomization in cryogenic combustion.* Ph. D. thesis, Université Nice Sophia Antipolis. *(p. 5, 26, 311)*

Le Touze, C., A. Murrone, and H. Guillard (2015). Multislope MUSCL method for general unstructured meshes. *Journal of Computational Physics 284*, 389 – 418. *(p. 88, 321)*

Lebas, R., T. Menard, P. A. Beau, A. Berlemont, and F. X. Demoulin (2009). Numerical simulation of primary break-up and atomization: DNS and modelling study. *Int. J. Multiphase Flows 35*(3), 247–260. *(p. 26)*

Lefebvre, A. H. (1989). *Atomization and spray.* Hemisphere Publishing Corporation. *(p. 24)*

Lele, S. K. (1992). Compact finite difference schemes with spectral-like resolution. *Journal of Computational Physics 103*, 16–42. *(p. 85, 317)*

LeSaint, P. and P.-A. Raviart (1974). On a finite element method for solving the neutron transport equation. In *Mathematical aspects of finite elements in partial differential equations*, Math. Res. Center, Univ. of Wisconsin-Madison, Academic Press, New York, pp. 89–123. *(p. 92)*

LeVeque, R. J. (2002). *Finite volume methods for hyperbolic problems.* Cambridge Texts in Applied Mathematics. Cambridge: Cambridge University Press. *(p. 85, 86, 107, 108, 327)*

Levermore, C. (1996). Moment Closure Hierarchies for Kinetic Theories. *Journal of Statistical Physics 83*(5-6), 1021–1065. *(p. 311)*

Levermore, C. and W. Morokoff (1998). The Gaussian moment closure for gas dynamics. *SIAM Journal on Applied Mathematics 59*(1), 72–96. *(p. 52, 58, 60)*

Liu, X.-D., S. Osher, and T. Chan (1994). Weighted essentially non-oscillatory schemes. *Journal of Computational Physics 115*(1), 200 – 212. *(p. 88)*

Liu, Y., M. Vinokur, and Z. Wang (2006). Spectral difference method for unstructured grids i: Basic formulation. *Journal of Computational Physics 216*(2), 780 – 801. *(p. 85, 97)*

López-Morales, M., J. R. Bull, J. Crabill, T. D. Economon, D. E. Manosalvas, J. Romero, A. Sheshadri, J. E. Watkins, D. M. Williams, F. Palacios, and A. Jameson (2014). Verification and validation of HiFiLES: a High-Order LES unstructured solver on multi-GPU platforms. In *32nd AIAA Applied Aerodynamics Conference, AIAA Aviation*, Atlanta, GA. *(p. 98)*

Lord Rayleigh, J. (1894). *The theory of sound.* Macmillan and Company, London. *(p. 89)*

Lorini, M., F. Bassi, A. Colombo, and A. Ghidoni (2016). High-order implementation of a non-local transition model in a DG solver for turbomachinery applications. *Computers and Fluids 127*, 115 – 130. *(p. 323)*

Lu, H., J. Zhu, D. Wang, and N. Zhao (2016). Runge-Kutta discontinuous Galerkin method with front tracking method for solving the compressible two-medium flow. *Computers and Fluids 126*, 1 – 11. *(p. 93)*

Marble, F. (1970). Dynamics of dusty gases. *Ann. Rev. Fluid Mech. 2*, 397–446. *(p. 58)*

Marchioli, C., M. Salvetti, and A. Soldati (2008). Some issues concerning large-eddy simulation of inertial particle dispersion in turbulent bounded flows. *Physics of Fluids 20*(4), 040603. *(p. 269)*

Marchisio, D. and R. Fox (2005). Solution of population balance equations using the direct quadrature method of moments. *Journal of Aerosol Science 36*, 43–73. *(p. 69)*

Marchisio, D. and R. Fox (2013). *Computational Models for Polydisperse Particulate and Multiphase Systems.* Cambridge Series in Chemical Engineering. Cambridge University Press. *(p. 233)*

Marchisio, D., R. Vigil, and R. Fox (2003). Quadrature method of moments for aggregation - breakage processes. *Journal of Colloid and Interface Science 258*(2), 322–334. *(p. 68)*

Martin, C., L. Benoit, Y. Sommerer, F. Nicoud, and T. Poinsot (2006). LES and acoustic analysis of combustion instability in a staged turbulent swirled combustor. *AIAA journal 44*(4), 741–750. *(p. 6)*

Martinez, L. (2010). *Simulation aux grandes échelles de l'injection de carburant liquide dans les moteurs à combustion interne.* Ph. D. thesis, Institut National Polytechnique de Toulouse. *(p. 104, 320)*

Martinez, L., A. Adlï¿½ne Benkenida, and B. Cuenot (2010). A model for the injection boundary conditions in the context of 3d simulation of diesel spray: Methodology and validation. *Fuel 89*(1), 219 – 228. *(p. xix, 6, 29, 30)*

Martinez-Ruiz, D., J. Urzay, A. L. Sánchez, A. Liñán, and F. A. Williams (2013). Dynamics of thermal ignition of spray flames in mixing layers. *Journal of Fluid Mechanics 734*, 387–423. *(p. 6)*

Mas-Gallic, S. and P. A. Raviart (1987). A particle method for first-order summetric systems. *Numer. Math. 51*, 323–352. *(p. 42)*

Mashayek, F., F. Jaberi, R. Miller, and P. Givi (1997). Dispersion and polydispersity of droplets in stationary isotropic turbulence. *International Journal of Multiphase Flow 23*, 337–355. *(p. 9, 37)*

Masi, E. (2010). *Étude théorique et numérique de la modélisation instationnaire des écoulements turbulents anisothermes gaz-particules par une approche Euler-Euler.* Ph. D. thesis, Institut National Polytechnique de Toulouse. *(p. 10, 46, 54)*

Masi, E. and Simonin (2014). Algebraic-Closure-Based Moment Method for unsteady Eulerian simulations of non-isothermal particle-laden turbulent flows at moderate Stokes numbers in dilute regime. *Flow Turbulence and Combustion 92*(1-2), 121–145. *(p. 46, 54)*

Masi, E. and O. Simonin (2012). An algebraic-closure-based moment method for unsteady Eulerian modeling of non-isothermal particle-laden turbulent flows in very dilute regime and high Stokes number. *Turbulence, Heat and Mass Transfer 7*, 1–12. *(p. 46, 54, 308)*

Masi, E., O. Simonin, E. Riber, P. Sierra, and L. Gicquel (2014). Development of an algebraic-closure-based moment method for unsteady Eulerian simulations of particle-laden turbulent flows in very dilute regime. *International Journal of Multiphase Flow 58*, 257–278. *(p. 54)*

Massot, M. (2007). *Eulerian multi-fluid models for polydisperse evaporating sprays*, Volume 492 of *CISM Courses and Lectures*, Chapter in "Multiphase Reacting Flows: Modelling and Simulation", *Udine, July 2006*, pp. 79–123. Springer Wien New York (2007). D.L. Marchisio and R.O. Fox Editors. *(p. 36, 56, 101, 106)*

Massot, M., A. Kumar, M. ans Gomez, and M. Smooke (1998). Counter-flow spray diffusion flames of heptan: computations and experiments. In *27th Symposium on Combustion*, pp. 1975–1984. *(p. 6)*

Massot, M., F. Laurent, D. Kah, and S. de Chaisemartin (2010). A robust moment method for evaluation of the disappearance rate of evaporating sprays. *SIAM J. Appl. Math 70*(8), 3203–3234. *(p. 10, 69)*

Maxey, M. R. (1987). The gravitational settling of aerosol particles in homogeneous turbulence and random flow fields. *Journal of Fluid Mechanics 174*, 441–465. *(p. 33, 166, 168)*

Maxey, M. R. and J. J. Riley (1983). Equation of motion for a small rigid sphere in a nonuniform flow. *Physics of Fluids 26*(4), 883–889. *(p. 31)*

McGraw, R. (1997). Description of aerosol dynamics by the quadrature method of moments. *Aerosol Science and Technology 27*, 255–265. *(p. 10, 68)*

McKinley, G. H. and M. Renardy (2011). Wolfgang von ohnesorge. *Physics of Fluids 23*(12), 1–7. *(p. 25)*

Mead, L. and N. Papanicolaou (1984). Maximum entropy in the problem of moments. *J. Math. Phys. 25*, 2404–2417. *(p. 68, 69)*

Meftah, H. (2008). *Simulation numérique directe d'un spray en évaporation : Analyse et modélisation du mélange turbulent et des transferts thermiques.* Ph. D. thesis, Université de Rouen. *(p. 147, 156)*

Menard, T., S. Tanguy, and A. Berlemont (2007). Coupling level set/VOF/ghost fluid methods: Validation and application to 3D simulation of the primary break - up of a liquid jet. *International Journal of Multiphase Flow 33*, 510–524. *(p. 5, 26, 318)*

Mercier, D. (2018). *Large Eddy Simulation of disperse phase in turbulent flows with two way coupling.* Ph. D. thesis, Université Paris-Saclay, France. *(p. 308, 311)*

Miller, R. and J. Bellan (2000). Direct numerical simulation and subgrid analysis of a transitional droplet laden mixing layer. *Phys. Fluid 12*(3), 650–671. *(p. 9, 37)*

Minier, J. P. (2015). On lagrangian stochastic methods for turbulent polydisperse two-phase reactive flows. *Progress in Energy and Combustion Science 50*, 1–62. *(p. 270)*

Minier, J. P. and E. Peirano (2001). The pdf approach to polydispersed turbulent two phase flows. *Physics Reports 352*(1-3), 1–214. *(p. 43, 270)*

Moreau, M. (2006). *Modélisation numérique directe et des grandes échelles des écoulements turbulents gas-particules dans le formalisme eulérien mésoscopique.* Ph. D. thesis, Institut National Polytechnique de Toulouse. *(p. 249, 317)*

Moreau, M., B. Bédat, and O. Simonin (2010). Development of gas-particle euler-euler LES approach: a priori analysis of particle sub-grid models in homogeneous isotropic turbulence. *Flow Turbulence and Combustion 84(2)*, 295–324. *(p. 11, 270, 271, 273, 274, 275, 303, 307)*

Mossa, J.-B. (2005). *Extension polydisperse pour la description Euler-Euler des écoulements diphasiques réactifs.* Ph. D. thesis, Institut National Polytechnique de Toulouse. *(p. 66)*

Moureau, V., P. Domingo, and L. Vervisch (2011a). From large-eddy simulation to direct numerical simulation of a lean premixed swirl flame: Filtered laminar flame-pdf modeling. *Combustion and Flame 158*(7), 1340 – 1357. *(p. xxx, 320, 321)*

Moureau, V., P. Domingo, and L. Vervisch (2011b). High performance computing design of a massively parallel CFD code for complex geometries. *Comptes Rendus Mï¿½canique 339*(2), 141 – 148. *(p. 320)*

Mueller, M., G. Blanquart, and H. Pitsch (2009). Hybrid method of moments for modeling soot formation and growth. *Combustion and Flame 156*(6), 1143 – 1155. *(p. 67)*

Murrone, A. and P. Villedieu (2011). Numerical modeling of dispersed two-phase flows. *Aerospace Lab 2*, 34–46. *(p. 65, 321)*

Neau, H., J. Laviéville, and O. Simonin (2010). High parallel computing performance for particle-laden reactive flows. In *7th International Conference on Multiphase Flow, ICMF*, Tampa. *(p. 323)*

Nguyen, T. T., F. Laurent, R. O. Fox, and M. Massot (2016). Solution of population balance equations in applications with fine particles: mathematical modeling and numerical schemes. *Journal of Computational Physics*, 1–42. submitted, available on HAL `https://hal.archives-ouvertes.fr/hal-01247390`. *(p. 41, 69)*

Novikov, E. A. (1964). Functionals and the random-force method in turbulence theory. *Zh. Eksp. Teor. Fiz. 44*, 1919. *(p. 273)*

Obligado, M., T. Teitelbaum, A. Cartellier, P. Mininni, and M. Bourgoin (2014). Preferential concentration of heavy particles in turbulence. *Journal of Turbulence 15*(5), 293–310. *(p. 33)*

O'Brien, E. (1980). *Finite Volume Methods: Foundation and Analysis*, Chapter in "Turbulent Reacting Flows", pp. 185–218. Springer-Verlag, Heidelberg. Libby, P.A. and Williams, F. A. Editors. *(p. 39)*

O'Connor, J., M. P. Musculus, and L. M. Pickett (2016). Effect of post injections on mixture preparation and unburned hydrocarbon emissions in a heavy-duty diesel engine. *Combustion and Flame 170*, 111 – 123. *(p. 3)*

Oefelein, J., V. Sankaran, and T. Drozda (2007). Large Eddy Simulation of swirling particle-laden flow in a model axisymmetric combustor. *Proceedings of the Combustion Institute 31*(2), 2291–2299. *(p. 320)*

Ohnesorge, W. V. (1936). Formation of drops by nozzles and the breakup of liquid jets. *Zeitschrift für Angewandte Mathematik und Mechanik (Journal of Applied Mathematics and Mechanics) 16*(4), 355–358. *(p. 25)*

O'Rourke, P. J. (1981). *Collective drop effects on vaporizing liquid sprays.* Ph. D. thesis, Princeton University. *(p. 9, 34, 43, 313)*

Ortner, C. and E. Süli (2007). Discontinuous Galerkin Finite Element approximation of nonlinear second-order elliptic and hyperbolic systems. *SIAM Journal on Numerical Analysis 45*(4), 1370–1397. *(p. 92)*

Osher, S. (1984). Riemann solvers, the entropy condition, and difference approximations. *SIAM Journal on Numerical Analysis 21*(42), 217–235. *(p. 88)*

Osher, S. and R. Fedkiw (2001). Level set methods: An overview and some recent results. *Journal of Computational Physics 169*(2), 463–502. *(p. 26)*

Osher, S. and F. Solomon (1982). Upwind schemes for hyperbolic systems of conservation laws. *Mathematics of Computation 38*(132), 339–374. *(p. 86)*

Overholt, M. R. and S. B. Pope (1998). A deterministic forcing scheme for direct numerical simulations of turbulence. *Computers and Fluids 27*(1), 11–28. *(p. 150)*

Pai, M. and S. Subramaniam (2012). Two-way coupled stochastic model for dispersion of inertial particles in turbulence. *Journal of Fluid Mechanics 700*, 29–62. *(p. 26, 37)*

Palacios, F., J. Alonso, K. Duraisamy, M. Colonno, J. Hicken, A. Aranake, A. Campos, S. Copeland, T. Economon, A. Lonkar, T. Lukaczyk, and T. Taylor (2013). Stanford university unstructured (su^2): An open-source integrated computational environment for multi-physics simulation and design. In *51st AIAA Aerospace Sciences Meeting including the New Horizons Forum and Aerospace Exposition*, Grapevine, Texas. *(p. 321)*

Pandya, R. and F. Mashayek (2002). Two-fluid Large-Eddy Simulation approach for particle-laden turbulent flows. *International Journal of Heat and Mass Transfer 45*, 4753–4579. *(p. 11, 270, 271, 272, 273)*

Pankajakshan, R., B. Mitchell, and L. Taylor (2011). Simulation of unsteady two-phase flows using a parallel Eulerian-Lagrangian approach. *Computers and Fluids 41*(1), 20 – 26. *(p. 38)*

Parmentier, J.-F., O. Simonin, and O. Delsart (2012). A functional subgrid drift velocity model for filtered drag prediction in dense fluidized bed. *AIChE Journal 58*(4), 1084–1098. *(p. 276)*

Patnaik, G. and J. Boris (2010). FAST3D-CT: an LES model for urban aerodynamics model. In *International Symposium on Computational Wind Engineering*, Durham NC. *(p. 87, 318)*

Paulhiac, D. (2015). *Modélisation de la combustion d'un spray dans un brûleur aéronautique.* Ph. D. thesis, INP Toulouse. *(p. 7)*

Peiro, J. and S. Sherwin (2005). *Finite Difference, Finite Element and Finite Volume Methods For Partial Differential Equations*, Volume 1, Chapter in "Handbook of Materials Modeling", pp. 2415–2446. Springer. *(p. xxi, 85, 91)*

Péra, O. (2005). *Simulation et modélisation de la dispersion turbulente, l'évaporation et la combustion d'écoulements diphasiques.* Ph. D. thesis, Université de Rouen. *(p. 147, 156)*

Philip, M. (2016). *Dynamics of light-round in multi-injector annular combustors.* Ph. D. thesis, Université Paris-Saclay. *(p. xxi, 95)*

Philip, M., M. Boileau, R. Vicquelin, E. Riber, T. Schmitt, B. Cuenot, D. Durox, and S. Candel (2015). Large eddy simulations of the ignition sequence of an annular multiple-injector combustor. *Proceedings of the Combustion Institute 35*(3), 3159 – 3166. *(p. xxi, 6, 105, 320)*

Pierce, C. D. and P. Moin (2004, 4). Progress-variable approach for Large-Eddy Simulation of non-premixed turbulent combustion. *Journal of Fluid Mechanics 504*, 73–97. *(p. 6)*

Pigeonneau, F. and P. Saramito (2016). Discontinuous Galerkin finite element method applied to the coupled Navier-Stokes/Cahn-Hilliard equations. In *9th International Conference on Multiphase Flow*, Firenze, Italy. *(p. 93)*

Pitsch, H. (2006). Large-Eddy Simulation of turbulent combustion. *Annual Review of Fluid Mechanics 38*(1), 453–482. *(p. 6)*

Pitsch, H. and L. Duchamp de Lageneste (2003). Large-Eddy Simulation of premixed turbulent combustion. In K. Bathe (Ed.), *Computational Fluid and Solid Mechanics 2003*, pp. 1096 – 1099. Oxford: Elsevier Science Ltd. *(p. 6)*

Poinsot, T., D. Haworth, and G. Bruneaux (1993). Direct simulation and modeling of flame-wall interaction for premixed turbulent combustion. *Combustion and Flame 95*(1), 118 – 132. *(p. 6, 317)*

Poinsot, T. and D. Veynante (2005). *Theoretical qnd Numerical Combustion.* Philadelphia: Edwards. *(p. 6)*

Pollack, M., S. Salenbauch, D. Marchisio, and C. Hasse (2016). Bivariate extensions of the extended quadrature method of moments (eqmom) to describe coupled droplet evaporation and heat-up. *Journal of Aerosol Science 92*, 53 – 69. *(p. 69)*

Pope, S. (1985). PDF methods for turbulent reactive flows. *Progress in Energy and Combustion Science 11*, 119–192. *(p. 39)*

Pope, S. (2000). *Turbulent flows.* Cambridge University. *(p. 4, 148, 149, 151, 154, 155, 251, 254, 266, 267, 268, 283, 285)*

Popinet, S. and S. Zaleski (1994). A front - traking algorithm for accurate representation of surface tension. NASA Langley Research Center Hampton, ICASE Report 94-24. *(p. 5, 26)*

Pozorski, J. and S. Apte (2009). Filtered particle tracking in isotropic turbulence and stochastic modelingof subgrid-scale dispersion. *International Journal of Multiphase Flows 35*(2), 118–28. *(p. 270)*

Presser, C., A. Gupta, and H. Semerjian (1993). Aerodynamic characteristics of swirling spray flames: Pressure-jet atomizer. *Combustion and Flame 92*(1-2), 25–44. *(p. 3)*

Quartapelle, L. and V. Selmin (1993). *High-order Taylor-Galerkin methods for non-linear multidimensional problems*, pp. 1374–1384. *(p. 90, 102)*

Ramkrishna, D. and A. G. Fredrickson (2000). *Population Balances: Theory and Applications to Particulate Systems in Engineering.* Academic Press. *(p. 68)*

Raviart, P. A. (1985). *An analysis of particle methods*, pp. 243–324. Berlin, Heidelberg: Springer Berlin Heidelberg. *(p. 42)*

Reed, W. and T. Hill (1973). Triangular mesh methods for the neutron transport equation. In *Proceedings cf the American Nuclear Society.* *(p. 92)*

Reeks, M. W. (1991). On a kinetic equation for the transport of particles in turbulent flows. *Phys. Fluids 3*, 446–456. *(p. 272, 281)*

Reeks, M. W. (1992). On the continuum equations for dispersed particles in nonuniform flows. *Physics of Fluids A 4*(6), 1290–1303. *(p. 272, 281)*

Refloch, A., B. Courbet, A. Murrone, P. Villedieu, C. Laurent, P. Gilbank, J. Troyes, L. Tessé, G. Chaineray, J. Dargaud, E. Quï¿½merais, and F. Vuillot (2011). Cedre software. *Aerospace Lab 2*, 131–140. *(p. 321)*

Renaud, A. (2015). *High-speed diagnostics for the study of flame stabilization and transient behaviour in a swirled burner with variable liquid-fuel distribution*. Ph. D. thesis, CentraleSupélec. *(p. 3, 25)*

Reveillon, J., J. Chesnel, B. Duret, and F. Demoulin (2013). Towards fully coupled modeling of liquid atomization and dispersed spray combustion. In *1st ERCOFTAC Conference on Simulation of multiphase flows in gasification and combustion*. *(p. 5, 26, 311)*

Reveillon, J. and F. Demoulin (2007). Effects of the preferential segregation of droplets on evaporation and turbulent mixing. *Journal of Fluid Mechanics 583*, 273–302. *(p. 33, 147, 150, 156, 158, 205, 315, 316, 318)*

Reveillon, J. and L. Vervish (2005). Analysis of weakly turbulent diluted - spray flames and spray combustion regimes. *J. Fluid Mech. 537*, 317–347. *(p. 9, 37)*

Riber, E. (2007). *Développement de la méthode de simulation aux grandes échelles pour les écoulements diphasiques turbulents*. Ph. D. thesis, INP Toulouse. *(p. 54, 55, 104, 276, 317)*

Riber, E., V. Moureau, M. Garcia, T. Poinsot, and O. Simonin (2009). Evaluation of numerical strategies for Large Eddy Simulation of particulate two-phase recirculating flows. *Journal of Computational Physics 228*(2), 539 – 564. *(p. 38, 105)*

Richard, S. (2005). *Simulation aux grandes échelles de la combustion dans les moteurs à allumage commandé*. Ph. D. thesis, Ecole Central Paris. *(p. 6)*

Richter, A., M. Vascellari, P. Nikrityuk, and C. Hasse (2016). Detailed analysis of reacting particles in an entrained-flow gasifier. *Fuel Processing Technology 144*, 95 – 108. *(p. 8, 28)*

Riley, J. and G. Paterson (1974). Diffusion experiments with numerically integrated isotropic turbulence. *Physics of Fluids 17*, 292–297. *(p. 8, 37)*

Ritz, W. (1909). On a new method for the solution of certain. variational problems of mathematical physics (in german). *Journal fur reine und angewandte Mathematik 135*, 1–61. *(p. 89)*

Rivière, B. (2008). *Discontinuous Galerkin Methods for Solving Elliptic and Parabolic Equations: Theory and Implementation*. SIAM, Philadelphia. *(p. 92)*

Roe, P. (1981). Approximate riemann solvers, parameter vectors, and difference schemes. *Journal of Computational Physics 43*(2), 357 – 372. *(p. 86)*

Rosso, M., H. Wang, and S. Elghobashi (2016). Dispersion of finite size droplets and solid particles in isotropic turbulence. In *9th International Conference on Multiphase Flow, ICMF*, Firenze, Italy. *(p. 8, 28)*

Roy, S., P. Arias, V. Lecoustre, D. Haworth, H. Im, and A. Trouvé (2014). Development of high fidelity soot aerosol dynamics models using method of moments with interpolative closure. *Aerosol Science and Technology 48*(4), 379–391. *(p. 67)*

Sabat, M., A. Larat, A. Vié, and M. Massot (2014). *Comparison of realizable schemes for the Eulerian simulation of disperse phase flows*, pp. 935–943. Springer International Publishing. *(p. 14, 100, 125)*

Sabat, M., A. Larat, A. Vié, and M. Massot (2014). On the development of high order realizable schemes for the Eulerian simulation of disperse phase flows: a convex-state preserving Discontinuous Galerkin method. *Journal of Computational Multiphase Flows 6*(3), 247–270. Selected for a special issue from the 8th International Conference on Multiphase Flow, Jeju, Korea. *(p. 14, 100)*

Sabat, M., A. Vié, A. Larat, and M. Massot (2016). Fully Eulerian simulation of 3D turbulent particle laden flow based on the Anisotropic Gaussian closure. In *Proceedings of the 9th International Conference on Multiphase Flow, Firenze, Italy*. *(p. 14)*

Sabat, M., A. Vié, A. Larat, and M. Massot (2018). Statistical description of turbulent particle-laden flows in the very dilute regime using the anisotropic gaussian moment method. (In preparation). *(p. 14)*

Saeedipour, M. and D. Priker, S. an Schneiderbauer (2016). Multiscale simulation of liquid jet disintegration and primary atomization using Eulerian-Lagrangian coupling. In *Proceedings of the 9th International Conference on Multiphase Flow, Firenze, Italy*. *(p. 5)*

Sagaut, P. (1998). *Large Eddy Simulation for incompressible flows*. Springer-Verlag Berlin and Heidelberg GmbH & Co. K. *(p. 4, 267, 268)*

Sainsaulieu, L. (1995). Contribution a la modélisation mathématique et numérique des écoulements diphasiques constitués d un nuage de particules dans un écoulement de gaz. *(p. 39, 57)*

Salenbauch, S., A. Cuoci, A. Frassoldati, C. Saggese, T. Faravelli, and C. Hasse (2015). Modeling soot formation in premixed flames using an extended conditional quadrature method of moments. *Combustion and Flame 162*(6), 2529 – 2543. *(p. 69)*

Sanchez, A. L., J. Urzay, and A. Liñán (2014). The role of separation of scales in the description of spray combustion. *Proceedings of the Combustion Institute 35*, 1549–1577. *(p. 6)*

Sander, M. and M. Kraft (2009). Stochastic particle method and sintering. In *Modeling and Computation of Nanoparticles in Fluid Flows, Lectures Notes of the von Karman Institute, NATO RTO- EN-AVT-169*, pp. 1–28. *(p. 43)*

Sanders, B. and S. Bradford (2006). Impact of limiters on accuracy of high-resolution flow and transport models. *J. Eng. Mech. 132*(1), 87–98.

(p. 326)

Sanjosé, M., J. Senoner, F. Jaegle, B. Cuenot, S. Moreau, and T. Poinsot (2011). Fuel injection model for Euler-Euler and Euler-Lagrange Large-Eddy Simulations of an evaporating spray inside an aeronautical combustor. *International Journal of Multiphase Flow 37*(5), 514 – 529. *(p. xix, 6, 10, 30, 55, 105)*

Schaal, K., A. Bauer, P. Chandrashekar, R. Pakmor, C. Klingenberg, and V. Springel (2015). Astrophysical hydrodynamics with a high-order discontinuous Galerkin scheme and adaptive mesh refinement. *Monthly Notices of the Royal Astronomical Society 453*(4), 4278–4300. *(p. xxx, 319)*

Schiller, L. and A. Naumann (1935). A drag coefficient correlation. *Zeitschrift des Vereines Deutscher Ingenieure 77*, 318–320. *(p. 313)*

Schoenawa, S. and R. Hartmann (2014). Discontinuous Galerkin discretization of the Reynolds-Averaged Navier-Stokes equations with the shear-stress transport model. *Journal of Computational Physics 262*, 194 – 216. *(p. 319)*

Schumann, U. (1977). Realizability of reynolds-stress turbulence models. *Physics of Fluids 20*(5), 721 – 725. *(p. 55)*

Schwamborn, D., T. Gerhold, and R. Heinrich (2006). The dlr tau-code: recent applications in research and industry. In *Proceedings of European Conference on Computational Fluid Dynamics*, TU-Delft. *(p. 322)*

Sekora, M. and P. Colella (2009). Extremum-preserving limiters for MUSCL and PPM. available at http://arxiv.org/abs/0903.4200v2. *(p. 319, 328)*

Selle, L., L. Benoit, T. Poinsot, F. Nicoud, and W. Krebs (2006). Joint use of compressible Large-Eddy Simulation and helmoltz solvers for the analysis of rotating modes in an industrial swirled burner. *Combustion and Flame 145*(1–2), 194–205. *(p. 6)*

Senoner, J., M. Sanjosé, T. Lederlin, F. Jaegle, M. Garcia, E. Riber, B. Cuenot, L. Gicquel, H. Pitsch, and T. Poinsot (2009). Combustion for aerospace propulsion Eulerian and Lagrangian Large-Eddy Simulations of an evaporating two-phase flow. *Comptes Rendus Mécanique 337*(6), 458 – 468. *(p. 32)*

Shinjo, J. and A. Umemura (2010). Simulation of liquid jet primary breakup: Dynamics of ligament and droplet formation. *International Journal of Multiphase Flow 36*(7), 513 – 532. *(p. 26)*

Shinjo, J. and A. Umemura (2011). Surface instability and primary atomization characteristics of straight liquid jet sprays. *International Journal of Multiphase Flow 37*(10), 1294 – 1304. *(p. 26)*

Shotorban, B. and S. Balachandar (2007). A Eulerian model for Large-Eddy Simulation of concentration of particles with small stokes numbers. *Phys. Fluids 19*, 118107. *(p. 11, 270, 271, 275, 277)*

Shotorban, B. and F. Mashayek (2006). A stochastic model for particle motion in Large Eddy Simulation. *Journal of turbulence 7*(18), 1–13. *(p. 270)*

Shotorban, B., K. K. Q. Zhang, and F. Mashayek (2007). Improvement of particle concentration prediction in Large-Eddy Simulation by defiltering. *Int. J. of Heat and Mass Transfer 50*, 3728–3739. *(p. 270)*

Shu, C.-W. (2001). A survey of strong stability preserving high order time discretizations. *(p. 92)*

Shu, C.-W. (2013). A brief survey on discontinuous Galerkin methods in computational fluid dynamics. *Advances in Mechanics 43*(6), 541 – 553. *(p. 92)*

Shu, C.-W. (2016). High order WENO and DG methods for time-dependent convection-dominated pdes: A brief survey of several recent developments. *Journal of Computational Physics 316*, 598 – 613. *(p. 88, 92)*

Shu, C.-W. and S. Osher (1988). Efficient implementation of essentially non-oscillatory shock-capturing schemes. *Journal of Computational Physics 77*(2), 439–471. *(p. 88)*

Shu, C.-W. and S. Osher (1989). Efficient implementation of essentially non-oscillatory shock-capturing schemes, II. *Journal of Computational Physics 83*(1), 32–78. *(p. 88)*

Sibra, A. (2015). *Modélisation et étude de l'évaporation et de la combustion de gouttes dans les moteurs à propergol solide par une approche eulérienne Multi-Fluide*. Ph. D. thesis, Ecole Centrale Paris, France. *(p. 58, 65, 66, 68, 74)*

Sierra, P. (2012). *Modeling the dispersion and evaporation of sprays in aeronautical combustion chambers*. Ph. D. thesis, INP Toulouse. *(p. 10, 46, 55)*

Simonin, O. (1996). *Continuum modeling of dispersed two-phase flows*, Volume 2 of *VKI Lecture Series*, Chapter in "Combustion and turbulence in two phase flows", pp. 79–123. von Karman Institue for Fluid Dynamics, Bruxelles. *(p. 39, 69)*

Simonin, O., E. Deutsch, and J. Minier (1993). Eulerian prediction of the fluid/particle correlated motion in turbulent two-phase flows. *Applied Scientific Research 51*, 275–283. *(p. 270, 275)*

Simonin, O., P. Février, and J. Lavieville (2002). On the spatial distribution of heavy particle velocities in turbulent flow: from continuous field to particulate chaos. *Journal of Turbulence 3*(1), 40. *(p. 32, 39, 54)*

Simonin, O., L. Zaichik, V. Alipchenkov, and P. Février (2006). Connection between two statistical approaches for the modelling of particle velocity and concentration distributions in turbulent flow: The Mesoscopic Eulerian Formalism and the two-point probability density function method. *Physics of Fluids 18*(12), 125107(1–9). *(p. 131, 157)*

Sirignano, W. A. (1999). *Fluid Dynamics and Transport of Droplets and Sprays*. Cambridge: Cambridge University Press. *(p. 31, 313, 316)*

Sirignano, W. A. (2010). *Fluid dynamics and transport of droplets and sprays, 2^{nd} edition*. Cambridge University Press. *(p. 6)*

Sitaraman, H. and R. Grout (2016). Balancing conflicting requirements for grid and particle decomposition in continuum-Lagrangian solvers. *Parallel Computing 52*, 1 – 21. *(p. 38, 42)*

Smagorinsky, J. (1963). General circulation experiments with the primitive equations. I : The basic experiment. *Monthly Weather Review 91(3)*, 99–164. *(p. 4, 269)*

Sommerfeld, M. and H.-H. Qiu (1998). Experimental studies of spray evaporation in turbulent flow. *International Journal of Heat and Fluid Flow 19*(1), 10 – 22. *(p. 3)*

Sornek, Rafal J.and Dobashi, R. and T. Hirano (2000). Effect of turbulence on vaporization, mixing, and combustion of liquid-fuel sprays. *Combustion and Flame 120*(4), 479 – 491. *(p. 3)*

Spalding, D. (1953). The combustion of liquid fuels. In *4th Symposium (International) on Combustion*, The Combustion Institute, Baltimore, pp. 847–864. *(p. 315)*

Springel, V. (2010). E pur si muove: Galilean-invariant cosmological hydrodynamical simulations on a moving mesh. *Monthly Notices of the Royal Astronomical Society 401*(2), 791–851. *(p. xxx, 322)*

Squires, K. and J. Eaton (1991a). Measurements of particle dispersion obtained from direct numerical simulations of isotropic turbulence. *Journal of Fluid Mechanics 226*, 1–35. *(p. 9, 37)*

Squires, K. and J. Eaton (1991b). Preferential concentration of particles by turbulence. *Physics of Fluids A: Fluid Dynamics 3*, 1169–1178. *(p. 9, 37, 166, 168)*

Stokes, G. (1846). Report on recent researches in hydrodynamics. *(p. 313)*

Strang, G. (1968). On the construction and comparison of difference schemes. *SIAM Journal on Numerical Analysis 5*(3), 507–517. *(p. 96)*

Strang, G. and G. Fix (1973). *An Analysis of the Finite Element Method.* Prentice Hall. *(p. 89)*

Struchtrup, H. (2005). *Macroscopic transport equations for rarefied gas flows.* Interaction of Mechanics and Mathematics. Berlin: Springer. Approximation methods in kinetic theory. *(p. 31)*

Subramaniam, S. (2001). Statistical modeling of sprays using the droplet distribution function. *Physics of Fluids 13*(3), 624–642. *(p. 41)*

Subramaniam, S. (2013). Lagrangian-Eulerian methods for multiphase flows. *Progress in Energy and Combustion Science 231*(2-3), 215–245. *(p. 8, 27, 43)*

Sun, R. and H. Xiao (2016). Sedifoam: A general-purpose, open-source CFD-DEM solver for particle-laden flow with emphasis on sediment transport. *Computers & Geosciences 89*, 207–219. *(p. 38)*

Sundaram, S. and L. Collins (1997). Collision statistics in an isotropic particle-laden turbulent suspension. part 1. direct numerical simulations. *Journal of Fluid Mechanics 335*, 75–109. *(p. 244)*

Sweby, P. (1984). High resolution schemes using flux limiters for hyperbolic conservation laws. *SIAM Journal on Numerical Analysis 21*(5), 995–1011.

(p. 325, 327)

Syred, N. (2006). A review of oscillation mechanisms and the role of the precessing vortex core (pvc) in swirl combustion systems. *Progress in Energy and Combustion Science 32*(2), 93 – 161. *(p. 2)*

Ta, M., F. Pigeonneau, and P. Saramito (2016). An implicit high order discontinuous Galerkin level set method for two-phase flow problems. In *9th International Conference on Multiphase Flow*, Firenze, Italy. *(p. 93)*

Tachibana, S., K. Saito, T. Yamamoto, M. Makida, T. Kitano, and R. Kurose (2015). Experimental and numerical investigation of thermo-acoustic instability in a liquid-fuel aero-engine combustor at elevated pressure: Validity of Large-Eddy Simulation of spray combustion. *Combustion and Flame 162*(6), 2621 – 2637. *(p. 3)*

Tambour, Y. (1980). A sectional model for evaporation and combustion of sprays of liquid fuel. *Isr. J. Technol. 18*, 47–56. *(p. 67)*

Tanguy, S. and A. Berlemont (2005). Development of a level set method for interface tracking: application to droplet collisions. *International Journal of Multiphase Flows 31*(9), 1015–1035. *(p. 5, 26, 318)*

Tenneti, S., R. Garg, and S. Subramaniam (2011). Drag law for monodisperse gas-solid systems using particle-resolved direct numerical simulation of flow past fixed assemblies of spheres. *International Journal of Multiphase Flows 37*(9), 1072–1092. *(p. 8, 28)*

Tenneti, S. and S. Subramaniam (2014). Particle-resolved direct numerical simulation for gas-solid flow model development. *Annual Review of Fluid Mechanics 46*(1), 199–230. *(p. 8, 28)*

Teukolsky, S. (2016). Formulation of discontinuous Galerkin methods for relativistic astrophysics. *Journal of Computational Physics 312*, 333 – 356. *(p. 93)*

Thomée, V. (2001). From Finite Differences to Finite Elements A short history of numerical analysis of partial differential equations. *Journal of Computational and Applied Mathematics 128*, 1–54. *(p. 84, 89)*

Thomine, O. (2011). *Développement de méthodes multi-échelles pour la simulation numérique des écoulements réactifs diphasiques*. Ph. D. thesis, Université de Rouen. *(p. 37, 147, 156, 318)*

Toro, E. (2009). *Riemann Solvers and Numerical Methods for Fluid Dynamics: A Practical introduction* (3 ed.). Springer. *(p. 85, 86, 87, 326)*

Toro, E. F., M. Spruce, and W. Speares (1994). Restoration of the contact surface in the HLL-Riemann solver. *Shock Waves 4*(1), 25–34. *(p. 86)*

Torres, D. J., Y. H. Li, and S.-C. Kong (2010). Partitioning strategies for parallel KIVA-4 engine simulations. *Computers and Fluids 39*(2), 301 – 309. *(p. 322)*

Torres, D. J. and M. F. Trujillo (2006). KIVA-4: An unstructured ALE code for compressible gas flow with sprays. *Journal of Computational Physics 219*(2), 943 – 975. *(p. 322)*

Tryggvason, G., J. Thomas, S. ans Lu, and B. Aboulhasanzadeh (2010).

Multiscale issues in DNS of multiphase flows. *Acta Mathematica Scientia 30*(2), 551 – 562. *(p. 8, 27)*

Turner, M., R. Clough, H. Martin, and L. Topp (1956). Stiffness and deflection analysis of complex structures. *Journal of Aeronautical Sciences 23*(9), 805–823. *(p. 89)*

Vallet, A., A. Burluka, and R. Borghi (2001). Development of a Eulerian model for the "atomization" of a liquid jet. *Atomization and Sprays 11*, 619–642. *(p. 26)*

van der Vegt, J. and H. van der Ven (1998). Discontinuous Galerkin Finite Element Method with Anisotropic Local Grid Refinement for Inviscid Compressible Flows. *Journal of Computational Physics 141*(1), 46 – 77. *(p. 92)*

van Leer, B. (1974). Towards the ultimate conservative difference scheme II. monotonicity and Conservation Combined in a Second-Order Scheme. *Journal of Computational Physics 14*, 361–370. *(p. 87, 326)*

van Leer, B. (1979). Towards the ultimate conservative difference scheme V. A second order sequel to Godunov's method. *Journal of Computational Physics 32*(1), 101–136. *(p. 87, 101, 110)*

van Leer, B. (1986). On numerical dispersion by upwind differencing. *Appl. Numer. Math. 2*, 379–384. *(p. 85)*

van Leer, B. (2006). Upwind and high-resolution methods for compressible flow: From donor cell to residual-distribution schemes. *Commun. Comput. Phys. 1*, 192–206. *(p. 85, 87, 325)*

Vance, M. W., K. D. Squires, and O. Simonin (2006). Properties of the particle velocity field in gas-solid turbulent channel flow. *Physics of Fluids 18*(6), 063302,1–13. *(p. 163)*

Vermorel, O., B. Bédat, O. Simonin, and T. Poinsot (2003). Numerical study and modelling of turbulence modulation in a particle laden slab flow. *Journal of Turbulence 4*(4), N25. *(p. 317)*

Versaevel, P. (1996). *Combustion laminaire diphasique: Etude théorique et expérimentale.* Ph. D. thesis, Ecole Centrale Paris. *(p. 315)*

Vervisch, L., R. Hauguel, P. Domingo, and M. Rullaud (2004). Three facets of turbulent combustion modelling: DNS of premixed V-flame, LES of lifted nonpremixed flame and RANS of jet-flame. *Journal of Turbulence 5*, N4. *(p. 6)*

Vervisch, L. and T. Poinsot (1998). Direct numerical simulation of non-premixed turbulent flame. *Annual Review on Fluid Mechanics 30*, 655–691. *(p. 6)*

Veynante, D. and L. Vervisch (2002). Turbulent combustion modeling. *Progress in Energy and Combustion Science 28*(3), 193 – 266. *(p. 6)*

Vié, A. (2010). *Simulation aux grandes échelles d' écoulements diphasiques turbulents à phase liquide dispersée.* Ph. D. thesis, Institut National Polytechnique de Toulouse. available at http://tel.archives-ouvertes.fr/tel-00620754. *(p. 105, 320)*

Vié, A., F. Doisneau, and M. Massot (2015). On the Anisotropic Gaussian closure for the prediction of inertial-particle laden flows. *Comm. in Comp. Physics 17*(1), 1–46. *(p. 10, 12, 52, 56, 58, 59, 60, 88, 101, 110, 112, 113, 137, 139, 188, 280)*

Vié, A., B. Franzelli, Y. Gao, T. Lu, H. Wang, and M. Ihme (2014). Analysis of segregation and bifurcation in turbulent spray flames: A 3d counterflow configuration. *Proceedings of the Combustion Institute 35*, 1675–1683. *(p. 7)*

Vié, A., S. Jay, B. Cuenot, and M. Massot (2013). Accounting for polydispersion in the Eulerian Large Eddy Simulation of the two-phase flow in an aeronautical-type burner. *Flow, Turbulence and Combustion 90*, 545–581. *(p. xix, 10, 30, 32, 55, 68)*

Vié, A., F. Laurent, and M. Massot (2013). Size-velocity correlations in hybrid high order moment/multi-fluid methods for polydisperse evaporating sprays: modeling and numerical issues. *Journal of Computational Physics 237*, 177–210. *(p. 10, 69, 88, 110, 111)*

Vié, A., E. Masi, O. Simonin, and M. Massot (2012). On the direct numerical simulation of moderate-stokes-number turbulent particulate flows using Algebraic-Closure-Based and Kinetic-Based Moment Methods. In *Proceedings of the summer program 2012, Center for Turbulence Research, Stanford University*, pp. 1–10. *(p. xxi, 55, 113, 114, 308)*

Vilar, F., P.-H. Maire, and R. Abgrall (2011). Cell-centered discontinuous Galerkin discretizations for two-dimensional scalar conservation laws on unstructured grids and for one-dimensional Lagrangian hydrodynamics. *Computers and Fluids 46*(1), 498 – 504. 10th ICFD Conference Series on Numerical Methods for Fluid Dynamics (ICFD 2010). *(p. 93)*

Vinkovic, I., C. Aguirre, S. Simoëns, and J.-N. Gence (2005). Couplage d'un modèle stochastique Lagrangien sous-maille avec une simulation grandes échelles. *Comptes Rendus Mécanique 333*, 325–330. *(p. 43)*

Vinkovic, I., C. Aguirre, S. Simoëns, and M. Gorokhovski (2006). Large Eddy Simulation of droplet dispersion for inhomogeneous turbulent wall flow. *International Journal of Multiphase Flow 32*(3), 344 – 364. *(p. 43, 270)*

Visbal, M. and D. Gaitonde (2002). On the use of higher-order finite-difference schemes on curvilinear and deforming meshes. *Journal of Computational Physics 181*(1), 155 – 185. *(p. 85)*

Volkov, K. (2007). Stochastic models of particle motion in a turbulent flow and their application for calculating internal flows. *Journal of Engineering Physics and Thermophysics 80*(3), 40–85. *(p. 43)*

Vu, T.-T., T. Ménard, and C. Dumouchel (2016). Application of a level-set/volume-of-fluid method and an immersed boundary method to the atomization of a liquid jet ejected from a complex-shaped injector. In *Proceedings of the 9th International Conference on Multiphase Flow, Firenze, Italy*. *(p. 5, 26)*

Wang, L. P. and M. R. Maxey (1993). Settling velocity and concentration distribution of heavy particles in homogeneous isotropic turbulence. *J. Fluid Mech. 256*, 27–68. *(p. 205)*

Wang, Q. and K. D. Squires (1996). Large Eddy Simulation of particle-laden turbulent channel flow. *Phys. Fluids 8*, 1207–1223. *(p. 270)*

Wang, Z. (2002). Spectral (Finite) Volume Method for Conservation Laws on Unstructured Grids. Basic Formulation. *Journal of Computational Physics 178*(1), 210 – 251. *(p. 97)*

Watanabe, H., R. Kurose, S. M. Hwang, and F. Akamatsu (2007). Characteristics of flamelets in spray flames formed in a laminar counterflow. *Combustion and Flame 148*(4), 234–248. *(p. 6)*

Weber, C. (1931). Disintegration of liquid jets. *Zeitschrift für Angewandte Mathematik und Mechanik (Journal of Applied Mathematics and Mechanics) 11*, 136–154. *(p. 24)*

Wells, M. and D. Stock (1983). The effects of crossing trajectories on the dispersion of particles in a turbulent flow. *Journal of Fluid Mechanics 136*, 31–62. *(p. 31)*

Williams, F. (1958). Spray combustion and atomization. *Physics of Fluids 1*, 541–545. *(p. 40)*

Williams, F. (1985). *Combustion Theory (Combustion Science and Engineering Series)*. ed F.A. Williams (Reading, MA: Addition - Wesley). *(p. 40)*

Witherden, F., A. Farrington, and P. Vincent (2014). PyFR: An open source framework for solving advection-diffusion type problems on streaming architectures using the flux reconstruction approach. *Computer Physics Communications 185*(11), 3028 – 3040. *(p. 97)*

Wright, D. L., R. McGraw, and D. E. Rosner (2001). Bivariate Extension of the Quadrature Method of Moments for Modeling Simultaneous Coagulation and Sintering of Particle Populations. *J. of Colloid and Interface Sci. 236*, 242–251. *(p. 68)*

Wunsch, D. (2009). *Theoretical and numerical study of collision and coalescence-Statistical modeling approaches in gas-droplet turbulent flows.* Ph. D. thesis, Institut National Polytechnique de Toulouse. *(p. 37)*

Xu, Y. and S. Subramaniam (2010). Effect of particle clusters on carrier flow turbulence: A direct numerical simulation study. *Flow, Turbulence and Combustion 85*(3), 735–761. *(p. 8, 27)*

Yang, Y., D. Wei, and C.-W. Shu (2013). Discontinuous Galerkin method for Krause's consensus models and pressureless Euler equations. *Journal of Computational Physics 252*, 109–127. *(p. 93, 114, 125)*

Yee, H. (1997). Explicit and implicit multidimensional compact high-resolution shock-capturing methods:formulation. *Journal of Computational Physics 131*(1), 216 – 232. *(p. 85)*

Yuan, C. and R. Fox (2011). Conditional quadrature method of moments for kinetic equations. *Journal of Computational Physics 230*(22), 8216–8246. *(p. 56, 57, 188)*

Yuan, C., F. Laurent, and R. Fox (2012). An extended quadrature method of moments for population balance equations. *Journal of Aerosol Science 51*, 1–23. *(p. 69)*

Zaichik, L. (1999). A statistical model of particle transport and heat transfer in turbulent shear flows. *Phys. Fluids 11*(6), 1521–1534. *(p. 273)*

Zaichik, L., V. Alipchenkov, and E. Sinaiski (2008). *Particles in Turbulent Flows*. Wiley-VCK. *(p. 274, 304)*

Zaichik, L., O. Simonin, and V. Alipchenkov (2003). Two statistical models for predicting collision rates of inertial particles in homogeneous isotropic turbulence. *Phys. Fluids 15*, 2995–3005. *(p. 284, 285)*

Zaichik, L., O. Simonin, and V. Alipchenkov (2009). An Eulerian approach for Large Eddy Simulation of particle transport in turbulent flows. *Journal of Turbulence 10*(4), 1–21. *(p. 11, 270, 271, 273, 274, 282, 284, 292, 298, 299, 304, 307)*

Zalesak, S. (1979). Fully multidimensional flux-corrected transport algorithms for fluids. *Journal of Computational Physics 31*(3), 335 – 362. *(p. 87)*

Zalesak, S. (1997). Introduction to Flux-Corrected Transport. I. SHASTA, A Fluid Transport Algorithm That Works. *Journal of Computational Physics 135*(2), 170 – 171. *(p. 87, 318)*

Zamansky, R., F. Coletti, M. Massot, and A. Mani (2014). Radiation induces turbulence in particle-laden fluids. *Physics of Fluids 26*(7), 071701–7. *(p. 11, 37, 42)*

Zamansky, R., F. Coletti, M. Massot, and A. Mani (2016). Turbulent thermal convection driven by heated inerial particles. *Journal of Fluid Mechanics submitted (in revision)*. *(p. 37, 42)*

Zamansky, R., I. Vinkovic, and M. Gorokhovski (2011). Solid particle acceleration in a high Reynolds number channel flow: DNS and LES with stochastic modelling of subgrid acceleration. *Journal of Fluids: Conference Series 333*(7), 1–13. *(p. 43)*

Zanotti, O., F. Fambri, M. Dumbser, and A. Hidalgo (2015). Space-time adaptive ADER discontinuous Galerkin finite element schemes with a posteriori sub-cell finite volume limiting. *Computers and Fluids 118*, 204 – 224. *(p. 93)*

Zhang, R., J. Zhu, A. Loula, and X. Yu (2016). Operator splitting combined with positivity-preserving discontinuous Galerkin method for the chemotaxis model. *Journal of Computational and Applied Mathematics 302*, 312 – 326. *(p. 93)*

Zhang, X. (2011). *Maximum-Principle-Satisfying and Positivity-Preserving High Order Schemes for Conservation Laws*. Ph. D. thesis, Brown University. *(p. 93, 101, 117)*

Zhang, X. (2016). A curved boundary treatment for discontinuous Galerkin schemes solving time dependent problems. *Journal of Computational Physics 308*, 153 – 170. *(p. 93)*

Zhang, X. and C.-W. Shu (2010). On maximum-principle-satisfying high order schemes for scalar conservation laws. *Journal of Computational Physics 229*(9), 3091–3120. *(p. 93, 101, 114)*

Zhang, X. and C.-W. Shu (2011, February). Positivity-preserving high order discontinuous Galerkin schemes for compressible euler equations with source terms. *J. Comput. Phys. 230*(4), 1238–1248. *(p. 93, 96)*

Zhang, X., Y. Xia, and C.-W. Shu (2012). Maximum-Principle-Satisfying and Positivity-Preserving High Order Discontinuous Galerkin Schemes for Conservation Laws on Triangular Meshes. *Journal of Scientific Computing 50*(1), 29–62. *(p. 93, 101, 114, 119)*

Zhu, H., R. Zhou, R. Yang, and A. Yu (2007). Discrete particle simulation of particulate systems: Theoretical developments. *Chemical Engineering Science 62*(13), 3378–3396. *(p. 37)*

Zhu, J., J. Qiu, T. Liu, and B. C. Khoo (2011). RKDG methods with WENO type limiters and conservative interfacial procedure for one-dimensional compressible multi-medium flow simulations. *Applied Numerical Mathematics 61*(4), 554 – 580. *(p. 92)*

Zhu, J., J. Qiu, C.-W. Shu, and M. Dumbser (2008). Runge-Kutta discontinuous Galerkin method using WENO limiters ii: Unstructured meshes. *Journal of Computational Physics 227*(9), 4330 – 4353. *(p. 92)*

Zimmer, L., R. Domann, Y. Hardalupas, and Y. Ikeda (2003). Simultaneous laser-induced fluorescence and mie scattering for droplet cluster measurements. *AIAA Journal 41*(11), 2170–2178. *(p. 33)*

Zuzio, D., G. Blanchard, and J. Estivalézes (2016). A large scale multi-fluid/dispersed phase approach for spray generation in aeronautical fuel injectors. In *Proceedings of the 9th International Conference on Multiphase Flow, Firenze, Italy.* *(p. 5, 26, 311)*